

**Stabilization and Confinement
of Hot, Dense, High-Beta Plasma**

**Final Report
September 1, 1998 – December 31, 2001
DOD-ONR grant N00014-98-1-0857**

submitted to the

**U. S. Department of Defense
Office of Naval Research**

Submitted by

The University of Nevada, Reno

- Principal Investigator -

**Dr. Bruno S. Bauer
Professor of Physics
Department of Physics/220
University of Nevada, Reno
Reno, NV 89557-0058**

DISTRIBUTION STATEMENT A

**Approved for Public Release
Distribution Unlimited**

**Coinvestigators: V.L. Kantsyrev, N. Le Galloudec, V. Makhin, R.C. Mancini,
G.S. Sarkisov, A.S. Shlyaptseva, and V.I. Sotnikov**

February 14, 2002

20020312 050

Table of Contents

Stabilization and Confinement of Hot, Dense, High-Beta Plasma

I.	Project summary	1
II.	Statement of work	2
III.	Results	3
1.	Overview	3
2.	Development and operation of the Nevada Terawatt Facility	5
2.1.	Power-flow measurements and SCREAMER modeling	6
2.2.	Laser and optical diagnostics	8
3.	Z-pinch physics	9
3.1.	Linear theory of z-pinch MHD instabilities	10
3.1.1.	MHRDR modeling of the $m=0$ instability with sheared axial flow, but no axial magnetic field	11
3.1.2.	References for Section 3.1	21
3.2.	Investigation of axial shear flow stabilization: conical arrays	22
3.2.1.	MHRDR modeling of conical array implosions	34
3.3.	Explosion of wires driven by Z-like and faster prepulses	39
3.3.1.	Experimental setup	41
3.3.2.	Experimental results	43
3.3.2.1.	Materials with high heat of vaporization (W, Mo, Ti, Ni, and Fe)	47
3.3.2.2.	Materials with low heat of vaporization (Au, Cu, Al, and Ag)	50
3.3.2.3.	Plasma expansion, deposition of Joule energy, and magnetic confinement	52
3.3.2.4.	Imaging spectroscopy	52
3.3.2.5.	Interferometry and shadowgraphy	55
3.3.3.	MHRDR one-dimensional simulations of wire explosions	58
3.3.3.1.	Comparison with results of Chittenden et al.	58
3.3.3.2.	Influence of coronal plasma on wire explosions	67
3.3.3.3.	Comparison with tungsten wire experiments	76
4.	X-ray/EUV diagnostics development and x-pinch experiments	82
4.1.	Plasma diagnostic research at the NTF	82
4.1.1.	2DXIS and 1DXIS	84
4.1.2.	Multichannel spectrometer "Polychromator"	89
4.1.3.	Multichannel time-gated x-ray pinhole camera	91
4.1.4.	X-ray polarimeter-spectrometers	91
4.1.5.	Future EUV plasma diagnostic for Zebra	93

Table of Contents (cont.)

4.2.	Physics of high-current x-pinch x-ray/EUV radiation sources	97
4.2.1.	Development and study of x-pinch backlighting	97
4.1.2.1.	Experimental procedure	97
4.1.2.2.	Experimental results	103
4.3.	References for Section 4	129

APPENDICES

Appendix A	Linear analysis of the shear flow stabilization of the global MHD instabilities based on the Hall fluid model
Appendix B	Linear analysis and MHD modeling of shear flow stabilization of the sausage instability
Appendix C	Conical wire-array implosions
Appendix D	MHRDR modeling of z-pinchs at the Nevada Terawatt Facility
Appendix E	Homogeneous electrical explosion of tungsten wire in vacuum
Appendix F	Deposition of joule energy at initial stage of wire explosion
Appendix G	Advanced x-ray and extreme ultraviolet diagnostics and first applications to x-pinch plasma experiments at the Nevada Terawatt Facility
Appendix H	X-ray temporal, spatial, and spectral study of 0.9 MA x-pinch Ti, Fe, Mo, W, and Pt radiation sources. Energetic electron beam and hard x-ray generation from x-pinchs.
Appendix I	Features of soft x-ray and x-ray radiation from point laser plasma and z-pinch sources transported by glass capillary converters (experiment)
Appendix J	Fields of optical waveguides as waves in free space
Appendix K	Powerful microfocus x-ray and hard x-ray 1-MA x-pinch plasma source for imaging, spectroscopy, backlighting, and polarimetry
Appendix L	Application of new five-channel x-ray/EUV spectrometer with an imaging transmission diffraction grating for study of z-pinch plasma sources
Appendix M	Multi-channel fast hard x-ray spectrometer with spatial resolution capability for extended z-pinch plasma sources
Appendix N	X-ray spectropolarimetry of high-temperature plasmas
Appendix O	X-ray spectropolarimetry and the effect of hot electrons on modeling of high-current x-pinch plasma spectra

Stabilization and Confinement of Hot, Dense, High-Beta Plasma

I. Project summary

The instability, turbulence, and transport of current-carrying plasma is a basic problem with widespread applications, from industrial to astrophysical plasmas. One especially important and interesting challenge is the understanding and control of high-beta plasma, in which the plasma pressure is comparable to the magnetic field pressure. In addition to improving our understanding of many naturally occurring plasmas, mastering the instabilities in such plasmas would permit higher plasma pressures to be confined by externally-produced magnetic fields and would improve the performance of plasma confined by internally-produced magnetic fields.

One of the most rapidly developing areas of plasma physics employs confinement by strong internally-produced magnetic fields: the plasma z-pinch. Despite its relative instability, the z-pinch is finding a wide array of applications, from an intense source of x-rays, to the development of thermonuclear fusion; and from the stripping and focusing of ions in accelerators, to the production of high pressures for equation of state studies. Much higher confining magnetic fields can be generated in a z-pinch plasma than can be produced by external coils.

This project investigated z-pinch instabilities and examined schemes to reduce them, at energy densities relevant to those in large, high-power z-pinches. Substantial strides were taken toward thoroughly diagnosing the plasma and making a detailed comparison between experiment, computer simulation, and theory. The research will help improve the understanding and control of hot, dense, current-carrying plasmas and will help clarify which magnetic field and plasma configurations result in optimum plasma and energy confinement.

II. Statement of work

Develop and operate a calibrated, high-repetition-rate 2-terawatt z-pinch (Zebra) at the Nevada Terawatt Facility (NTF). Develop x-ray, laser, optical, and power-flow diagnostics for the Zebra z-pinch. Investigate z-pinch physics with experiments, computer modeling, and theory.

III. Results

1. Overview

A calibrated, high-repetition-rate 2-terawatt z-pinch (Zebra) was developed, and new z-pinch physics was investigated. Investigation of axial-shear-flow z-pinch stabilization was initiated, with experiments, computer modeling, and theory. An experiment on single wires driven by current prepulses similar to, and faster than, those at Z (SNL) found that faster rising pulses are much more effective at exploding single tungsten wires than Z-like pulses. Experiments on x-pinch driven at 900 kA characterized x-pinch in an almost unexplored regime.

This report is organized according to the statement of work (given above). This section gives an overview of the accomplishments of the project. It summarizes the major achievements and indicates the sections in which they are described in detail.

1. A calibrated, high-repetition-rate 2-terawatt z-pinch research facility has been developed and operated at the Nevada Terawatt Facility (NTF) (Section 2). Experiments are being performed with Zebra, a high-repetition-rate 2-terawatt z-pinch (from Los Alamos National Laboratory). This device, the highest-power electrical generator at a U.S. university, forms the core of the NTF. Zebra will be joined by the Leopard laser, built using components of the Petawatt laser from LLNL (previously the most powerful laser in the world). A variety of diagnostics have been installed on Zebra, and significant progress has been made in organizing all experimental data in a user-friendly database, to facilitate detailed comparisons between theory and experiment.
2. Z-pinch physics has been investigated (Section 3):
 - A detailed analytical and numerical study has been initiated of z-pinch linear instability (Section 3.1, Appendix A, and Appendix B). The calculations aim to understand the growth of fluctuations observed in experiment and modeling, and to resolve the contradictory results on this topic in the literature, especially as regards stabilization by sheared axial flow. Axial shear flow stabilization has been investigated experimentally, with conical array implosions (Section 3.2 and Appendix C). Computer modeling of these experiments has been performed with MHRDR (Section 3.2.1 and Appendix D).
 - An experiment on single wires driven by current prepulses similar to, and faster than, those at Z (Section 3.3, Appendix E, and Appendix F) found that the characteristics of wire explosions depend dramatically on the rate of rise of the current, on the heat of vaporization of the wire material, and on the diameter of the wire. For substances with high vaporization energy (W, Mo, Ti, Ni, Fe, Au-plated W), faster rising pulses are much more effective at exploding single wires than Z-like pulses. Faster rising pulses may lead to a plasma less divided into cold core and unstable corona than has typically been produced. The measurements are being compared with MHRDR simulations at UNR.

3. Experimental research in the development of x-ray and EUV plasma diagnostics and sources has been performed (Section 4 and Appendices G-M).
 - A novel *two-dimensional* x-ray imaging spectrometer (2DXIS) has been built and partially tested. X-ray diagnostics on Zebra include (Section 4.1): a 5-channel tunable x-ray spectrometer ("Polychromator") with nanosecond time resolution; two one-dimensional x-ray imaging polarimeters/spectrometers (1DPS); two universal survey convex crystal spectrometers/pinhole cameras; and a multihole x-ray pinhole camera (constructed around a 6-strip 0.1-ns-gated MCP detector from SNL).
 - X-pinchs have been driven at 900 kA and investigated with novel diagnostics (Section 4.2, Appendix G, Appendix H, and Appendix K). The goal of these experiments is to develop new x-ray sources for radiography and to understand the final stage of the z-pinch MHD sausage ($m=0$) instability, when a z-pinch turns into a mini-diode.
4. Plasma spectroscopy modeling has been refined to meet the challenges of EUV and x-ray diagnostic development. The polarization of x-ray spectra have been calculated and initial comparisons have been made with experiment, with the aim of determining the magnetic field and the energetic non-Maxwellian component of the electron distribution function. K-shell and L-shell diagnostics of Mo plasma have been developed. These topics are described in Appendices N and O.

In addition to improving the understanding and control of hot, dense, current-carrying plasmas, this project is having an enormous educational impact in areas related to plasma physics. Many undergraduate, graduate, and postdoctoral students are engaged in the research and development described below, and are receiving a hands-on training in pulsed-power technology, advanced x-ray and laser diagnostics, computer modeling, plasma, atomic, and radiation physics, and related areas.

2. Development and operation of the Nevada Terawatt Facility

A calibrated, high-repetition-rate 2-terawatt z-pinch research facility has been developed and operated at the Nevada Terawatt Facility (NTF). Experiments have been performed with Zebra, a high-repetition-rate 2-terawatt z-pinch (2 MV, 1.2 MA, 100 ns, 200 kJ, 1.9 ohm final line impedance, formerly HDZP-II at LANL). Full-system shots have yielded new z-pinch data (Sections 3.2 and 4.2) and produced x-rays for the development of short-wavelength diagnostics (Section 4.1). Computer control and automation of the pulsed-power generator is partially complete.

Zebra is being operated under the supervision of the university's Environmental Health and Safety Office. Students and personnel are protected by an extensive system of electronic, mechanical, and administrative controls. Safety procedures have been documented, and staff are trained in safe high-voltage practices, forklift operation, overhead-crane operation, confined-space entry, radiation safety, laser safety, and lockout/tagout. Required life-safety improvements to the three-story Zebra high bay are complete, with a high degree of satisfaction by inspectors from the Office of the State Fire Marshal, the UNR Facilities Management Department, and the UNR Department of Environmental Health and Safety.

Experiments on Zebra have yielded new z-pinch data and produced x-rays for the development of short-wavelength diagnostics. Experiments on Zebra examined single-wire z-pinchs, conical-array implosions, and high-current x-pinchs.

Significant progress has been made in organizing all Zebra z-pinch experimental data in a user-friendly database, to facilitate detailed comparisons between theory and experiment. At present, the information stored describes, on a shot by shot basis, the experiment performed, the Zebra set-up, the load characteristics, the signal paths, and the data acquisition settings. The database is being continuously extended to include detailed information provided by the plasma diagnostics. In the future, the database will be integrated with data processing codes. To enhance the accessibility to data, the database will be posted on the NTF web site, which is being designed and developed in parallel.

The database resides on the central NTF server (HDZP2NT) and can be accessed for both viewing and entering data. Users navigate the data in the same way as the world wide web, which makes finding data easy and fast. The relational field of the database is the Shot Number. Users can search for information pertaining to specific shots or for data spread among several shots and several different tables. (E.g., users can filter the database to look only at the x-pinch shots.) Locating the database on a central server allows many people to access and modify the database simultaneously.

Zebra will be joined by the Leopard laser, built using components of the Petawatt laser from LLNL (previously the most powerful laser in the world). A 20 J, sub-picosecond laser is expected to be available for experiments, in conjunction with the Zebra z-pinch, in fall of 2003.

2.1. Power-flow measurements and SCREAMER modeling

Precise measurements are made of the current and voltage throughout Zebra, and to the load (Figure 2.1.1). About 20 current and voltage signals are recorded for each shot. These are vital for z-pinch science, for triggering diagnostics, for optimizing pulsed-power performance, and for diagnosing declines in performance. Six or more of the probes mentioned measure the current flowing through the load. Three differential B-dots symmetrically distributed around the load provide precise measurements. Their signals, in correlation with other measurements, significantly contribute to understanding the evolution of the z-pinch load. They are also used as input for numerical simulations of experiments. Two additional B-dots have been used during several wire array shots to measure the magnetic field diffusion inside the array or between nested arrays.

The comprehensive power-flow measurements agree in amplitude and timing with predictions of SCREAMER (SNL) power-flow modeling. The detailed Zebra SCREAMER model (with over 50 elements), developed in collaboration with SNL, predicts the current and voltage waveforms at key locations along Zebra, including the load region and the locations of the power flow probes. Some differences in waveform shape between Zebra and the SCREAMER model continue to be investigated. Increasing the accuracy and confidence of the current and voltage measurements in the load region of Zebra is a permanent focus of the power-flow work.

In addition to predicting the effects of current changes in the machine set-up, SCREAMER is run to help design major configuration and functional modifications of Zebra. This method was employed to design a diverter switch in the oil tank and several hardware parts for the load region. At present, this work is continued aiming to make Zebra appropriate for more complex experiments. The design of the Zebra vacuum chamber is being adapted to allow for laser – z-pinch interaction experiments. The current to the load will only be reduced by about 5%.

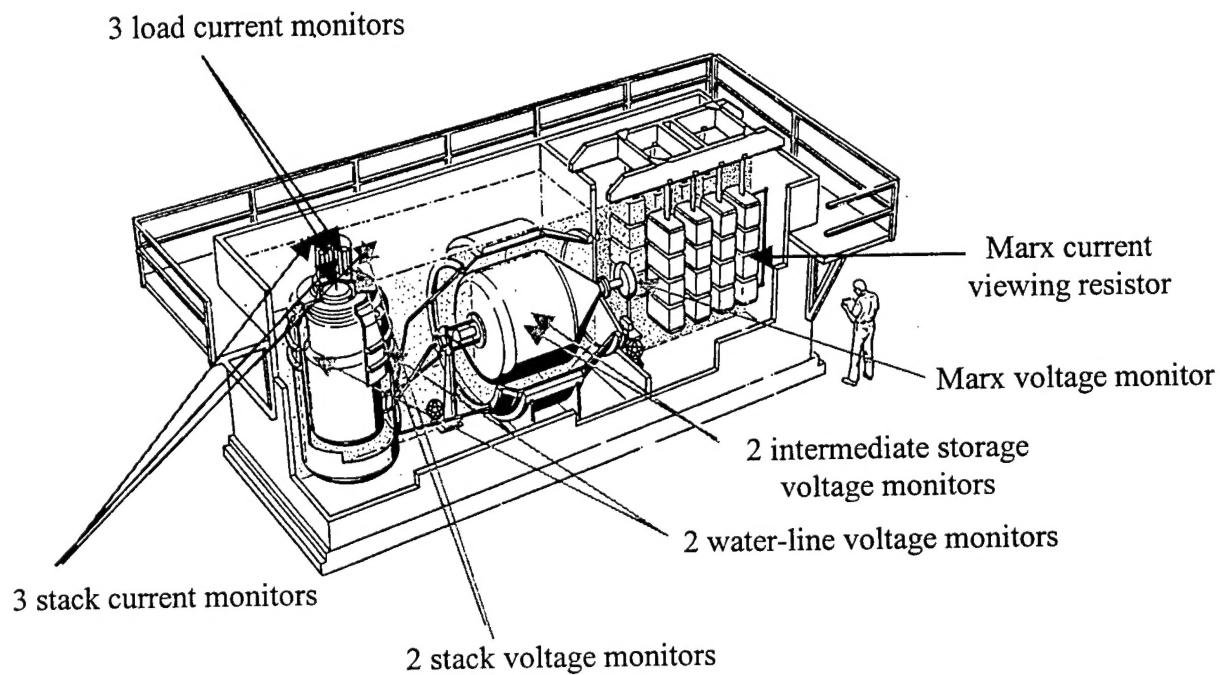


Figure 2.1.1. Precise measurements are available of the current and voltage throughout Zebra, and to the load. The locations of 14 of the current and voltage probes are shown.

2.2. Laser and optical diagnostics

Time-resolved laser absorption imaging and interferometry have been developed and used to study the formation of plasma from fine wires exploded by fast-rising, kA-level currents.

Development of laser polarimetry, collective Thomson scattering, and induced fluorescence diagnostics has been initiated. Detection equipment has been procured, including three pre-owned streak cameras (one IR-UV sensitive), a 3-grating, 0.5-m, imaging spectrometer, several CCD cameras, and a variety of optics. A flashlamp-pumped dye laser has been obtained (from TRW) for laser-induced fluorescence measurements. A few-mJ, nanosecond-pulse Nd:YLF laser has been procured for the imaging of laser absorption, interferometry, and Faraday rotation of polarization, and for subsequent amplification to 1 GW by the Quantel PG-48, to drive collective Thomson scattering.

3. Z-pinch physics

A detailed analytical and numerical study has been initiated of z-pinch linear instability (Section 3.1, Appendix A, and Appendix B). The calculations aim to understand the growth of fluctuations observed in experiment and modeling, and to resolve the contradictory results on this topic in the literature, especially as regards stabilization by sheared axial flow. Axial shear flow stabilization has been investigated experimentally, with conical array implosions (Section 3.2 and Appendix C). Computer modeling of these experiments has been performed with MHRDR (Section 3.2.1 and Appendix D).

An experiment on single wires driven by current prepulses similar to, and faster than, those at Z (Section 3.3, Appendix E, and Appendix F) found that the characteristics of wire explosions depend dramatically on the rate of rise of the current, on the heat of vaporization of the wire material, and on the diameter of the wire. For substances with high vaporization energy (W, Mo, Ti, Ni, Fe, Au-plated W), faster rising pulses are much more effective at exploding single wires than Z-like pulses. Faster-rising pulses may lead to a plasma less divided into cold core and unstable corona than has typically been produced. The measurements are being compared with MHRDR simulations at UNR.

X-pinchs have also been investigated (Section 4.2, Appendix L, Appendix M, and Appendix P) with experiments on Zebra at 900 kA, and novel diagnostics. The goal of these experiments is to develop new x-ray sources for radiography and to understand the final stage of the z-pinch MHD sausage ($m=0$) instability, when a z-pinch turns into a mini-diode.

3.1. Linear theory of z-pinch MHD instabilities

Fluctuations are small in the earliest stage of z-pinch development, and the growth of instabilities is then amenable to treatment by linear theory. A comprehensive theoretical description of this phase would be invaluable for comparison with experiment and simulation. However, such a description, for realistic conditions, is lacking, and, worse, some of the results in the literature are in contradiction (in particular, with respect to stabilization by sheared axial flow). A detailed analytical and numerical study has been initiated of z-pinch linear instability, to address this need.

A systematic analytical and simulation study of sheared flow stabilization of global MHD instabilities has been initiated for z-pinch plasma, including $m=0$ sausage and Rayleigh-Taylor modes and $m=1$ internal kinks. Sheared flows are of interest as a possible mechanism for the stabilization of MHD instabilities, because MHD instabilities grow on the pinch surface, where the density is low and the magnetic field is high. The flow stretches and eliminates MHD modulations, mixing unstable modes with different wavelengths. This can restrict the growth of the modes to a nondestructive level. We first of all need to understand z-pinch behavior in the linear stage of development of the instability.

It should also be pointed out that appearance of short scales due to the mixing associated with the presence of sheared flow means that it is necessary to include in the model the Hall term and finite Larmor radius effects. This is the reason why for the linear stage, we shall use equations that contain the Hall term and finite Larmor radius effects, in addition to the standard MHD terms, in the presence of sheared axial flow and axial magnetic field. These equations form a more general set than has apparently been used before. These equations will be used to define eigenfunctions and eigenvalues which could exhibit unstable solutions to the perturbed equilibria. This will identify the region in parameter space where the instability can take place and to determine the linear growth rate of the instability to compare with the results of the simulations. By varying these parameters, we will try to find optimal regimes for stabilization, which will still be effective for plasma compression. We will look for conditions that can be realized experimentally. These linear studies will also help resolve the discrepancy in the effectiveness of axial flow shear as a stabilizing agent.

To date, to perform a linear stability analysis we derived equations that contain the Hall term in addition to the standard MHD terms, in the presence of externally imposed axial and azimuthal sheared flows and axial magnetic field. This is well suited for calculations relevant to Zebra. Then the problem can be treated numerically following the development in time of an initial perturbation. After several growth times the solution will converge to the fastest growing mode, defining real and imaginary parts of ω . This method has been used to study z-pinch stability in tokamak plasma by Coppins et al. (1984), and to study ideal MHD instabilities in tokamaks (Sykes and Wesson, 1974; Bateman et al., 1974). A numerical code, WOLF, has been developed to solve the resultant system of linearized equations.

As a first step we investigated the instability of $m=0$ mode in the presence of the axial shear flow with the Hall term included, but with zero axial magnetic field and zero azimuthal shear flow. The numerical solutions reveal that shear flow in the absence of the Hall term considerably

reduces the growth rate of the $m=0$ instability (for our set of parameters ~ 4 times) and narrows the excited wave spectrum in k space in comparison with the ideal MHD limit. Inclusion of the Hall term into the model leads to the increase of the growth rate and it confirms the earlier suggestion of Coppins et al. (1984) that the Hall term can play destabilizing role.

In the future we plan to examine the growth rate behavior for a much broader parameter range, with the inclusion of azimuthal sheared flow and axial magnetic field, in order to create a general picture of $m=0$ instability development and the ways to reduce the amount of energy going into this mode.

The derived equations can also be used to investigate the development of the kink instability in the presence of axial and azimuthal sheared flow, the Hall term and axial magnetic field, and to identify the factors that can lead to considerable reduction or even suppression of the kink mode instability.

The logical extension of the linear analysis is the simulation study of the nonlinear development of the sausage instability. We plan to carry out 2D simulations using the Eulerian Magnetohydrodynamic Radiative Code (MHRDR). The simulation results will allow us to understand how the inclusion of sheared flow and the Hall term influence the nonlinear stage of instability development. While the linear stage defines the energy going into the unstable wave spectrum, nonlinear wave-wave coupling transfers this wave energy to other modes, whose dissipation determines the saturation amplitude of the resultant turbulence.

The linear theory results are presented in Appendices A and B. MHRDR simulation results, for the same problem, are presented in the next section (and in Appendix D).

3.1.1. MHRDR modeling of the $m=0$ instability with sheared axial flow, but no axial magnetic field

The linear analysis of the $m=0$ instability development and above results from the code WOLF is being cross-checked against the results of MHRDR simulations for the initial growth stage of the instability. This gives credibility to the performance of both numerical tools, and increased confidence in the subsequent nonlinear evolution calculated by MHRDR.

The MHRDR simulation results (Figures 3.1.4–3.1.7) are in agreement with the numerical linear theory solutions for the growth rate (Figure 3.1.3). For the unstable wave with $k_z r_0 = 6$ from Figure 3.1.3 we find a growth rate $\gamma \sim 1.25$ in the absence of sheared flow ($V_{0z} = 0$ and $\varepsilon = 0$) and $\gamma \sim 0.3$ in the presence of sheared axial flow ($V_{0z} = 1.5 V_{Ti}$ and $\varepsilon = 0$). (In MHRDR, the growth rate can also be obtained from the time dependence of the axial kinetic energy. These values are also in agreement with the linear theory results.)

The MHRDR simulations were initiated with Bennett equilibrium profiles for magnetic field and density. This is a 2D problem in the r - z plane, with the azimuthal magnetic field B_θ perpendicular to the plane of the simulation. Periodic boundary conditions are not currently available in MHRDR, so metal boundaries of the simulation box were used. A constant current

flux flowing from the bottom of the simulation box along z axis was created. This current flux had a Bennett radial profile.

The current density profile of the Bennett equilibrium is

$$j_z = \frac{j_{z \max}}{(1 + (\frac{r}{a})^2)^2}, \quad j_{z \max} = \frac{c}{\pi} \frac{B_{\max}}{a},$$

where $a = \frac{r_0}{3}$ is the coordinate of the maximum of the magnetic field in Bennett equilibrium and r_0 is the radius of a metal cylinder.

The current profile of the Bennett equilibrium is

$$J_z = \frac{J_{z \max} (\frac{r}{a})^2}{1 + (\frac{r}{a})^2}, \quad J_{z \max} = \pi a^2 j_{z \max}.$$

The density profile of the Bennett equilibrium is

$$\rho_0 = \frac{\rho_{\max}}{(1 + (\frac{r}{a})^2)^2}, \quad \rho_{\max} = M_H n_{00} [\frac{kg}{m^3}].$$

The magnetic field profile of the Bennett equilibrium is

$$B_{0\theta} = \frac{2rB_{\max}}{a(1 + (\frac{r}{a})^2)}.$$

The initial density perturbations for this problem were

$$\rho_{pert} = ampl * \rho_{\max} * \exp(-0.5 * (\frac{r-a}{b})^2) * \sin(kz)$$

where $ampl$ was chosen in the range $1.0e-5 \leq ampl \leq 1.0e-2$.

The initial density distribution was $\rho_{initial} = \rho_0 + \rho_{per}$.

A similar procedure was used to initialize the other variables.

The following initial simulation parameters were chosen for hydrogen plasma:

- atomic density $n_{00} = 10^{18} \frac{1}{cm^3}$, corresponding to a mass density $\rho_{0max} = 1.67 \cdot 10^{-3} \frac{kg}{m^3}$;
- temperature $T = 1ev = 11605 K$.

The axial length of simulated region was chosen to contain many wavelengths of the most unstable modes: $L_z \approx 30r_0$.

The simulation results (Figures 3.1.4–3.1.7) are in agreement with the numerical linear theory solutions for the growth rate, presented in Appendix D. For the unstable wave with $k_z r_0 = 6$ we find for the growth rate $\gamma \sim 1.25$ in the absence of a shear flow ($V_{0z} = 0$ and $\varepsilon = 0$) and $\gamma \sim 0.3$ in the presence of a shear flow ($V_{0z} = 1.5 V_{Ti}$, and $\varepsilon = 0$). In MHDRD value of the growth rate can be obtained from the time dependence of the axial kinetic energy. These values are in agreement with the linear theory results.

The boundary conditions and input decks are given, following the simulation results (Figures 3.1.4–3.1.7).

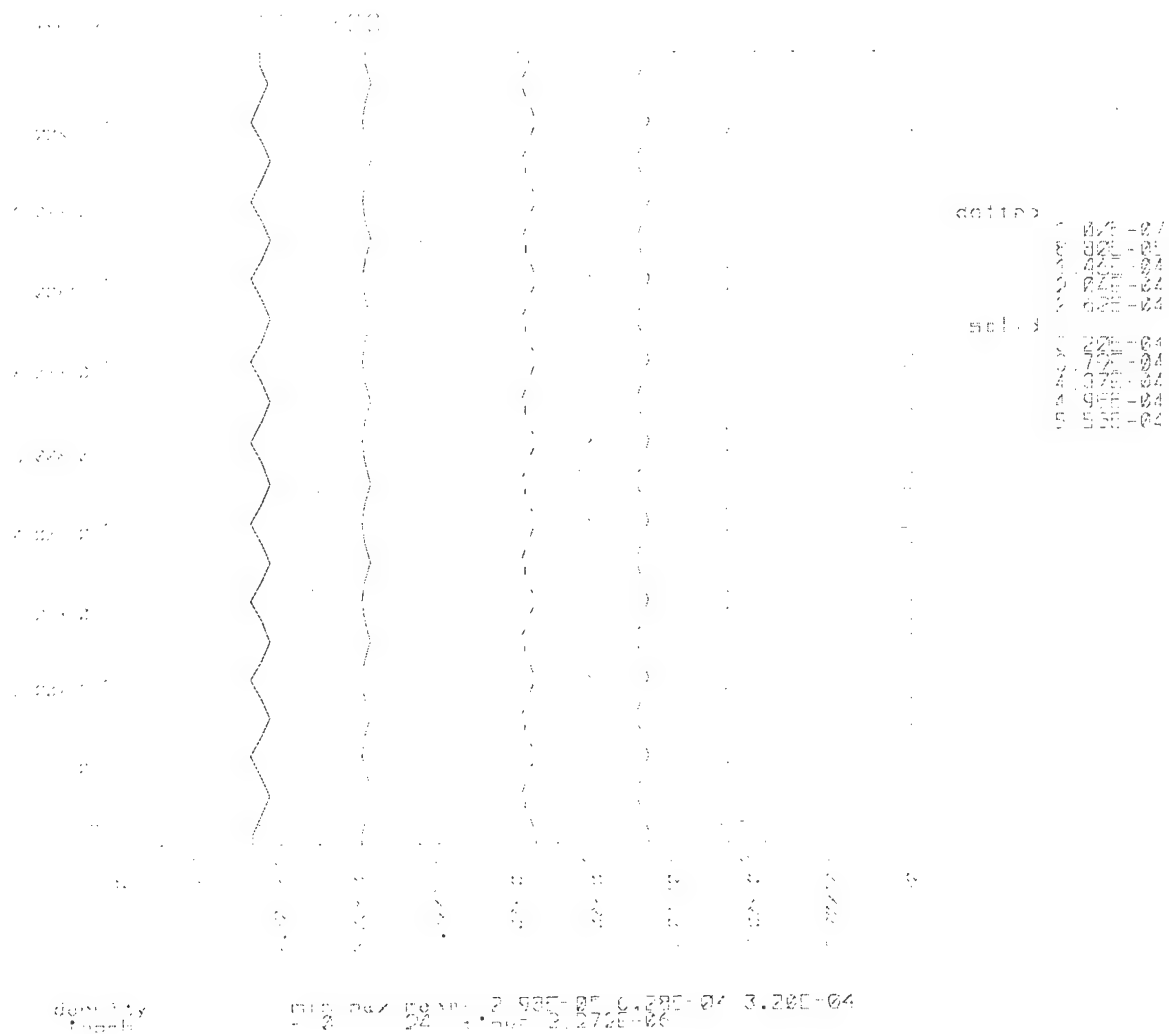


Figure 3.1.4. Contour lines of density with growing perturbations ($k_z r_0 = 6$). 2D MHRDR simulation of the sausage ($m=0$) instability, from an initial Bennett profile without sheared flow ($V_{0z} = 0$).

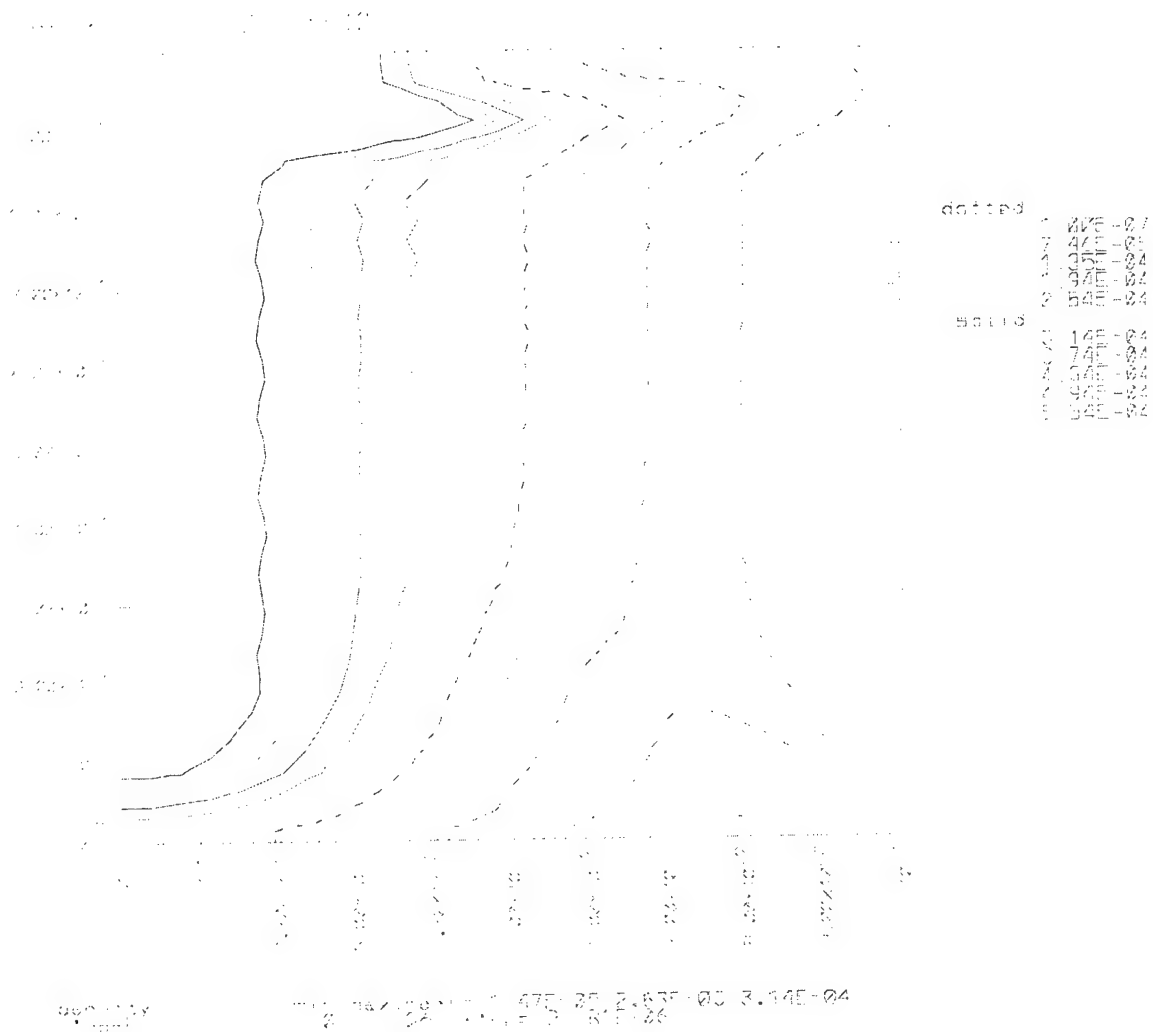


Figure 3.1.5. Contour lines of density with growing perturbations ($k_z r_0 = 6$). 2D MHRDR simulation of the sausage ($m=0$) instability, from an initial Bennett profile with sheared axial flow ($V_{0z} = 1.5 V_{Ti}$).

The following boundary conditions were used.

On the left border (r=0): 111111711

For ρ

$$1:: 1 -- \frac{d\rho}{dn} = 0$$

For normal velocity (radial) VR

$$2:: 1 -- V_r = 0$$

For tangential velocity VZ

$$4:: 1 -- \frac{dV_z}{dn} = 0$$

For electron specific energy EI

6:: 1 -- EI – zero-temperature, electrically conducting wall.

For magnetic field perpendicular to the plane of computation

8:: 7 -- BP – cylindrical axis of symmetry

On the right border (r=r0): 1111551111

For ρ

$$1:: 1 -- \frac{d\rho}{dn} = 0$$

For normal velocity (radial) VR

$$2:: 1 -- V_r = 0$$

For tangential velocity VZ

$$4:: 1 -- \frac{dV_z}{dn} = 0$$

For electron specific energy EI

6:: 5 -- EI – thermally insulating, electrically conducting wall (or mirror, $\frac{dEI}{dn} = 0$).

For magnetic field perpendicular to the plane of computation

8:: 1 -- BP – tangential current density = 0 (conducting wall or mirror).

On the bottom (z=0) border : 1111551111

For ρ

$$1:: 1 -- \frac{d\rho}{dn} = 0$$

For tangential velocity (radial) VR

$$2:: 1 -- \frac{dV_r}{dn} = 0$$

For normal velocity VZ

$$4:: 1 -- V_z = 0$$

For electron specific energy EI

$$6:: 5 -- \text{EI -- thermally insulating, electrically conducting wall (or mirror, } \frac{dEI}{dn} = 0 \text{)} .$$

For magnetic field perpendicular to the plane of computation

$$8:: 1 -- \text{BP -- tangential current density} = 0 \text{ (conducting wall or mirror).}$$

On the upper (z=Lz) border: 1111551111

For ρ

$$1:: 1 -- \frac{d\rho}{dn} = 0$$

For tangential velocity (radial) VR

$$2:: 1 -- \frac{dV_r}{dn} = 0$$

For normal velocity VZ

$$4:: 1 -- V_z = 0$$

For electron specific energy EI

$$6:: 5 -- \text{EI -- thermally insulating, electrically conducting wall (or mirror, } \frac{dEI}{dn} = 0 \text{)} .$$

For magnetic field perpendicular to the plane of computation

$$8:: 1 -- \text{BP -- tangential current density} = 0 \text{ (conducting wall or mirror).}$$

MHRDR input file for problem described above

```
program=lin1
initmon=1,1
tstop=1.9e-4
dtedit=1e-4
dtdump=1e-5
longid=linear stability
model=18
matl=,,,-201,1.0,1.00797,77.038,1.0e-6,1.6667
cutoff=1e-6
xgrid=40,0.0,1.0e-1,,
ygrid=40,0.0,30.0e-1
dtmin=1e-19
dtmax=1e-5
dtinit=1e-11
chgmax=.3
rad=1.0,0.0
itcon=1.0,0.0
res=1.0,0.0
dtref=1,1e4,10,10
bdrycon= 111111711,1111151111,1111551111,1111551111
initfyl=inpMHRDR
```

post-processor

```
mode=1
4plot
cplot=ro,,,,
dtedit=1e-5
cplot=te,,,,
cplot=pr,,,,
cplot=bp
mode=1
4plot
kline=13
dtedit=1e-5
plotnum=ro,11
plotnum=te,11
plotnum=pr,11
plotnum=bpt,11
```

3.1.2. References for Section 3.1

- S. Appl and M. Camenzind, The stability of the current-carrying jets, *Astron. Astrophys.* **256**, 354 (1992).
- T.D. Arber and D.F. Howell, The effect of sheared axial flow on the linear stability of the Z-pinch, *Phys. Plasmas* **3**, 554 (1996).
- G. Bateman, W. Schneider, and W. Grossman, *Nucl. Fusion* **14**, 669 (1974).
- G. Bateman, *MHD Instabilities*, MIT Press, Cambridge, 1978.
- M. Coppins, D.J. Bond, and M.G. Haines, A study of the stability of the Z pinch under fusion conditions using the Hall fluid model, *Phys. Fluids* **27**, 2886 (1984).
- E. Corbelli and G. Torricelli-Ciamponi, *Phys. Fluids B* **2**, 828 (1990).
- C.L. Hedrick and J.-N. Leboeuf, Landau fluid equations for electromagnetic and electrostatic fluctuations, *Phys. Fluids B* **4**, 3915 (1992).
- B.B. Kadomtsev, Hydromagnetic stability of a plasma, *Reviews of Plasma Physics*, vol.2, 1966.
- P. Sheehey and I. Lindemuth, Hall and two-temperature magnetohydrodynamic simulation of deuterium-fiber-initiated Z- pinches, *Phys. Plasmas*, **4**, 146 (1997).
- U. Shumlak, C.W. Hartman, Sheared flow stabilization of the $m=1$ kink mode in z-pinches, *Phys. Rev. Letters* **75**, 3285 (1995).
- A. Sykes and J.A. Wesson, *Nucl. Fusion* **14**, 645 (1974).
- F. Winterberg, *Beitr. Plasmaphys.* **25**, 117 (1985).

3.2. Investigation of axial shear flow stabilization: conical arrays

Axial shear flow stabilization of MHD instabilities would significantly extend z-pinch applications. As a first approach to shear flow z-pinch stabilization research at NTF, conical array implosion experiments have been initiated, in parallel with MHD modeling. The main objective is to determine and study the parameters range for which a shear flow created along the z-axis can stabilize a z-pinch plasma. In our experiments, the z-pinch to be stabilized is a single exploding wire, a load known as prone to MHD instabilities. To avoid the need of using a separate generator for creating the axial plasma flow, we use for this purpose a conical wire array surrounding the wire, so that Zebra powers both the plasma to be stabilized and the stabilizing plasma. The $\mathbf{j} \times \mathbf{B}$ implosion of a conical load is expected to exhibit a zippering effect along its axis, similar to that observed in plasma focus or Marshall gun type experiments. The collision of plasma structures arriving at oblique directions to the z-axis produces in turn a plasma flow with an axial velocity component.

In previous x-pinch and v-pinch experiments on Zebra, we have observed that planar configurations of wires making angles with and symmetrically distributed about the z-axis lead to jetting towards the axis and to the formation of a relatively dense plasma on axis. To assure momentum conservation, the axial plasma structure has to move along the axis in a jet-like fashion.

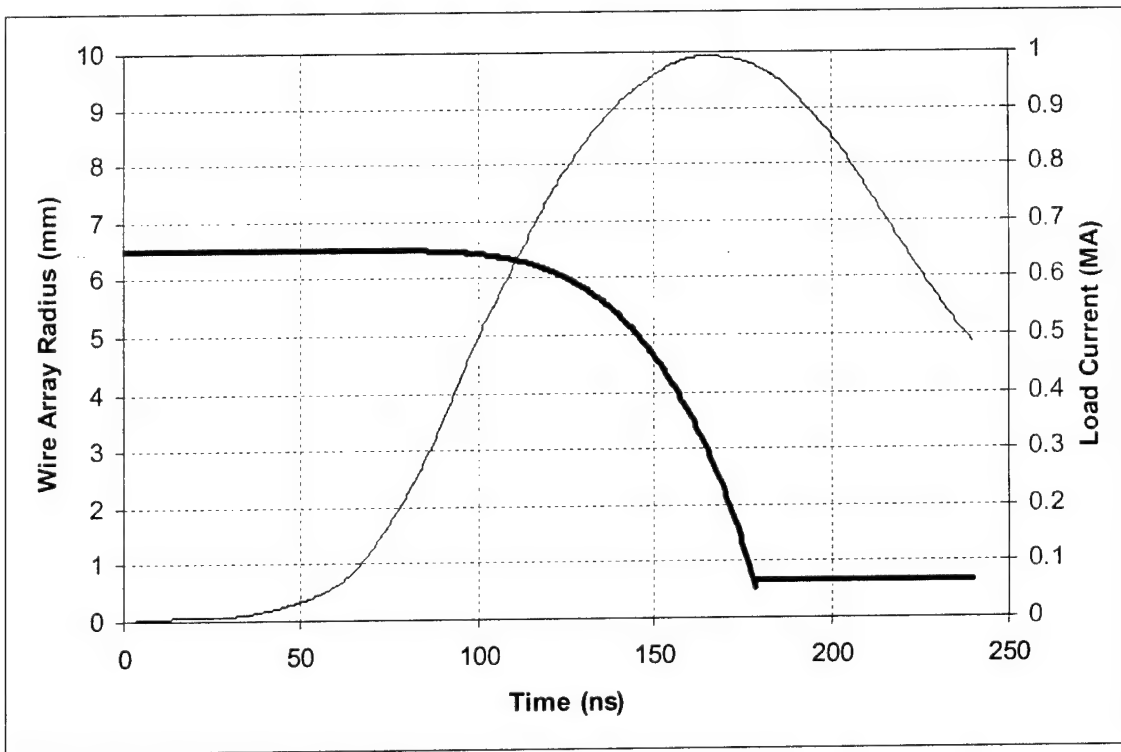


Figure 3.2.1. OD simulation of a cylindrical array implosion. The calculation is carried out for an array made of 8 Al wires 15.2 μm thick and 20 mm long placed on a circle 13 mm in diameter, with a central Ti wire 76 μm thick. The calculation is performed for an actual Zebra load current waveform (thinner line).

The experiments are being designed on basis of simple 0D calculations. At present we are using a cylindrical wire array model (a 0D simulation code for conical arrays is under development). The array mass and diameter are determined by such calculations performed for a typical Zebra current waveform. The simulation results are also used for diagnostics timing and synchronization. One result of a 0D calculation is given in Fig. 3.2.1. The array the implosion of which is modeled is made of 8 Al wires $15.2\text{ }\mu\text{m}$ thick and 20 mm long placed on a circle 13 mm in diameter, with a central Ti wire $76\text{ }\mu\text{m}$ thick. The calculation is performed for an actual Zebra load current waveform. The presence of the central wire is taken into account by subtracting from the total current the amount flowing through this wire, in the assumption that the current division calculated for cold wires is valid for the whole duration of the implosion.

In addition to these numerical constraints, other elements are taken into account when specifying the experimental parameters. Previous experiments with different types of loads suggested that the optimum load mass from the point of view of power coupling is about $800\text{ }\mu\text{g}$. Loads with masses around this value have displayed maximum conversion efficiency of electrical energy to x-rays.

The diagnostics available for this experimental campaign are almost exclusively x-ray diagnostics. To enhance the sensitivity of this type of measurements, namely the spectral contrast, we have decided to use two different materials for the central wire and for the surrounding array, respectively. Taking into account the expertise of the x-ray spectroscopic diagnostics group at NTF, Titanium and Aluminum are used in the first series of tests for the central wire and for the array, respectively.

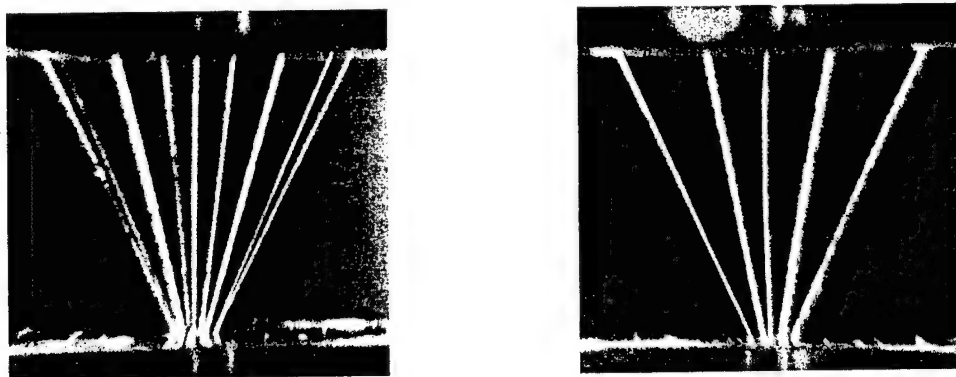


Figure 3.2.2. The conical array to be used for Z-SHOT#73 (03/14/01) photographed from two directions. It shows good symmetry and good wire alignment. The cone tip points towards the cathode. The load dimensions are given in the text.

Corroborated, the above considerations led us to choose $152\text{ }\mu\text{m}$ thick Ti wire for the central wire, and $15.2\text{ }\mu\text{m}$ diameter Al for the 8-wires outer array. The outcome of the first conical array shot suggested the use of a thinner central wire. Ti wire with $76\text{ }\mu\text{m}$ diameter has been chosen. All loads shot in this series have been 20 mm high. To date, two conical arrays (Fig. 3.2.2) have been shot, each consisting of 8 outer Al wires and a central Ti. The conical structure had a small radius of 2.5 mm (cathode) and a large radius of 23 mm (anode), giving a tip angle of about 54 degrees. As reference for the effect of the Al plasma flowing along the central wire, two single 76

μm Ti wire shots and two cylindrical arrays (Fig. 3.2.3) with 76 μm Ti central wire have been performed in the same Zebra operating conditions. The cylindrical array consisted of 8 parallel Al wires, placed on a 12.7 mm diameter circle.

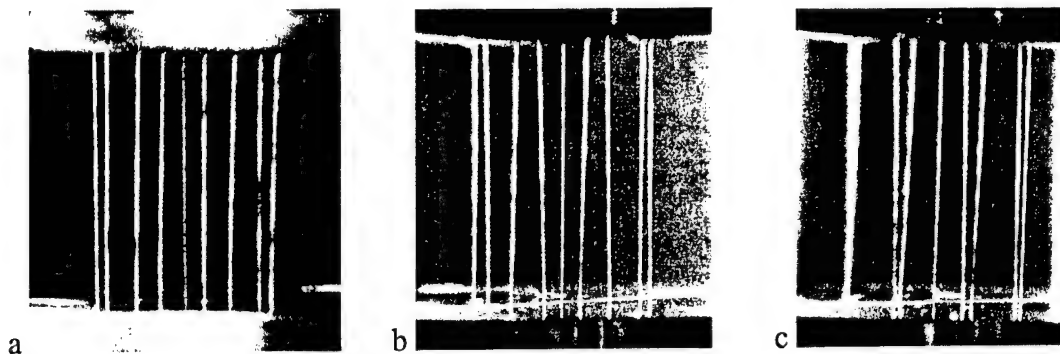


Figure 3.2.3. a. The cylindrical array used for Z-SHOT#79 (04/04/01). The photograph shows that the wires are not perfectly parallel. b. and c. The cylindrical array used for Z-SHOT#80 (04/09/01). In this case, the wires have not been parallel or equally spaced. The cylindrical array load dimensions are given in the text.

The experiments are carried out on the Zebra pulsed-power generator. The Marx capacitors are charged at 85 kV corresponding to about 150 kJ stored energy. For this set-up, the load current typically reaches about 0.9 MA, with 70 ns rise time (from 10% to 90%) and about 120 ns current rise to peak intensity.

An extensive set of x-ray diagnostics instruments and techniques is employed in these experiments. They are all described in detail in the Section 4.1 of this report. High-resolution x-ray emission spectra are recorded with 2 spectrographs employing a KAP crystal ($2d = 26.62 \text{ \AA}$, for both Al and Ti) and, respectively, a LiF crystal ($2d = 4.027 \text{ \AA}$ for Ti K-shell radiation). A pinhole grating is used to record a lower resolution spectrum with 1D space-resolution. The x-ray emitting load is imaged with two time-integrated multi-pinhole cameras (PHC) and a gated x-ray imager (GXI or MCPH). The GXI records for each shot six pairs of frames starting every 17 ns, and with 8 ns exposure time each. The two simultaneous frames in each pair are illuminated through different filters that expose them to different spectral ranges: one set of 6 frames records both Al and Ti K-shell radiation, while the other 6 are only sensitive to the Ti K-shell emission. The space resolution of the GXI is 250 μm . The time-integrated PHCs are sensitive in the same spectral ranges as the GXI and have space resolutions of 580 μm and 65 μm , respectively. The x-ray emission rate is monitored with a photo-conductive detector (PCD) and an x-ray diode (XRD). The XRD is equipped with a 5 μm aluminized kimfoil filter that makes it responsive to the Al and Ti K-shell radiation. The PCD, with an 8 μm Be filter, is most sensitive to the Ti K-shell radiation. A fast Ni bolometer is used to record the total energy emitted in the spectral range 10 eV to 10 keV.

The MHD modeling is carried out with the LANL code MHRDR. Several particularities of this 2D (r-z) code make it difficult to use for simulating the experiments as described above. The spatial coordinates available allow only the modeling of azimuthally symmetrical shells; the

behavior of individual wires cannot be tracked. Moreover, it is difficult to account for a time-varying magnetic field inside the conducting shell, therefore the current division among the wires forming the array and the central wire is hard to simulate. MHRDR can account for only one material during one run. To make possible a comparison of the simulated and the experimental results, the test load has to be built of only one material. The code outputs that can be directly compared with experimental results consist mainly of density and temperature maps at given moments or time-evolution of the density and temperature at a given location. In the experiments presented here, the diagnostics that comes the closest to give such information is the time-gated x-ray imaging (GXI or MCPH; see Section 4.1. of this Report). It provides images of the plasma regions that are both hot enough to emit x-rays, and dense, so that a comparison with the simulation results is not straightforward.

Before making some comments on the experimental results, a description of the following graphs and images might be useful. The XRD (middle-thickness line) and PCD signals are plotted together with the load current (thickest line, slowest varying signal), on the same time scale. The rectangular signals below the 0 line represent the GXI gates (their FWHM equals the exposure time); their amplitude is arbitrary. In all the diagrams, $t = 0$ is arbitrarily chosen at the moment when the load current intensity $I_{\text{load}} = 500$ kA. The time-integrated images are reproduced in positive format, while the time-gated images are represented as negatives. In all images the anode is towards the top of the reproduction. The GXI images shown more to the right are recorded later.

The single 76 μm Ti wire z-pinch experiments produced typical results. The time-integrated x-ray images show straight chains of bright spots (Fig. 3.2.4). (The larger, round formation appearing on all time-integrated images is an artifact due to hard x-rays.) This spatial pattern is accompanied by a numerous series of sharp pulses in the time-resolved x-ray emission signals. All these details are indicating that the z-pinch plasma observed is dominated by instabilities, especially necking instabilities.

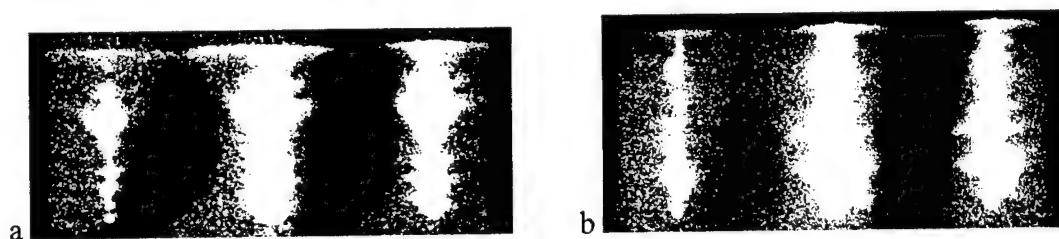


Figure 3.2.4. Time integrated x-ray images of single 76 μm Ti wire z-pinch plasma recorded on shots #74 (a) and #75 (b), respectively.

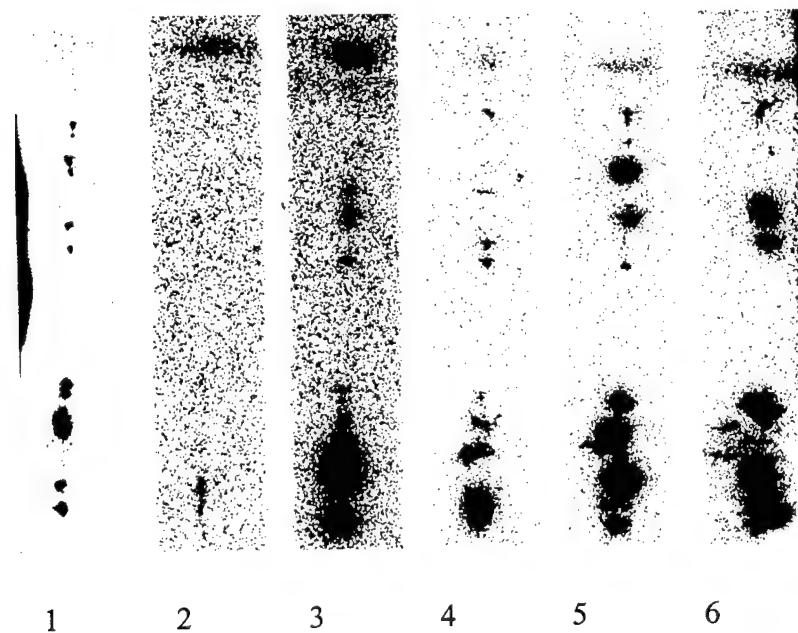
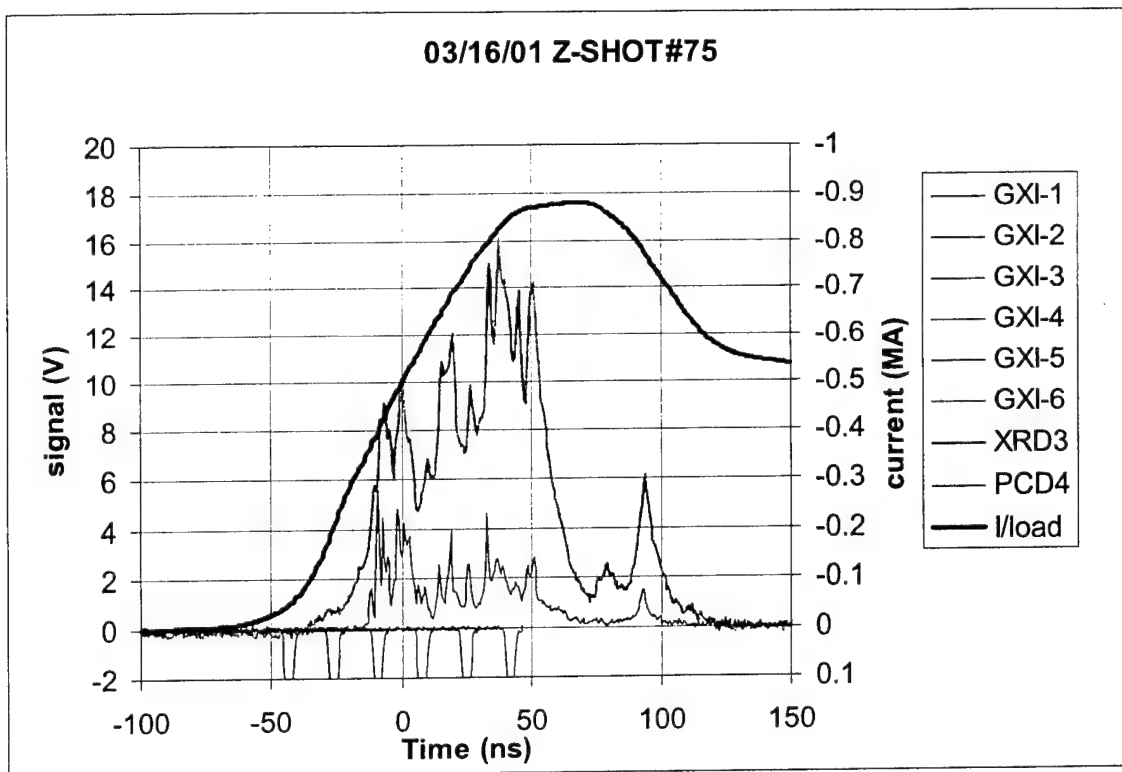


Figure 3.2.5. X-ray signals, load current, and time-gated images recorded for shot #75, for a single 76 μm Ti wire z-pinch plasma. The moments when the GXI frames were recorded are indicated on the graph. Harder x-ray images were recorded in the upper half of the GXI pictures.

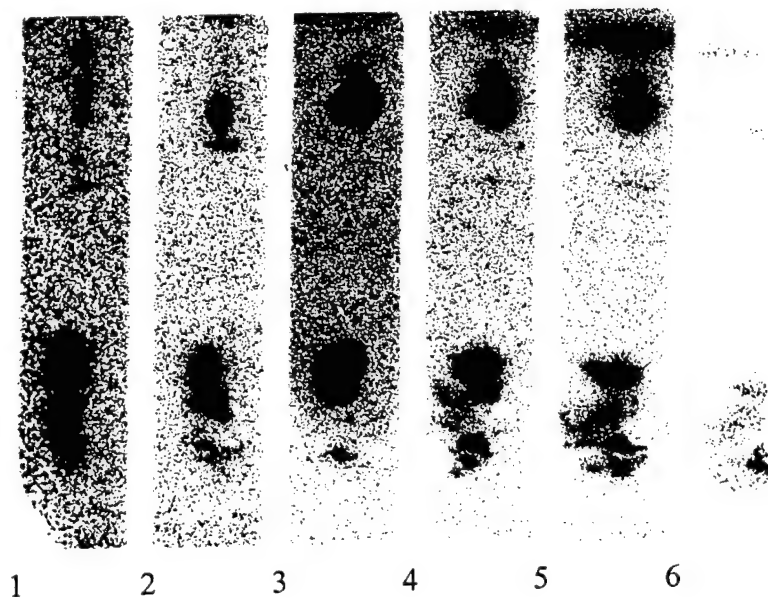
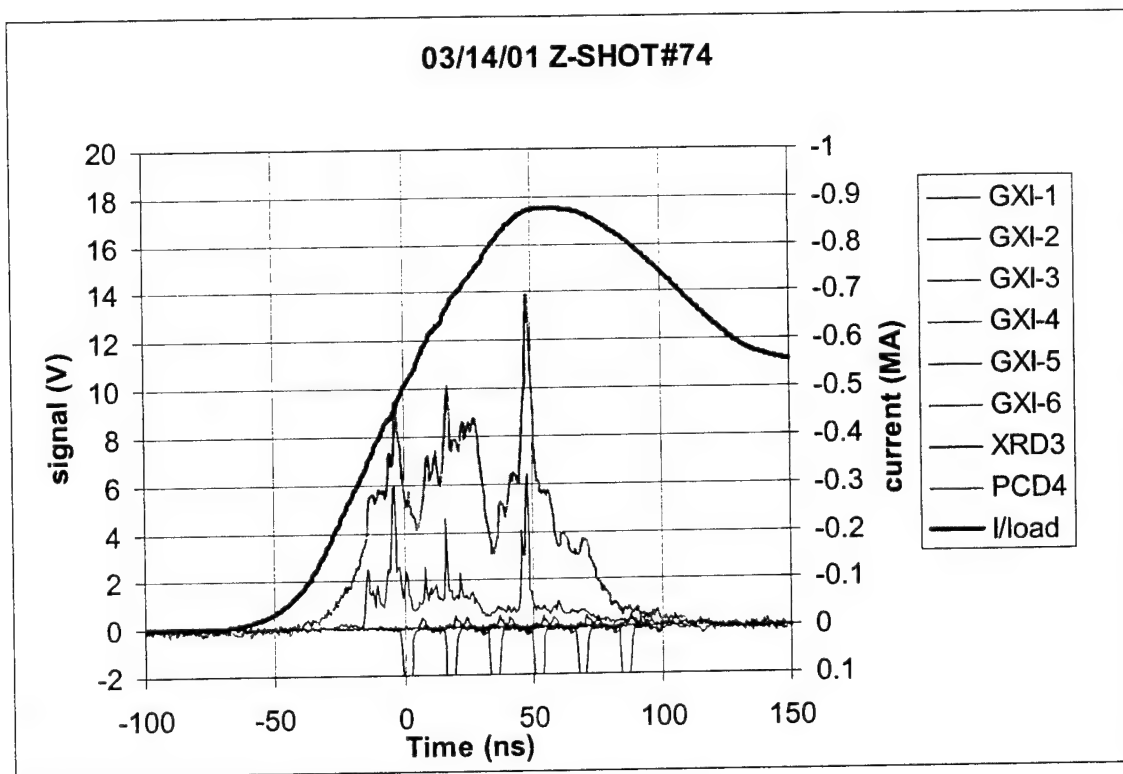


Figure 3.2.6. X-ray signals, load current, and time-gated images recorded for shot #74, for a single 76 μm Ti wire z-pinch plasma. The moments when the GXI frames were recorded are indicated on the graph. Harder x-ray images were recorded in the upper half of the GXI pictures.

The time-gated images recorded on shots #74 and #75 form a sequence that describes the evolution of the single wire z-pinch from the beginning of the current flow, showing the bright spots formation, and ending with the plasma disruption. Although the histories of the two discharges are not identical, the initial and final stages of the z-pinch evolution can be clearly distinguished.

Although generally unwanted, the marked and reproducible instability of the single wire z-pinch plasma is a good starting point for this investigation. As more accurate reference for the action of the conical arrays on the stability of the central wire, two cylindrical arrays with central wire have been tested in Zebra shots.

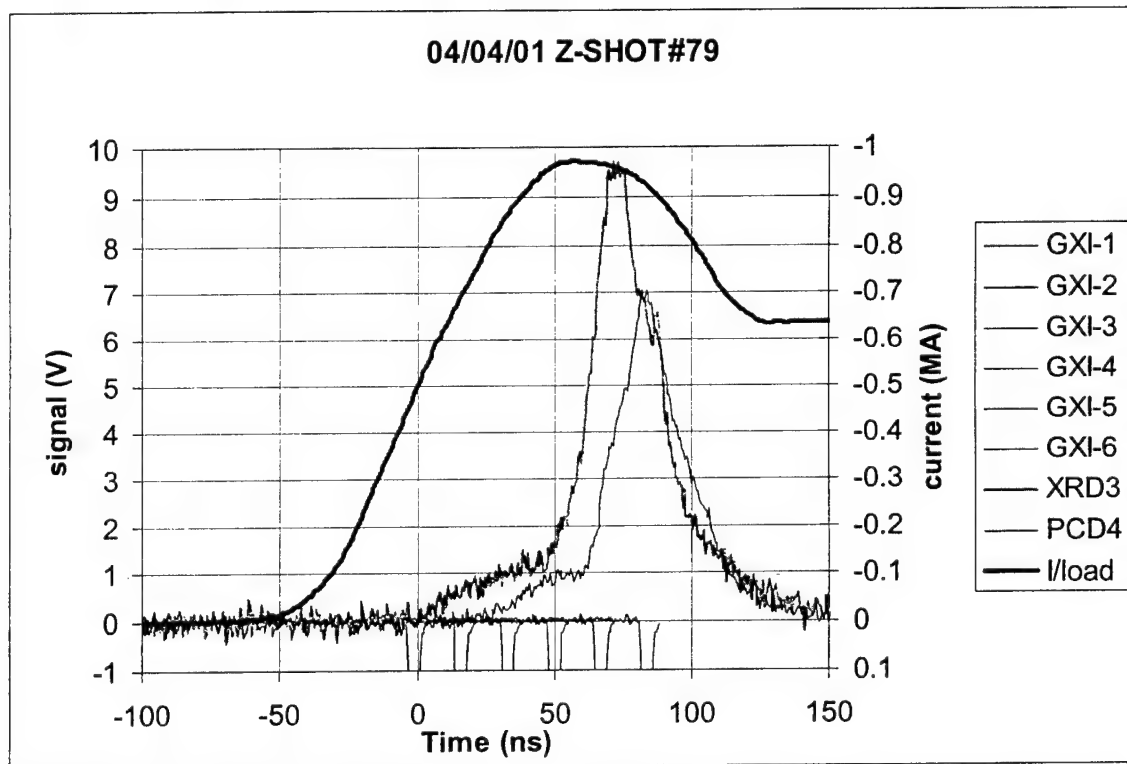


Figure 3.2.7. X-ray and load current signals recorded for a cylindrical array made of 8 Al wires 15.2 μm thick and a central 76 μm Ti wire (shot #79).

The two cylindrical arrays (Fig. 3.2.3) exhibited very similar behavior in spite of their quite different initial condition. The x-ray emission rate, as recorded by the XRD (Fig. 3.2.7 and Fig. 3.2.8), shows a long, slowly rising pedestal followed by a single, wide pulse with slow rise and decay. The harder radiation signal from the PCD shows a similar time-evolution. Although the pulse starts and peaks about 10 ns later than in the case of the XRD signal, the decays occur almost simultaneously. The peak of the x-ray emission occurs at about the moment of maximum compression predicted by a simple 0D simulation (Fig. 3.2.1). It is interesting to note that the overall emission follows the time-evolution of the compression. This type of signals has been

observed before in the case of large-gap wire-arrays, when the wires explode and are accelerated towards the axis as individual entities.

One very interesting feature of this test is the almost complete lack of Ti K-shell radiation. This is indicated especially by the spectra, but also by the absence of any features in the images recorded in a spectral range inaccessible (too hard) to the Al radiation. This result indicates that not enough current flows through the 76 μm Ti wire to transform it into a hot plasma. The plasma (electron) temperature determined from the Al spectrum was not higher than about 390 eV for the shot #79. This temperature is not enough to excite the K-shell emission of Ti. On the other hand, this observation seems to agree with a simple current division estimate that tells that only 10% of the total load current can flow through the central wire. More experiments, with local current measurements, are needed to clarify this observation.

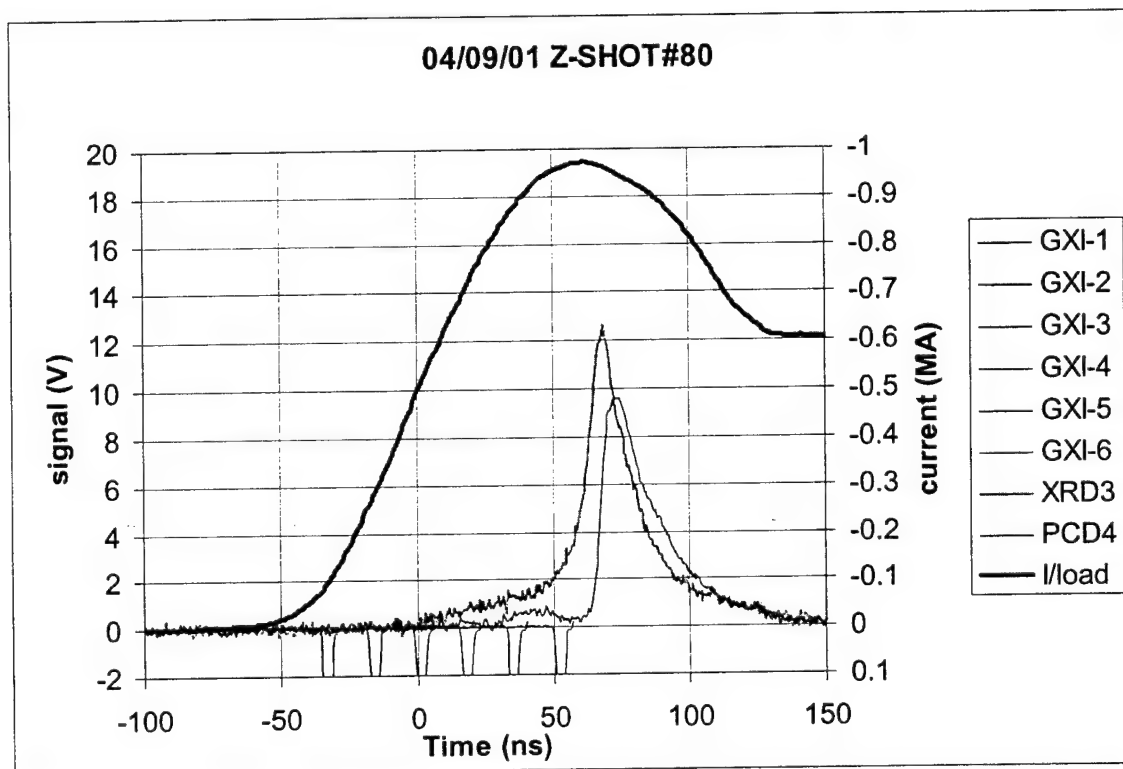


Figure 3.2.8. X-ray and load current signals recorded for a cylindrical array made of 8 Al wires 15.2 μm thick and a central 76 μm Ti wire (shot #80).

The time-gated x-ray images of the cylindrical array show the formation of very unstable z-pinch plasma. Both necking and kink instabilities can be observed to appear and evolve during the discharge. The question arises if and how much the kink modes (with very different pitches for the shots presented) are influenced by the initial condition of the wire arrays (Fig. 3.2.3).

The conical array implosions on central wire display results very different from both the single wire tests and the cylindrical array with central wire ones. While the x-ray emission rate signals seem to have an intermediate structure, the x-ray images evidence different features.

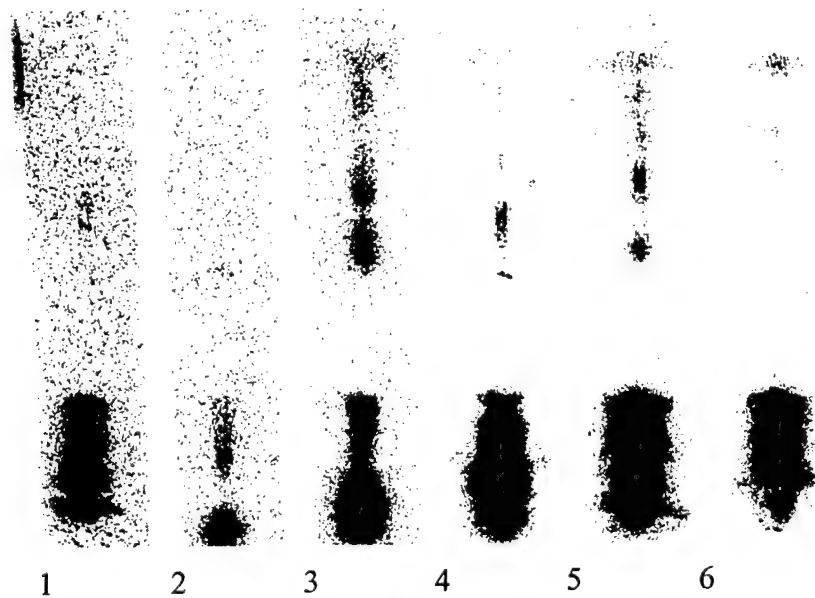
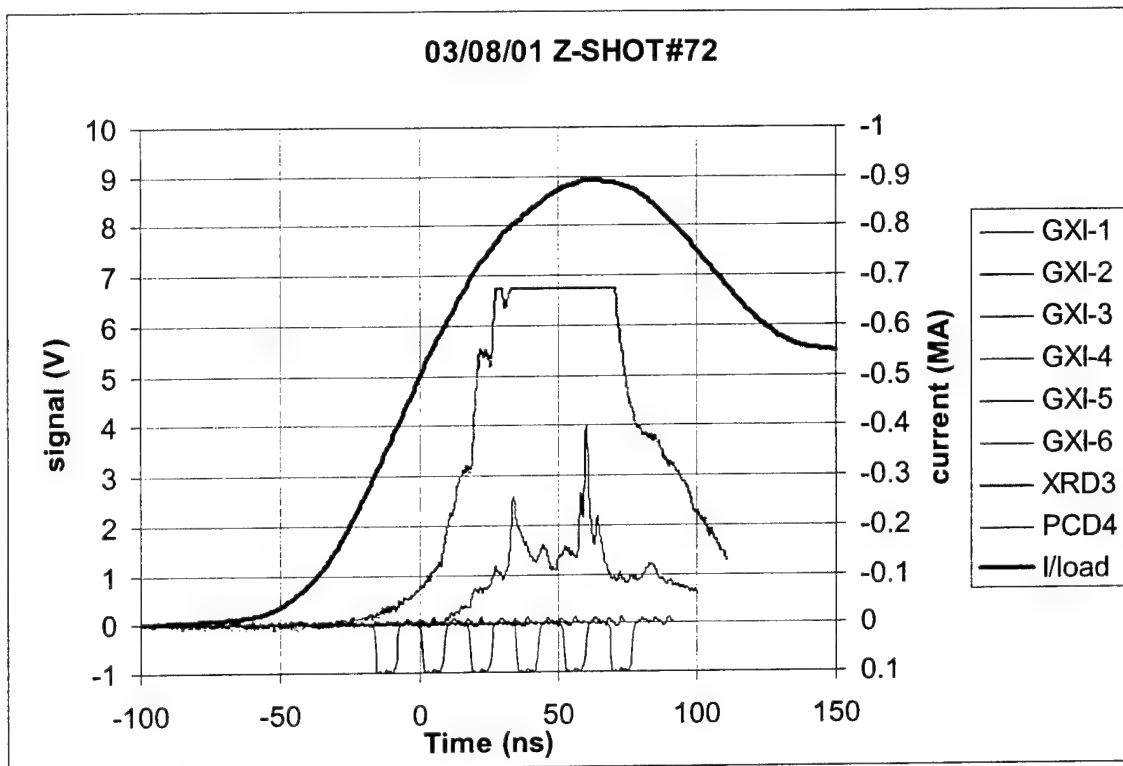


Figure 3.2.9. X-ray and load current signals recorded for a conical array made of 8 Al wires 15.2 μm thick and a central 152 μm Ti wire (shot #72). The moments when the GXI frames were recorded are indicated on the graph. Harder x-ray images are shown in the upper half of the GXI pictures. The anode end of the softer x-ray images is artificially truncated.

The x-ray signals (Fig. 3.2.9 and 3.2.10) do not have the triangular shape observed in the case of the cylindrical arrays, but do not have as many pulses as displayed by the single-wire z-pinch measurements. The rise- and fall-time of the peaks observed is slower than for the single wire peaks. This appearance of the signals suggests a plasma development with intermediate stability when compared with the reference cases.

The time-gated x-ray pictures (Fig. 3.2.9 and 3.2.10) support this image. The frames sensitive to lower x-ray energies show less structure than either the single wires or the cylindrical arrays. The harder x-ray images evidence only a few larger spots. They also indicate the formation of relatively hot Ti plasma, as opposed to the cylindrical array case. For these shots, K-shell Ti spectra have been recorded with features similar to those observed in single wire z-pinch plasmas, and indicating electron temperatures higher than 1 keV. This emission seems to origin from a small region near the cathode, clearly visible in the time-integrated harder x-ray images. Actually the time-gated images also show that most of the Ti emission occurs in the cathode half of the pinch, where the cone tip was originally.

Correlating all this information agrees with the idea of a plasma shell forming initially in the cathode vicinity. As the current increases, the collapsing shell moves along the axis in a zipper-like fashion. The GXI images actually clearly show a plasma blob that forms at the cathode surface, and then migrates along the z-axis in the anode direction. The displacement speed of this plasma structure is of about $2 \cdot 10^5$ m/s for both conical arrays tested. MHRDR simulations predict a similar structure and evolution, but moving more than 5 times faster.

The plasma temperature determined from the Al spectra can be as high as 450 eV, definitely higher than for the cylindrical array. A possible explanation is that in the case of the conical array only part of the wires mass gets accelerated towards the axis. In this way roughly the same amount of energy gets thermalized when the plasma is compressed on axis, but it is shared by less particles. The difference between the temperature determined from the Al spectra and that estimated from the Ti ones is due to the fact that the spectroscopic calculations have been applied to spectra both space- and time-integrated.

The GXI frames 2 soft and frame 3 hard (Fig. 3.2.9) show a wire-like core. The width of this structure is less than 175 μm , corresponding to the initial diameter of the central wire, 152 μm . In the next frames only this structure's edges still emit harder radiation. This tube-like emitting structure suggests that most of the Ti wire material remains cold during the discharge. The time-integrated x-ray images also show a cold, non-emitting core, on the z-pinch axis. In turn, this points again to the insufficient current flowing through the central wire.

From the stabilization point of view, we have to notice that in the presence of the conical array, the Ti central wire shows less and larger bright spots than a single Ti wire. When the conical array is not employed, the spots are distributed more uniformly along the pinch, and they are brighter and smaller.

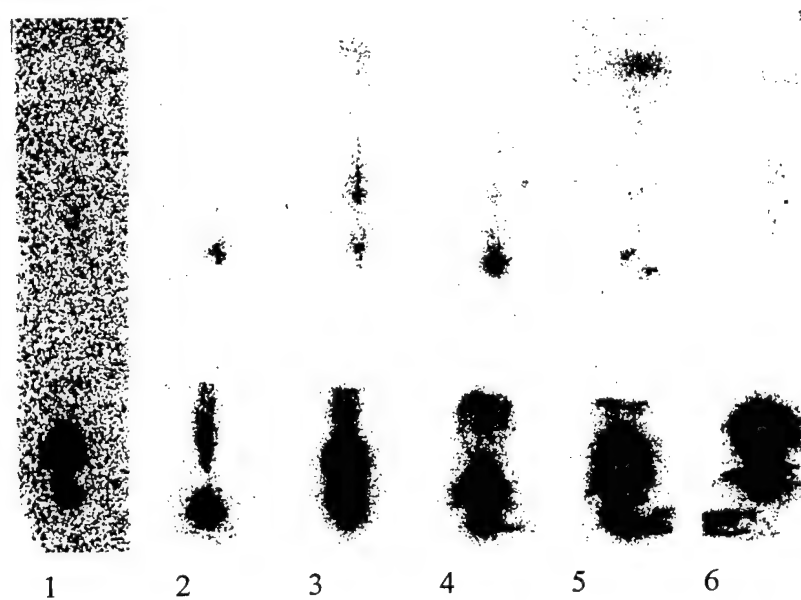
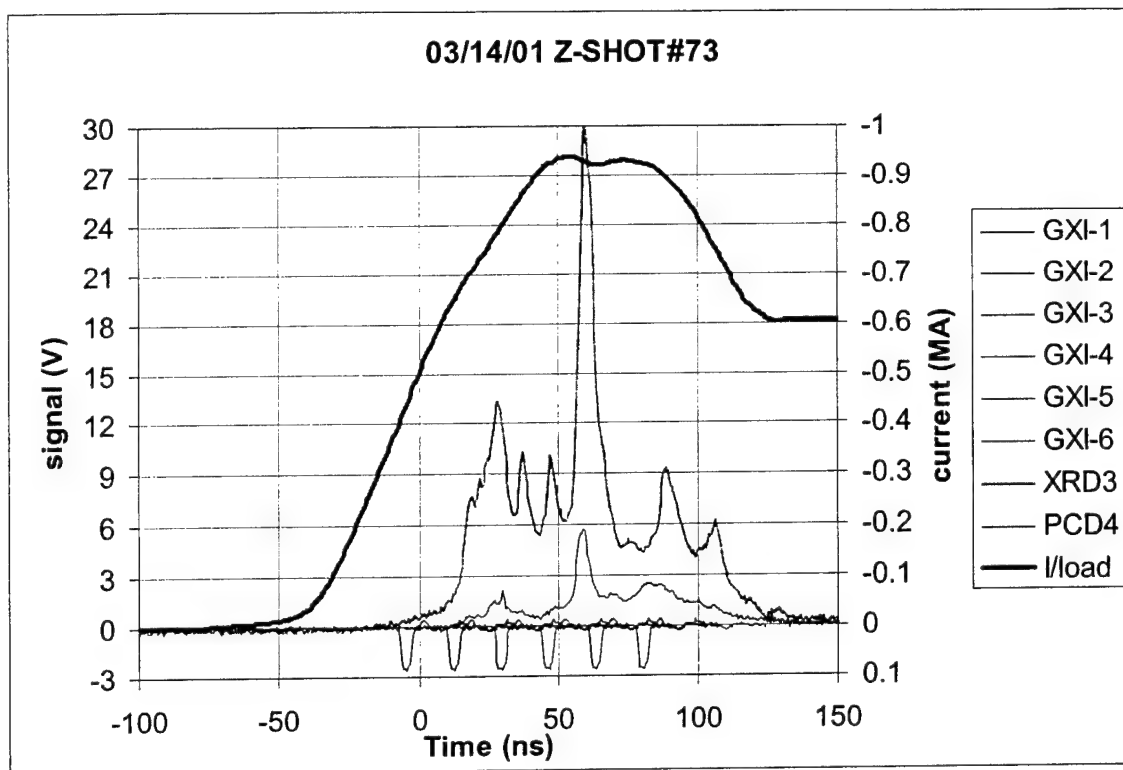


Figure 3.2.10. X-ray and load current signals recorded for a conical array made of 8 Al wires $15.2\text{ }\mu\text{m}$ thick and a central $76\text{ }\mu\text{m}$ Ti wire (shot #73). The moments when the GXI frames were recorded are indicated on the graph. Harder x-ray images are shown in the upper half of the GXI pictures. The anode end of the softer x-ray images is artificially truncated.

These first tests in the shear flow stabilization experimental campaign raised several important questions. How is the current divided among the wires forming the array, on one hand, and the central wire, on the other hand? How much of a dense core remains in the central wire?

An answer to the first question can be given by direct measurement. At present we are working on adding current measurements closer to and inside the load. Additional diagnostics would help our understanding of the phenomena observed. Among them, the optical and laser imaging diagnostics would also help improve the quality of the comparison between the experimental results and the ones obtained by simulation.

In parallel complementary loads will be added to the study. A much finer wire (most probably 20 μm Ti) will be used on axis, so that the available current will be enough to convert it into plasma. In this way the stabilizing effect of the conical array can be studied in more valid conditions. As reference, as well as to observe the stability of a flowing plasma, conical and cylindrical arrays with no central structure will be used in future experiments. These tests, along with some with a central wire made of the same material as the array, are also useful for testing the MHRDR simulations.

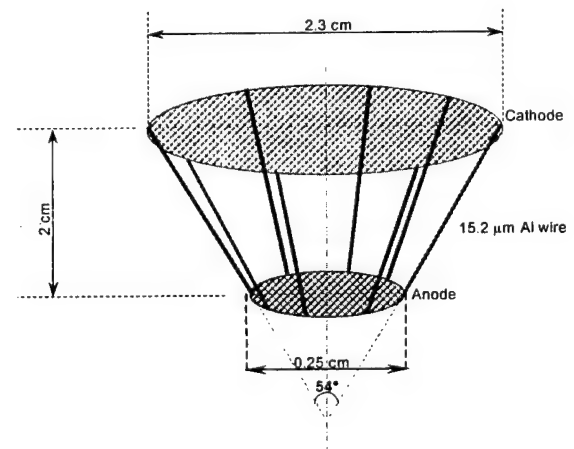
3.2.1. MHRDR modeling of conical array implosions

Theoretical and computational studies have revealed the stabilization effect of a sheared axial flow of plasma. We have initiated experimental and computational studies of conical wire arrays (with and without a central wire) to study the effect of shear flows on z-pinch stabilization. The purpose of these studies is: 1) To determine the magnitude of sheared flow attainable with conical wire arrays, and 2) To assess the effect of the resulted shear flow on the stability of a wire located in the center of the array. The possibility of using the resulted shear flow in a staged z-pinch geometry is also a goal for future studies.

2D r-z MHD simulations of conical wire arrays have been started using MHRDR, a 2D-MHD, Eulerian simulation code. As initial conditions it was assumed that the wire array had merged into an uniform shell 1-mm-thick, and with a temperature of 1 eV, at 20 ns from the beginning of the current rise (56.5 kA total initial current). For these simulations a one temperature model was used, coupled to SESAME tables for resistivities, opacities, and the equation of state. The computational mesh had 48 cells in r and 40 cells in z. The calculations were carried out up to 100 ns. The background density and temperature of the vacuum region were 10^{-4} kg/m^3 , and 0.025 eV, respectively.

Figure 3.2.11. Conical wire array parameters:

- wire material: Aluminum ($Z=13$)
- wire diameter: $15.2 \mu\text{m}$
- number of wires: 8
- array diameter @ anode: $0.9 \text{ inch} = 2.286 \text{ cm}$
@cathode: $0.1 \text{ inch} = 0.254 \text{ cm}$
- array radius: @anode: 11.43 mm
@cathode: 1.27 mm
- height: 2 cm
- total current: 1MA / rise time 130 ns
(0-100%)
- total mass in the array: $78.4 \mu\text{g}$
- angle to vertical: 27°



Computer simulation parameters (warm start):

- shell thickness: 1mm
- shell temperature: 1 eV
- shell inner small radius: 0.77 mm
- shell outer small radius: 1.77 mm
- shell inner large radius: 10.93 mm
- shell outer large radius: 11.93 mm
- volume of conical shell: $0.81 \times 10^{-6} \text{ m}^3$
- density of shell: 0.097 kg/m^3

The following pictures show contour plots of the plasma density beginning at 20 ns and up to 100 ns. The horizontal axis is the array radius (meters) and the vertical axis is the array height (meters).

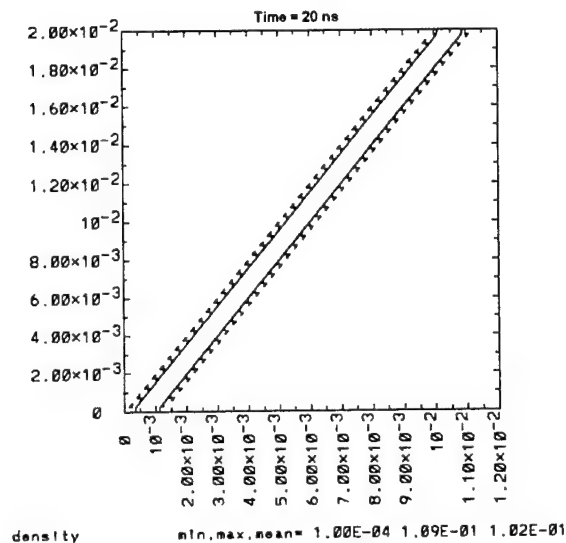


Figure 3.2.12a. Plasma density at 20 ns.

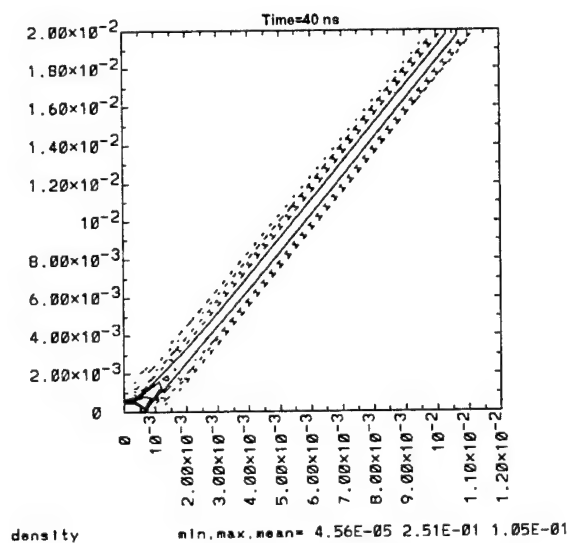


Figure 3.2.12b. Plasma density at 40 ns.

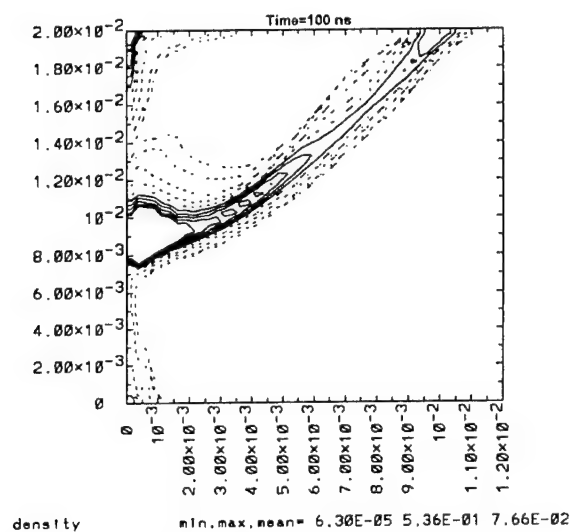
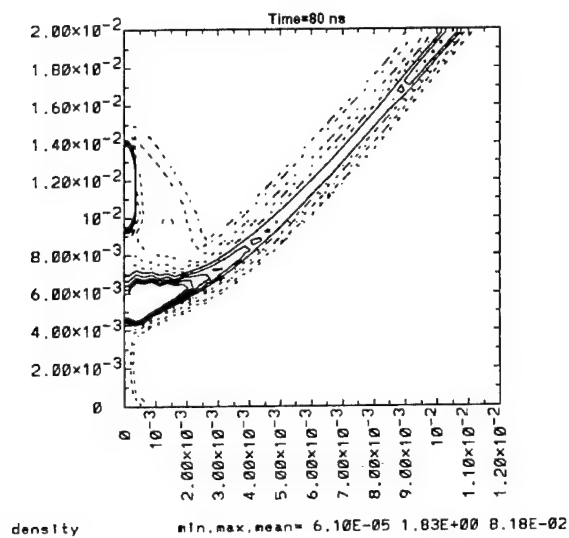
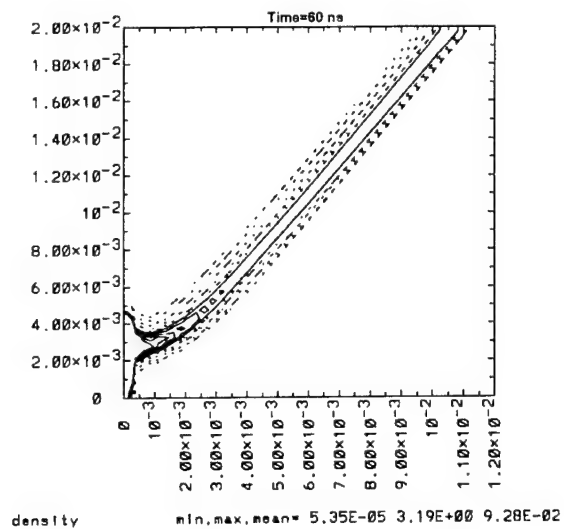


Figure 3.2.12c-e. Plasma density at 60, 80, and 100 ns.

The simulation shows that it is possible to obtain large axial velocities with a large shear close to the pinch axis, as shown in the following two figures.

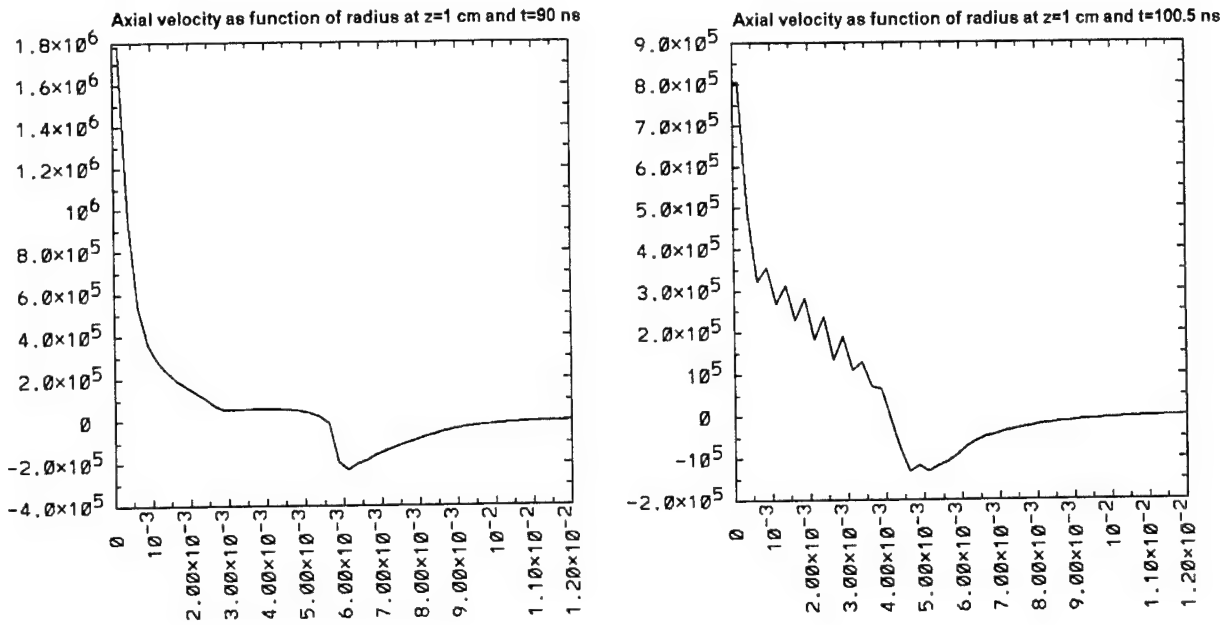


Figure 3.2.13. Axial velocity as a function of radius at the z-pinch midplane, at 90 and 100.5 ns.

Velocities much larger than the ion sound speed are obtained on the axis at 75 ns and 90 ns (high Mach numbers) suggesting that conical arrays are appropriate for studies of z-pinch stabilization with shear flow.

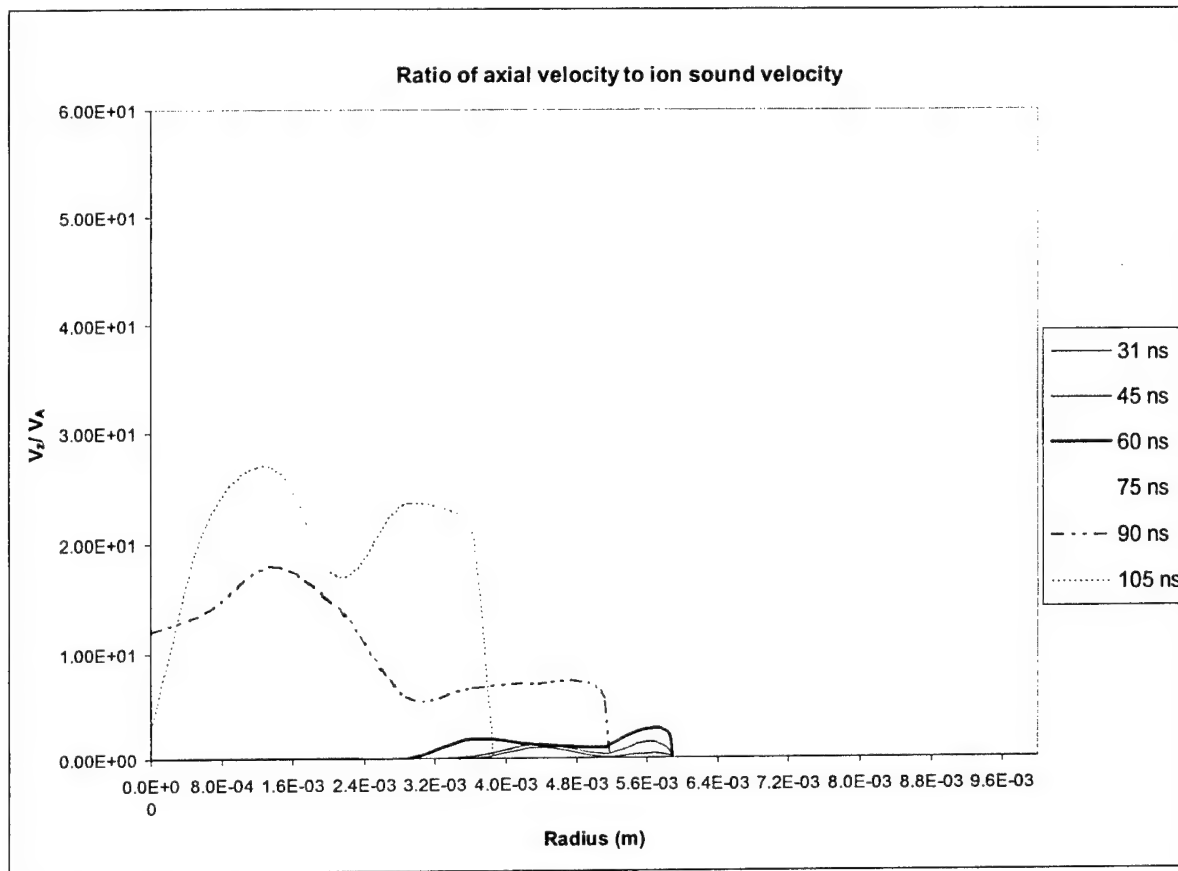


Figure 3.2.14. Ratio of axial velocity to ion sound velocity, as a function of radius, at various times.

These simulations do not take into account the development of Rayleigh-Taylor instability so we expect that future results will be somehow different. Better initial conditions (temperature and density profiles; initial magnitude of the current + start time) for the 2D r-z conical array are expected to result from 1D/2D r-z cold start simulations of single wire explosions. Two temperature models, coupled to SESAME tables will be used in the future. Experiments will provide additional data needed for the code calibration, in order to better optimize and predict the results of future experiments. The next step will be simulations of conical array implosions on central wire and the study of the effect of the shear flow produced in this way on the pinch stability.

3.3. Explosion of wires driven by Z-like and faster prepulses

The heating and expansion of wires with current prepulses similar to, and faster than, those at Z (SNL) has been investigated. Individual W, Mo, Ti, Ni, Fe, Au, Cu, Al, Ag, or Au-plated W wires of diameter 4-40 μm are exploded with a fast kiloampere pulse fed from a 9-m-long 50-ohm coax. The wire current, voltage, emitted light, and wire expansion velocity are measured as a function of time with electrical, optical, and laser diagnostics, throughout the explosion. Exploding wires will also be observed with x-ray backlighting, with several x-pinch backlighters driven by Zebra, and with gated optical imaging.

The characteristics of the wire explosions are observed to depend dramatically on the rate of rise of the current, on the heat of vaporization of the wire material, and on the diameter of the wire.

The efficiency of heating of fine wires driven by high current is observed to improve dramatically with an increased rate of rise of the driving current. Wires were driven by a 12.6-J electrical pulse, with, alternately, a 40-80 A/ns current rise (4-8 kV/ns voltage rise) or a 10-20 A/ns current rise (0.8-1.6 kV/ns voltage rise). The slower rise is characteristic of the prepulse through individual wires on Z, where wires are exploded with a prepulse current that rises at 23-29 A/ns (7 kA/ns applied for 50 ns to an array of 240-300 fine wires). Fast-rising current pulses produce an expansion many times faster than that produced by slow-rising current pulses.

The absorption of energy by high-current-driven wires is a two-stage process. Initially, the wire heats efficiently. Suddenly, a low-resistance plasma forms around the wire, and most of the current is shunted into it. The voltage collapses, the power absorbed by the load decreases, and that power mostly goes into the plasma rather than into the wire. The heating of the wire becomes very inefficient. The load can contain a cold, even solid, core for a long time.

Increasing the rate of rise of the driving current pulse is a new method to increase the efficiency of wire heating. Previously, the energy absorbed was increased by delaying the onset of plasma formation, either by degassing the wire¹ or by insulating it². Here it is shown that the energy absorbed can also be increased by increasing the rate of rise of the driving current pulse. This dramatically increases the energy absorbed by all wires, whether untreated, degassed, or insulated. Remarkably, the time to flashover, from the start of the pulse, decreases only a little for a substantially faster rising pulse. Thus the energy absorbed by the wire, prior to flashover, can be increased dramatically, by steepening the pulse rise.

A fast-rising prepulse, in conjunction with preheated or insulated wires, could yield a plasma without a cold core, quicken the formation of a plasma shell from wire arrays, and lead to increased x-ray power from wire-array implosions. The initial perturbations for the magneto-Rayleigh-Taylor instability (that degrades plasma compression) arise in the plasma formed from the exploded wire array. Increased peak x-ray power correlates with decreased wire gap, presumably because this leads to earlier merging of the exploding wires and formation of a

¹ S.A. Pikuz, T.A. Shelkovenko, A.R. Mingaleev, D.A. Hammer, and H.P. Neves, *Phys. Plasmas*, 6, 4272 (1999).

² D.B. Sinars, T.A. Shelkovenko, S.A. Pikuz, M. Hu, V. M. Romanova, K.M. Chandler, J.B. Greenly, D.A. Hammer, and B.R. Kusse, *Phys. Plasmas Lett.* 7, 429 (2000).

smoother plasma shell. Efficient explosion of array wires, minimizing the cold-core / hot-corona phenomenon, would lead to earlier merging of the exploded wires into a plasma shell. This shell might be smoother, because perturbations would have less time to grow while the shell was forming.

For substances with high vaporization energy (W, Mo, Ti, Ni, Fe, Au-plated W), in particular, a fast-rising current pulse deposits much more energy into a fine wire than does a slower-rising, Z-like pulse. For both the fast-rising and slow-rising pulses, the load resistance increases many times from its room-temperature value, as the wire heats, and then collapses in a few ns to a very small value, when flashover occurs. The time to flashover, from the start of the pulse, is only a little shorter (e.g., 30 ns vs. 40 ns, for a 16.2- μm -diameter tungsten wire) for the fast-rising pulse than for the slow one. This results in a substantial increase in the energy absorbed by the wire (e.g., 3 times more, for a 16.2- μm -diameter tungsten wire), prior to flashover, when it is driven by the fast-rising pulse. After flashover, heating of the wire becomes very inefficient. Thus, for example, with the slow-rising pulse through a 16.2- μm -diameter tungsten wire, the wire does not melt before flashover, and the electrical pulse mostly just disintegrates the wire into solid parts, with a piece often remaining attached to the cathode after the discharge. In contrast, with the fast-rising pulse, a 16.2- μm -diameter tungsten wire melts before flashover, and subsequently explodes at ~ 1 km/s.

Low-vaporization-energy-material (Au, Cu, Al, Ag) wires quickly become completely transparent to 905 nm light for fast explosions (no opaque central region persists). Al wires become transparent sooner than Au or Cu wires. In contrast, an opaque central region persists at least 100 ns for slow-rising-current explosions. The expanding radial density distribution is thus markedly different for fast-rise and slow-rise current pulses, for the same wire and the same pulse energy.

For fast explosions of 20.3- μm -diameter wires, the velocity of wire expansion is inversely proportional to the square of the heat of vaporization of the wire material. Al and Fe don't quite follow this relationship, possibly because of oxidation of the wire surface.

For fast explosions of W wires, the expansion velocity increases with the wire diameter. Smaller-diameter wires absorb more Joule energy per atom and still expand more slowly than larger-diameter wires. This indicates that their higher internal kinetic pressure is compensated by their higher inward magnetic field pressure, which is inversely proportional to square of the wire diameter. During the fast pulse, 7.9- μm - and finer-diameter W wires experience a magnetic pressure in excess of the critical pressure of tungsten (337Mpa). In this case, as the wire is heated, an overcritical phase transition from liquid takes place — liquid tungsten transforms into gas and plasma without separation into liquid and gas phases.

A summary description of the experiment and the main results follows. The measurements are being compared with MHRDR simulations at UNR (Section 3.3.3).

3.3.1. Experimental setup

The experimental setup is shown in Figures 3.3.1 and 3.3.2. A 50-kV Maxwell 40167 trigger amplifier triggers a 100-kV Maxwell 40151-B pulse generator with a stored energy of 12.6 J that provides the current and voltage used to drive the wire explosions. A 50- Ω , 9-m coaxial transmission line delivers the positive-voltage pulse from the generator to the wire. The setup produces a fast pulse with a 170 A/ns current rise into a short-circuit, or, with an inductor inserted before the generator output, a slower pulse with a 22 A/ns current rise into a short-circuit. The slower rise is characteristic of the prepulse through individual wires on Z. The electrical pulse is applied to a single wire that is 2 cm in length and varies in diameter from 4 to 40 μm . The wire forms the central conductor of a coaxial line evacuated to a pressure of $\sim 10^{-5}$ torr before the explosion to prevent arcing between the anode and the cathode or surrounding coaxial ground.

The current flowing through the wire is measured with a 2-GHz bandwidth shunt resistor, and the voltage drop across the wire is measured with a low inductance, passive high-voltage probe (100kV, 1.5ns rise time). The current into the wire and the voltage at the output of the transmission line are now also measured with a Bdot and a Ddot probe. From current and voltage data, the resistive component of the voltage, the load resistance, and the joule heating of the load can be determined throughout the wire explosion. The difference between the current entering the anode-side of the wire and leaving the cathode-side of the wire is also measured; this corresponds to current lost through arcing to the return-current outer conductor.

The evolution of light energy emitted from the exploding wire is monitored by a PIN diode with a rise time of less than 1 ns. The diode is one focal length behind a large collecting lens, so that the efficiency of light collection is equal for all points in the plasma, within a 1-cm wide by 2-cm long window. This provides comparative information on the emitted-light power of different wire substances and diameters.

Streak camera (Hamamatsu C-1587-01) shadow images of the wire during the explosion are obtained using a high-power diode laser (905 nm, 10 W, 200 ns, 0.1 ns jitter) as a backlighter (a long-pulse Nd-glass laser – 527 nm, 100 mJ, 50 ns – was previously used). From these streak images, the plasma expansion velocity (at the sharp plasma density jump from 10^{20} cm^{-3} to an order of magnitude higher or more) and the starting time of the explosion are determined.

Time-integrated (open-shutter) visible-light CCD images of wire explosions give information on the 2-dimensional structure of the energy deposition in visible light in and around the wire loads.

An imaging spectrometer (Chromex 500is with a 100 grooves/mm grating, recorded by a CCD camera) observes the optical spectrum emitted, showing the impurities in the explosion and allowing an estimate of the temperature.

Interferometry and shadowgraphy have been used to observe the electron density profile and the development of plasma instabilities.

The current, voltage, PIN diode, and streak-camera-sync-output waveforms are captured by a 4-channel, 1-GHz digital scope (Tektronix TDS 684C, 5 GS/s), with a time axis cross-correlated to that of the streak camera images.

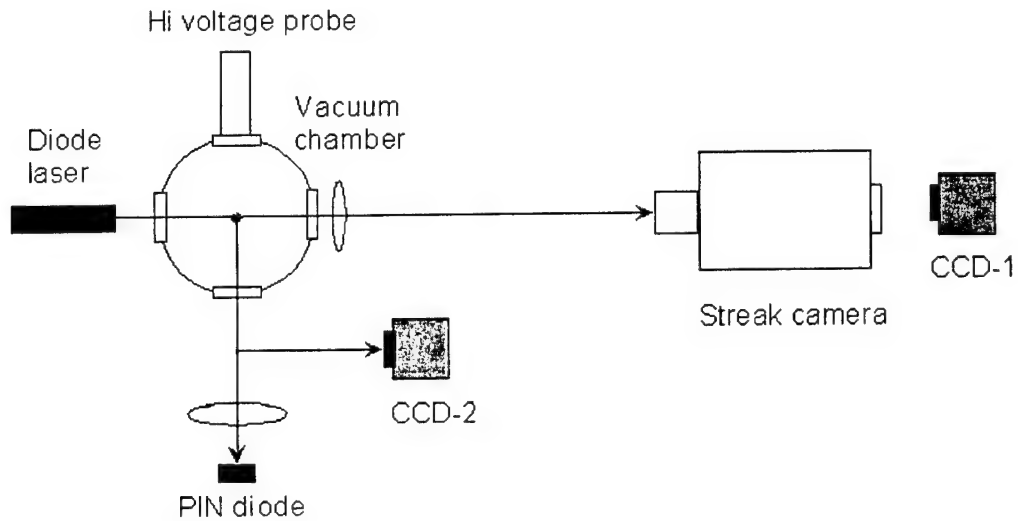


Figure 3.1.1. Experimental setup

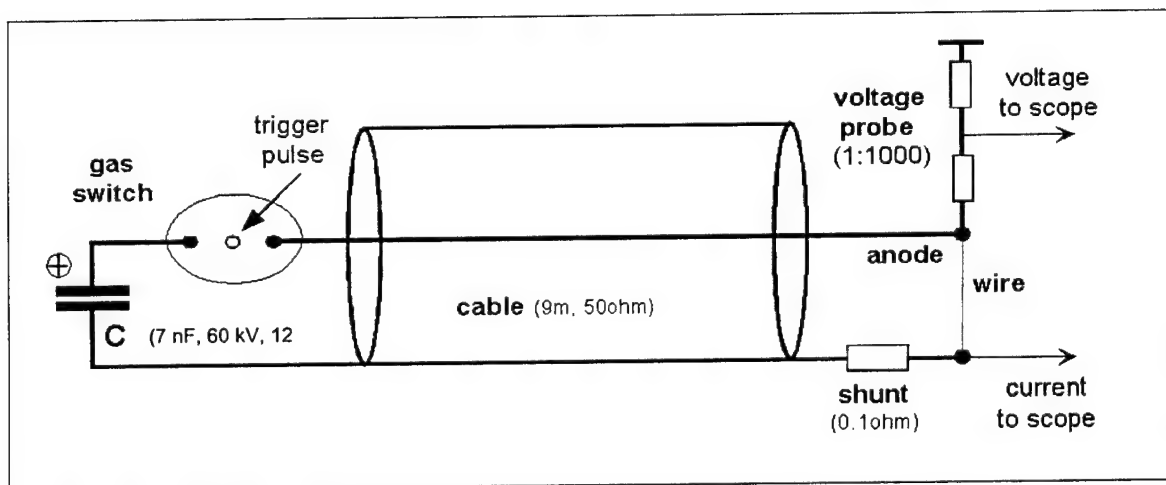


Figure 3.3.2. Electrical schema of experiment

3.3.2. Experimental results

The experimental results are considerably different for substances with a high heat of vaporization (W, Mo, Ti, Ni, Fe) than for those with a low heat of vaporization (Au, Cu, Al, Ag). Au-plated W represents an interesting combination of the two material types. An Au-plated W wire initially follows the behavior of an Au wire, and subsequently, the behavior of a W wire.

In this section, the increase in energy deposition with a fast-rising pulse is shown for 16.2- μ m-diameter W wires. Results for other wire materials and diameters are presented in subsequent sections.

Typical time-integrated images of exploding 16.2- μ m diameter and 2-cm long W wires (Fig. 3.3.3) show big differences in the energy deposition structure between the explosions driven by fast and slow pulses. The fast pulse produces a homogeneous "cylindrical" (a) or a "conical" (b) structure. The "conical" explosion (b) is wider at the anode and narrower at the cathode side. The slow pulse results in many arcs between the positively charged wire and the ground cylinder 2.8 cm away. Part of wire is left unvaporized (d) after the slow pulse shot (c). For the cylindrical (a) and the conical (b) explosion modes, the region surrounding the wire glows brightly. For the slow pulse case (c), the light emission is over an order of magnitude less, and comes mostly from the arcs.

The velocity of expansion is dramatically greater for the fast pulse explosion than for the slow pulse case (Fig. 3.3.4, with data from the shots shown in Fig. 3.3.3). The velocity of expansion in the middle of the 16.2- μ m diameter W wire is 0.83 km/s for the fast cylindrical explosion mode (Figs. 3.3.4a and 3.3.3a), 0.59 km/s for the fast conical explosion mode (Figs. 3.3.4b and 3.3.3b), and 0.15 km/s for the slow-pulse explosion (Figs. 3.3.4c and 3.3.3c). In the slow-pulse explosion, the wire expands only in the region where the off-axis lightning is absent. The wire remains unvaporized in the region with off-axis lightning. The wire starts to expand after the voltage reaches the maximum value, i.e., after flashover. The expansion proceeds at a constant speed, indicating minimal heating of the wire after flashover.

The temporal evolution of voltage (1), current (2), and deposited joule energy (3) for fast cylindrical (a) and slow (b) explosion modes of 16.2- μ m diameter W wire is presented in Fig. 3.3.5. For both types of explosions, the voltage reaches a maximum and then collapses in a few ns to a very small value, when flashover occurs. The power into the load is 7 times greater for the fast pulse than for the slow one, peaking at 60 MW in the first case, and at 9 MW in the latter. The time to flashover, from the start of the pulse, is only a little shorter (30 ns vs. 40 ns) for the fast-rising pulse than for the slow one. The result is that 3 times more energy is absorbed by the wire, when it is driven by the fast-rising pulse.

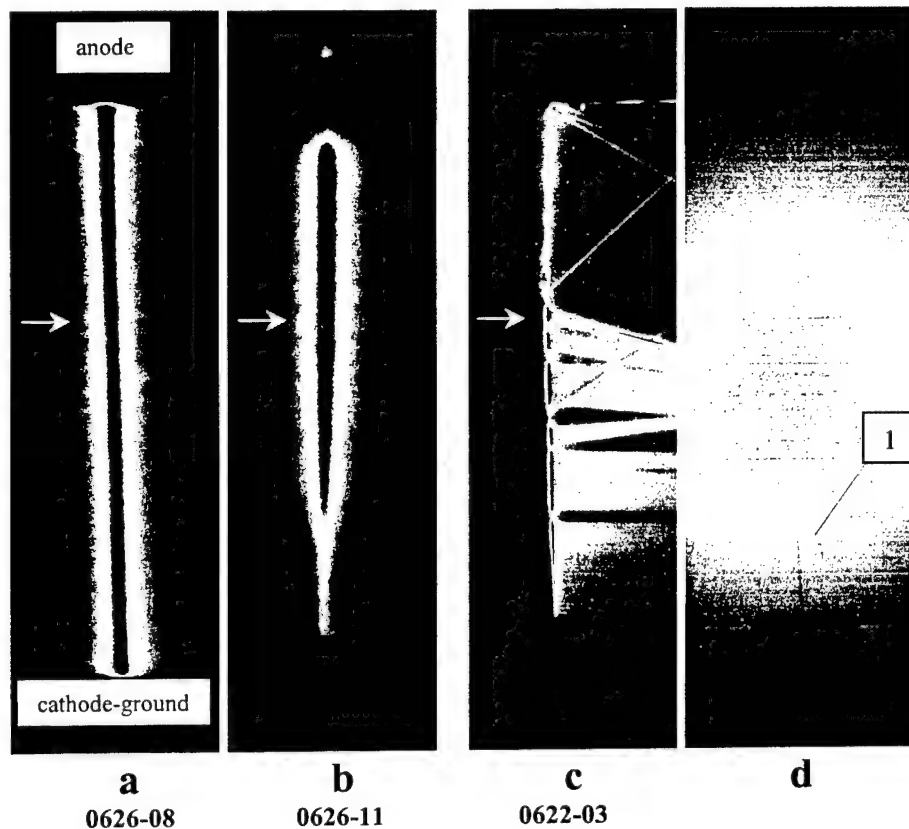


Figure 3.3.3. Time-integrated CCD images of 16.2- μm diameter and 2-cm long W wire explosion: (a) fast cylindrical explosion; (b) fast conical explosion; (c) slow explosion -- note off-axis arcing; (d) the cathode-anode gap after the shot (c) -- note unvaporized wire (1). The arrows on (a-c) show the cross-section imaged to the streak camera to investigate the velocity of the wire expansion (Fig. 3.3.4.).

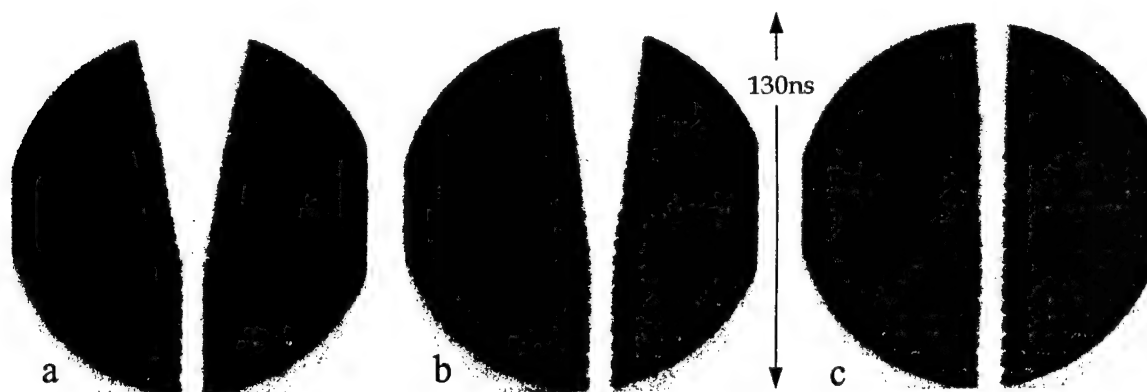


Figure 3.3.4. Radius-time (R-T) streaked laser-shadow images of the expansion in the middle of the 16.2- μm diameter W wire. R-T images (a), (b), (c) correspond to time-integrated images (a), (b), (c) in Fig. 3.3.3

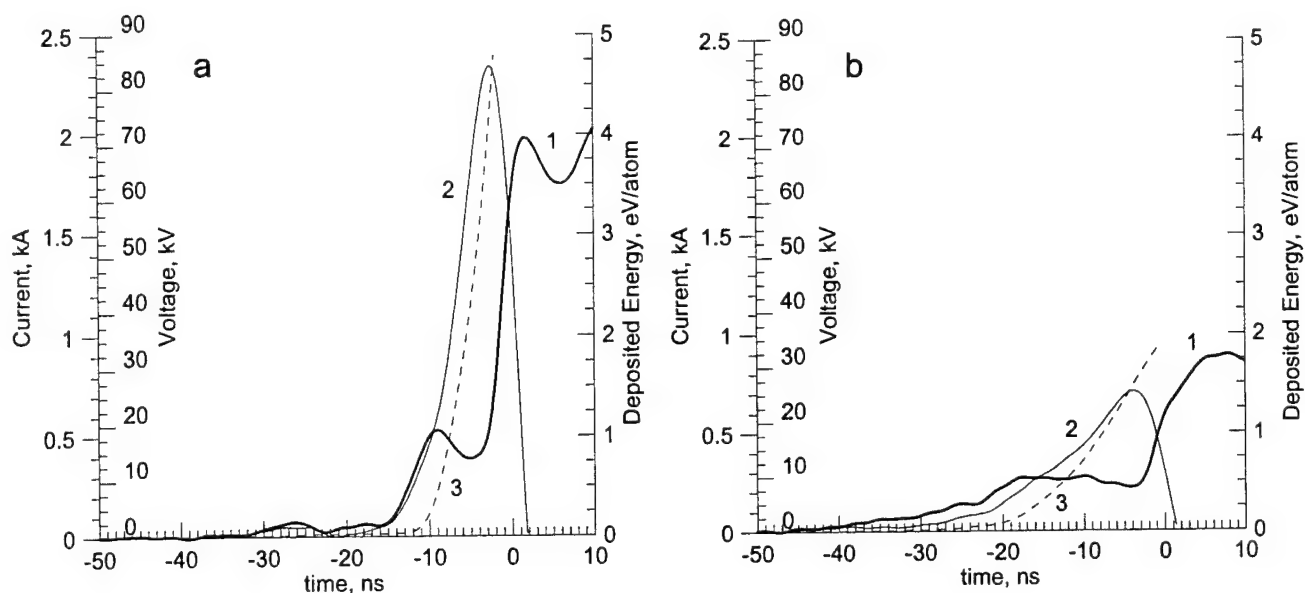


Figure 3.3.5. Temporal evolution of the current (1), voltage (2), and deposited joule energy (3) for fast (a) and slow (b) explosions of 16.2- μm W wires.

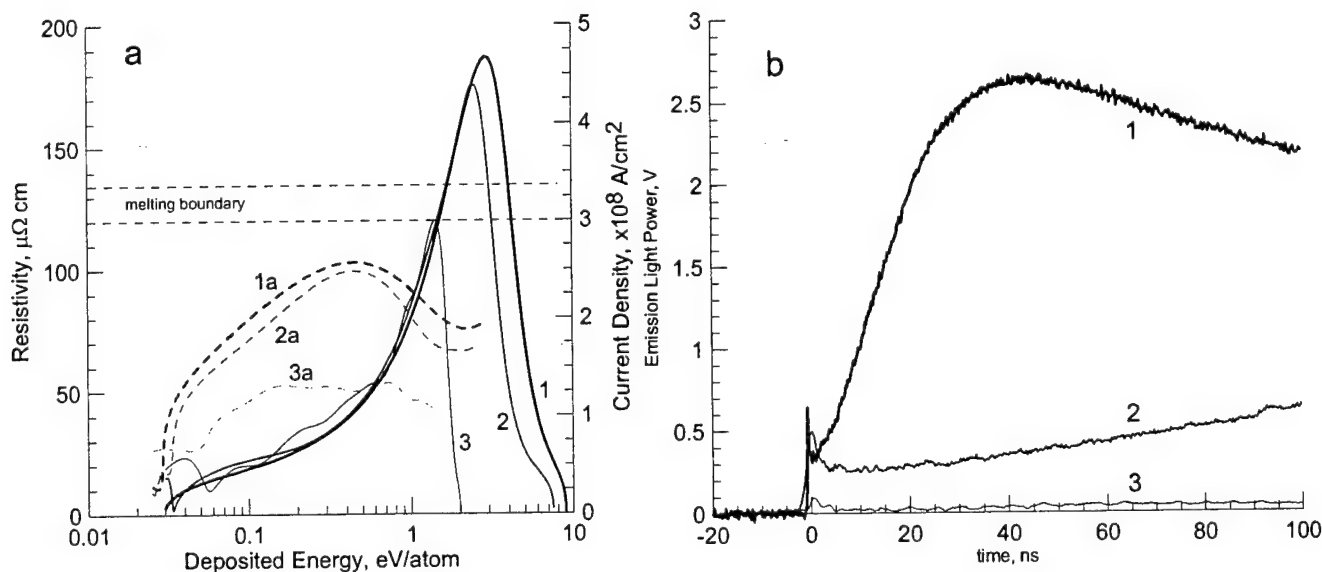


Figure 3.3.6. (a) Dependence on deposited energy of load resistivity (1,2,3) and corresponding current density (1a, 2a, 3a) for the fast cylindrical (1,1a), fast conical (2,2a), and slow (3,3a) explosion modes of 16.2- μm W wires. (b) Evolution of the emitted light power for the fast cylindrical (1), fast conical (2), and slow (3) explosion modes of these wires.

The dependence of load resistivity and current density on deposited energy for fast cylindrical (1), conical (2), and slow (3) explosion modes is presented in Fig. 3.3.6a. Initially, all three resistivity curves (1,2,3) coincide. The only difference is the point at which flashover occurs -- at 3 eV/atom, 2.5 eV/atom, and 1.5 eV/atom for the fast cylindrical (1), fast conical (2), and slow (3) explosion modes, respectively. For fast explosions the wire resistivity (1) reaches 180-200 $\mu\Omega\cdot\text{cm}$, far above the melting boundary [5], corresponding to the saturation plateau in [13]. In contrast, the resistivity with the slow-rising pulse (3) only reaches 120 $\mu\Omega\cdot\text{cm}$, below the melting boundary [5].

The current densities before and at flashover (Fig.3.3.6a) are substantial -- $2 \times 10^8 \text{ A/cm}^2$ for fast-rising pulses, and $1 \times 10^8 \text{ A/cm}^2$ in the slow-rising case. The magnetic field at the wire surface at flashover is 100 kG and 50 kG, for the fast- and slow-rising pulses, respectively. For a uniformly distributed current, this corresponds to a difference in magnetic pressure (B^2/μ_0), between the surface and the center of the wire, of 80 MPa and 20 MPa, respectively -- about 20% and 5% of the critical pressure for W. The high magnetic field perhaps delays flashover, which occurs at higher deposited energy and higher current density for the fast-rising pulse than for the slow-rising one.

The temporal evolution of the light emission from fast cylindrical (1), fast conical (2) and slow (3) explosions of 16.2- μm diameter W wires is presented in Fig. 3.3.6b. The extremely fast rising initial spike of light (at time $t = 0$) coincides in time with the rapid increase in current and the rapid decrease in voltage (Fig. 3.3.5), i.e., with flashover. Fast explosions (especially in cylindrical mode (1)) yield the most light. The radiation is over an order of magnitude weaker for wires driven by the slow-rising pulse. Interestingly, the temporal shape of radiation shown in Fig. 3.3.6b is typical only for W. Other substances give significantly different temporal shapes for the radiation, indicating quite different evolutions of the wire core and coronal plasma. For the fast cylindrical mode of explosion, the temporal shape of the radiation depends very strongly and distinctly on the wire material, but not much on the wire diameter.

In the following sections, results for other wire materials and diameters are presented.

3.3.2.1. Materials with high heat of vaporization (W, Mo, Ti, Ni, and Fe)

Energy deposition varies dramatically between the fast and slow explosions of W, Mo, Ti, and Au-plated W wires (Figure 3.3.7). For the fast-pulse explosion (170 A/ns), the Joule-energy deposition is uniform along the wire axis. This likely indicates uniform current flow along the wire. On the other hand, in the slow-pulse explosion (22 A/ns) of these wires, the energy deposition is not uniform. Variegated off-axis arcing to the coaxial outer cylinder (transmission-line ground) occurs for all wire diameters (Figure 3.3.8). This indicates significant leakage of electrical energy, and lesser deposition of Joule energy inside the wire. For planar off-axis arcing, some of the wire even remains unevaporated after the shot (Figure 3.3.9). (The off-axis arcing occurs preferentially in the direction of minimum distance between the wire and the coaxial outer cylinder; the wire load is slightly displaced from the axis of symmetry of the outer cylinder). The exception to the rule is the 4- μ m-diameter W wire, for which fast-pulse explosions result in off-axis arcing about 90% of the time. The small radius of this wire promotes electron emission and arcing.

In fast-pulse explosions, W, Mo, Ti, and Au-plated W wires display two types of energy deposition: cylindrical and conical explosions (Figure 3.3.10). The cylindrical explosion shows the ideal uniform deposition of energy along the wire, with no dependence of emitted light intensity on the axial location. In the conical explosions, more energy is deposited at the anode than at the cathode.

Fast-current-rise explosions also produce more light than slow-current-rise ones, in accord with more energy deposition into the wire (Figure 3.3.11). Fast cylindrical explosions also emit more than conical ones. The first sharp peak in the emission coincides with the rising current front. For fast explosions, the subsequent evolution varies very specifically with the material, increasing for high-heat-of-vaporization materials, and decreasing for low-heat-of-vaporization materials (Figure 3.3.12). Au-plated W wire represents an interesting combination of the two material types. It initially follows the behavior of an Au wire, and subsequently, with 20 ns retardation, the behavior of a W wire (Figure 3.3.13).

When arcing is absent (fast explosions), the region around the wire becomes luminous (compare Figures 3.3.7a and 3.3.7b). With better energy deposition, enough hot expanding material is produced to be observed.

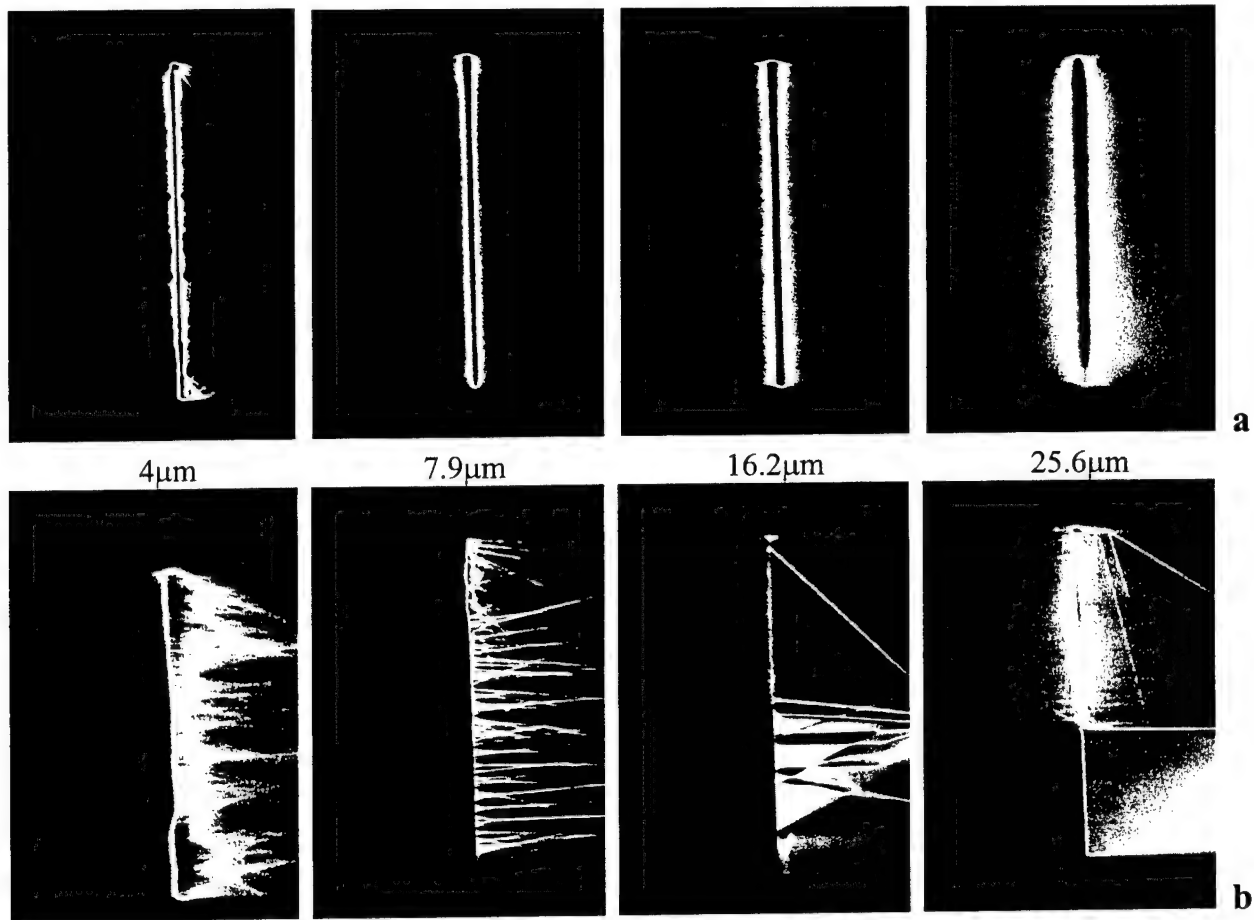


Figure 3.3.7. (a) Time-integrated CCD images of W wire explosions driven by a fast-rising pulse for four wire diameters, showing uniform energy deposition along the wire. The wire substance and diameter are given below each image. (b) Images of slow-pulse explosions for the same wire substances and diameters. Off-axis arcing to opposite current cylinder indicates big leakage of electrical energy.

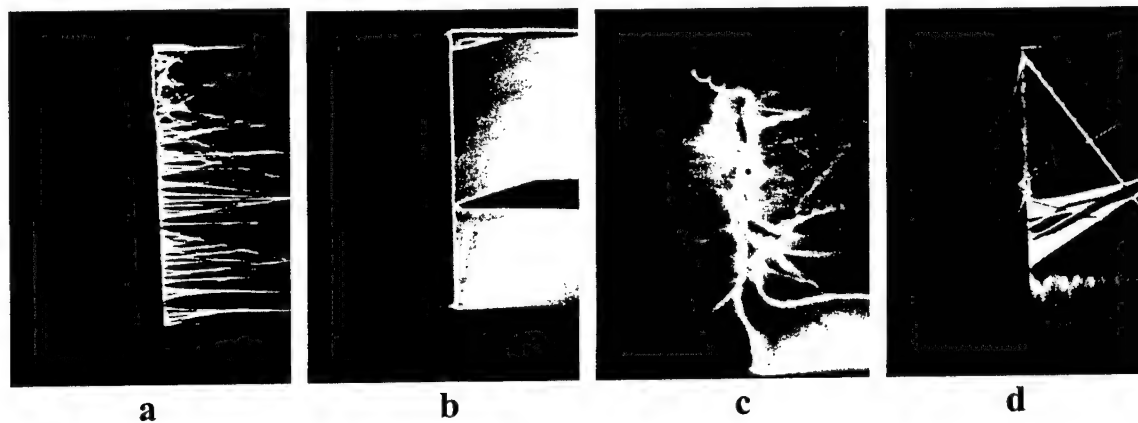


Figure 3.3.8. Different types of arcing for slow exploding W wire. Linear arc (a), planar arc (b), linear arc with kink instability (c), planar arc with aurora instability (d).

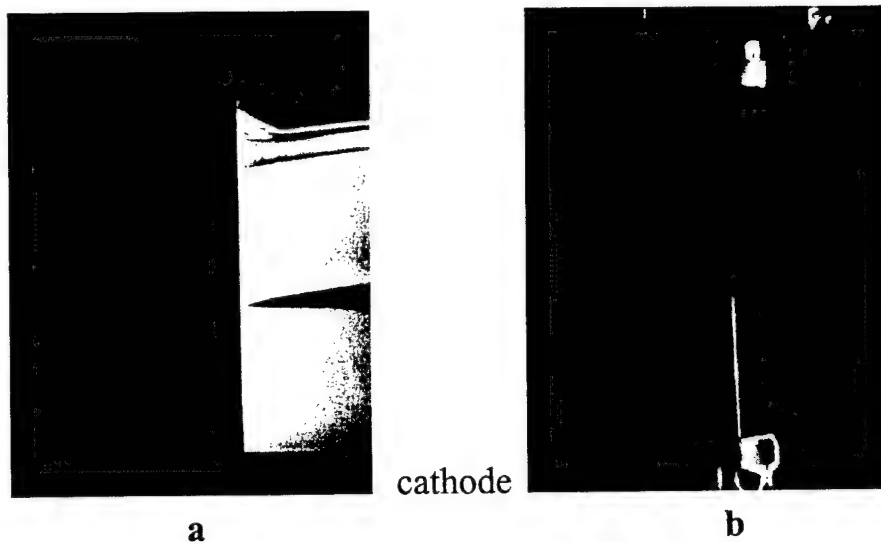


Figure 3.3.9. Slow-pulse explosion of 10.2- μm -diameter W wire: during explosion (a) and after explosion (b). After planar off-axis arcing cathode part of the wire remains unevaporated.

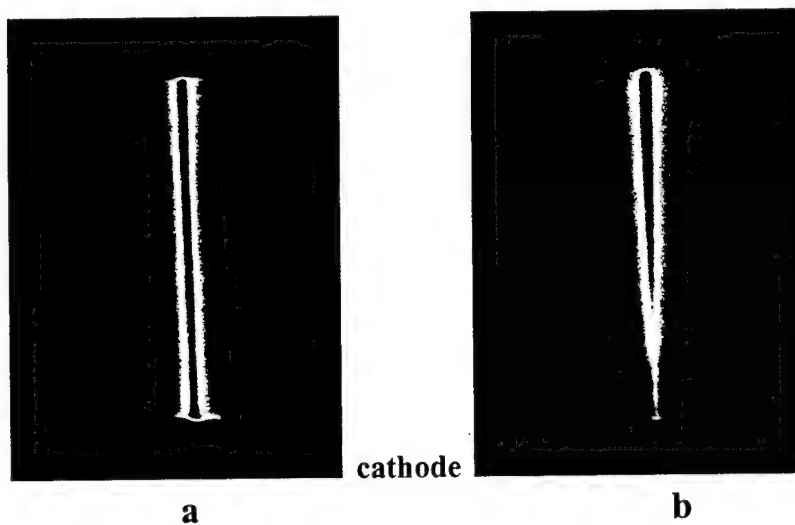


Figure 3.3.10. Two modes of fast-pulse explosions of 12.7- μm -diameter W wires. There is homogeneous deposition energy for cylindrical explosion (a). In the conical explosion (b), more energy is deposited at the anode than at the cathode.

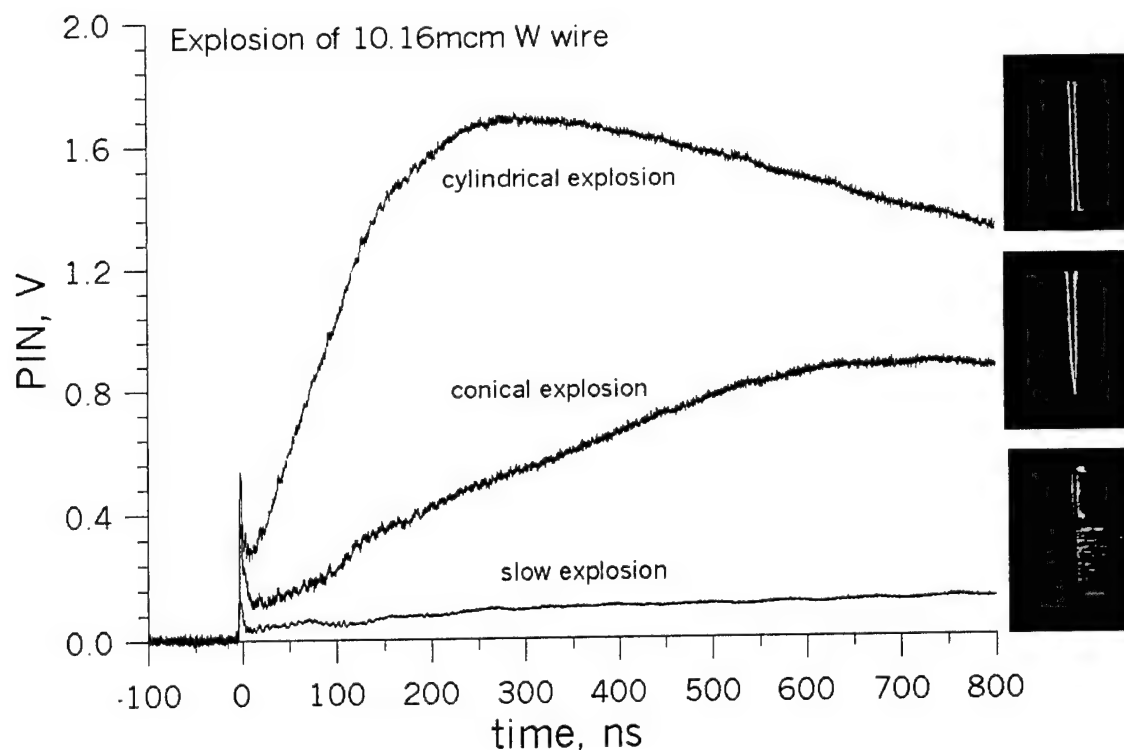


Figure 3.3.11. Emission of the light for different regimes of explosion of 10.2- μ m-diameter W wires.

3.3.2.2. Materials with low heat of vaporization (Au, Cu, Al, and Ag)

No off-axis arcing is observed in either fast or slow explosions of Au, Cu, Al, or Ag wires. Both rates of current rise give good quasi-cylindrical explosions and uniform deposition of energy along the wire. However, in slow-pulse explosions, the radial extent of the region of deposited energy is nearly twice as great as in fast-pulse explosions, although the light emitted is significantly less, and the velocities of wire expansion are slower (by a factor of 2-4, for Al and Au). Although no off-axis arcing was observed for these materials, arcing along the wire surface may cause some of the difference between fast and slow explosions.

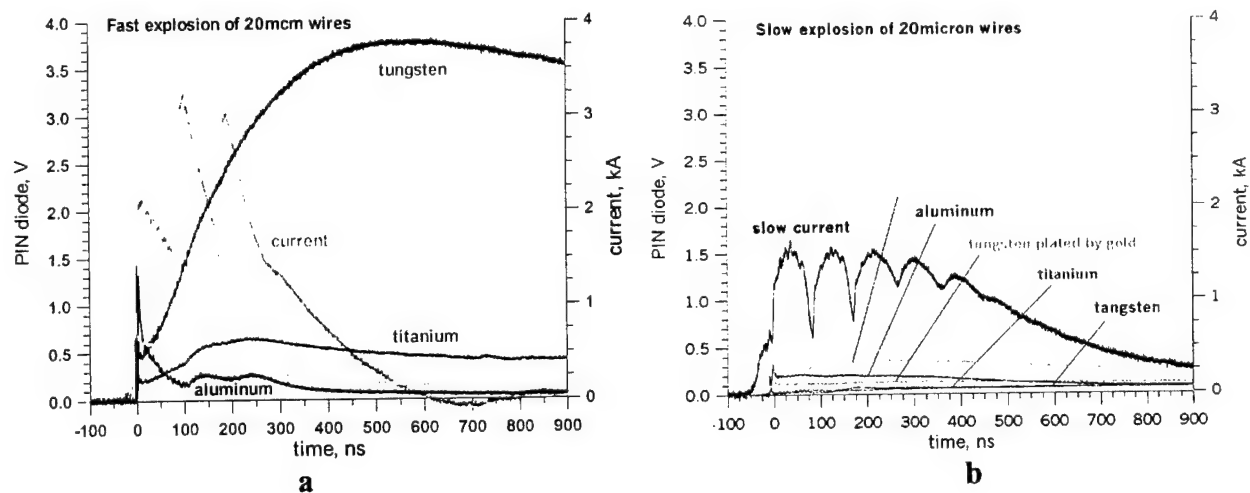


Figure 3.3.12. Emission of light for fast (a) and slow-pulse (b) explosion for 20.3- μ m-diameter wires of different substances. Fast exploding wire gives bigger amplitude and characteristic light radiation.

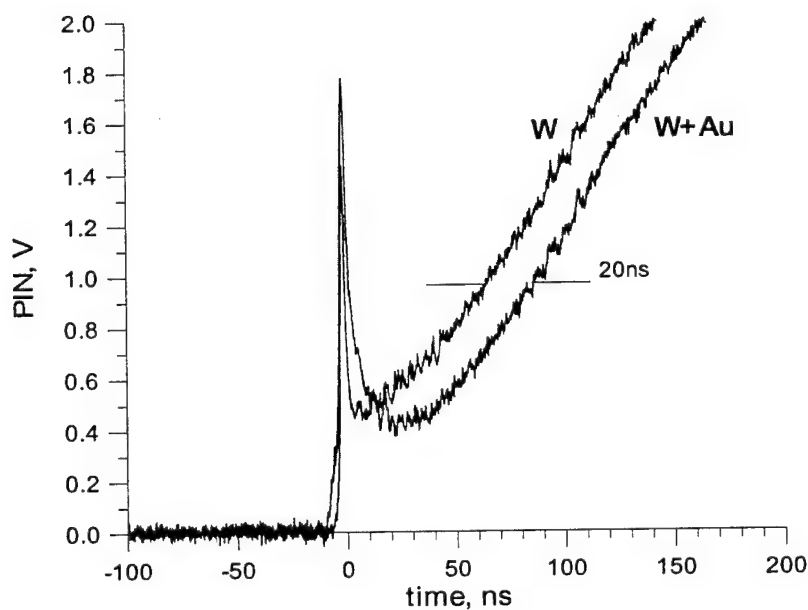


Figure 3.3.13. Emission of light from 20- μ m-diameter W, Au-coated W wires for fast-pulse exploding mode. Gold coating burns out in 20 ns.

3.3.2.3. Plasma expansion, deposition of Joule energy, and magnetic confinement

Magnetic pressure can slow the expansion of exploding wires and change the manner in which plasma is formed.

The expansion velocity of exploding wires as a function of substances and diameters was measured with laser backlighting (532 nm and 905 nm) imaged to a streak camera (Hamamatsu C-1587-01). Typical radius-time diagrams for fast-exploded W wires are presented on Figure 3.3.14 (time flows from the bottom to the top). The 10.2- μm diameter wire explodes with velocity 0.33 km/s, while the thicker 20.3- μm wire explodes with greater velocity, 1.12 km/s. Slow-pulse-driven W wires explode with a velocity nearly 10 times less than fast-pulse-driven ones. For fast explosions of W wires, the expansion velocity is inversely proportional to the wire diameter (Figure 3.3.15). For fast explosions of 20.3- μm -diameter wires, the velocity of wire expansion is inversely proportional to the square of the heat of vaporization of the wire material (Figure 3.3.16). Al and Fe don't quite follow this relationship, possibly because of oxidation of the wire surface.

The evolution of the deposited Joule energy per atom for fast-pulse explosions of W wires as a function of wire diameter is shown in wire Figure 3.3.17. The specific Joule energy absorbed increases with decreasing wire diameter.

Smaller-diameter wires thus absorb more Joule energy per atom and still expand more slowly than larger-diameter wires. This indicates that their higher internal kinetic pressure is compensated by their higher inward magnetic field pressure, which is inversely proportional to square of the wire diameter. Under the same current, a 4- μm -diameter wire will experience 25 times more magnetic field pressure than a 20- μm -diameter wire. During the fast pulse, 7.9- μm - and finer-diameter W wires experience a magnetic pressure in excess of the critical pressure of tungsten (337 Mpa). In this case, as the wire is heated, an overcritical phase transition from liquid takes place – liquid tungsten transforms into gas and plasma without separation into liquid and gas phases.

Interestingly, low-vaporization-energy-material wires quickly become completely transparent to 905 nm light for fast explosions (no opaque central region persists). Al wires become transparent sooner than Au or Cu wires. In contrast, an opaque central region persists at least 100 ns for slow-rising-current explosions and for W wires. The expanding radial density distribution is thus markedly different for fast-rise and slow-rise current pulses, for the same wire and the same pulse energy.

3.3.2.4. Imaging spectroscopy

An imaging optical spectrometer (Chromex 500is with a 100 grooves/mm grating, recorded by a CCD camera) is being used to observe the impurities in the explosion and estimate the temperature. Time-integrated, spatially-resolved (along the wire axis) spectra for fast explosions of 10.6- μm -diameter Al and 7.9- μm -diameter W wires are presented in Figures 3.3.18 and 3.3.19. Spectral lines from H and Cu impurities are observed, in addition to Al and W

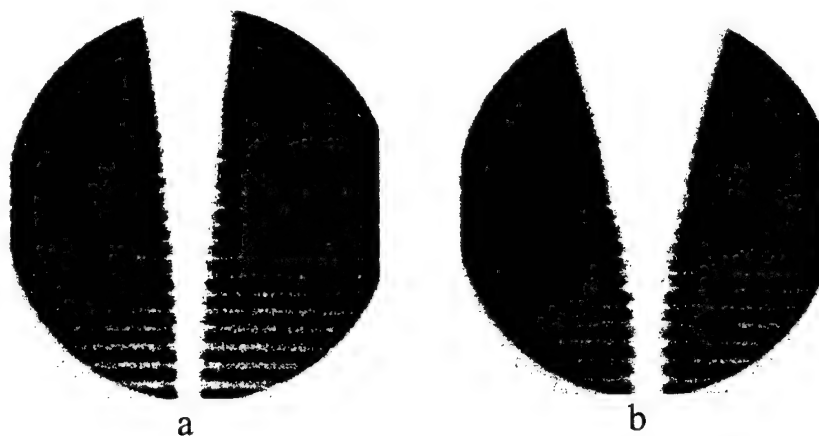


Figure 3.3.14. RT-diagram of fast exploded W wire with diameter (a) 10.2 μm and (b) 20.3 μm .

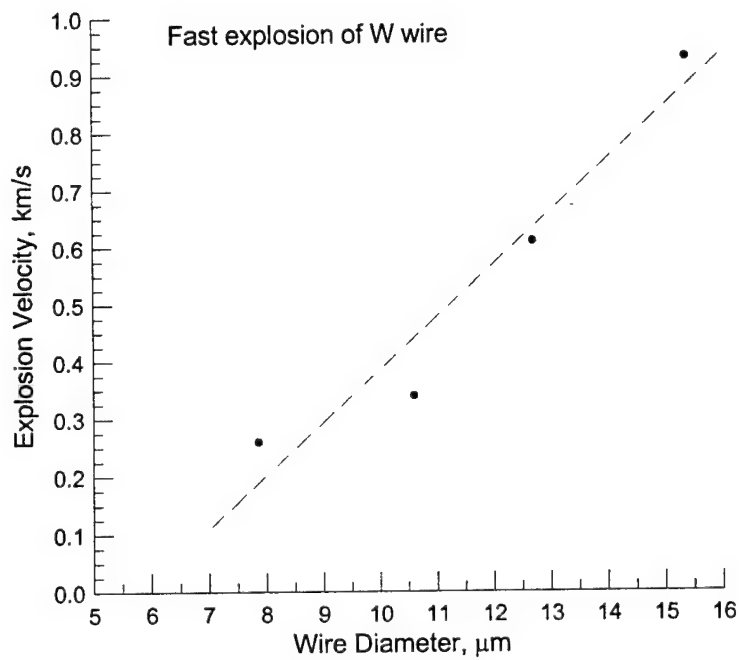


Figure 3.3.15. Dependence of the explosion velocity of fast exploding W wire from wire diameter.

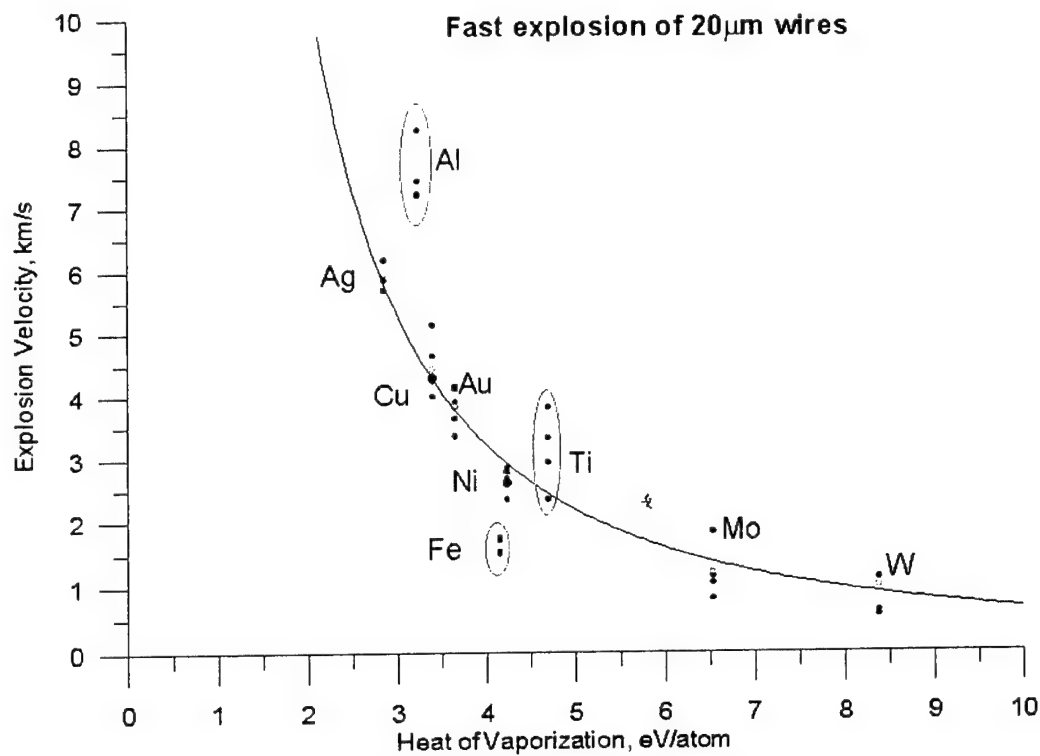


Figure 3.3.16. Dependence of the explosion velocity from heat of vaporization for fast exploding 20.3 μ m wires of different substances.

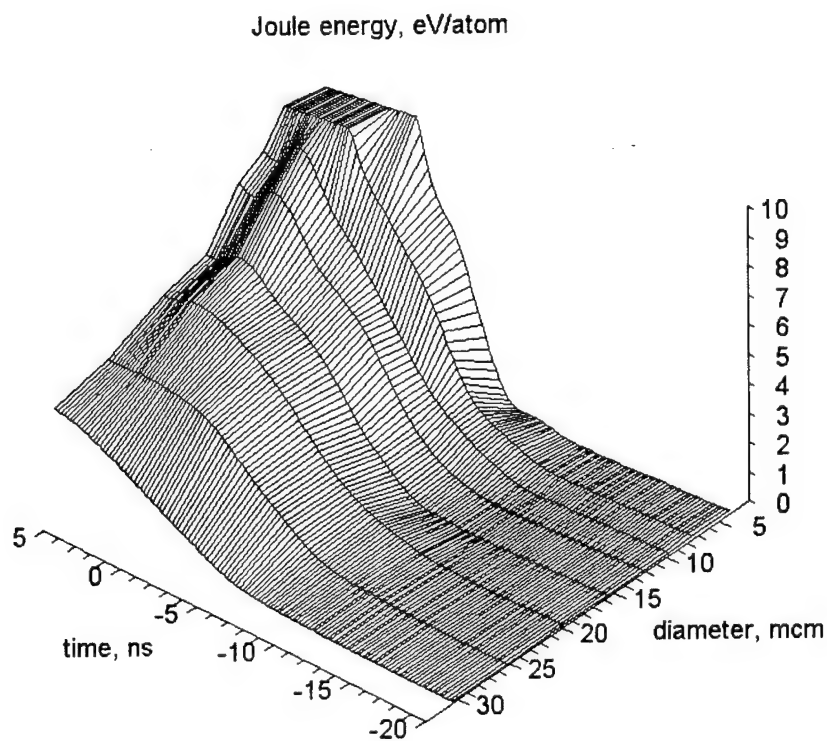


Figure 3.3.17. Evolution of the specific Joule energy for different diameters of fast exploding W wires.

emissions. The ratio of the intensities of the Al^{+2} lines at 448 nm and at 452.9 nm suggests an electron temperature³ of about 5 eV. The temperature of the Al appears higher near the anode and cathode than in between, in concordance with the greater brightness near the anode and cathode seen in the time-integrated CCD images of the Al wire explosions. Time resolved imaging spectroscopy is planned.

3.3.2.5. Interferometry and shadowgraphy

Interferometry and shadowgraphy have been used to observe the electron density profile and the development of plasma instabilities. A Q-switched Nd-glass laser (527 nm, 100 mJ, 20 ns) probed the plasma. The images of wire explosions were captured on CCD camera. An air-wedge shearing interferometer⁴ (Figures 3.3.20) was used, consisting of two 3-degree glass wedges placed between a lens and the CCD camera. The wedges are pressed together, forming a small air gap between them. The reflected beams from the two internal faces of the gap create an interference pattern in the overlapped region in the imaging plane.

Laser interferograms of wire explosions (Figure 3.3.21) were used to estimate the electron density at the initial stage of fast-exploding 12.7- μm -diameter W wires. A cylindrical expansion of the wire is observed, with no disturbance of the interference fringes 65 ns and 140 ns after the start of the current pulse. Estimation of the electron density gives a value less than 10^{19} cm^{-3} in the outer region of the wire. These interferograms, along with two-dimensional shadowgrams (using the same laser), found no evidence of instability in the first 100 ns of explosion. The wire expansion is cylindrically symmetric.

³ J. Bailey, Time-resolved optical spectroscopy measurements of pre-pulse plasma formation on Z, presented at the 26th IEEE ICOPS, Monterey, CA, June 20-24, 1999, USA.

⁴ G.S. Sarkisov, Shearing interferometer with an air wedge for the electron density diagnostics in a dense plasma, Instr. Exp. Techniques, 3, No.5, 727-731 (1996).

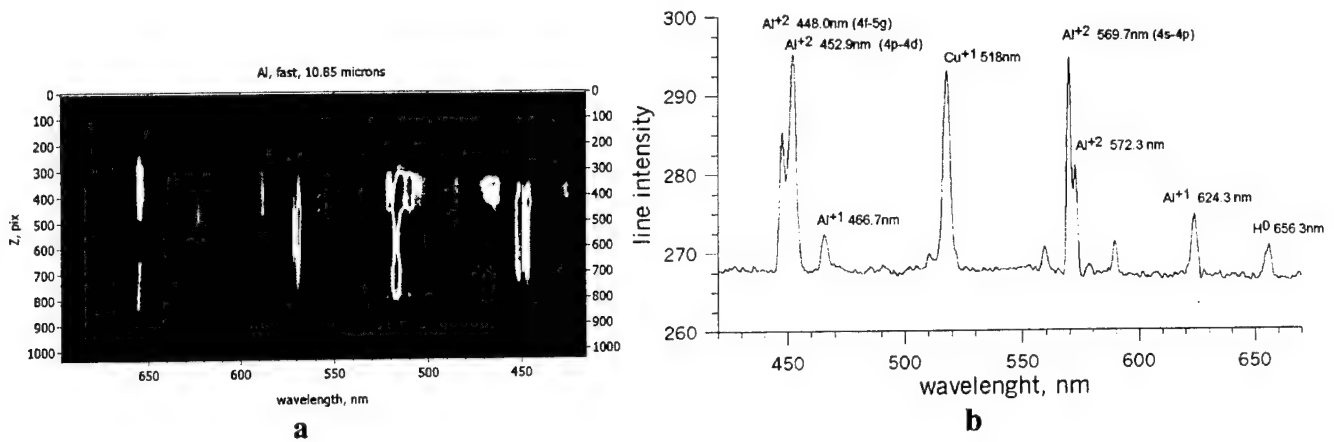


Figure 3.3.18. Spectra of fast exploding 10.9- μm -diameter Al wire (a), and spectral distribution of the line intensity in the middle cross-section (b).

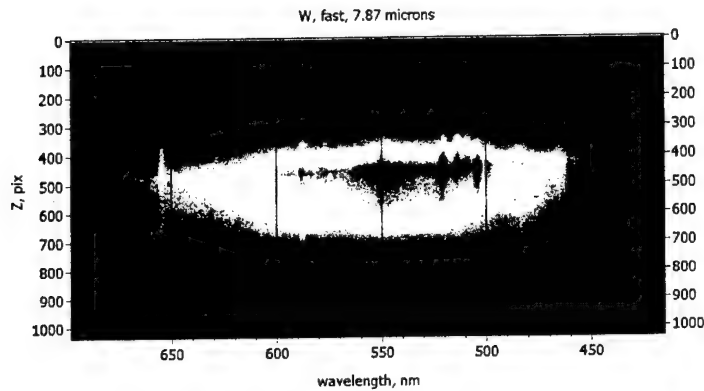


Figure 21. Spectra of fast exploding 7.9 μm W wire.

Figure 3.3.19. Spectra of fast-exploding 7.9- μm -diameter W wire.

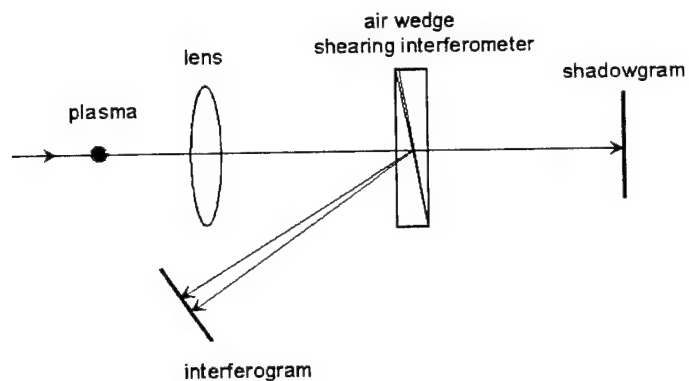


Figure 3.3.20. Optical scheme of shearing interferometer with air wedge.

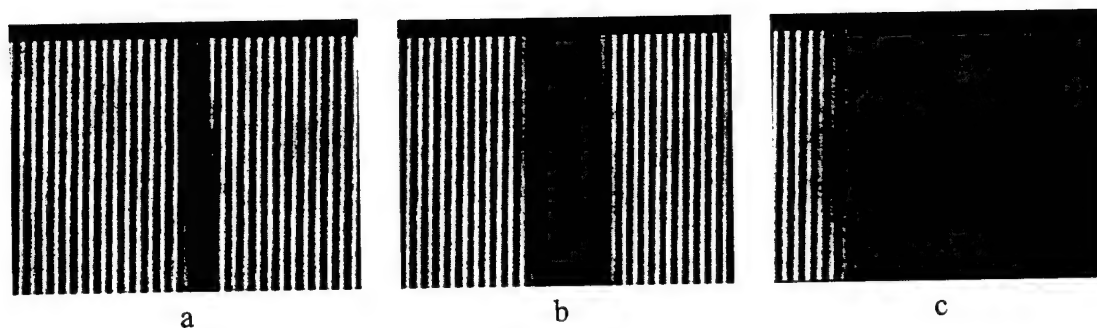


Figure 3.3.21. Interferogram of fast exploding 12.7- μm -diameter W wires before the shot (a) and in a shot (b, c). Probing moments are 65 ns (b) and 140 ns (c).

3.3.3. MHRDR one-dimensional simulations of wire explosions

Modeling has been initiated of the initial stage of wire explosions using the 1D version of the Eulerian Magnetohydrodynamic Radiative Code MHRDR. The parameters of the simulations are those of the experiments described above. The properties of the wire material are modeled by the Los Alamos SESAME tables:

- 201: atomic number, ionic charge, and normal density
- 301: equation of state
- 602: electrical conductivity (modified by Desjarlais, and Rosenthal, SNL for "room" temperatures)
- 505: Plankian opacity (except for tungsten, molybdenum, and gold, for which analytical expressions for radiated flux are implemented).

A test of the MHRDR code, comparing its results with the 1D simulation results of Chittenden et al., is presented first (section 3.3.3.1). This is followed (section 3.3.3.2) by a simulation that examines the strong influence of a coronal plasma on the evolution of wire explosions. Finally (section 3.3.3.3), modeling results for tungsten wire explosions are given, and initial comparisons with the experiments described above.

3.3.3.1. Comparison of MHRDR 1D simulations of the initial stages of a wire explosion with the numerical results of Chittenden et al.

In order to make a comparison with 1D simulation results presented in the paper by Chittenden et al. (Phys. Rev. E, Vol. 61, No. 4, April 2000), MHRDR 1D simulations with identical initial and boundary conditions for an Al wire explosion were carried out. The simulations were initiated with "cold-start" conditions (a solid aluminum wire with mass density $\rho = 2.7 \times 10^3 \text{ kg/m}^3$, at "room" temperature $T = 0.026 \text{ eV}$). The wire diameter $15 \text{ }\mu\text{m}$. It was surrounded by a low density "background plasma" ($\rho = 1.0 \times 10^{-4} \text{ kg/m}^3$, $T = 0.026 \text{ eV}$). The background-plasma approach has proven satisfactory⁵ for z-pinch problems with "cold" and "warm" starts. The current waveform used in simulations was the same as in the Chittenden et al. paper.

The grid was chosen with a ratio of neighbor cells 1.115 and a total length in the radial (r) direction of $4.5 \times 10^{-4} \text{ m}$ ($450 \text{ }\mu\text{m}$). The "cutoff" density was $1.0 \times 10^{-2} \text{ kg/m}^3$. In MHRDR, thermal conduction, ohmic heating (but not resistive diffusion), and shock heating are turned off when density drops below the cutoff density.

In figures 3.3.3.1-3.3.3.6 are presented MHRDR simulation results (Figs. 3.3.3.1, 3.3.3.3, and 3.3.3.5) and simulation results from the paper by Chittenden et al. (Figs. 3.3.3.2, 3.3.3.4, and 3.3.3.6) for mass density, current density, electron temperature, and total pressure versus radius at 10, 25, and 40 nsec. One can easily see that they are not identical especially at 25 and 40 nsec.

⁵I. Lindemuth, A boundary condition for computational magnetohydrodynamics, J. Comp. Physics **25**, 104-117 (1977).

This difference in results at 25 and 40 nsec could be connected with differences in the physical models implemented in these codes. In the Chittenden et al. code, in the equation describing the internal energy, an ionization energy sink term is included. Moreover, the electron-ion collision frequency is modified to include an artificially high anomalous resistivity connected with lower hybrid drift turbulence in the region of low density. Also, we used the new, modified-for-low-("room")-temperatures version of the SESAME electrical conductivity tables (Desjarlais, Rosenthal, SNL). The importance of these modifications in the SESAME conductivity tables was shown by Atchison et. al (LANL) (2D02, ICOPS 2000).

In the near future we plan to resolve these differences collaborating with Dr. Chittenden (Imperial College, UK).

The input file for the MHRDR simulations with initial and boundary conditions similar to Chittenden et. al. (Phys. Rev. E, Vol. 61, No. 4, April 2000) is given following figures 3.3.3.1-3.3.3.6.

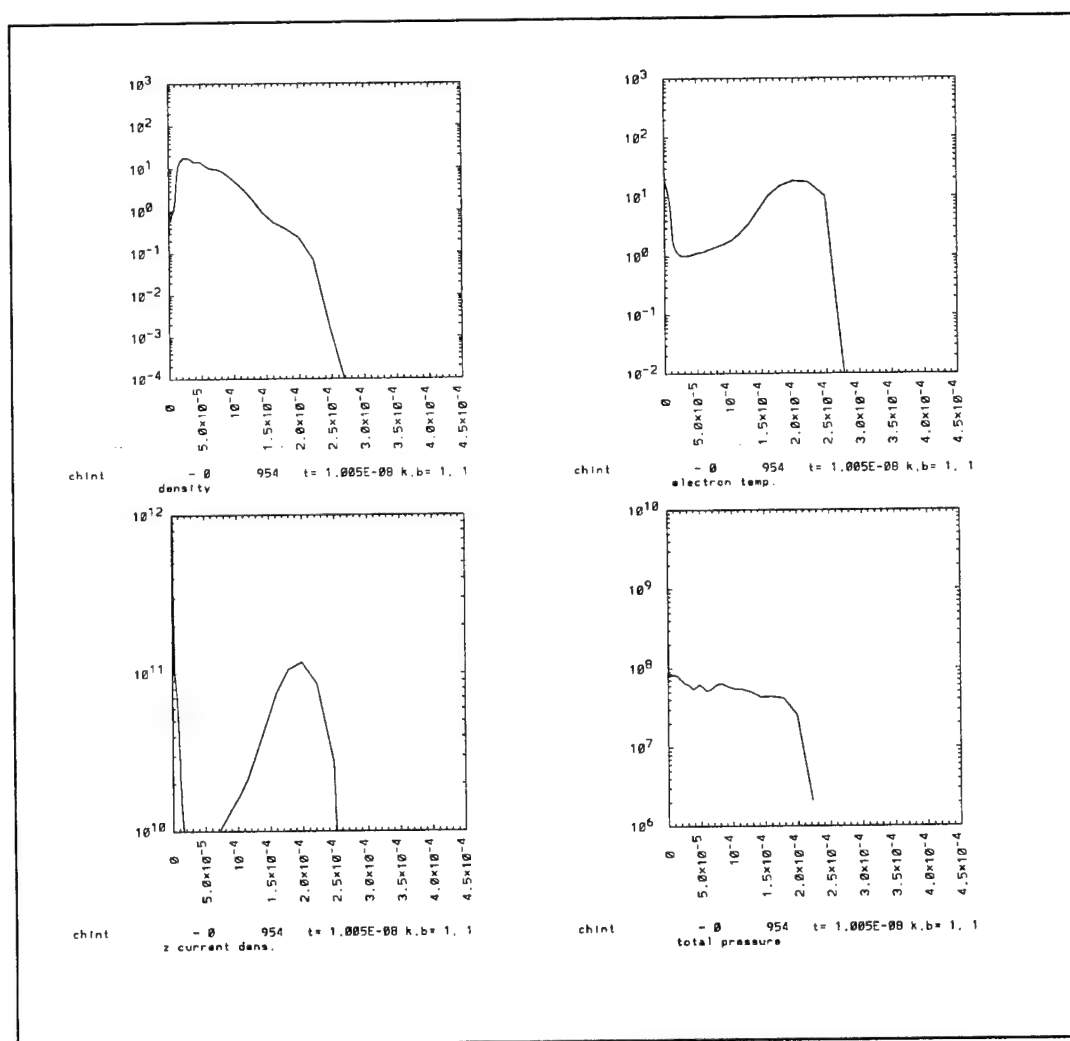


Figure 3.3.3.1. MHRDR simulation: mass density, current density, electron temperature, and total pressure versus radius at 10 nsec.

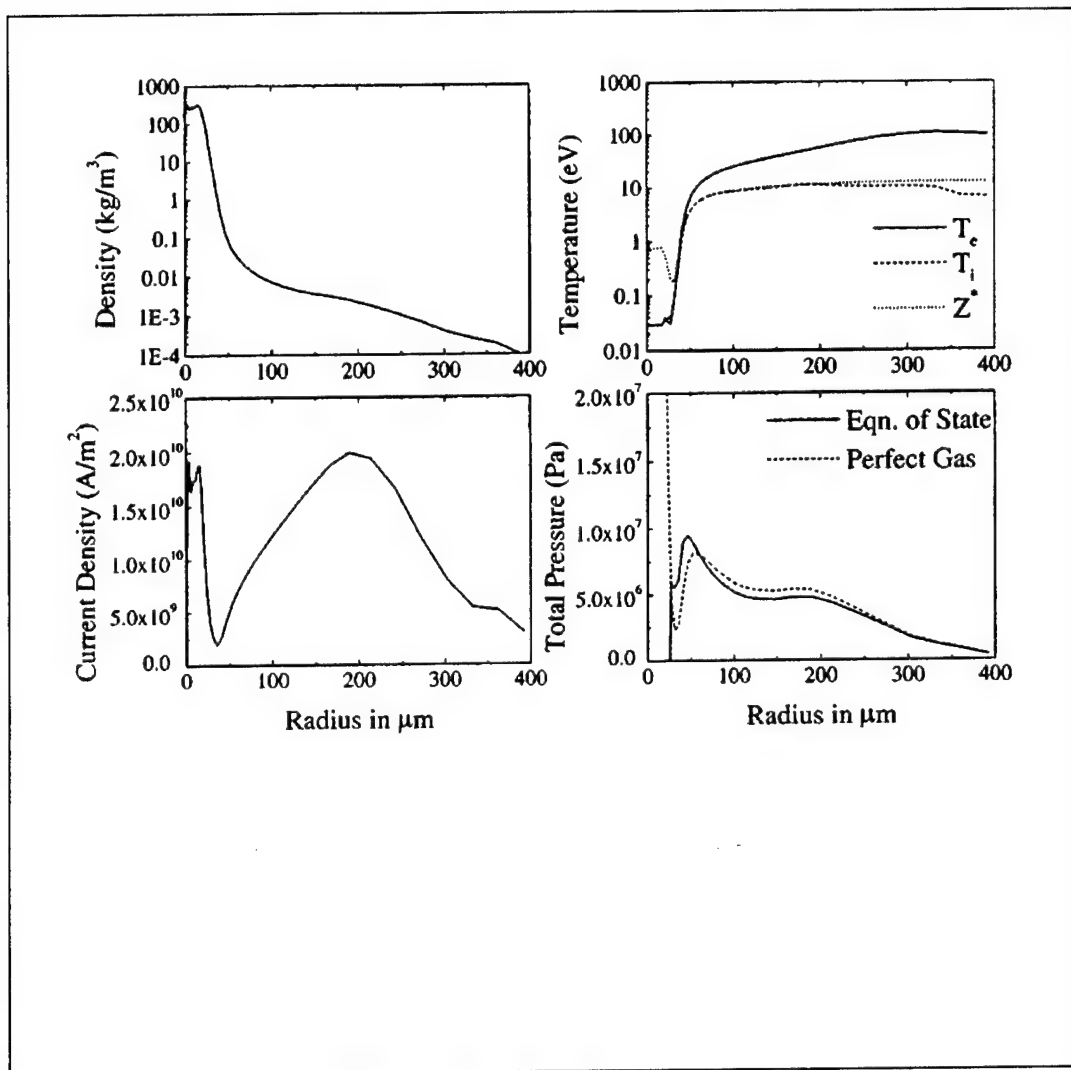


Figure 3.3.3.2. Chittenden et al. simulation: mass density, current density, electron temperature, and total pressure versus radius at 10 nsec.

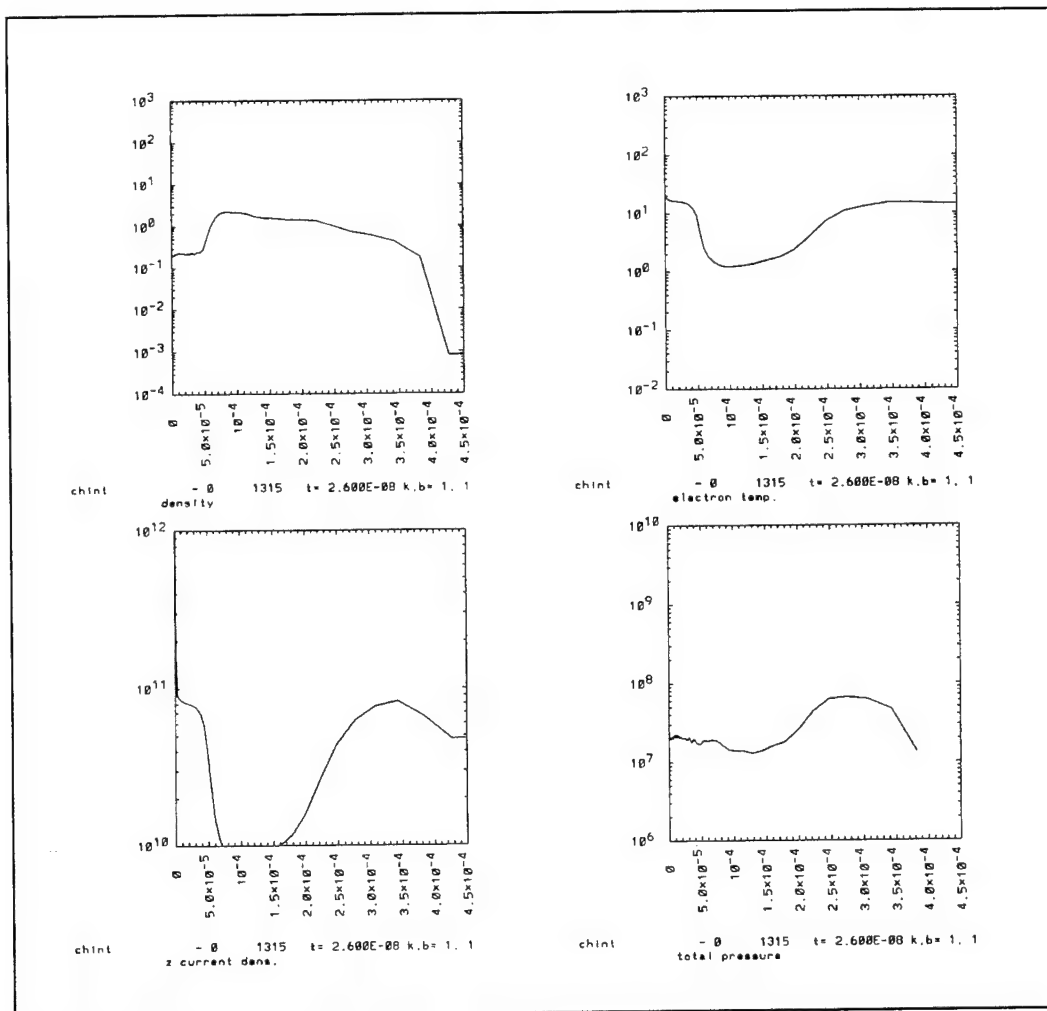


Figure 3.3.3.3. MHRDR simulation: mass density, current density, electron temperature, and total pressure versus radius at 25 nsec.

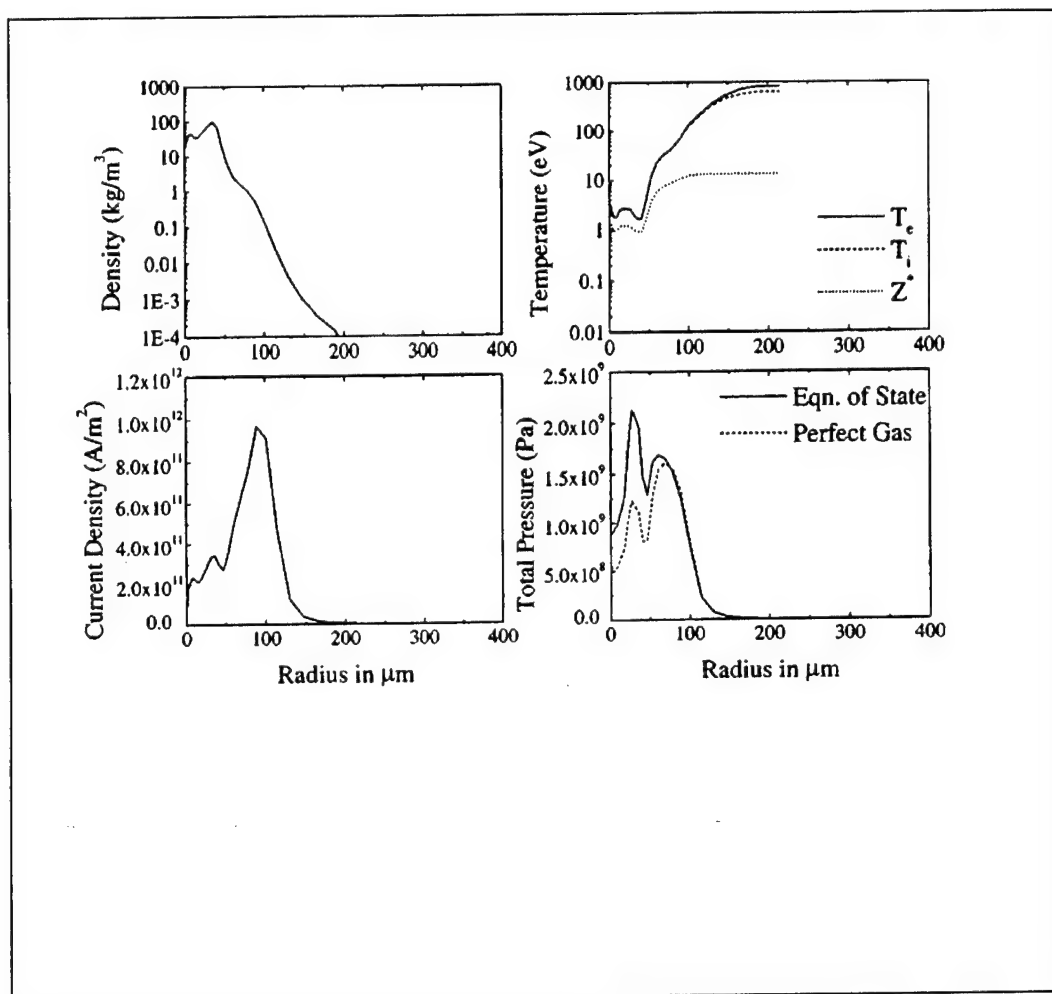


Figure 3.3.3.4. Chittenden et al. simulation: mass density, current density, electron temperature, and total pressure versus radius at 25 nsec.

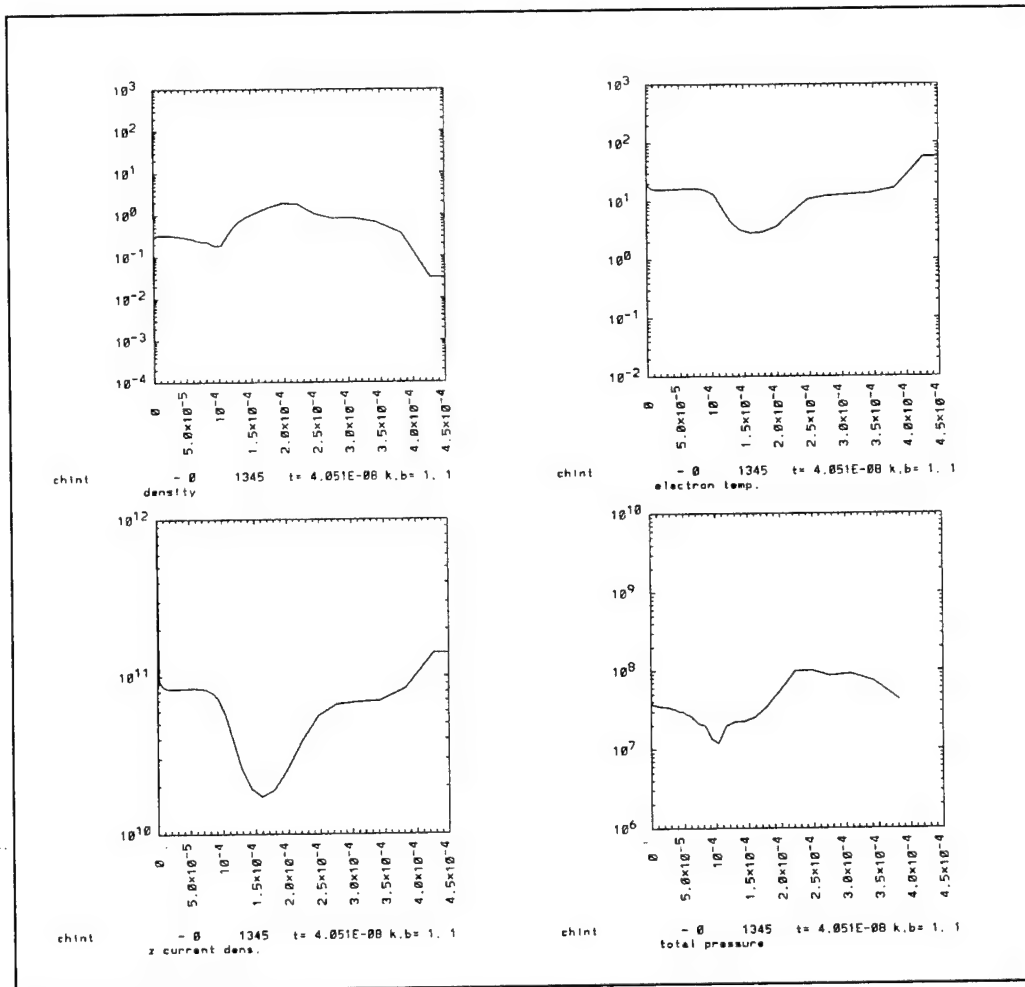


Figure 3.3.3.5. MHRDR simulation: mass density, current density, electron temperature, and total pressure versus radius at 40 nsec.

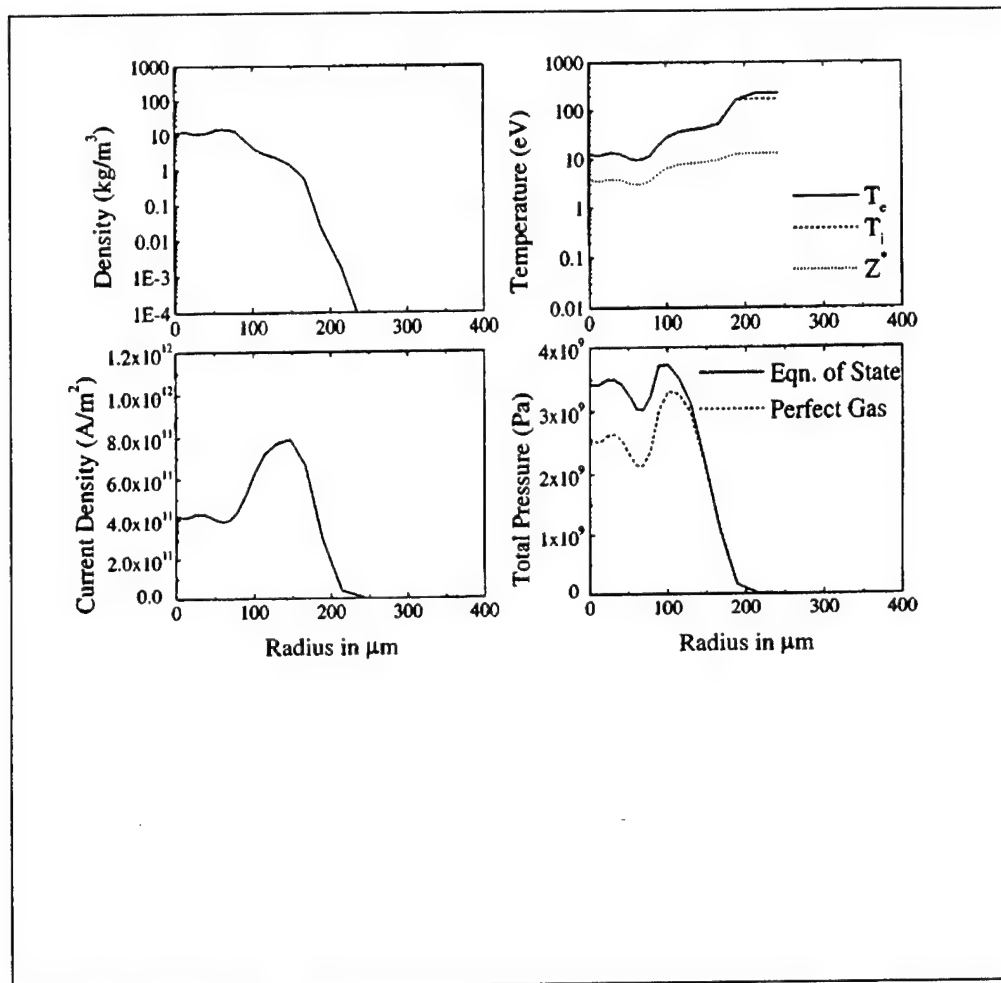


Figure 3.3.3.6. Chittenden et al. simulation: mass density, current density, electron temperature, and total pressure versus radius at 40 nsec.

The input file for the MHRDR simulations with initial and boundary conditions similar to Chittenden et. al. (Phys. Rev. E, Vol. 61, No. 4, April 2000) is as follows.

```
program=chitt

initmon=1,1
tstop=4.01e-8
!TSTOP=4.01e-10
dtedit=2e-9
dtdump=2e-9
longid=aluminium wire data Phys.Ref.v61,n4,4370,2000
model=14
!prnttbl=1
matl=,sesame,3716,101
matl=,sesame,3716,201
matl=,sesame,3716,301
!matl=,sesamr,29373,601
matl=,sesamr,29373,602
!matl=,sesamr,29373,603
!matl=,sesou,13716,504
matl=,sesou,13716,505
rad=0,0
!matl=,,,-201,13.0,26.9815,2.7e3,1e-0,1.6667
cutoff=1.0e-2
xgrid=100,0.0,4.5e-4,1.1150
init=1e-4,.026, , , , 0.0, , 7.5e-6,5e-4
init=2.7e3,.026, , , , 0.0, , 7.5e-6
!linearb=,0.0, , , 7.5e-6
dtmin=1e-19
dtmax=1e-9
dtinit=5e-10
chgmax=.3
dtref=1,1e4,10,10
!cktwid=.02
itabl=0.0,0.0,25.0e3,20.0e-9,50.0e3,40.0e-9
itabl=100.0e3,60.0e-9,125.0e3,80.0e-9
itabl=150.0e3,100.0e-9,127.0e3,120.0e-9
bdrycon=1111111711,1111551311
bkgrnd=1e-4, .026

!mode=17
!plot=tiz
!chantyp=tiz,1
!mode=2
!plot=kez,11,1e-7,1e5
!plot=ker,11,1e-7,1e5
!plot=thr,11,1e-7,1e5
!mode=8
!plot=ro
```

```

!rof=1,7.5e1,3e2
!tef=1,10,100
mode=4
4plot
plotnum=los
plotnum=l
plotnum=iz
plotnum=vb
plotnum=se
plotnum=fck
plotnum=vit
plotnum=rp
plotnum=vp
plotnum=ndt
plotnum=dt,11
plotnum=cpu
plotnum=rmx
plotnum=roc
mode=2
4plot
plotnum=e+l
plotnum=tot
plotnum=con
plotnum=rad
plotnum=ohm
plotnum=shk
plotnum=pdv
plotnum=iec
plotnum=mas
plotnum=kin
plotnum=thr
plotnum=mag
plotnum=flx
plotnum=te>,11
plotnum=ate,
plotnum=nrt,11
plotnum=oln
plotnum=fip
mode=1
4plot
dtedit=2e-9
plotnum=ro,11,1.0e-4,1e3
plotnum=te,11,1e-2,1e3
!plotnum=ti,11
!plotnum=bpt,11
plotnum=jz,11,1.0e10,1.0e12
plotnum=pr,11,1.e6,4.0e9

```

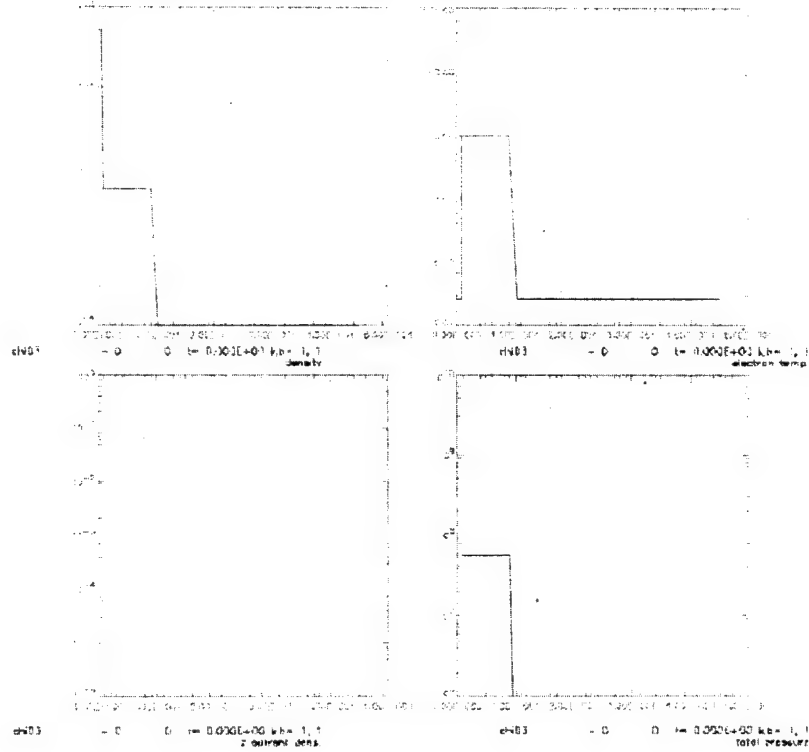
3.3.3.2. MHRDR 1D simulations of the influence of coronal plasma on wire explosions

Experiments demonstrate a strong dependence of wire explosions on the surface preparation of the wire (heating, coating with oil, aging, oxidation), and on the current rise rate. Different surface preparations and current rise rates change the time to formation of a coronal plasma around the wire. Formation of a coronal plasma can dramatically change the energy deposition into the wire, as seen by the following simulations.

MHRDR simulations of the explosion of a thin aluminum wire were performed with and without an initial coronal aluminum plasma. A surrounding density corona plasma of not less than 1% of the total wire mass was used, because MHRDR is a hydrodynamic code. This prevents applicability of MHRDR for lower plasma densities when kinetic effects should be taken into account. A 2-temperature (T-ions and T-electrons) model (in MHRDR definition it is model=15) was used, with a 1D simulation. SESAME tables 303 and 304 were used for the electron and ion EOS. In the future, MHRDR will be upgraded to model more than one material at a time, to be able to model oil and aluminum oxide on the wire.

Below are presented simulation results of density, current density, electron temperature, and pressure versus radius in moments $t = 0, 2, 4, 10$ ns for two different initial setups. In the first case (chi03), a $15\text{ }\mu\text{m}$ aluminum wire was surrounded by hot plasma with radius 10^{-4} m , density 0.3 kg/m^3 and temperature 10 eV . The comparison of these with the case when surrounding coronal plasma was absent (chi04) shows a significant delay of the wire explosion in the first case. This is connected with the fact that the current rapidly switches to the coronal plasma and a strong decrease in the deposition of energy into the wire takes place.

Aluminum wire with coronal plasma at $t = 0$ ns



Aluminum wire without coronal plasma at $t = 0$ ns

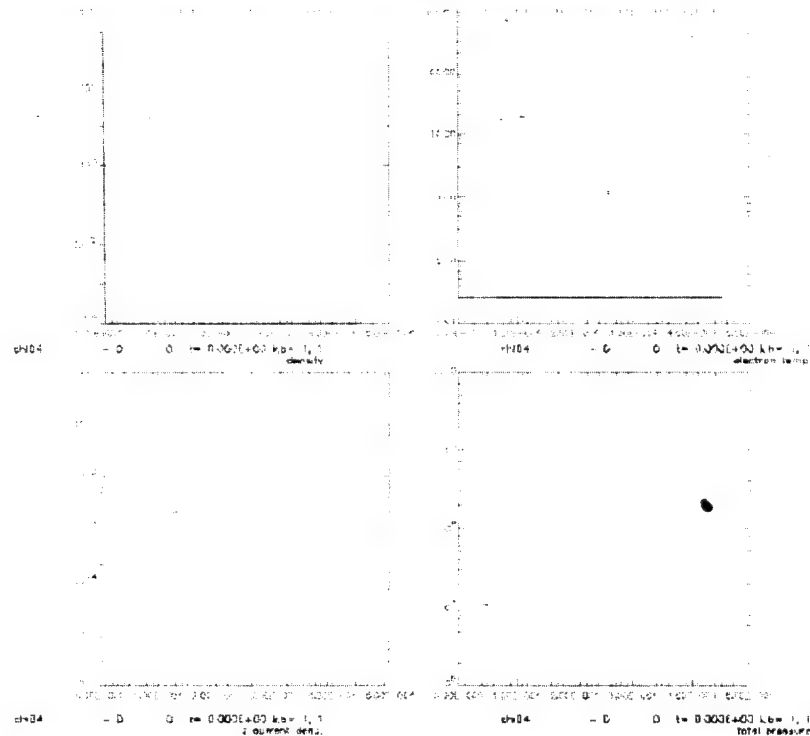
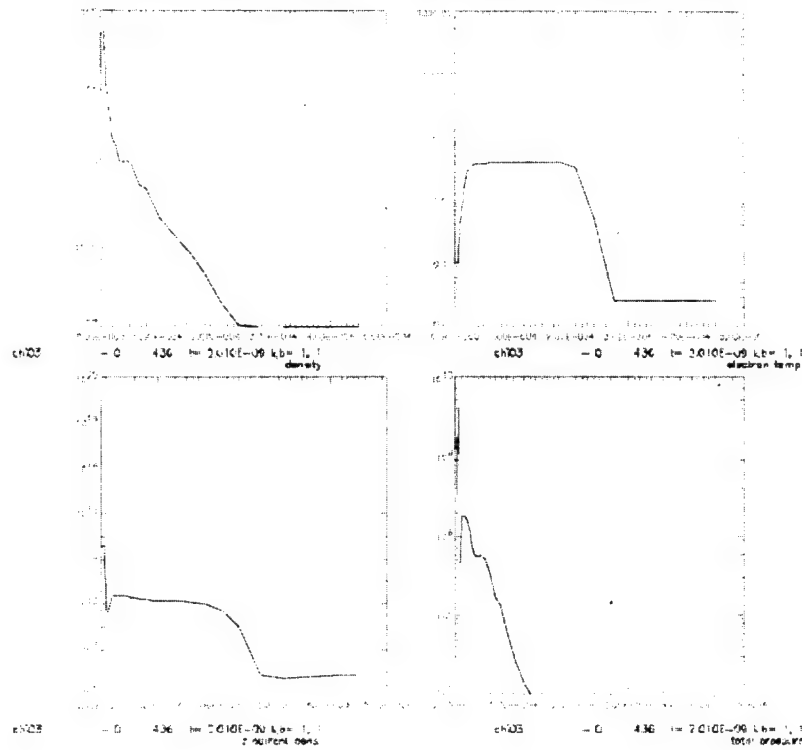


Figure 3.3.3.7. MHRDR simulation of Al wire explosion with and without corona: mass density, current density, electron temperature, and total pressure versus radius at 0 nsec.

Aluminum wire with coronal plasma at $t = 2\text{ns}$



Aluminum wire without coronal plasma at $t = 2\text{ns}$

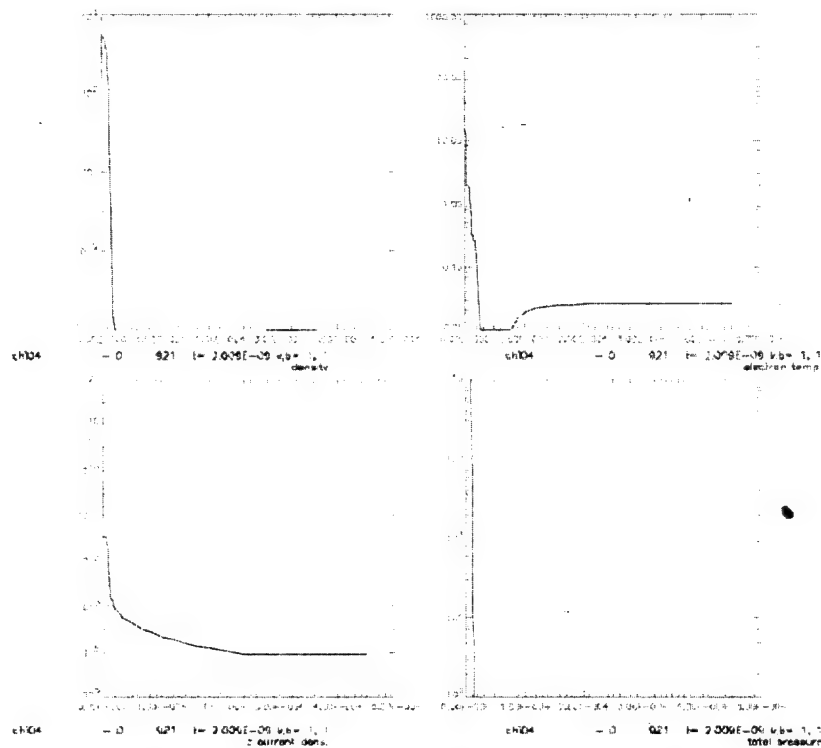
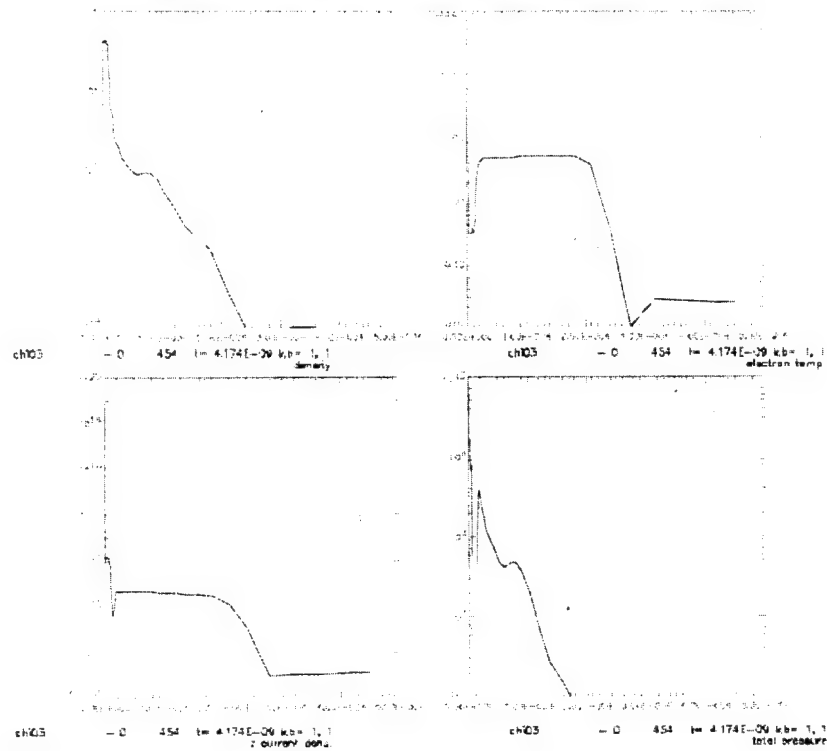


Figure 3.3.3.8. MHRDR simulation of Al wire explosion with and without corona: mass density, current density, electron temperature, and total pressure versus radius at 2 nsec.

Aluminum wire with coronal plasma at $t = 4$ ns



Aluminum wire without coronal plasma at $t = 4$ ns

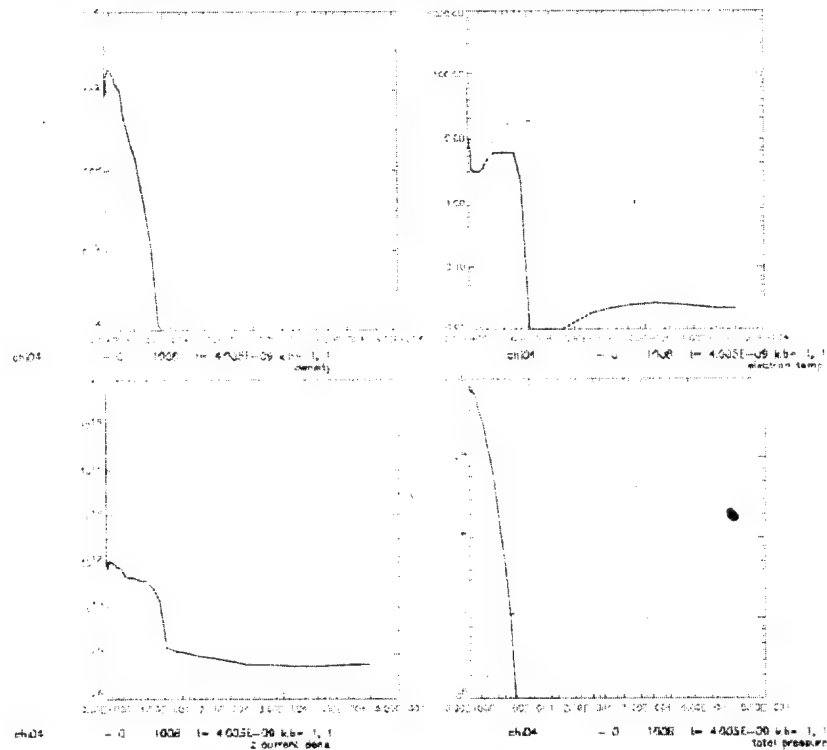
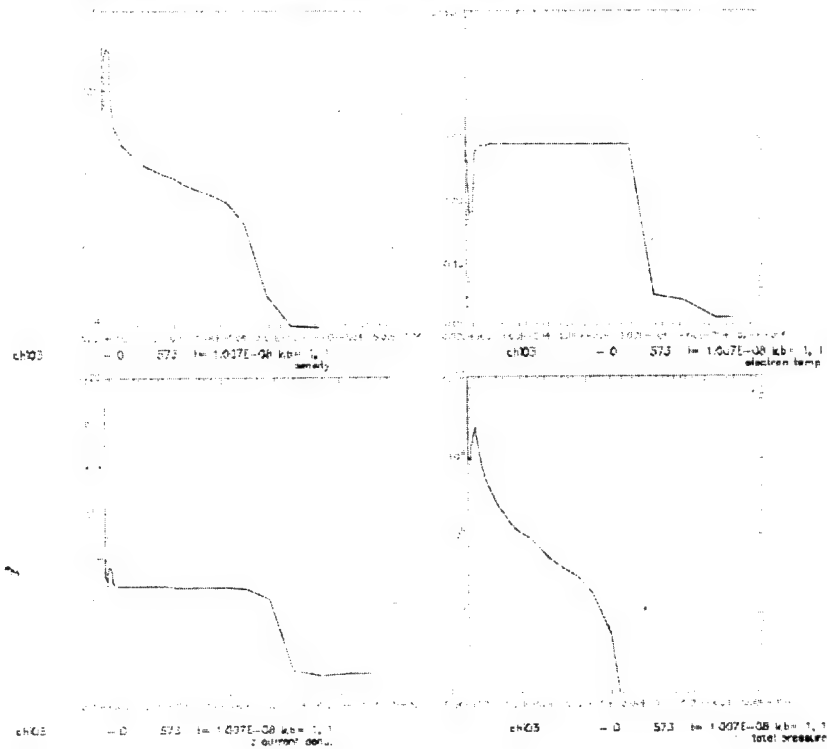


Figure 3.3.3.9. MHRDR simulation of Al wire explosion with and without corona: mass density, current density, electron temperature, and total pressure versus radius at 4 nsec.

Aluminum wire with coronal plasma at $t = 10$ ns



Aluminum wire without coronal plasma at $t = 10$ ns

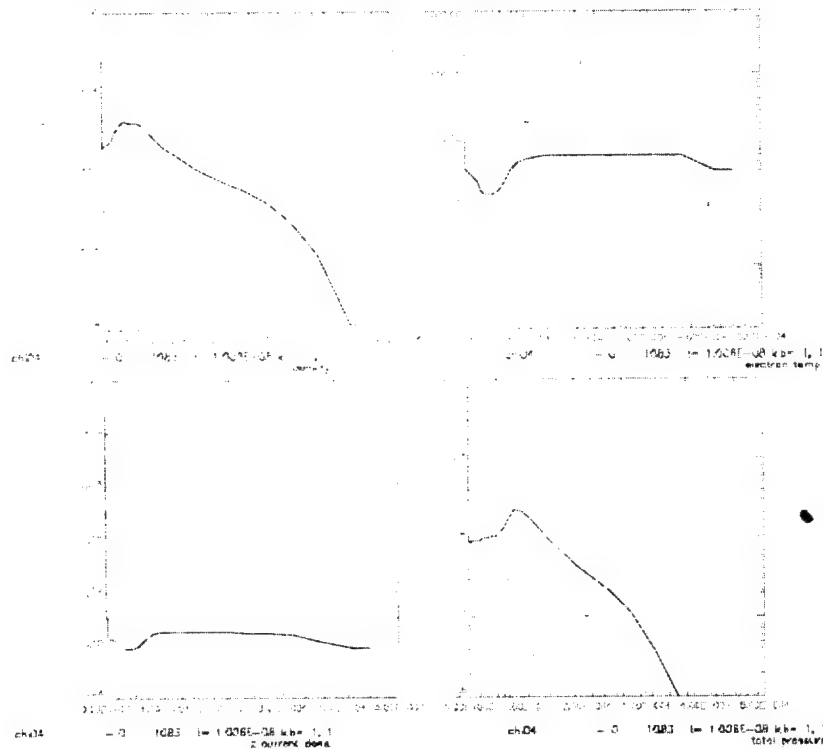


Figure 3.3.3.10. MHRDR simulation of Al wire explosion with and without corona: mass density, current density, electron temperature, and total pressure versus radius at 10 nsec.

The input file for the above MHRDR simulations of an Al wire corona with an initial plasma corona is as follows.

program=chi03

```
initmon=1,1
tstop=5.01e-8
dtedit=2e-9
dtdump=1e-9
longid=aluminum wire with coronal plasma
!model=14
!model=31
!model=7
model=15
!prnttbl=1
!matl=,sesame,3716,101
matl=,sesame,3717,201
!matl=,sesame,3717,301
matl=,sesame,3717,303
matl=,sesame,3717,304
!matl=,sesamr,29373,601
matl=,sesamr,29373,602
!matl=,sesamr,29373,603
!matl=,sesou,13716,504
matl=,sesou,13716,505
matl=,sesou,13716,502
cutoff=1.0e-2
rad=0
!xgrid=100,0.0,4.5e-4,1.1150
xgrid=100,0.0,4.5e-4,1.15
init=0.3,10.0,10.0,0.0, , ,0.0, ,7.5e-6,1.0e-4
init=1.0e-4,0.026, , , ,0.0, ,1.0e-4,5e-4
init=2.7e3,.026, , , ,0.0, ,7.5e-6
!linearb=,0.0, , ,7.5e-6
dtmin=1e-19
dtmax=1e-9
dtinit=5e-10
chgmax=.3
dtref=1,1e4,10,10
!cktwid=.02
itabl=0.0,0.0,25.0e3,20.0e-9,50.0e3,40.0e-9
itabl=100.0e3,60.0e-9,125.0e3,80.0e-9
itabl=150.0e3,100.0e-9,127.0e3,120.0e-9

bdrycon=1111111711,1111551311
bkgrnd=1.0e-4, 0.026

!mode=17
```

```
!plot=tiz
!chantyp=tiz,1
!mode=2
!plot=kez,11,1e-7,1e5
!plot=ker,11,1e-7,1e5
!plot=thr,11,1e-7,1e5
!mode=8
!plot=ro
!rof=1,7.5e1,3e2
!tef=1,10,100
mode=4
4plot
plotnum=los
plotnum=l
plotnum=iz
plotnum=vb
plotnum=se
plotnum=fck
plotnum=vit
plotnum=rp
plotnum=vp
plotnum=ndt
plotnum=dt,11
plotnum=cpu
plotnum=rmx
plotnum=roc
```

```
mode=2
4plot
plotnum=e+l
plotnum=tot
plotnum=con
plotnum=rad
plotnum=ohm
plotnum=shk
plotnum=pdv
plotnum=iec
plotnum=mas
plotnum=kin
plotnum=thr
plotnum=mag
plotnum=flx
plotnum=te>
plotnum=ti>
plotnum=fip
plotnum=aro
plotnum=ate
plotnum=ati
plotnum=nrt
plotnum=oln
```

```

mode=1
4plot
dtedit=2e-9
plotnum=ro,11,1.0e-4,1e3
plotnum=te,11,1e-2,1e3
!plotnum=ti,11
!plotnum=bpt,11
!plotnum=jz,11,1.0e10,1.0e12
plotnum=jz,11
plotnum=pr,11,1.e6,4.0e9

```

program=chi04

```

initmon=1,1
tstop=5.01e-8
dtedit=2e-9
dtdump=1e-9
longid=aluminum wire
!model=14
!model=31
!model=7
model=15
!prnttbl=1
!matl=,sesame,3716,101
matl=,sesame,3717,201
!matl=,sesame,3717,301
matl=,sesame,3717,303
matl=,sesame,3717,304
!matl=,sesamr,29373,601
matl=,sesamr,29373,602
!matl=,sesamr,29373,603
!matl=,sesou,13716,504
matl=,sesou,13716,505
matl=,sesou,13716,502
cutoff=1.0e-2
rad=0
!xgrid=100,0.0,4.5e-4,1.1150
xgrid=100,0.0,4.5e-4,1.15
!init=0.3,10.0,10.0,0.0, , ,0.0, ,7.5e-6,1.0e-4
!init=1.0e-4,0.026, , , ,0.0, ,1.0e-4,5e-4
init=1.0e-4,0.026, , , ,0.0, ,7.5e-6,5e-4
init=2.7e3,.026, , , ,0.0, ,7.5e-6
!linearb=,0.0, , ,7.5e-6
dtmin=1e-19
dtmax=1e-9
dtinit=5e-10

```

```
chgmax=.3  
dtref=1,1e4,10,10  
!cktwid=.02  
itabl=0.0,0.0,25.0e3,20.0e-9,50.0e3,40.0e-9  
itabl=100.0e3,60.0e-9,125.0e3,80.0e-9  
itabl=150.0e3,100.0e-9,127.0e3,120.0e-9
```

```
bdrycon=1111111711,1111551311  
bkgrnd=1.0e-4, 0.026
```

3.3.3.3. MHRDR 1D simulations of tungsten wire explosions and comparison with experiments

Simulations were performed for wires with diameter 20 μm , with the width of the moving simulation grid equal to 100 μm at the beginning of the run. "Cold-start" initial conditions for the computations were a solid tungsten wire ($\rho = 19.35 \times 10^3 \text{ kg/m}^3$, $T = 0.025 \text{ eV}$) surrounded by a low-density "background plasma" ($\rho = 1.0 \cdot 10^{-4} \text{ kg/m}^3$, $T = 0.025 \text{ eV}$). The current in simulations corresponded to the current load table used in the experiment.

This was the first attempt to simulate cold-start thin metallic wire explosions with MHRDR. Previous MHRDR simulations with a cold start were carried out only for solid, cryogenic deuterium fibers (density $\rho = 88 \text{ kg/m}^3$) (Sheehey, al, Phys. Fluids B 4 (11), November 1992).

Results of MHRDR simulations are presented in Figs. 3.3.3.11 (initial conditions), 3.3.3.12 (right before expansion), and 3.3.3.13 (just after expansion). Simulations were carried out for two regimes: without and with radiation losses.

When radiation losses are not included, the simulation reproduces the explosion of the Tungsten wire observed during the experiment. The main features observed during the experiment were: time of explosion at 22th ns for modified shifted-in-time cyclogram of the current, and speed of explosion 0.99 km/s. The first feature (time of explosion) was in agreement with experiment, but the speed of expansion from simulation was much higher (700 times higher). This is a strong indicator that it is very important to use a correct model for radiation losses in MHRDR in order to obtain better agreement with the experiment in terms of expansion speed.

When radiation losses were included, the simulation didn't reveal a wire explosion, in contradiction with observations. In this case, the temperature didn't increase inside the core of the wire. Thus it is important to modify the radiation model implemented in MHRDR to correctly predict the behavior of the wire.

More efforts will be applied to produce reliable simulation results with MHRDR. The simulations were carried out without opacity tables for Tungsten. These will be included in the simulation model soon.

Following figures 3.3.3.11-3.3.3.13 is the input file for MHRDR simulations with initial and boundary conditions from Sarkisov et. al. experiment 0419-03-W.

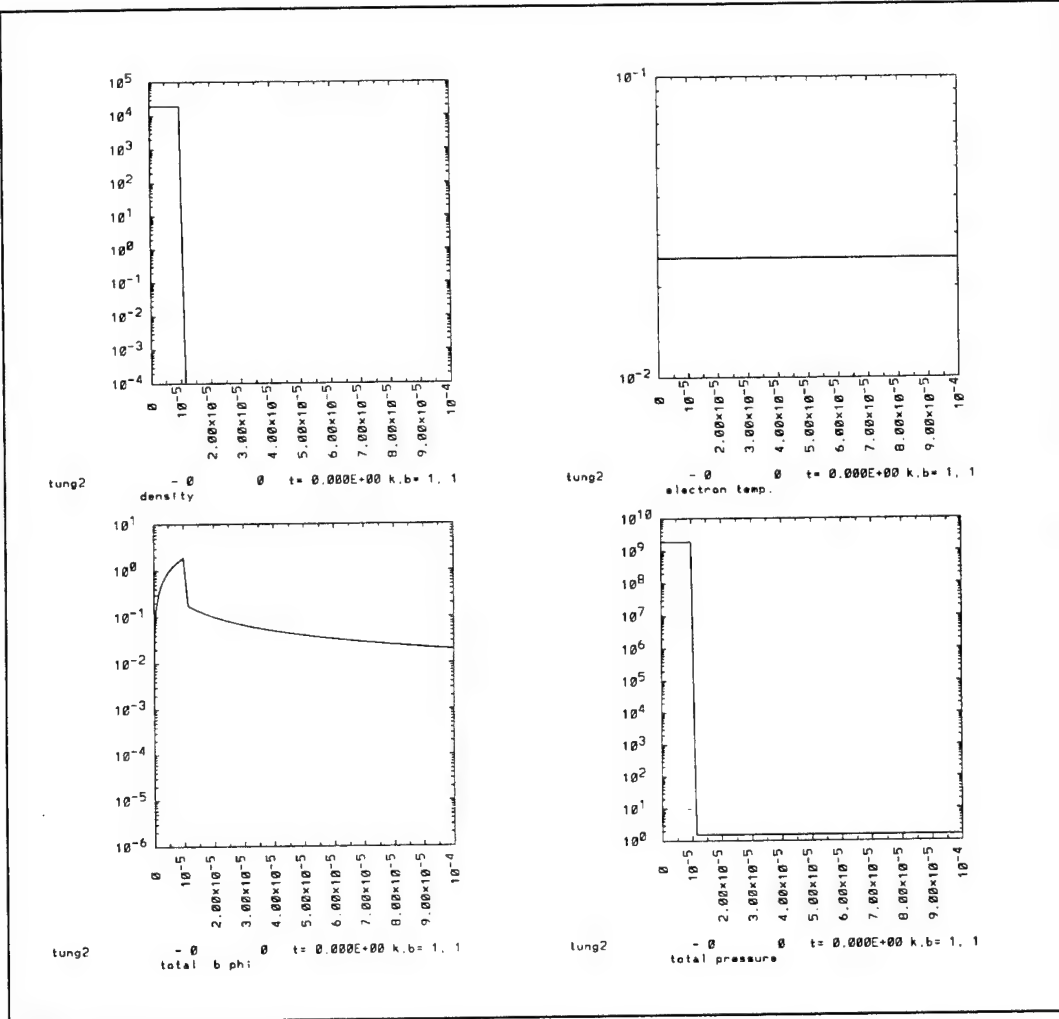


Figure 3.3.3.11. MHRDR simulation: initial mass density, azimuthal magnetic field, electron temperature, and total pressure versus radius ($t = 0$ ns).

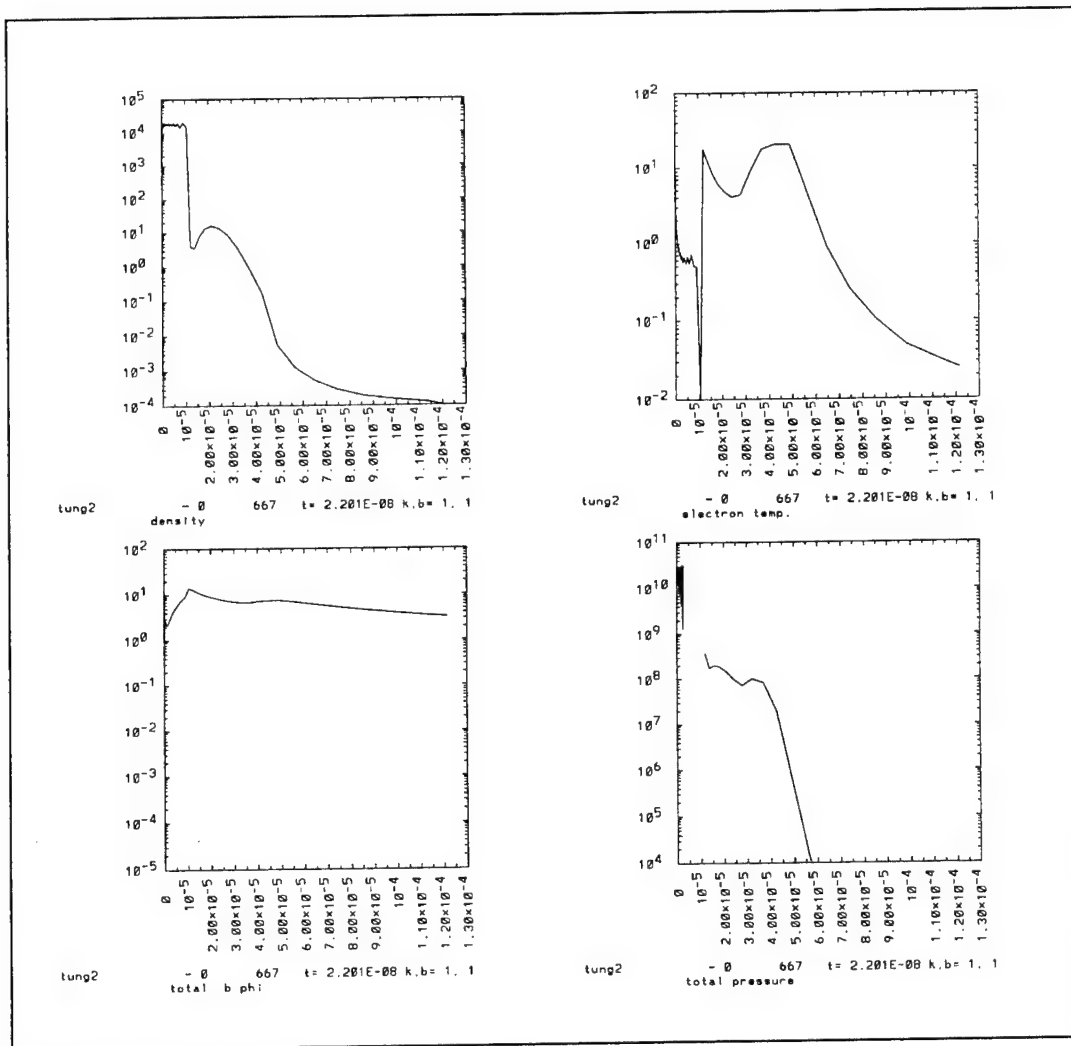


Figure 3.3.3.12. MHRDR simulation: mass density, azimuthal magnetic field, electron temperature, and total pressure versus radius, just before expansion ($t = 22$ ns).

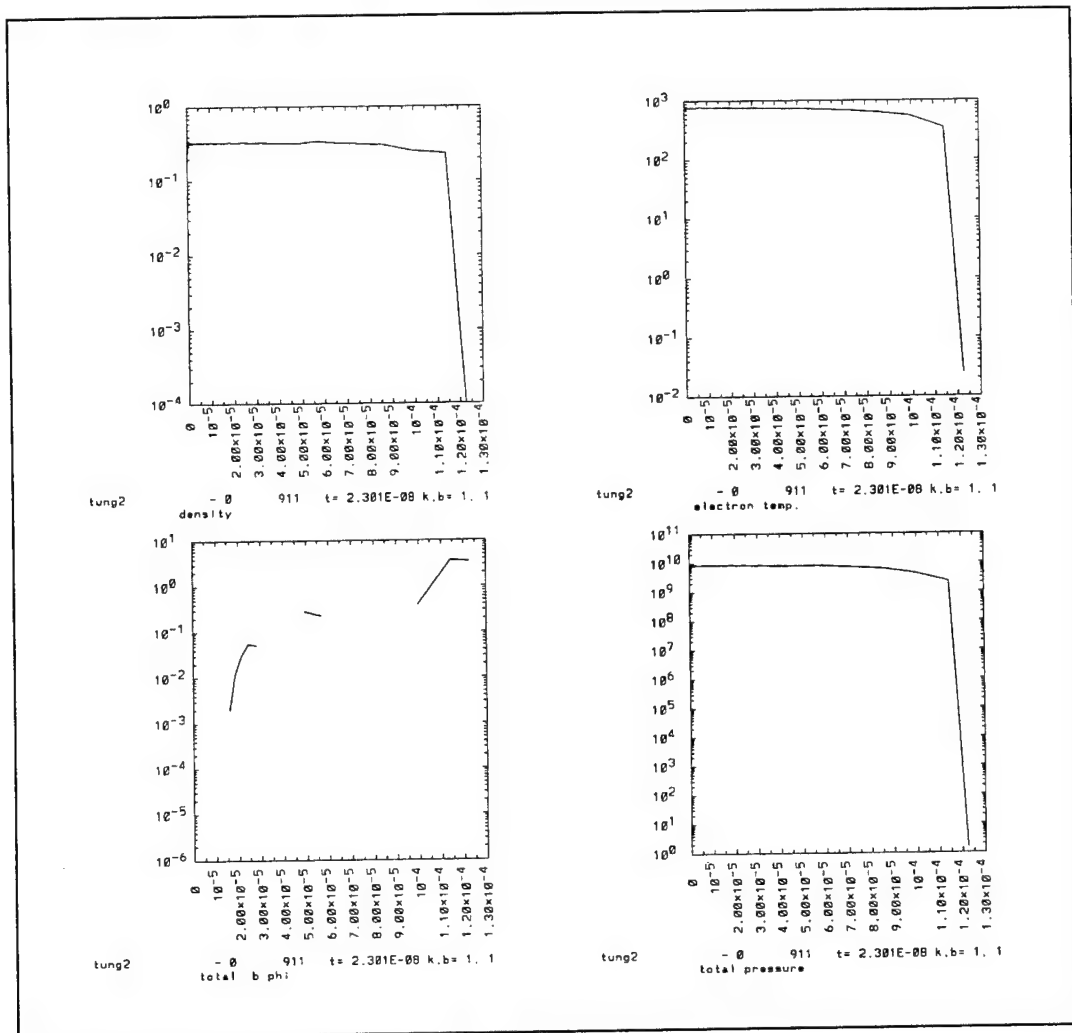


Figure 3.3.3.13. MHRDR simulation: mass density, azimuthal magnetic field, electron temperature, and total pressure versus radius, just after expansion ($t = 23$ ns).

The input file for MHRDR simulations with initial and boundary conditions from Sarkisov et. al. experiment 0419-03-W is as follows.

```
program=tungs

initmon=1,1
tstop=28.e-9
dtedit=2e-8
dtdump=1e-9
!chngdmp=23.5,1.0e-11,2e-8
longid=tungsten wire z-pinch
model=14
!prnttbl=1
matl=,sesame,3541,101
matl=,sesame,3541,201
matl=,sesame,3541,301
!matl=,sescu,23541,601
!matl=,sescu,23541,602
matl=,sesamr,29354,602

cutoff=1e-2
xgrid=50,0.0,1.0e-4,1.15
init=1e-4,.025, , , ,10.0, ,10.0e-6,2e-4
init=19.35e3,.025, , , ,0.0, ,10.0e-6
linearb=,95.52, , ,10.0e-6
dtmin=1e-40
dtmax=1e-9
chgmax=.3
dtref=1,1e4,10,10
cktwid=.02
rad=0.0,0
gridmov=1
gridv=1.0e-4,0,1.2e-4,2e-8,1.4e-4,5e-8
gridv=1.6e-4,10.0e-8
!itabl=95.52,0,412.13,17.6e-9,1352.04,20.0e-9,2045.29,25.0e-9
!itabl=2106.75,30.0e-9,1659.45,95.0e-9,1659.45,100.0e-9
itabl=95.52,0,412.13,17.6e-9,1652.04,20.0e-9,2345.29,25.0e-9
itabl=2406.75,30.0e-9,1959.45,95.0e-9,1659.45,100.0e-9
bdrycon=1111511711,3533333333
bkgrnd=1e-4, .025

!mode=17
!plot=tiz
!chantyp=tiz,1
!mode=2
!plot=kez,11,1e-7,1e5
!plot=ker,11,1e-7,1e5
```

```

!plot=thr,11,1e-7,1e5
!mode=8
!plot=ro
!rof=1,7.5e1,3e2
!tef=1,10,100
mode=4
4plot
plotnum=los
plotnum=l
plotnum=iz
plotnum=vb
plotnum=se
plotnum=fck
plotnum=vit
plotnum=rp
plotnum=vp
plotnum=ndt
plotnum=dt,11
plotnum=cpu
plotnum=rmx
plotnum=roc
mode=2
4plot
plotnum=e+l
plotnum=tot
plotnum=con
plotnum=rad
plotnum=ohm
plotnum=shk
plotnum=pdv
plotnum=iec
plotnum=mas
plotnum=kin
plotnum=thr
plotnum=mag
plotnum=flx
plotnum=te>,11
plotnum=ate,
plotnum=nrt,11
plotnum=oln
plotnum=fip
mode=1
4plot
!tstart=23.5e-9
dtedit=1e-9
plotnum=ro,11
plotnum=te,11
plotnum=pr,11
plotnum=bpt,11

```

4. X-ray/EUV diagnostics development and x-pinch experiments

Contents:

- 4.1. Plasma diagnostic research at the NTF (V. Kantsyrev, A. Shlyaptseva, and S. Fuelling [EUV spectrometer]).
- 4.2. Physics of High-Current X-Pinch X-ray/EUV Radiation Sources (V. Kantsyrev and A. Shlyaptseva).
 - 4.2.1. Development and study of x-pinch x-ray backlighting.
 - 4.2.2. X-ray spectropolarimetry for the study of energetic electron distribution functions and magnetic fields in z-pinch plasma.
 - 4.2.3. Study of the influence of a suprathermal e-beam generated in z-pinch plasma on the structure of K- and L-spectra of multicharged ions.

Participation in data analysis and illustrations preparation: D. Fedin, S. Hansen, N. Ouart, S. Keely, H. LeBeau, D. Chamberlain.

4.1. Plasma diagnostic research at the NTF

Plasma diagnostic research at the NTF includes the development of x-ray and EUV plasma spectroscopy and x-ray backlighting [1,2]. X-ray and EUV plasma spectroscopy and x-ray backlighting are effective methods of measuring density, temperature, and other profiles of high-density plasmas. X-ray and EUV spectra of a wide variety of chemical elements can be produced on Zebra, and fundamental studies of atomic processes of multiply charged ions in moderate- and high-density z-pinch plasmas have been initiated. A new plasma diagnostic, x-ray spectropolarimetry [3,4], is being applied to z-pinch plasmas containing a directed electron beam, to obtain information about the electron distribution function and the magnetic field

Plasma density, temperature, flow, charge states, and magnetic field must be measured with a detailed space- and time-resolved short-wavelength spectroscopy. The NTF-Zebra x-ray and EUV diagnostics (Figures 4.1 and 4.2) include passive devices (spectrometers, pinhole imagers, and filtered x-ray diode arrays). Several types of x-ray spectrometers have been developed, tested and used in z-pinch experiments at the NTF. Active devices like a x-ray backlighter will be added soon. All experiments were proved under vacuum better than 5×10^{-6} torr. Each vacuum beamline has strong permanent magnets to protect the x-ray devices against the damage from z-pinch ion beams.

The status of the NTF x-ray/EUV diagnostics is:

1. Side-on two-dimensional glass-capillary imaging x-ray time-gated spectrometer (2DXIS): testing in progress (see description below).
2. Side-on one-dimensional time-gated spectrometer (1DXIS—based on a 2DXIS chamber and a MCP detector): operational. Spectrometer parameters: λ from several ten Å to 0.5 Å (different flat crystals or multilayer mirrors), observation for one shot $\Delta\lambda = 0.5$ Å, spectral resolution $\Delta\lambda/\lambda \approx 1000$, temporal resolution $\Delta\tau = 1-8$ ns, number of frames 4, inter-frame time 3-20 ns, spatial resolution 1-5 mm.
3. Side-on multichannel time-gated pinhole camera (GXI): operational. Camera parameters: 6 frames (1-8 ns), inter-frame time 1-20 ns, spatial resolution 100-250 μm , λ from 1 Å to 10 Å (two rows of images behind two different filters).
4. Side-on 6-channel “Polychromator” spectrometer with a transmission grating spectrometer: operational (see description below).
5. Side-on one-dimensional x-ray imaging time-integrated crystal spectrometer / time-integrated survey low-resolution pinhole camera: operational. Spectrometer parameters: λ from 0.5 Å to 20 Å (different convex crystals), spectral resolution $\Delta\lambda/\lambda = 700-800$, spatial resolution 2-7 mm. Camera parameters: spatial resolution 580 μm , λ from 1 Å to 10 Å (three images behind three different filters).
6. Side-on time-integrated high-resolution pinhole camera: operational. Camera parameters: spatial resolution 10-70 μm , λ from 1 Å to 10 Å (two images behind two different filters, multilayer x-ray film package).
7. Side-on and end-on one-dimensional x-ray imaging time-integrated polarimeter-spectrometers: side-on is operational, end-on: testing in progress (see description below).
8. Side-on filtered fast PCD and XRD detectors: operational. Detectors parameters: $\lambda \approx 500-0.1$ Å, time resolution ≈ 0.2 ns.
9. Side-on Ni x-ray bolometer: operational. Bolometer parameters: $\lambda \approx 600-0.1$ Å.
10. End-on hard x-ray time –integrated imaging detector with filtered x-ray films: operational. Parameters of the detector: energy 25-200 keV.
11. Side-on hard x-ray time –integrated imaging detector with filtered x-ray films: operational. Parameters of the detector: energy 25-200 keV.
12. Hard x-ray detector (photomultiplier with scintillator): operational. Device parameters: time resolution several ns, energy \approx MeV.
13. Side-on and end-on hard x-ray fast detectors with spatial resolution capability: in development. Detector parameters: energy $\approx 10-200$ keV, time resolution $\approx 0.2 - 0.5$ ns.
14. Extreme ultraviolet (EUV) imaging diagnostic beam line: in development (see description below).

New x-ray and EUV diagnostics (parts 1, 4, 6) on Zebra are based on the use of crystals in conjunction with glass capillary converters (GCCs) [1,5,6] and multilayer mirrors (MLMs). The GCCs collect, guide, focus, filter [5,6-8] and polarize [6,9] a wide spectrum of short-wavelength radiation. The MLMs and crystal elements are used for dispersing, focusing and polarizing a narrow bandwidth of radiation. The GCCs consist of a bundle of glass or quartz capillaries. EUV, soft x-ray, and x-ray radiation is guided along straight or slightly curved capillaries by multiple grazing-incidence reflections from the inner capillary surfaces [7,8,10]. The GCCs were used in plasma diagnostics as hard x-ray filters in a soft x-ray pinhole camera, and were proposed as an imaging and filtering x-ray streak camera element [1,5,6,11]. GCCs have been used as a new device for enhancing the flux density of x-ray and EUV radiation on the entrance slit of any type of a short-wavelength spectrometer (a coefficient of an enhancement of the flux density was $\eta \approx 10$ -100 in a wide spectral region $0.1 \text{ nm} < \lambda < 100 \text{ nm}$) [6,12] (Figure 4.2). A GCC also serves as a high-transmission window for differential pumping [5,6], and a collecting/focusing element in a glass-capillary monochromator-concentrator device [5].

4.1.1. The x-ray and EUV two-dimensional imaging capillary spectrometer (2DXIS) and one-dimensional imaging spectrometer (1DXIS) for z-pinch plasma diagnostics

Space and time resolution for hot z-pinch or laser plasmas spectroscopy are essential, as these plasmas contain strong gradients and evolve rapidly. A broad range of wavelengths must be measured, both to accurately determine the electron energy distribution and to simultaneously observe a variety of atomic processes. For example, to compile two-dimensional (2-D) maps of electron density N_e and electron temperature T_e , an entire 2-D monochromatic plasma image must be captured on each shot, as shot-to-shot reproducibility is limited. These criteria are unfortunately not simultaneously satisfied by current spectroscopic methods. A spatial resolution of better than $5\text{-}10 \text{ }\mu\text{m}$ can be achieved now, however, for an extended source as a z-pinch, the average distortion of the image generally increases up to $50\text{-}100 \text{ }\mu\text{m}$ or more for plasma columns $20\text{-}50 \text{ mm}$ in length [13]. However, glass-capillaries offer a way to break up and manipulate an x-ray image for spectroscopic analysis. EUV, soft x-ray and x-ray radiation diagnostics stand to redefine the state of the art in the measurement of plasma parameters: a multiband, two-dimensional imaging spectrometer 2DXIS [14].

A novel Two-Dimensional X-ray Imaging Spectrometer (2DXIS) consists of an entrance pinhole imaging camera for experiments with SNL-Z scale z-pinches (or imaging x-ray mirror for the NTF-Zebra machines), the number of individual glass capillary channels, a joint crystal, and a time-gated imaging detector. The scheme is shown in Figure 4.4. The 2DXIS uses GCC to add an extra dimension to the spectrometer throughput. The GCC multiplex transforms a two-dimensional image of the plasma into an output array of spatially separated pixels (Figs.4, 5). Cross-talk between pixels is prevented by using a separating of pixels with thin plate sheets (optical insulator) and a mask (to limit the angular distribution of the x-rays). The beam array is then spectrally dispersed by a crystal or a multilayer mirror, recorded by a temporally-gated imager, and reconstituted as an image by a computer. The result is a time-gated x-ray spectrum for each plasma image point.

The array of these 2-D x-ray imaging spectrometers, each observing essentially-identical plasma images, would yield an array of spectral images, at multiple times and in multiple wavelength bands. The choice of a spatial resolution, a field of view, a wavelength range, and a spectroscopic resolution is such that measured spectra, in conjunction with theory and computer modeling, yield two-dimensional maps of important plasma parameters such as electron temperature and density, and ionization state.

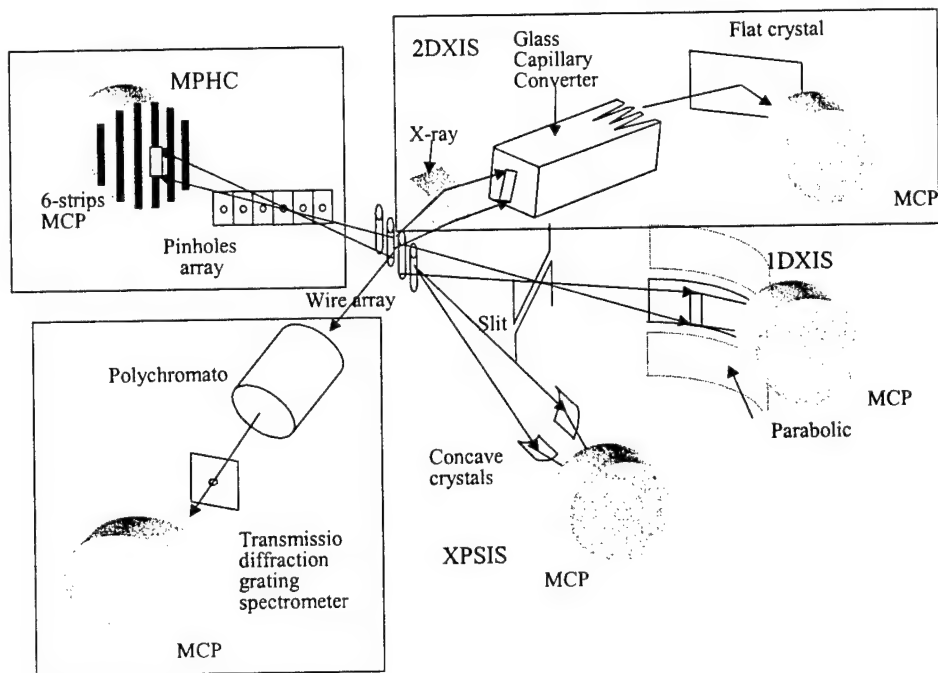


Figure 4.1. The scheme of new x-ray and EUV diagnostics at the NTF. 2DXIS-the two-dimensional EUV and x-ray imaging spectrometer with glass capillary optic and a MCP time-gated multi-strip imager. This device had been converted to a one-dimensional time-resolved x-ray spectrometer by removing the GCC and installing an imaging slit between a plasma and a crystal (MLM). MCPH-the multichannel x-ray pinhole camera with a MCP time-gated multi-strip imager. Polychromator: the 5-channel time-resolved crystal (MLM) spectrometer with an additional transmission grating spectrometer channel. XPSIS: the x-ray polarization-sensitive imaging spectrometer. Modification of the device with crossed-placed concave focusing crystals is shown. 1DXIS: the future one-dimensional x-ray imaging spectrometer with a set of parabolic crystals for study of z-pinchs with large dimensions.

New results have been obtained [15] from the experimental study and theoretical modeling of the nonuniform output angular distribution of keV and sub-keV radiation transported by different types of glass mono- and polycapillary converters from an x-ray plasma source. The distribution of output radiation from a capillary with an internal polycapillary structure (diameter of channels 35-40 μm , diameter of the polycapillary structure 220 μm) is much more uniform than that from a

simple hollow capillary. A new design for polycapillary converters for the 2DXIS has been developed in collaboration with Collimated Holes, Inc. (Campbell, CA), using these results. The throughput and output angular distribution of Ti K-shell radiation through different capillaries is being characterized using Zebra as a radiation source.

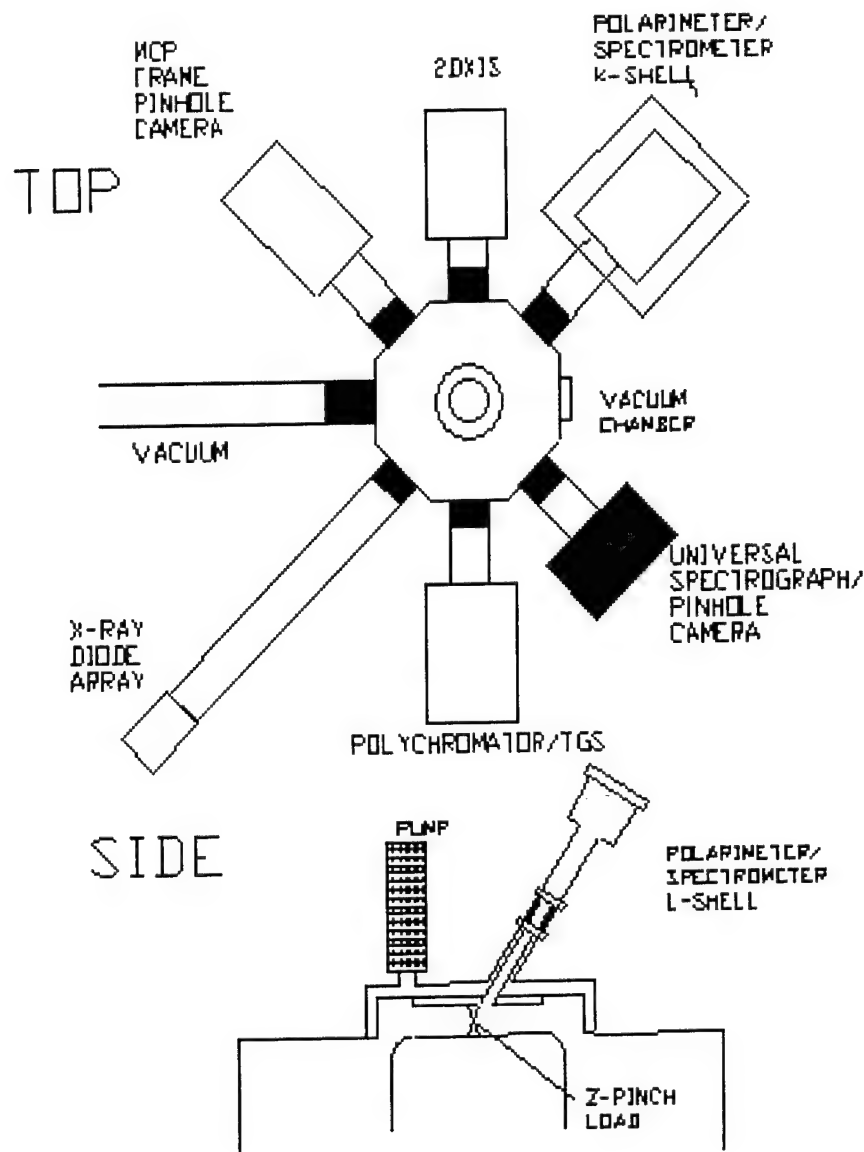


Figure 4.2. X-ray diagnostics at the Nevada Terawatt Facility. The vacuum discharge chamber with the vertical XPSIS channel beamline and cryopump is in the center of the picture. At the right and the left is the diagnostic supporting platform that has a mechanical contact with a vacuum discharge chamber of Zebra only through soft bellows into diagnostics beamlines. Several x-ray spectrometers and imaging systems are seen on the photo around the discharge chamber.

The 2DXIS was tested with a laser plasma x-ray source at the X-ray Diagnostic Developing Laboratory of the NTF. Output channels (total number about 80) are used to obtain an array of time-resolved spectra that covers the full plasma evolution. A comparison of parameters of the 2DXIS with traditional 2D spectrographs with a spherical curved dispersive element [14,16,17] is shown in Table.1. The sensitivity of the spectrometer must be enough for registration of spatial and frame time resolved x-ray and EUV spectra in a single shot of a z-pinch or laser plasma facility. Our theoretical estimations of a sensitivity of a 2DXIS spectrometer were in a good matching with our experimental results of measurements of a sensitivity of one channel of a 2DXIS with a laser-plasma source of x-rays. From these comparisons it was shown, that 2DXIS can be applied to study a z-pinch plasma of the powerful facilities (SNL-Z scale) during the evolution of an implosion of a Z-pinch plasma, even for spectroscopic dopants in plasmas with a concentration of about 10 % [16].

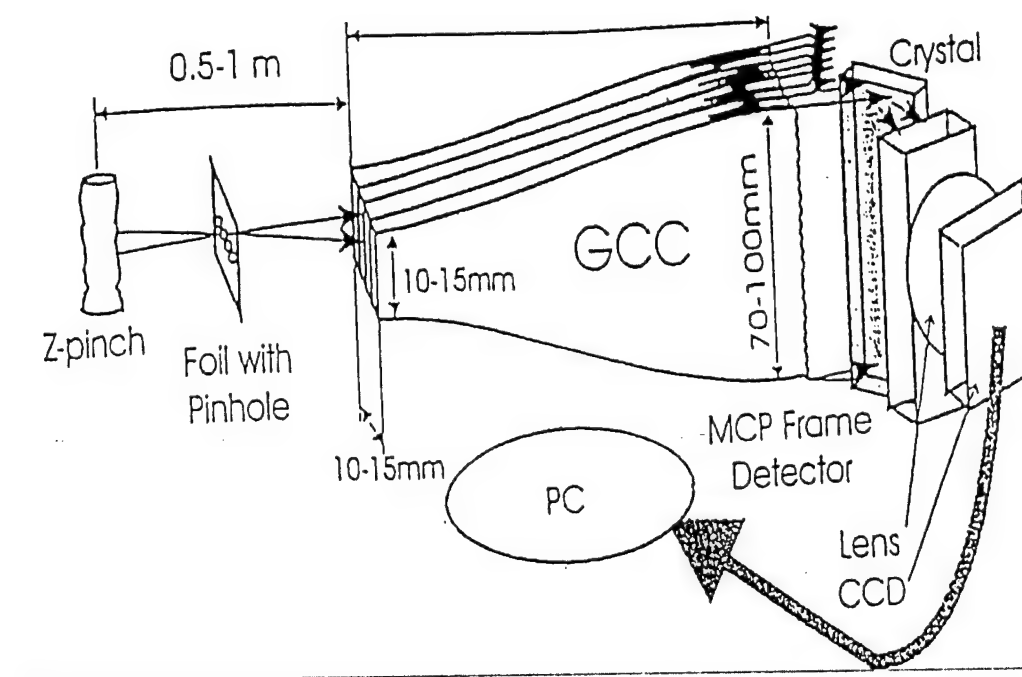


Figure 4.3. The two-dimensional EUV/X-ray imaging spectrometer (2DXIS) decomposes an image into pixels, separates and spectrally disperses these pixels, and records spectra with a time-gated MCP intensifier.

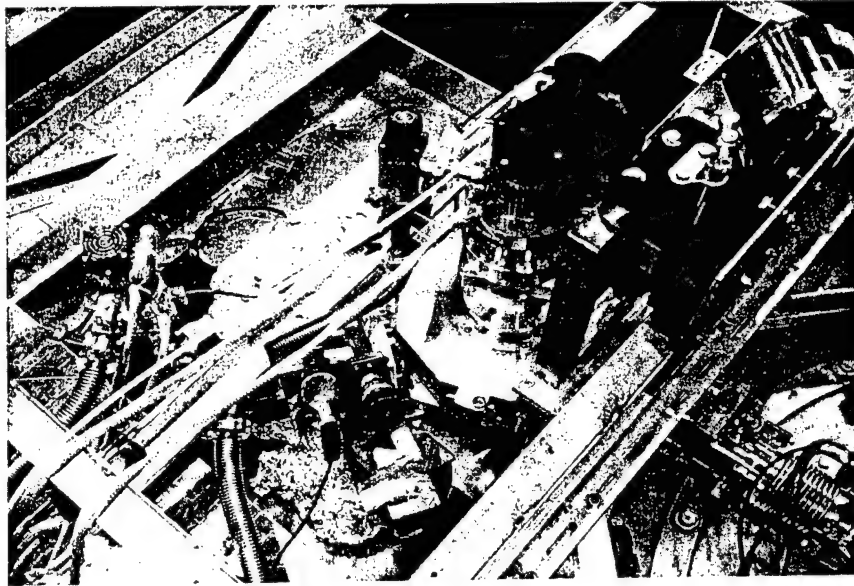


Figure 4.4. The 2DXIS (1DXIS) is prepared for experiments at the NTF (view from the top). At the right the diagnostic beamline with bellow and protection magnet is seen. In the center the main vacuum chamber of 2DXIS (1DXIS) is shown with a turbo-vacuum pump and an x-ray MCP time-gated multi-strip imager. At the left a x-ray MCP time-gated multi-strip imager and a part of MCP vacuum system are seen.

Table 1. Comparison of the parameters of the prototype 2DXIS with traditional 2D spectrographs with a spherical curved dispersive element [13,17,18] for z-pinch studies.

	2DXIS	2D spectrograph
Spectral resolution ($\lambda/\Delta\lambda$):		
crystals	700 – 1000	1000 [14,16]
MLMs	50 – 100	50-100 [16]
Spatial resolution (for z-pinch plasma):	100 -- 250 μm	100 μm
Number of output individual spectra	4-5 x 20	1
Time resolution (gated)	1-2 ns	1-2 ns
Wavelength observation band $\Delta\lambda$:		
single shot exposure	$\lambda/10 - \lambda/20$	$\lambda/25 - \lambda/50$
multi shot exposure	$\lambda/3$	-----
with rotation of a crystal (MLM)		

Testing of the 2DXIS at the NTF will begin in May-June 2001 with a Mo V-pinch test plasma object.

The 2DXIS has been used without a glass-capillary array and with an additional imaging slit between plasma and crystal, becoming a one-dimensional x-ray spectrometer with a time-multigated registration of x-ray spectra (1DXIS). First results of application of the 1DXIS for x-pinch experiments are described below.

4.1.2. Multichannel spectrometer "Polychromator"

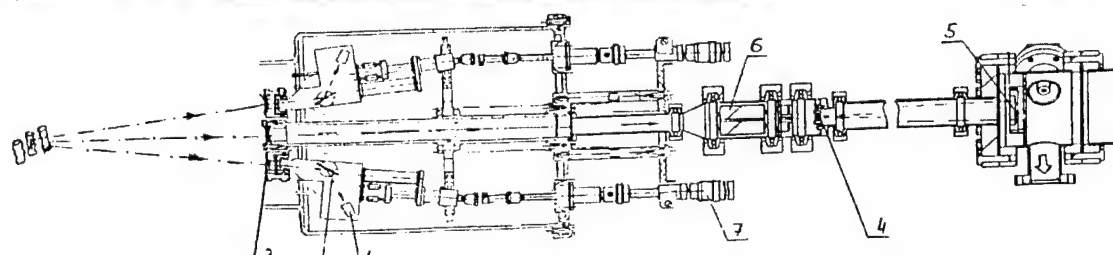
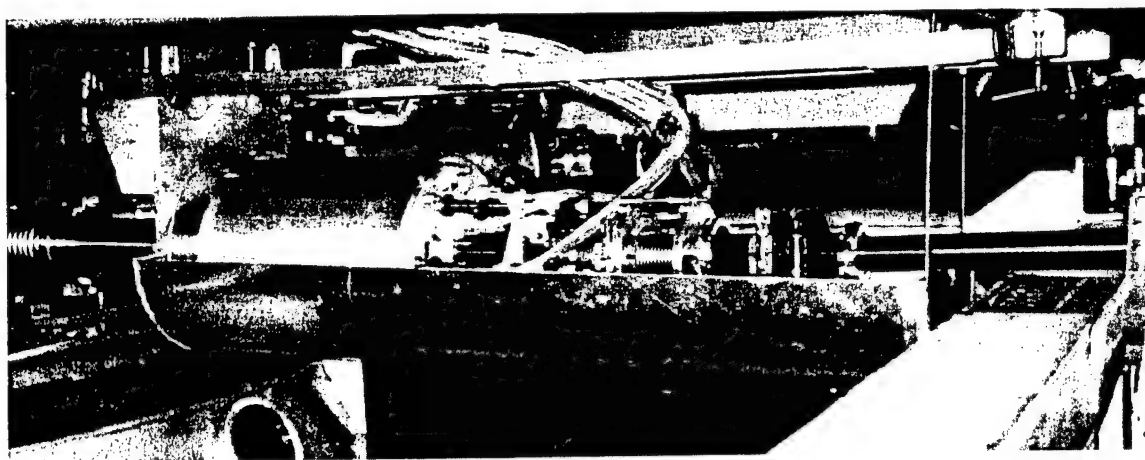
The monitoring of a time evolution of x-ray/EUV spectral lines from hot dense plasmas is very important for estimation of temperature and density behavior. A new 5-channel spectrometer (Figure 4.5) is designed for registration of x-ray emission from hot dense plasmas with spectral and temporal resolution [19]. An introduced device has 5 high spectral and temporal resolution channels based on Si [20] or PCD [21] x-ray detectors and crystals or MLMs as dispersing elements. Depending on the type of a dispersing element one can observe different groups of spectral lines with good spectral and temporal resolution. For spectroscopic measurements with spatial and temporal resolution, a channel based on a transmission diffraction grating spectrometer (TGS) and a gated imager can be added.

A set of different dispersing elements (crystals and MLMs) defines an observed spectral region (Table 2). Currently we use three crystals for studying *K*- and *L*- shell radiation: KAP ($2d=26.63$ Å), PET 002 ($2d=8.742$ Å), and LiF 200 ($2d=4.027$ Å). This set of crystals can record radiation in a very wide spectral region (from 1 Å to 25 Å). For studying EUV radiation we use multilayer mirrors (MLM) with $2d=61.5$ Å and $2d=197.2$ Å. All channels are independent from each other providing an opportunity to set the particular spectral region for each channel. Adjustment to a chosen wavelength is made by means of a precision linear translation stage for each channel without disturbing of vacuum conditions. Translation stages are connected with a mechanism of a crystal turning in the way that the incidence angle of radiation depends linearly on a fine screw position. The special design of the "Polychromator" also allows us to choose the particular dispersing elements, which can be the best for a spectral region under investigation.

The "Polychromator" has been used in the NTF x-pinch and conical and cylindrical array z-pinch experiments.

The sixth channel of the device shown in Figure 4.6 was designed for registration of a soft x-ray radiation in a spectral region of 20-80 Å. In this channel a transmission diffraction grating is used as a dispersing element. A transmission diffraction grating has a number of advantages in comparison with traditional grazing incidence spectrometers employed for spectroscopic measurements in this wavelength region. Spectrometers based on transmission diffraction gratings have better efficiency practically independent of a wavelength. For a grating used in our spectrometer, diffraction efficiency is ~7% in the first order. Spectrometers with pinhole gratings provide reasonable spatial resolution for all wavelengths under investigation. A flat registration surface allows us to use a gated microchannel plate detector (MCP) and to obtain simultaneously spatial, spectral and temporal resolution. Our spectrometer is designed to work with both an x-ray film and a MCP. A spectrometer proposed to be used in our experiments was tested at

several facilities such as a synchrotron radiation source, z-pinch, gas-puff and laser produced plasmas.



- | | | |
|-------------------------------------|-----------------------|----------------------|
| 1. Fast x-ray diodes (5 units) | 2. Crystals (5 units) | 3. Filters (5 units) |
| 4. Transmission Grating | 5. MCP Imager | 6. Magnetic Shield |
| 7. Wavelength controllers (5 units) | 8. Z-pinch plasma | |

Figure 4.5. Polychromator at the NTF (top) and its detailed drawing (bottom) .

Table 2. 6-channel "Polychromator" X-ray Spectrometer Characteristics.

5 -channel spectrometer	Transmission grating spectrometer (TGS)
Spectral region: 0.5 - 50 Å (3 crystal channels and MLM channel) 120 -240 Å (MLM channel)	Spectral region: 20 - 80 Å
Spectral resolution: 400-600	Spectral resolution: 20-50
Field of view: variable with spatial resolution: 3 - 5 mm	Spatial resolution: 150-200 μm
Time resolution: 0.2 - 0.5 ns.	Possible time resolution (gated): 1 - 2 ns.

4.1.3. Multichannel time-gated x-ray pinhole camera

The multichannel x-ray pinhole camera (MCPH) with a MCP time-gated multi-strip imager (Figs. 4.1, 4.6) has been constructed around a 6-strip 0.1-0.2 ns-gated MCP detector from Sandia National Laboratories, and installed at the NTF. This camera has been successfully used in x-pinch plasma experiments at the NTF for study of evolution of hot plasma with spatial and time resolution [22]. MCPH parameters are: magnification $\frac{1}{2}$, distance from a z-pinch plasma 70 cm, spatial resolution 100-250 μm , λ from 1 \AA to 10 \AA (two rows of images behind two different filters), MCP imager 6 gold striplines. Time frames 1, 2, 4, 6, or 8 ns, 6 frames (1-8 ns), inter-frame time 1-20 ns.

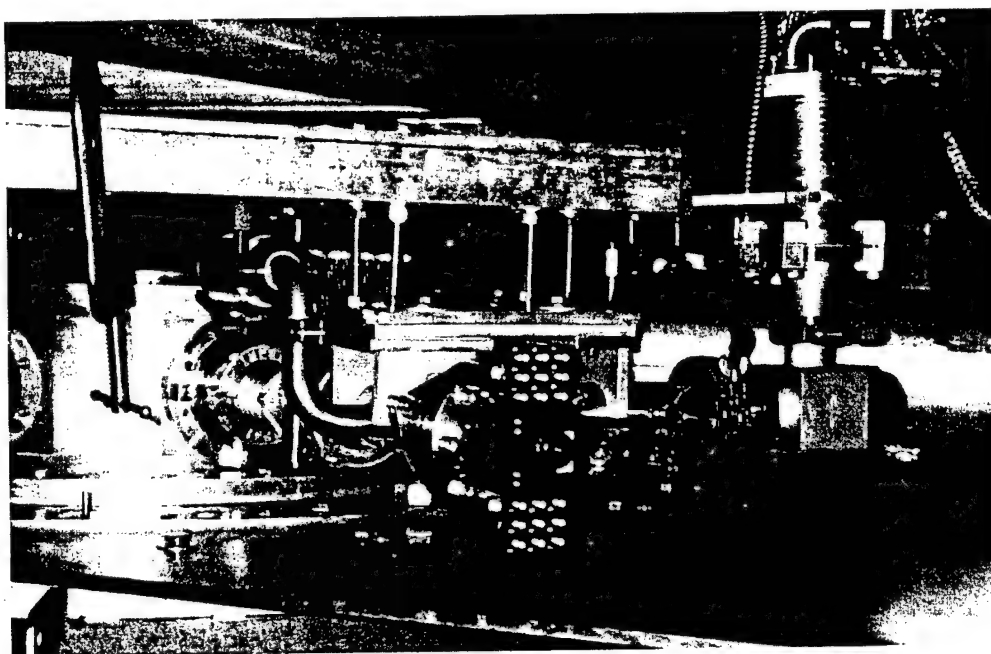


Figure 4.6. The multichannel x-ray pinhole camera (MCPH) at the NTF.

4.1.4. X-ray polarimeter-spectrometers

X-ray spectropolarimetry is a new powerful method to study energetic electron distribution functions and magnetic fields in hot plasma [3, 4]. This diagnostic method first suggested in 1981 [22] employs two identical spectrometers, that registered x-ray spectra in one direction of view on plasma, with a different orientation of dispersion planes in respect of a z-pinch discharge axis: one perpendicular and another parallel to the axis.

X-pinch at the NTF generate strong electron beams and are good for comparing polarization measurements and theory [2,4]. Preliminary calculations and modeling indicate that, for example, K-shell Ti lines, in particular a He-like resonance line and satellite lines, can be used to diagnose electron beams (or an alignment of the excited levels including autoionizing levels). The magnetic field will have no influence on their polarization. On the other hand, the L-shell Ti

lines are very good candidates for the diagnostics of magnetic field through line polarization [3,4]. Two sets of polarimeters/ spectrometers (XPSIS) with several convex crystals were designed for registration of polarization-sensitive K-shell and L-shell spectra produced by Ti or Fe x-pinch plasmas [4]. We applied these XPSIS (Figure 4.7) in first experimental polarization-sensitive measurements of K-shell Ti emission generate by x-pinch plasmas at the NTF [4].

In addition, "Polychromator" can be used for the detailed time-resolved investigation of polarization-dependent spectra simultaneously recorded by five channels with identical crystals (or MLMs) located at five different positions around direction of view on z-pinch plasma. These polarization-dependent spectra collected simultaneously at different angles of the diffraction from identical crystals represent a very valuable source of information about the electron distribution function in plasmas when the appropriate theoretical modeling is provided.

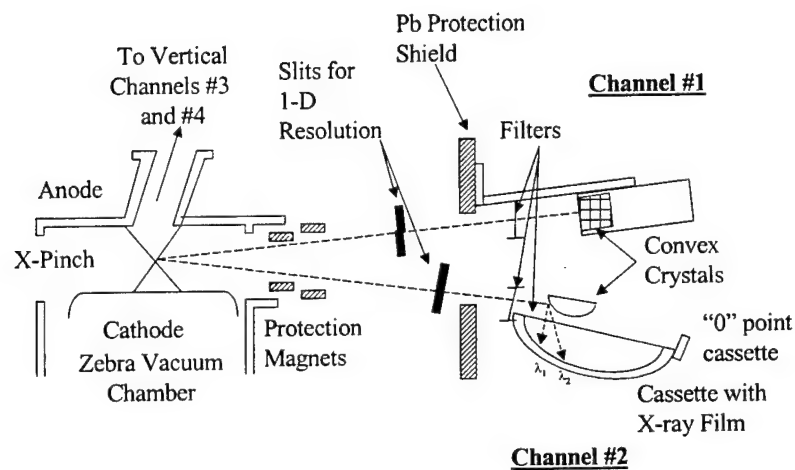


Figure 4.7. Experimental setup including a one-dimensional x-ray polarimeter/spectrometer for polarization measurements.

4.1.5. Future EUV plasma diagnostic for Zebra

A McPherson VUV spectrometer Model 225 was obtained from the Naval Research Laboratory, disassembled, with some vital parts missing. The instrument has been restored but we are still waiting for one slit assembly and a new grating. As soon as we have the slit, we can start testing and calibrating the instrument.

In the meantime, we have modeled the optical path of the EUV beamline using the raytracing software Zemax (Figs 4.8 & 4.9). Several configurations have been modeled. The best results were achieved using a 4" flat mirror, which will be exposed to fragments of the wire explosions, and a 6" toroidal mirror with curvatures of 2000 mm and 2015.34 mm. Since the curvatures are so close, we can make a fixture that bends a standard 2000 mm spherical mirror by about 22 μm , so that we achieve the needed curvatures. That this can be done has been proven in the literature.

In addition, we have modeled the mirror vacuum chamber that host the flat 4" (Figs. 4.10 & 4.11). In order to ease the design of this chamber, we can purchase an off-the-shelf 5- or 6-way cross that only requires some modifications. The 6" mirror will be housed in an ISO 200 (8") vacuum chamber, that consists of a standard ISO 200 tube adapter and a blank flange. Each mirror will be adjustable by an in-vacuo manipulator. Upon acceptance of the design, the mirror chamber can be manufactured at the physics' machine shop.

We will use one of the empty diagnostics ports of the Zebra vacuum chamber. The EUV light emission from the z-pinch plasma is deflected by a 4" mirror onto the toroidal 6" mirror (Figures 4.10 & 4.11). The 4" flat mirror will be exposed to fragments of the wire explosion and has a limited life expectancy. It needs to be replaced more often, and is therefore made easily accessible. In addition, the hard x-ray plasma emissions can deteriorate the Al/MgF mirror coating over time. We opted for this configuration, since only a relatively inexpensive 4" mirror needs to be exchanged. The light is deflected downwards and collected by a 6" toroidal mirror, which deflects and focuses the light onto the entrance slit of the spectrometer (Figures 4.10 & 4.11). Great care has been taken to ensure that the grating is adequately filled for a plasma object of 2 cm height (Figure 4.9). Other configurations, like a combination of a spherical and a cylindrical mirror, or other light pathways showed much poorer focusing and improper illumination of the grating.

In order to fill the grating, the F/number of the spectrometer has to be taken into account, which had to be balanced with the requirement to place the exposed optics at least 1 m away from the center of the Zebra vacuum chamber. The final design places the 4" mirror 1.5 m away from the chamber center.

In addition to the geometric optics, the wavelength regime has to be taken into account. For the toroidal mirror and also for the grating we will use an iridium coating for best performance in the VUV, while we can get away with Al/MgF coating for the flat mirror because of the shallow angle of incidence (40 degree). We want to study the region from 1000 \AA to 1400 \AA using a pulsed MCP with either film or CCD readout. The Model 225, equipped with a 600 g/mm grating, has a dispersion of 16.6 $\text{\AA}/\text{mm}$ which gives ~ 25 mm of spectrum of the wavelength region at the image plane. With a slit width of 0.200 mm the resolution is about 3.3 \AA .

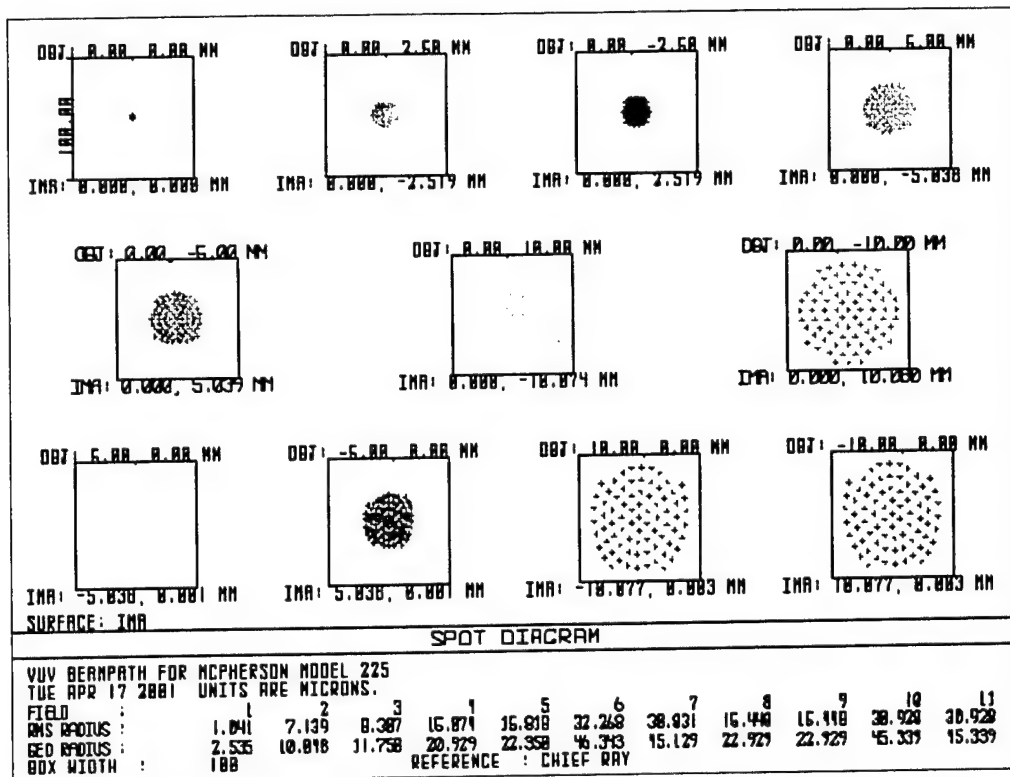


Figure 4.8. Raytracing of a 20 mm x 20 mm object onto the image plane. The box size is 100 μm x 100 μm .

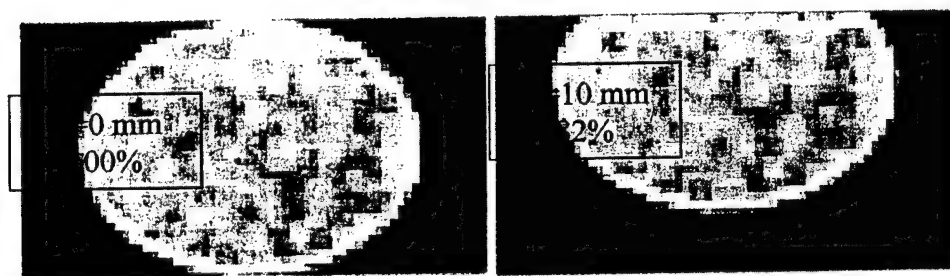


Figure 4.9. Raytracing results for two spots of the 20 mm image (object height is Y). For the outermost part of the object, the grating is still filled by 82% of the original rays.

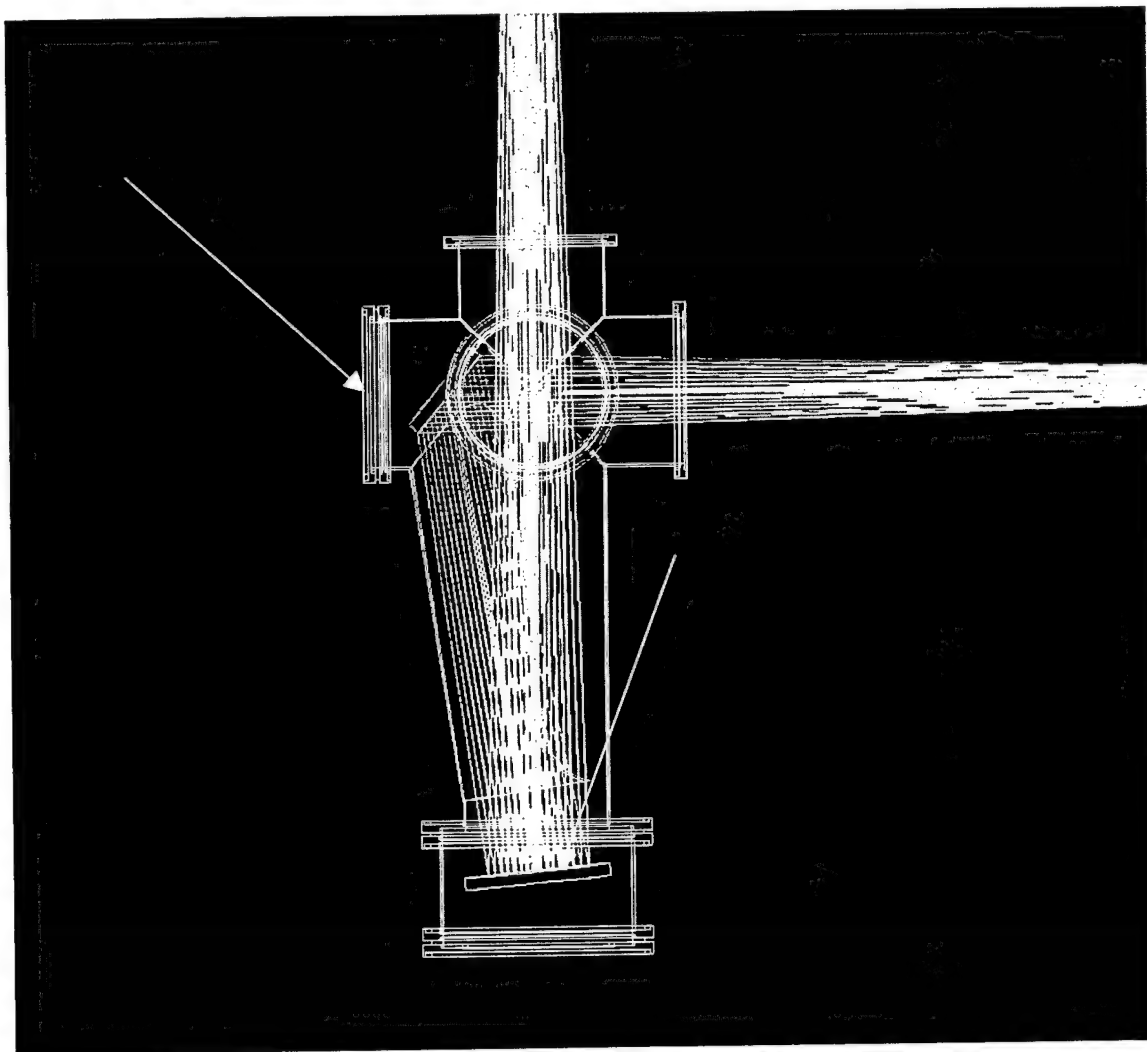


Figure 4.10. Pro/E solid model detail of the mirror chamber. The upper ports are of ISO 160 (6"); the lower ports with the toroidal mirror chamber are of ISO 200 (8"). Mirror manipulators are mounted on the ISO blank flanges for easy access to the mirrors and equipped with vacuum feedthroughs for mirror adjustments.

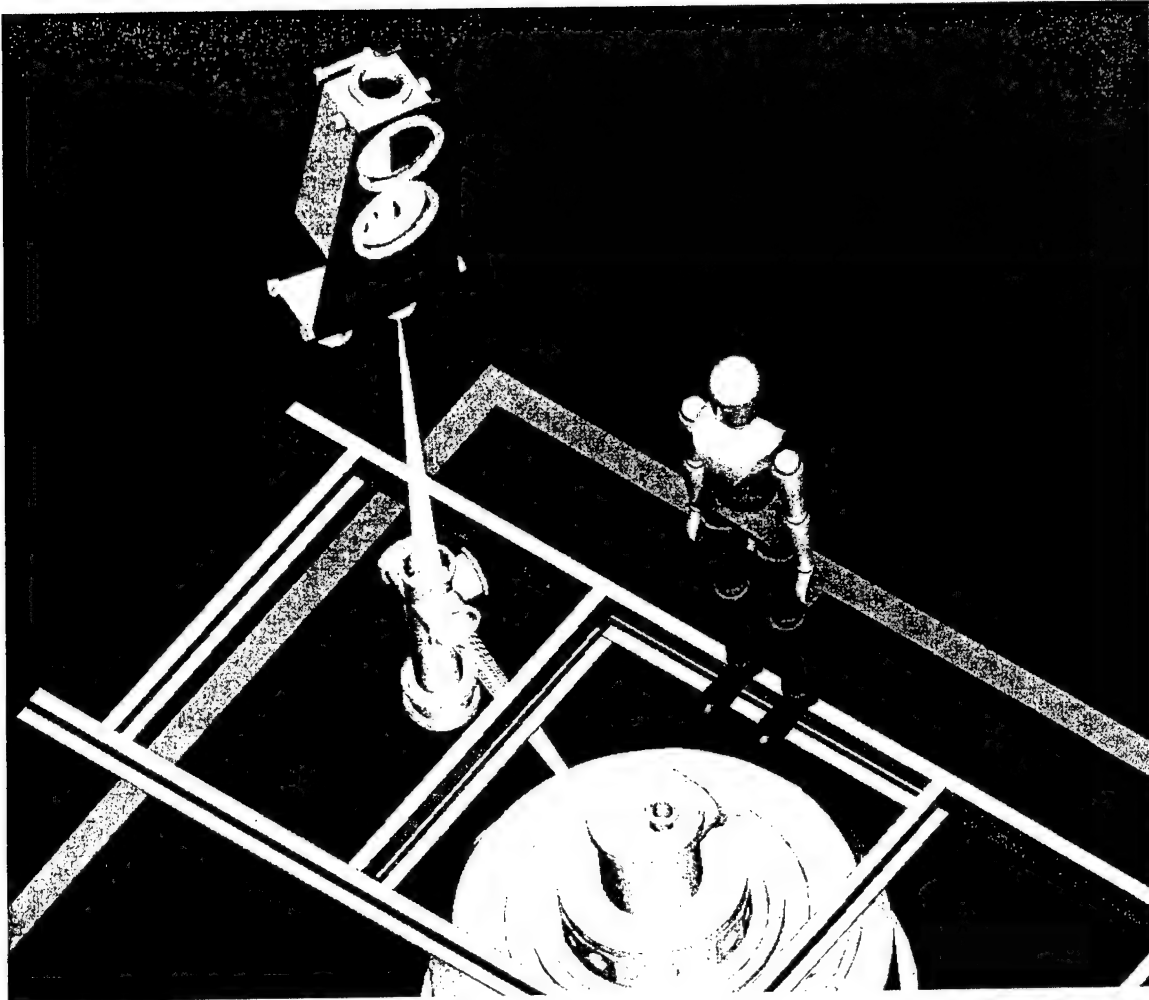


Figure 4.11. Pro/E model of VUV plasma diagnostic beamline. The mirror chambers are far enough from the Zebra assembly, in order to not interfere with regular maintenance operations. The water around the beamline parts will be displaced by a 'boat' which is not shown here.

4.2. Physics of high-current x-pinch x-ray/EUV radiation sources

4.2.1. Development and study of x-pinch backlighting

Zebra is being used to drive x-pinchs, to study and develop powerful pulsed soft x-ray point sources for x-ray and EUV plasma spectroscopy and x-ray backlighting. The x-pinch is being studied because it is the only x-ray source to offer simultaneously high spatial resolution (from 3-5 to 100 μm) and nanosecond time resolution [23]. X-pinchs consist of two or more thin crossed wires driven by a pulsed-power generator. Applying more than 100 kA peak current to the wires creates a hot, dense plasma along the original positions of the wires. At the contact point, the wires converge, and the magnetic field of the full current compresses, heats, and finally necks off the plasma, forming a bright plasma point and a microscopic x-ray diode [23]. Early x-pinchs have been used in both monochromatic and direct point-source backlighting [23], the main two x-ray backlighting schemes.

The long-term goals of these x-pinch experiments at the NTF are:

1. to develop a new (harder) x-ray backlighting source to determine a z-pinch load density profile [2];
2. to test x-ray spectropolarimetry, a powerful new tool for studying the anisotropy of high-temperature plasmas[4];
3. to examine the final stage of the MHD sausage ($m=0$) instability (production of a mini-diode).

X-pinch experiments on Zebra aim to characterize and understand x-pinch behavior as a function of current, and to see if a higher current (0.9 MA vs. 0.2-0.4 MA) can be used to make x-pinch sources brighter, harder (shorter wavelength), or faster (shorter pulse). X-pinchs have been made from a wide variety of materials, from Al to Pd [23], but have mostly been driven by currents of 0.2-0.4 MA, or less. At higher currents, the authors are only aware of one x-pinch publication [24], on an Al x-pinch driven by 0.8 MA. Here (section 4.2.1.2.), the results on Ti, Fe, Mo, W and Pt x-pinchs driven by 0.9 MA are reported. Important results are spot sizes, radiation pulse widths, wire diameters and symmetry of x-pinch hardware necessary to avoid multiple strikes and resulting multiple x-ray bursts, spectra of the radiation, the total radiated energy, how these parameters scale with a mass density of wires (current dependence will be study in near future).

4.2.1.1. Experimental procedure

X-pinchs were made by positioning two thin, straight, crossed Ti, Fe, Mo, W or Pt wires, of a diameter 20-152 μm , between the cathode and anode of the Zebra pulsed-power generator, with the wire contact on the axis of the cathode-anode gap (Figure 4.12). Driving the x-pinch with 0.9 MA yields bright, nanoseconds-duration K-shell, L-shell or M-shell x-ray bursts from a small bright spot where the wires intersect. The diameter and length of wires were varied to change the mass of z-pinch loads. Two configurations of x-pinchs were tested: wire twisted (at angle of rotation $\alpha \approx 25^\circ$ - 30°) and planar-loop (Figures 4.12 and 4.13). Other loads for comparison with

x-pinches, such as single wires and V-pinches, were also tested (see Section 4.3). An inner view of Zebra discharge chamber and views of anode and cathode electrodes are shown in Figures 4.14-4.16.

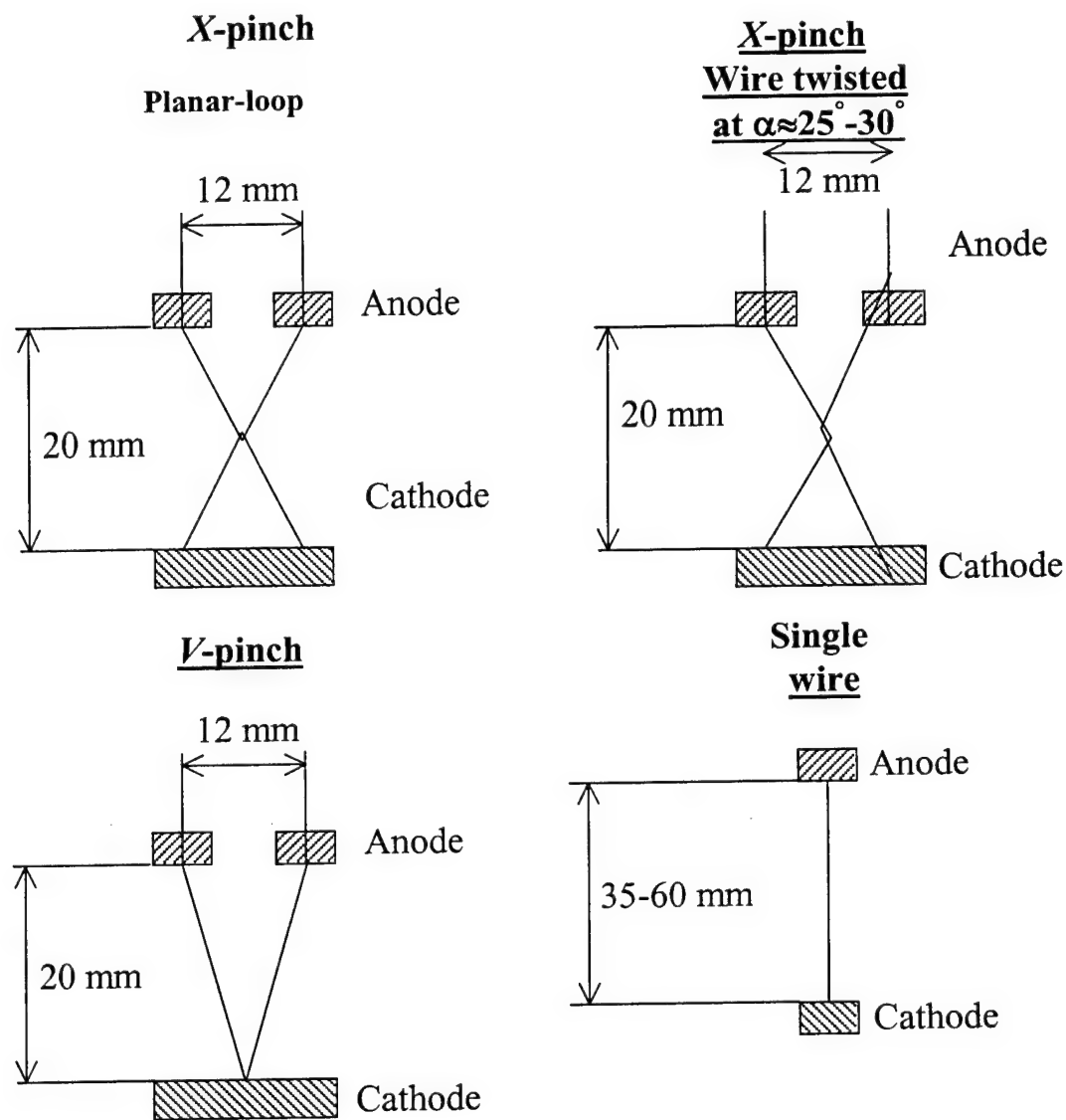


Figure 4.12. Main configurations of loads in the NTF plasma experiments.

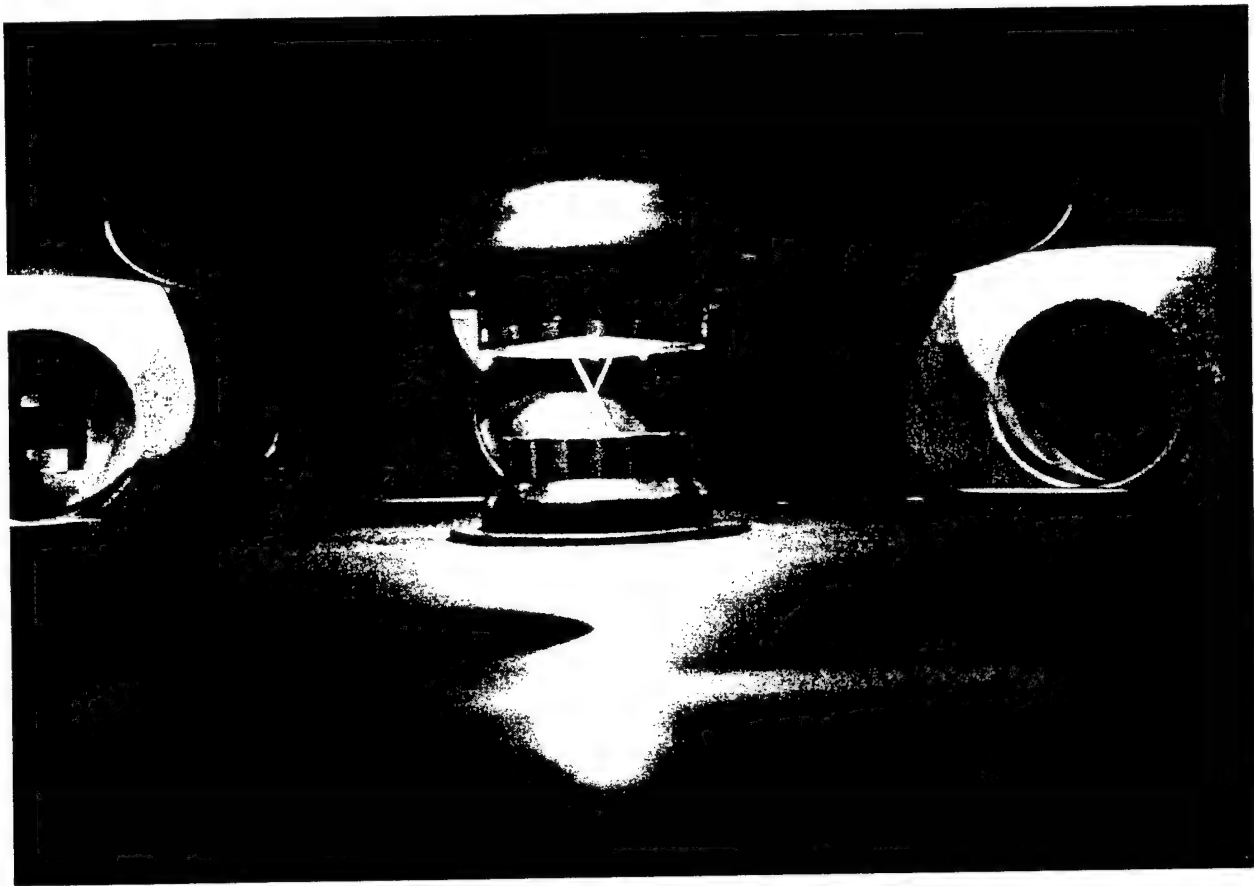


Figure 4.13. The x-pinch load in the NTF discharge chamber. Anode is at the top.

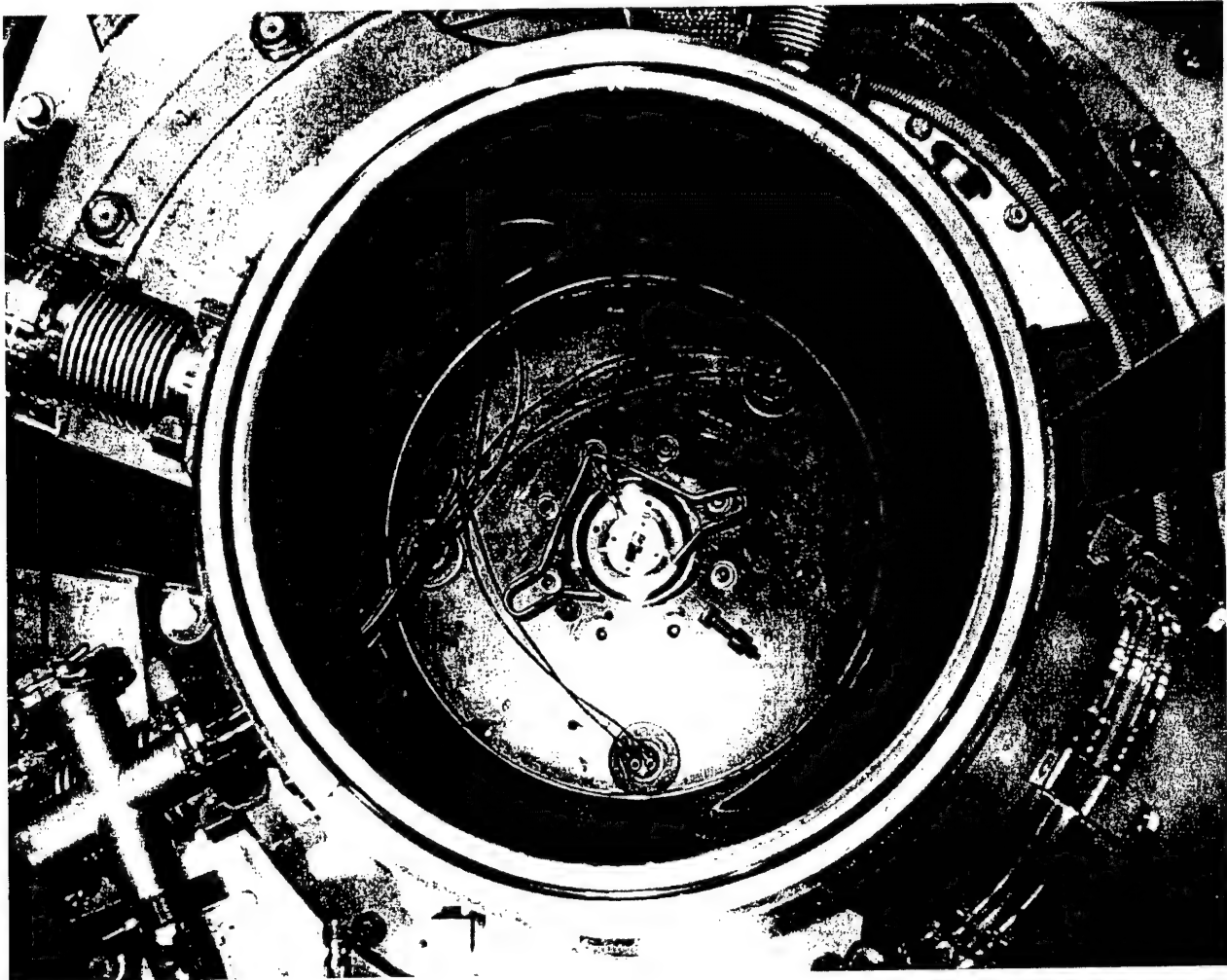


Figure 4.14. View from the top on an anode plate of Zebra. An anode cap for an x-pinch and wire holders are at the center.

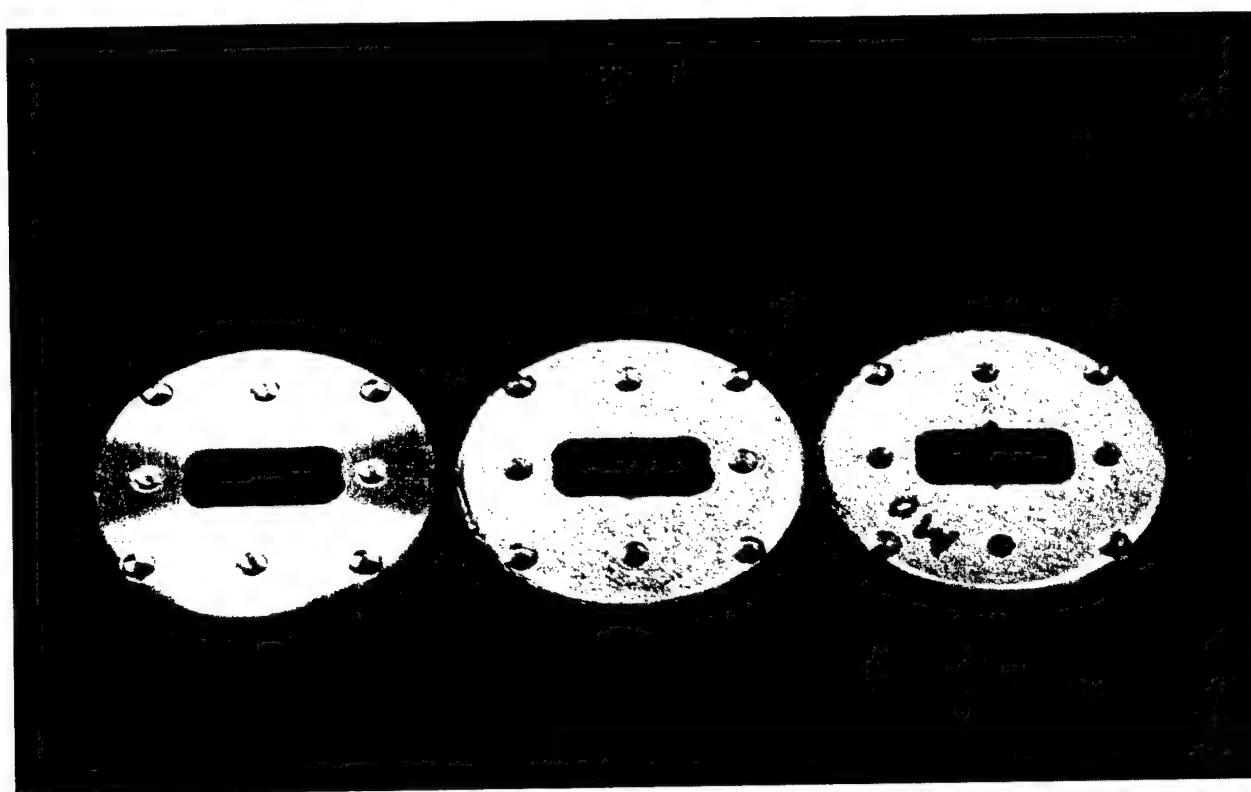


Figure 4.15. An anode electrode before (left) and after the shot for Fe (center) and Mo x-pinches (right). A strong increasing of the diameter of holes in plate for Mo is clearly seen.

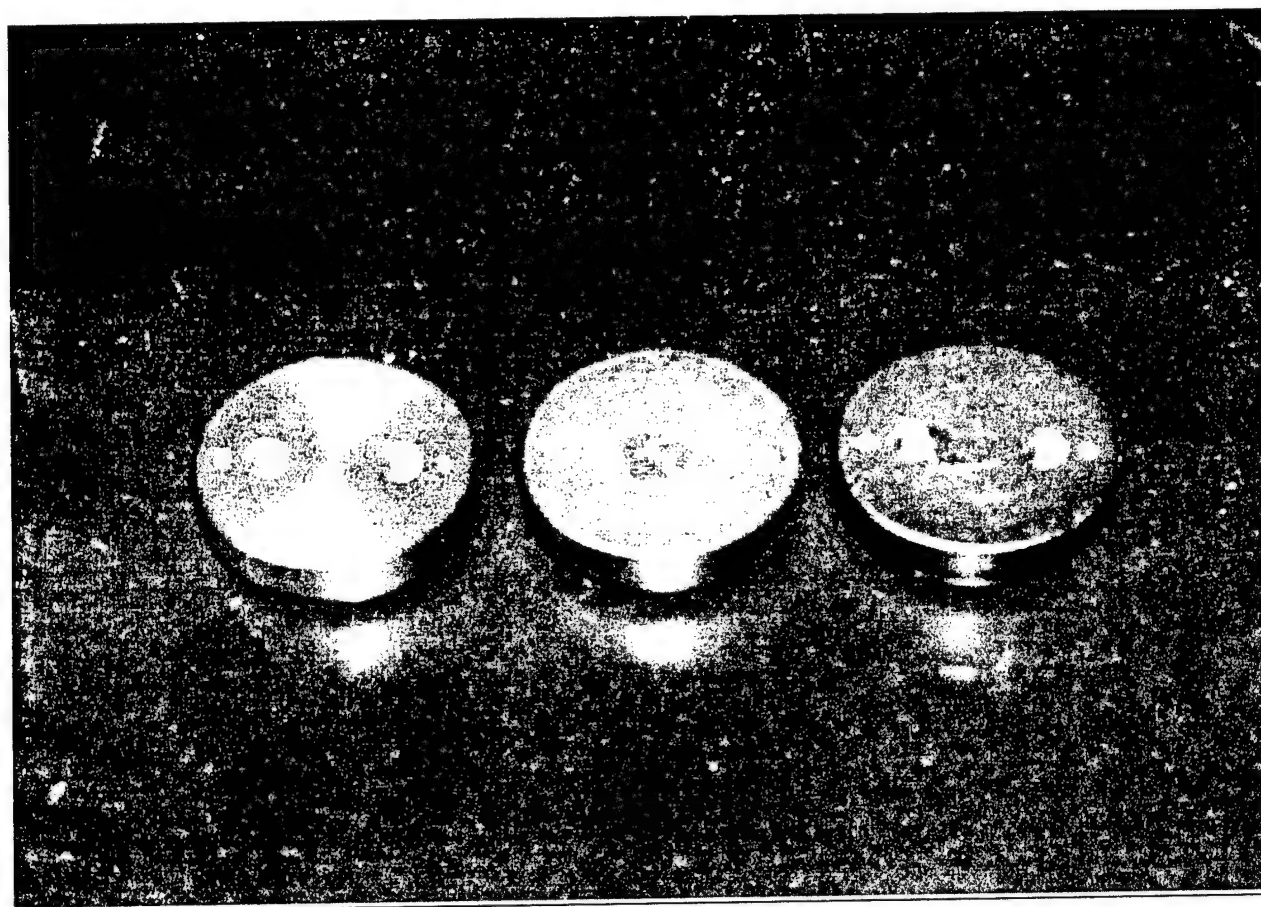


Figure 4.16. A cathode electrode before (left) and after the shot (center and right). The central electrode spot corresponds to a symmetrical x-pinch implosion, the right one to asymmetrical one with multiple strikes which result in multiple x-ray bursts.

4.2.1.2. Experimental results

4.2.1.2.1. Spatial structure of high-current x-ray sources

The high peak current (0.8-0.9 MA) quickly vaporizes and strongly ionizes the wires. Time-integrated and time-gated x-ray pinhole images show the location of the wires, with a bright spot at the cross point (Figs. 2-6). Ti and Fe K-shell, Mo L-shell, W and Pt M-shell and harder radiation is emitted from the cross point of the wires. High-resolution filtered pinhole camera images (GXI) show that the continuum and harder radiation come from a region that can be smaller than several hundred μm , in the same location as the K-shell, L-shell and M-shell sources. Ongoing experiments are attempting to determine whether source sizes comparable to the extremely small (2-5 μm) source size observed in x-pinchs at a lower current (0.2-0.4 MA) [3] can be achieved at a high current.

The structure of x-pinchs driven by a high current (0.8-0.9 MA) is more complicated than that of low-current (0.2-0.4 MA) x-pinchs [2].

First, a strong, energetic electron beam is not only directed to the center of the anode (between the wires), but also toward the anode ends of the wires [2]. The total energy of this beam is more than 10% of the discharge energy, based on the energy needed to generate the observed holes in the center of the anode and at the points of connection of the wires with the anode (Figure 4.15; also see the results of an e-beam study in Section 4.2.1.2.4). Such an energetic electron beam influences the plasma x-ray spectra. For example, polarization of K-shell spectra of Ti is observed[4]. Moreover, we observed a strong hard x-ray beam that is directed to the center of the anode (between the wires). Photon energy of this beam is more than 100-150 keV (Mo x-pinch) compare with 50-100 keV x-ray radiation in direction perpendicular to the x-pinch axis (see the results of a hard x-beam study in Section 4.2.1.2.4).

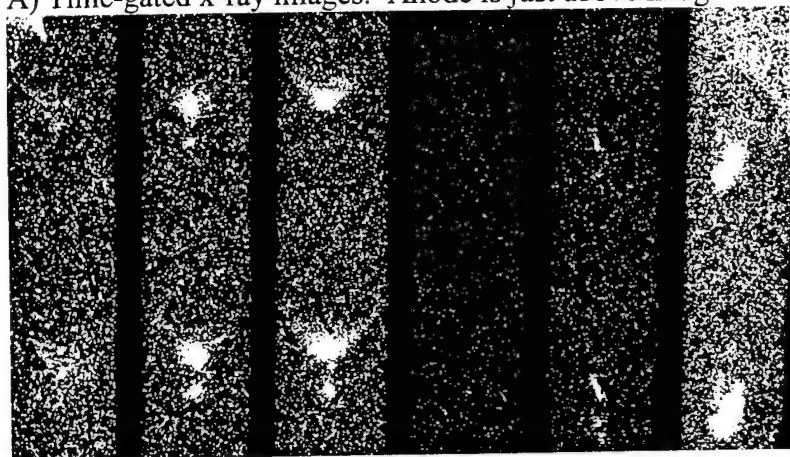
Second, strong jets are observed (mostly in softer-than-K-shell Ti and Fe, or L-shell Mo x-ray continuum emissions) directed toward the discharge axis, perpendicular to the wires (Figs. 17-21, 23-24) [2]. Stagnation of these jets on the axis of discharge forms a strong efficiently radiated in x-ray region jet directed to the anode (see below). The same effect was observed for the V-pinch configuration, that can be used to study plasma jet generation (Figure 4.25). These small jets have a period that varying from 1 to 2 mm for Ti, Fe and Mo. They are presumably spikes of the Rayleigh-Taylor instability of the accelerated wires. The luminous jets and their wires are observed on the anode- and cathode-sides of the contact. But brightness of anode side of images were always much stronger (Figs. 20, 21), indicating that they are luminous (in the spectral band recorded) because of excitation by fast electrons beams originating from the necked-off contact. Spots of damage in a center of a cathode have been observed in shots when we observed some jets directed to cathode (Figs. 16, 20, 21).

A comparison of time-gated x-ray images with time-integrated images and x-ray diodes signals shows that the x-ray source had a minimum size of 0.1-0.5 mm, and moved at a distance of 1.5-2 mm along the discharge axis during the discharge (Figs. 17-23). In most discharges development of a bright spot at the cross point occurs during the first part of the current pulse. Anode and cathode jets appear to be formed during all period of x-ray generation. In most cases the

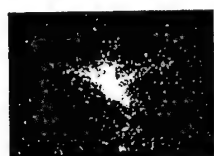
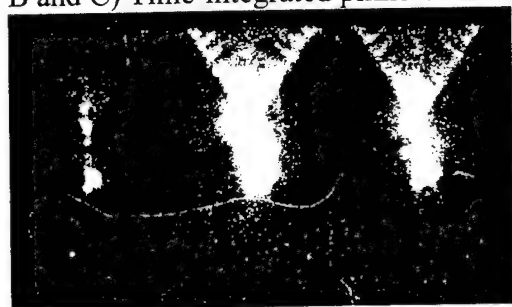
development of anode-wire directed electron beams occurs when current reached value of 0.5-1.0 from maximum.

Time-integrated and time-gated pinhole images, and time integrated pinhole transmission grating (TGS) images show the location of the wires, with bright spots at the cross point of x-pinch (see below). K-shell, L-shell, M-shell and harder radiation is emitted from the cross point of Ti, Fe, Mo, W and Pt wires. The size and shape of the emitting region depend on the observed spectral region, type of wires material and method of connection of wires. High resolution time-gated GXI and time integrated images show that the line, continuum and harder radiation comes from a region that can be smaller than 30-65 μm (resolution of time-integrated pinhole camera), in the same location as the Ti, Fe K-shell, Mo L-shell or W, Pt M-shell sources (ongoing NTF experiments are attempting better resolution to 10-12 μm). The minimum size of this region is 2.5-4 mm for Ti K-shell and 2-3 mm for Fe K-shell, Mo L-shell or W, Pt M-shell radiation (time-integrated image) for planar-loop x-pinch. For wire-twisted Ti x-pinch this is 4-6 mm. Typically this region includes from 3 to 7-8 hot bright spots (each smaller than 30-65 μm -the resolution of camera) for the x-pinch with wire-twisted connection.

A) Time-gated x-ray images. Anode is just above images. Top image $\lambda < 3.5 \text{ \AA}$



A) 1 2 3 4 5 6 Lower image $\lambda < 5 \text{ \AA}$
 B and C) Time-integrated pinhole camera images; anode is at top of images.



12mm

B) $\lambda < 3 \text{ \AA}$ $\lambda < 7 \text{ \AA}$ $\lambda < 4 \text{ \AA}$ C) $\lambda < 4 \text{ \AA}$
 D) GXI frames (correspond to A): 1 2 3 4 5 6

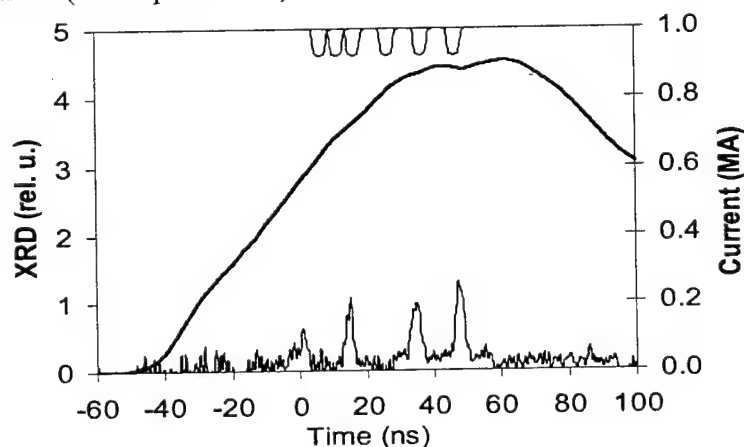
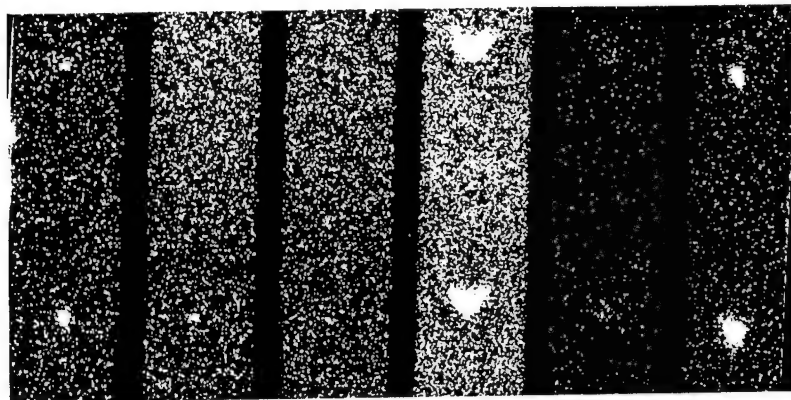


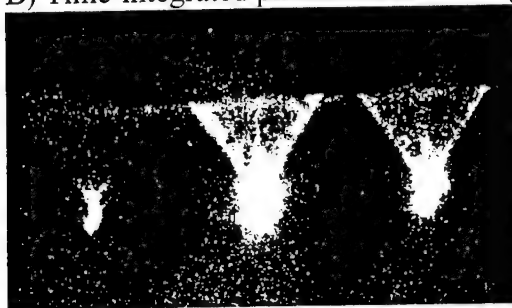
Figure 4.17. X-ray images and signals from a Ti wire-twisted x-pinch with 30- μm wire diameter and 20-mm anode-cathode gap (shot #29, May 17, 2000). A) Gated x-ray images. Spatial resolution 100 μm . Top image on each strip filtered for $\lambda < 3.5 \text{ \AA}$, the lower image for $\lambda < 5 \text{ \AA}$. B) Time-integrated pinhole camera images (Kodak DEF-5 x-ray film), with the same view as in A. Spatial resolution 580 μm . C) Time-integrated pinhole camera image as in B), but with a view from the top, at 9 degrees from vertical. Spatial resolution 200 μm . D) X-pinch current (thick smooth line), GXI frames, and XRD (with 5 μm Kimfoil filter; lower thin spiky line) response versus time.

A) 1 2 3 4 5 6 Anode is just above images.
Top image $\lambda < 5\text{\AA}$



Lower image $\lambda < 3.5\text{\AA}$

B) Time-integrated pinhole camera images; anode is at top of images.



B) $\lambda < 3\text{\AA}$ $\lambda < 7\text{\AA}$ $\lambda < 4\text{\AA}$

12mm

C) GXI frames (correspond to A): 1 2 3 4 5 6

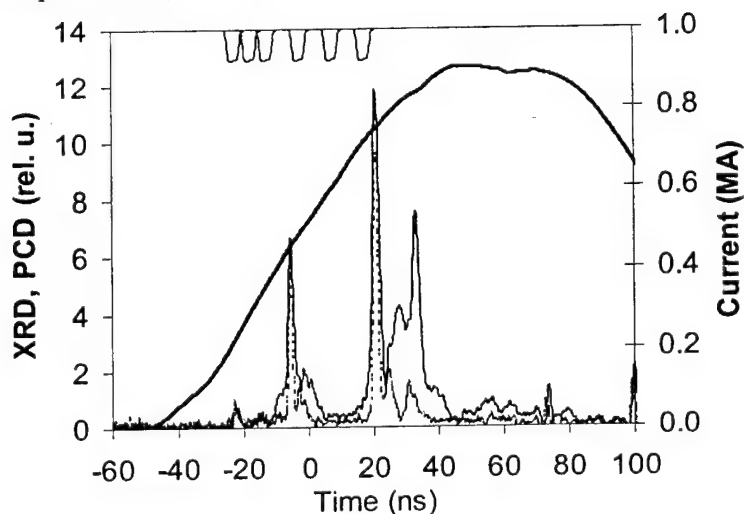
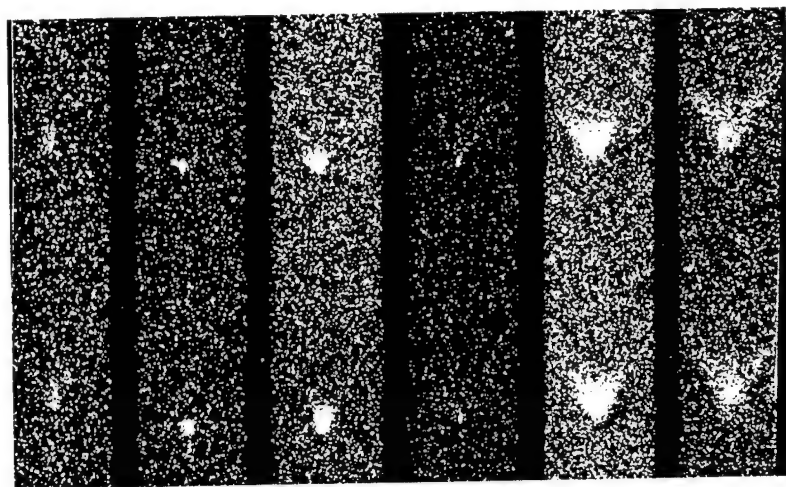


Figure 4.18. X-ray images and signals from a Ti wire-twisted x-pinch with 30- μm wire diameter and 20-mm anode-cathode gap (shot #30, May 18, 2000). A) Gated x-ray images. Spatial resolution 100 μm . Top image on each strip filtered for $\lambda < 3.5\text{\AA}$, the lower image for $\lambda < 5\text{\AA}$. B) Time-integrated pinhole camera images (Kodak DEF-5 x-ray film), with the same view as in A. Spatial resolution 580 μm . C) X-pinch current (thick smooth line), GXI frames, XRD (with 5 μm Kimfoil filter; thin solid spiky line), and PCD (with 8 μm Be filter; dotted lower spiky line) response versus time.

A) Time-gated x-ray images.

Anode is just above images.
Top image $\lambda < 3.5 \text{ \AA}$



A) 1 2 3 4 5 6 Lower image $\lambda < 5 \text{ \AA}$

B) Time-integrated pinhole camera images; anode is at top of images.



B) $\lambda < 3 \text{ \AA}$ $\lambda < 7 \text{ \AA}$ $\lambda < 4 \text{ \AA}$

C) GXI frames (correspond to A): 1 2 3 4 5 6

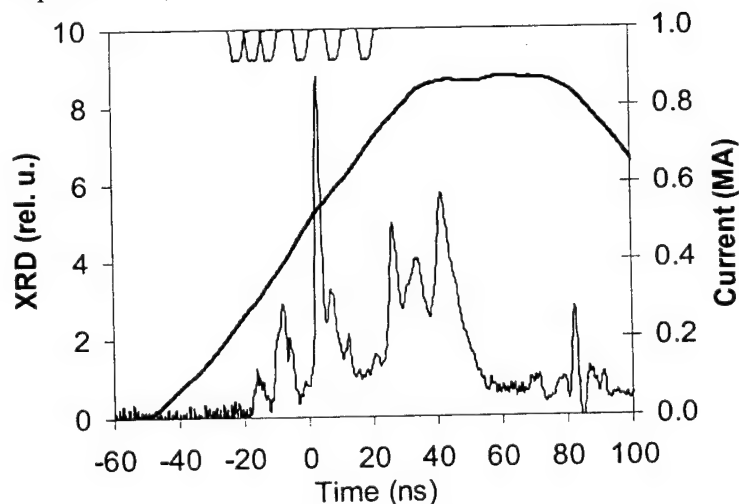
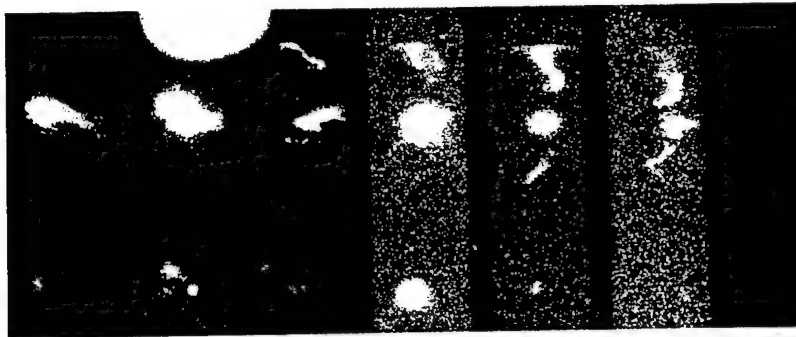


Figure 4.19. X-ray images and signals from an Fe planar-loop x-pinch with 19- μm wire diameter and 20-mm anode-cathode gap (shot #32, May 24, 2000). A) Gated x-ray images. Spatial resolution 100 μm . Top image on each strip filtered for $\lambda < 3.5 \text{ \AA}$, the lower image for $\lambda < 5 \text{ \AA}$. B) Time-integrated pinhole camera images (Kodak DEF-5 x-ray film), with the same view as in A. Spatial resolution 580 μm . C) X-pinch current (thick smooth line), GXI frames, and XRD (with 5 μm Kimfoil filter; thin spiky line) response versus time.

A) Time-gated x-ray images.

Anode is just below images.
Top image $\lambda < 10 \text{ \AA}$



A) 6 5 4 3 2 1

Lower image $\lambda < 3.5 \text{ \AA}$

B) Time-integrated pinhole camera images; anode is at top of images.



B) $\lambda < 2.6 \text{ \AA}$ $\lambda < 7.9 \text{ \AA}$ $\lambda < 5 \text{ \AA}$

C) GXI frames (correspond to A) : 1 2 3 4 5 6 (see below time axis).

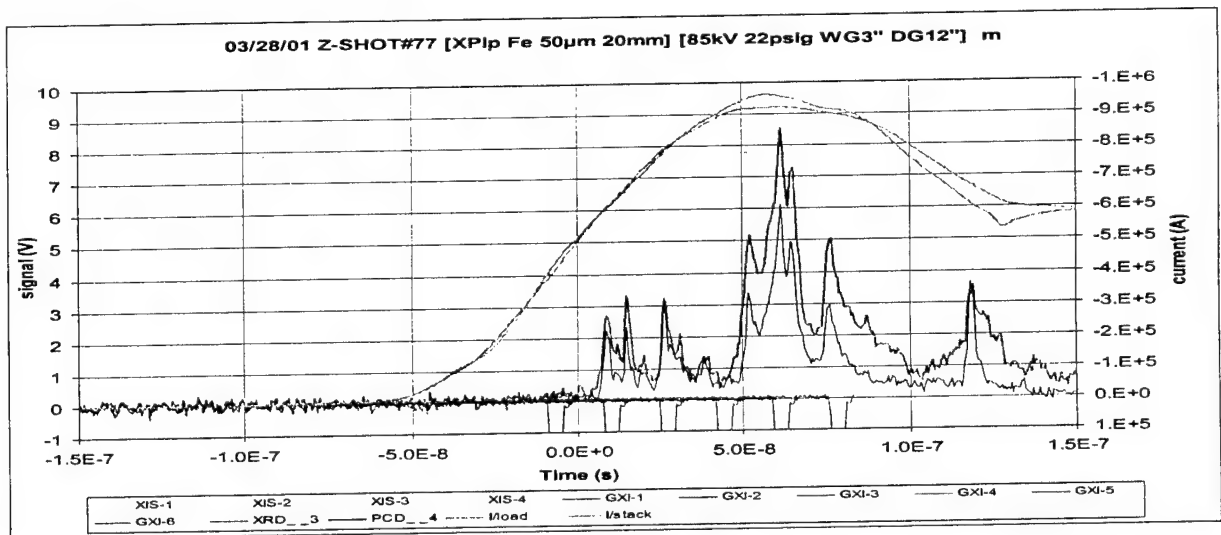
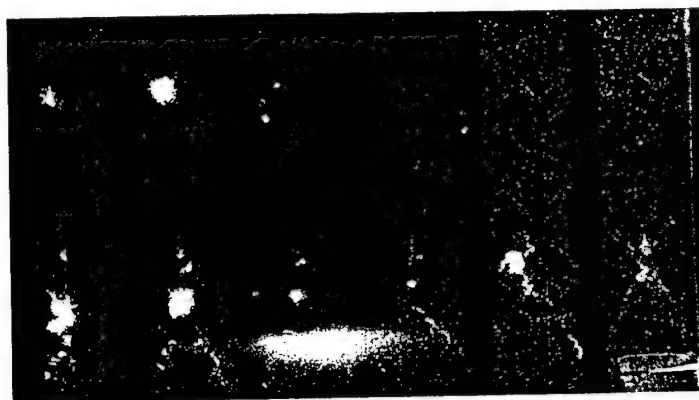


Figure 4.20. X-ray images and signals from a Fe planar-loop x-pinch with a 50- μm wire diameter and a 20-mm anode-cathode gap (shot #77, March 28, 2001). A) Gated x-ray images. Frame 4 ns. Spatial resolution 230 μm . Top image on each strip filtered for $\lambda_{1/10} < 10 \text{ \AA}$, the lower image for $\lambda_{1/10} < 3.5 \text{ \AA}$. B) Time-integrated pinhole camera images (Kodak DEF-5 x-ray film), with the same view as in A. Spatial resolution 580 μm . C) X-pinch current (thick smooth line), GXI frames, XRD (with 5 μm Kimfoil filter) and PCD (with 8 μm Be filter) response versus time.

A) Time-gated x-ray images.

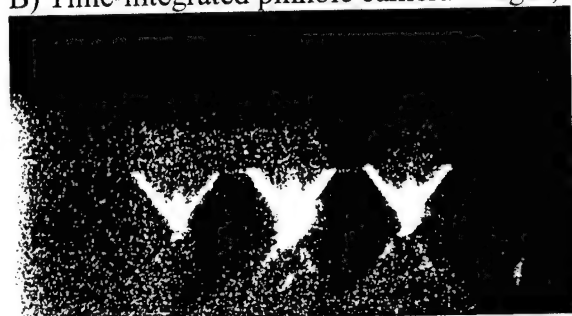
Anode is just below images.

Top image $\lambda < 3.5 \text{ \AA}$



A) 6 5 4 3 2 1 Lower image $\lambda < 10 \text{ \AA}$

B) Time-integrated pinhole camera images; anode is at top of images.



B) $\lambda < 2.6 \text{ \AA}$ $\lambda < 7.9 \text{ \AA}$ $\lambda < 5 \text{ \AA}$

C) GXI frames (correspond to A): 1 2 3 4 5 6 (see below time axis).

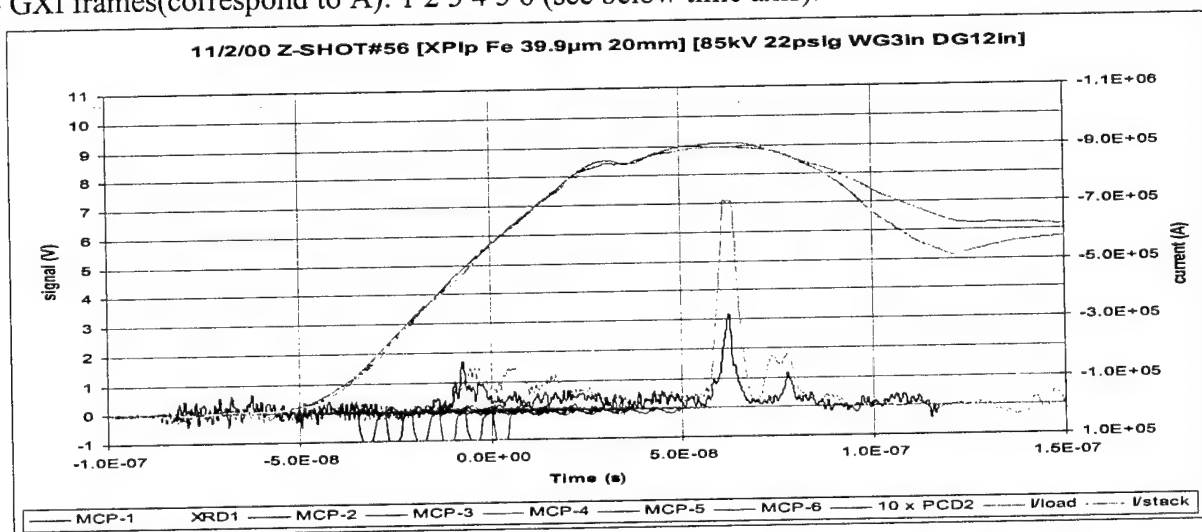


Figure 4.21. X-ray images and signals from a Fe planar-loop x-pinch with a 39.9- μm wire diameter and a 20-mm anode-cathode gap (shot #56, November 02, 2000). A) Gated x-ray images. Frame 4 ns. Spatial resolution 230 μm . Top image on each strip filtered for $\lambda_{1/10} < 10 \text{ \AA}$, the lower image for $\lambda_{1/10} < 3.5 \text{ \AA}$. B) Time-integrated pinhole camera images (Kodak DEF-5 x-ray film), with the same view as in A. Spatial resolution 580 μm . C) X-pinch current (thick smooth line), GXI frames, XRD (with 8 μm Be filter) and PCD (with 25 μm kapton filter) response versus time.

A) Time-gated x-ray images.

Anode is just below images.
Top image $\lambda < 3.5 \text{ \AA}$



A) 1 2 3 4 5 6

Lower image $\lambda < 10 \text{ \AA}$

B) Time-integrated pinhole camera images; anode is at top of images.



B) $\lambda < 5 \text{ \AA}$ $\lambda < 7.9 \text{ \AA}$ $\lambda < 2.6 \text{ \AA}$

C) GXI frames (correspond to A) : 1 2 3 4 5 6 (see below time axis).

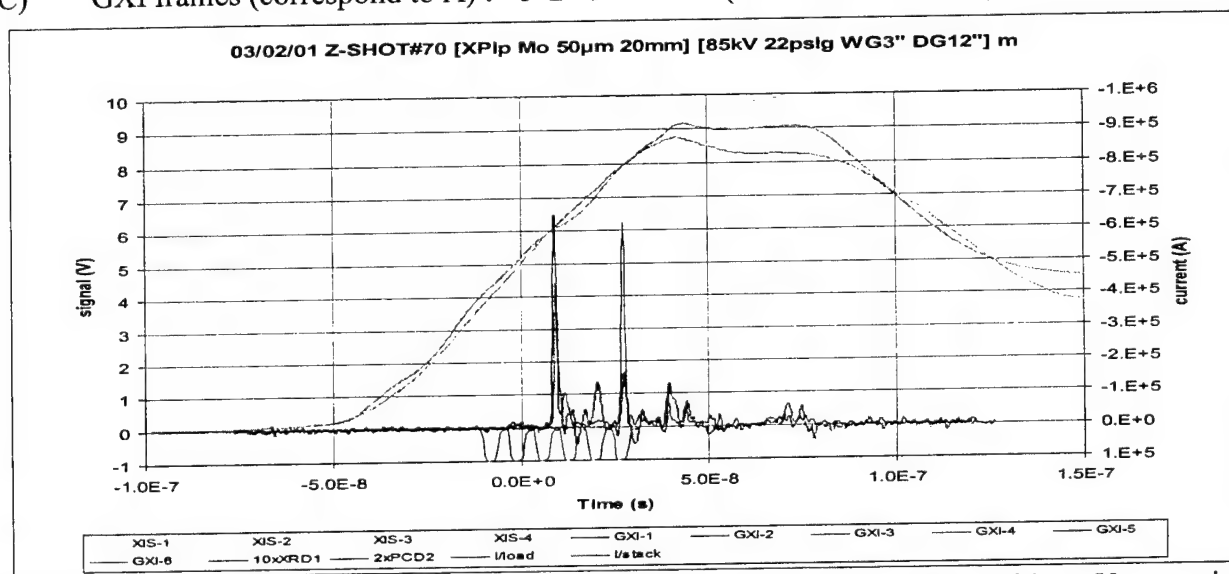


Figure 4.22. X-ray images and signals from a Mo planar-loop x-pinch with a 50- μ m wire diameter and a 20-mm anode-cathode gap (shot #70, March 02, 2001). A) Gated x-ray images. Frame 4 ns. Spatial resolution 230 μ m. Top image on each strip filtered for $\lambda_{1/10} < 10 \text{ \AA}$, the lower image for $\lambda_{1/10} < 3.5 \text{ \AA}$. B) Time-integrated pinhole camera images (Kodak DEF-5 x-ray film), with the same view as in A. Spatial resolution 580 μ m. C) X-pinch current (thick smooth line), GXI frames, XRD (with 8 μ m Be filter) and PCD (with 25 μ m kapton filter) response vs. time.

A) Time-gated x-ray images; frame time & number are above & below strips.

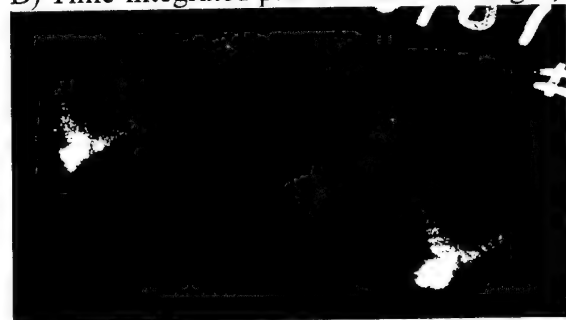
Anode is just below images.

Top image $\lambda < 10 \text{ \AA}$



Lower image $\lambda < 3.5 \text{ \AA}$

B) Time-integrated pinhole camera images; anode is at top of images.



B) $\lambda < 3.5 \text{ \AA}$

$\lambda < 10 \text{ \AA}$

C) GXI frames (correspond to A):

1 2 3 4 5 6 (see below time axis).

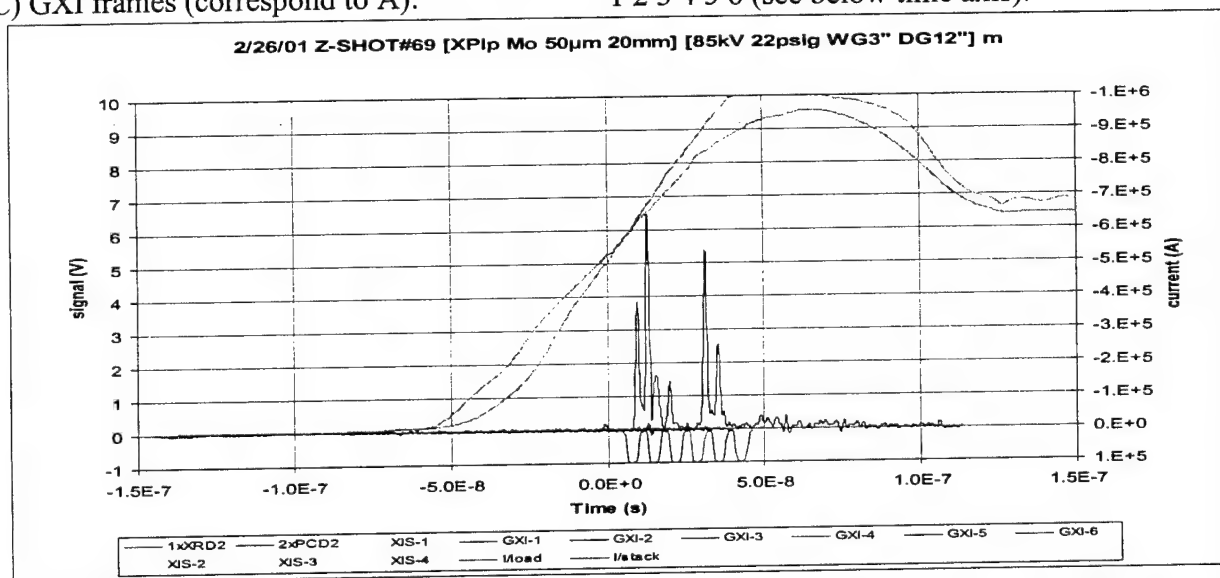


Figure 4.23. X-ray images and signals from a Mo planar-loop x-pinch with a 50- μm wire diameter and a 20-mm anode-cathode gap (shot #69, February 26, 2001). A) Gated x-ray images. Frame 4 ns. Spatial resolution 230 μm . Top image on each strip filtered for $\lambda_{1/10} < 10 \text{ \AA}$, the lower image for $\lambda_{1/10} < 3.5 \text{ \AA}$. B) Time-integrated pinhole camera images (Kodak DEF-5 x-ray film), with the same view as in A. Spatial resolution 580 μm . C) X-pinch current (thick smooth line), GXI frames, XRD (with 8 μm Be filter) and PCD (with 25 μm kapton filter) response vs. time.

A) Anode is just above images.



$\lambda < 5\text{\AA}$ $\lambda < 7.9\text{\AA}$ $\lambda < 2.6\text{\AA}$

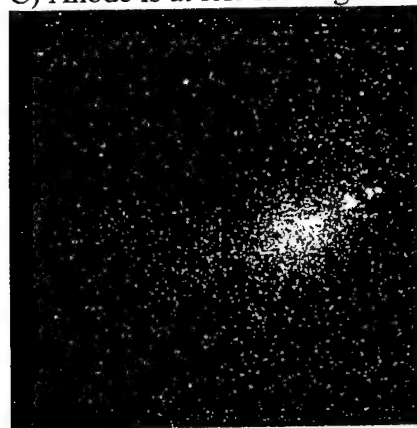
B) Anode is at bottom of image.



$\lambda < 7.9\text{\AA}$

----- 650 μm

C) Anode is at left of image



----- 650 μm

$\lambda < 2\text{\AA}$

Figure 4.24. X-ray images from a Mo planar-loop x-pinch with a 50- μm wire diameter and a 20-mm anode-cathode gap (shot #70, March 02, 2001). A) Time-integrated pinhole camera images (Kodak DEF-5 x-ray film). Spatial resolution 580 μm . B) Time-integrated pinhole camera images (Kodak DEF-5 x-ray film). Spatial resolution 60 μm . C) Time-integrated pinhole camera images (Kodak DEF-5 x-ray film). Spatial resolution 60 μm . Spot at the right from hot spots images is a result of penetration of hard x-ray through Pt/Ir pinhole substrate.

For the planar-loop x-pinch a number of hot spots is reduced to 1-5. The size of these spots depends on spectral region of registration. For example, for a Mo x-pinch it has been reduced from several hundred μm to smaller than 30—70 μm when a spectral region of observation has been changed from 4-10 \AA (Mo L-shell) to 1.5-2 \AA (continuum with planckian spectra) (Figure 4.24). These short-wavelength hot spots are located in shape of a chain along a central axis of an x-pinch near the cross point of wires.

The minimum size of an emitting region was found for a Mo x-pinch with a 50 μm diameter of wires (about 200 $\mu\text{g}/\text{cm}$ mass density). The minimum size of emitting region for Ti and Fe L-shell measured with TGS is 3-6 mm. This region includes several small sources of radiation with a minimum size 200 μm (TGS resolution).

A comparison of time-gated x-ray images with time-integrated images and PCD/XRD signals shows that a x-ray image of the source moved for a distance of several mm along the discharge axis during the discharge with a maximum speed from 5×10^6 cm/s (Ti and Fe) to 5×10^7 cm/s (Mo). The direction of movement can change to opposite during a discharge.

We found that the quality of an x-pinch structure (from the point of view of minimization of an effective size of a source and a number of hot spots) is in strongly dependent on the original symmetry of the x-pinch and its planarity. For example, shots #56 (Fe), # 70 (Mo) correspond to a good symmetry, whereas shots 32, 77 (Fe) and shot 69 (Mo) reflect bad original symmetry due to problems with some deformation of an anode plate under vacuum. An estimated accuracy of an x-pinch structure must be at least 3-5 % from a maximum dimension of structure.

The x-pinch structure at high current is shown below (Fig. 4.25).

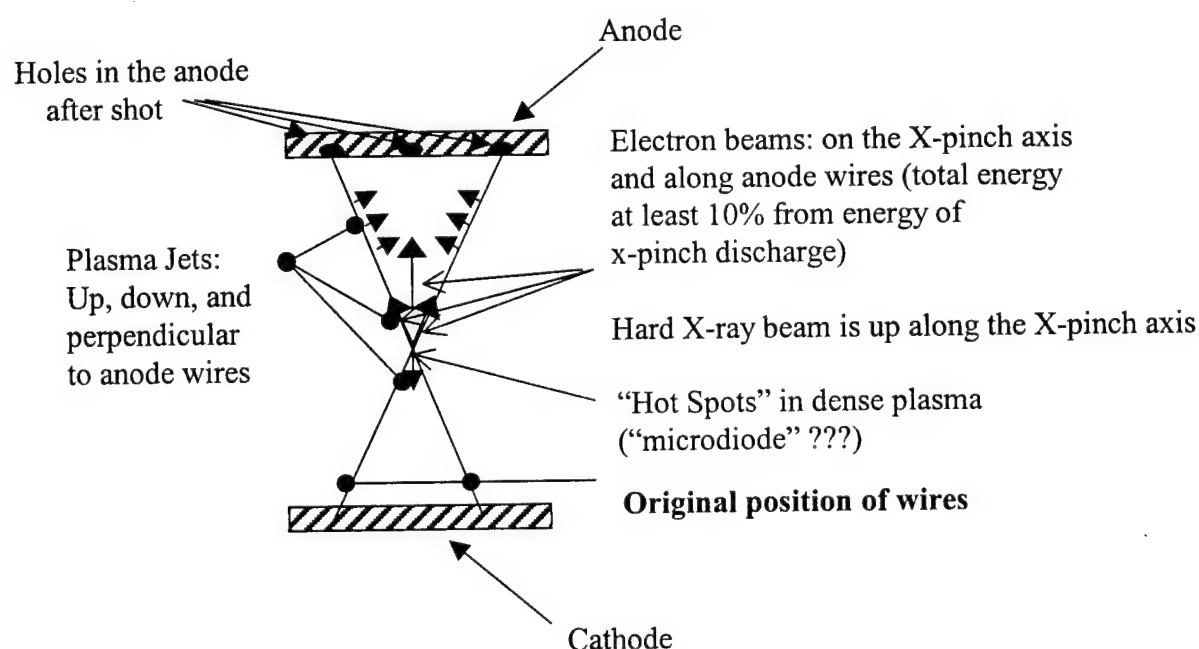


Figure 4.25. The structure of an x-pinch at a high current.

4.2.1.2.2. Time and energy scaling of high-current x-pinch x-ray/EUV pulses

Statistics were collected on the time and energy scaling of high-current x-pinch x-ray/EUV emission. Optimization of the emission would require more x-pinch shots than have been taken to date. In the tables and figures below, each data point represents an average value from two to five pulses.

The fast (0.2 ns) PCD are filtered by Be or kapton and XRD are filtered by kimfoil measure x-pinch emission. The "Polychromator" measures duration of selected spectral lines. The Ni bolometer (from SNL) measures the total x-ray/EUV energy radiated from x-pinch. For all x-pinch PCD, XRD and "Polychromator" signals are distributed in 1-5 pulses with different duration (Table 3), compared with 7-10 or more for single wires and a v-pinch.

X-ray bursts appear before the current reaches maximum (Figs. 4.17-4.23). Often x-ray pulses occurred in two or three groups, in the narrow time intervals after the start of the current.

Table 3. Minimum pulse duration of high current x-pinch.

	PCD (filter)	XRD (filter)	XRD (filter)
Ti	2.2 ± 0.4 ns (Be $8\mu\text{m}$)	4 ± 1 ns (kimfoil $5\mu\text{m}$)	
Fe	1.3 ± 0.7 ns (Be $8\mu\text{m}$)	3.7 ± 0.7 ns (kimfoil $5\mu\text{m}$)	
Mo	1.1 ± 0.5 ns (kapton $25\mu\text{m}$)	1.2 ± 0.7 ns (Be $8\mu\text{m}$)	15-20 ns (kimfoil $5\mu\text{m}$)
W	1.1 ± 0.7 ns (kapton $25\mu\text{m}$)	1.1 ± 0.7 ns (Be $8\mu\text{m}$)	15-20 ns (kimfoil $5\mu\text{m}$)
Pt	1.2 ± 0.7 ns (kapton $25\mu\text{m}$)	1.1 ± 0.7 ns (Be $8\mu\text{m}$)	

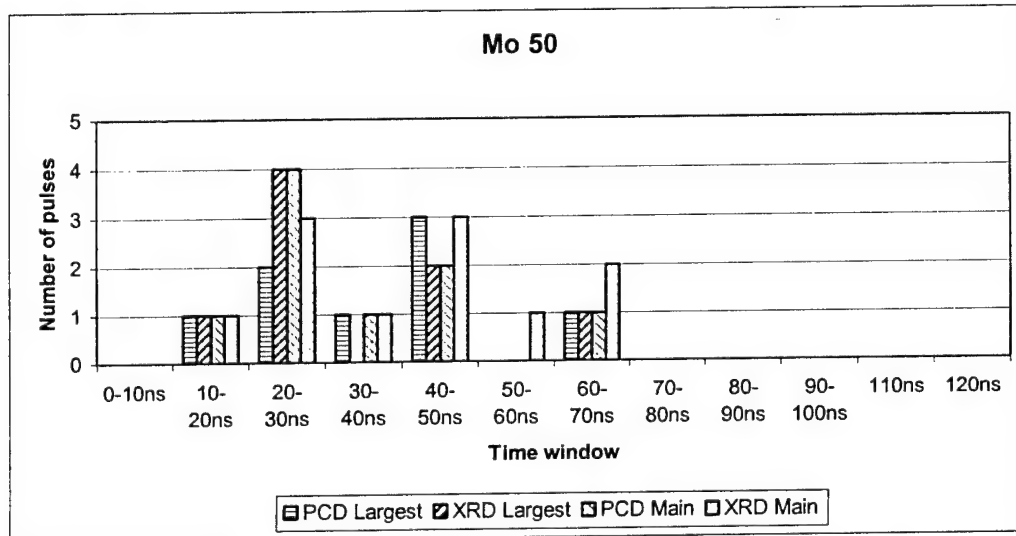


Figure 4.26. The time distribution of PCD and XRD signals for 50 μm Mo x-pinch ($I \approx 0.9$ MA). Largest: the signals with a maximum amplitude. Main: signals with amplitude from 0.9 to 0.3 of the largest value. The data are based on 5 shots.

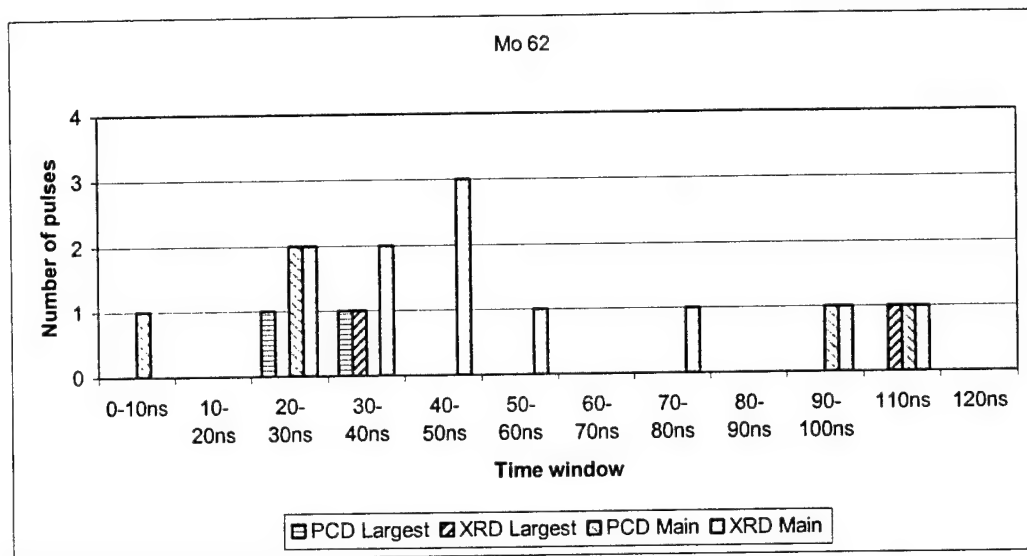


Figure 4.27. The time distribution of PCD and XRD signals for 62 μm Mo x-pinch ($I \approx 0.9$ MA). Largest: the signals with a maximum amplitude. Main: signals with amplitude from 0.9 to 0.3 of the largest value. The data are based on 2 shots.

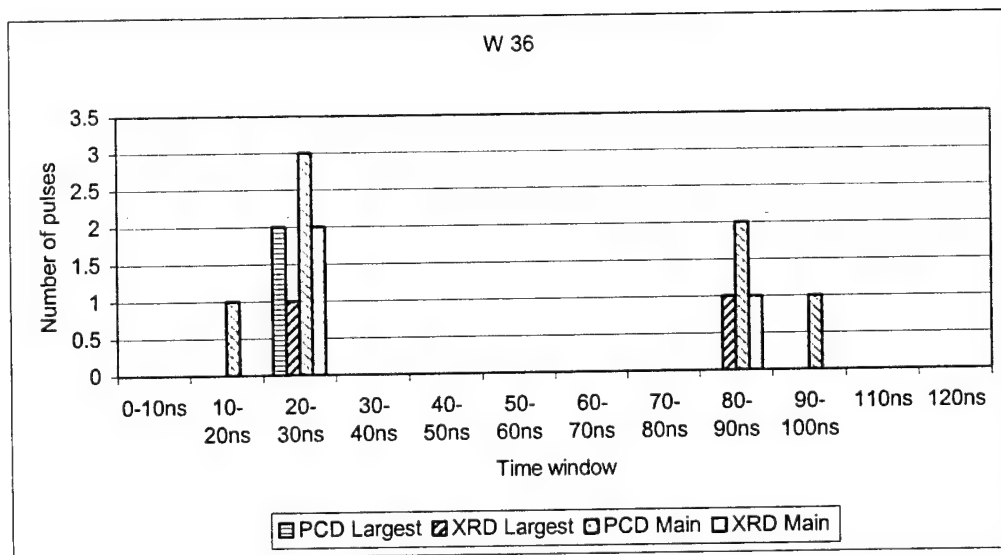
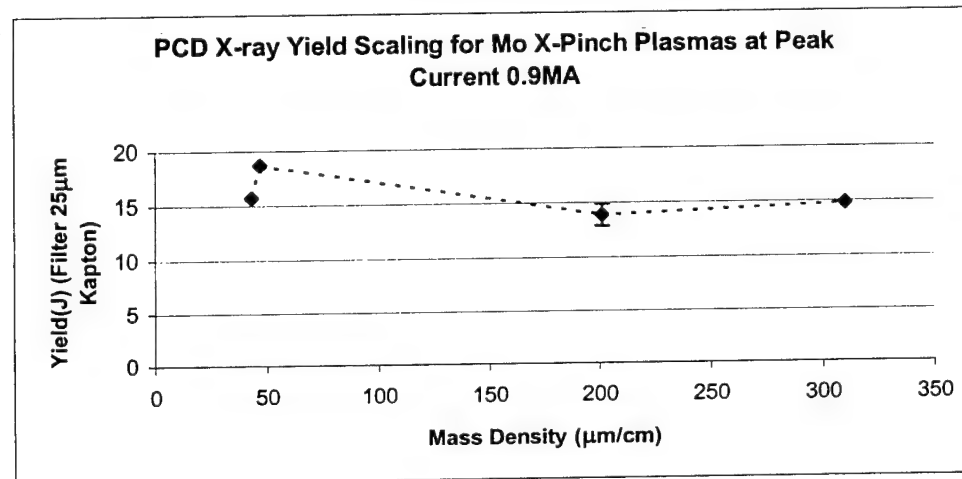
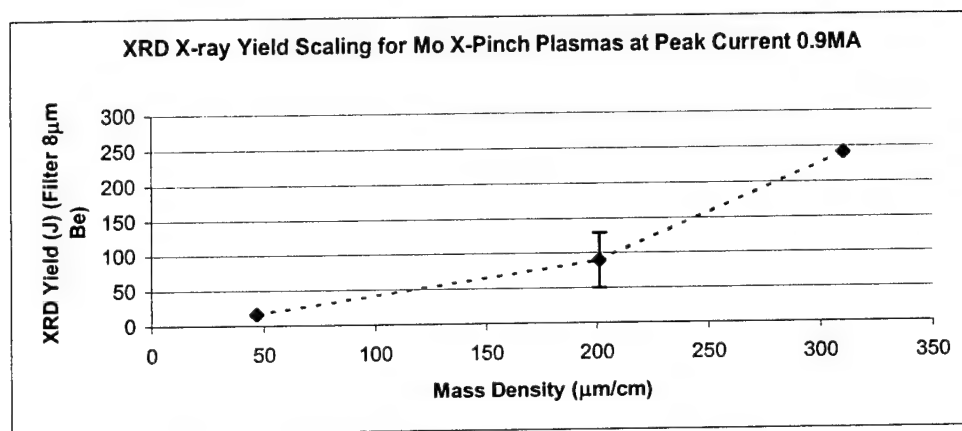
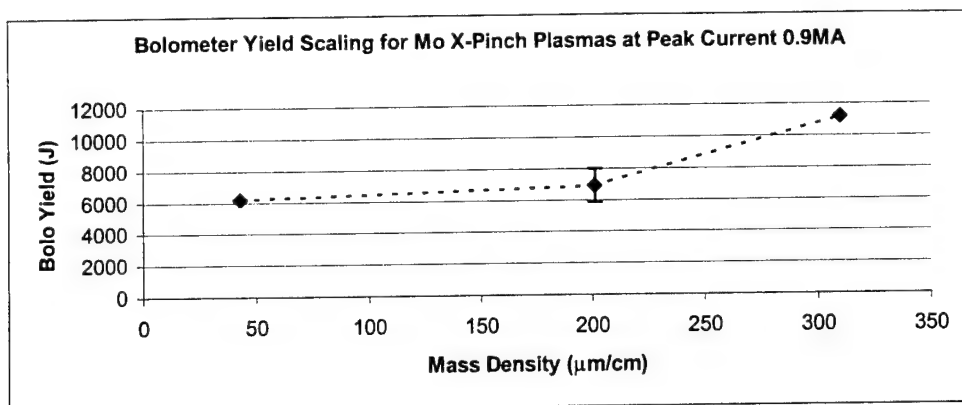
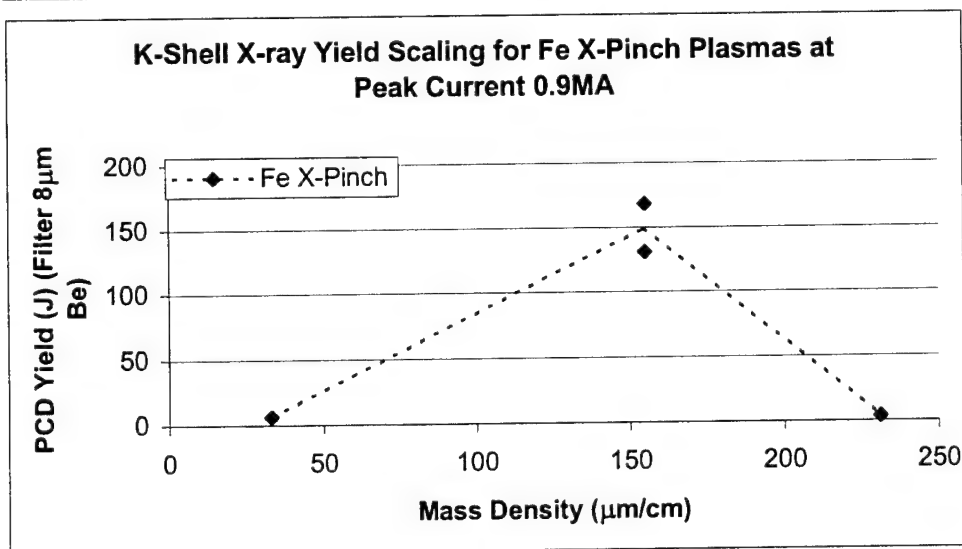
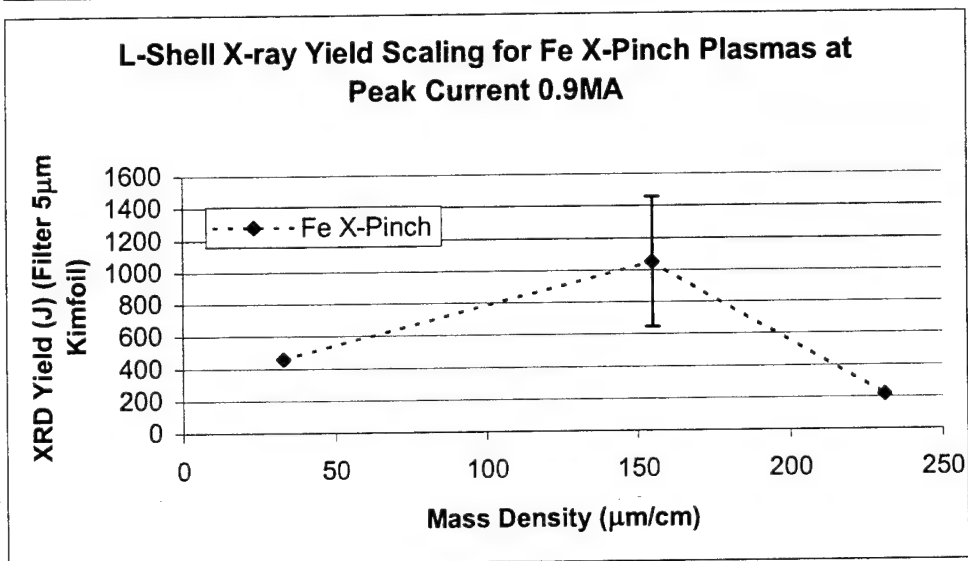
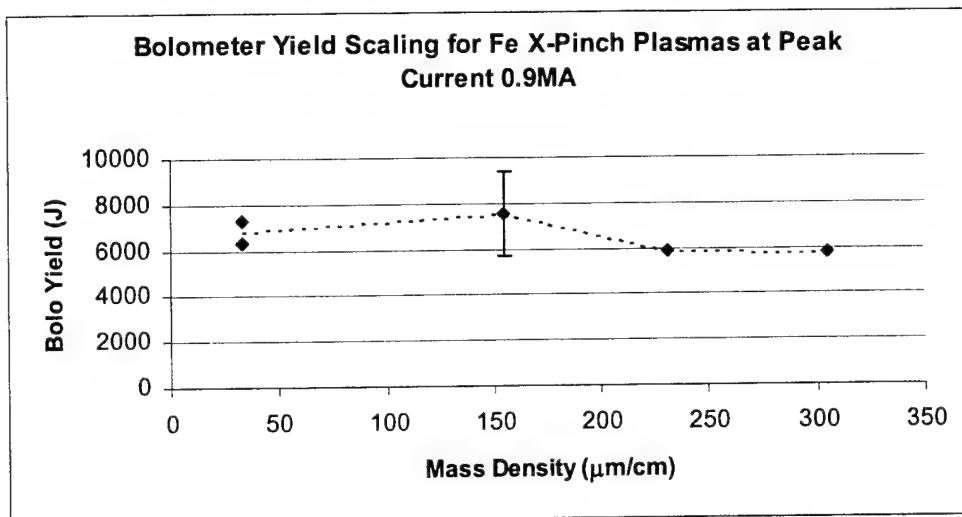


Figure 4.28. The time distribution of PCD and XRD signals for 36 μm W x-pinch ($I \approx 0.9$ MA). Largest: the signals with a maximum amplitude. Main: signals with amplitude from 0.9 to 0.3 of the largest value. The data are based on 2 shots.

The energy scaling of x-ray/EUV pulses from Ti, Fe, Mo, W and Pt x-pinchs, single wires, and a v-pinch is given in the figures below.





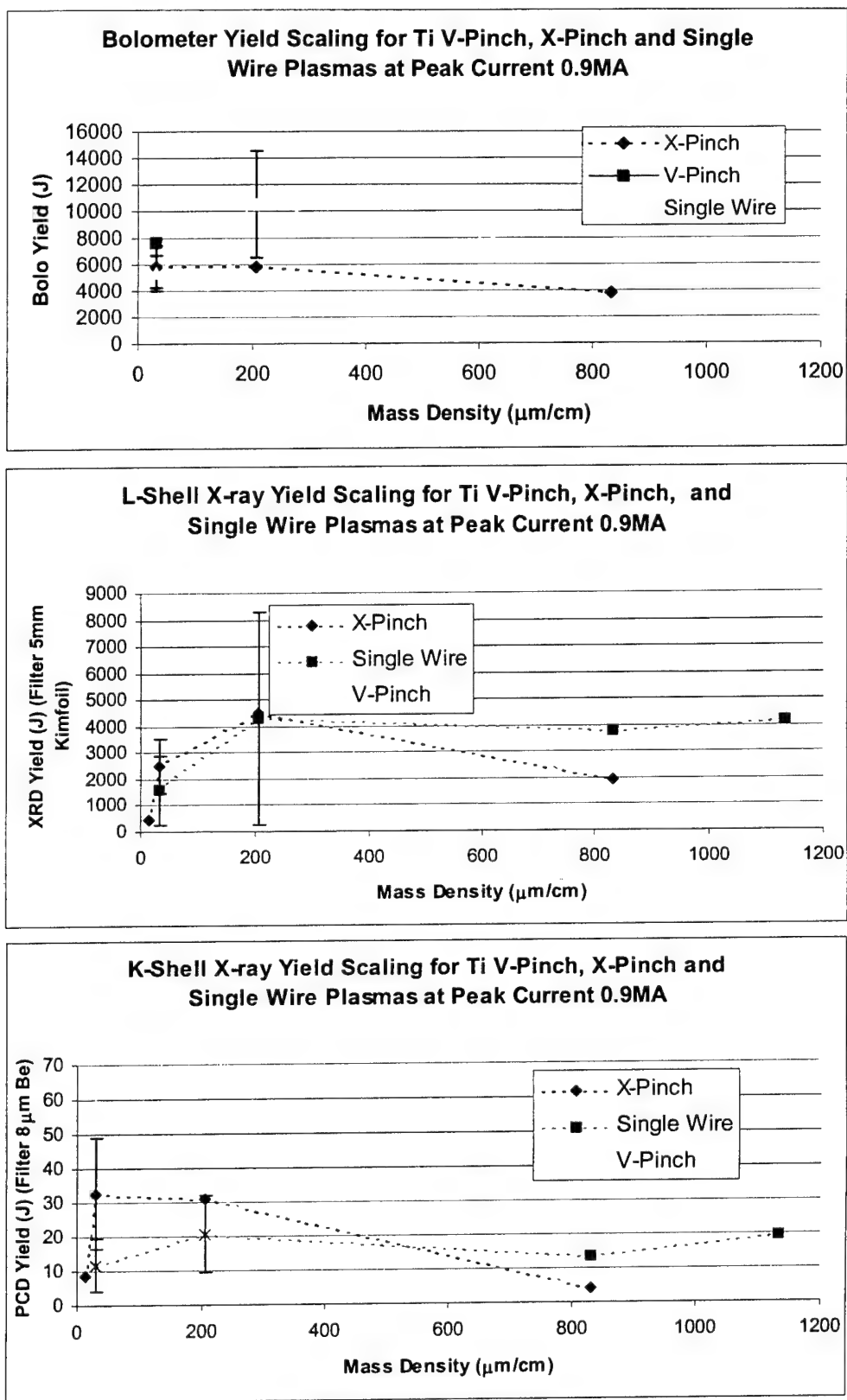


Figure 4.29. The variation of x-ray yield with linear mass density of the x-pinch loads. The dashed lines indicate trends.

The maximum total energy for x-pinch was more than 10-11 kJ for Mo x-pinch, 7-8 kJ for Fe, Pt and W, and 6 kJ for Ti.

Determination of the optimum yield for a Mo x-pinch is ongoing. Maximum XRD signals (L-shell and 0.7-1 keV continuum) were about 250J, and PCD signals (L-shell and 2 keV continuum) were about 15 J.

For a Fe x-pinch optimum yields were obtained with a mass density of 150 $\mu\text{g}/\text{cm}$. Fe x-pinch irradiated up to 1 kJ in L-shell and 0.25 keV in continuum (XRD signals), and about 150 J in K-shell and several keV continuum (PCD).

Optimum yields for Ti x-pinch were obtained with a mass density of 200 $\mu\text{g}/\text{cm}$. The total K-shell radiation was 30-40 J. The total L-shell radiation was 3-4.5 kJ. All these parameters are approximately 3-10 times bigger than those for a lower current (0.2-0.4 MA) Ti x-pinch or for single wire Ti z-pinch at 0.6-0.7 MA.

The M-shell and 0.7-1 keV continuum (XRD) yield for W varied from 25 to 6-7 J, and L-shell and 2 keV continuum (PCD) changed from 20 to 5-6 J. The statistics of Pt shots were not conclusive.

4.2.1.2.3. X-ray spectra of high-current x-pinch sources

4.2.1.2.3.1. Time-integrated spectra

Some of time-integrated spectra produced by high-current x-pinchs are shown below. Currently, the identified spectra of Ti, Fe and Mo are being processed to measure the main parameters of an x-pinch plasma (electron temperature and density), and to record polarization-dependent spectra. Most of x-ray spectra of Ti, Fe, Mo, W and Pt have been recorded with time-integrated one-dimensional convex crystal spectrographs (shorter than 1.7-1.8 nm). For study of Ti K-shell, Fe and Mo L-shell, W M-shell x-pinchs spectra with time-gated resolution, a one-dimensional x-ray imaging spectrometer (1DXIS) has been used. For study of soft x-ray emission (from 2.0 to 8.0 nm) a time-integrated one-dimensional transmission-grating spectrometer (TGS) was applied. A "Polychromator" spectrometer has been installed and used to study the time evolution of selected x-ray spectral lines from x-pinchs.

Figure 4.30 shows a $K\alpha$ spectrum produced by a Ti x-pinch at 0.9 MA. All Ti spectra have the spectroscopic features seen here; including the prominent $He\alpha$ resonance line, the $He\beta$ and $He\gamma$ lines, the hydrogen-like $Ly\alpha$ resonance line, and their satellites. Line radiation of Li- to F-like Ti ions is also observed, along with a cold $K\alpha$ Ti lines. From the Ti x-pinch spectra, radiation of He-like and H-like ions dominates, $T_e \approx 1.5$ -2 keV, and Ti He-like radiation is polarized [2,4]. The strong electron beam was observed in the Ti x-pinch experiments.

Soft x-ray spectra of Ti include strong L-shell radiation. The analysis of these experimental results is in progress.

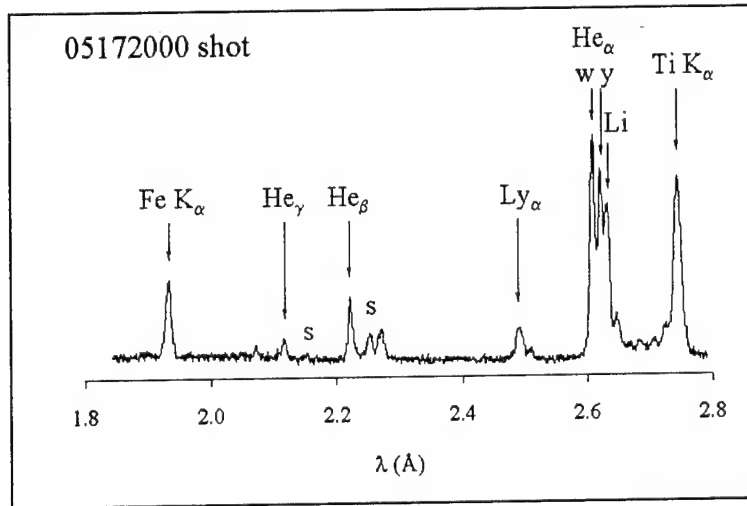


Figure 4.30. Ti x-pinch spectrum (30 μ m diameter wires).

For Fe x-pinches, only He-like ions were observed, along with weak L-shell spectral lines and cold $K\alpha$ lines. The weakness of L-shell spectra can be explained by the influence of strong opacity.

X-ray spectra of Mo include very strong L-shell and intense "cold" K lines (Figs. 31,32). W and Pt x-pinch spectra include weak M-shell and strong "cold" L-shell spectral lines respectively (Figs. 4.31, 4.33 – 4.35).

From the Mo L-shell x-pinch spectra, radiation of Na-like and Ne-like ions dominates, $T_e \approx 0.8$ keV. Polarization of Mo L-shell x-pinch spectra will be studied in near future.

Analysis of W and Pt M-shell experimental results is in progress.

"Cold" Mo K-shell and W, Pt L-shell spectra have been recorded because intensity of "cold" spectral lines is associated with a strength of an electron beam in an x-pinch plasma, and can be used for study of characteristics of an e-beam. Such beam has been observed in almost all NTF high-current x-pinch experiments (see preliminary analysis in Section 4.2.1.2.4 of this report).

Strong Fe $K\alpha$ and $K\beta$ were observed in all "cold" Ti, Mo, W and Pt x-pinch spectra, as a result of bombarding of a stainless steel anode by an electron beam. In addition, K spectra of stainless steel impurities (Cr and Ni) have been seen (Figure 4.32). This is an evidence of high sensitivity of our x-ray spectrographs, because concentration of Cr and Ni was only several percentages.

4.2.1.2.3.2. Time-resolved spectra

The first results of the study of Mo L-shell x-pinch spectra with a time-gated one-dimensional x-ray imaging spectrometer (1DXIS) have demonstrated that shape of spectra changed dramatically during the shot and this instrument can improve our understanding of processes in z-pinch plasma. The experiments are in progress.

The alignment of the "Polychromator" was improved and corrected to a new source position using a He-Ne laser and new procedure. In order to confirm alignment correctness during one of the shots we install a set of five identical crystals (α -quartz) and adjust all channels to the same spectral line (Figure 4.36). Difference in waveforms was within the limits of crystal reflections and detectors sensitivity variations, which gave us a proof of alignment.

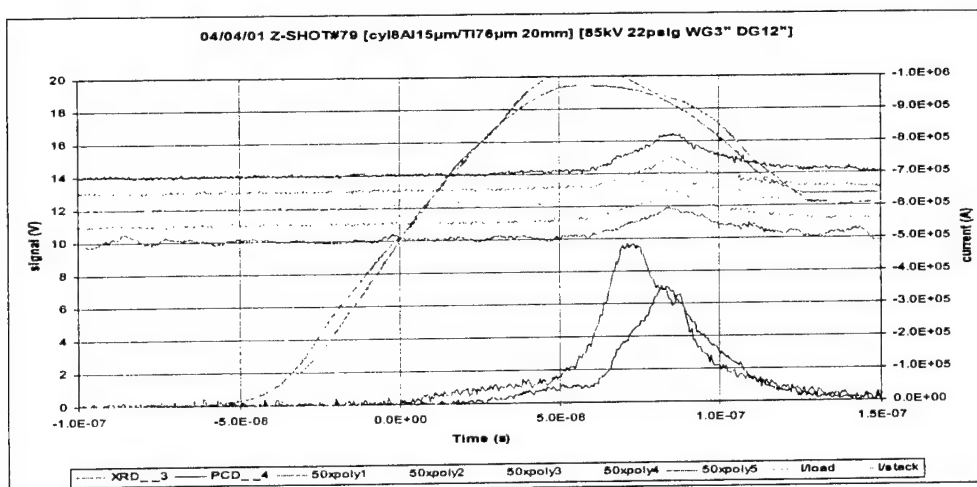


Figure 4.36. X-ray signals from an Al /Ti cylindrical wire array (Al 15 μm x8, 76 μm Ti central wire) (shot # 79, April 04, 2001). “Polychromator”($\lambda=2.74$ \AA , “cold” $K_{\alpha}\text{Ti}$) PCD (with 8 μm Be filter) and XRD (with 5 μm kimfoil filter) response versus the time. Note that maximum of “Polychromator” signals correlated in time with a PCD signal (Ti K-shell radiation).

For next shots two of the α -quartz crystals were substituted by KAP crystals to observe temporal behavior of softer lines. A waveform from the first (He-like Al) (Figure 4.37) channel was completely out of scale, at the same time a signal from a H-like Al channel was barely visible, which is an evidence of predominance of the He-like line of Al in plasma emission. Analysis of signals from three other channels with α -quartz crystals (adjusted to Ti lines) shows no significant difference in temporal evolution and these lines were more intensive than H-like Al and much less intensive than He-like. The waveforms of the signal are very close to a signal from PCD and approximately 5 ns later than a signal from XRD, which was filtered for softer radiation.

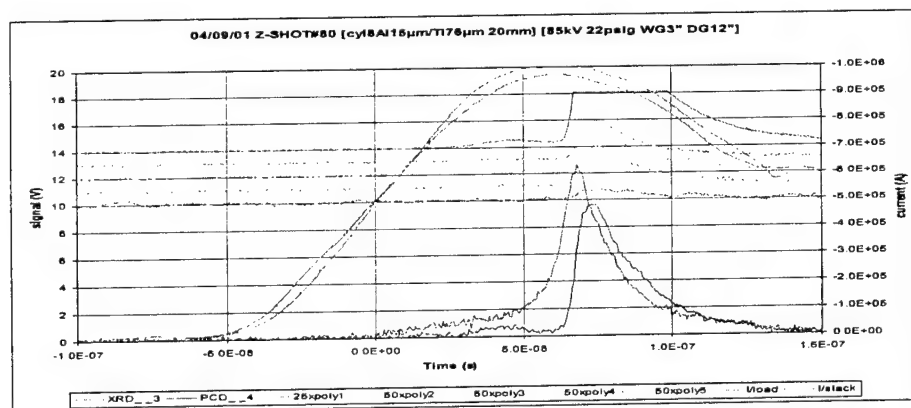


Figure 4.37. X-ray signals from an Al /Ti cylindrical wire array (Al 15 μm x8, 76 μm Ti central wire) (shot # 80, April 09, 2001). “Polychromator”(chan.1: $\lambda=7.765$ \AA , He-like Al; chan.2,3,4: $\lambda=2.74$ \AA , “cold” $K_{\alpha}\text{Ti}$; chan.5: $\lambda=7.174$ \AA , H-like Al) PCD (with 8 μm Be filter) and XRD (with 5 μm kimfoil filter) response versus the time. Note that maximum of “polychromator” Ti signals correlated in time with a PCD signal (Ti K-shell radiation).

For the analysis of experiments with 50 μm Mo x-pinch employing a "Polychromator", one channel with a KAP crystal was adjusted to Ne-like lines at 5.21 \AA , two channels with α -quartz crystals were adjusted to another Mo L-shell lines and the last channel with α -quartz was adjusted to Fe K_{α} line (1.94 \AA) (Figure 4.38). One can see the difference between time evolutions of different Mo spectral lines (for example, a wide pulse at $\lambda=5.21$ \AA , Ne-like line after maximum of a current) which can provide with temporal evolution of electron density and temperature. Fe K_{α} line shows that the peak of an electron beam appears twice at the time of maximum temperature and density at approximately 60 and 90% of a current maximum.

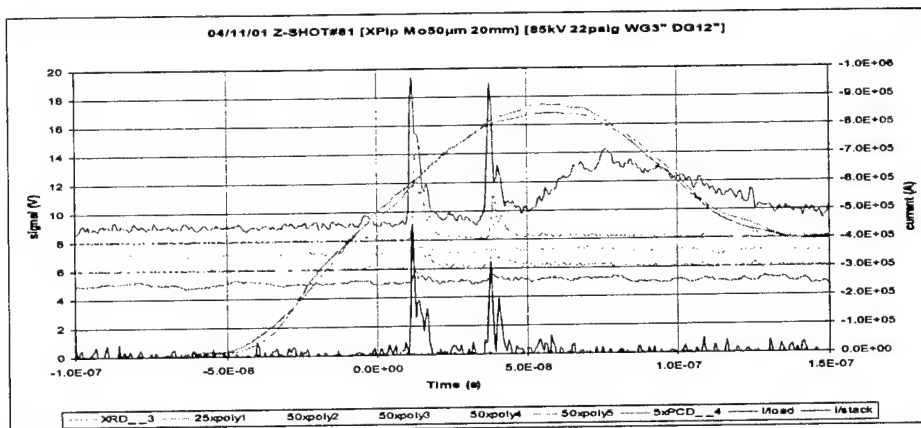


Figure 4.38. X-ray signals from an 50 μm Mo x-pinch (shot # 81, April 11, 2001). "Polychromator" (chan.1: $\lambda=5.21$ \AA , Ne-like Mo; chan.2: $\lambda=4.80$ \AA , Na-like Mo; chan.3: $\lambda=1.94$ \AA , "cold" $K_{\alpha}\text{Fe}$; chan.4: $\lambda=4.41$ \AA , Ne-like Mo; chan.5: $\lambda=5.5$ \AA , continuum, control line). PCD (with 25 μm kapton filter) response versus the time. Note that maximum of "Polychromator" Ti signals correlated in time with a PCD signal (Ti K-shell radiation).

4.2.1.2.4. High-energy electron and x-ray beams in high-current x-pinches: first NTF hard x-ray backlighting experiments

Previous studies of x-pinch plasma sources at lower (200-300 kA) currents [23] show that this is a perspective source for x-ray radiography in a 1-10 keV spectral region. Our studies at sufficiently higher currents (~900 kA) also confirm a possibility to use an x-pinch as a source for backlighting purposes even with harder x-rays. Presence of a very powerful high energy electron beam in plasma can lead to generation of hard x-ray radiation in a cross point as a result of interaction of this beam with a matter and a local magnetic field.

A strong, energetic electron beam is directed not only to the center of the anode (between the wires), but also toward the anode ends of the wires [2]. The experimental estimation of a width of Fe K_{α} spectral lines (generated on a steel anode) in x-pinch experiments has shown that a diameter of such electron beam in high-current x-pinches may be smaller as 1mm.

The total energy of x-pinch electron beam is at least from 2-4% (Fe) to 16-20 % (Mo) of the x-pinch discharge energy (Figure 4. 40). The estimation is based on the energy needed to generate the observed holes in the center of the anode and at the points of connection of the wires with the anode (experimental estimations are shown that total energy divided in ratio 1:1 between a central hole and both connection holes) (see Figs. 15, 25).

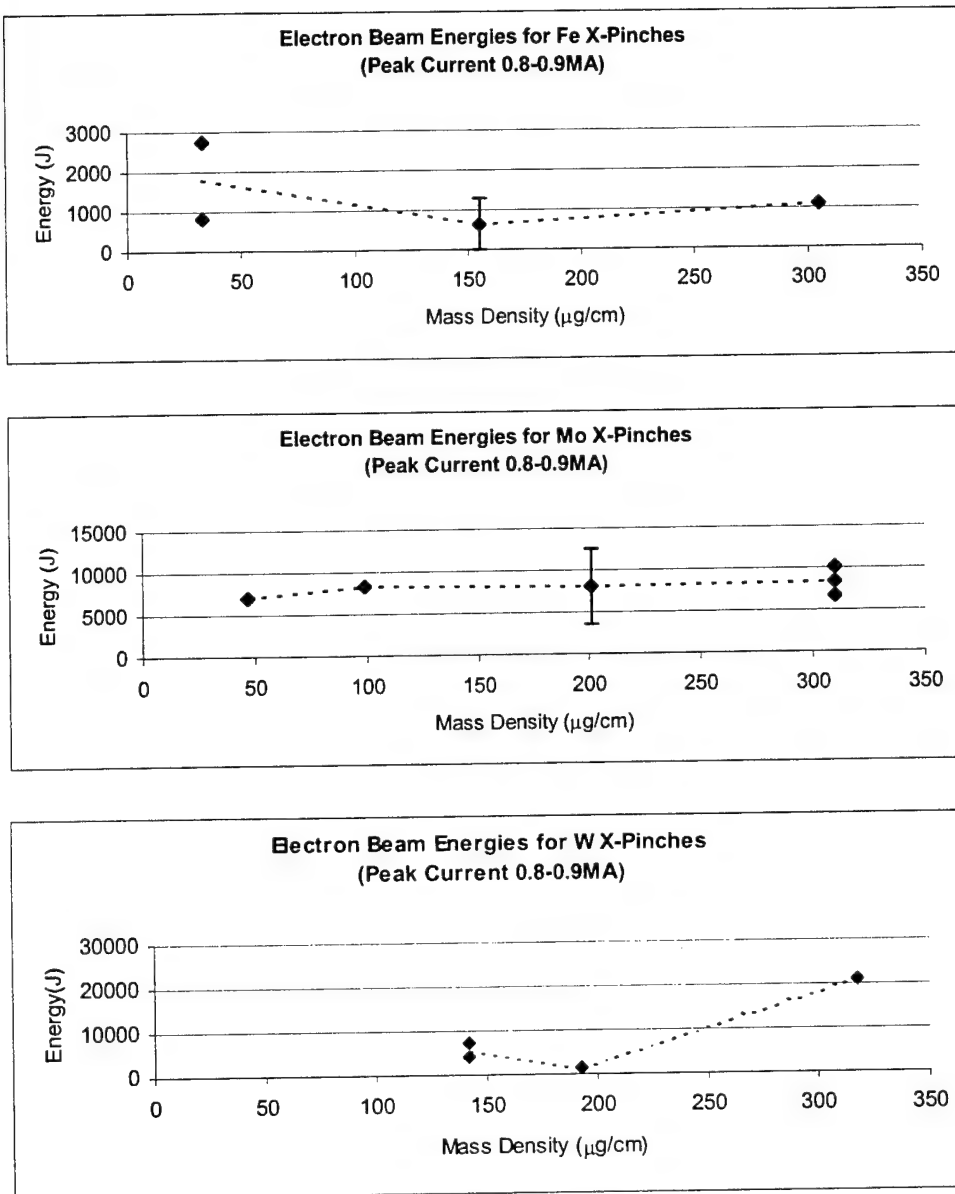


Figure 4.39. The experimental estimation of the energy needed to generate the observed holes at the points of connection of the wires with the anode of an x-pinch vs. mass density of wires.

Several tests of the NTF Mo and Fe x-pinch as a hard x-ray backlighter source were carried out with a static test object. As test objects set of materials with different absorption properties was used. One of the sets was placed in end-on beam line and another in side-on line (Figure 4.40). In order to roughly control spectral distribution of hard x-rays, step filters with different attenuation were placed in front of the film in both beamlines. Optical densities of images after filters and objects were measured by a commercial densitometer. For calibration, an x-ray tube Philips BV22 with a W anode at 100 kV was used.

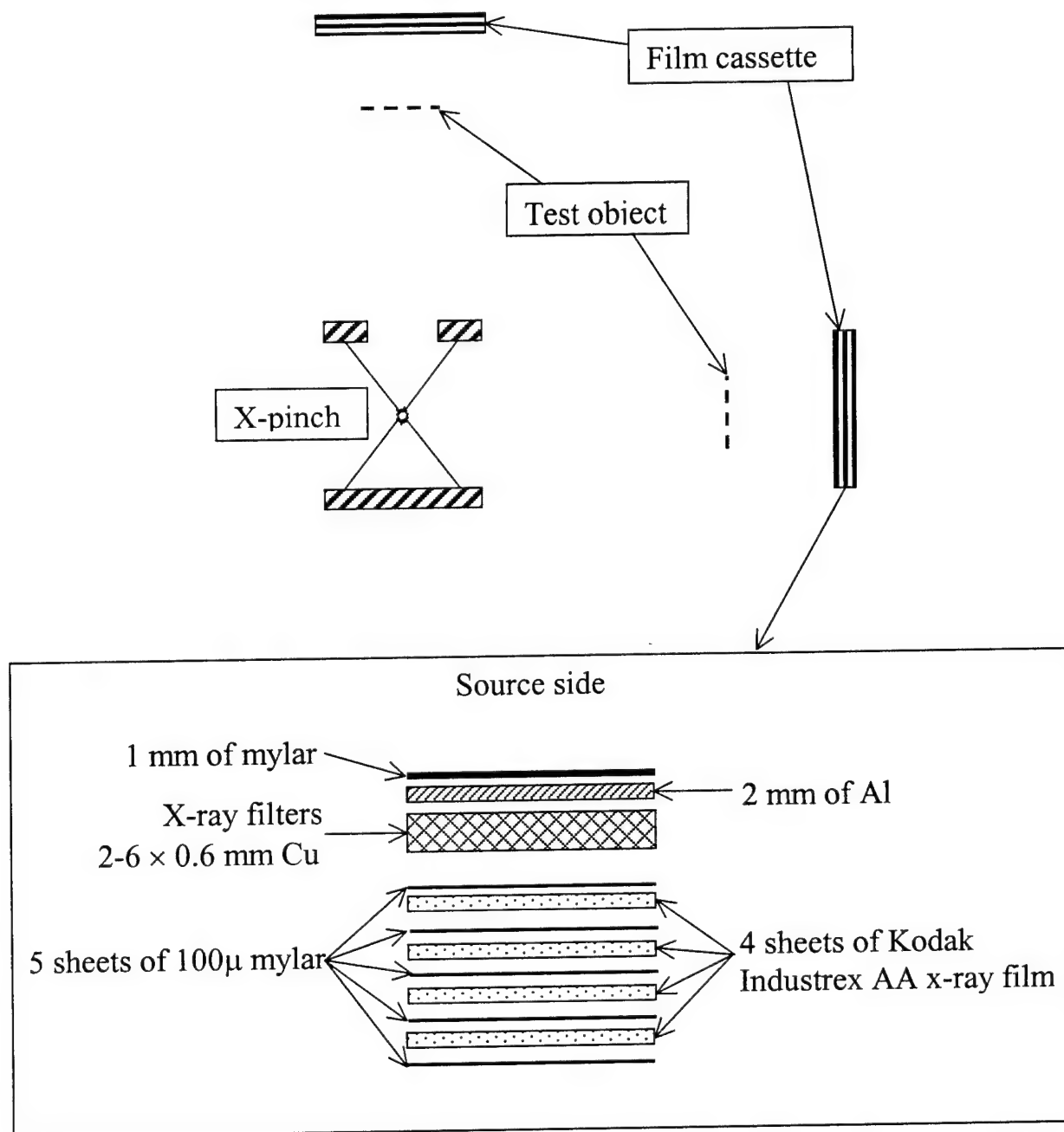


Figure 4.40. The scheme of hard x-ray backlighting experiments.

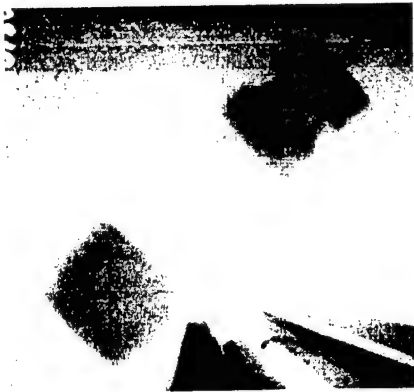


Figure 4.41. Hard x-ray image of two hollow steel parts (diameter 15-17mm) and an Al tube (diameter 1-12 mm) connected by a 1 m thick Cu wire. A part of calibrator-attenuator at the bottom. Shot #71 (03/05/01) 50 μ m Mo x-pinch. End-on beamline. 3.0-mm Cu filter. Al tube is barely seen. An inner structure of steel parts is seen in part.



Figure 4.42. Hard x-ray image of two hollow steel parts (diameter 10-15 mm) and two Al tubes (diameter 15-18 mm) connected by a 1 mm thick Cu wire. Shot #81 (04/11/01) 50 μ m Mo x-pinch. Side-on beamline. 3.0-mm Cu filter. A structure of an Al tube is seen. An inner structure of steel parts is not seen.



Figure 4.43. Hard x-ray image of a flat steel part (thickness 2.5 mm) and an Al tube (diameter 10-12 mm) from Figure 4.41 connected by a 1 mm thick Cu wire. A part of a calibrator-attenuator is at the left. Shot #69 (02/26/01) 50 μ m Mo x-pinch. End-on beamline. 1.8-mm Cu filter. An inner structure of an Al tube is clearly seen.

The preliminary results of x-pinch and x-ray tube experiments show that a x-pinch is an effective source of hard x-ray radiation at high current conditions. A rough estimation of spectral regions available for radiography gives us values between 100-200 keV end-on and 50-100 keV side-on for a Mo x-pinch, and 50-100 keV end-on for a Fe x-pinch. Spatial resolution in experiments was approximately 0.3-0.4 mm. A size of a source was about 1mm. Experiments are in progress.

Time duration measurements of a hard x-ray beam will be performed soon. If these measurements will confirm a short pulse (at least as PCD or XRD signals), then high brightness and small size of such hard x-ray sources could meet some minimal conditions for an additional backlighter on SNL-Z or ATLAS.

4.3. References for Section 4

1. V. Kantsyrev, B. Bauer, A. Shlyaptseva, R. Bruch, R. Phaneuf, "New optical instrumentation for hot plasma imaging, polarimetry, and spectroscopy, using glass capillary converters and multilayer mirrors", *Proc. Fourth Intern. Conf. "Dense Z-pinches" (1997), AIP Proc., CP409*, pp. 499 - 502, 1997.
2. V. Kantsyrev*, B. Bauer, A. Shlyaptseva, D. Fedin, S. Hansen, R. Presura**, S. Batie, A. Oxner, B. LeGalloudec, H. Faretto, D. Chamberlain, N. Ouart, A. Jones, H. LeBeau, M. Gharaibeh, "Advanced x-ray and EUV diagnostics and first application to x-pinch plasma experiments at the Nevada Terawatt Facility", *Rev. Sci. Instrum.*, v.72, 1(II), pp.663-667(2000).
3. A. Shlyaptseva, A. Petrashen, V. Kantsyrev, S. Kazantsev, U. Safronova, "X-ray line polarization plasma spectroscopy: polarization database and plasma diagnostics.", *NIFS Proc. (Japan) 44*, pp. 138-140 (2000).
4. A.S. Shlyaptseva, S. B. Hansen, V.L. Kantsyrev, B.S. Bauer, D.A. Fedin, N. Ouart, S.A. Kazantsev, A.G. Petrashen, U.I. Safronova, "X-ray spectropolarimetry of high-temperature plasmas", submitted to *Rev. Sci. Instrum.*, v.72, 1(II), pp. 1241-1244(2000).
5. V. Kantsyrev, R. Bruch, P. Phaneuf, N. Publicover, "New concepts for x-ray, soft x-ray, and EUV optical instrumentation including applications in spectroscopy, plasma diagnostics, and biomedical microscopy: A status report", *Journ. X-ray Sci. Technol.*, 7, pp.139 - 158, 1997.
6. V. Kantsyrev, R. Bruch, "New optical methods for short wavelength hot plasma diagnostics", *Rev.Sci. Instrum.*, 68, 1(II), pp. 770 - 773, 1997.
7. O. Ananyin, Yu. Bykovsky, V. Kantsyrev, Yu. Kozyrev, "Source of x-rays", *Certificate of Authorship 520863, filed 15 October 1974 (USSR)(Bull.Izobret. USSR, N 11, 229, 1979)*.
8. P. Mallozzi, H. Epstein, R. Jung, D. Applebaum, B. Fairand, W. Gallagher, R. Uecker, M. Muckerheide, "Laser plasma as a source of x-rays for medical applications", *J.Appl.Phys.* 45, pp. 1891-1895, 1974.
9. V. Kantsyrev, R. Bruch, A.Shlyaptseva, "Spectrometer - polarimeter", The US Patent Applic., 60/014,483, filed April, 01,1996.
10. V. Arkad'ev, A. Kolomiitsev, M. Kumakhov, I. Ponomarev, I. Knoddeev, Yu. Chertov, I. Shakhparonov, "Wide-band x-ray optics with large angular aperture", *Sov.Phys. Usp.* , 32, pp. 271 - 279, 1989.
11. V. Kantsyrev, O. Petrukhin, A. Shlyaptseva, N. Mingaliev, S. Pikuz, V. Romanova, T. Shelkovenko, A. Faenov, "Investigating the characteristics of x-ray radiation from hot plasma by means of glass capillary converters", *Quantum Electronics*, 23, 12, 1026 - 1029, 1993.
12. V. Kantsyrev, R. Bruch, M. Bailey, A. Shlyaptseva, "Enhancement of the flux density of line radiation in the extreme ultraviolet and soft x-ray spectral region for spectroscopic and plasma diagnostic applications using glass capillary converters", *Appl. Phys. Lett.* 66, 3567 (1995).

13. E. Forster, R. Hutcheon, O. Renner, I. Uschmann, M. Vollbrecht, M. Nantel, A. Klisnick, P. Jaegle, "High-resolution x-ray imaging of extended lasing plasmas", *Appl. Opt.*, 36, 4, pp.831-840, 1997.
14. B. Bauer, V. Kantsyrev, "Capillary spectrometer", The US Patent, #5,991,024, filed May 29, 1998 (Prov. Appl. filed May, 30, 1997).
15. V. Kantsyrev, D. Fedin, S. Kukhlevsky, B. Bauer, N. Ouart, "Features of soft x-ray and x-ray radiation from a point laser plasma and z-pinch sources transported by glass capillary converters (experiment). *Proc. SPIE*, 4144, pp. 128-135 (2000).
16. V. Kantsyrev, B. Bauer, D. Fedin, A. Shlyaptseva, S. Hansen, I. Paraschiv, "Novel x-ray and EUV two-dimensional glass capillary spectrometer for Z-pinch plasma diagnostics", *Proc. SPIE*, 3766, pp. 410-417, 1999.
17. A.Ya. Faenov, S.A. Pikuz, A.I. Erko, B.A. Brunetkin, V.M. Dyakin, G.V. Ivanenkov, A.R. Mingaliev, T.A. Pikuz, V.M. Romanova, T.A. Shelkovenko, "High-performance x-ray spectroscopic devices for plasma microsources investigations", *Phys. Scripta*, 52, pp. 333-338, 1994.
18. V. Kantsyrev, K.Takasugi, K.Tatsumi, T. Miyamoto, A.S. Shlyaptseva, "The structural, spectral and temporal properties of x-ray in regions $\lambda = 3.4 \text{ nm} - 4.6 \text{ nm}$ and $\lambda = 1.0 \text{ nm}$ emitted from the Ar gas-puff z-pinch plasma", *Proc. Intern. Conf. On Plasma Physics (ICPP 96)*, Nagoya, Japan, pp. 1106 - 1109, 1996.
19. D. Fedin, V. Kantsyrev, B. Bauer, A. Shlyaptseva, I. Brytov, "Polychromator" five channel x-ray/EUV spectrometer with imaging transmission grating for plasma diagnostics", *Proc. SPIE*, 3764, pp. 80-84, 1999. R.Korde, J.S.Cable, L.R.Canfield, "One Gigarad passivating nitrided oxides for 100% internal quantum efficiency silicon photodiodes", *IEEE Transactions on Nuclear Science*, 40, 6, pp. 1655-59, 1993.
20. R.B.Spielman, L.E.Ruggles, R.E.Pepping, S.P.Breeze, J.S.McGurn, K.W.Struve, "Fielding and calibration issues for diamond photoconducting detectors" *Rev. Sci. Instrum.* 68(1) pp.782-785 1997.
21. A. Shlyaptseva, A. Urnov, A. Vinogradov, "On diagnostics of suprathermal electrons in high-temperature plasmas.", P.N. Lebedev Phys. Intitute (USSR), Rep.#193, pp.1-19 (1981).
22. A. Shlyaptseva, A. Urnov, A. Vinogradov, "On diagnostics of suprathermal electrons in high-temperature plasmas.", P.N. Lebedev Phys. Intitute (USSR), Rep.#193, pp.1-19 (1981).
23. S.A. Pikuz, T.A. Shelkovenko, V.M. Romanova, G.S. Sarkisov, D.A. Hammer, D.F. Acton, "Studies of X-pinch plasma structure using high resolution x-ray optical and imaging spectroscopy methods", *AIP Proc. CP 409*, pp.429-436 (1997).
24. D. H. Kalantar, D.A. Hammer, K.C. Mittal, N. Qi, F.C. Young, S.J. Stephanakis, P.G. Burkhalter, G. Mehlman, D.A. Newman, "K-shell x-ray yield scaling for aluminum x-pinch plasmas", *J. Appl.Phys.*, 73, pp.8134-8139(1993).

APPENDIX A

Linear Analysis of the Shear Flow Stabilization of the Global MHD Instabilities Based on the Hall Fluid Model

V.I. Sotnikov, I. Paraschiv, V. Makhin, and B.S. Bauer, UNR
J.-N. LeBoeuf and J.M. Dawson, UCLA

Submitted to Phys. Plasmas

Linear analysis of the shear flow stabilization of the global MHD instabilities based on the Hall fluid model.

V. I. Sotnikov, I. Paraschiv, V. Makhin, B.S. Bauer,

University of Nevada, Reno, NV 89557-0058

J. N. Leboeuf, J. M. Dawson,

University of California, Los Angeles, CA 90095-1547

(Received

Abstract

A systematic study of the linear stage of sheared flow stabilization of z-pinch plasmas based on the Hall fluid model with equilibrium that contains sheared flow and axial magnetic field is presented. The study begins with a general set of equations that permit evaluation of the combined effect of sheared flow and axial magnetic field on the development of the $m = 0$ sausage and $m = 1$ kink instabilities, with the Hall term included in the model. Inclusion of sheared flow, axial magnetic field and the Hall term allows the z-pinch system to be taken away from the region in parameter space where ideal MHD is applicable to a regime where non-ideal effects tend to govern stability. The problem is then treated numerically following the development in time of an initial perturbation. The numerical results as a function of sheared flow, axial magnetic field and Hall term are reported.

PACS numbers: 52.30.Cv, 47.65 + a, 52.35.Py, 52.58.Lq

I. INTRODUCTION

Theory and computations have examined several possible z-pinch stabilization techniques, including axial sheared flow.¹⁻⁴ With sheared axial flows included in the equilibrium it is found that substantial stabilization of internal modes is possible for some equilibrium profiles. The guiding principle is to take the z-pinch system away from the region in parameter space where ideal MHD is applicable to a regime where non-ideal effects⁵ such as the Hall term⁶⁻⁷ and axial sheared flow tend to govern stability. The calculations inform the experimental approach to higher densities and longer confinement times.

This paper focuses on the effects of axial sheared flow on the $m = 0$ sausage instability, in the presence of the Hall and axial magnetic field. The results are compared with those of ideal MHD.

Sheared flows are of interest as a possible mechanism for the stabilization of MHD instabilities, because MHD instabilities grow on the pinch surface, where the density is low and the magnetic field is high. The flow stretches and eliminates the MHD modulations, mixing the unstable modes with different wave lengths. This restricts the growth of the modes to a nondestructive level. We first of all need to understand z-pinch behavior in the linear stage of development of the instability.

We shall use equations that contain the Hall term in addition to the standard MHD terms, in the presence of sheared axial flow. These equations form a more general set than has apparently been used before. These equations will be used to define eigenfunctions and

eigenvalues that could exhibit unstable solutions to the perturbed equilibria . This will identify the region in parameter space where the instability can take place and determine the linear growth rate of the instability. We will consider conditions realized experimentally.

This paper is organized as follows. The linear stability analysis is initiated in Section 2. Results for the $m=0$ sausage instability in the presence of sheared axial flow and the Hall term are given in Section 3. Results for the sausage instability in the presence of sheared flow and axial magnetic field presented in Section 4. Section 5 offers a discussion and conclusions.

II. LINEAR STABILITY ANALYSIS

We shall treat the problem numerically following the development in time of an initial perturbation. After several growth times the solution will converge to the fastest growing mode, defining real and imaginary parts of ω . This method has been used for linear studies of z-pinch stability in tokamak plasmas by⁸, ideal MHD instabilities in tokomaks.⁹⁻¹⁰

Using this approach, we have derived the linearized system of equations which describes the development of the $m = 0$ sausage and $m = 1$ kink instabilities in the presence of axial and azimuthal sheared flow, axial magnetic field, and the Hall term. It has the following form:

$$\frac{\partial P_1}{\partial t} + (\vec{v}_0 \nabla) P_1 = -(\vec{v}_1 \nabla) P_0 - \Gamma P_0 (\nabla \vec{v}_1) \quad (1)$$

$$\begin{aligned} \rho_0 \frac{\partial \vec{v}_1}{\partial t} + \rho_0 (\vec{v}_0 \nabla) \vec{v}_1 = & -\nabla P_1 - \rho_1 (\vec{v}_0 \nabla) \vec{v}_0 - \rho_0 (\vec{v}_1 \nabla) \vec{v}_0 + \\ & \frac{1}{4\pi} (\nabla \times \vec{B}_1) \times \vec{B}_0 + \frac{1}{4\pi} (\nabla \times \vec{B}_0) \times \vec{B}_1 \end{aligned} \quad (2)$$

$$\frac{\partial \rho_1}{\partial t} + \vec{v}_0 \nabla \rho_1 = -\vec{v}_1 \nabla \rho_0 - \rho_0 (\nabla \vec{v}_1) \quad (3)$$

$$\begin{aligned} \frac{\partial \vec{B}_1}{\partial t} = & \nabla \times [\vec{v}_1 \times \vec{B}_0] + \nabla \times [\vec{v}_0 \times \vec{B}_1] - \tilde{\varepsilon} \nabla \times \left[\frac{1}{n_0} [(\nabla \times \vec{B}_0) \times \vec{B}_1] \right] - \\ & - \tilde{\varepsilon} \nabla \times \left[\frac{1}{n_0} [(\nabla \times \vec{B}_1) \times \vec{B}_0] \right] - \tilde{\varepsilon} \nabla \times \left[\frac{n_1}{n_0^2} [(\nabla \times \vec{B}_0) \times \vec{B}_0] \right] \end{aligned} \quad (4)$$

$$\text{where } \tilde{\varepsilon} = \frac{c}{4\pi e}$$

The following equilibrium conditions were used to derive equations (1) - (4):

$$\rho_0 (\vec{v}_0 \nabla) \vec{v}_0 = -\nabla P_0 + \frac{1}{4\pi} (\nabla \times \vec{B}_0) \times \vec{B}_0 \quad (5)$$

$$\nabla \times [\vec{v}_0 \times \vec{B}_0] - \tilde{\varepsilon} \nabla \times \left[\frac{1}{n_0} (\nabla \times \vec{B}_0) \times \vec{B}_0 \right] = 0 \quad (6)$$

$$(\vec{v}_0 \nabla) P_0 = 0 \quad (7)$$

$$(\vec{v}_0 \nabla) \rho_0 = 0 \quad (8)$$

$$\nabla \cdot \vec{v}_0 = 0 \quad (9)$$

For radially dependent equilibria with $P_0(r)$, $n_0(r)$, $B = B_{0\theta}(r) e_\theta + B_{0z}(r) e_z$ and $v = v_{0\theta}(r) e_\theta + v_{0z}(r) e_z$, equations (6) – (9) are satisfied automatically. From equation (5) we have the following condition for such equilibria:

$$\frac{1}{Mn_0} \frac{\partial}{\partial r} \left[P_0 + \frac{B_{0z}^2}{8\pi} + \frac{B_{0\theta}^2}{8\pi} \right] + \frac{1}{Mn_0} \frac{B_{0\theta}^2}{4\pi r} = \frac{v_{0\theta}^2}{r} \quad (5^*)$$

This equilibrium condition does not include axial speed $v_{0z}(r)$. It means that axial speed is a free parameter of our problem. This results in a great variety of possible equilibrium profiles with different axial sheared flows.

In cylindrical coordinates the system of equations (1 – 4) has the form:

$$\rho_0 \frac{\partial v_{1r}}{\partial t} = -i\rho_0 K v_{1r} + 2\rho_0 r \Omega_0 \Omega_1 - \frac{\partial R}{\partial r} + \frac{i}{4\pi} S B_{1r} - \frac{1}{2\pi} \frac{B_{0\theta}}{r} B_{1\theta} + \frac{v_{0\theta}^2}{r} \rho_1 \quad (10)$$

$$\rho_0 r \frac{\partial \Omega_1}{\partial t} = -i\rho_0 K r \Omega_1 - \rho_0 \left(2\Omega_0 + r \frac{\partial \Omega_0}{\partial r} \right) v_{1r} - \frac{im}{r} R + \frac{i}{4\pi} S B_{1\theta} + \frac{1}{4\pi} \frac{1}{r} \frac{\partial}{\partial r} (r B_{0\theta}) B_{1r} \quad (11)$$

$$\rho_0 \frac{\partial v_{1z}}{\partial t} = -i\rho_0 K v_{1z} - \rho_0 \frac{\partial v_{0z}}{\partial r} v_{1r} - i k_z R + \frac{i}{4\pi} S B_{1z} + \frac{1}{4\pi} \frac{\partial B_{0z}}{\partial r} B_{1r} \quad (12)$$

$$\frac{\partial P_1}{\partial t} = -iK P_1 - \frac{\partial P_0}{\partial r} v_{1r} - \Gamma P_0 \operatorname{div} \vec{v}_1 \quad (13)$$

$$\frac{\partial \rho_1}{\partial t} = -iK \rho_1 - \frac{\partial \rho_0}{\partial r} v_{1r} - \rho_0 \operatorname{div} \vec{v}_1 \quad (14)$$

$$\begin{aligned}
\frac{\partial B_{1r}}{\partial t} = & -iKB_{1r} + iSv_{1r} - \\
& -\tilde{\varepsilon} \left\{ \frac{im}{r} \frac{1}{n_0} B_{1r} \frac{\partial B_{0z}}{\partial r} - ik_z \frac{1}{n_0} B_{1r} \frac{1}{r} \frac{\partial}{\partial r} (rB_{0\theta}) \right\} - \\
& -\tilde{\varepsilon} \left\{ \frac{im}{r} \frac{1}{n_0} B_{0\theta} \left(\frac{im}{r} B_{1z} - ik_z B_{1\theta} \right) + ik_z \frac{1}{n_0} B_{0z} \left(\frac{im}{r} B_{1z} - ik_z B_{1\theta} \right) \right\}
\end{aligned} \tag{15}$$

$$\begin{aligned}
\frac{\partial B_{1\theta}}{\partial t} = & -iKB_{1\theta} + \left(r \frac{\partial \Omega_0}{\partial r} - \Omega_0 \right) B_{1r} + \left(\frac{B_{0\theta}}{r} - \frac{\partial B_{0\theta}}{\partial r} \right) v_{1r} + iSv_{1\theta} - B_{0\theta} \operatorname{div} \vec{v}_1 - \\
& -\tilde{\varepsilon} \left\{ ik_z \left[\frac{B_{1z}}{n_0} \frac{\partial B_{0z}}{\partial r} - \frac{B_{1\theta}}{n_0} \frac{1}{r} \frac{\partial}{\partial r} (rB_{0\theta}) \right] + \frac{\partial}{\partial r} \left[\frac{B_{1r}}{n_0} \frac{\partial B_{0z}}{\partial r} \right] \right\} - \\
& -\tilde{\varepsilon} \left\{ ik_z \left[\frac{B_{0z}}{n_0} (ik_z B_{1r} - \frac{\partial B_{1z}}{\partial r}) - \frac{B_{0\theta}}{n_0} \left(\frac{1}{r} \frac{\partial}{\partial r} (rB_{1\theta}) - \frac{im}{r} B_{1r} \right) \right] - \frac{\partial}{\partial r} \left[\frac{B_{0\theta}}{n_0} \left(\frac{im}{r} B_{1z} - ik_z B_{1\theta} \right) \right] \right\} + \\
& -\tilde{\varepsilon} ik_z \frac{n_1}{n_0^2} \left\{ B_{0z} \frac{\partial B_{0z}}{\partial r} + \frac{B_{0\theta}}{r} \frac{\partial}{\partial r} (rB_{0\theta}) \right\}
\end{aligned} \tag{16}$$

$$\begin{aligned}
\frac{\partial B_{1z}}{\partial t} = & -iKB_{1z} + \left(\frac{\partial v_{0z}}{\partial r} \right) B_{1r} - \left(\frac{\partial B_{0z}}{\partial r} \right) v_{1r} + iSv_{1z} - B_{0z} \operatorname{div} \vec{v}_1 - \\
& -\tilde{\varepsilon} \left\{ \frac{1}{r} \frac{\partial}{\partial r} \left[\frac{B_{1r}}{n_0} \frac{\partial}{\partial r} (rB_{0\theta}) \right] + \frac{im}{r} \left[\frac{B_{1z}}{n_0} \frac{\partial B_{0z}}{\partial r} + \frac{B_{1\theta}}{n_0} \frac{1}{r} \frac{\partial}{\partial r} (rB_{0\theta}) \right] \right\} + \\
& +\tilde{\varepsilon} \left\{ \frac{1}{r} \frac{\partial}{\partial r} \left[\frac{rB_{0z}}{n_0} \left(\frac{im}{r} B_{1z} - ik_z B_{1\theta} \right) \right] + \frac{im}{r} \left[\frac{B_{0z}}{n_0} (ik_z B_{1r} - \frac{\partial B_{1z}}{\partial r}) - \frac{B_{0\theta}}{n_0} \frac{1}{r} \frac{\partial}{\partial r} (rB_{1\theta}) + \frac{im}{r} \frac{B_{0\theta} B_{1r}}{n_0} \right] \right\} - \\
& +\tilde{\varepsilon} \frac{im}{r} \frac{n_1}{n_0^2} \left\{ B_{0z} \frac{\partial B_{0z}}{\partial r} + \frac{B_{0\theta}}{r} \frac{\partial}{\partial r} (rB_{0\theta}) \right\}
\end{aligned} \tag{17}$$

The following notations were used in the system of equations (10-17)

$$R = P_1 + \frac{1}{4\pi} B_{0\theta} B_{1\theta} + \frac{1}{4\pi} B_{0z} B_{1z}$$

$$S = \frac{m}{r} B_{0\theta} + k_z B_{0z}$$

$$v_{0\theta} = r\Omega_0 \quad v_{1\theta} = r\Omega_1 \quad \varepsilon = \frac{c}{4\pi e}$$

$$K = m\Omega_0 + k_z v_{0z}$$

The system of equations (10 – 17) has a rather general form, includes as a special case all previously examined cases, and can be used to study stabilization effects connected with the axial and azimuthal shear flow, axial magnetic field and the Hall term. In the absence of the Hall term, azimuthal sheared flow, and axial magnetic field, it can be reduced to the system studied by³ for sheared flow stabilization of $m=0$ sausage and $m = 1$ kink modes. In the absence of axial and azimuthal sheared flow and axial magnetic field, it coincides with the system studied by⁶ to examine the stability of the $m = 0$ sausage mode in the presence of the Hall term.

III. DEVELOPMENT OF THE SAUSAGE INSTABILITY IN THE PRESENCE OF SHEAR FLOW AND THE HALL TERM

As the first step we have investigated the instability of the $m = 0$ mode in the presence of the axial shear flow with the Hall term included, but with zero axial magnetic field ($B_{0z} = 0$) and zero azimuthal shear flow ($\Omega_0 = 0$). In this case the system of equations (10 – 17) can be reduced to :

$$\rho_0 \frac{\partial v_{1r}}{\partial t} = -i\rho_0 k_z v_{0z} v_{1r} - \frac{\partial}{\partial r} \left(P_1 + \frac{1}{4\pi} B_{0\theta} B_{1\theta} \right) - \frac{1}{2\pi} \frac{B_{0\theta}}{r} B_{1\theta} \quad (18)$$

$$\rho_0 \frac{\partial v_{1z}}{\partial t} = -\rho_0 k_z v_{0z} v_{1z} - \rho_0 \frac{\partial v_{0z}}{\partial r} v_{1r} - ik_z \left(P_1 + \frac{1}{4\pi} B_{0\theta} B_{1\theta} \right) \quad (19)$$

$$\frac{\partial \rho_1}{\partial t} = -ik_z v_{0z} \rho_1 - \frac{\partial \rho_0}{\partial r} v_{1r} - \rho_0 \frac{1}{r} \frac{\partial}{\partial r} (r v_{1r}) - i \rho_0 k_z v_{1z} \quad (20)$$

$$\frac{\partial P_1}{\partial t} = ik_z v_{0z} P_1 - \frac{\partial P_0}{\partial r} v_{1r} - \Gamma P_0 \frac{1}{r} \frac{\partial}{\partial r} (r v_{1r}) - i \Gamma P_0 k_z v_{1z} \quad (21)$$

$$\begin{aligned} \frac{\partial B_{1\theta}}{\partial t} = & -ik_z v_{0z} B_{1\theta} - \frac{\partial}{\partial r} (v_{1r} B_{0\theta}) - ik_z v_{1z} B_{0\theta} + \epsilon i k_z \frac{B_{1\theta}}{n_0} \frac{1}{r} \frac{\partial}{\partial r} (r B_{0\theta}) \\ & - \epsilon i k_z \frac{n_1}{n_0^2} \frac{B_{0\theta}}{r} \frac{\partial}{\partial r} (r B_{0\theta}) - \epsilon i k_z r B_{1\theta} \frac{\partial}{\partial r} \left(\frac{B_{0\theta}}{r n_0} \right) \end{aligned} \quad (22)$$

The system of equations (18 – 22) was solved numerically with the following boundary and initial conditions. At $r = 0$, they are from the requirement for the solutions to be regular:

$$B_{1\theta} = 0 \quad v_{1r} = 0 \quad \frac{\partial v_{1z}}{\partial r} = 0 \quad \frac{\partial P_1}{\partial r} = 0 \quad \frac{\partial \rho_1}{\partial r} = 0 \quad (23)$$

at the edge of the metal cylinder $r = R_0$ they are:

$$\frac{\partial}{\partial r} (r B_{1\theta}) = 0 \quad v_{1r} = 0 \quad \frac{\partial v_{1z}}{\partial r} = 0 \quad \frac{\partial P_1}{\partial r} = 0 \quad \frac{\partial \rho_1}{\partial r} = 0 \quad (24)$$

If a Bennett equilibrium (constant electron drift velocity across the pinch) is used as initial conditions, then

$$B_{0\theta} = \frac{\sqrt{2} r B_{\max}}{a \left(1 + \left(\frac{r}{a} \right)^2 \right)} \quad P_0 = \frac{P_0(r=0)}{\left(1 + \left(\frac{r}{a} \right)^2 \right)^2} \quad (25)$$

where B_{\max} is the maximum magnetic field and a is the radius of B_{\max}

If a parabolic equilibrium (constant current density across the pinch) is used instead, then

$$B_{0\theta} \sim r \quad P_0 \sim P_{0\max} (1 - r^2) \quad (26)$$

where $P_{0\max}$ is the pressure on the axis, and r is the normalized radius.

We now present the results of the numerical solution of the system of equations (18 – 22). This system of equations describes the linear development of the sausage instability in the presence of axial sheared flow and the Hall term.

To solve the system of equations (18 – 22) numerically the following dimensionless variables were used:

$$r = \frac{\tilde{r}}{\tilde{r}_0} \quad \text{where } \tilde{r}_0 \text{ is the radius of a conducting cylinder and } \tilde{r} \text{ is the radial dimensional coordinate.}$$

$$t = \frac{V_{Ti}}{\tilde{r}_0} \tilde{t} \quad \text{nondimensional time}$$

$$B = \frac{\tilde{B}}{\tilde{B}(\tilde{r}_0)} \quad \text{where } \tilde{B}(\tilde{r}_0) = (4\pi M \bar{n} V_{Ti}^2)^{1/2}$$

$$\bar{n} = \frac{\tilde{N}}{\pi \tilde{r}_0^2}, \quad \tilde{N} \text{ - is ion line density and } V_{Ti} \text{ is ion thermal velocity.}$$

$$P = \frac{\tilde{P}}{M \bar{n} V_{Ti}} \quad \text{nondimensional pressure}$$

$$n = \frac{\tilde{n}}{\bar{n}} \quad \text{nondimensional density}$$

and parameter ϵ in the Hall term is equal to $\epsilon = c / (\omega_{pi} r_0)$, the ratio of the ion collisionless skin depth to the radius of the cylinder. When $\epsilon = 0$ the Hall term is not included into the model.

The development of the sausage instability has been analyzed numerically for the following set of parameters:

a) Fig. 3, Ideal MHD limit in the presence of the shear flow and in the absence of the Hall term ($V_{0z} = 0, 1, 2, 2.5; \epsilon = 0$).

b) Fig. 4, In the presence of the sheared flow and the Hall term ($V_{0z}=1,2,3$; $\epsilon = 0.01$).

c) Fig. 5, In the presence of the sheared flow and the Hall term ($V_{0z}=1,2,3$ $\epsilon = 0.1$).

where V_{0z} is the maximum sheared flow velocity and the shear flow profile was chosen in the form $V_z(r) = V_{0z} \cdot r^2$. Density and magnetic field profiles for the Bennett equilibrium with the radius of maximum B equal to $a = r_0 / 3$ are presented in Fig. 1 and 2.

The numerical solutions for all five cases with the Bennett equilibrium profile are presented in Fig. 3 -5. The smallest growth rate among the five cases (a-c) under consideration corresponds to the case (a) when sheared flow is included in the model but there is no input from the Hall term (parameter $\epsilon = 0$). Sheared flow significantly reduces the growth rate and narrows the excited wave spectrum in kz -space. With inclusion of the Hall term in the model the growth rate of the instability starts to grow, especially in the short wavelength part of the spectrum. This confirms previously obtained simulation results by⁶ for $m=0$ mode in a z -pinch plasma in the absence of sheared flow, where the destabilizing effect of the Hall term on the instability development was also observed.

The dependence of the growth rate on ϵ for the Bennett equilibrium profile is shown in Fig. 6. For this type of equilibrium the Hall term plays a destabilizing role and the growth rate increases with increasing ϵ .

We have also investigated the $m=0$ sausage instability development for the parabolic equilibrium profile. On Fig. 7 it is shown that in the absence of the Hall term ($\epsilon = 0$) the shear flow reduces the growth rate of the instability.

The numerical solutions for the growth rate with the parabolic equilibrium profile are presented on Fig. 8. As one can see, the behavior of the growth rate is different from the

case with the Bennett equilibrium profile. With increase of ϵ the growth rate now slightly decreases. It can be seen from the solutions for the cases ($V_{0z} = 1.5$; $\epsilon = 0$) and ($V_{0z} = 1.5$; $\epsilon = 0.01$). However, for larger values of ϵ the growth rate starts to grow with ϵ , as can be seen in the case ($V_{0z} = 1.5$; $\epsilon = 0.1$). Similar growth rate behavior was observed for the equilibrium profile II in the absence of the shear flow in the paper⁶.

The results of the numerical solution of the system of equations (18–22) for the $m=0$ mode were compared when possible and appeared to be in agreement with the previously obtained results for the instability of the $m=0$ mode in terms of the growth rate value, particularly in the papers by⁶ (instability of the $m=0$ mode was investigated in the presence of the Hall term but without sheared flow) and³ (stabilization of the $m=0$ mode in the presence of sheared flow but without the Hall term was studied).

It is also worth mentioning that numerical solutions presented represent the solutions of the system of equations (18–22) after they have converged to the solution corresponding to the fastest growing mode with a constant growth rate. These growth rates were the same for all five variables in the equations. This can represent an additional check for the correctness of the obtained numerical solutions.

It is well known that the Bennett equilibrium is MHD stable for $\Gamma > 2$ and exactly that result was obtained from the numerical solution. All these together makes us to believe that the obtained numerical results are correct.

IV. DEVELOPMENT OF THE SAUSAGE INSTABILITY IN THE PRESENCE OF THE AXIAL MAGNETIC FIELD

In the presence of an axial magnetic field B_{0z} , shear flow and the Hall term equations

(10 – 17) in dimensionless variables have the following form:

$$\rho_0 \frac{\partial v_{1r}}{\partial t} = -i\rho_0 k_z v_{0z} v_{1r} - \frac{\partial}{\partial r} (P_1 + B_{0z} B_{1z}) - \frac{1}{r^2} \frac{\partial}{\partial r} (r^2 B_{0\theta} B_{1\theta}) + ik_z B_{0z} B_{1r} \quad (27)$$

$$\rho_0 \frac{\partial v_{1\theta}}{\partial t} = -i\rho_0 k_z v_{0z} v_{1\theta} + ik_z B_{0z} B_{1\theta} + \frac{B_{1r}}{r} \frac{\partial}{\partial r} (r B_{0\theta}) \quad (28)$$

$$\rho_0 \frac{\partial v_{1z}}{\partial t} = -\rho_0 k_z v_{0z} v_{1z} - \rho_0 \frac{\partial v_{0z}}{\partial r} v_{1r} - ik_z (P_1 + B_{0\theta} B_{1\theta}) + \frac{\partial B_{0z}}{\partial r} B_{1r} \quad (29)$$

$$\frac{\partial \rho_1}{\partial t} = -ik_z v_{0z} \rho_1 - \frac{1}{r} \frac{\partial}{\partial r} (r \rho_0 v_{1r}) - i\rho_0 k_z v_{1z} \quad (30)$$

$$\frac{\partial P_1}{\partial t} = -ik_z v_{0z} P_1 - \frac{\partial P_0}{\partial r} v_{1r} - \Gamma P_0 \frac{1}{r} \frac{\partial}{\partial r} (r v_{1r}) - i\Gamma P_0 k_z v_{1z} \quad (31)$$

$$\frac{\partial B_{1r}}{\partial t} = -ik_z v_{0z} B_{1\theta} + ik_z v_{1r} B_{0z} + \epsilon k_z \frac{B_{1r}}{n_0} \frac{1}{r} \frac{\partial}{\partial r} (r B_{0\theta}) - \epsilon k_z^2 \frac{B_{0z}}{n_0} B_{1\theta} \quad (32)$$

$$\begin{aligned}
\frac{\partial B_{1\theta}}{\partial t} = & -ik_z v_{0z} B_{1\theta} - \frac{\partial}{\partial r} (v_{1r} B_{0\theta}) - ik_z v_{1z} B_{0\theta} + ik_z B_{0z} v_{1\theta} + \\
& \epsilon k_z \left(2 \frac{B_{1\theta} B_{0\theta}}{n_0} + \frac{B_{1\theta} B_{0\theta}}{n_0^2} \frac{\partial n_0}{\partial r} + \frac{B_{0z}}{n_0} \frac{\partial B_{1z}}{\partial r} - \frac{B_{1z}}{n_0} \frac{\partial B_{0z}}{\partial r} - \frac{B_{0z}}{n_0} \frac{\partial B_{0z}}{\partial r} \frac{n_1}{n_0^2} \right) + \\
& - \epsilon k_z \frac{n_1}{n_0^2} \frac{B_{0\theta}}{r} \frac{\partial}{\partial r} (r B_{0\theta}) + \epsilon k_z^2 \frac{B_{0z}}{n_0} B_{1r}
\end{aligned} \tag{33}$$

$$\begin{aligned}
\frac{\partial B_{1z}}{\partial t} = & -ik_z v_{0z} B_{1z} + \frac{\partial v_{0z}}{\partial r} B_{1r} - \frac{1}{r} \frac{\partial}{\partial r} (r B_{0z} v_{1r}) - \epsilon \frac{1}{r} \frac{\partial}{\partial r} \left[\frac{B_{1r}}{n_0} \frac{\partial}{\partial r} (r B_{0\theta}) \right] \\
& - \epsilon k_z \left[\frac{1}{r} \frac{\partial}{\partial r} \left(\frac{r B_{0z} B_{1\theta}}{n_0} \right) \right]
\end{aligned} \tag{34}$$

Here we present numerical solution of equations (22-30) only when the Hall term was not included into the mode ($\epsilon = 0$). In the presence of the Hall term eigenfunctions representing the solution are located very close to the boundary and experience strong dependence from the boundary conditions. This in turn results in inaccurate values for the growth rate defined from the numerical solution. In the future we plan to apply another approach connected with the use of shooting code¹³ to overcome this difficulty. The set of equations (22-30) was solved numerically with parabolic profile chosen for initial equilibrium.

$$B_{0\theta} = r$$

$$P_0 = 1 - r^2$$

The following cases were investigated:

1. In the absence of the shear flow ($V_{0z} = 0$) and the Hall term ($\epsilon = 0$)

axial magnetic field B_{0z} had values $B_{0z} = 0$, $B_{0z} = 0.1$ and $B_{0z} = 0.2$.

Numerical solution for this case is presented on Fig. 9.

2. In the presence of the shear flow ($V_{0z} = 1.5$) without the Hall term ($\epsilon = 0$)

axial magnetic field B_{0z} had values $B_{0z} = 0$, $B_{0z} = 0.1$ and $B_{0z} = 0.2$.

Numerical solution for this case is presented on Fig. 10.

The instability growth rates presented on Fig 9 and 10 show that combination of the shear flow and axial magnetic field leads to substantial decrease of the growth rate and considerably narrows the excited wave spectrum for $m = 0$ mode.

V. SUMMARY, DISCUSSION, AND CONCLUSIONS

In this paper, we have developed a general analytic formulation for linear z-pinch stability to MHD modes with inclusion of the Hall term, sheared flow (axial and azimuthal), and axial magnetic field. We have presented numerical solutions of the resulting equations as an initial value problem with fixed boundaries. The stability of the $m=0$ sausage mode was examined under several conditions: with the Hall term and axial sheared flow but without axial magnetic field with Bennett and parabolic equilibrium profiles; with axial sheared flow and axial magnetic field but without the Hall term with parabolic equilibrium profile. These results were of course compared to the standard ideal MHD case.

Our main results are that axial sheared flow decreases the growth rate of the sausage instability in all cases where it is present. The axial magnetic field is further stabilizing when it is present as is well known¹¹⁻¹² and reproduced here. Our results are closest to recent work by¹².

The Hall term on the other hand has a destabilizing effect for the Benette equilibrium on the $m=0$ mode when included. In the case of the parabolic profile we observed the reduction of the growth rate for the small values of the parameter ϵ and increase in the growth rate for the larger values of ϵ . This is in agreement with results obtained by⁶ and with the MHRDR code by⁷.

AKNOWLEDGMENTS

The authors wish to acknowledge valuable discussions with I. Lindemuth, P. Sheehey and L. Rudakov.

This work was supported by the Department of Energy.

¹F. Winterberg, Beitr. Plasmaphys., **25**, 117 (1985).

²U. Shumlak, C.W. Hartman, Phys. Rev. Letters, **75**, 3285 (1995).

³T. D. Arber and D.F. Howell, Physics of Plasmas **3**, 554 (1996).

⁴S. Appl and M. Camenzind, Astronomy and Astrophysics **354**, 256 (1992).

⁵M. G. Haynes and M. Coppins, Phys. Rev. Lett. **66**, 1462 (1991).

⁶M. Coppins, D.J. Bond, and M.G. Haines, Phys. Fluids, **27**, 2886 (1984).

⁷P. Sheehey, I. Lindemuth, Phys. Plasmas, **4**, 146 (1997).

⁸A. Sykes and J.A. Wesson, Nucl. Fusion, **14**, 645 (1974).

⁹G. Bateman, W. Schneider, and W. Grossman, Nucl. Fusion **14**, 669 (1974).

¹⁰G. Bateman, MHD Instabilities, MIT Press, Cambridge, (1978).

¹¹J.P. Freidberg, *Ideal Magnetohydrodynamics* (Plenum, New York, 1987)

¹²A.B. Bud'ko, Sov. Phys. Tech. Phys., **34(b)**, 914 (1989).

¹³C.L. Hedrick and J-N. Leboeuf, Phys. Fluids B, **4**, 3915 (1992).

Figure Captions

FIG. 1. Density profile for the Bennett equilibrium with the radius of maximum B equal to $a = r_0 / 3$.

FIG. 2. Magnetic field profile for the Bennett equilibrium with the radius of maximum B equal to $a = r_0 / 3$

FIG. 3. Growth rate of the $m = 0$ sausage instability in the ideal MHD limit in the presence of the shear flow and in the absence of the Hall term ($V_{0z} = 0, 1, 2, 2.5$; $\epsilon = 0$).

FIG. 4. Growth rate of the $m = 0$ sausage instability in the presence of the sheared flow and the Hall term ($V_{0z} = 1, 2, 3$; $\epsilon = 0.01$). V_{0z} is the maximum sheared flow velocity and the shear flow profile was chosen in the form $V_z(r) = V_{z0} \cdot r^2$.

FIG. 5. Growth rate of the $m = 0$ sausage instability in the presence of the sheared flow and the Hall term ($V_{0z} = 1, 2, 3$; $\epsilon = 0.1$). V_{0z} is the maximum sheared flow velocity and the shear flow profile was chosen in the form $V_z(r) = V_{z0} \cdot r^2$.

FIG. 6. Dependence of the growth rate on ϵ for the Bennett equilibrium profile with and without the shear flow.

FIG. 7. Growth rate of the $m = 0$ sausage instability for the parabolic equilibrium profile with and without the shear flow in the absence of the Hall term ($\epsilon = 0$).

FIG. 8. Growth rate of the $m = 0$ sausage instability for different values of parameter $\epsilon = (0, 0.01, 0.1)$ corresponding to the Hall term, for the parabolic equilibrium profile in the presence of the shear flow.

FIG. 9. Growth rate of the $m = 0$ sausage instability for the parabolic equilibrium profile, when axial magnetic field B_{0z} had values $B_{0z} = 0$, $B_{0z} = 0.1$ and $B_{0z} = 0.2$ in the absence of the shear flow ($V_{0z} = 0$) and the Hall term ($\epsilon = 0$).

FIG. 10. Growth rate of the $m = 0$ sausage instability for the parabolic equilibrium profile in the presence of the shear flow ($V_{0z} = 1.5$) without the Hall term ($\epsilon = 0$), when axial magnetic field B_{0z} had values $B_{0z} = 0$, $B_{0z} = 0.1$ and $B_{0z} = 0.2$.

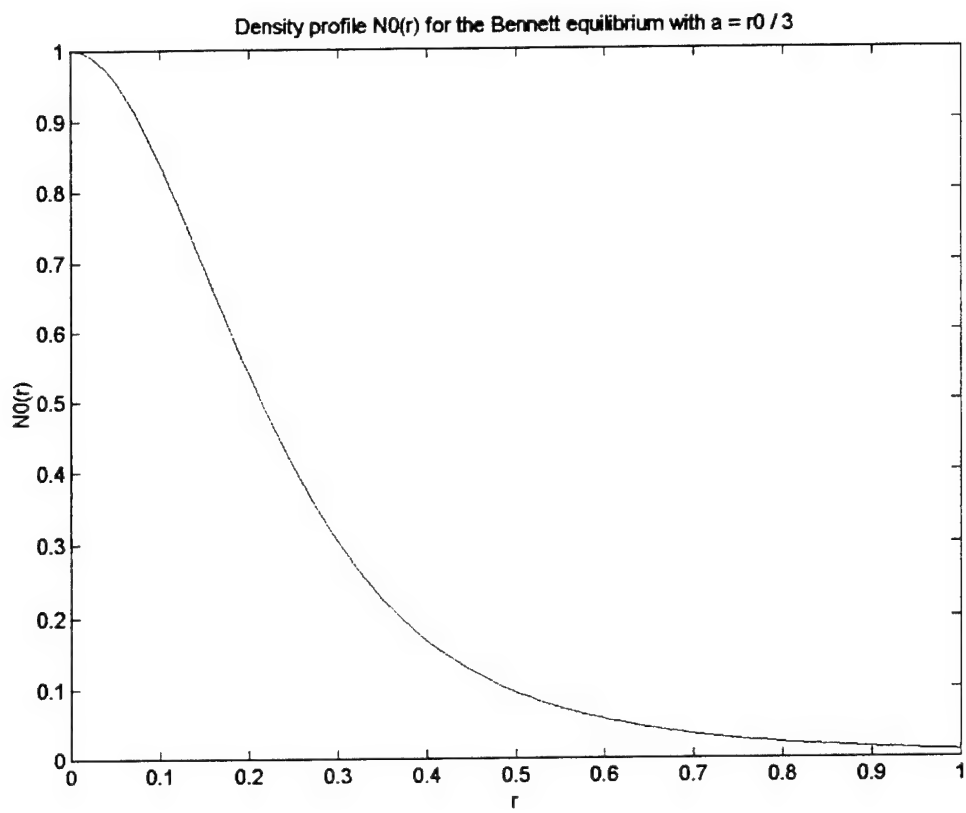


FIG. 1

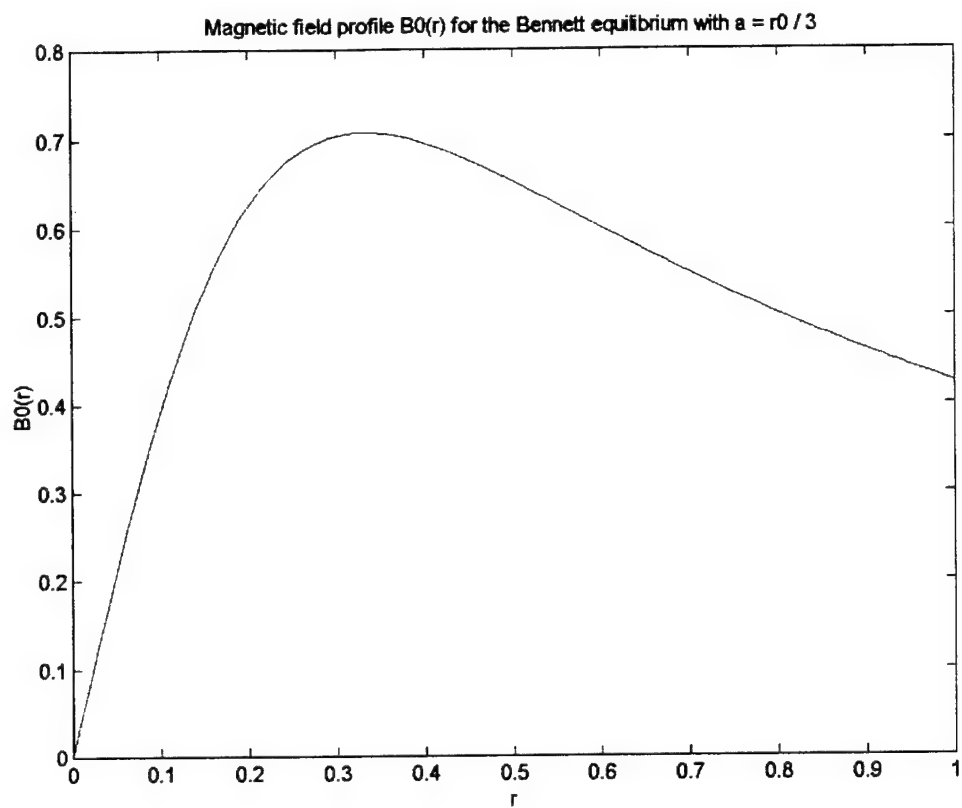


FIG. 2

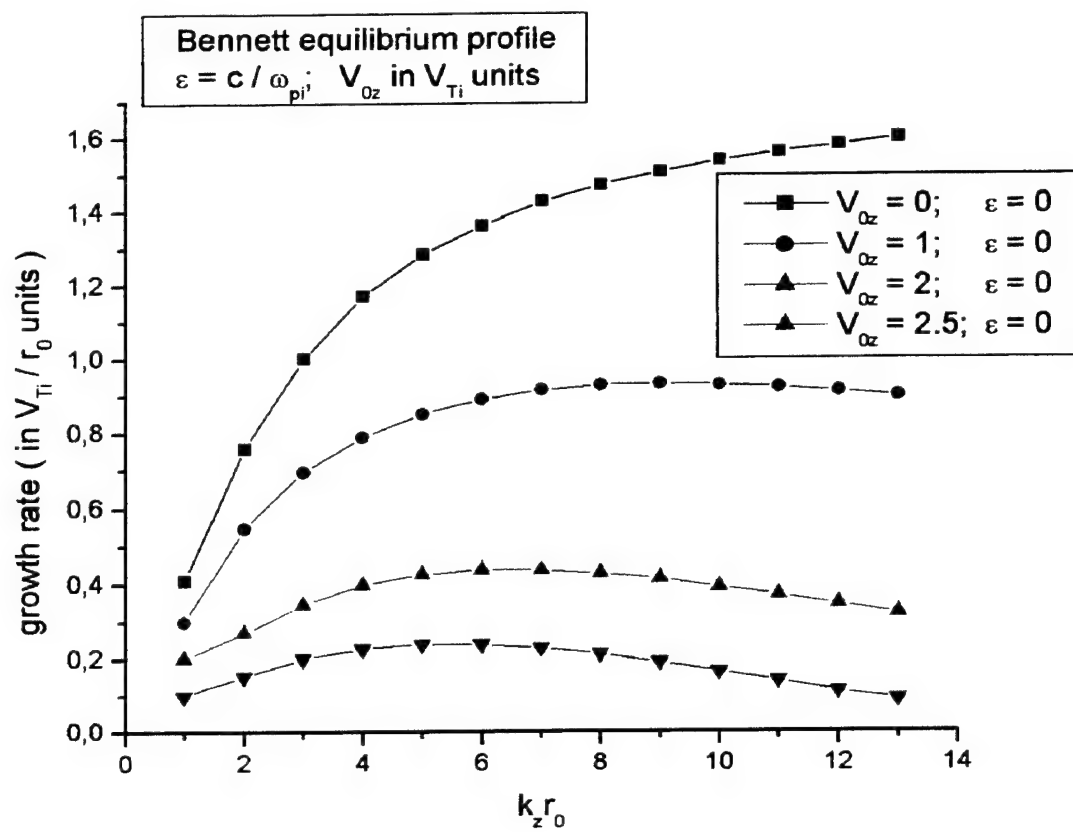


FIG. 3

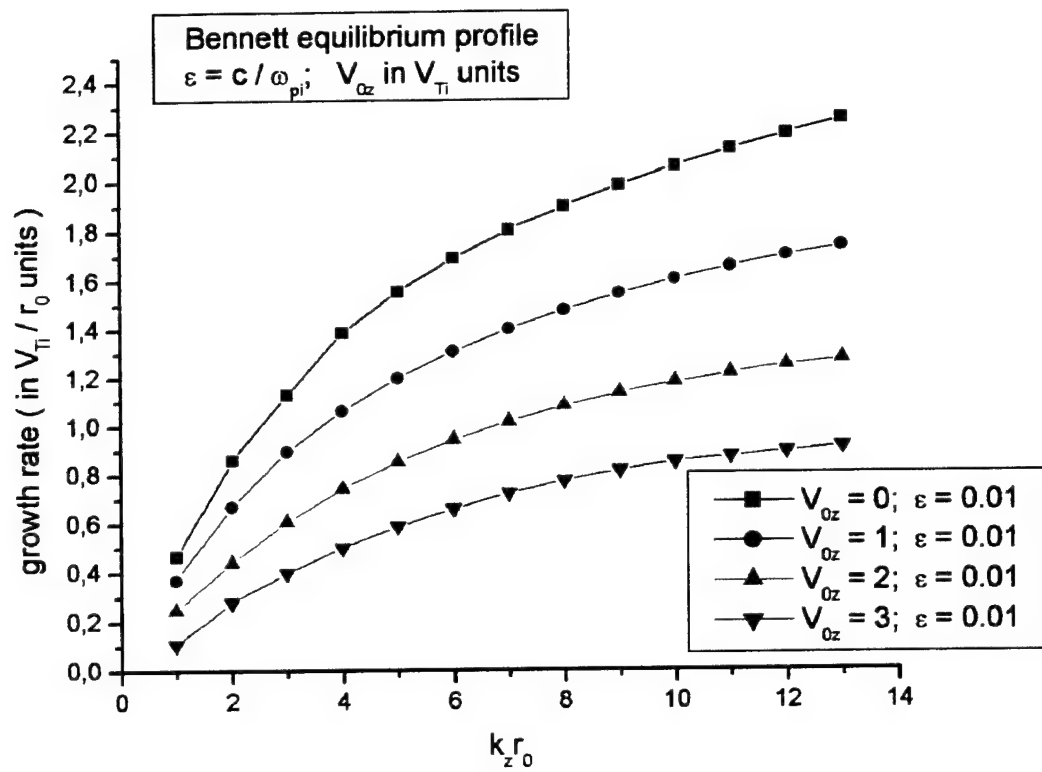


FIG. 4

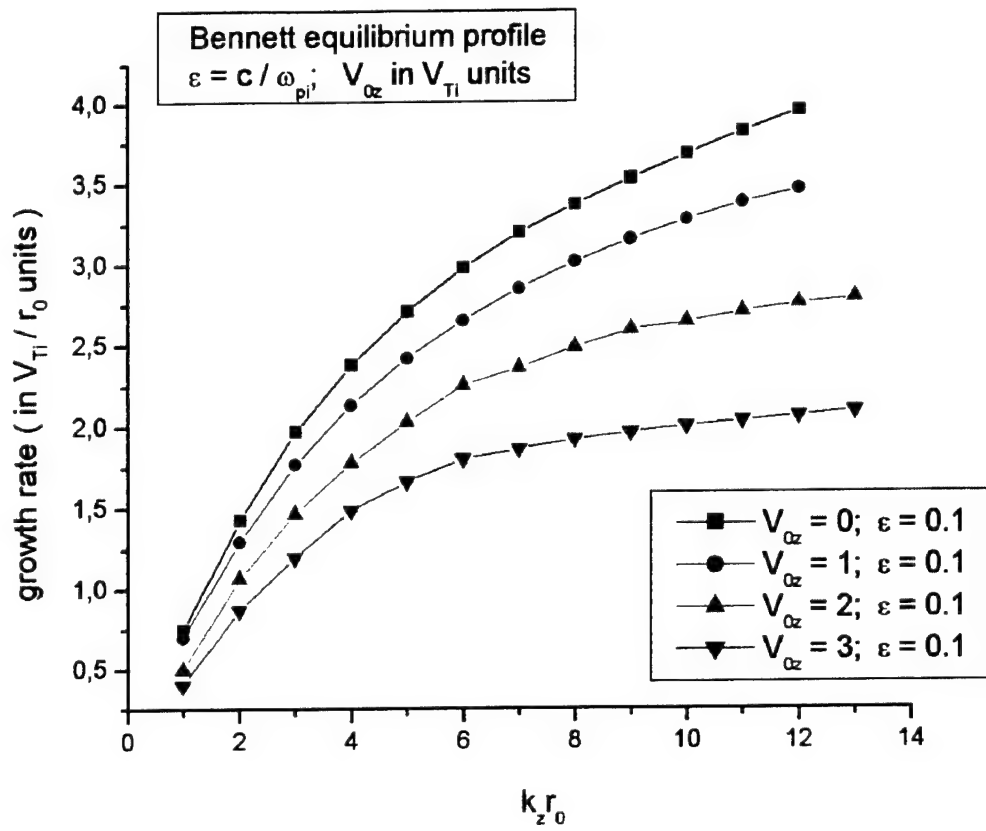


FIG. 5

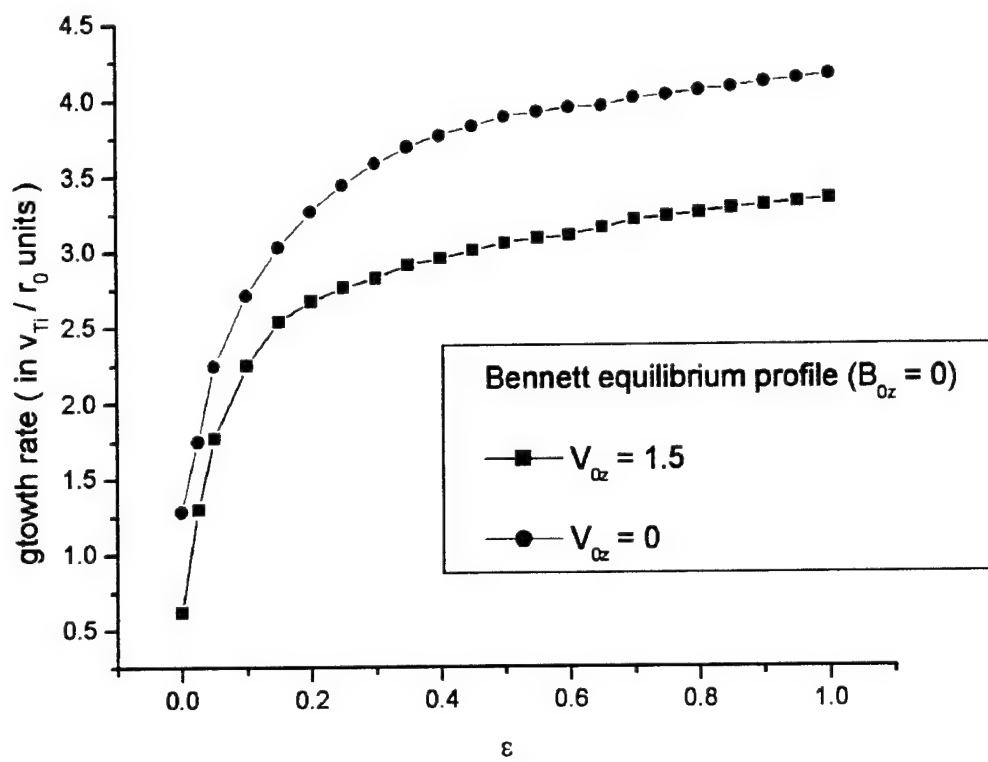


FIG. 6

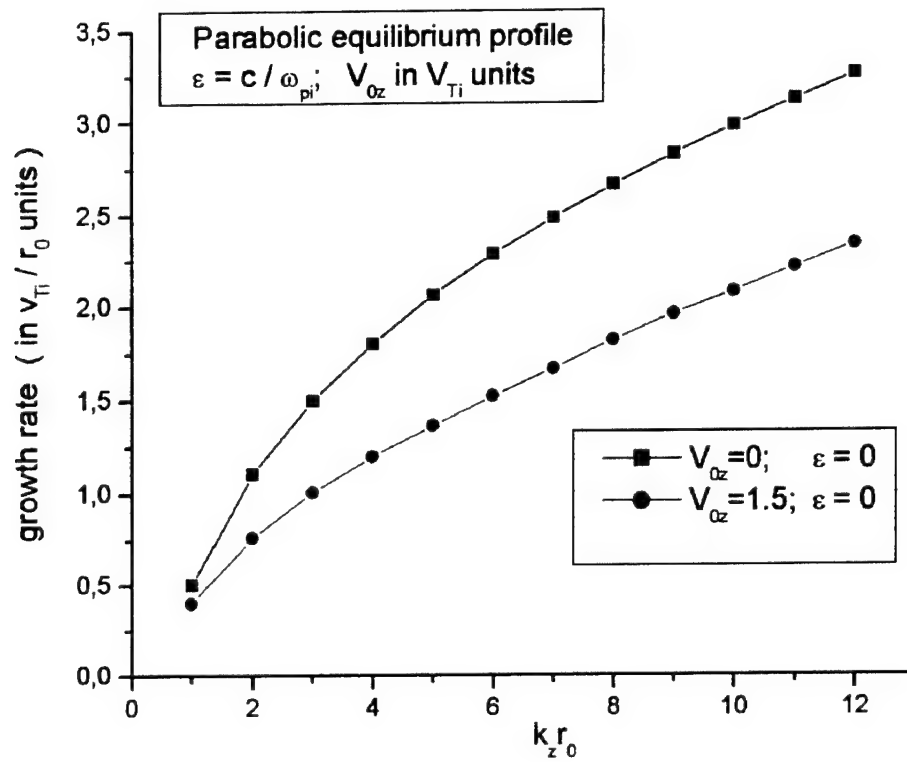


FIG. 7

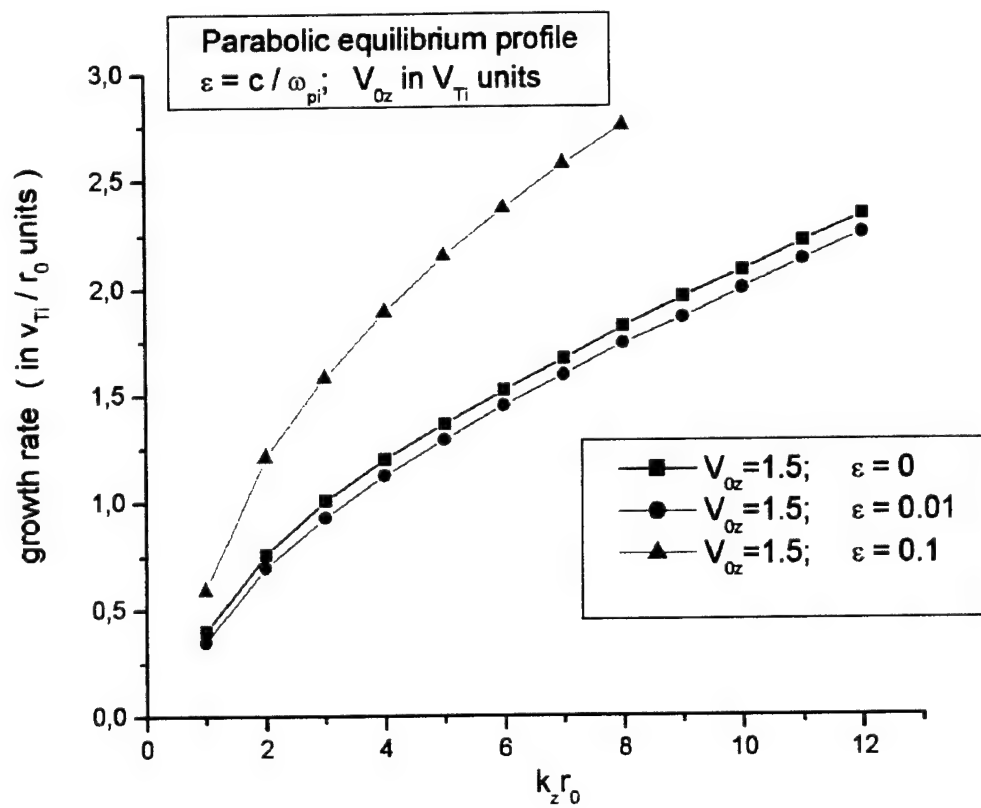


FIG. 8

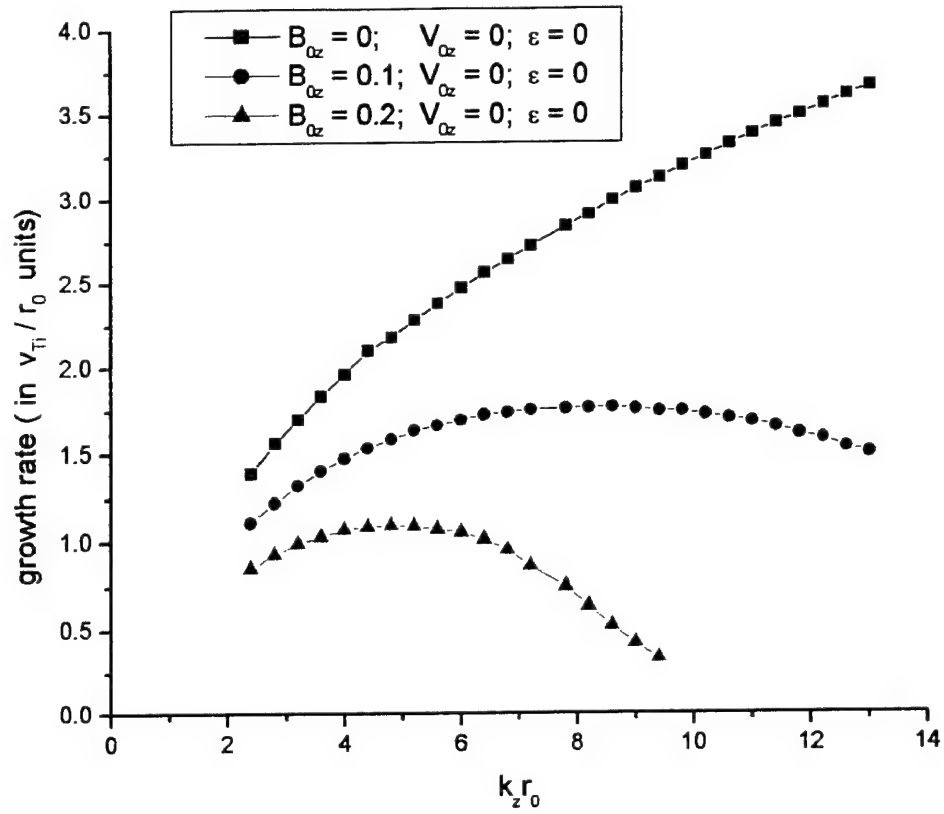


FIG. 9

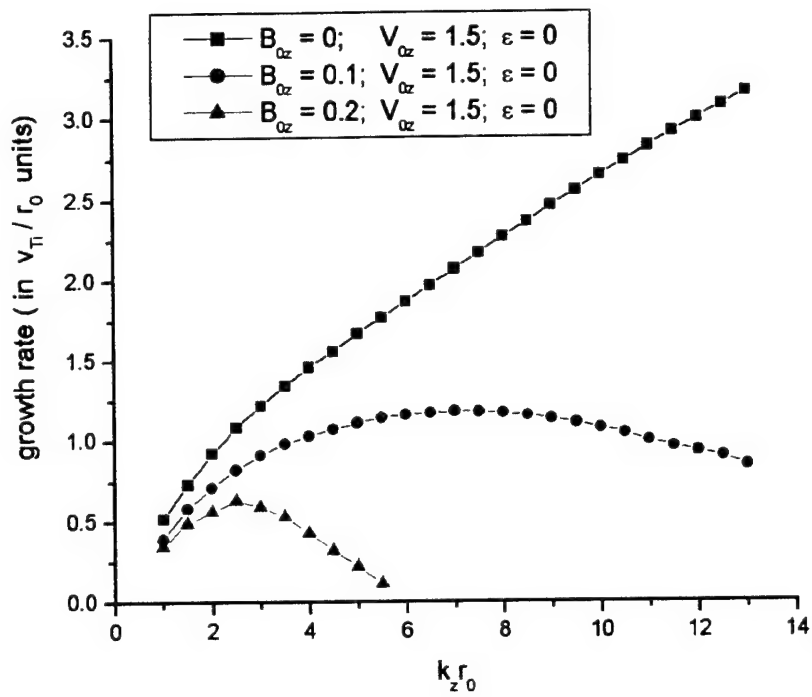


FIG. 10

APPENDIX B

Linear Analysis and MHD Modeling of Shear Flow Stabilization of the Sausage Instability

V.I. Sotnikov, V. Makhin, I. Paraschiv, and B.S. Bauer, UNR
J.-N. LeBoeuf and J.M. Dawson, UCLA
I. Lindemuth and P. Sheehey, LANL

PPPS-2001, Las Vegas, NV, June 17-22, 2001

Linear analysis and MHD modeling of sheared flow stabilization of the sausage instability

V. I. Sotnikov, V. Makhin, I. Paraschiv, B.S. Bauer

University of Nevada, Reno, NV 89557-0058

J. N. Leboeuf, J. M. Dawson

University of California, Los Angeles, CA 90095-1547

I. Lindemuth, P. Sheehey

Los Alamos National Laboratory, Los Alamos, NM 87544

Abstract

A systematic study of the linear stability of z-pinch plasmas with equilibria that contain sheared flow based on the linearized MHD equations and 2D MHD simulations using MHRDR code is presented. The study begins with a linearized set of equations that permit evaluation of the effect of sheared flow on the $m = 0$ sausage instability, with the Hall term included in the model. Inclusion of sheared flow and the Hall term allows the z-pinch system to be taken away from the region in parameter space where ideal MHD is applicable to a regime where non-ideal effects tend to govern stability. The problem is then treated numerically following the development in time of an initial perturbation. The numerical results as a function of sheared flow and Hall term are reported. The linear stage of the instability development is also compared with the 2D MHRDR simulation results. To initiate MHRDR simulations Bennett equilibrium profiles for magnetic field and density were chosen with simulation region in r-z plane and with the azimuthal magnetic field B_θ perpendicular to the plane of the simulations. Linear theory solutions for the growth rate appeared to be in a good agreement with the MHRDR simulation results.

I. ITRODUTION

Theory and computations have examined several possible z-pinch stabilization techniques, including axial sheared flow [1-4]. With sheared axial flows included in the equilibrium it is found that substantial stabilization of internal modes is possible for some equilibrium profiles. The guiding principle is to take the z-pinch system away from the region in parameter space where ideal MHD is applicable to a regime where non-ideal effects [5] such as the Hall term [6-8] and axial sheared flow [8] tend to govern stability. The calculations will guide the experimental approach to higher densities and longer confinement times.

This paper focuses on the effects of axial sheared flow on the $m = 0$ sausage instability, with and without the Hall term included into the model. The results are compared with 2D MHRDR simulation of the $m = 0$ instability with the Bennett equilibrium profile.

Sheared flows are of interest as a possible mechanism for the stabilization of MHD instabilities, because MHD instabilities grow on the pinch surface, where the density is low and the magnetic field is high. The flow stretches and eliminates the MHD modulations, mixing the unstable modes with different wave lengths. This restricts the growth of the modes to a nondestructive level. We first of all need to understand z-pinch behavior in the linear stage of development of the instability.

We shall use equations derived in [8] that contain the Hall term in addition to the standard MHD terms, in the presence of sheared axial flow. These equations form a more general set than has apparently been used before. These equations will be used to define eigenfunctions and eigenvalues that could exhibit unstable solutions to the perturbed

equilibria . This will identify the region in parameter space where the instability can take place and determine the linear growth rate of the instability.

This paper is organized as follows. The linear stability analysis is initiated in Section 2, where results for the $m=0$ sausage instability in the presence of sheared axial flow and the Hall term are presented. MHRDR simulation results for the sausage instability in the presence of sheared flow for the same initial and boundary conditions as in Section 2 are presented in Section 3. Section 4 offers a discussion and conclusions.

II. LINEAR STABILITY ANALYSIS

We shall treat the problem numerically following the development in time of an initial perturbation. After several growth times the solution will converge to the fastest growing mode, defining real and imaginary parts of ω . This method has been used for linear studies of z -pinch stability in cylindrical plasmas by [9], and for ideal MHD instabilities in tokomaks [10-12].

Using this approach, the linearized system of equations which describes the development of the $m = 0$ sausage and $m = 1$ kink instabilities in the presence of axial and azimuthal sheared flow, axial magnetic field, and the Hall term was derived in [8]. In the case of the sausage ($m = 0$) instability it has the following form:

$$\rho_0 \frac{\partial v_{1r}}{\partial t} = -i\rho_0 k_z v_{0z} v_{1r} - \frac{\partial}{\partial r} \left(P_1 + \frac{1}{4\pi} B_{0\theta} B_{1\theta} \right) - \frac{1}{2\pi} \frac{B_{0\theta}}{r} B_{1\theta} \quad (1)$$

$$\rho_0 \frac{\partial v_{1z}}{\partial t} = -\rho_0 k_z v_{0z} v_{1z} - \rho_0 \frac{\partial v_{0z}}{\partial r} v_{1r} - i k_z \left(P_1 + \frac{1}{4\pi} B_{0\theta} B_{1\theta} \right) \quad (2)$$

$$\frac{\partial \rho_1}{\partial t} = -ik_z v_{0z} \rho_1 - \frac{\partial \rho_0}{\partial r} v_{1r} - \rho_0 \frac{1}{r} \frac{\partial}{\partial r} (r v_{1r}) - i \rho_0 k_z v_{1z} \quad (3)$$

$$\frac{\partial P_1}{\partial t} = ik_z v_{0z} P_1 - \frac{\partial P_0}{\partial r} v_{1r} - \Gamma P_0 \frac{1}{r} \frac{\partial}{\partial r} (r v_{1r}) - i \Gamma P_0 k_z v_{1z} \quad (4)$$

$$\begin{aligned} \frac{\partial B_{1\theta}}{\partial t} = & -ik_z v_{0z} B_{1\theta} - \frac{\partial}{\partial r} (v_{1r} B_{0\theta}) - ik_z v_{1z} B_{0\theta} + \tilde{\varepsilon} ik_z \frac{B_{1\theta}}{n_0} \frac{1}{r} \frac{\partial}{\partial r} (r B_{0\theta}) \\ & - \tilde{\varepsilon} ik_z \frac{n_1}{n_0^2} \frac{B_{0\theta}}{r} \frac{\partial}{\partial r} (r B_{0\theta}) - \tilde{\varepsilon} ik_z r B_{1\theta} \frac{\partial}{\partial r} \left(\frac{B_{0\theta}}{r n_0} \right) \end{aligned} \quad (5)$$

where $\tilde{\varepsilon} = \frac{c}{4\pi e}$

For radially dependent equilibria with $P_0(r)$, $n_0(r)$, $B_{0\theta}(r)$ and

$v_{0z}(r)$ the following equilibrium condition was used to derive equations (1) - (5):

$$\frac{1}{M n_0} \frac{\partial}{\partial r} \left[P_0 + \frac{B_{0\theta}^2}{8\pi} \right] + \frac{1}{M n_0} \frac{B_{0\theta}^2}{4\pi r} = 0 \quad (6)$$

This equilibrium condition does not include axial speed $v_{0z}(r)$. It means that axial speed is a free parameter of our problem. This results in a great variety of possible equilibrium profiles with different axial sheared flows.

The system of equations (1 – 5) was solved numerically with the following boundary and initial conditions. At $r = 0$, they are from the requirement for the solutions to be regular:

$$B_{1\theta} = 0 \quad v_{1r} = 0 \quad \frac{\partial v_{1z}}{\partial r} = 0 \quad \frac{\partial P_1}{\partial r} = 0 \quad \frac{\partial \rho_1}{\partial r} = 0 \quad (23)$$

at the edge of the metal cylinder $r = R_0$ they are:

$$\frac{\partial}{\partial r}(rB_{1\theta}) = 0 \quad v_{1r} = 0 \quad \frac{\partial v_{1z}}{\partial r} = 0 \quad \frac{\partial P_1}{\partial r} = 0 \quad \frac{\partial \rho_1}{\partial r} = 0 \quad (24)$$

If a Bennett equilibrium (constant electron drift velocity across the pinch) is used as initial conditions, then

$$B_{0\theta} = \frac{\sqrt{2}rB_{\max}}{a \left(1 + \left(\frac{r}{a} \right)^2 \right)} \quad P_0 = \frac{P_0(r=0)}{\left(1 + \left(\frac{r}{a} \right)^2 \right)^2} \quad (25)$$

where B_{\max} is the maximum magnetic field and a is the radius of B_{\max}

We now present the results of the numerical solution of the system of equations (1 – 5).

This system of equations describes the linear development of the sausage instability in the presence of axial sheared flow and the Hall term.

To solve the system of equations (1 – 5) numerically the following dimensionless variables were used:

$$r = \frac{\tilde{r}}{\tilde{r}_0} \quad \text{where } \tilde{r}_0 \text{ is the radius of a conducting cylinder and } \tilde{r} \text{ is the radial dimensional coordinate.}$$

$$t = \frac{V_{Ti}}{\tilde{r}_0} \tilde{t} \quad \text{nondimensional time}$$

$$B = \frac{\tilde{B}}{\tilde{B}(\tilde{r}_0)} \quad \text{where } \tilde{B}(\tilde{r}_0) = (4\pi M \bar{n} V_{Ti}^2)^{1/2}$$

$$\bar{n} = \frac{\tilde{N}}{\pi \tilde{r}^2}, \quad \tilde{N} - \text{is ion line density and } V_{Ti} \text{ is ion thermal velocity.}$$

$$P = \frac{\tilde{P}}{M \bar{n} V_{Ti}} \quad \text{nondimensional pressure}$$

$$n = \frac{\tilde{n}}{\bar{n}} \quad \text{nondimensional density}$$

and parameter ϵ which appears in the dimensionless equation for magnetic field in the Hall term is equal to $\epsilon = c / (\omega_{pi} r_0)$, the ratio of the ion collisionless skin depth to the radius of the cylinder. When $\epsilon = 0$ the Hall term is not included into the model.

The development of the sausage instability has been analyzed numerically for the following set of parameters:

- a) Fig. 3, Ideal MHD limit in the presence of the shear flow and in the absence of the Hall term ($V_{0z} = 0, 1, 2, 2.5$; $\epsilon = 0$).
- b) Fig. 4, In the presence of the sheared flow and the Hall term ($V_{0z} = 1, 2, 3$; $\epsilon = 0.01$).
- c) Fig. 5, In the presence of the sheared flow and the Hall term ($V_{0z} = 1, 2, 3$; $\epsilon = 0.1$).

where V_{0z} is the maximum sheared flow velocity and the shear flow profile was chosen in the form $V_z(r) = V_{z0} \cdot r^2$. Density and magnetic field profiles for the Bennett equilibrium with the radius of maximum B equal to $a = r_0 / 3$ are presented in Fig. 1 and 2.

The numerical solutions for all five cases with the Bennett equilibrium profile are presented in Fig. 3 -5. The smallest growth rate among the five cases (a-c) under consideration corresponds to the case (a) when sheared flow is included in the model but there is no input from the Hall term (parameter $\epsilon = 0$). Sheared flow significantly reduces the growth rate and narrows the excited wave spectrum in kz -space. With

inclusion of the Hall term in the model the growth rate of the instability starts to grow, especially in the short wavelength part of the spectrum. This confirms previously obtained simulation results by [6] for $m=0$ modes in a z-pinch plasma in the absence of sheared flow, where the destabilizing effect of the Hall term on the instability development was also observed.

The dependence of the growth rate on ϵ for the Bennett equilibrium profile is shown in Fig. 6. For this type of equilibrium the Hall term plays a destabilizing role and the growth rate increases with increasing ϵ .

The results of the numerical solution of the system of equations (1–5) for the $m=0$ mode were compared when possible and appeared to be in agreement with the previously obtained results for the instability of the $m=0$ mode in terms of the growth rate value, particularly in the papers by [6]. There, instability of the $m=0$ mode was investigated in the presence of the Hall term but without sheared flow and stabilization of the $m=0$ mode in the presence of sheared flow but without the Hall term was studied.

It is also worth mentioning that numerical solutions presented represent the solutions of the system of equations (1-5) after they have converged to the solution corresponding to the fastest growing mode with a constant growth rate. These growth rates were the same for all five variables in the equations. This can represent an additional check for the correctness of the obtained numerical solutions.

It is well known that the Bennett equilibrium is MHD stable for $\Gamma > 2$ and exactly that result was obtained from the numerical solution. All of these taken together lead us to believe that the obtained numerical results are correct.

III. MHRDR MODELING OF THE SAUSAGE INSTABILITY

In this section investigation of the linear stage of the sausage instability development will be carried out using the magnetohydrodynamic code MHRDR, developed by I.

Lindemuth and P. Sheehey at LANL. Our aim is to compare

simulation results with the results of linear theory. This benchmarks not only the MHRDR code but also the linear initial value solver.

To initiate MHRDR simulations, Bennett equilibrium profiles for magnetic field and density were chosen. This is a 2D problem with the simulation region in the r - z plane and with the azimuthal magnetic field B_θ perpendicular to the plane of simulations. We cannot impose periodic boundary conditions in MHRDR and have consider a simulation box with metal boundaries with the z - axis corresponding to the axial direction and r -axis to the radial direction. The initial current density profile was taken as Bennett profile in the radial direction

$$j_z = \frac{j_{z \max}}{(1 + (\frac{r}{a})^2)^2} \quad (7)$$

with $j_{z \max} = \frac{c}{\pi} \frac{B_{\max}}{a}$ and where $a = \frac{r_0}{3}$ is the radial location of the magnetic field

maximum in the Bennett equilibrium . Here r_0 is the radius of a metal cylinder.

Initial density perturbations for this problem were chosen of the form:

$$\rho_{pert} = ampl * \rho_{\max} * \exp(-0.5 * (\frac{r-a}{h})^2) * \sin(kz) \quad (8)$$

where $ampl$ was taken to be in the range $1.0e-5 \leq ampl \leq 1.0e-2$. Initial perturbations for pressure, magnetic field, and speed were of the same form.

The following initial simulation parameters were chosen for hydrogen plasma:

density $n_{00} = 10^{18} \frac{1}{\text{cm}^3}$, which corresponds to the mass density $\rho_{0\text{max}} = 1.67 \cdot 10^{-3} \frac{\text{kg}}{\text{m}^3}$.

The temperature of the plasma was taken at $T = 1\text{ev}$.

The length of the simulation region in the z direction was chosen so that many wavelengths of the most unstable modes could fit inside the simulation box $L_z \approx 10r_0$.

The wave vector k_z in the expression (8) for the perturbed quantities was such that $k_z r_0 = 6$. According to the results of the numerical solution (Fig. 3) this gives $\gamma = 1.36$ for the growth rate of the instability in the absence of sheared flow ($V_{0z} = 0$ and $\varepsilon = 0$) and $\gamma = 0.39$ in the presence of sheared flow with $V_{0z} = 2$ and $\varepsilon = 0$.

In the MHRDR simulations, we shall follow the growth of this unstable mode and will find the growth rate of this mode using the growth in time of the perturbed kinetic energy of the plasma in the z direction. This is what is used in this code to calculate of the growth rate of the unstable mode defined as a perturbation to the initial conditions. Simulation results are presented in Figs. 7 – 10. In Fig. 7 and Fig. 8 the contour lines of density and azimuthal magnetic field with growing perturbations defined in the initial conditions ($k_z r_0 = 6$) in the absence of the sheared flow ($V_{0z} = 0$ and $\varepsilon = 0$) corresponding to the sausage instability ($m = 0$) with Bennett initial profiles are presented. In Fig.9 and Fig.10 the contour lines of density and azimuthal magnetic field in the presence of sheared flow with $V_{0z} = 2$ are presented. In both cases the contour lines were plotted at the same time from the start of simulations. The growth of the perturbations, as is seen in the simulation results, is suppressed when the sheared flow is included in the model. Simulation results presented in Figures 7 –10 are in agreement with the numerical linear theory solutions for the growth rate, presented in Figure 3. In MHRDR, the value of the growth rate can be obtained from the time dependence of the

axial kinetic energy. For the unstable wave number of $k_z r_0 = 6$, we found for the growth rate $\gamma \sim 1.37$ in the absence of sheared flow ($V_{0z} = 0$ and $\varepsilon = 0$) and $\gamma \sim 0.35$ in the presence of sheared ($V_{0z} = 1.5 V_{Ti}$, and $\varepsilon = 0$). This is in good agreement with the linear theory results.

IV. SUMMARY, DISCUSSION, AND CONCLUSIONS

In this paper, we investigated the development of the sausage ($m = 0$) instability in the presence of axial sheared flow and compared results of the linear stability analysis with simulation results obtained using the MHRDR code. Results of the linear stability analysis with inclusion of the Hall term into the model are presented as well. For the linear stability analysis, we have presented numerical solutions of the linearized MHD equations as an initial value problem with fixed boundaries. The stability of the $m=0$ sausage mode was examined under several conditions: with the Hall term and axial sheared flow, and with Bennett equilibrium profile. We also carried out 2D MHRDR simulations of the $m = 0$

instability with the same initial input parameters as for the linear stability analysis.

This allowed us to compare MHRDR simulation results with the linear stability analysis and to benchmark the MHRDR code and the linear initial value solver. Comparisons of the results have shown very good agreement between the linear theory predictions and the MHRDR simulations.

Our principal results are that axial sheared flow decreases the growth rate of the sausage instability in all cases where it is present. The Hall term on the other hand has a

destabilizing effect for the Bennett equilibrium on the $m=0$ mode when included This is in agreement with results obtained by [6] and with the MHRDR code by [7].

AKNOWLEDGMENTS

The authors wish to acknowledge valuable discussions with L. Rudakov.

The work at the University of Nevada, Reno was supported by the U.S. Department of Energy and Sandia National Laboratories.

The work at the University of California at Los Angeles was supported by the U.S. Department of Energy under contract no. DE-FG03-01ER54617.

REFERENCES

- [1] F. Winterberg, *Beitr. Plasmaphys.*, vol. 25, pp. 117-122, Jan. 1985.
- [2] U. Shumlak, C.W. Hartman, "Sheared flow stabilization of the $m = 1$ kink mode in Z pinches", *Phys. Rev. Letters*, vol. 75, pp 3285-3288, Nov. 1995.
- [3] T. D. Arber and D.F. Howell, "The effect of sheared axial flow on the linear stability of the Z-pinch", *Phys. Plasmas*, vol.3, pp 554-560, Feb. 1996.
- [4] S. Appl and M. Camenzind, "The stability of the current-carrying jets", *Astronomy and Astrophysics*, vol. 354, pp 256-269. Feb. 1992.
- [5] M. G. Haynes and M. Coppins, "Universal diagram for regimes of Z-pinch stability" *Phys. Rev. Lett.*, vol. 66, pp. 1462-1464, Jul. 1991.
- [6] M. Coppins, D.J. Bond, and M.G. Haines, "A study of the stability of the Z pinch

- under fusion conditions using the Hall fluid model” , *Phys. Fluids*, vol 27, pp 2886-2289, Dec. 1984.
- [7] P. Sheehey, I. Lindemuth, “Hall and two-temperature magnetohydrodynamic simulation of deuterium-fiber-initiated Z pinches, *Phys. Plasmas*, vol. 4, pp. 146-158, Jan. 1997.
- [8] V.I Sotnikov, I. Paraschiv, V. Makhin, B.s. Bauer, J-N. Leboeuf, J.M. Dawson, “Linear analysis of stabilization of global MHD instabilities, based on the Hall fluid model”, Submitted to the *Phys. Plasmas*, Jul. 2001.
- [9] A. Sykes and J.A. Wesson, *Nucl. Fusion*, vol. 14, pp. 645-654, Apr.1974.
- [10] G. Bateman, W. Schneider, and W. Grossman, *Nucl. Fusion*, vol. 14, pp. 669-676 Apr. 1974.
- [11] G. Bateman, *MHD Instabilities*. Cambridge: MIT Press, 1978, pp. 86-92.

Figure Captions

FIG. 1. Density profile for the Bennett equilibrium with the radius of maximum B equal to $a = r_0 / 3$.

FIG. 2. Magnetic field profile for the Bennett equilibrium with the radius of maximum B equal to $a = r_0 / 3$

FIG. 3. Growth rate of the $m = 0$ sausage instability in the ideal MHD limit in the presence of the sheared flow and in the absence of the Hall term ($V_{0z} = 0, 1, 2, 2.5$; $\varepsilon = 0$).

FIG. 4. Growth rate of the $m = 0$ sausage instability in the presence of the sheared flow and the Hall term ($V_{0z} = 1, 2, 3$; $\varepsilon = 0.01$). V_{0z} is the maximum sheared flow velocity and the sheared flow profile was chosen of the form $V_z(r) = V_{0z} \cdot r^2$.

FIG. 5. Growth rate of the $m = 0$ sausage instability in the presence of the sheared flow and the Hall term ($V_{0z} = 1, 2, 3$; $\varepsilon = 0.1$). V_{0z} is the maximum sheared flow velocity and the sheared flow profile was chosen of the form $V_z(r) = V_{0z} \cdot r^2$.

FIG. 6. Dependence of the growth rate on ε for the Bennett equilibrium profile with and without sheared flow.

FIG. 7. The contour lines of density with growing perturbations ($k_z r_0 = 6$).

2D MHRDR simulation results of the $m=0$ sausage instability for a Bennett initial profile without sheared flow ($V_{0z} = 0$).

FIG. 8. The contour lines of azimuthal magnetic field with growing perturbations ($k_z r_0 = 6$). 2D MHRDR simulation results of the $m=0$ sausage instability for a Bennett initial profile without sheared flow ($V_{0z} = 0$).

FIG. 9 The contour lines of density with growing perturbations ($k_z r_0 = 6$).
2D MHRDR simulation results of the $m=0$ sausage instability for a Bennett initial profile with sheared flow ($V_{0z} = 2V_{Ti}$).

FIG. 10. The contour lines of azimuthal magnetic field with growing perturbations ($k_z r_0 = 6$). 2D MHRDR simulation results of the $m=0$ sausage instability of a Bennett initial profile with sheared flow ($V_{0z} = 2V_{Ti}$)

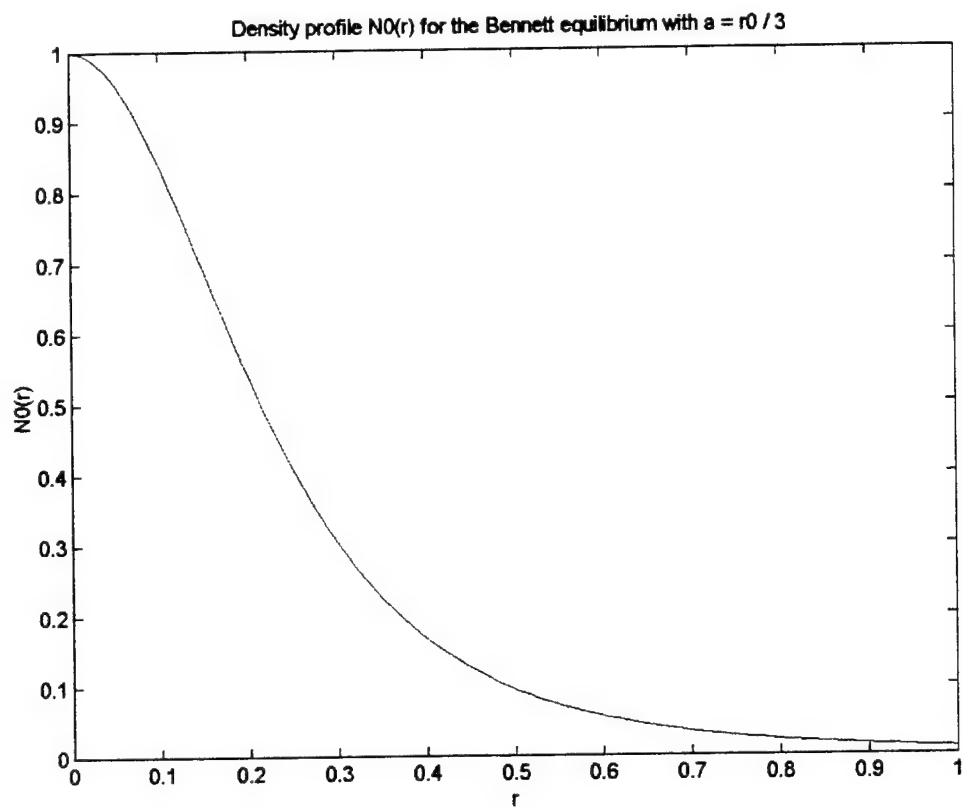


FIG. 1

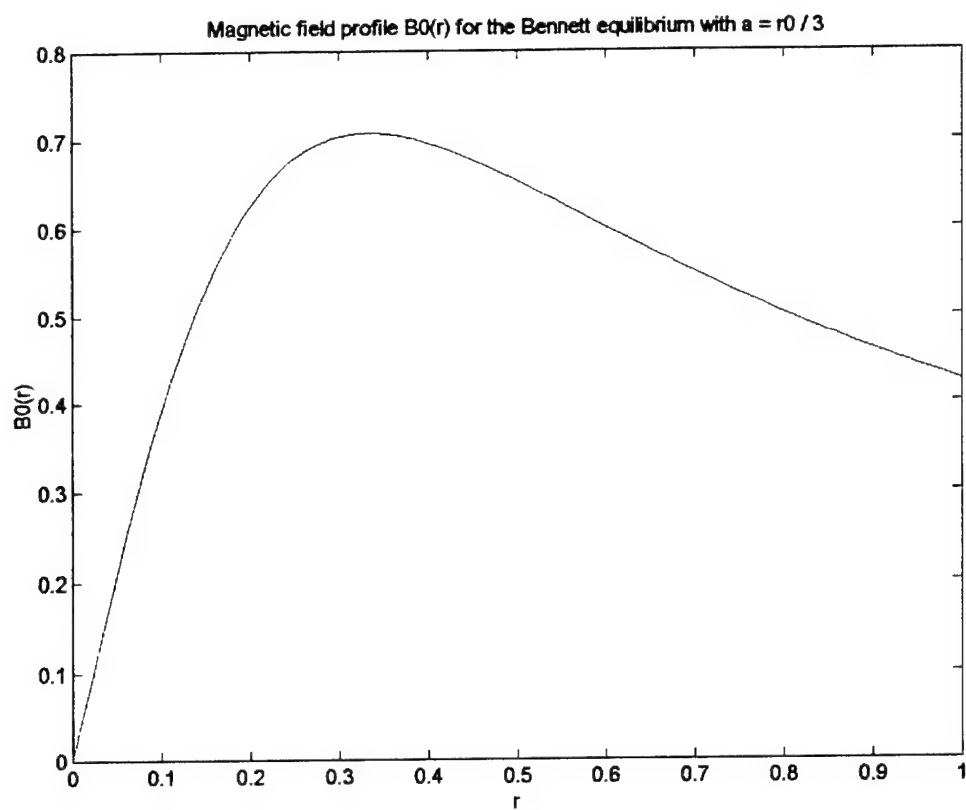


FIG. 2

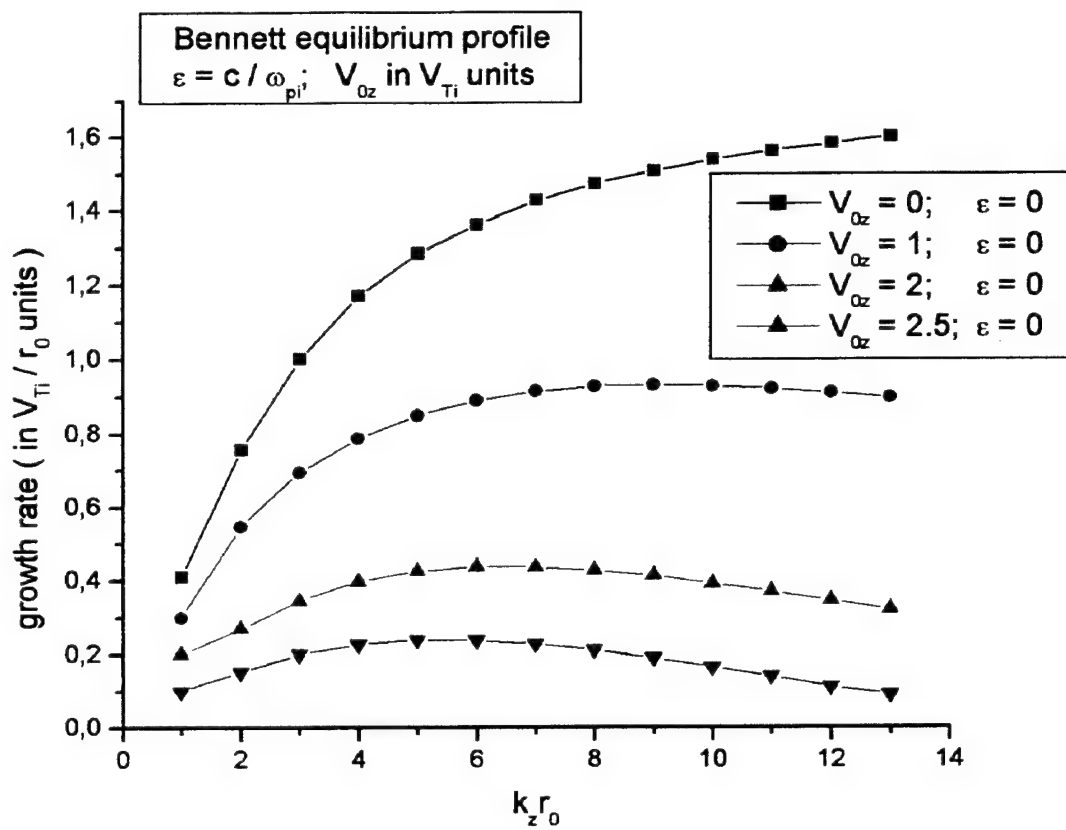


FIG. 3

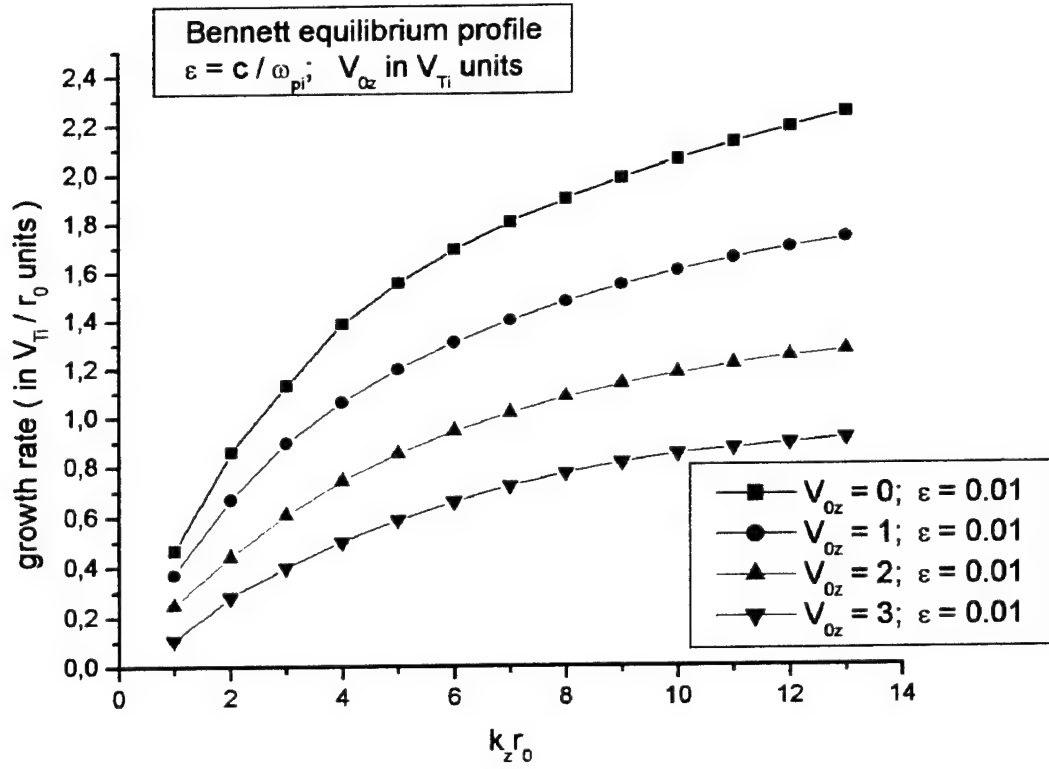


FIG. 4

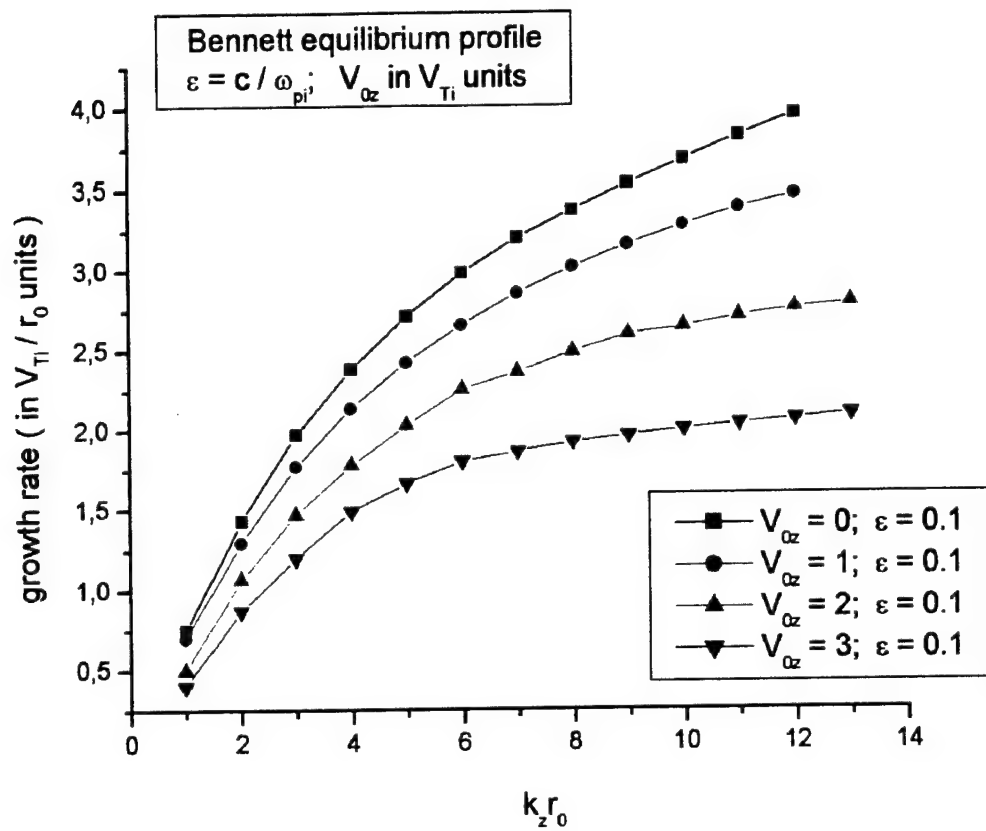


FIG. 5

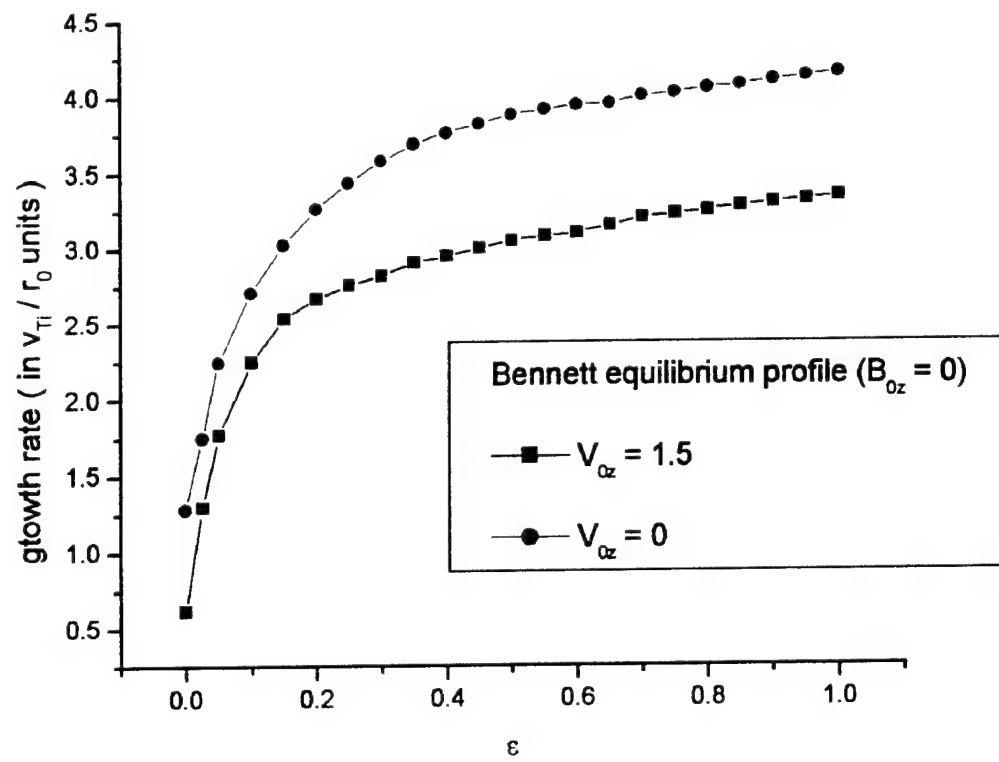
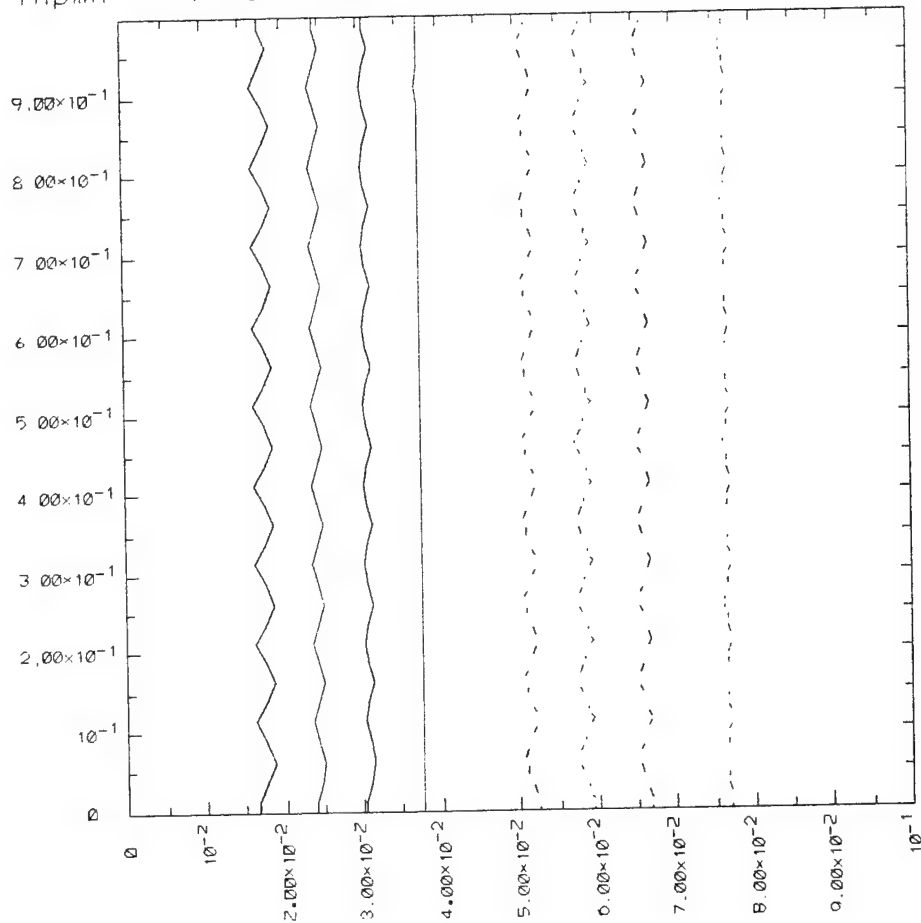


FIG. 6

inpmh 1 10/ 9/00



density inpmh min. max. mean = $2.98E-05$ $6.28E-04$ $3.20E-04$
 1 0 24 t = $5.272E-06$

FIG. 7

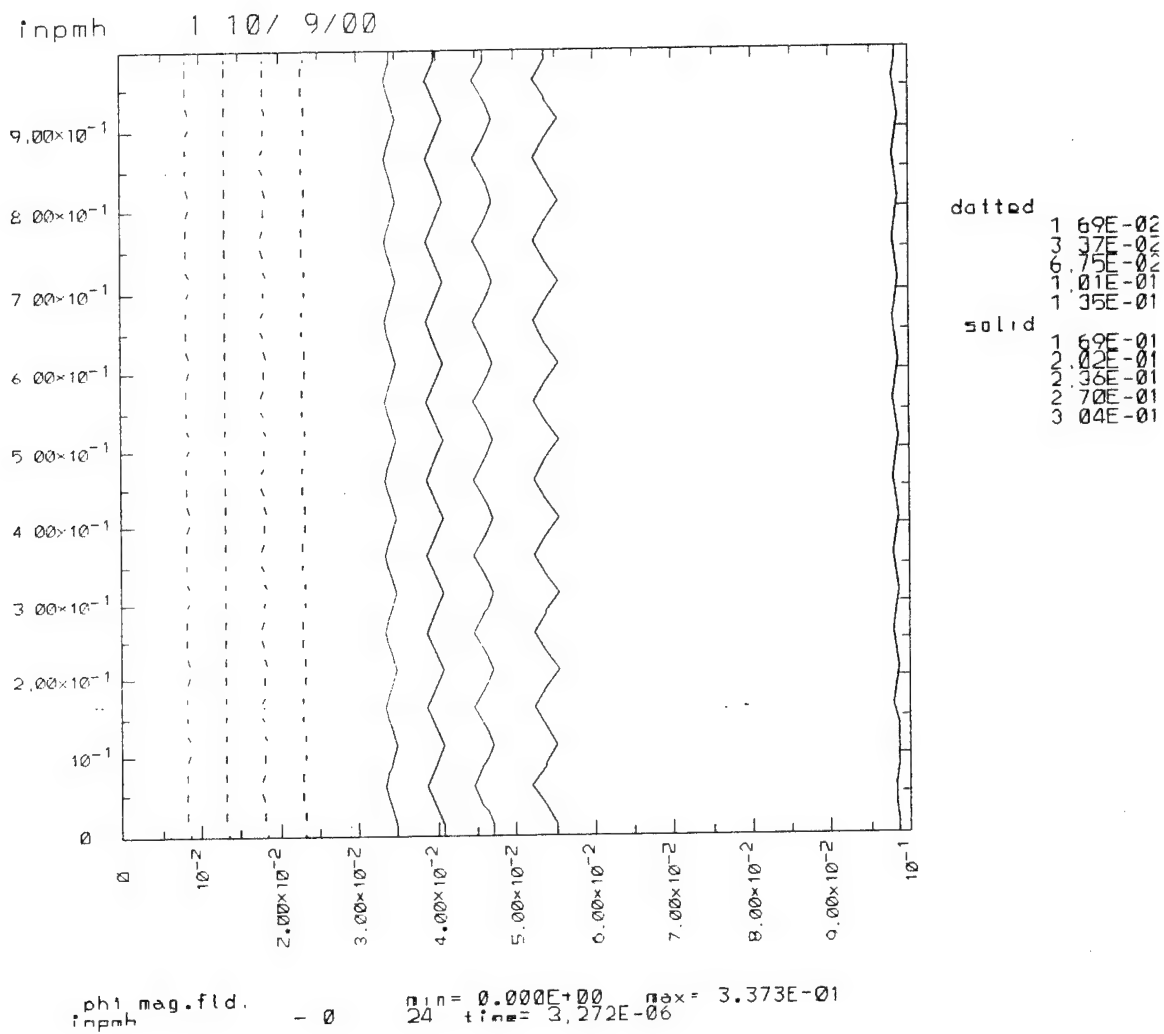
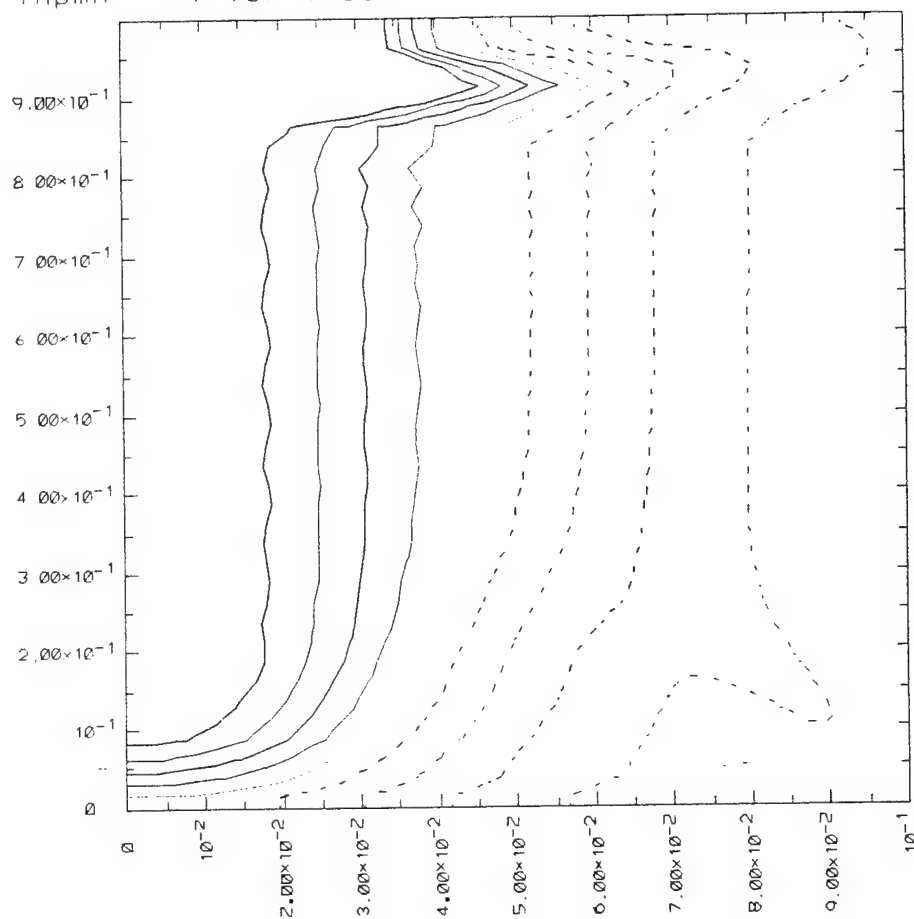


FIG. 8

inpmh 1 10/ 9/00



dotted
 1 00E-07
 7 46E-05
 1 35E-04
 1 94E-04
 2 54E-04
 solid
 3 14E-04
 3 74E-04
 4 34E-04
 4 94E-04
 5 54E-04

density
 inpmh min. max. mean = 1.47E-05 2.63E-03 3.14E-04
 0 26 time = 3.18E-06

FIG. 9

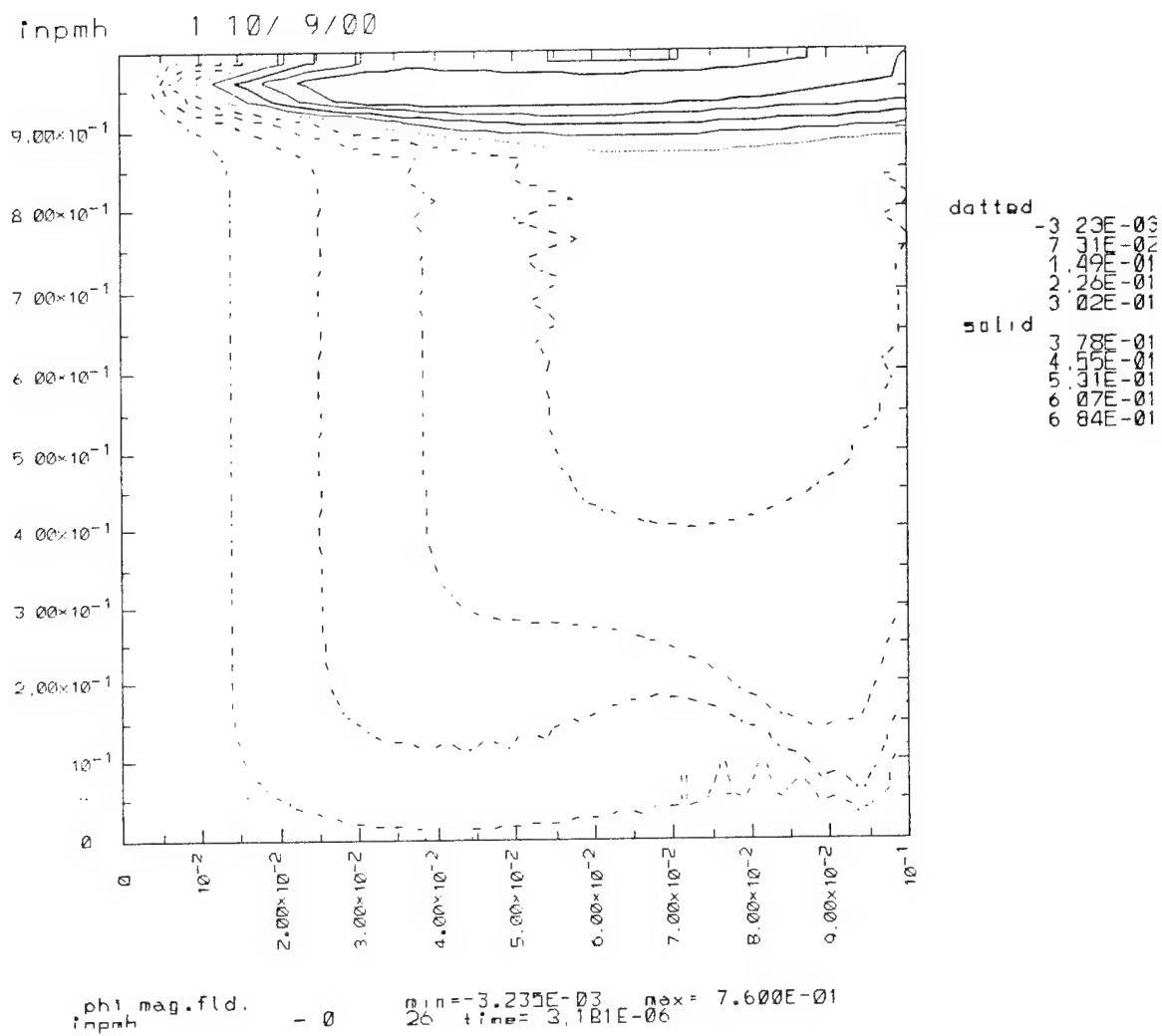


FIG. 10

APPENDIX C

Conical Wire-Array Implosions

R. Presura, B.S. Bauer, V.L. Kantsyrev, A.S. Shlyaptseva,
F. Winterberg, S. Fuelling, N. Le Galloudec, I. Paraschiv, D. Fedin,
S. Hansen, D. McCrorey, H. LeBeau, N. Quart, S. Rogowski,
S. Batie, and A. Oxner, UNR

PPPS-2001, Las Vegas, NV, June 17-22, 2001

Conical Wire-Array Implosions^{*}

- notes

N
T
F

R. Presura, B. S. Bauer, V. L. Kantsyrev,
A. S. Shlyaptseva, F. Winterberg, S. Fuelling, N. Le Galloudec,
I. Paraschiv, D. Fedin, S. Hansen, D. McCrorey,
H. LeBeau, N. Quart, S. Rogowski, S. Batie, A. Oxner,

Nevada Terawatt Facility, University of Nevada, Reno

* Work supported by DOE, SNL, and UNR



Lake Tahoe

Conical Wire-Array Implosions - notes

N
T
F

Conical array implosion experiments have been initiated at NTF, in parallel with MHD modeling, as a first approach to shear flow z-pinch stabilization research. The main objective is to determine and study the parameters range for which a shear flow created along the z-axis can stabilize a z-pinch plasma.

In our experiments, the z-pinch to be stabilized is a single exploding wire, a load known as prone to MHD instabilities. To create the axial plasma flow, we use a conical wire array surrounding the central wire, both being powered by Zebra. The $\mathbf{j} \times \mathbf{B}$ implosion of a conical load is expected to exhibit a zippering effect along its axis, similar to that observed in plasma focus or Marshall gun type experiments. The collision of plasma structures arriving at oblique directions to the z-axis produces in turn a plasma flow along the axis.

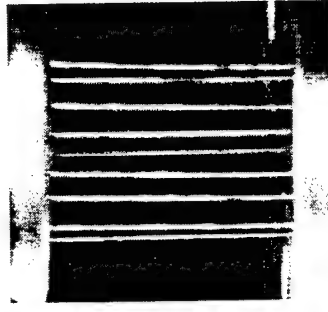
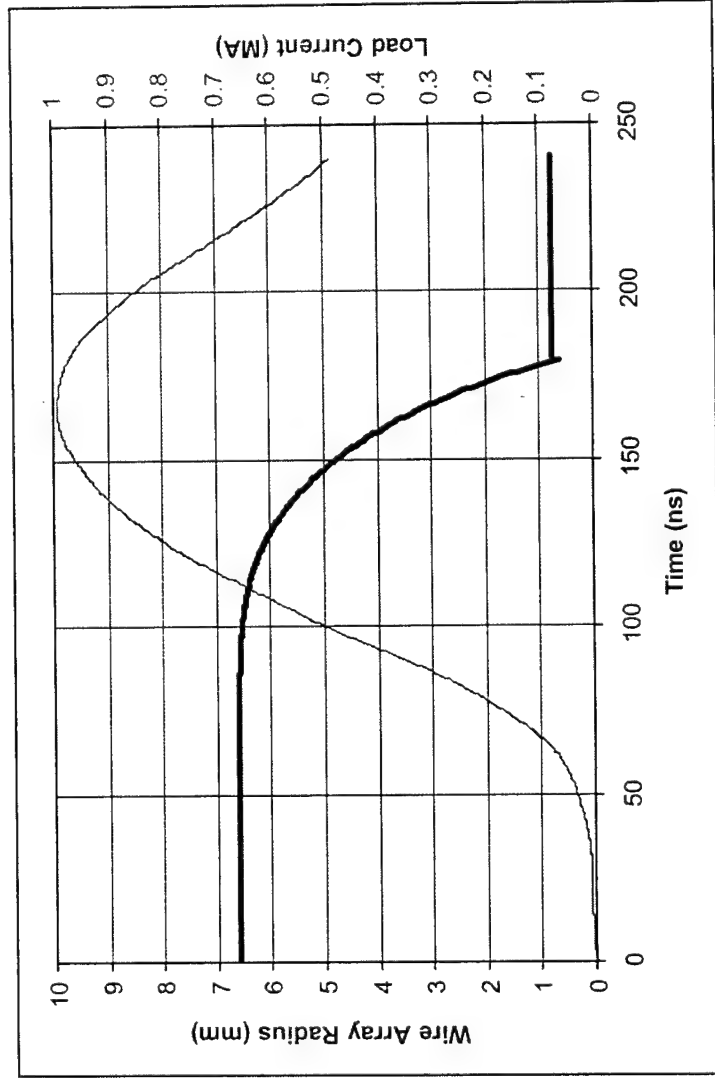
This type of behavior has been observed in previous x-pinch and v-pinch experiments on Zebra. Such planar configurations of wires making angles with and symmetrically distributed about the z-axis lead to jetting towards the axis and to the formation of a relatively dense, axially moving plasma on axis.



Lake Tahoe

The experiments are being designed on basis of simple 0D calculations

N T F



Cylindrical array:
 8 x 15.2 μm Al wires
 20 mm high
 13 mm diameter
 40 $\mu\text{g}/\text{cm}$

Central wire:
 76 μm Ti
 200 $\mu\text{g}/\text{cm}$

0D simulation of a cylindrical array implosion, performed for an actual Zebra load current waveform.



Lake Tahoe

The parameter space is being explored systematically

N T F

Load type	Central wire	Array diameters	Zebra Shots
Single wire	Ti 76 μ m		Z-SHOT#74 Z-SHOT#75
Cylindrical array with central wire	Ti 76 μ m	13 mm / 13 mm	Z-SHOT#79 Z-SHOT#80
Conical array with central wire	Ti 152 μ m	2.5 mm / 23 mm	Z-SHOT#72
Conical array with central wire	Ti 76 μ m	2.5 mm / 23 mm	Z-SHOT#73
Conical array with central wire	Ti 20 μ m	2.5 mm / 23 mm	Z-SHOT#85
Conical array with central wire	Ti 20 μ m	7.5 mm / 18 mm	Z-SHOT#87
Conical array with no central wire		2.5 mm / 23 mm 7.5 mm / 18 mm	
Cylindrical array with no central wire		13 mm / 13 mm	



Lake Tahoe

An extensive set of x-ray diagnostics is employed in these experiments

N T F

High resolution x-ray spectroscopy

- KAP crystal spectrograph (Al and Ti spectra)
- LiF crystal spectrograph (Ti K-shell)

Low resolution x-ray spectroscopy with 1D space resolution

- pinhole grating

Pinhole x-ray imaging

- two time integrated multi-pinhole cameras (580 μm and 65 μm resolution)
- gated x-ray imager (6 frames x 4 ns FWHM each 17 ns x 2 filters; 250 μm)

X-ray emission rate

- photoconductive detector (Ti K-shell radiation)
- x-ray diode (Al and Ti radiation)

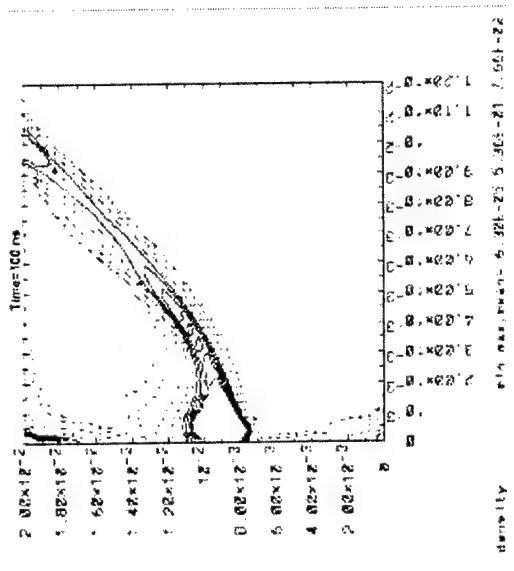
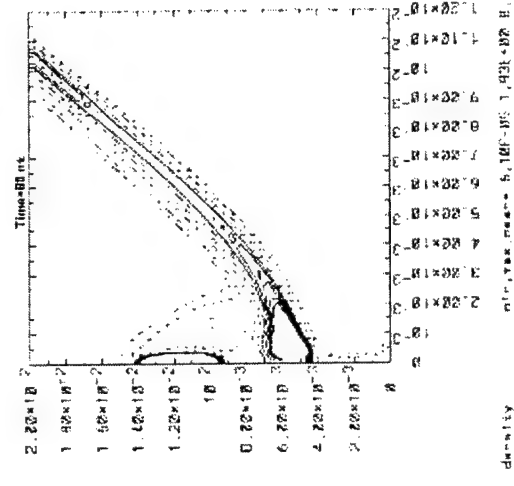
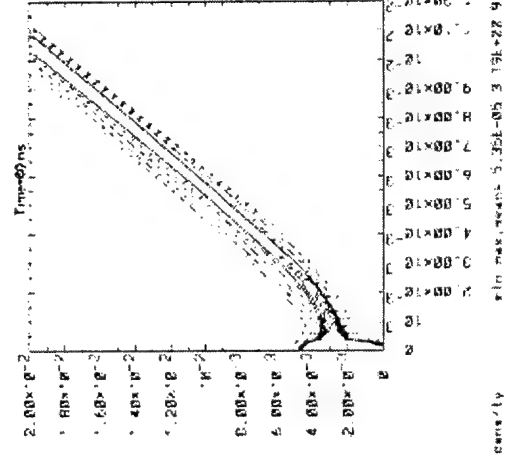
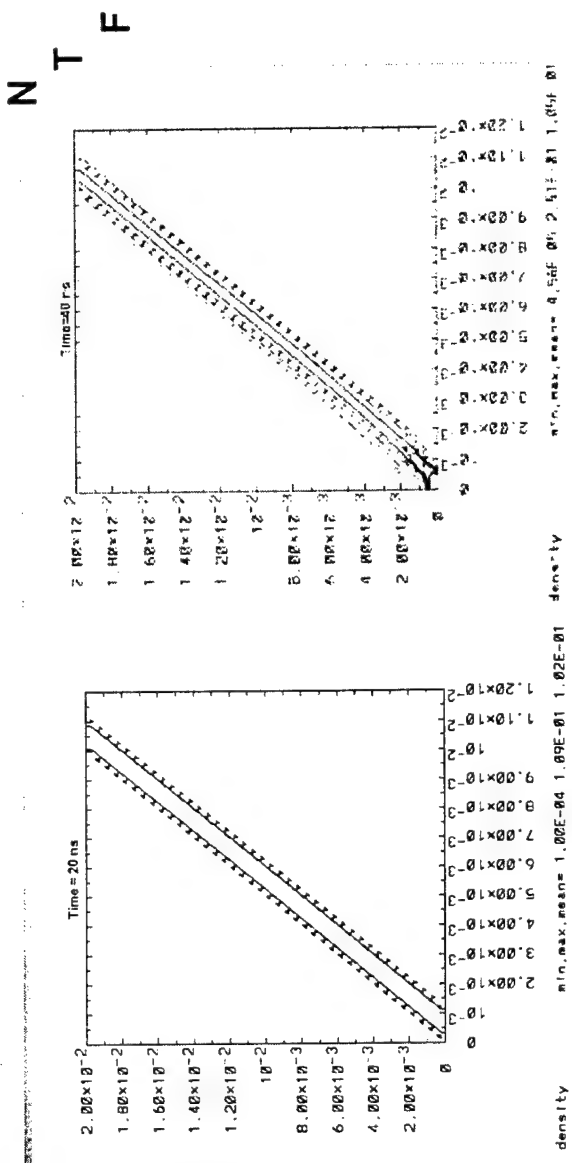
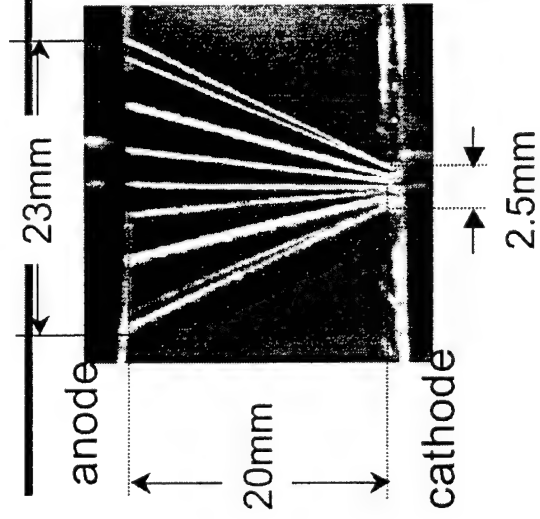
X-ray to VUV total emission energy

- fast Ni bolometer (10 eV to 10 keV)



Lake Tahoe

The density evolution is simulated with MHRDR

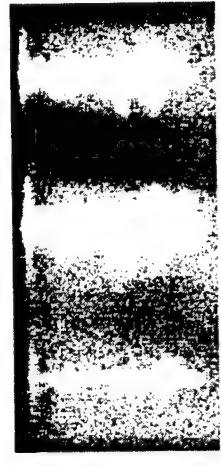


Lake Tahoe

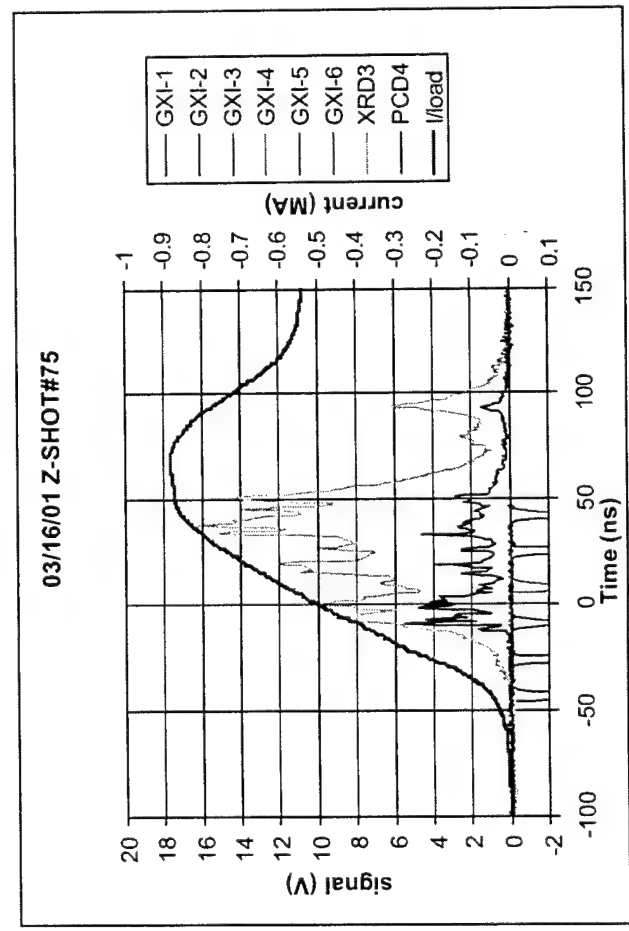
PPPS 2001 - Las Vegas, June 2001

Single wire (76 μm Ti) experiments evidenced the formation of bright-spots chains

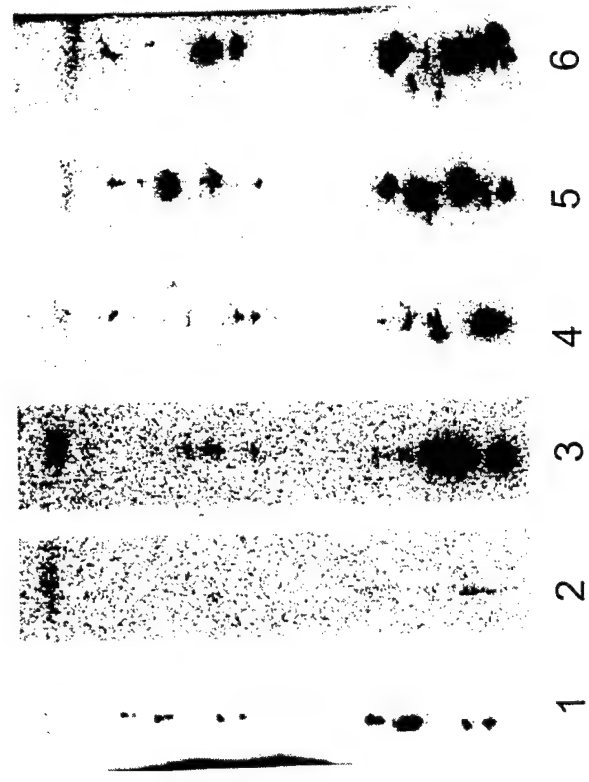
N T F



3 time-integrated x-ray images.
Anode on top.



In the gated x-ray images, the upper row of 6 frames recorded harder x-rays.



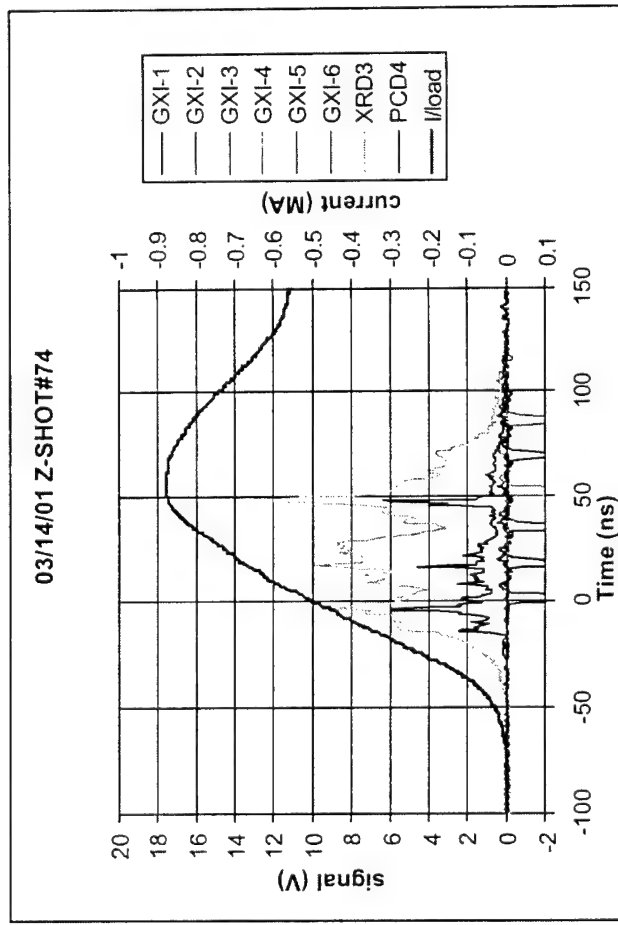
Lake Tahoe

Single wire (76 μm Ti) experiments evidenced the formation of bright-spots chains

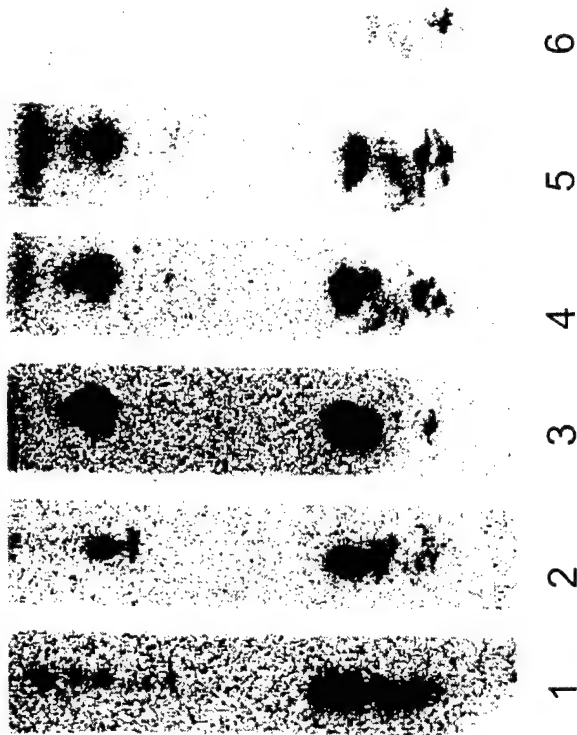
N
T
F



3 time-integrated x-ray images.
Anode on top.



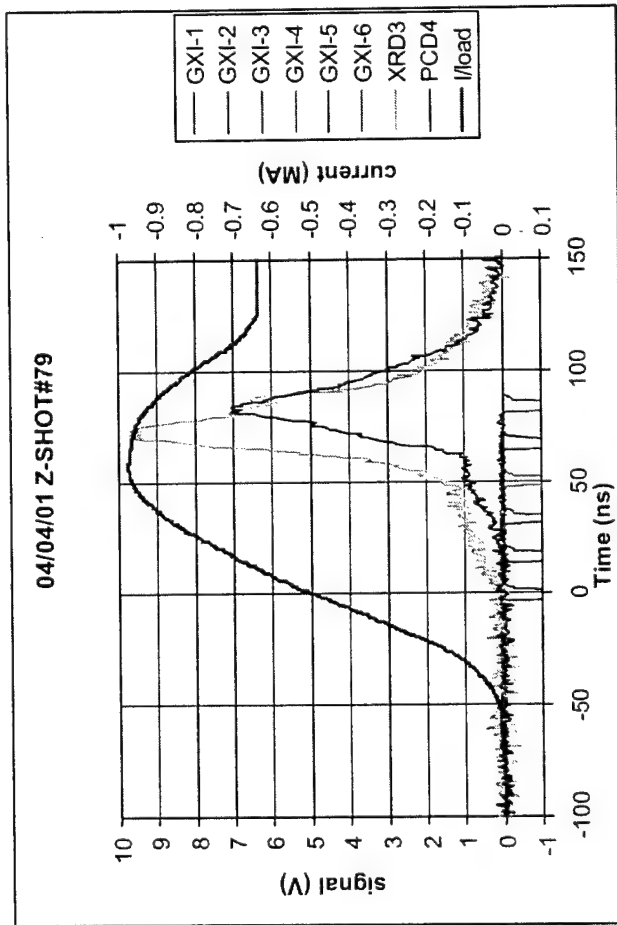
In the gated x-ray images, the upper row of 6 frames recorded harder x-rays.



Lake Tahoe

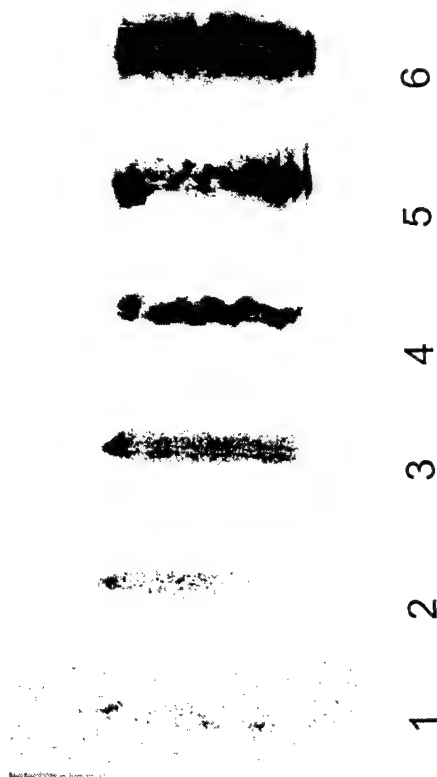
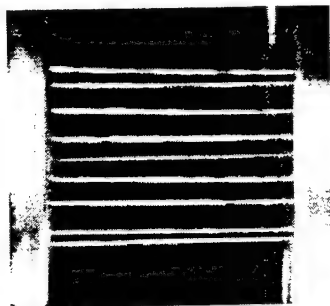
Cylindrical array implosions on central wire

N
T
F



Cylindrical array:
 8 x 15.2 μm Al wires
 20 mm high
 13 mm diameter
 40 $\mu\text{g}/\text{cm}$

Central wire:
 76 μm Ti
 200 $\mu\text{g}/\text{cm}$



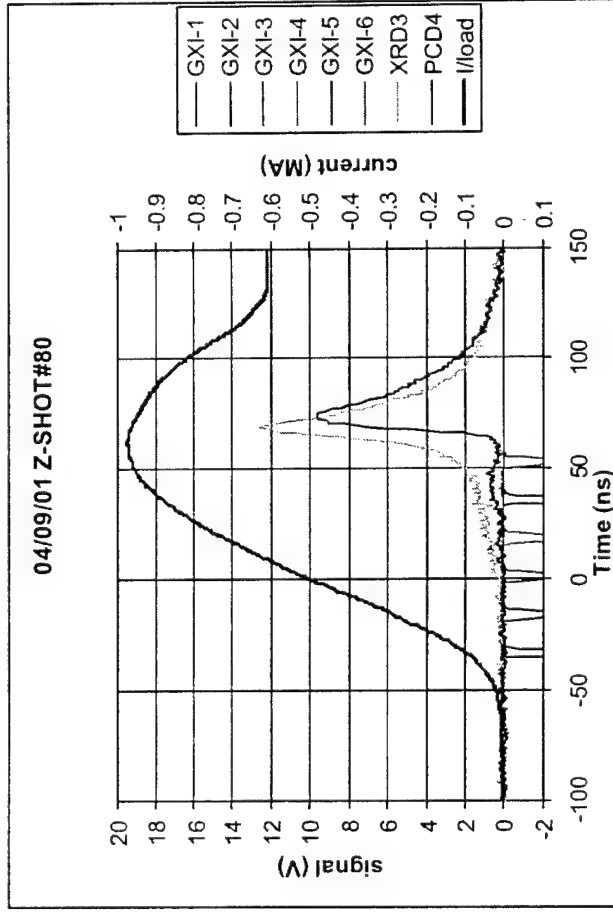
In the gated x-ray images, only the softer radiation channels are presented.
 No Ti K-shell radiation was recorded for the cylindrical array shots.



Lake Tahoe

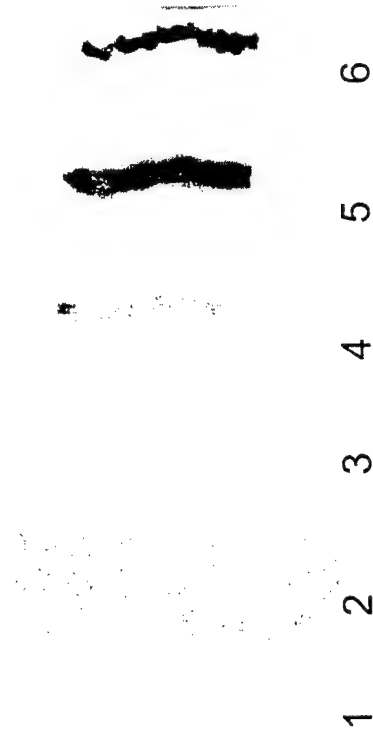
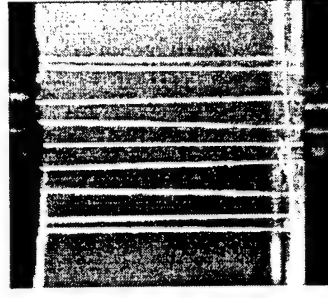
Cylindrical array implosions on central wire

N
T
F



Cylindrical array:
8 x 15.2 μm Al wires
20 mm high
13 mm diameter
40 $\mu\text{g}/\text{cm}$

Central wire:
76 μm Ti
200 $\mu\text{g}/\text{cm}$



In the gated x-ray images, only the softer radiation channels are presented.
No Ti K-shell radiation was recorded for the cylindrical array shots.



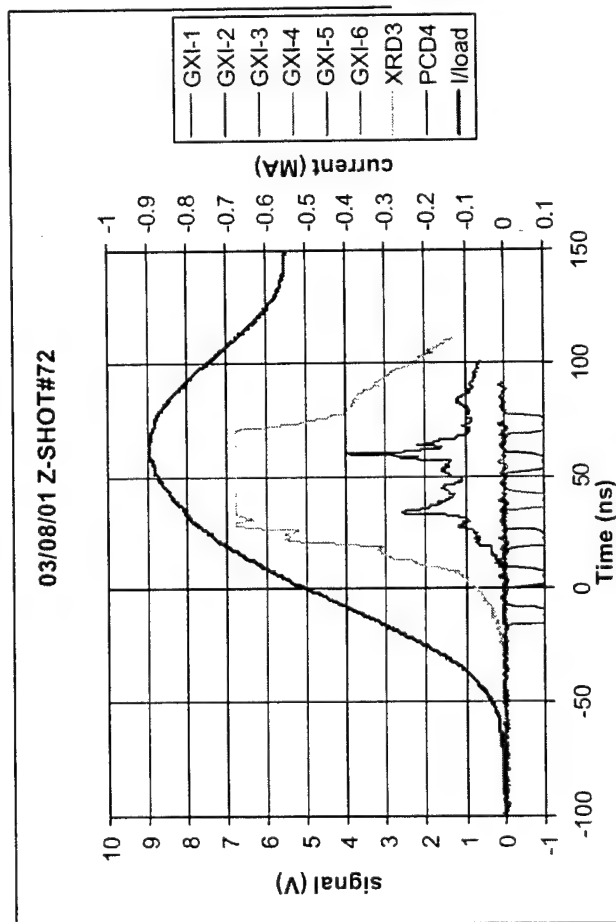
Lake Tahoe

Conical array implosions on central wire

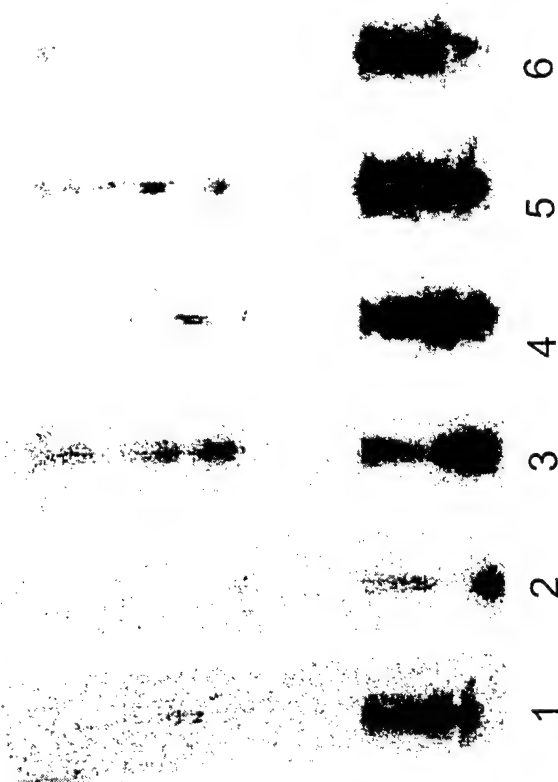
N T F

Conical array:
8 x 15.2 μm Al wires
20 mm high
2.5/23 mm diameter

Central wire:
152 μm Ti
800 $\mu\text{g/cm}$



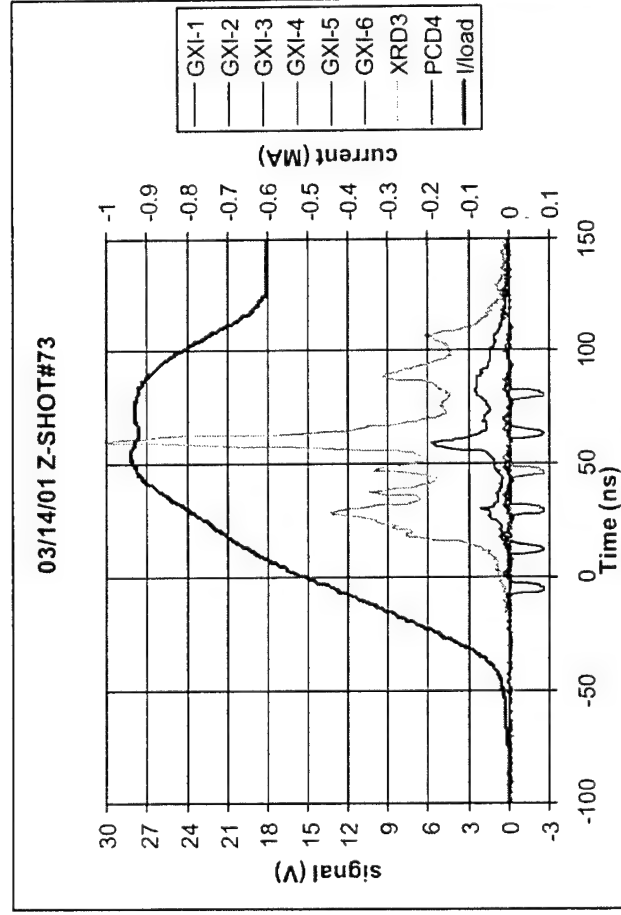
In the gated x-ray images, the upper row of 6 frames recorded harder x-rays.



Lake Tahoe

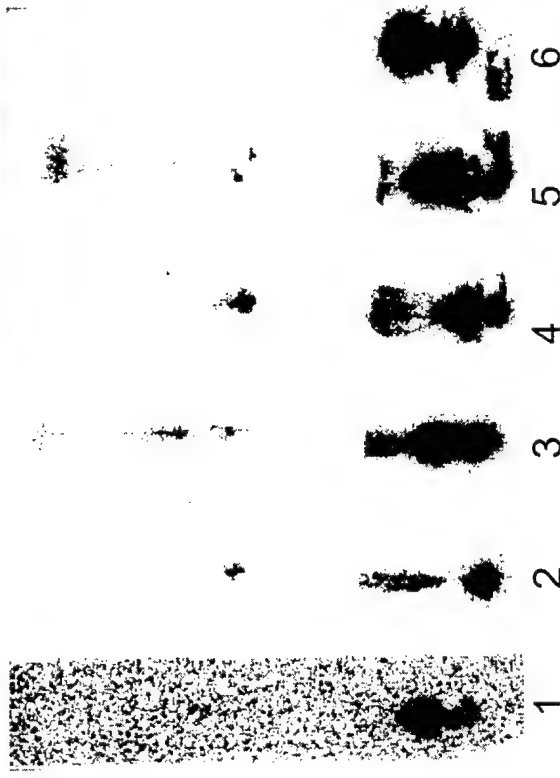
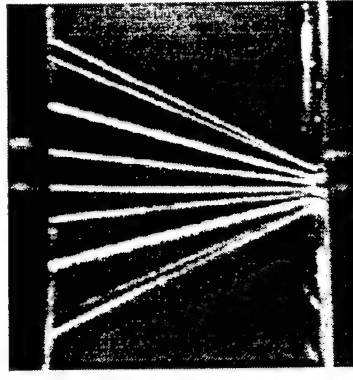
Conical array implosions on central wire

N
T
F



Conical array:
 8 x 15.2 μm Al wires
 20 mm high
 2.5/23 mm diameter

Central wire:
 76 μm Ti
 200 $\mu\text{g/cm}$

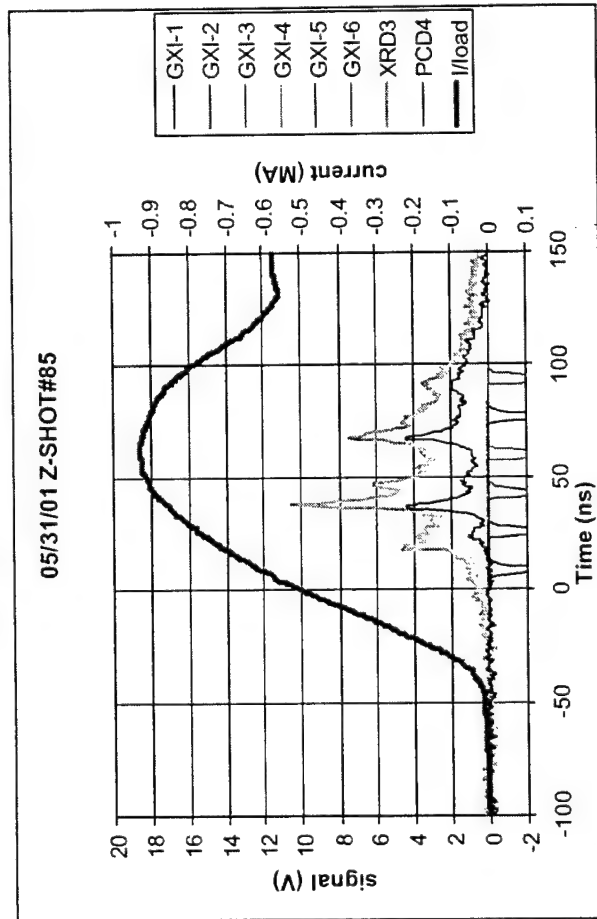


In the gated x-ray images, the upper row of 6 frames recorded harder x-rays.



Lake Tahoe

Conical array implosions on central wire



Conical array:

8 x 15.2 μm Al wires
20 mm high
2.5/23 mm diameter

Central wire:

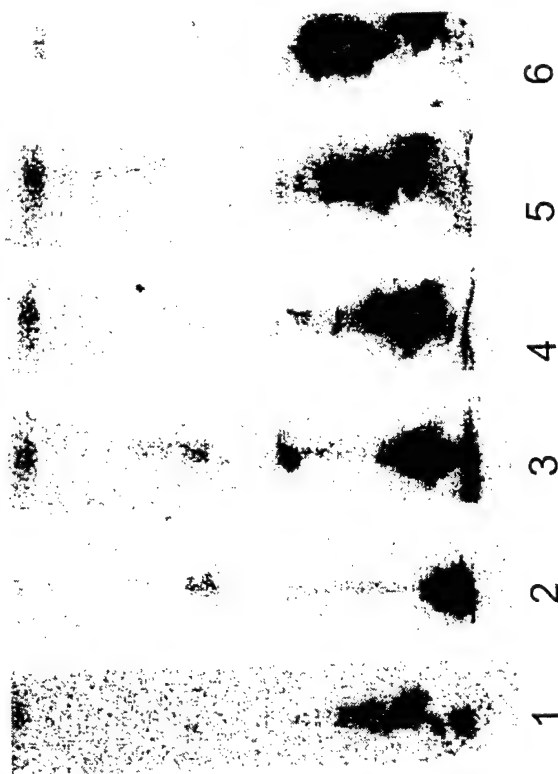
20 μm Ti
14 $\mu\text{g/cm}$

In the gated x-ray image
the upper row of 6 frame
recorded harder x-rays.

N T F



3 time-integrated x-ray images.
Anode on top.



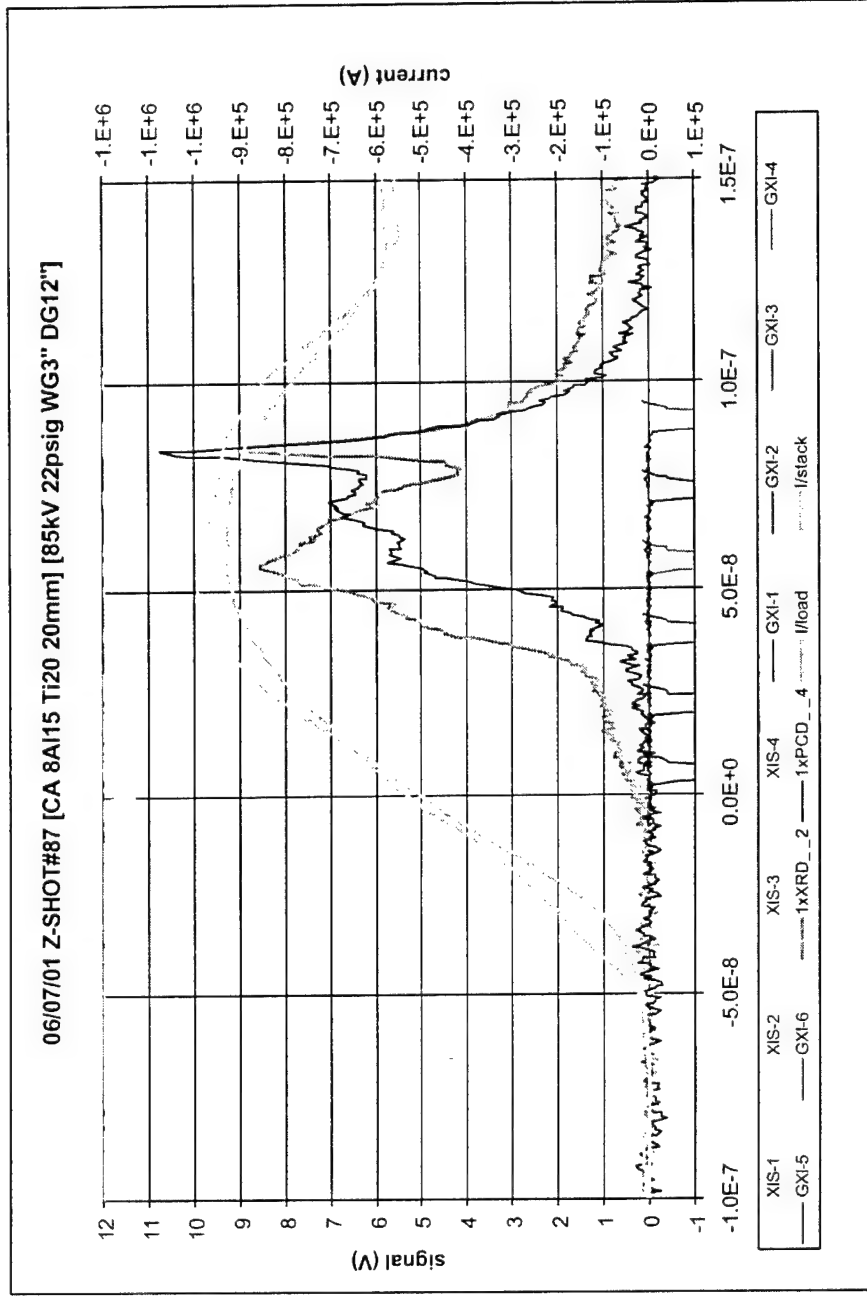
Lake Tahoe

PPPS 2001 - Las Vegas, June 2001

Conical array implosions on central wire

N
T
F

- Conical array:
 8 x 15.2 μ m Al wires
 20 mm high
 7.5/18 mm diameter
- Central wire:
 20 μ m Ti
 14 μ g/cm



Lake Tahoe

Conical array implosions on central wire

- comments

N
T
F

The time-gated x-ray pictures sensitive to lower x-ray energies show less structure than either the single wires or the cylindrical arrays. The harder x-ray images evidence only a few larger spots or an uninterrupted column (for 20 μm Ti). They also indicate the formation of relatively hot Ti plasma, as opposed to the cylindrical array case. For these shots, K-shell Ti spectra have been recorded with features similar to those observed in single wire z-pinch plasmas, indicating electron temperatures higher than 1 keV (more than 1.7 keV for 20 μm). The plasma temperature determined from the Al spectra can be as high as 450 eV, higher than for the cylindrical array (less than 390 eV).

A plasma shell forms initially near the cathode. As the current increases, the collapsing shell moves along the axis in a zipper-like fashion. The GXI images actually clearly show a plasma blob that forms at the cathode surface, and then migrates along the z-axis in the anode direction. The displacement speed of this plasma structure is about $2 \cdot 10^5$ m/s. MHRDR simulations predict a similar structure and evolution, but moving more than 5 times faster.

For thicker wires, GXI frames show a core less than 175 μm wide, corresponding to the initial diameter of the central wire, 152 μm . In the next frames only this structure's edges still emit harder radiation. This tube-like emitting structure suggests that most of the Ti wire material remains cold during the discharge. This points to insufficient current flowing through the central wire. For 20 μm Ti, the structure is column-like.



Lake Tahoe

Comments on data

N
T
F

Single wire z-pinch plasma is markedly and reproducibly unstable to $m=0$ instabilities.

Cylindrical array implosions exhibited almost complete lack of Ti K-shell radiation (in both spectra and images). This result indicates that not enough current flows through the 76 μm Ti wire to transform it into a hot plasma. The plasma temperature determined from the Al spectrum was not higher than about 390 eV for the shot #79, much less than necessary to excite the K-shell emission of Ti. The time-gated x-ray images of the cylindrical array show the formation of very unstable z-pinch plasma. Both necking and kink instabilities can be observed to appear and evolve during the discharge. The question arises if and how much the kink modes (with very different pitches for the shots presented) are influenced by the initial condition of the wire arrays.

The conical array implosions on central wire display results very different from both the single wire tests and the cylindrical array with central wire ones. While the x-ray emission rate signals seem to have an intermediate structure, the x-ray images evidence different features. This appearance of the signals suggests a plasma development with increased stability when compared with the reference cases.



Lake Tahoe

Conclusions

N T F

These first experimental results raised several questions:

- How is the current divided among the wires forming the array, on one hand, and the central wire, on the other hand?
 - current measurements closer to and inside the load are being developed
- How much of a dense core remains in the central wire?
 - x-ray backlighting will be implemented

Complementary loads will be added to the study, including arrays with higher Z than the central wire.

Comparisons of the experimental results with MHRDR simulations will continue. To improve the quality of these comparisons, optical and laser imaging diagnostics are going to be implemented.



Lake Tahoe

APPENDIX D

MHRDR Modeling of Z-Pinches at the Nevada Terawatt Facility

V. Makhin, B.S. Bauer, V.I. Sotnikov, A.S. Shlyaptseva,
N. Le Galloudec, I. Paraschiv, and M. Angelova, UNR
I. Lindemuth and P. Sheehey, LANL

PPPS-2001, Las Vegas, NV, June 17-22, 2001

P4-B12, PPPS-2001, June 21, 2001

MHRDR Modeling of Z-Pinches at the Nevada Terawatt Facility*

V.Makhin, B.S.Bauer, V. I. Sotnikov, A.Shlyaptseva,

N.Le Galloudec, I.Paraschiv, and M.Angelova

University of Nevada, Reno, 89557

I.Lindemuth, P.Sheehy

Los Alamos National Laboratory, Los Alamos, NM, 87545

* work supported by DOE, UNR, ONR, SNL, and NSF

Abstract

1D modeling of the initial state of wire explosions (“cold start” with updated SESAME tables) was examined using 1D version of the Eulerian Magnetohydrodynamic Radiative Code (MHRDR). Simulations were carried out for two regimes: with (black body radiative model) and without radiative losses. Results of the simulations revealed strong dependence of the time of explosion and expansion speed of the wire on the implemented radiative model. This shows that it is necessary to accurately include radiative losses to model “cold start” wire explosions.

2D modeling of the $m=0$ sausage instability with sheared axial flow. The MHRDR simulations were used to obtain the growth rate of the $m=0$ sausage instability in plasma column with initial Bennett equilibrium profile with and without shear flow. These growth rates appeared to be in good agreement with growth rates calculated from the linearized MHD equations (see poster P4-B11). Stabilization of internal sausage modes by conical shell implosions. 2D MHRDR simulations were carried out to investigate the development of the $m=0$ sausage mode in the presence of the axial shear flow produced by conical shell implosions. These results show that conical shell implosions appear to be an effective practical way in obtaining high Mach number, high density axial shear flows. Internal $m=0$ modes developed in the presence of the Bennett equilibrium profile were suppressed by the implosion of the conical shell.

MHRDR 1D Simulations of the Initial Stages of Wire Explosion

Simulations were initiated for so called “cold” start conditions for (solid aluminum wire with mass density $\rho=2.7 \cdot 10^3 \text{ kg/m}^3$, and “room” temperature $T=0.026 \text{ eV}$).

Diameter of wire was $15 \text{ }\mu\text{m}$. Surrounded low density “background plasma” in MHRDR simulations was chosen with parameters $\rho=1.0 \cdot 10^{-4} \text{ kg/m}^3$, $T=0.026 \text{ eV}$. The grid in simulations was chosen with the ratio of neighbor cells 1.115 and total length in r direction $4.5 \cdot 10^{-4} \text{ m}$ ($450 \text{ }\mu\text{m}$). The “cutoff” density was $1.0 \cdot 10^{-2} \text{ kg/m}^3$. In MHRDR, thermal conduction, ohmic heating (but not resistive diffusion), and shock heating are turned “off” when density drops below “cutoff” density. On Fig. 1-6 are presented MHRDR simulation results (Fig. 1,3,5) for mass density, current density, electron temperature and total pressure versus radius at 10, 25, and 40 ns. We also used new modified for low (“room”) temperatures region version of SESAME electrical conductivity tables (Desjarlais, Rosenthal, SNL). The importance of these modifications in conductivity SESAME tables was shown by Atchison et. al (LANL) calculations (2D02, ICOPS 2000).

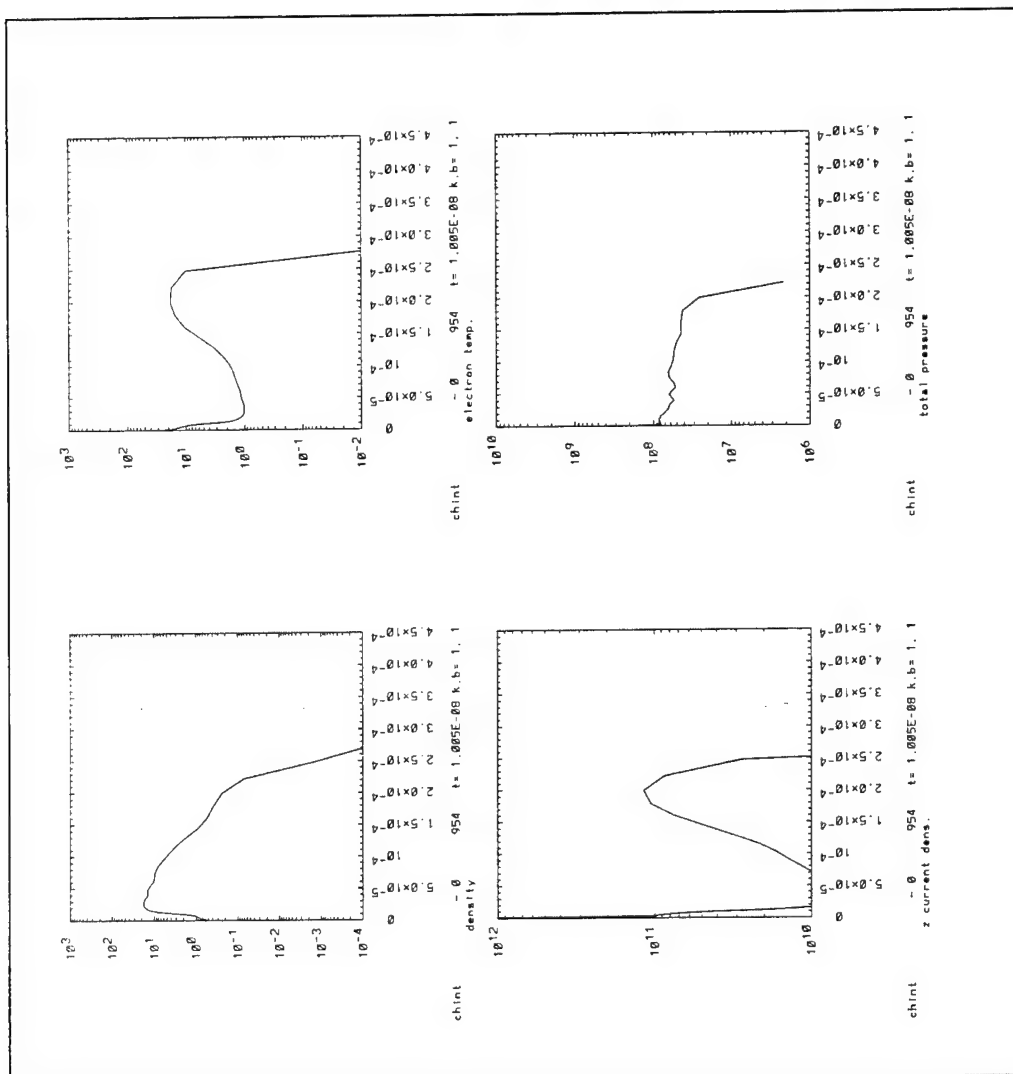
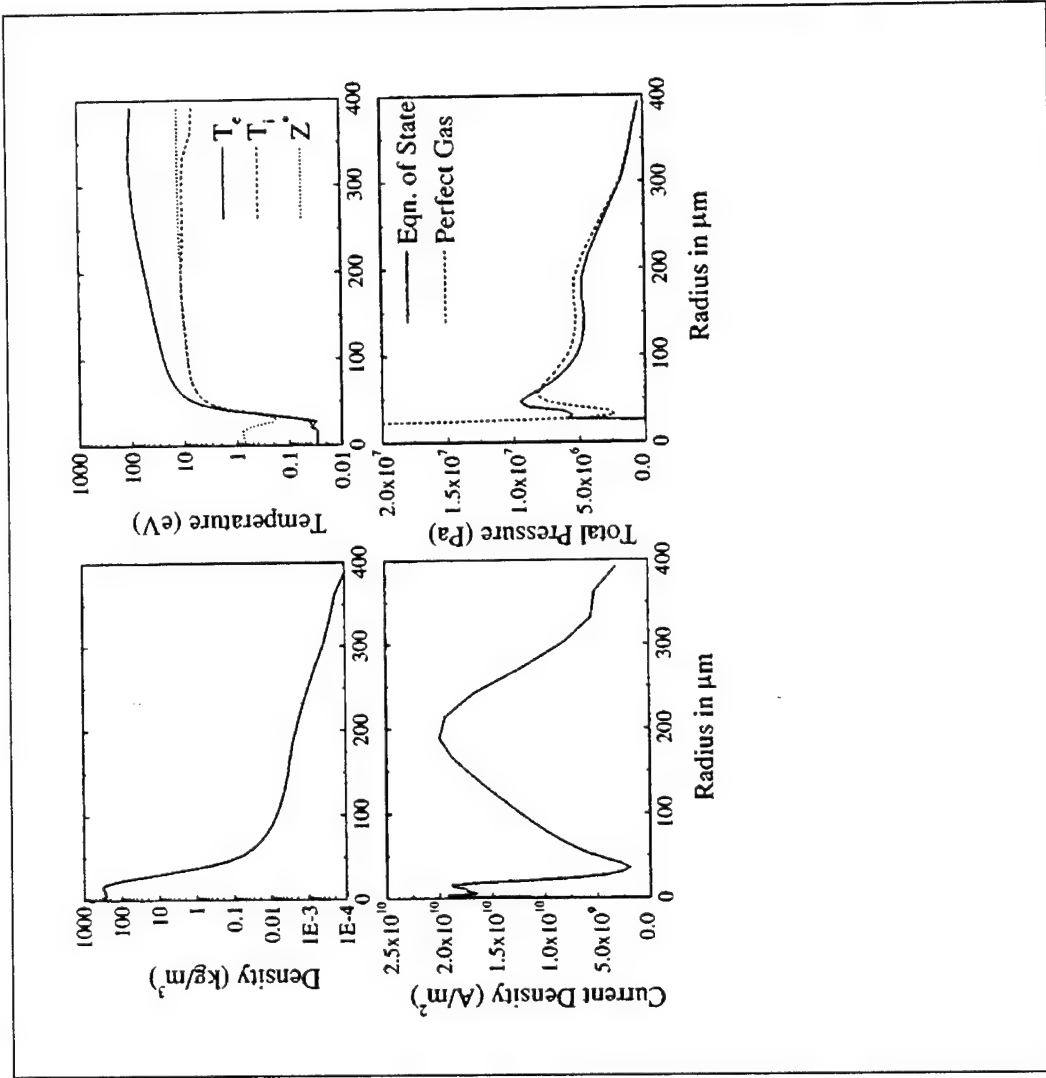


Fig. 1

Fig. 2



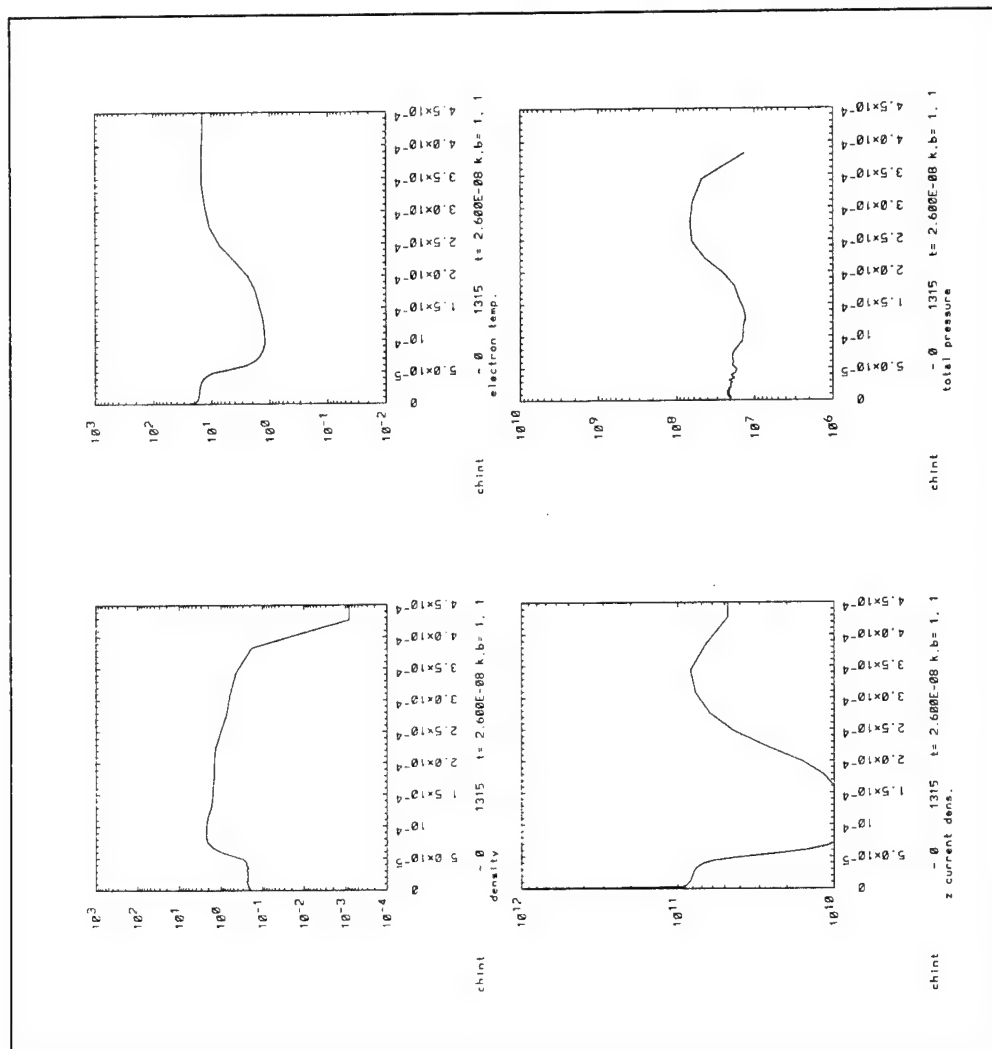


Fig. 3

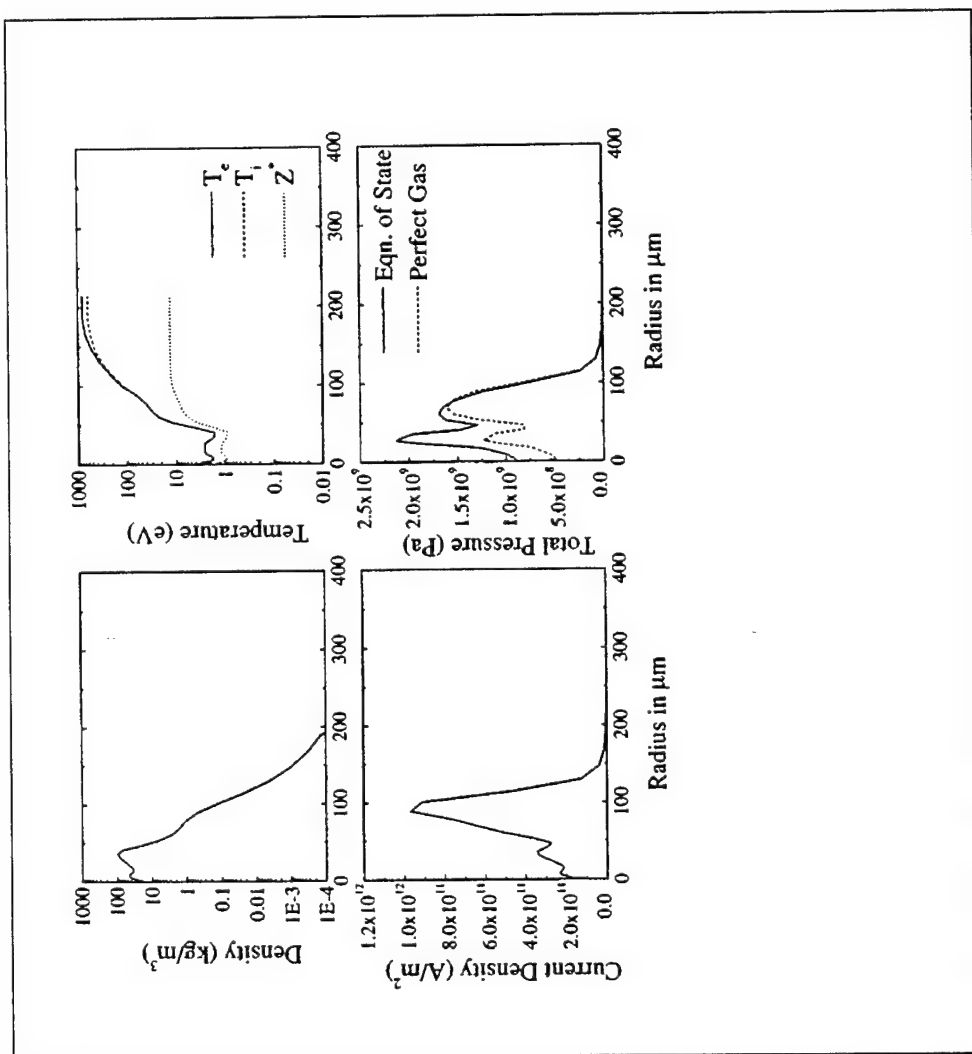


Fig. 4

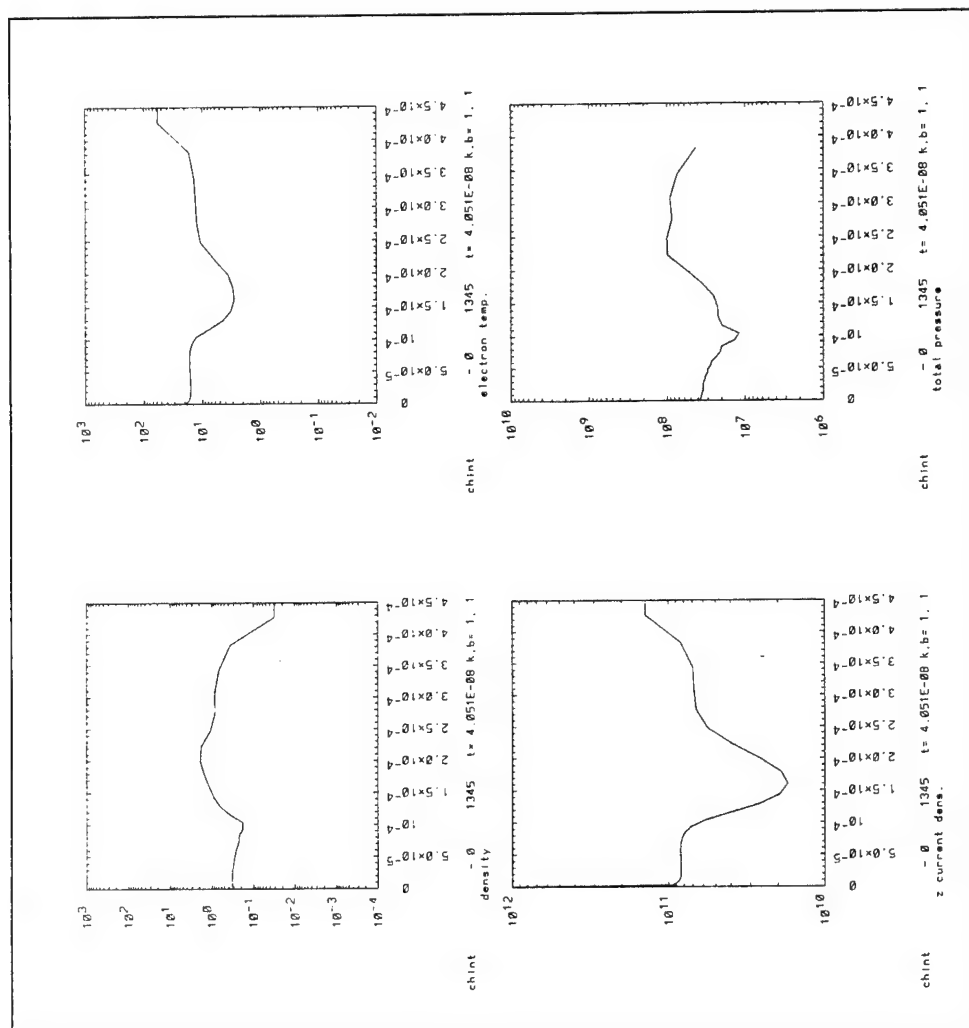


Fig. 5

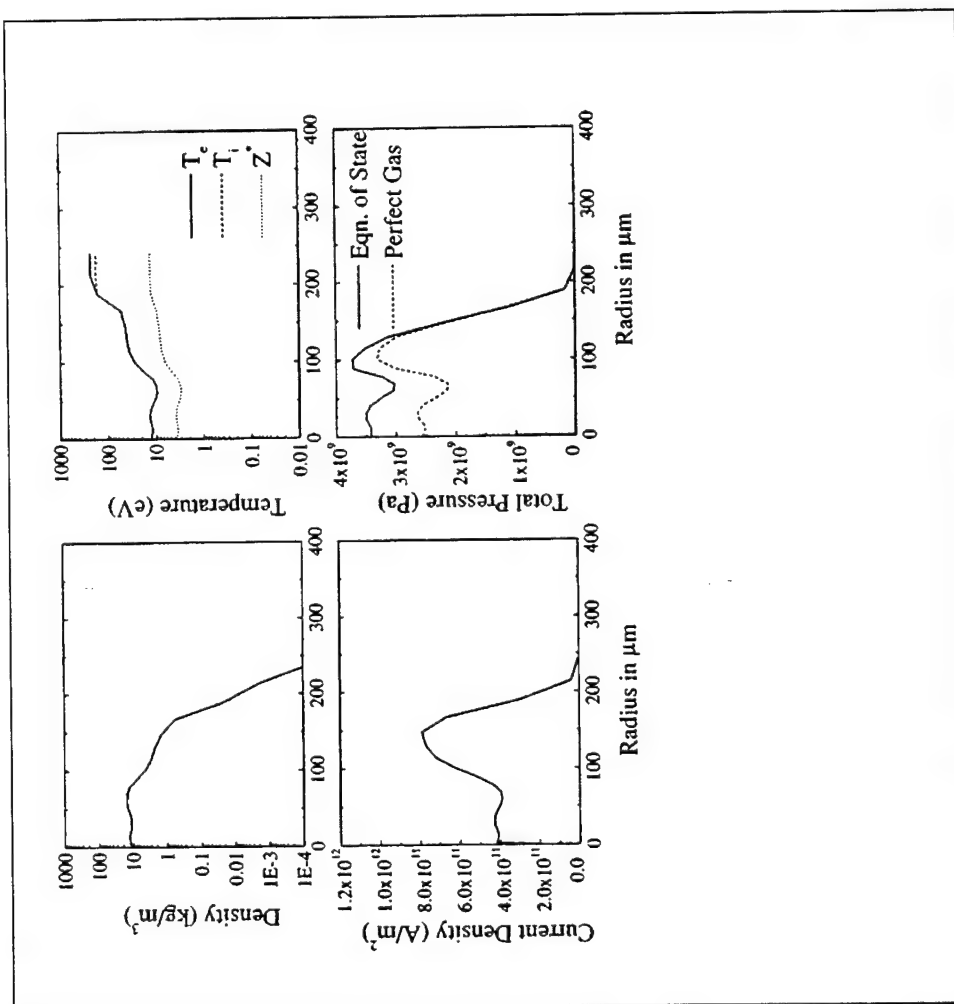


Fig. 6

Influence of coronal plasma on Z-pinch wire electric explosions

Recently held experiments indicate (SNL) strong dependence of regime of development of the explosion from the characteristics of the coated wire oil, which can lead to a delay in appearance of the coronal plasma around the naked wire.

It is important to investigate the rate of the energy deposition into the wire with and without the coronal plasma.

We used surrounding density corona plasma not less than 1% of the total wire mass. This is connected with the fact that MHRDR is a hydrodynamic code. This prevents applicability of MHRDR for lower plasma densities when kinetic effects should be taken into account.

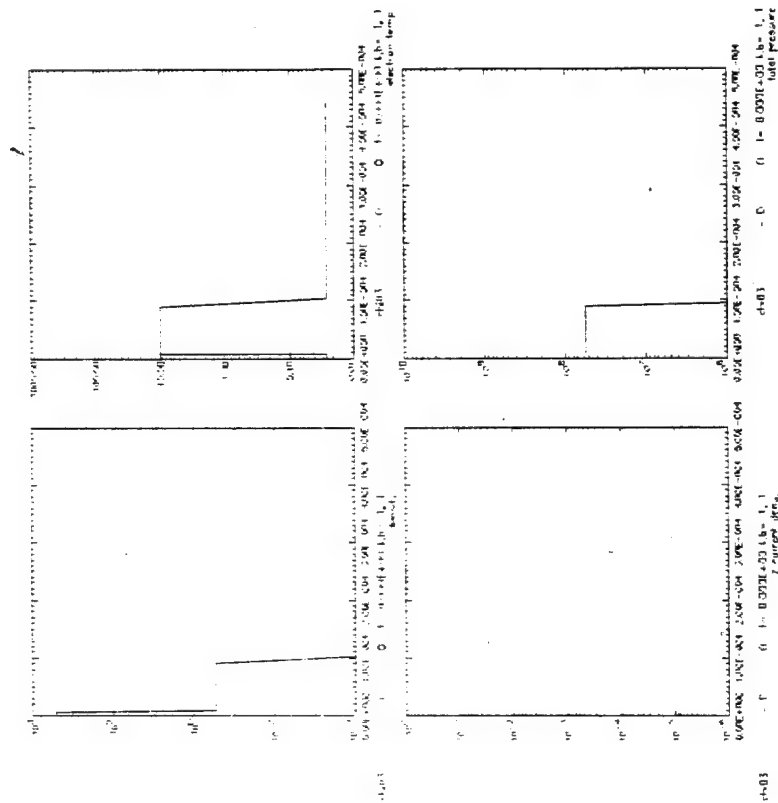
Taking into account that MHRDR is only one-material code below we present the simulation results with initial setup corresponding to thin aluminum wire with and without coronal aluminum plasma.

In this paragraph we present the simulation results showing the influence of the surrounding coronal plasma on Z-pinch wire explosions.

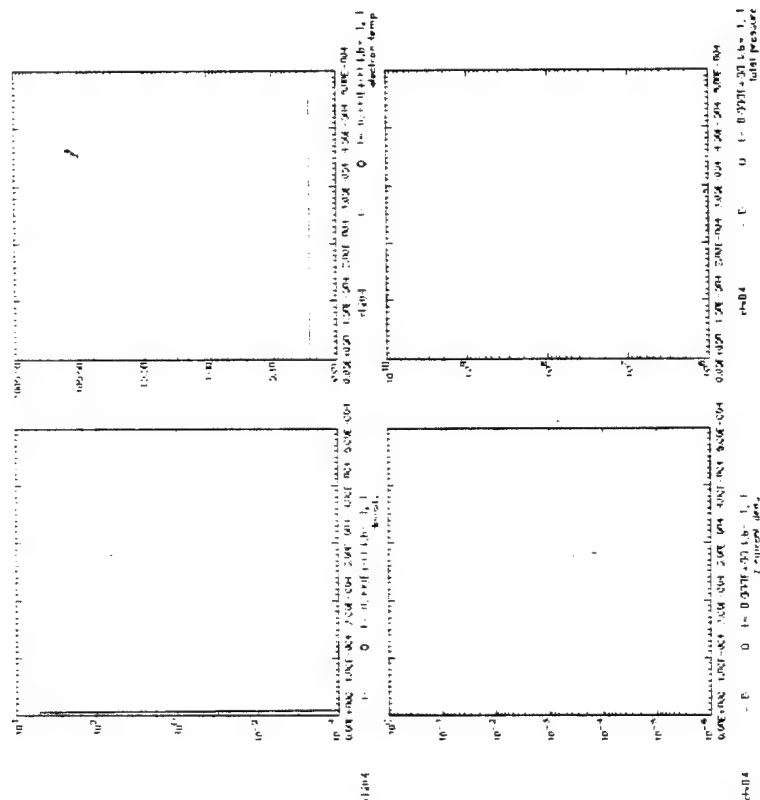
We are using 2-Temperature (T-ions and T-electrons) model (in MHRDR definition it is model=15) in 1D case. SESAME tables 303 and 304 were used for electron and ion EOS.

Below are presented simulation results of density, current density, electron temperature, and pressure versus radius in moments $t=0, 2, 4, 10$ ns for two different initial setups. In the first case $15\mu\text{m}$ aluminum wire was surrounded by hot plasma with radius= 10^{-4} m, density 0.3 kg/m^3 and temperature 10 eV. The comparison of these with the case when surrounding coronal plasma was absent shows significant delay of wire explosion in the first case. This is connected with the fact that the current rapidly switches to the coronal plasma and decrease in deposition of the energy into the wire takes place.

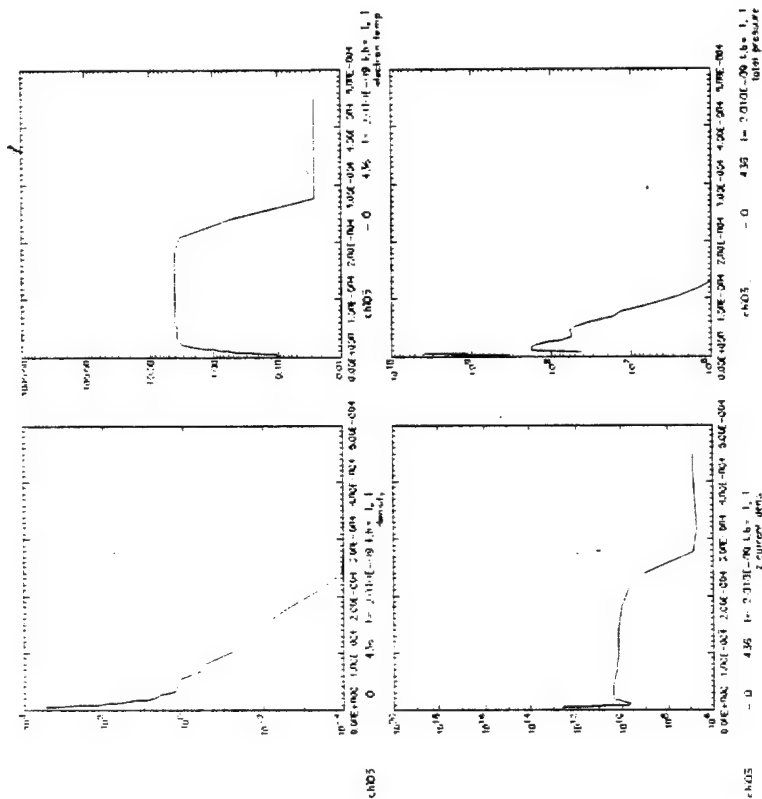
Aluminum wire with coronal plasma at $t=0$



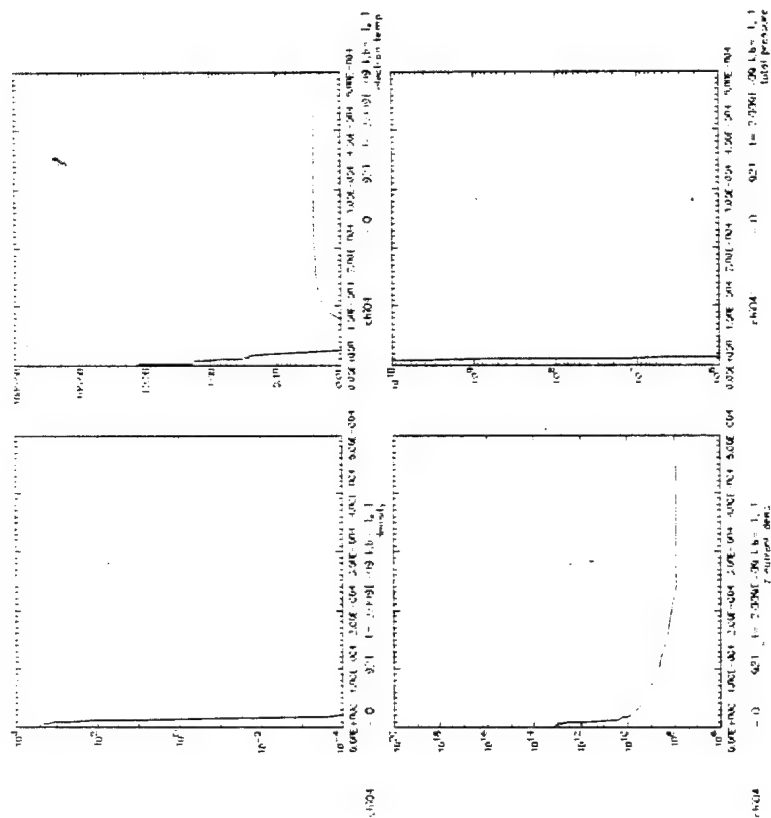
Aluminum wire without coronal plasma at t=0



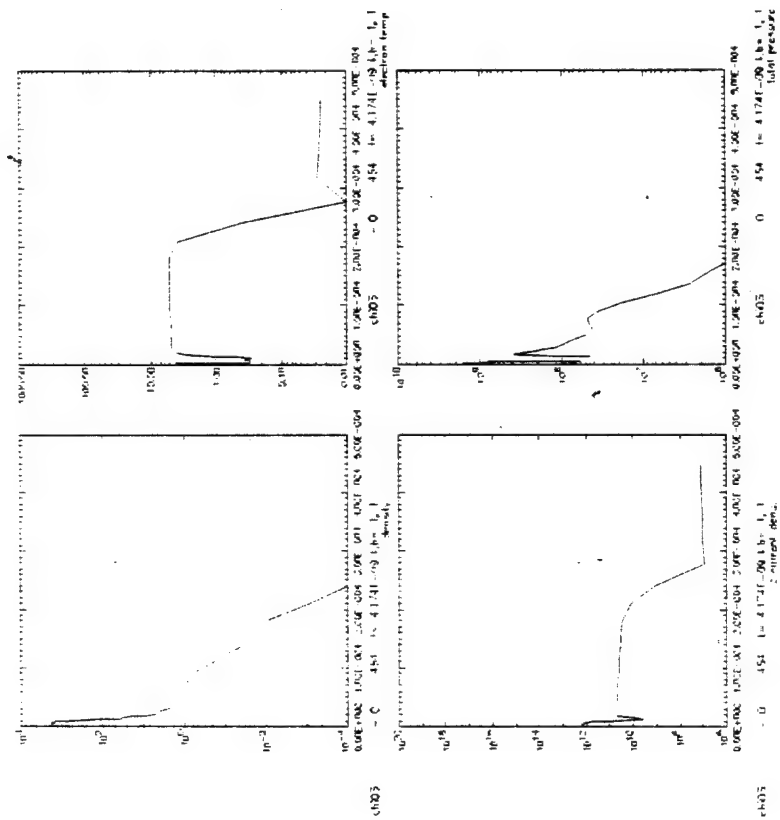
Aluminum wire with coronal plasma at $t=2\text{ns}$



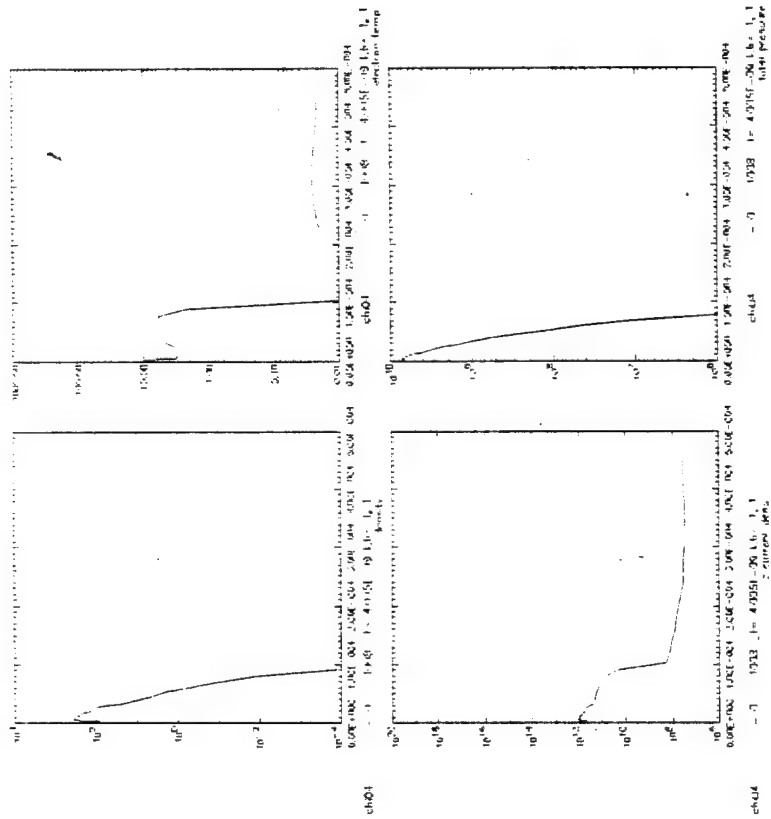
Aluminum wire without coronal plasma at $t=2\text{ns}$



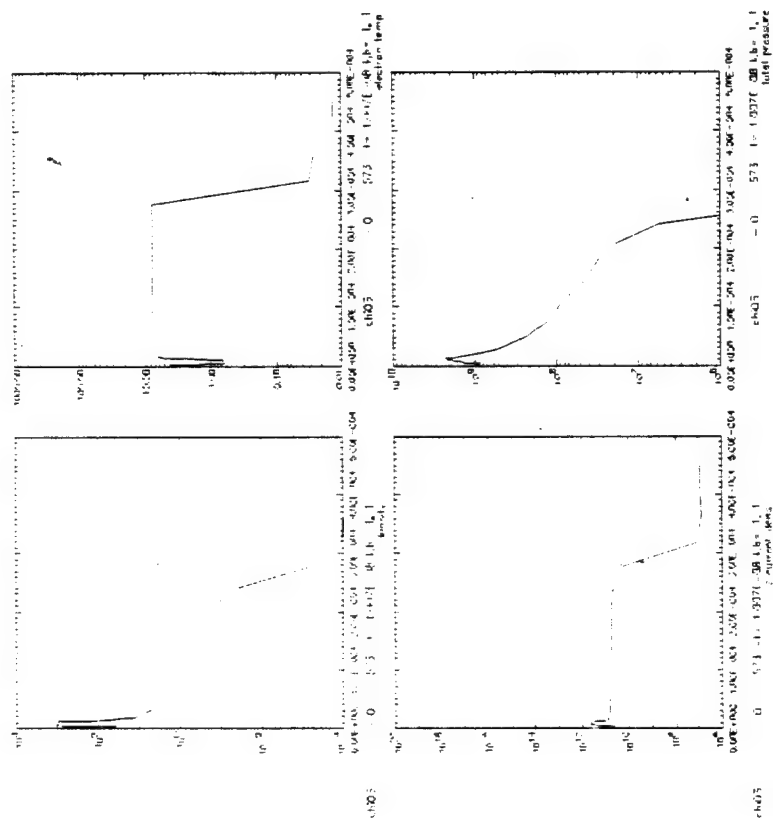
Aluminum wire with coronal plasma at $t=4\text{ns}$



Aluminum wire without coronal plasma at $t=4\text{ns}$

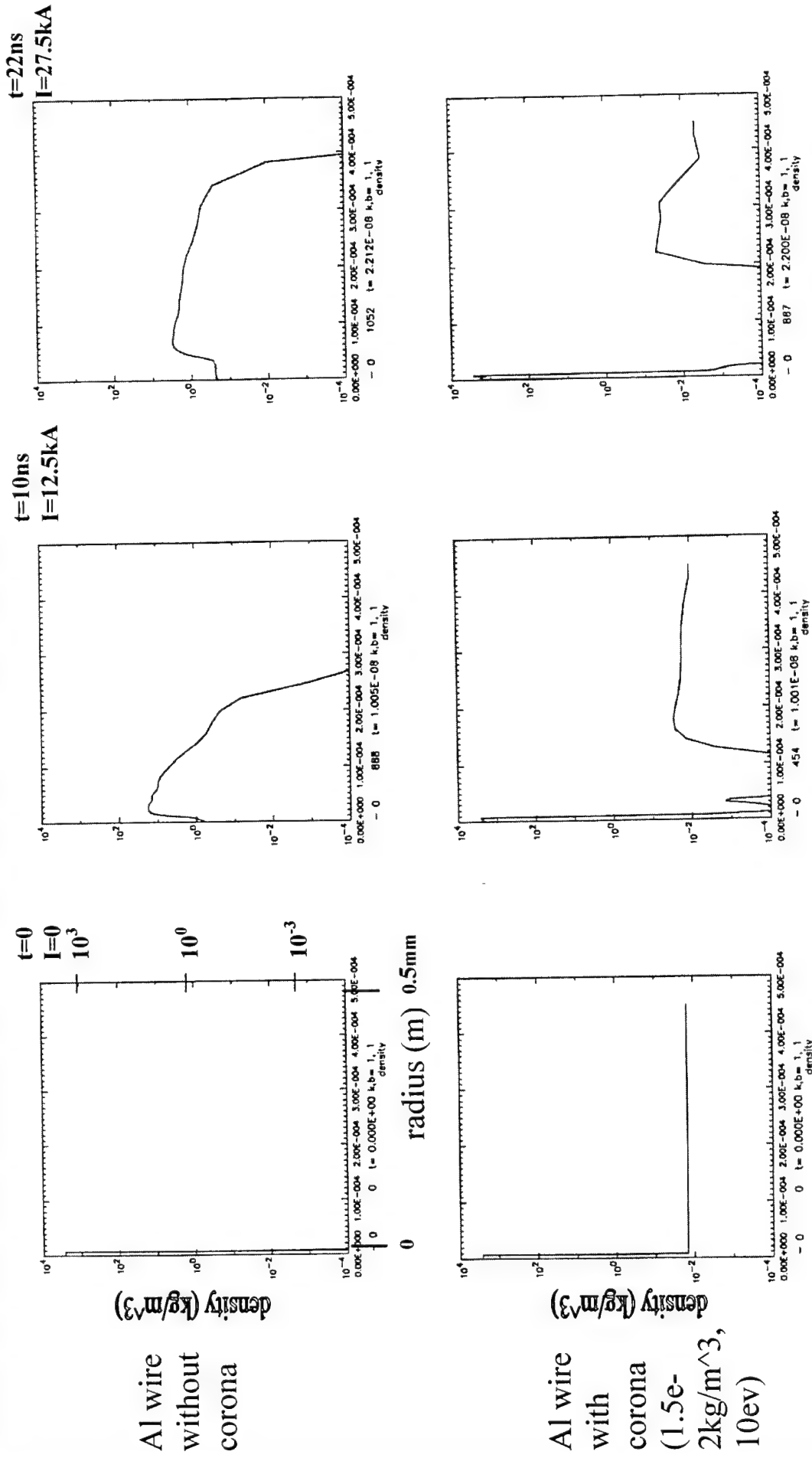


Aluminum wire with coronal plasma at $t=10\text{ns}$



Coronal plasma can greatly influence Z-pinch

MHRDR cold-start simulation of Z main pulse: 15 μm -diameter Al wire, $I(t)=(1.25\text{kA/ns})t$



Initial stage of the Tungsten wire explosion using 1D MHRDR simulation results

Initial parameters used in simulations were identical to those used in the experiments conducted by G. Sarkisov, et.al. at UNR.

To carry out simulations for Tungsten thin wire explosion the Los Alamos SESAME tables were used: 201 – atomic number, ionic charge, and normal density; 301 – equation of state, 602 – electrical conductivity (modified by Desjarlais, Rosenthal, SNL for “room” temperature region).

Simulations were performed for wire with diameter 20 μm with the dimension of the moving simulation grid equal to 100 μm at the beginning of the run. “Cold-start” initial conditions for the computations were a solid titanium wire ($\rho=19.35 \cdot 10^3 \text{ kg/m}^3$, $T=0.025 \text{ eV}$) surrounded by a low density “background plasma” with parameters ($\rho=1.0 \cdot 10^{-4} \text{ kg/m}^3$, $T=0.025 \text{ eV}$). The current in simulations corresponded to the current load table used in the experiment. This was a first attempt to simulate “cold” start thin metallic wire explosions using MHRDR code. Previous MHRDR simulation with “cold” start were carried out only for solid, cryogenic deuterium fiber (density ($\rho=88 \text{ kg/m}^3$) (Sheehy. al, Phys. Fluids B 4 (11), November 1992).

Results of MHRDR simulations are presented on Fig. 7 (initial conditions), 8 (right before expansion), 9 (just after expansion). Simulations were carried out for two regimes: without and with radiation losses.

In the first case when radiation losses are not included simulation results reproduce explosion of the Tungsten wire observed during the experiment. The main features observed during the experiment were: time of explosion at 22th ns for modified shifted in time cyclorama of the current, speed of explosion 0.99 km/s. The first feature (time of explosion) was in agreement with experiment, but speed of expansion from simulation was much higher (700 times higher). This is a strong indicator that it is very important to use right model for radiation losses in MHRDR code in order to obtain better agreement with the experiment in terms of expansion speed.

In the second case when radiation losses were included simulation results didn't reveal wire explosion what is in contradiction with observations. In this case we didn't observe increase in temperature inside the core of the wire. It means that it is important to modify the radiation model implemented in MHRDR to correctly predict behavior of the wire during the experiment.

Obviously more efforts are needed to produce reliable simulation results with MHRDR code.

It is worthwhile to mention that our simulations were carried out without opacity tables for Tungsten. In future we plan to include them into simulation model.

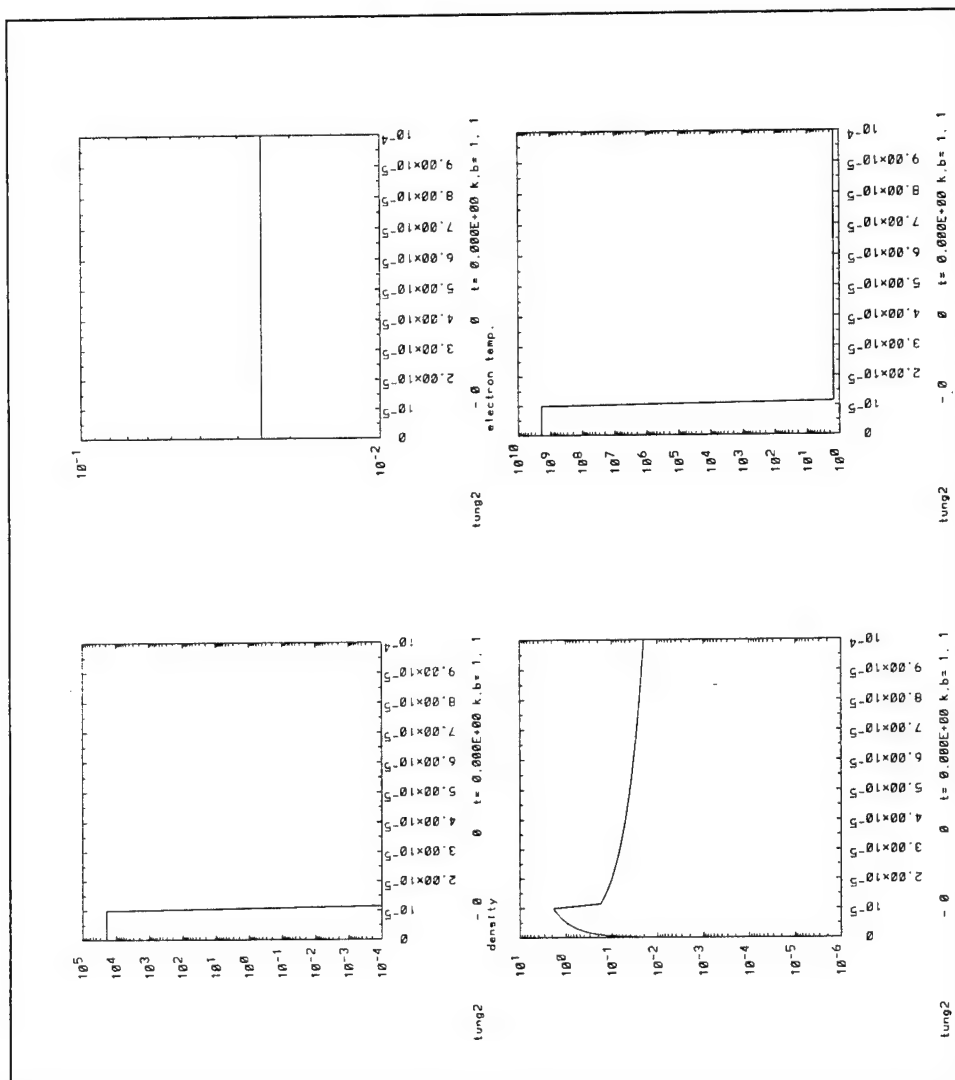


Fig. 7

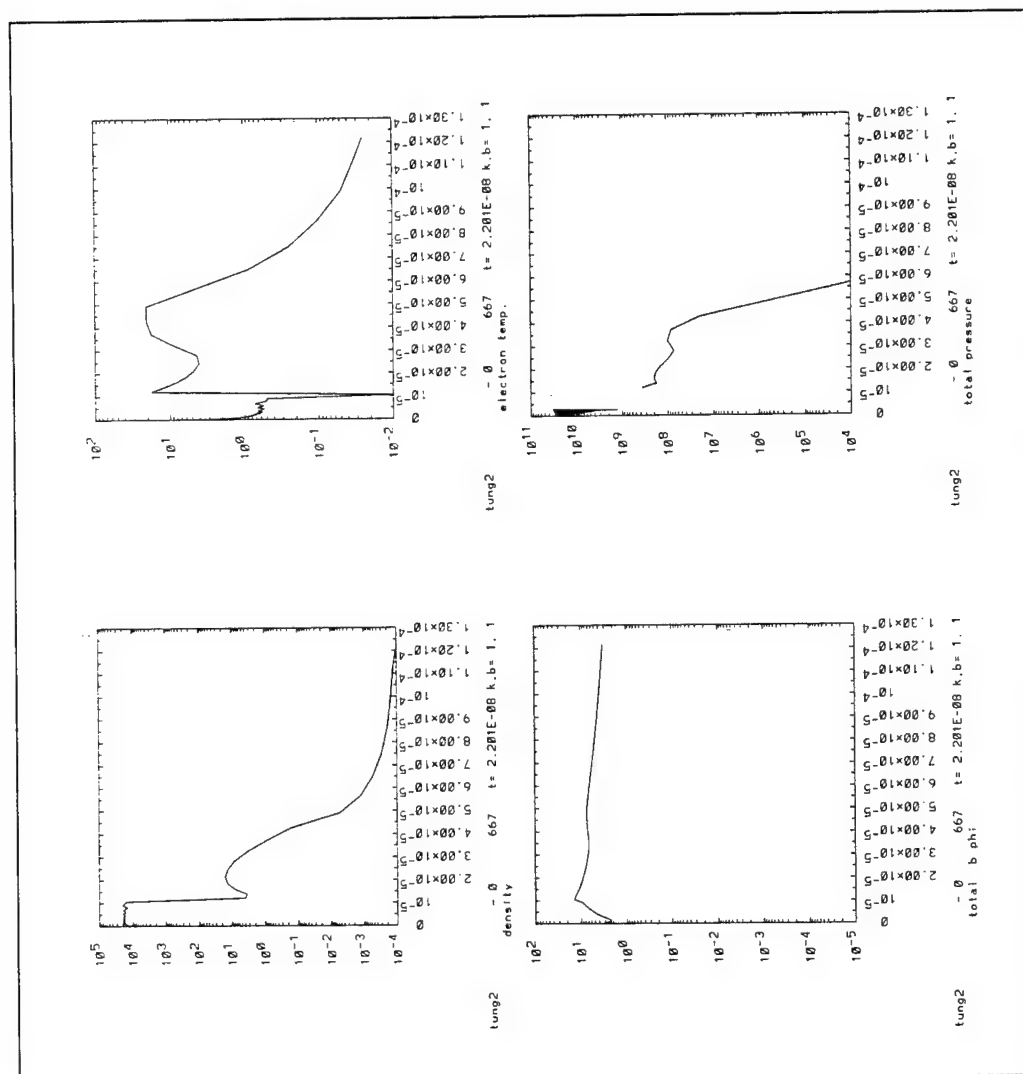


Fig. 8

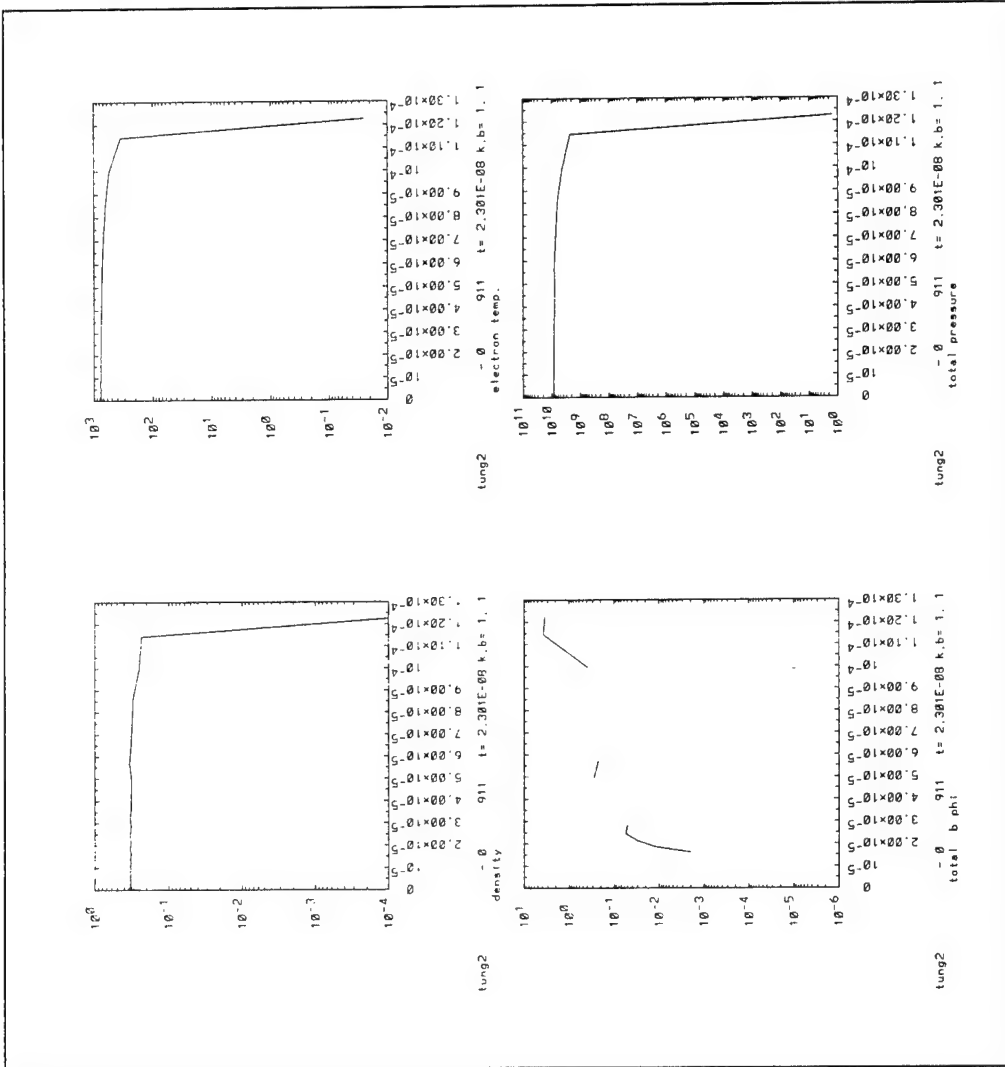


Fig.9

MHRDR simulations of the $m=0$ instability

To initiate MHRDR simulations Bennett equilibrium profiles for magnetic field and density were chosen. This is 2D problem with simulation region in r - z plane with the azimuthal magnetic field B_θ perpendicular to the plane of simulations. We can't impose periodic boundary conditions in MHRDR and we consider metal boundaries of the simulation box with the axis z corresponding to the axial direction and axis r in radial direction. It is also necessary to create constant current flux flowing from the bottom of the simulation box along z axis. This current flux should have Bennett profile in radial direction

Current density profile in Bennett equilibrium

$$j_z = \frac{j_{z \max}}{(1 + (\frac{r}{a})^2)^2} \quad j_{z \max} = \frac{c}{\pi} \frac{B_{\max}}{a}$$

where $a = \frac{r_0}{3}$ is a coordinate of the maximum of magnetic field in Bennett equilibrium and r_0 is a radius of a metal cylinder.

Current profile in Bennett equilibrium

$$J_z = \frac{J_{z\max} \left(\frac{r}{a}\right)^2}{1 + \left(\frac{r}{a}\right)^2}$$

$$J_{z\max} = \pi a^2 j_{z\max}$$

Density profile in Bennett equilibrium

$$\rho_0 = \frac{\rho_{\max}}{\left(1 + \left(\frac{r}{a}\right)^2\right)^2}$$

$$\rho_{\max} = M_H n_{00} \left[\frac{kg}{m^3}\right]$$

Magnetic field profile of the Bennett equilibrium

$$B_{0\theta} = \frac{2rB_{\max}}{a\left(1 + \left(\frac{r}{a}\right)^2\right)}$$

Initial perturbations for this problem we taken as follows

$$\rho_{pert} = ampl * \rho_{\max} * \exp\left(-0.5 * \left(\frac{r-a}{b}\right)^2\right) * \sin(kz)$$

where $ampl$ was chosen in the range $1.0e-5 \leq ampl \leq 1.0e-2$.

The final initial distribution was taken in the form

$$\rho_{initial} = \rho_0 + \rho_{per}.$$

Similar procedure was used for other variables.

The following initial simulation parameters we chosen for hydrogen plasma

Atomic Density

$$n_{00} = 10^{18} \frac{1}{cm^3}$$

what corresponds to mass density

$$\rho_{0max} = 1.67 \cdot 10^{-3} \frac{kg}{m^3}$$

Temperature

$$T = 1ev = 11605 K$$

Length of simulation region in z direction was chosen from considerations that many wavelength of the most unstable modes could be placed inside the simulation box.

$$L_z \approx 30r_0$$

We used the following boundary conditions

On the left border (r=0): 1111111711

$\frac{d\rho}{dn} = 0$; $V_r = 0$; $\frac{dV_z}{dn} = 0$; EI – zero-temperature, electrically conducting wall; for magnetic field perpendicular to the plane of computation BP – cylindrical axis of symmetry

On the right border (r=r0): 1111551111

$\frac{d\rho}{dn} = 0$; $V_r = 0$; $\frac{dV_z}{dn} = 0$; For electron specific energy EI – thermally insulating, electrically conducting wall (or mirror, $\frac{dEI}{dn} = 0$) ; for magnetic field perpendicular to the plane of computation BP – tangential current density = 0 (conducting wall or mirror).

On the bottom (z=0) border : 1111551111

$\frac{d\rho}{dn} = 0$; $\frac{dV_r}{dn} = 0$; $V_z = 0$; EI – thermally insulating, electrically conducting wall (or mirror, $\frac{dEI}{dn} = 0$) ; for magnetic field perpendicular to the plane of computation BP – tangential current density = 0 (conducting wall or mirror).

On the upper (z=Lz) border: 1111551111

$\frac{d\rho}{dn} = 0$; $\frac{dV_r}{dn} = 0$; $V_z = 0$; EI – thermally insulating, electrically conducting wall (or mirror, $\frac{dEI}{dn} = 0$) For magnetic field perpendicular to the plane of computation BP – tangential current density = 0 (conducting wall or mirror).

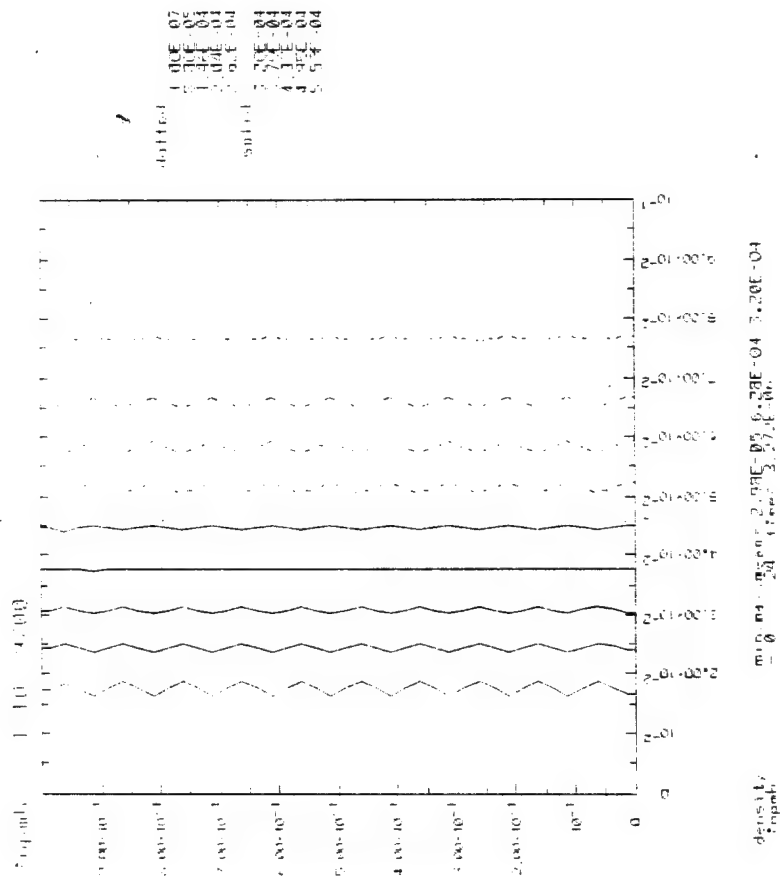


Figure 4

The contour lines of density with growing perturbations ($k_z r_0 = 6$).

2D MHRDR simulation results of $m=0$ sausage instability with Bennett initial profile without a shear flow ($V_{0z} = 0$).

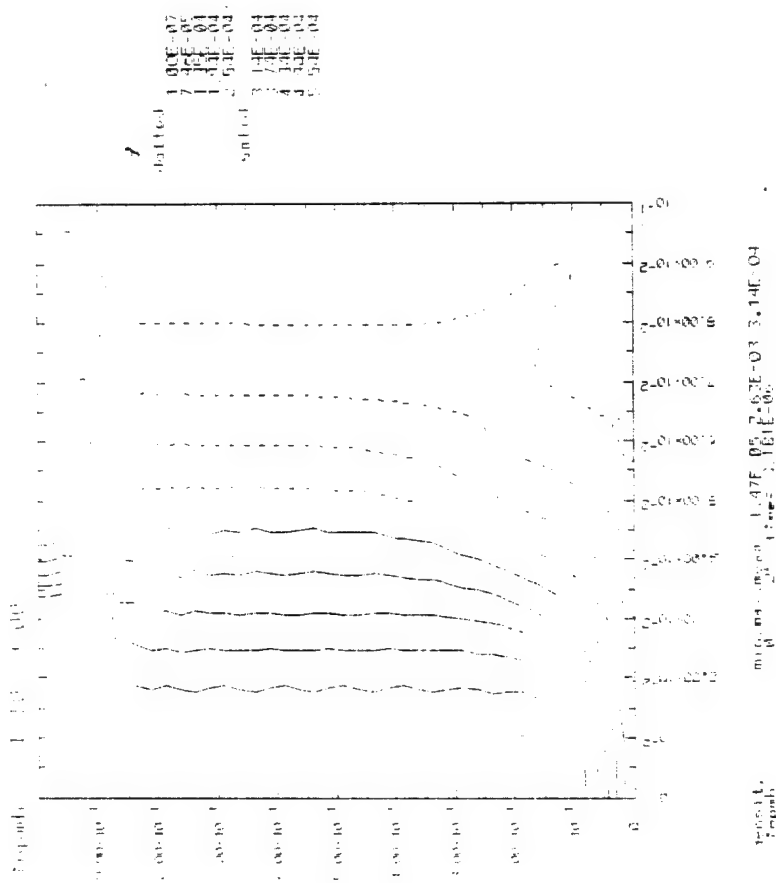


Figure 5

The contour lines of density with growing perturbations ($k_z r_0 = 6$).
 2D MHRDR simulation results of $m=0$ sausage instability with Bennett initial profile with a shear
 flow ($V_{0z} = 1.5 V_{Ti}$).

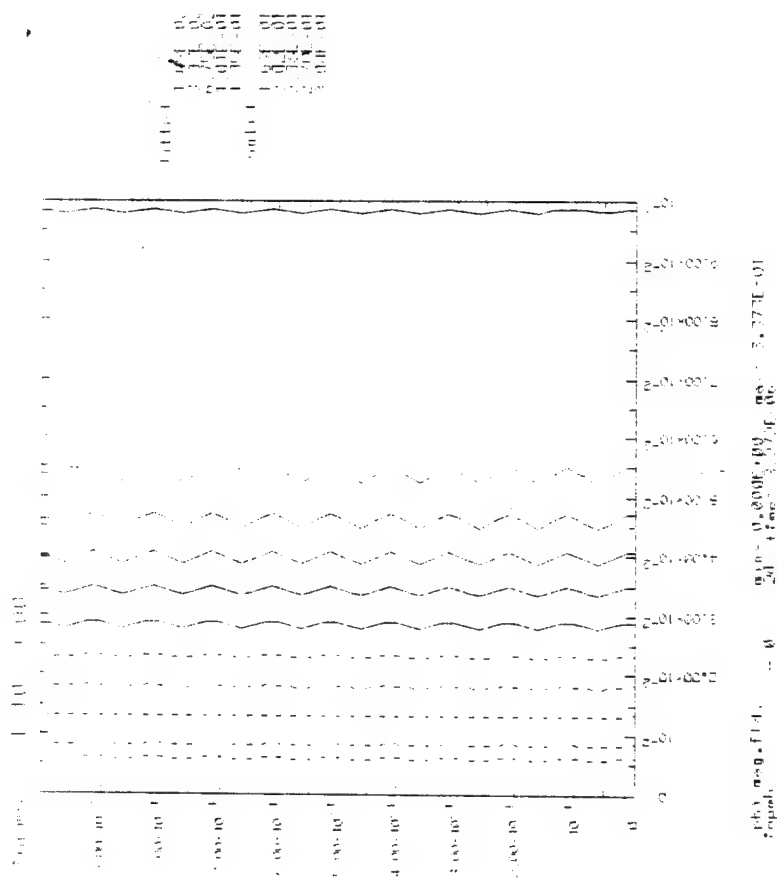


Figure 6

The contour lines of azimuthal magnetic field with growing perturbations ($k_z r_0 = 6$).

2D MHRDR simulation results of $m=0$ sausage instability with Bennett initial profile without a shear flow ($V_{0z} = 0$).

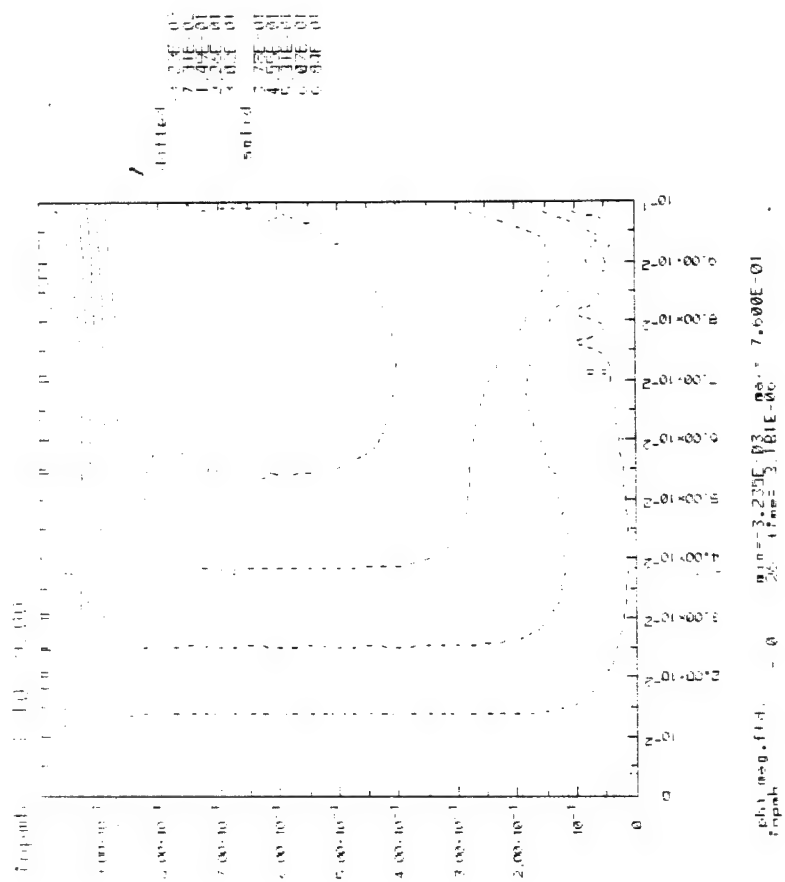


Figure 7

The contour lines of azimuthal magnetic field with growing perturbations ($k_z r_0 = 6$).
 2D MHRDR simulation results of $m=0$ sausage instability with Bennett initial profile with a shear
 flow ($V_{0z} = 1.5 V_{Ti}$)

Simulation results presented on Figures 4 –7 are in agreement with the numerical linear theory solutions for the growth rate, presented on Figure 3. For the unstable wave with $k_z r_0 = 6$ from Figure 3 we find for the growth rate $\gamma \sim 1.25 \dots$ in the absence of a shear flow ($V_0 z = 0$ and $\varepsilon = 0$) and $\gamma \sim 0.3$ in the presence of a shear flow ($V_{0z} = 1.5 V_{Ti}$, and $\varepsilon = 0$). In MHD RD value of the growth rate can be obtained from the time dependence of the axial kinetic energy. These values are in agreement with the linear theory results.

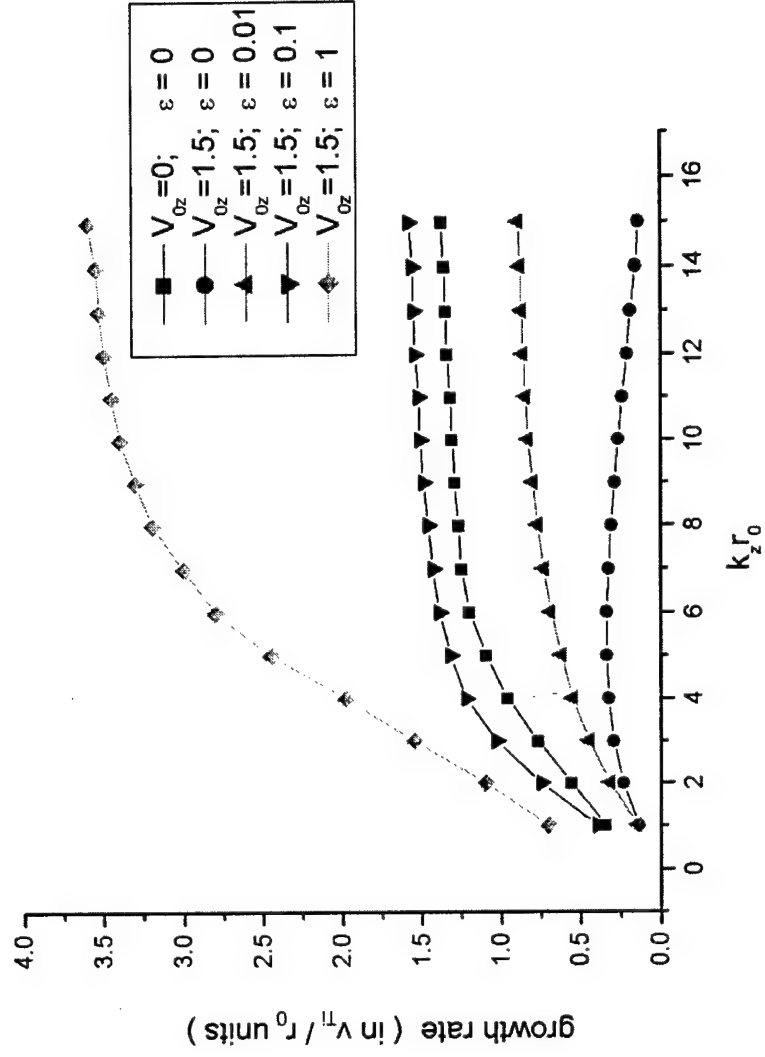
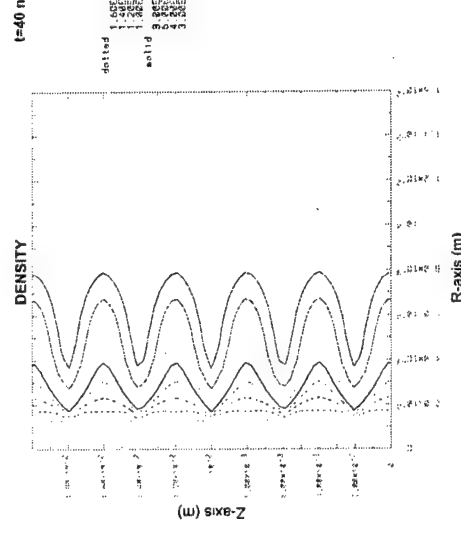
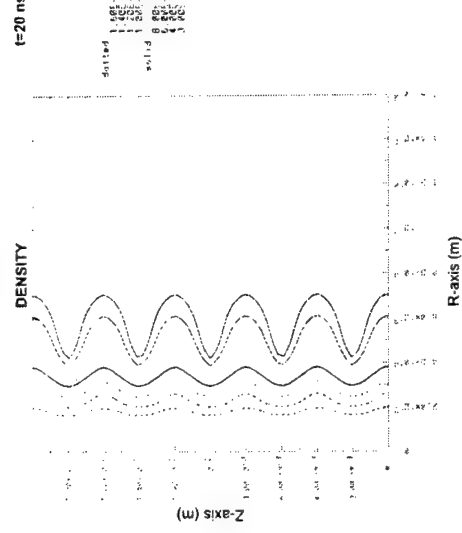
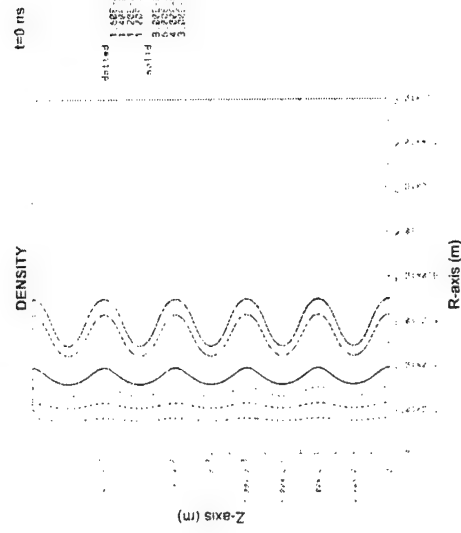


Figure 3

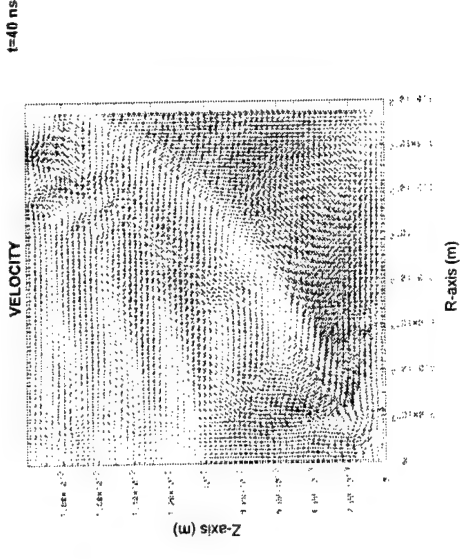
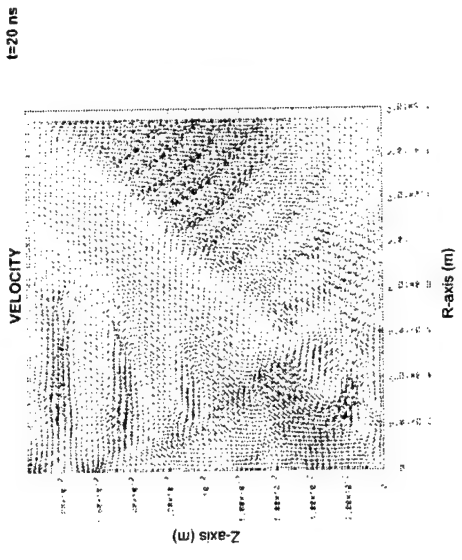
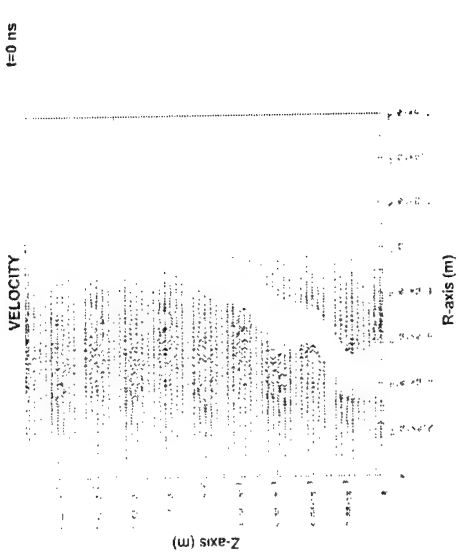
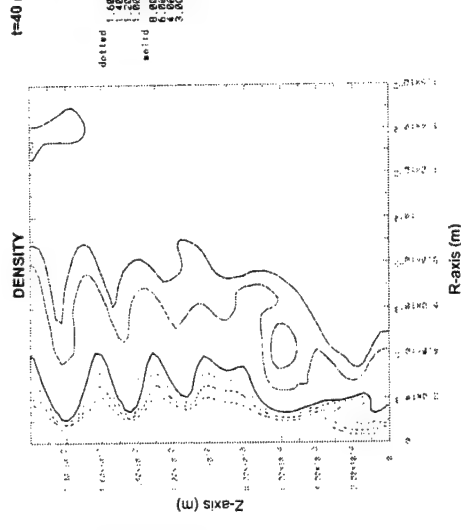
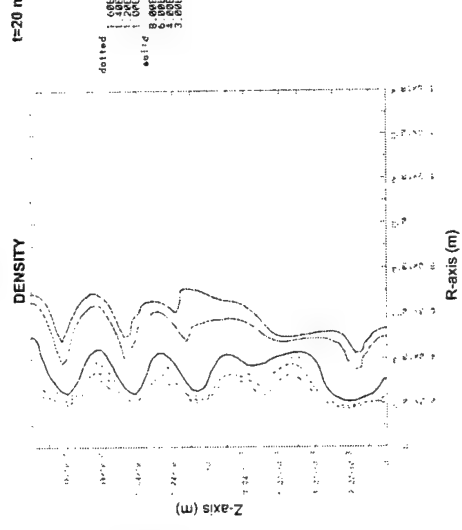
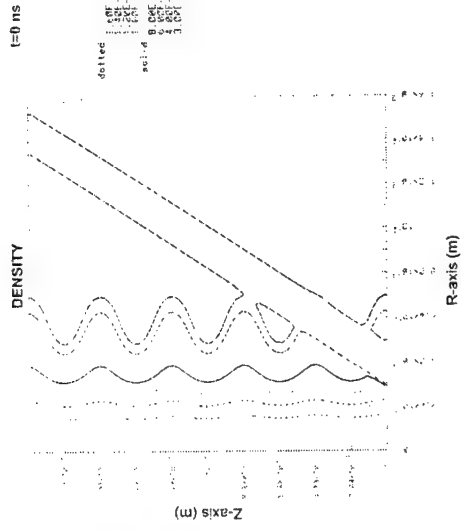
STABILIZATION OF M-F INTERFACIAL MODES WITH COLLIMATED AXIAL FLOWS PRODUCED BY CONICAL SHELL IMPLSIONS

- Simulations were performed in the ideal MHD conditions: infinite conductivity, no radiation losses, no thermal conduction losses, ideal gas equation of state
- All boundaries are electrically conductive walls with reflective boundary conditions
- Two simulations are presented:
 - *Bennett equilibrium* on which a pure mode perturbation with 10% amplitude is superimposed. The growth of the initial perturbation is followed up to 100 ns.
 - *Conical shell* on the same perturbed Bennett equilibrium. The growth of the initial perturbation is studied in this new configuration and compared to the previous results
- Bennett equilibrium: hydrogen, temperature 300 eV, maximum density 10^{24} m^{-3}
- Conical shell: hydrogen, temperature 10 eV, density $2 \times 10^{23} \text{ m}^{-3}$, shell thickness 2 mm, shell maximum current 200 kA
- Computational domain: length 1.55 cm, height 2 cm, grid $93 (r) \times 63 (z)$
- Initial perturbation: $kr_0 = 24$ (k is the wavenumber and r_0 is the radius), amplitude is 10 % from the maximum equilibrium quantities.

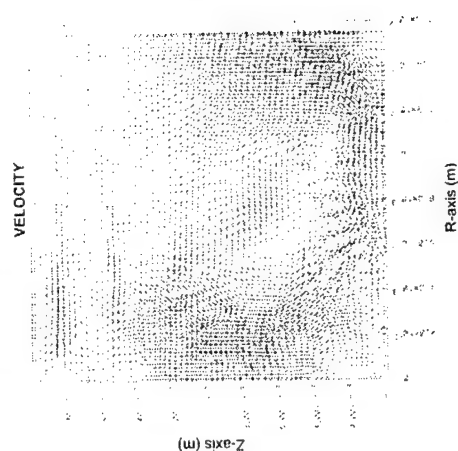
Bennett without conical shell



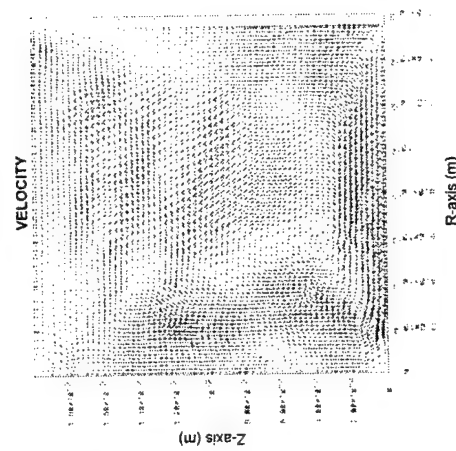
Bennett with conical shell



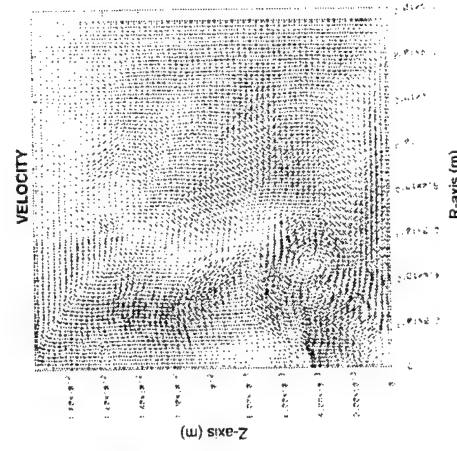
t=60 ns



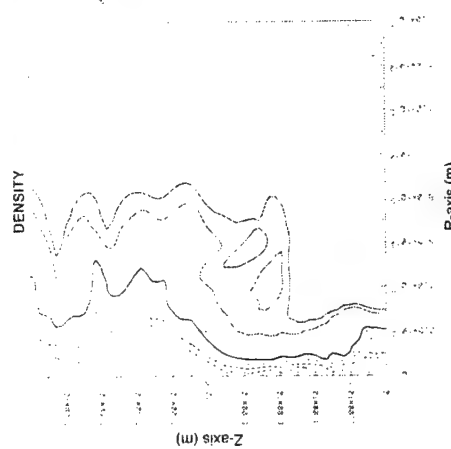
t=80 ns



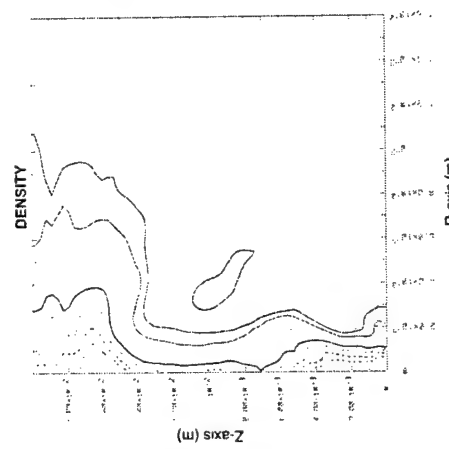
t=100 ns



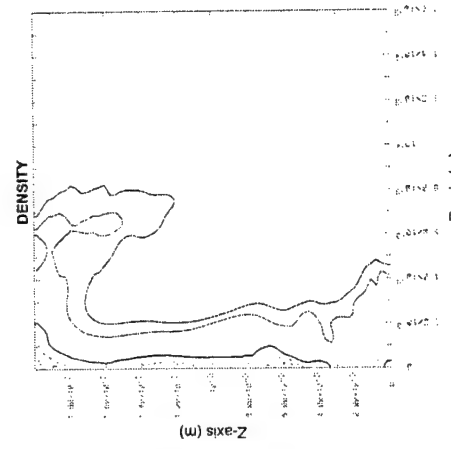
t=60 ns



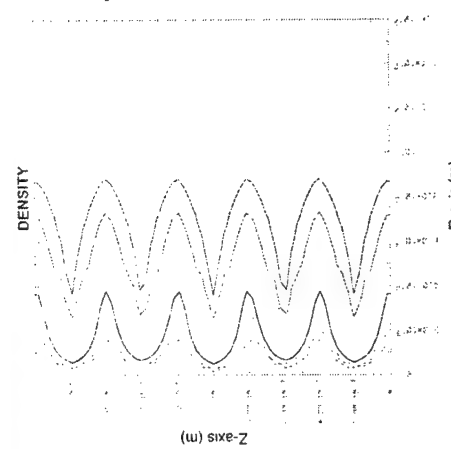
t=80 ns



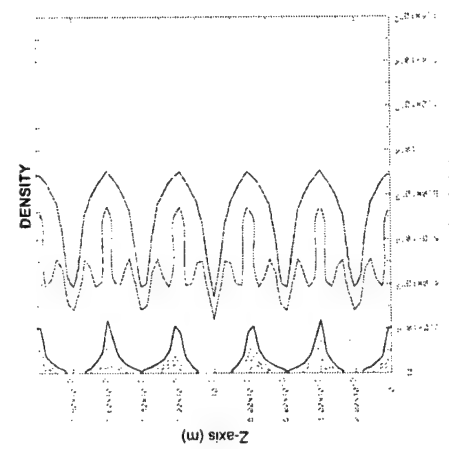
t=100 ns



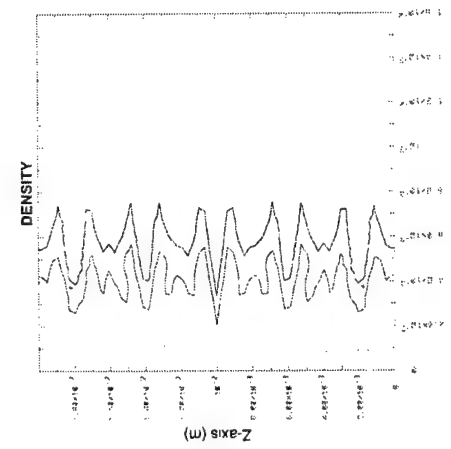
t=60 ns



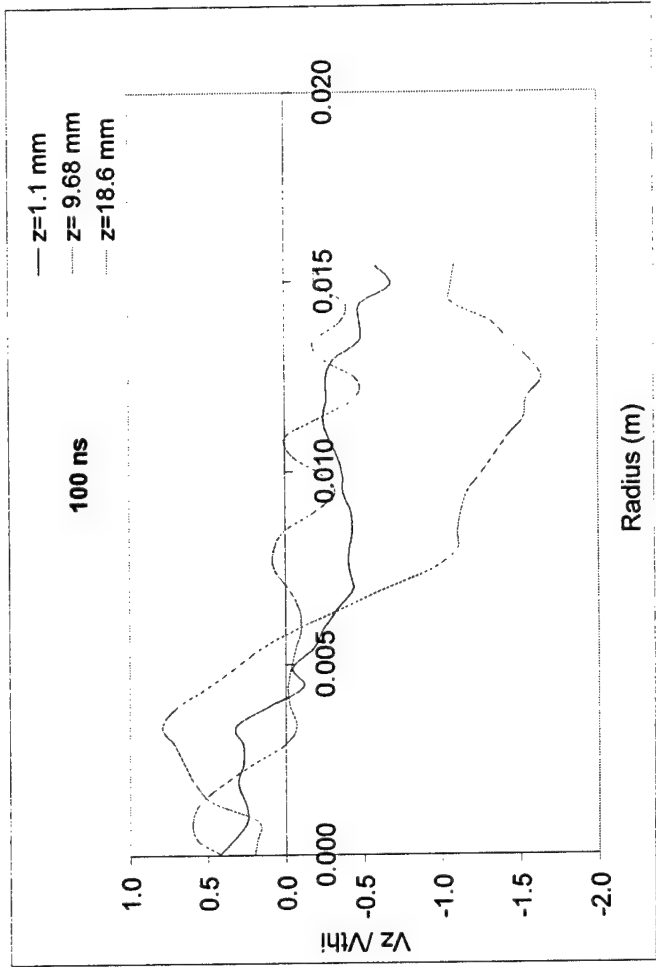
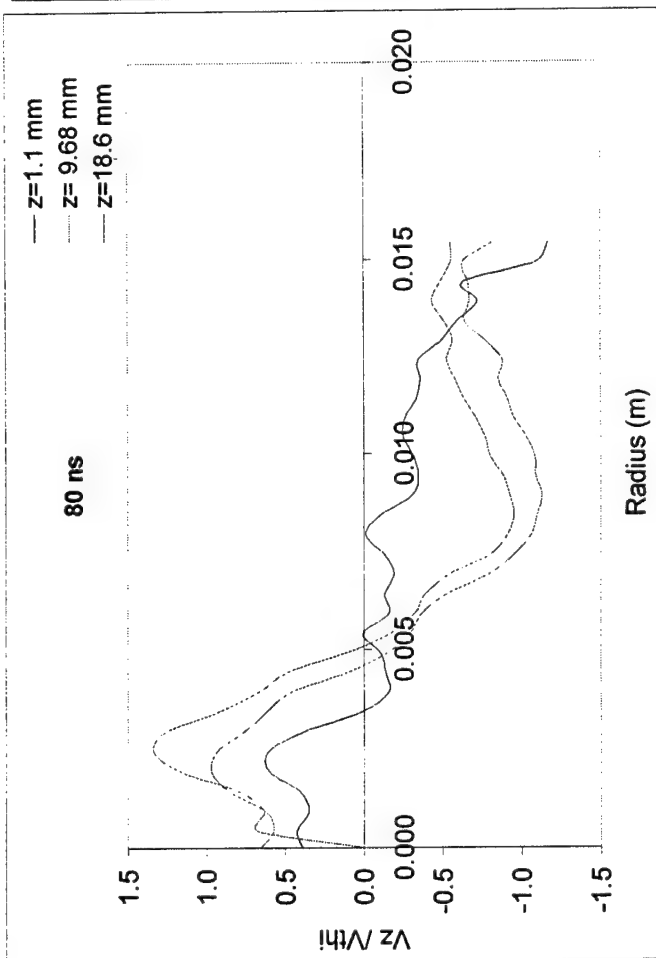
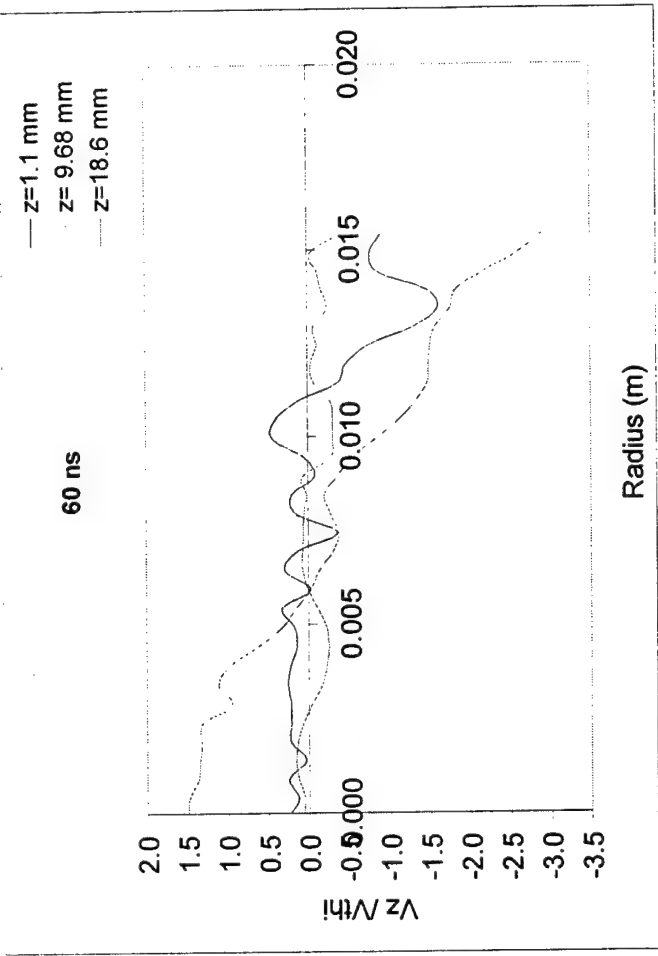
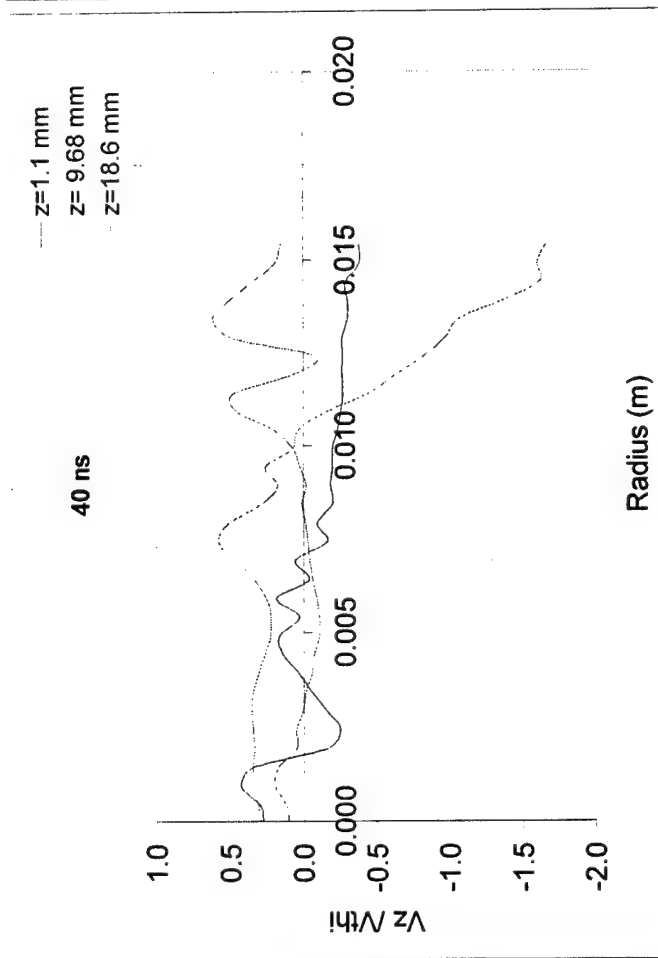
t=80 ns



t=100 ns



RATIO OF AXIAL VELOCITY TO ION THERMAL VELOCITY



- The growth of the internal modes of the sausage instability was studied for a perturbed Bennett equilibrium with and without a conical plasma shell
- The parameters of the conical shell were chosen so that the implosion kinetic energy would be comparable to the instability kinetic energy, and the mitigation of the linear stage instability development could be easily observed from the density contour plots
- For the implosion of the conical shell on a perturbed equilibrium the instability development was suppressed over a duration of about 100 ns (from the linear theory the instability growth time was found to be of about 60 ns)
- Flow velocities of order of 10^5 m/s were obtained on the z-axis, with maximum Mach numbers of about 1.5. The shear in these flows proved to be enough to destroy the instability structure
- We have demonstrated here the stabilizing effect of conical shell implosions on the sausage modes of a diffuse z-pinch. For the future we plan to investigate the effect of conical shell produced flows on the sausage instability development for a free-boundary z-pinch as well.

APPENDIX E

Homogeneous Electrical Explosion of Tungsten Wire in Vacuum

G.S. Sarkisov and B.S. Bauer, UNR
J.S. De Groot, UC Davis

JETP Letters **73**, 74-79 (2001)

Homogeneous Electrical Explosion of Tungsten Wire in Vacuum¹

G. S. Sarkisov^{*,2}, B. S. Bauer^{*}, and J. S. De Groot^{***}

^{*} Department of Physics, University of Nevada, Reno, NV 89557

^{**} e-mail: sarkisov@unr.edu.

^{***} Department of Applied Science, University of California, Davis, CA 95616

Received December 13, 2000

Experimental results on Joule energy deposition upon initiation of a fast electrical explosion of 16- μm tungsten wire in vacuum at current densities of more than 10^8 A/cm^2 are reported. We have found that explosion with a fast current rise time ($\sim 170 \text{ A/ns}$ into a short) results in homogeneous and enhanced deposition of electrical energy into the tungsten before surface flashover. The maximum tungsten wire resistivity reaches the value of up to $\sim 185 \mu\Omega \text{ cm}$ before surface flashover that significantly exceeds the melting boundary and corresponds to temperature of $\sim 1 \text{ eV}$. The highest values for light radiation and expansion velocity of wire $\sim 1 \text{ km/s}$ were observed for the fast explosion. For the explosion mode with a slower current rise time ($\sim 22 \text{ A/ns}$ into a short), we observed the existence of an "energy deposition barrier" for tungsten wire. At slow explosion mode, the current is reconnected to the surface shunting discharge before melting. The maximum tungsten wire resistivity in this case reaches the value of $\sim 120 \mu\Omega \text{ cm}$, which is less than indicative of melting. Also, the energy deposition along the wire is strongly inhomogeneous and wire is disintegrated into parts. We attribute the early reconnection of the current to the surface discharge for the slow explosion to high electron emission from the wire surface, which starts before melting. © 2001 MAIK "Nauka/Interperiodica".

PACS numbers: 52.80.Qj

A better understanding of the initial stage in the electrical explosion of refractory metal wires is extremely important for modern Z-pinch physics. The impressive result [1, 2] of 1.8 MJ of X rays radiated in 5 ns FWHM, achieved on Z-facility at Sandia National Laboratories, crucially depends on mitigating the Rayleigh–Taylor instability, which degrades plasma compression. The initial perturbations for this instability arise in the plasma shell formed from the exploded wire array. Increased peak X-ray power correlates with decreased wire gap, presumably because this leads to the formation of a smoother plasma shell. Similarly, the dynamics of single-wire Z-pinches depends on how energy is initially absorbed by the load.

It is assumed [3] that surface impurities, such as absorbed gases and hydrocarbons, play an important role in energy deposition processes. It is supposed that heated fast vaporizing impurities create a gas shell around the wire and, after field flashover, the current is switched from the wire to the ionized gas shell. The effectiveness of Joule energy deposition decreases after flashover. The main strategy to avoid the influence of

the early surface flashover is preliminary heating of the wire in vacuum for surface degasation. Preheating the wire has been shown [4] to increase the mass and uniformity of the plasma surrounding the cold core. Nevertheless, the maximum wire resistivity in experiments [4] did not reach the level of tungsten melting and the deposited energy was less than the energy needed for vaporization. The other approaches to increase energy deposition before surface flashover were: dielectric coating of the wire [5], explosion of the wire in oil [6], in deionized water [7], and in gas [8]. It has been shown that electrical explosion of tungsten wire in a dense medium and with a coating results in enhanced energy deposition before surface flashover.

We have found a new approach to significantly enhance the efficiency and homogeneity of the electrical explosion of pure tungsten wire in vacuum. In our experiments, we find, for the first time, a connection between the rate of energy deposition and the absolute value and homogeneity of deposited energy into the tungsten wire before surface flashover. For energy deposition rate of $\sim 0.1 \text{ (eV/atom)/ns}$, we observe an "energy deposition barrier," when surface flashover reconnects current from the wire to the surface before melting. In this case, the wire becomes mainly disintegrated into parts. Parts of the wire that absorbed some energy are expanding with a velocity of $\sim 0.1\text{--}0.2 \text{ km/s}$.

¹ This article was submitted by the authors in English.

² On leave from Lebedev Physics Institute, Russian Academy of Sciences, Moscow, 117924, Russia.

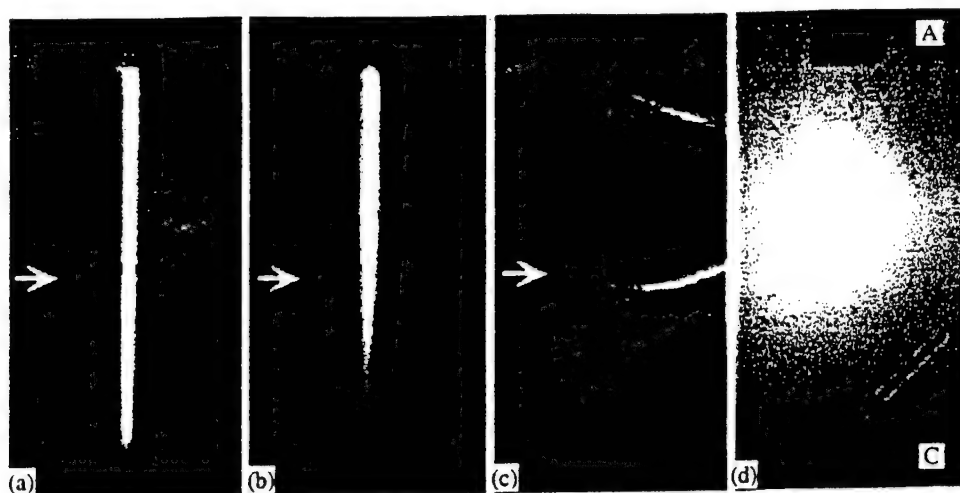


Fig. 1. Time-integrated CCD images of a 16- μ m diameter 2-cm long tungsten wire explosion: (a) fast "cylindrical" explosion (shot 0626-08); (b) fast "conical" explosion (shot 0626-11); (c) slow explosion with peripheral vacuum arcs (shot 0801-06); (d) the cathode-anode gap after a slow explosion with unvaporized wire (black arrow). The white arrows show the cross section imaged to the streak camera to investigate the velocity of the wire expansion (Fig. 2). Positions of the anode (A) and cathode (C) are marked on image (d).

For a faster energy deposition rate, ~ 0.7 (eV/atom)/ns, we observe a qualitative and quantitative breakthrough in the energy deposition processes. Tungsten wire was exploded homogeneously and the deposited energy was ~ 3 times higher. In this case, we observe strong light emission synchronized with surface flashover and the wire expansion velocity reaches the value ~ 1 km/s.

A 120 kV Maxwell 40151-B pulse generator with stored energy of 12.6 J (7 nF, 60 kV) provides the current and voltage used to drive the wire explosions. A 50- Ω 9-m coaxial transmission line delivers the positive-voltage pulse from the generator to the wire. The setup produces a fast pulse with a ~ 170 A/ns current rise into a short circuit (voltage rate ~ 11 kV/ns in an open circuit), or, with an inductor inserted before the generator output, a slower pulse with a ~ 22 A/ns current rise into a short circuit (voltage rate ~ 1 kV/ns into an open circuit). The slower rise is characteristic of the prepulse through individual wires on the Z-facility at Sandia National Laboratories. The electrical pulse is applied to a single tungsten wire 2 cm in length and 16 μ m in diameter. The wire forms the central conductor of a coaxial line evacuated to a pressure of $\sim 10^{-5}$ torr to prevent early gas breakdown.

The current flowing through the wire is measured with a 2-GHz bandwidth shunt resistor, and the voltage drop across the wire is measured with a resistive high-voltage probe (100 kV, 1.5 ns rise time). From current and voltage data, the resistive component of the voltage, the load resistance, and the Joule heating of the wire can be determined throughout the wire explosion. The evolution of space-integrated light intensity emitted from the exploding wire is monitored by a PIN

diode with a rise time of less than 1 ns. The light is focused by a $f/0.7$ lens with a focal length of 50.3 mm. Streak camera shadowgrams of the wire during the explosion are obtained using a high-power diode pulsed laser back lighter (905 nm, 10 W, 200 ns). From these streaked images, the plasma expansion velocity and the starting time of the explosion are determined. Time-integrated visible-light CCD images of wire explosions give information on the 2-dimensional structure of the energy deposition. We also analyze the time-integrated emission spectra using a visible imaging spectrometer.

Typical time-integrated images of exploding 16- μ m diameter and 2-cm long W wire are shown in Fig. 1. There are big differences in the energy deposition structure between the explosions driven by fast and slow pulses. The fast pulse produces a homogeneous "cylindrical" (a) or a "conical" (b) structure. The "conical" explosion (b) is wider at the anode and narrower at the cathode side. The slow pulse results in many peripheral vacuum arcs between the wire and the ground cylinder 2.8 cm away. Part of the wire is left unvaporized (d) after the slow pulse shot (c). For the cylindrical (a) and the conical (b) explosion modes, the region surrounding the wire is glowing brightly. For the slow pulse case (c), the light emission is over an order of magnitude less, and comes mostly from the peripheral vacuum arcs.

The velocity of expansion is dramatically greater for the fast pulse explosion than for the slow pulse case (Fig. 2, data from the shots shown in Fig. 1). The velocity of expansion in the middle of the 16- μ m diameter W wire is 0.83 km/s for the fast cylindrical explosion

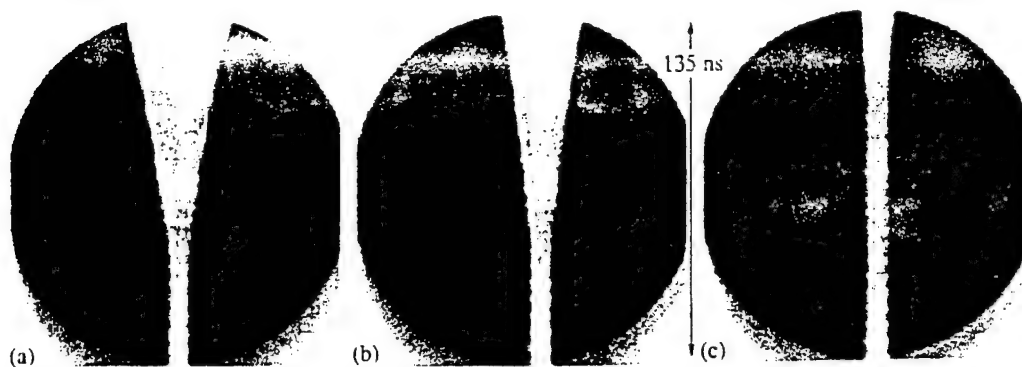


Fig. 2. Radius vs. time (R - T) streaked laser shadowgrams of the expansion in the middle plane of the 16- μ m diameter W wire. R - T images (a), (b), and (c) correspond to time-integrated images (a), (b), and (c) in the cross sections marked by white arrows in Fig. 1.

mode (Figs. 2a and 1a), 0.59 km/s for the fast conical explosion mode (Figs. 2b and 1b), and 0.15 km/s for the slow-pulse explosion (Figs. 2c and 1c). In slow-pulse explosion, the wire expands only in the region where the peripheral vacuum arcs are absent. The wire remains unevaporized in the arcing region. The wire starts to expand after the voltage reaches the maximum value, i.e., after surface flashover. The expansion proceeds at a constant speed, indicating minimal heating of the wire after flashover.

Optical spectra for the fast and slow explosion of 16- μ m W wire contain a high level of continuum radiation combined with spectral lines of W and some light species.

Temporal evolution of current (1), voltage (2), deposited Joule energy (3), and light emission (4) for fast cylindrical (a) and slow (b) explosion modes of 16- μ m W wire is presented in Figs. 3a and 3b. For both types of explosions, we can see the same feature: after reaching the maximum value, the voltage drops fast and then becomes inductive. The rate of specific energy deposition for the fast explosion is seven times higher than for slow one [~ 0.7 (eV/atom)/ns for fast explosion and ~ 0.1 (eV/atom)/ns for slow explosion]. The maximum electrical power for the fast explosion reaches the value of ~ 61 MW and ~ 5.5 MW for slow one. The extremely fast rising (~ 2 ns initial spike) light intensity for the fast cylindrical explosion coincides in time with the rapid decrease in voltage and rapid increase in current, i.e., with surface flashover. Fast explosions yield the most powerful light emission. The first radiation peak is 4–5 times weaker for wires driven by the slow explosion.

There is a large difference in the long-time behavior of light emission for fast and slow explosion modes. The fast explosion mode gives a strong (3–4 times) increase in the light after the first peak during ~ 500 ns and a slow drop during ~ 5 – 10 μ s. For slow explosion mode, light intensity is only dropping after the first

peak. Interestingly, the long-scale temporal shape of radiation for fast exploding mode is typical only for W . Other substances give significantly different temporal shapes for the radiation, indicating quite different conditions of the wire core and coronal plasma. For the fast cylindrical mode of explosion, the temporal shape of the radiation depends very strongly and distinctly on the wire material, but not much on the wire diameter.

The dependence of load resistivity (1), current density (2), electrical power (3), and magnetic field pressure (4) on deposited Joule energy for fast cylindrical (c) and slow (d) explosion modes is presented in Fig. 3c and 3d. During the voltage increase, we can attribute recovered value of resistivity to the property of the wire. When the voltage starts to drop, the current splits between wire and surface flashover and we cannot attribute the recovered value of the resistivity to the only wire or flashover property. The resistivity curves (1) in Figs. 3c and 3d for fast and slow exploding wires coincide for low value of energy deposition. The only difference is the point at which surface flashover occurs (~ 3 eV/atom for the fast cylindrical mode and ~ 1.5 eV/atom for the slow explosion mode). For fast explosions, the wire resistivity (1) reaches ~ 185 $\mu\Omega$ cm, far above the melting boundary [9] corresponding to the saturation plateau in [10]. In contrast, the resistivity with the slowly rising pulse (3) only reaches ~ 120 $\mu\Omega$ cm, which is below the melting boundary [9]. The maximum current densities before flashover (Figs. 3c, 3d) are substantial, ~ 250 MA/cm² for fast pulses and ~ 130 MA/cm² in the slow case. The maximum magnetic field at the wire surface before flashover is ~ 131 kG and ~ 67 kG for the fast and slow pulses, respectively. The maximum of the average pressure inside the wire is approximately equal to the magnetic-field pressure on the wire surface and corresponds to ~ 135 MPa for the fast explosion and ~ 36 MPa for the slow explosion modes. The magnetic-field pressure in the fast explosion mode is 40% of the critical pressure for W ($p_{cr} = 337$ MPa, [11]) and can suppress boiling at

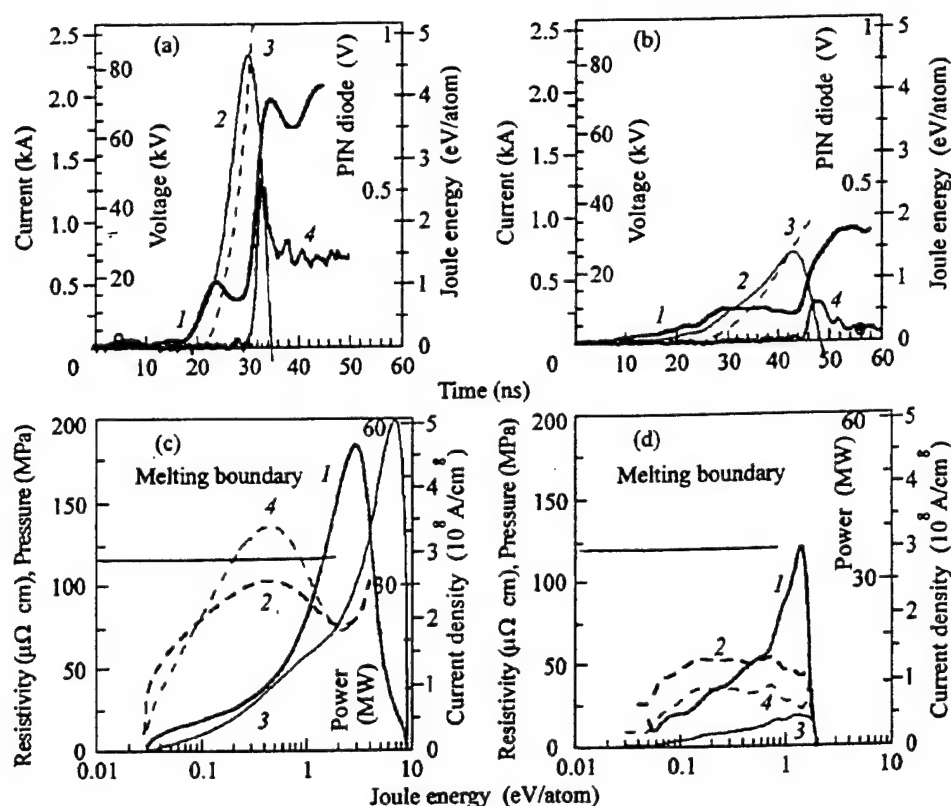


Fig. 3. Temporal evolution of (1) current, (2) voltage, (3) deposited Joule energy, and (4) emission light intensity for (a) fast and (b) slow explosions of 16- μm W wires. Dependence of (1) wire resistivity, (2) current density, (3) electrical power, and (4) magnetic-field pressure on the deposited Joule energy for (c) fast and (d) slow explosions. Magnetic field induction corresponding to current density (2) in (c) and (d) has a maximum value of 131 kG and 67 kG, respectively.

liquid–gas phase transition. In this case, we can assume a homogeneous expansion of the W wire.

The results of our experiments suggest the following scenario for the initial stages of the electrical explosion of tungsten wire. For the slow explosion mode, current flows through the wire and increases the temperature for the first ~ 45 ns. Before melting, the surface flashover starts. Current switches from the wire to surface flashover during a few nanoseconds and practically stops the heating of the substance. In this case, wire becomes mainly disintegrated on a macroparts.

Let now dwell on flashover reasons. The tungsten is known as a strong electron emitter. It has been found in [6] that, in rapid electrical heating of fine W wire in a vacuum, there is “anomalous electron emission” phenomenon when thermal electrons emission exceeds the normal value by ~ 100 times before melting. Emitted electrons may be a “trigger” for the ionization of vapors surrounding the wire and the creation of a low-resistance plasma shell [12]. Ionization of the vapor shell can be due to direct electron–atom collisions or/and photoionization by X-ray and UV radiation generated

in the collisions of emitted electrons with high-density wire surface. The strong electron emission from the W wire creates an “energy deposition barrier” to effective heating of the substance up to vaporization.

We can support this flashover scenario, because, in the slow pulse case, effective wire resistivity stops to grow at the level of W wire melting. Furthermore, we observe a set of peripheral vacuum arcs (Fig. 1c), which can be initiated by electron emission from the wire during the negative period of the electrical pulse (~ 400 ns after explosion initiation). The high level of continuum radiation in the optical spectra for the fast and slow explosion modes may support the electron emission hypothesis, because it is well known that the interaction of electrons with the wire generates bremsstrahlung radiation. There is another argument for the electron emission hypothesis. Experiments with W wire coated with vacuum pump oil demonstrate significantly higher values of deposited energy and expansion velocity than with uncoated wire. In this case, oil can “deactivate” emitted electrons because of high density at the metal–

oil interface. We will describe in detail these experiments in future publications.

We found one of the first descriptions of "wire disintegration regime" in [13] and in recent investigations using high-resolution X-ray back lighting [14]. It has been found that in slow explosion mode (~ 10 – 20 A/ns), W wire is disintegrated into longitudinal and radial parts, separated into drops [15, 16], destroyed into microscopic sol with sizes on the order of electron free path in a metal ~ 10 nm [17].

Energy deposition into the W wire is significantly improved in the fast implosion regime. In this case, surface flashover starts far after melting. The W wire resistivity reaches a maximum value of $\sim 185 \mu\Omega$ cm, which is beyond the melting level for W [9] and corresponds to the saturation plateau under normal density [10]. For this value of wire resistivity (at normal density), the temperature before the surface flashover is supposed to be ~ 1 eV [10]. For the fast explosion mode, the wire is heated at a larger value of current density and magnetic field than for the slow mode. In this case, the larger magnetic insulation of the wire may result in the surface flashover occurring at a temperature that is much higher than the melting temperature. The first narrow peak in light emission, which coincides with time of flashover, can be attributed to the radiation of the exited atoms and recombination of the ions produced due to the ionization of a vapor shell surrounding the wire. Analysis of the role of electron emission in the explosion of the refractory metals wire at current densities $\sim 10^6$ – 10^7 A/cm² can be found in [18].

There is no essential difference between the fast cylindrical (Fig. 1a) and the fast conical (Fig. 1b) explosion modes. For the fast conical explosion mode, electron emission may start the flashover at smaller values of absorbed energy and the maximum resistivity does not reach resistivity plateau [10] but passes through the melting level. For the fast cylindrical explosion mode, flashover starts at higher absorbed energy (close to the vaporization energy) and the maximum resistivity reaches the plateau [10]. The conical deposition energy was observed for many substances with large vaporization energy: W, Mo, Pt, Ti, Ni, Fe and was never observed for low vaporization energy substances: Au, Cu, Al and Ag. We will discuss this effect in latter publications.

In our experiments, the energy necessary to start wire melting is 1.5 eV/atom, which is ~ 1.8 times as large as the tabulated value. This agrees with the observation of increased specific heat capacity before melting, discussed in [18]. The high magnetic pressure may also play a certain role in increasing the energy deposition.

Finally, let us summarize the major results of this work. It has been shown that the quality of the electrical explosion of tungsten wire is critically dependent on the rate of energy deposition. The processes vary from electrical disintegrating of the wire into macroscopic

parts (under slow-pulse mode ~ 22 A/ns) to the homogeneous explosion with a large value of deposited energy (under fast-pulse mode ~ 170 A/ns). The main barrier to enhanced energy deposition in the slow explosion mode is caused by the initiation of high thermal electron emission before wire melting. Current becomes reconnected to the surface flashover, and heating of the wire stops. This "energy deposition barrier" can be avoided by increasing the wire heating rate. In this case, heating occurs at higher current density so that larger magnetic field may restrict the electron emission before melting. In the fast explosion mode, the wire resistivity reaches a value of $\sim 185 \mu\Omega$ cm, which is a plateau for normal density of tungsten [10]. In this case, the temperature of the wire before expansion reaches the values of ~ 1 eV, the energy deposition is homogeneous along the axis, and expansion velocity reaches a maximum value of ~ 1 km/s.

The effect of significant enhancement of energy deposition before surface flashover with increasing energy deposition rate was observed for all available pure metal wires (Mo, Pt, Ti, Ni, Fe, Ag, Cu, Al, and Ag); we will discuss the results in future publications.

We gratefully acknowledge V. Kantsyrev for assistance at the initial stage of the project, D. McCrorey for assistance in conducting the experiment, H. Fareto and B. LeGalloudec for assistance in initiating the high voltage pulser, A. Oxner and B. Brinsmead for help in fixing problems with experimental equipment, and V. Sotnikov for useful discussions. Special thanks to P. Sasorov, G. Oleinik, and R. Baksht for reading our paper and valuable remarks. This work was supported by DOE-NV, SNL, DOE-EPSCoR, and UNR.

REFERENCES

1. T. W. Sanford, G. O. Allshouse, B. M. Marder, *et al.*, Phys. Rev. Lett. **77**, 5063 (1996).
2. R. B. Spielman, C. Deeney, G. A. Chandler, *et al.*, Phys. Plasmas **5**, 2105, (1998).
3. F. D. Bennett, in *Progress in High Temperature Physics and Chemistry*, Ed. C. A. Rouse (Pergamon, Oxford, 1968), Vol. 2, p.3.
4. S. A. Pikuz, T. A. Shelkovenko, A. R. Minglaev, *et al.*, Phys. Plasma **6**, 4272 (1999).
5. D. B. Sinars, T. A. Shelkovenko, S. A. Pikuz, *et al.*, Phys. Plasmas **7**, 429 (2000).
6. S. V. Lebedev and S. E. Khaikin, Zh. Éksp. Teor. Fiz. **26**, 723 (1954); **26**, 629 (1954).
7. R. B. Baksht, I. M. Datsko, A. F. Korostelev, *et al.*, Fiz. Plazmy **9**, 1224 (1983) [Sov. J. Plasma Phys. **9**, 706 (1983)].
8. F. H. Webb, H. H. Hilton, P.H. Levine, and A. V. Tollestrup, in *Exploding Wires*, Ed. by W. G. Chace and H. K. More (Plenum, New York, 1962), Vol. 2, p. 37.
9. *Electrical Resistivity Handbook*, Ed. by G. T. Dyos and T. Farrell (Peter Peregrinus, London, 1992).

10. M. P. Desjarlais, *Contrib. Plasma Phys.* (2001) (in press).
11. M. M. Martynyuk and I. Kasimkhodzhaev, *Zh. Fiz. Khim.* **48**, 1243 (1974).
12. S. V. Lebedev, *High Temp.* **8**, 240 (1970).
13. N. N. Sobolev, *Zh. Éksp. Teor. Fiz.* **17**, 655 (1947); **17**, 987 (1947).
14. S. A. Pikuz, T. A. Shelkovenko, D. B. Sinars, *et al.*, *Phys. Rev. Lett.* **83**, 4313 (1999).
15. L. Zernow and G. Woffinden, in *Exploding Wires*, Ed. by W. G. Chace and H. K. More (Plenum, New York, 1959), p. 170.
16. J. Nasilowski, in *Exploding Wires*, Ed. by W. G. Chace and H. K. More (Plenum, New York, 1964), Vol. 3, p. 259.
17. F. G. Carioris, B. R. Fish, and G. W. Royster, in *Exploding Wires*, Ed. by W. G. Chace and H. K. More (Plenum, New York, 1962), Vol. 2, p. 299.
18. S. V. Lebedev and A. I. Savvatimskii, *Usp. Fiz. Nauk* **144** (2), 215 (1984) [*Sov. Phys. Usp.* **27** (10), 749 (1984)].

APPENDIX F

Deposition of Joule Energy at Initial Stage of Wire Explosion

G.S. Sarkisov and B.S. Bauer, UNR
J.S. De Groot, UC Davis

42nd APS-DPP Conference, Oct 23-27, 2000

Deposition of the Joule Energy at Initial Stage of Wire Explosion

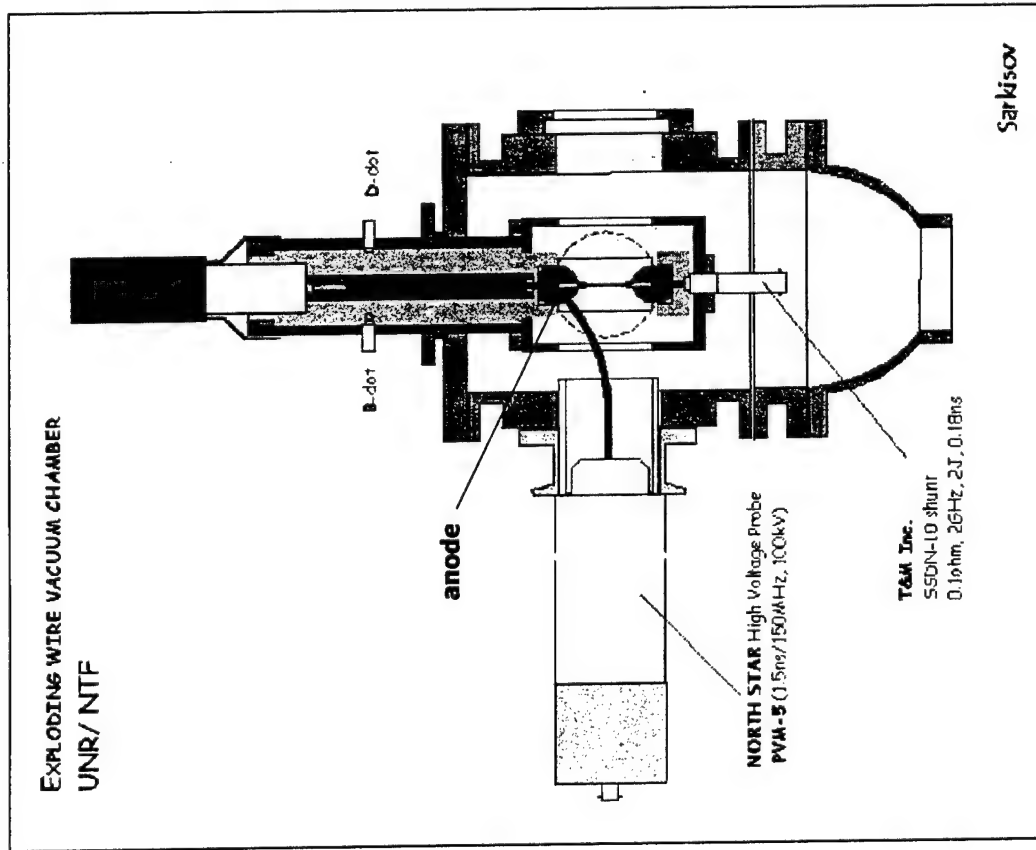
Gennady Sarkisov, Bruno Bauer (UNR)
John De Groot (UCD)

42nd APS DPP 2000, October 23-27,
Quebec City, Canada



Vacuum chamber for exploding wire experiments

N-7
T
F

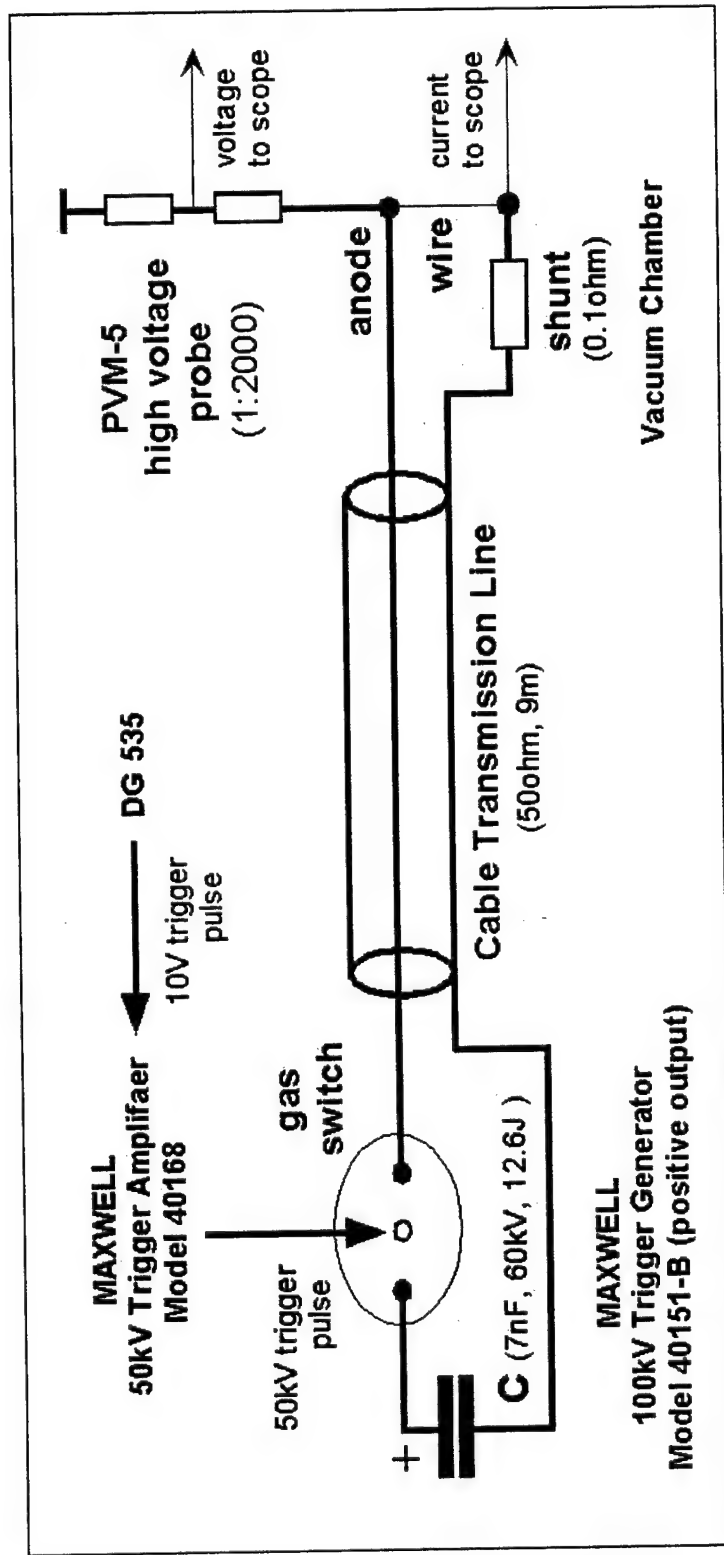


ON-LINE DIAGNOSTICS

1. Current (0.1ohm, 2GHz shunt)
2. Voltage (150MHz, 1.5ns rise)
3. B-dot and V-dot
4. PIN diode for visible light (<1ns rise)
5. Diode laser + streak-camera imaging
6. Visible spectrograph
7. Time integral CCD imaging

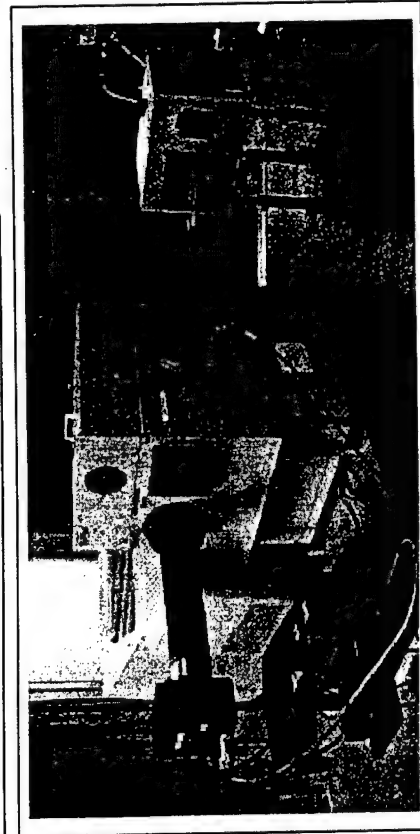
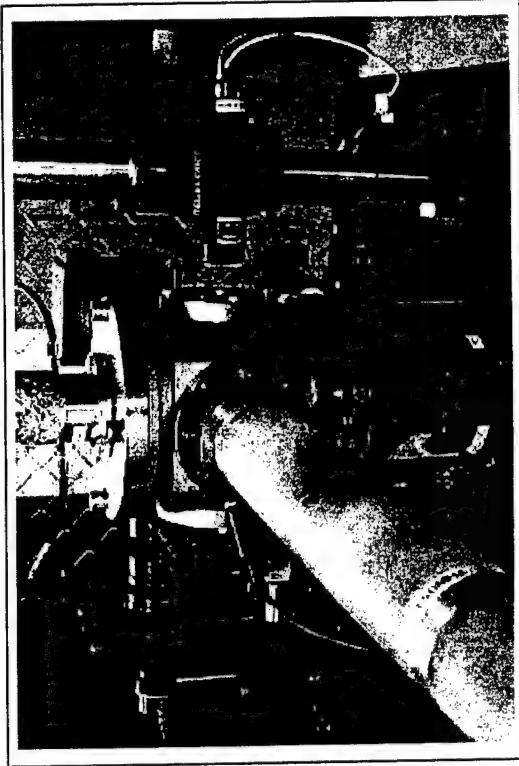
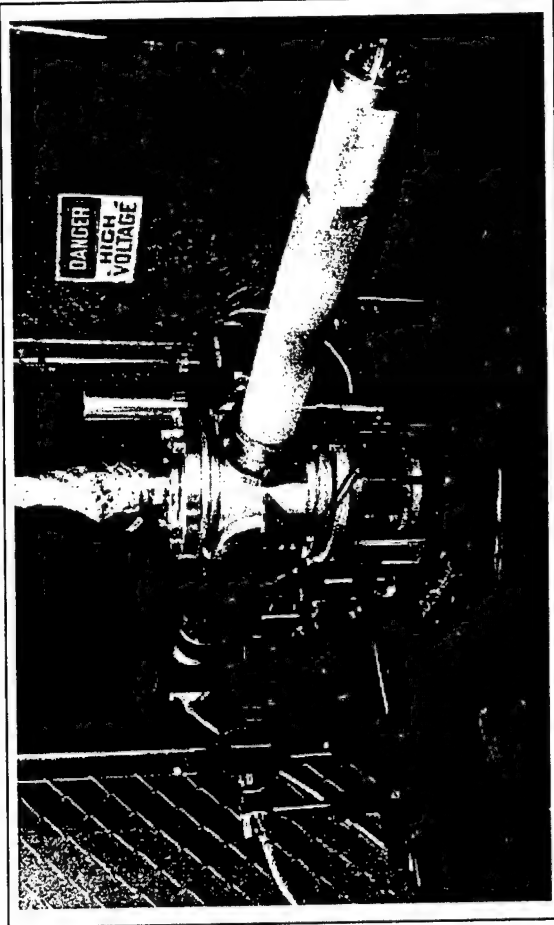
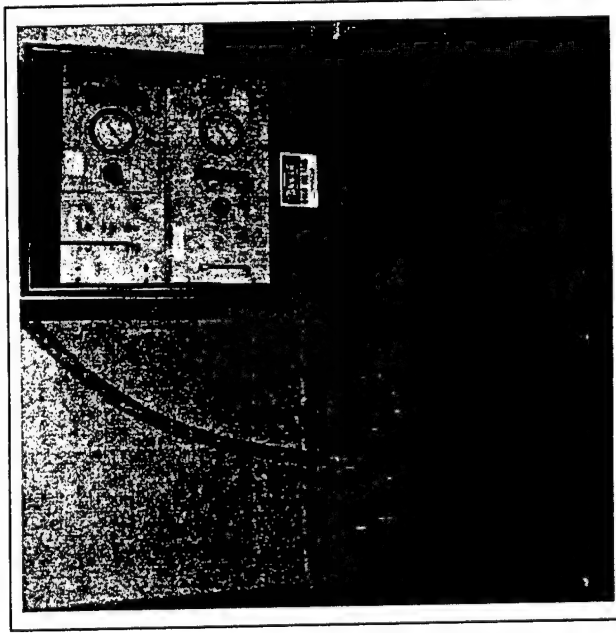
Electrical diagram of installation

N7
TF



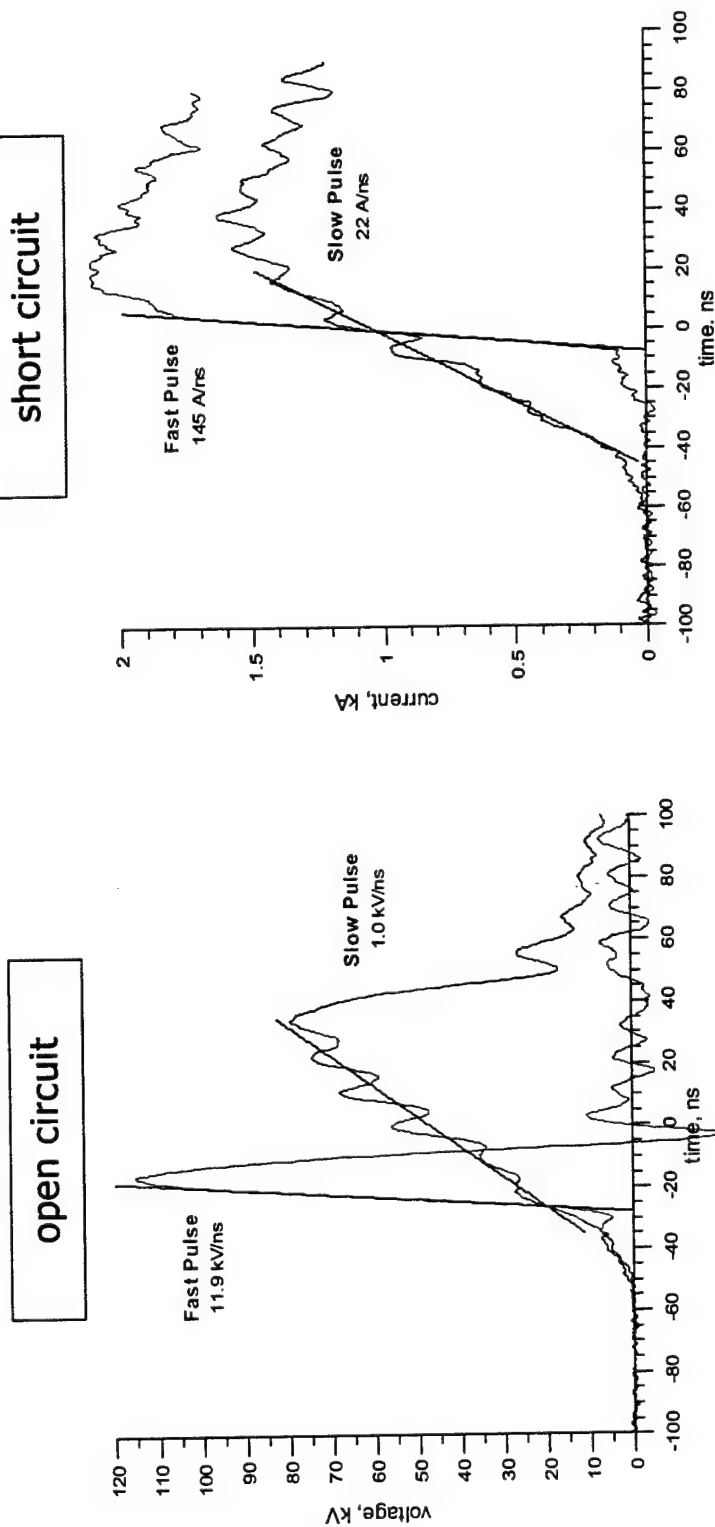
Experimental setup

N-7
T-7
Z-F



Fast & Slow regimes of wire explosion

N
T
F

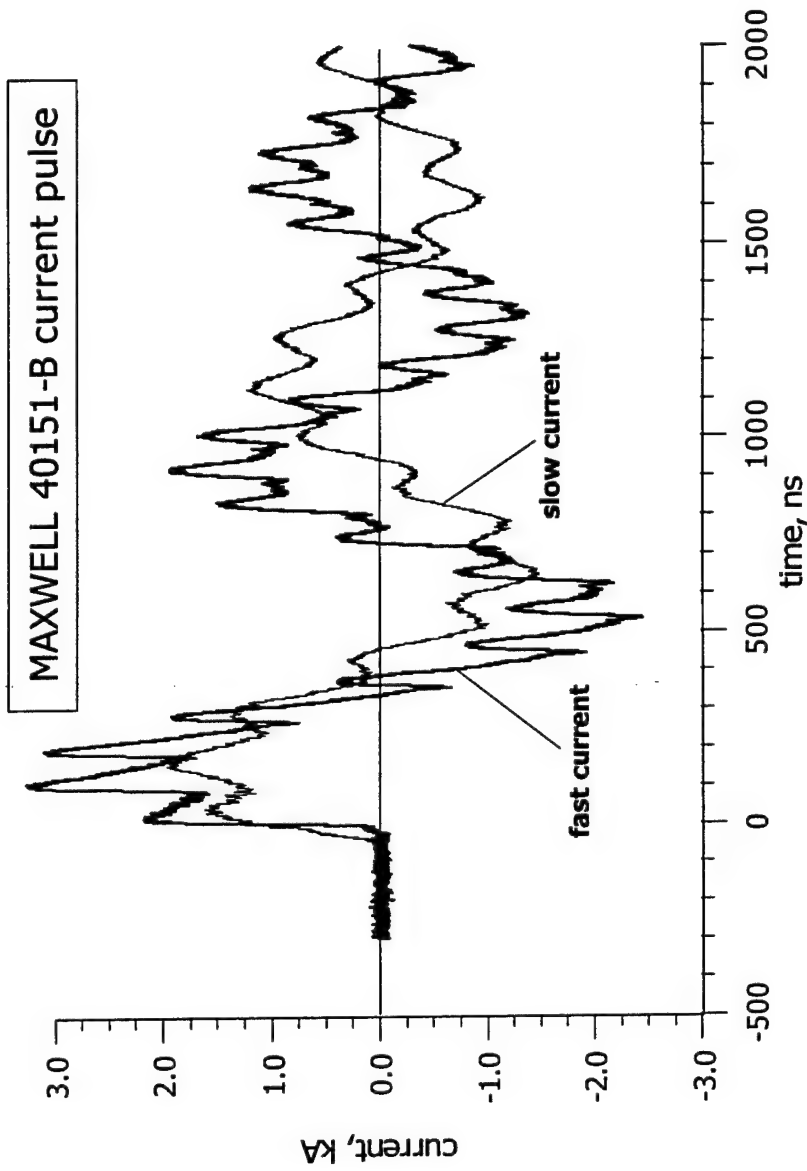


- MAXWELL 40151-B high voltage pulser test shorts



Fast & Slow current on short circuit

N
T
F

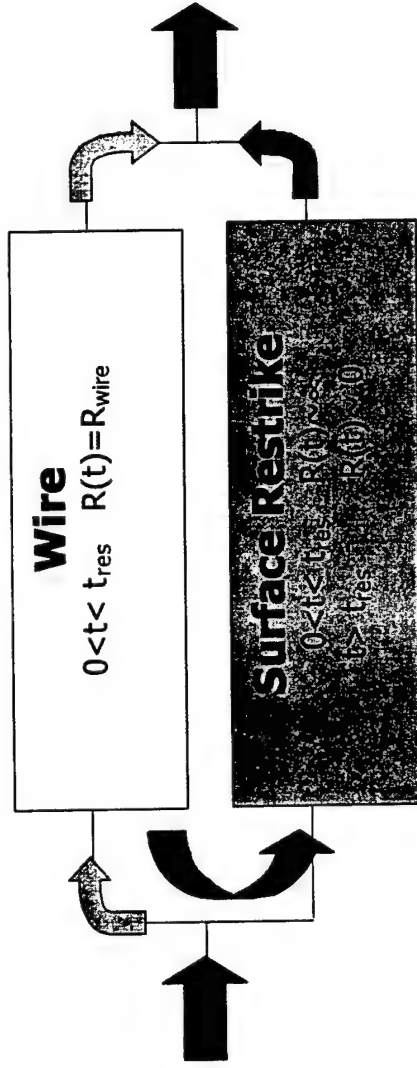


- Current pulsation due to reflection in a double length cable ($\sim 100\text{ns}$)



Two parallel resistors model for wire initiation

N-7
T-F



1. At $0 < t < t_{res}$ current flows through the wire (heating, phase transitions);
2. After $t > t_{res}$, due to surface restrike all current switches from the wire to the plasma shell;
3. After surface restrike wire heating is due to electron/radiation transport from surrounding hot plasma shell to the wire core;
4. Condition of the wire at the moment of the surface restrike dependent on wire substance and explosion mode.



Effect of Fast & Slow rate of energy deposition for tungsten wire

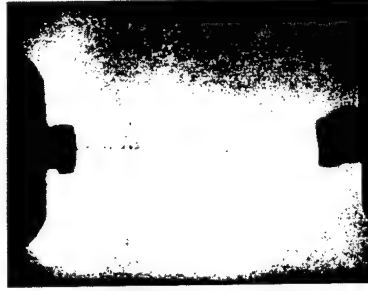
N₂
T
F

Slow explosion



During
explosion

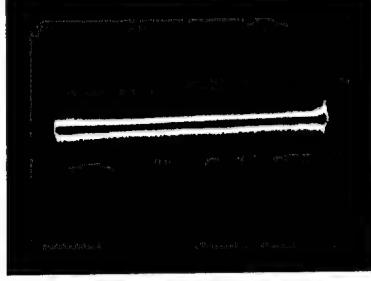
After
explosion



Poor energy deposition; Wire destroyed into parts; Rest of the wire remains at the same place; Vacuum arcing during negative period of pulse (+500ns)

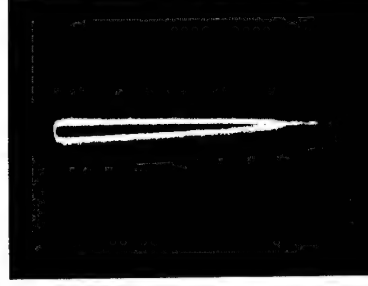


Fast explosion



1. Cylindrical Explosion
(homogeneous)

anode



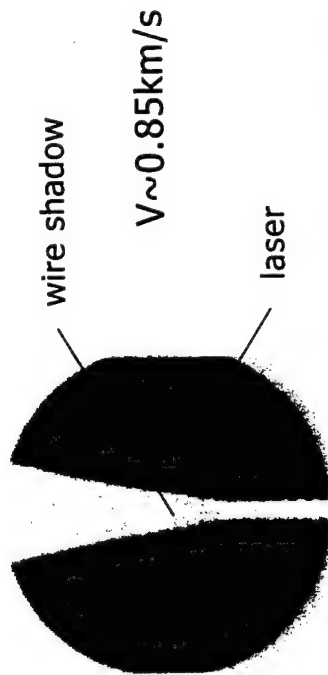
2. Conical Explosion
(non-homogeneous:
anode-better, cathode-
worse)

Good energy deposition; Wire totally vaporized; Expansion velocity ~1km/s; No arcing; Big light emission; Non stable to axial homogeneity of energy deposition

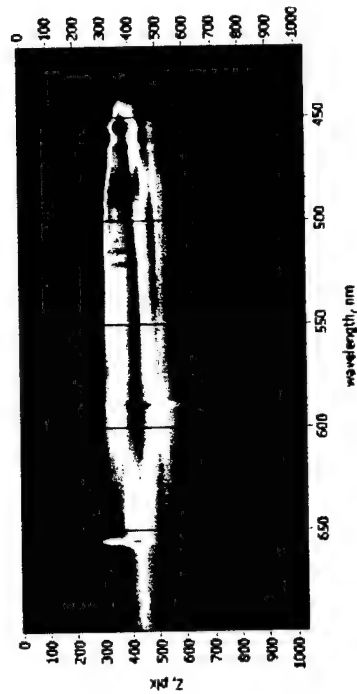
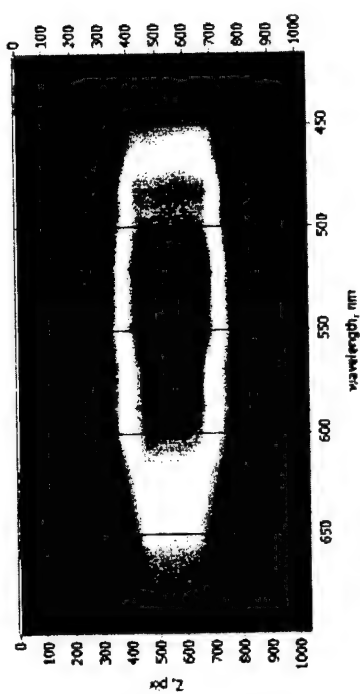
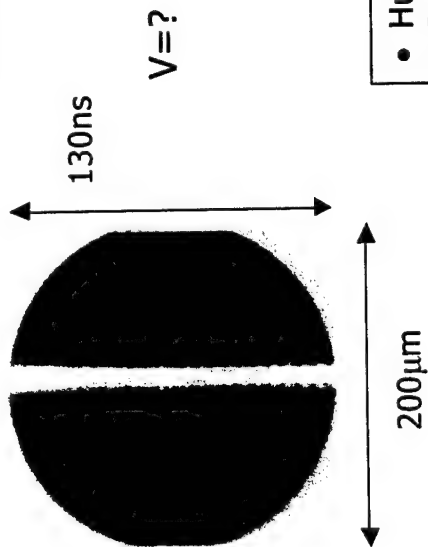
Explosion velocity & visible integral spectra for W wire explosion

N7
TF

Fast explosion



Slow explosion

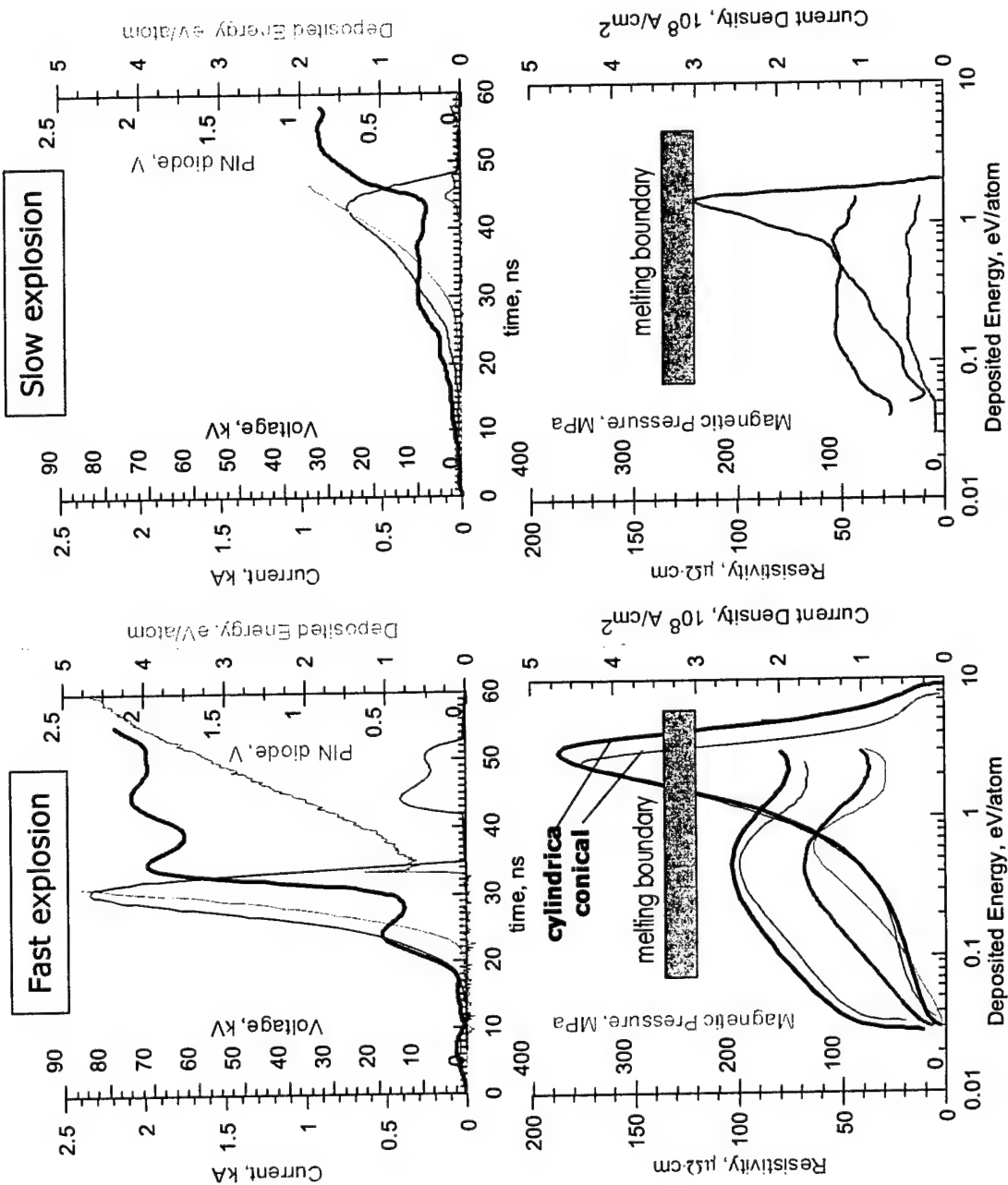


- Huge level of bremsstrahlung radiation for W wire explosion;
- In slow explosion wire survives or expanding with small velocity $\sim 0.1-0.2 \text{ km/s}$;



Reconstruction of explosion parameters for 16 μ m W wires

N-7
T-7
L-7
F



"Energy Deposition Barrier" for tungsten wire explosion

N7
TF

SOME CONCLUSIONS:

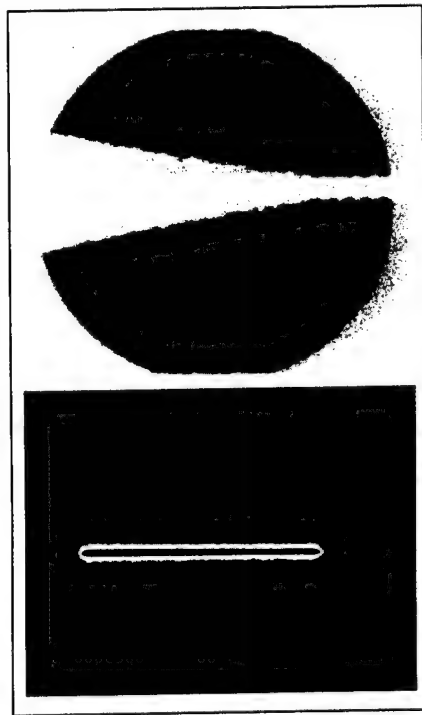
- In slow explosion mode ($dE/dt \sim 0.1(\text{eV/atom})/(\text{ns})$) current reswitches to surface restrike BEFORE MELTING ($120-135\mu\Omega\cdot\text{cm}$);
- It's because before the melting tungsten gives rise to ANOMALOUSLY HIGH ELECTRONIC EMISSION;
- This electronic emission plays important role in creation of surface restrike;
- Creation of hi-conductive plasma shell takes some finite time ($\sim 30-40\text{ns}$);
- Electronic emission creates some "energy deposition barrier" by reswitching current from the wire to the plasma shell before the wire melts;
- Vacuum arcing from non-melted wire to the ground happens during negative period of pulse, through the $\sim +500\text{ns}$ after current start.
- In fast explosion mode ($dE/dt \sim 0.7(\text{eV/atom})/(\text{ns})$) current reswitches to surface restrike AFTER MELTING;
- It happens because we deposit fast enough big enough value of energy before surface restrike reswitches the current;
- Wire resistivity before the expansion reaches value $\sim 185\mu\Omega\cdot\text{cm}$, that corresponds to plateau for normal density of W (SESAME table, M. Desjarlais, SNL);
- Tungsten temperature before the expansion reaches value $\sim 1\text{eV}$ (from SESAME);
- Wire expands after voltage collapse with velocity $\sim 1\text{km/s}$.



Explosion of the 16 μ m W wire coated with oil

N
T
F

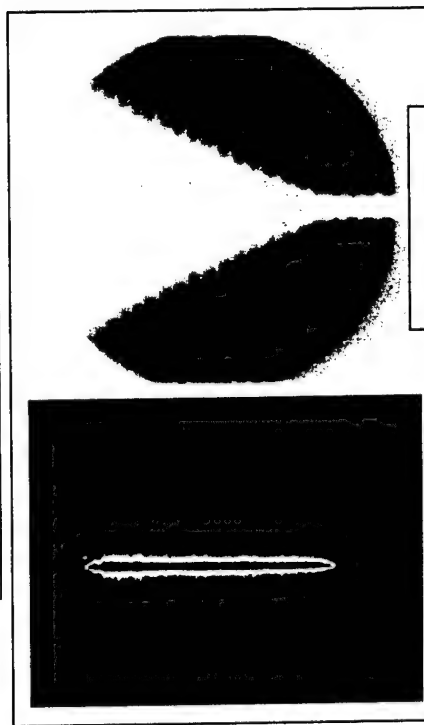
Clean wire



Fast

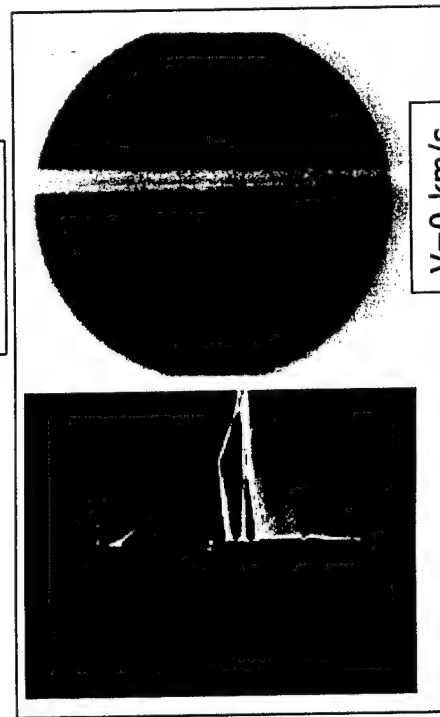
V=0.8 km/s

Coated with oil wire

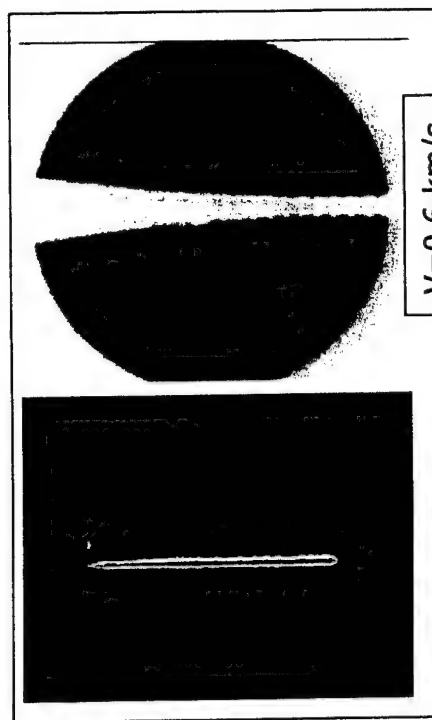


V=2.2 km/s

Slow



V=0 km/s



V=0.6 km/s



Explosion of the 16 μ m W wire in the air

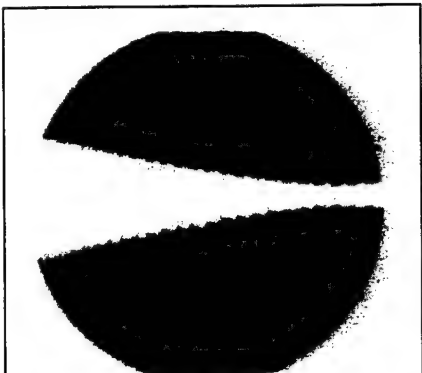
N7
T
F

In the air

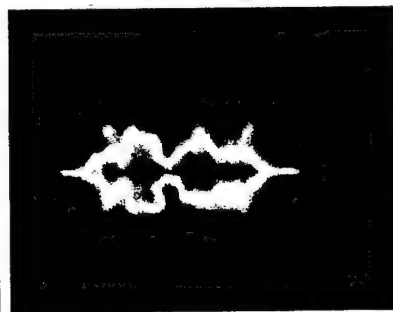
Fast



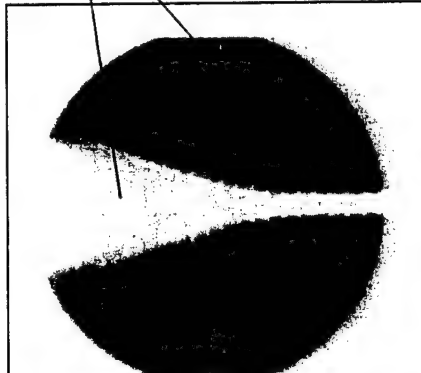
$V=0.9$ km/s



Slow

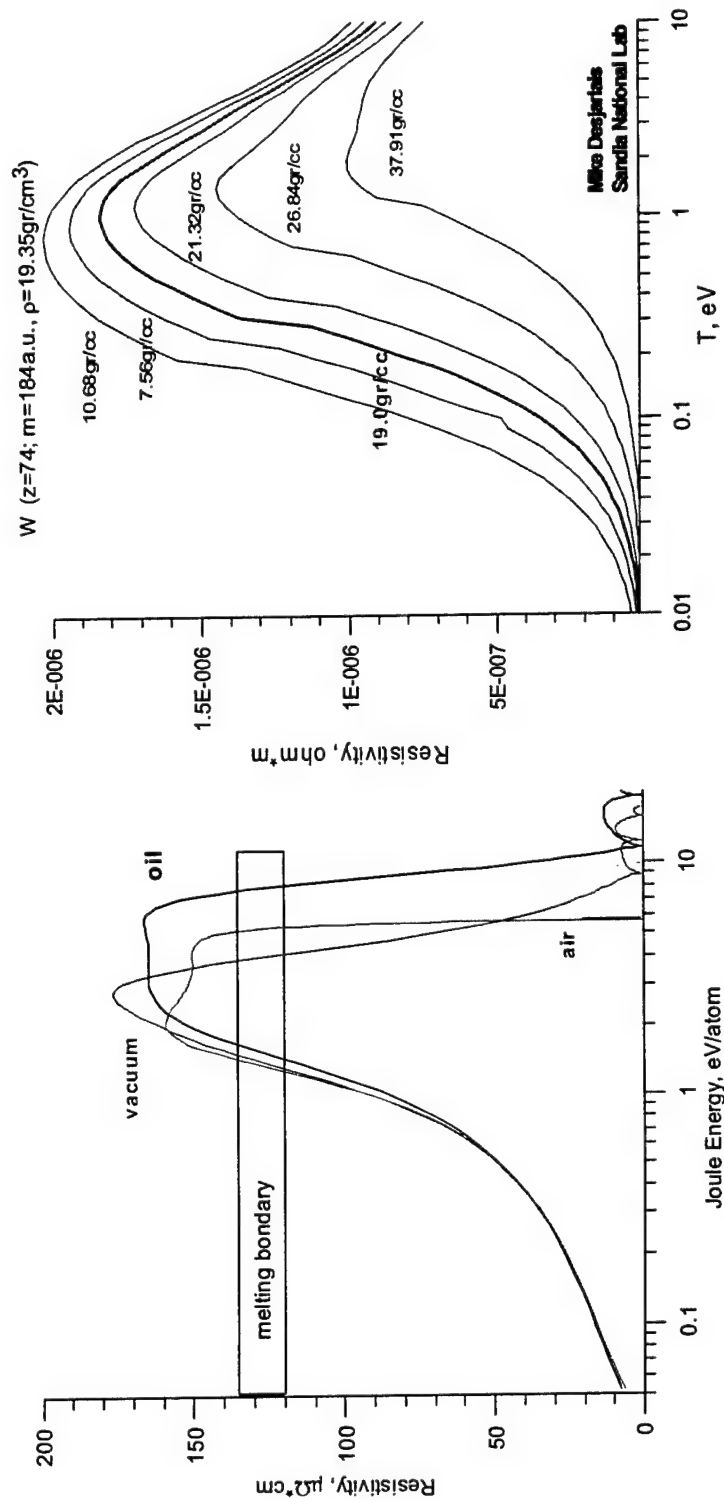


$V_w=1.3$ km/s
 $V_{shock}=12$ km/s
($M=40$)



Oil-coating and Air-explosion effects on 16μm W wire resistivity

N7
T-F



- Oil coating and explosion in the air results in depositing more energy into the wire before the surface restrike than in case of explosion of clear W in vacuum;
- At explosion in the air we observe generation of the strong shock-wave with $M \sim 40$.



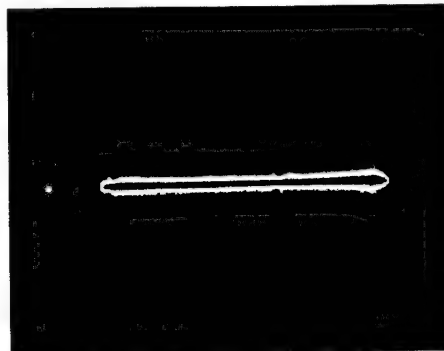
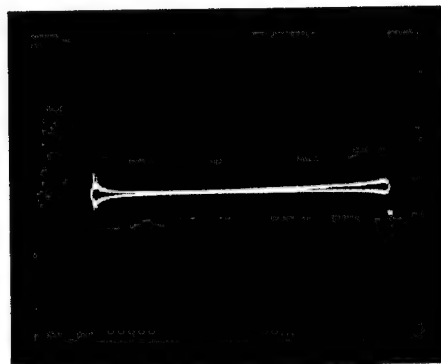
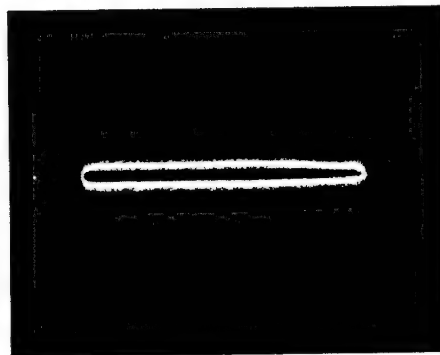
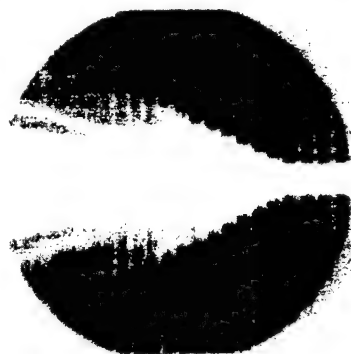
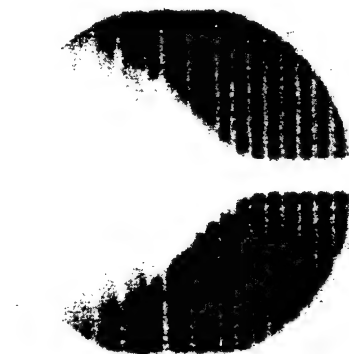
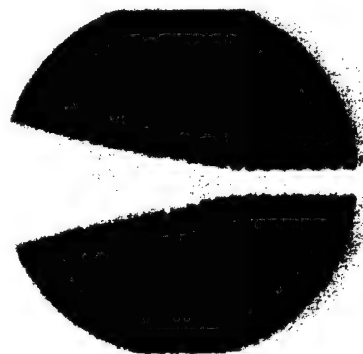
Fast explosion of the 20 μ m tungsten wire coated with 0.7 μ m of gold

N
T
F

Tungsten
1.1 km/s

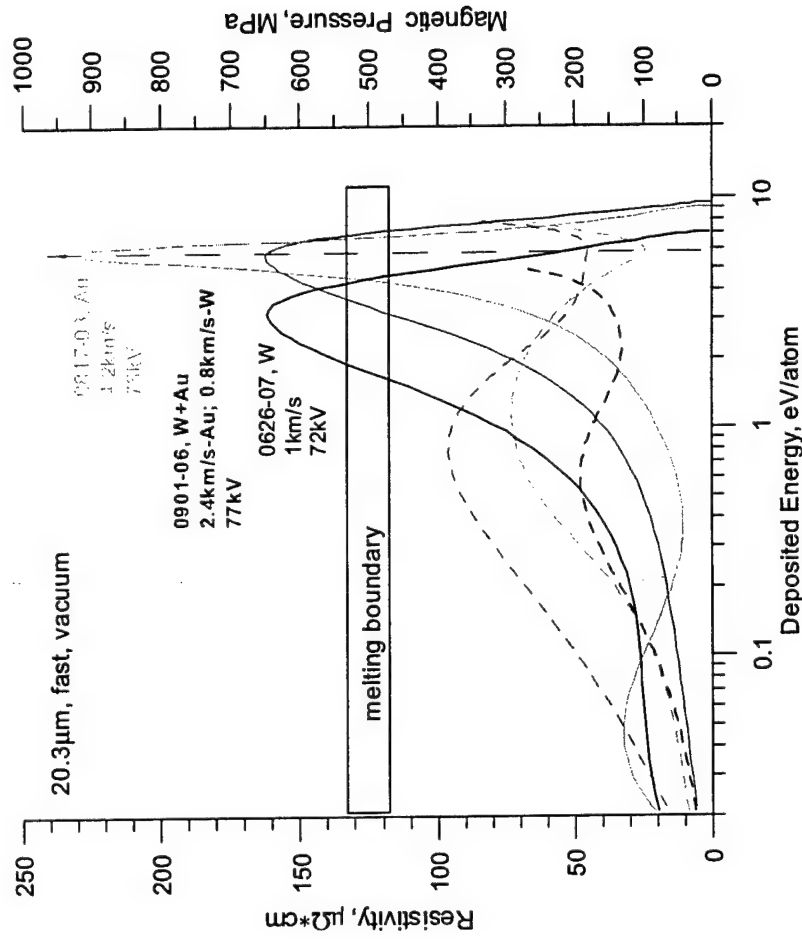
Gold
4.2km/s

Tungsten + Gold
0.8 km/s 2.4 km/s



Gold-coating effect on resistivity and energy absorption

N7
T
F

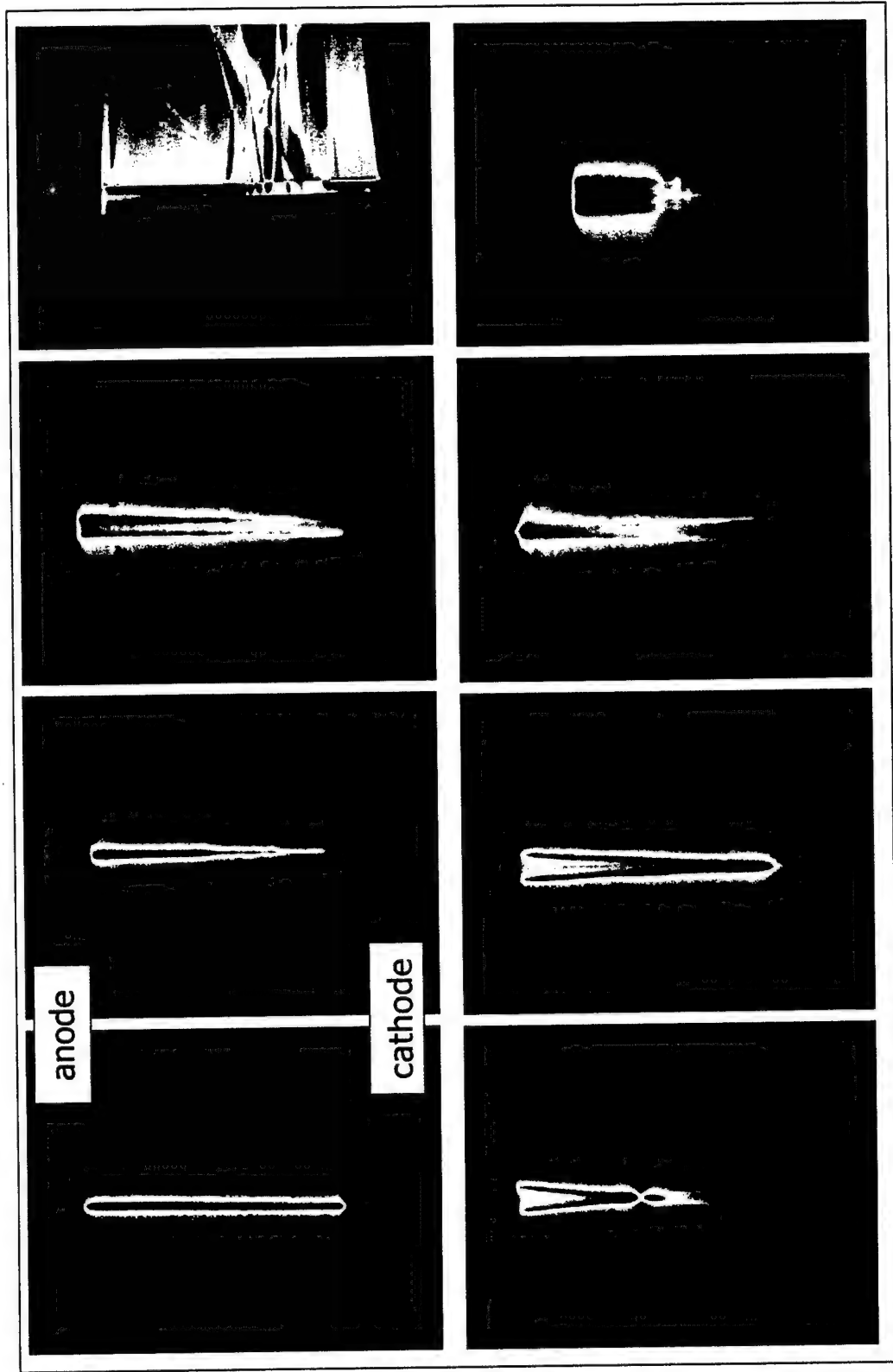


- Resistivity maximum for W+Au wire displaces to the bigger absorbed energy than clear W wire (~ 2 times more);
- The surface restrike for Au and W+Au wires starts under the same deposited energy $\sim 6 \text{ eV/atom}$.



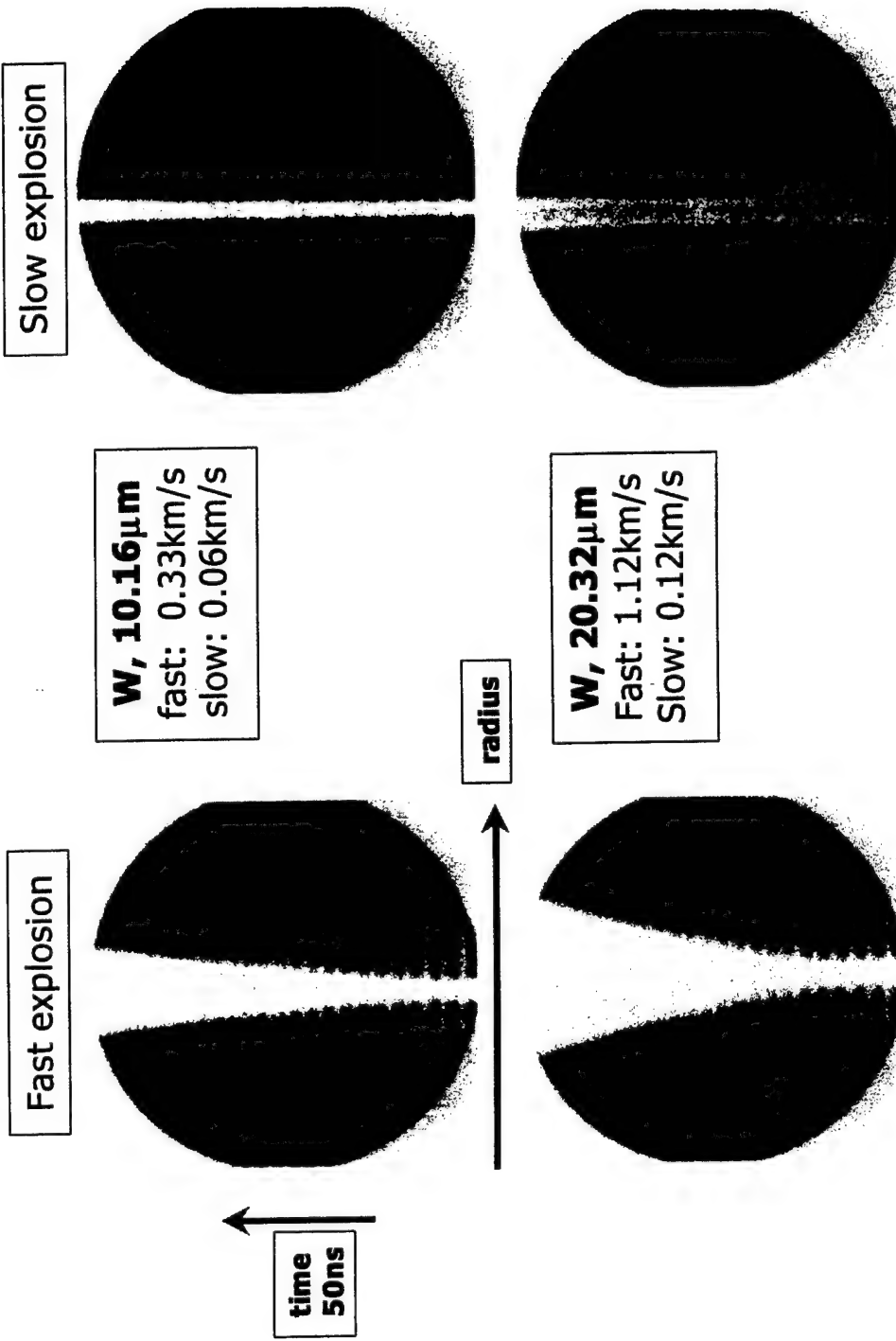
Homogeneity of energy deposition vs. target shape of for W wires

N7
TF



Streak camera images with laser back lighter for W wire

N
T
F



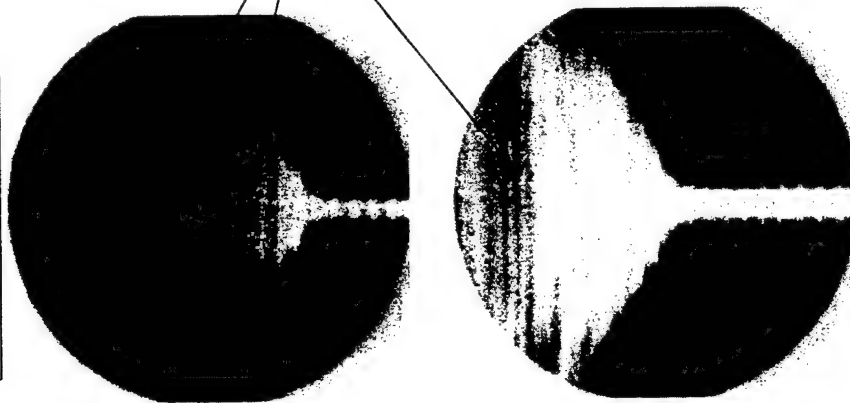
- Velocity of fast explosion dropping with decreasing wire diameter
- Velocity of the slow explosion ~ 10 times less
- Mo and Ti have the same behavior like W



Fast and slow explosion of Al wire

N-T
Z-F

Fast explosion



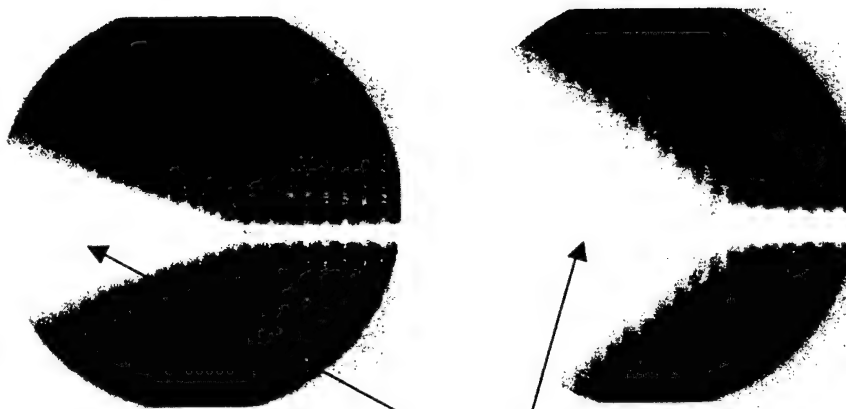
Al, 10.16 μ m
fast: 6.34km/s
slow: 1.61km/s

Plasma column
transparency

Non-transparent
cone

Al, 20.32 μ m
fast: 7.45km/s
slow: 3.47km/s

Slow explosion

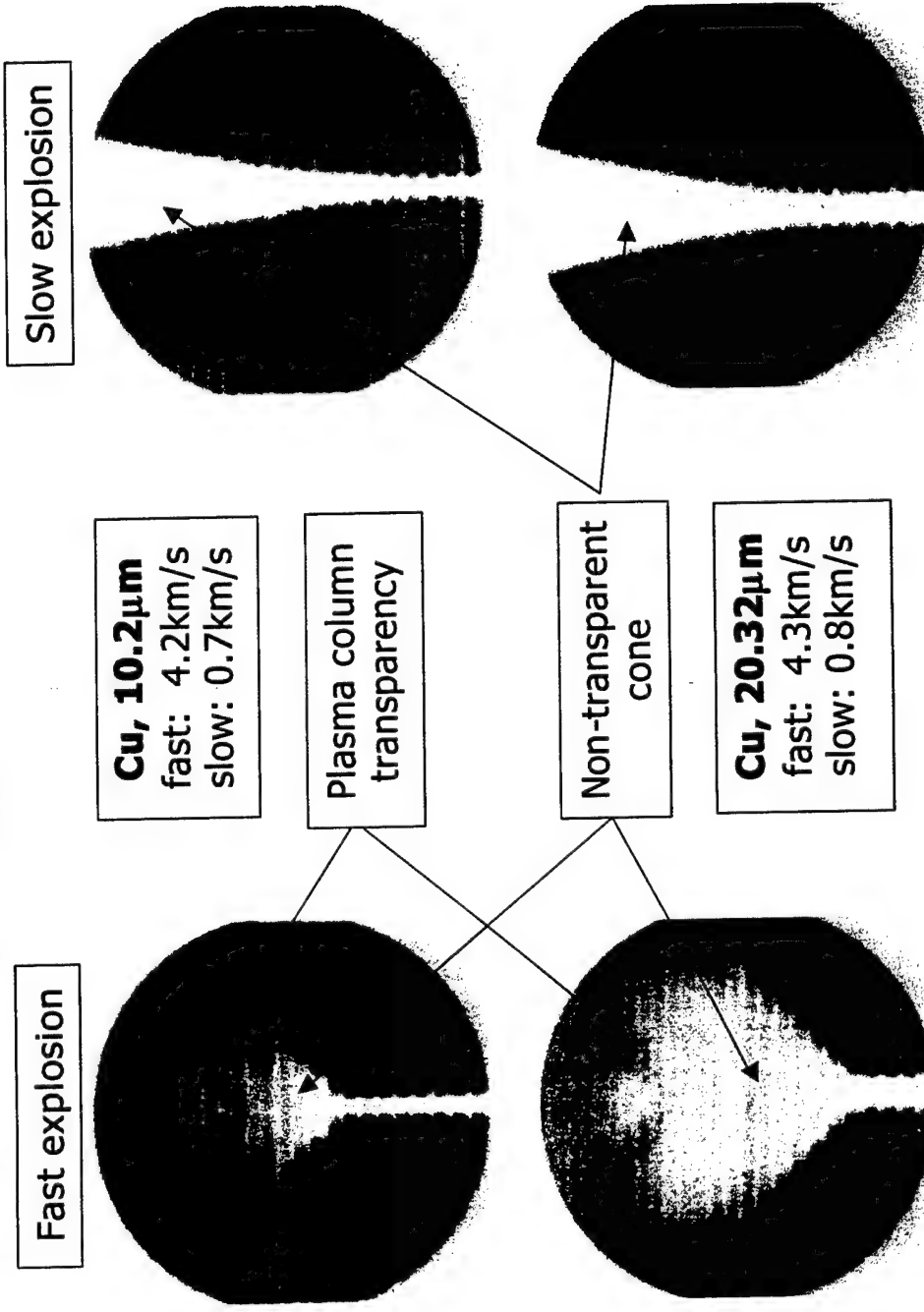


- Fast exploding 10 μ m Al becomes transparent in \sim 15ns after expansion starts
- Slow exploding Al remains non-transparent all observation time



Fast and slow explosion of Cu wire

N
T
F

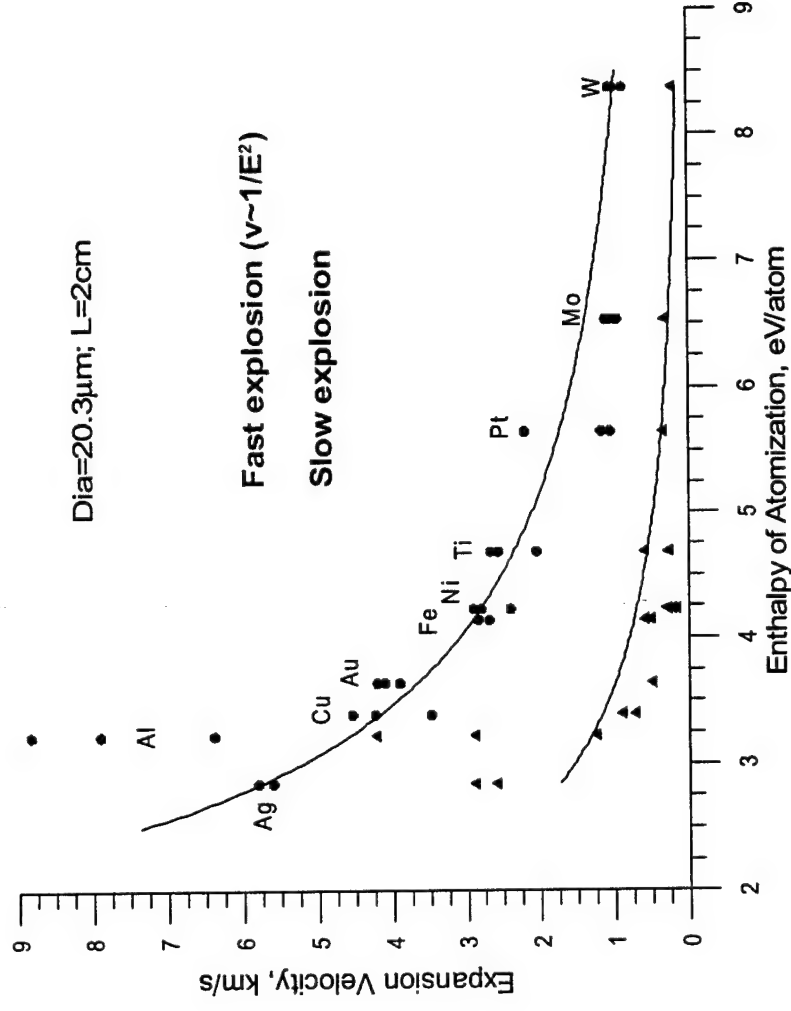


- Both Cu wire show the same explosion velocity
- Fast exploding 10 μ m Cu become transparent in first ~20ns after explosion start
- Slow exploding Cu remain non-transparent all observation time



Explosion velocity for different substances

N
I
F

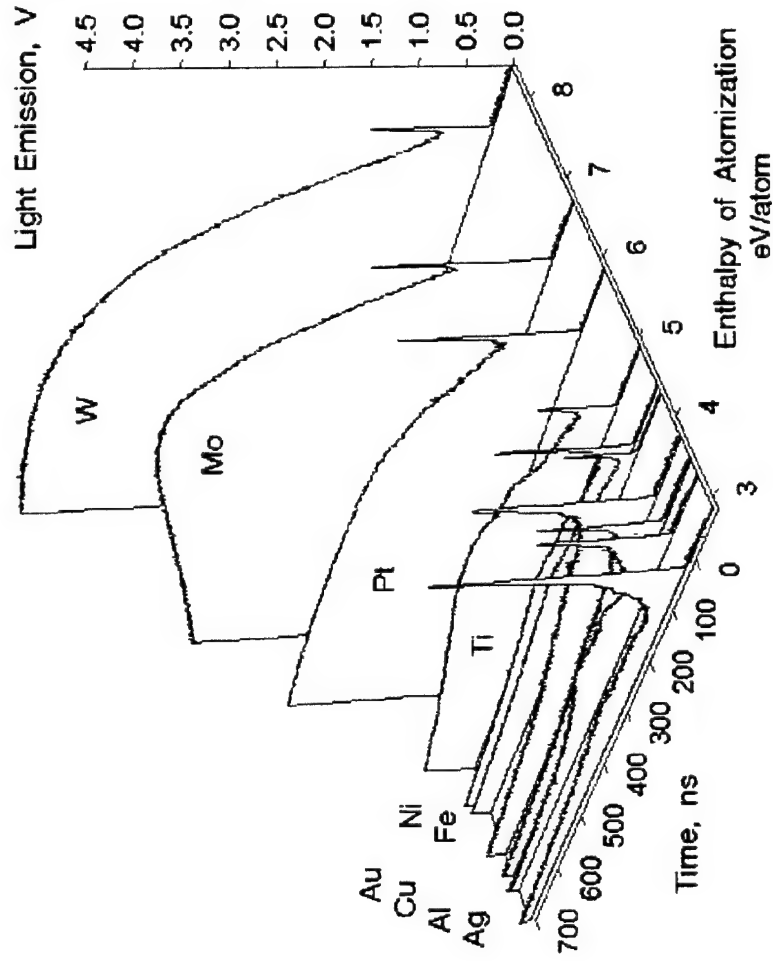


- Small atomization energy substances expand faster due to more joule energy absorbed before surface restrike;
- Slow explosion mode gives 2-4 times smaller expansion velocity;
- Al shows bigger velocity due to influence of dielectric Al_2O_3 coating on the surface;



Evolution of Light Emission vs Enthalpy of Atomization of Substance

N-T-F



- Systematical change of light emission shape has been found;
- Low atomization energy substances give wider first peak and lower following amplitude;
- Refractory metals give narrow first peak and bigger further light emission



Deposition energy structure vs. wire substances. Part 1

N₂
T
F

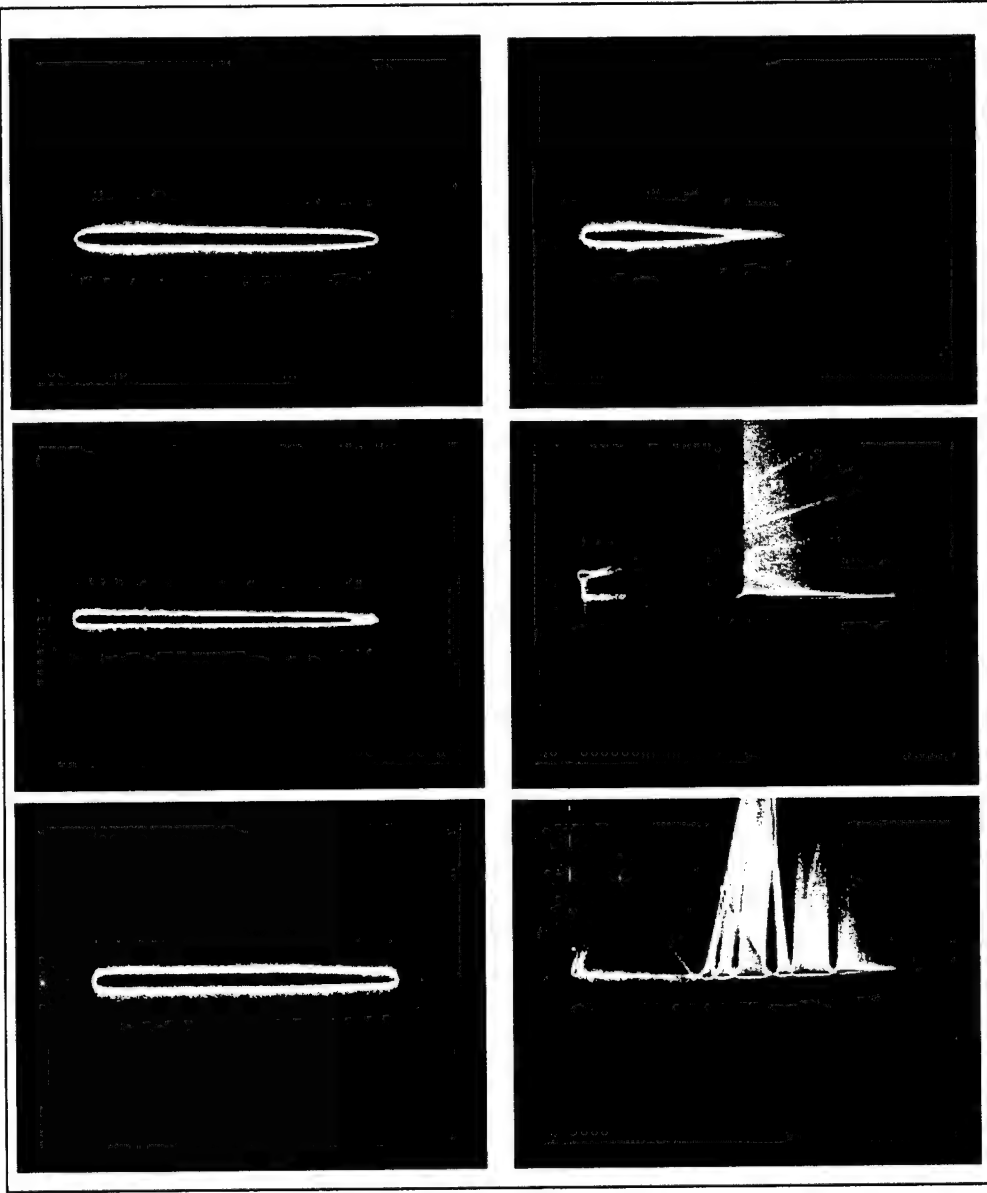
W (8.4eV/atom)

Mo (6.5eV/atom)

Pt (5.7eV/atom)

Fast

Slow



Deposition energy structure vs. wire substances. PART 2

N-T-F

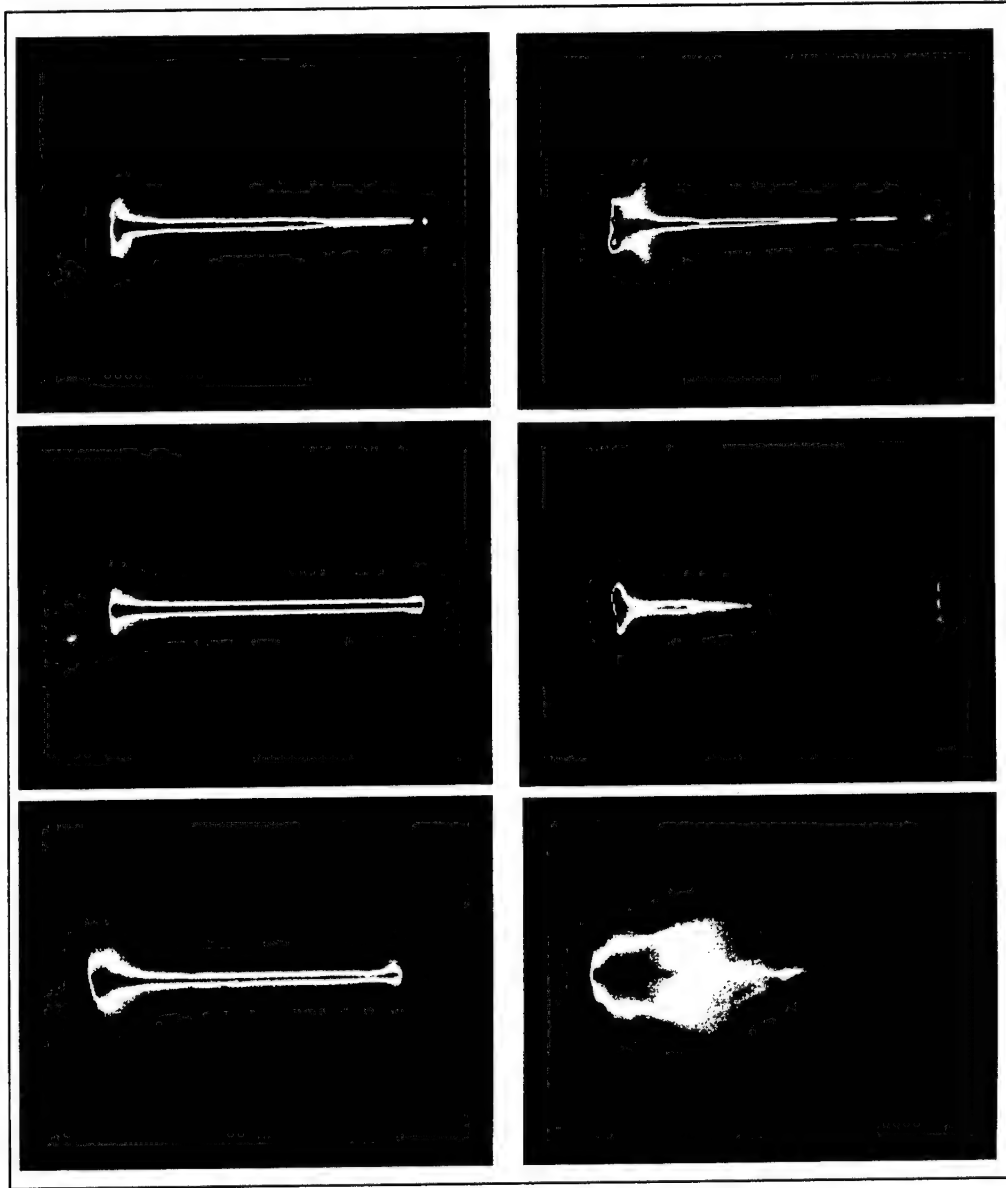
Ti (4.7eV/atom)

Ni (4.2eV/atom)

Fe (4.1eV/atom)

Fast

Slow



Deposition energy structure vs. wire substances. PART 3

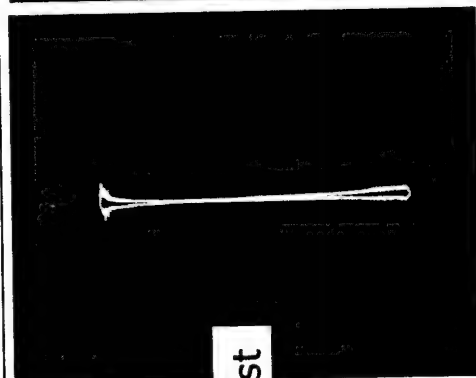
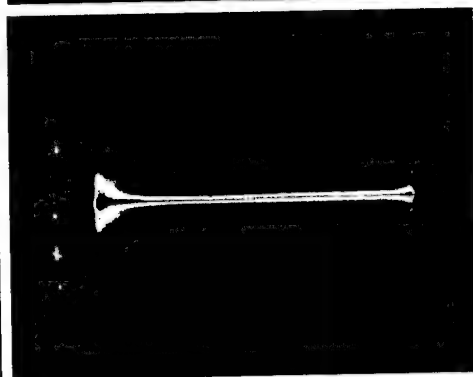
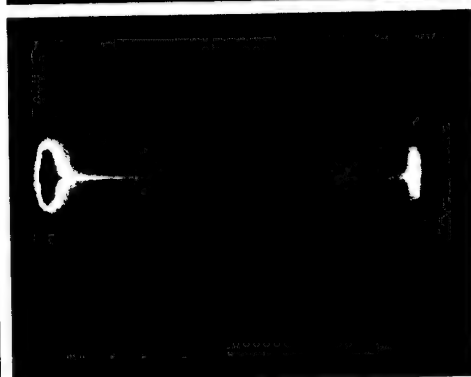
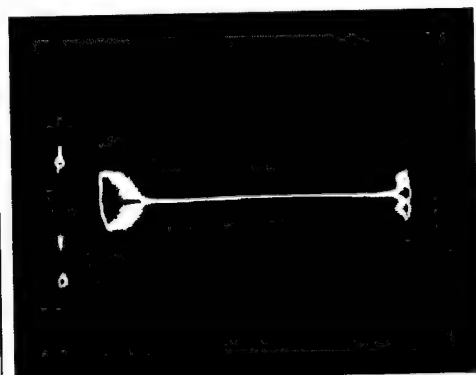
N
T
F

Ag (2.9eV/atom)

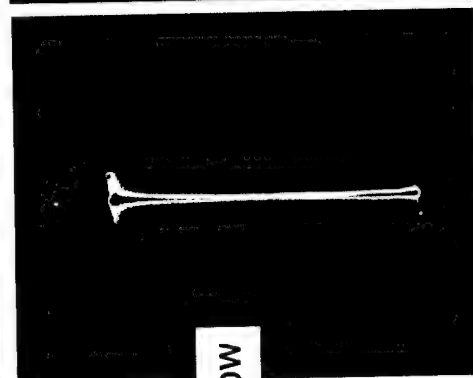
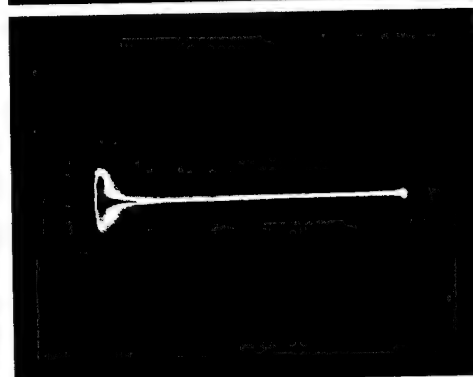
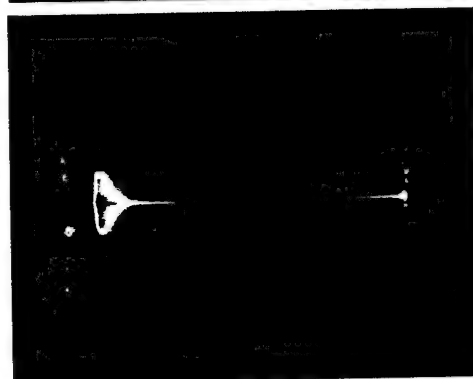
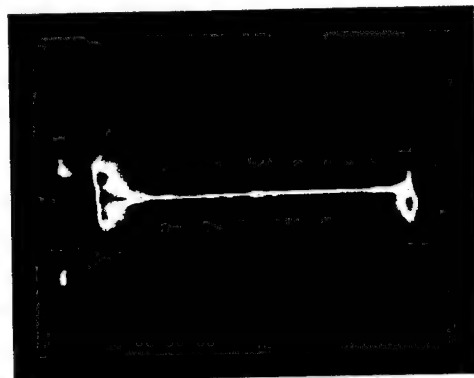
Al (3.2eV/atom)

Cu (3.4eV/atom)

Au (3.6eV/atom)



Fast

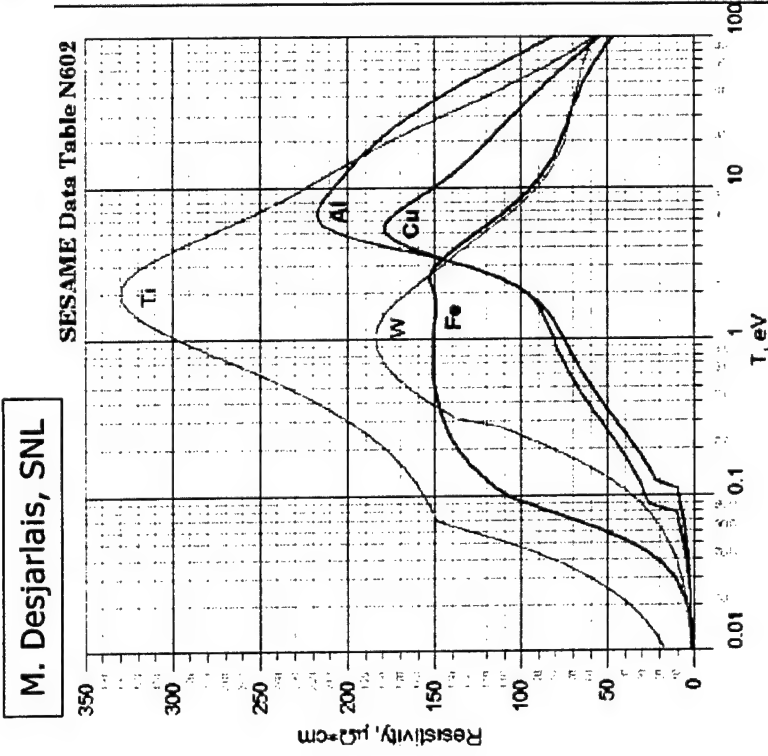
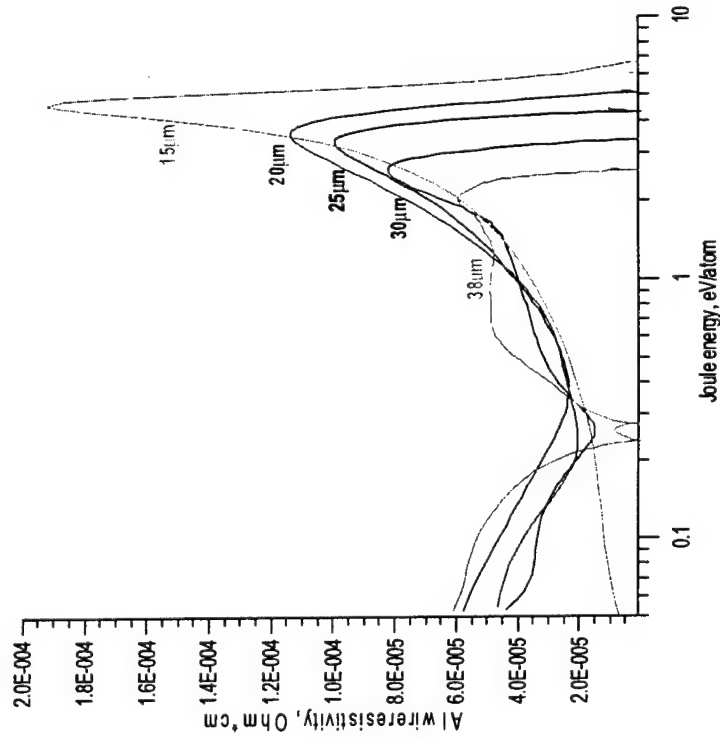


Slow



Resistivity for different diameters Al wires

N
T
F

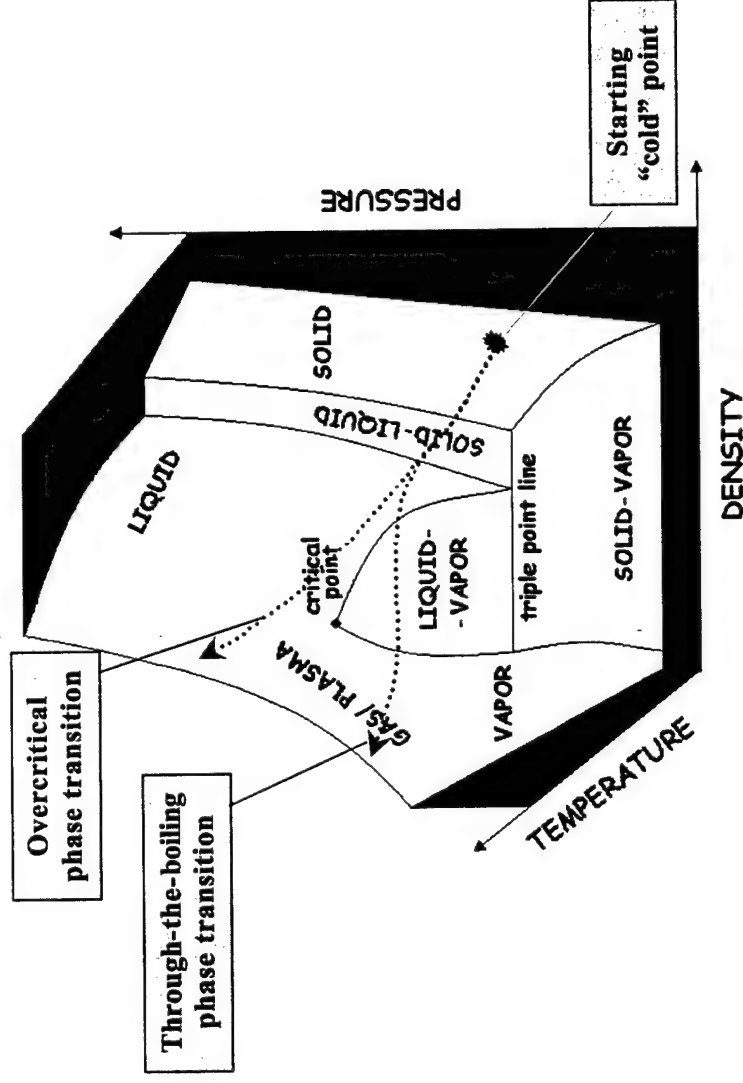


- Maximum resistivity is displaced into bigger absorption energy with decreasing wire diameter;
- Value of max resistivity increases with decreasing wire diameter;
- Small diameter wire collect more specific energy
- According to SESAME database 15mkm Al wire reaches temperature before the expansion ~5eV



3D Surface of Phase Transitions

N-7
T-F



- Slow explosion follows through the boiling to the gas-plasma stage, cold core is a main sign of this transition;
- In fast explosion ($P_{mf} > nkT$) wire reaches gas-plasma stage without phase separation (no boiling), no cold core inside, wire expands like gas volume;
- Overcritical explosion gives homogeneous gas-plasma column



APPENDIX G

Advanced X-Ray and Extreme Ultraviolet Diagnostics and First Applications to X-Pinch Plasma Experiments at the Nevada Terawatt Facility

V.L. Kantsyrev, B.S. Bauer, A.S. Shlyaptseva, D.A. Fedin,
S. Hansen, R. Presura, S. Batie, W. Brinsmead, H. Faretto,
B. Le Galloudec, A. Oxner, D. Chamberlain, N. Quart,
A. Jones, H. LeBeau, and M. Gharaibeh

Rev. Sci. Instrum. **72**, 663-666 (2001)

Advanced x-ray and extreme ultraviolet diagnostics and first applications to x-pinch plasma experiments at the Nevada Terawatt Facility

V. Kantsyrev,^{a)} B. Bauer, A. Shlyaptseva, D. Fedin, S. Hansen, R. Presura,^{b)} S. Batie, W. Brinsmead, H. Fareto, B. Le Galloudec, A. Oxner, D. Chamberlain, N. Ouart, A. Jones, H. LeBeau, and M. Gharaibeh

Department of Physics, University of Nevada, Reno, Nevada 89557-0058

(Presented on 20 June 2000)

A wide variety of x-ray and extreme ultraviolet (EUV) diagnostics are being developed to study z-pinch plasmas at the Nevada Terawatt Facility at the University of Nevada, Reno. Time-resolved x-ray/EUV imaging and spectroscopy, x-ray polarization spectroscopy, and backlighting will be employed to measure profiles of plasma temperature, density, flow, and charge state, and to investigate electron distribution functions and magnetic fields. The instruments are state-of-the-art applications of glass capillary converters (GCC), multilayer mirrors (MLM), and crystals. New devices include: a novel GCC-based two-dimensional imaging spectrometer, a six-channel crystal/MLM spectrometer ("polychromator") with a transmission grating spectrometer, and two sets of x-ray/EUV polarimeters/spectrometers. An x-pinch backlighter is under development. X-ray polarimeter/spectrometer, a survey spectrometer, a multichannel time-gated x-ray pinhole camera, and filtered fast x-ray diodes have observed the structure of Ti and Fe x pinches driven by a 0.9 MA current. X-ray yield and pulse duration depend sensitively on the wire load. © 2001 American Institute of Physics. [DOI: 10.1063/1.1315646]

I. INTRODUCTION

The core of the Nevada Terawatt Facility (NTF) is Zebra, a z-pinch machine with a maximum voltage of 2 MV, a maximum current of 1.2 MA, a rise time of 100 ns, a maximum stored energy of 200 kJ, a 1.9 Ω pulse-forming line impedance, and a repetition-rate of up to seven shots per day, known formerly as HDZP-II at Los Alamos National Laboratory. New x-ray and extreme ultraviolet (EUV) diagnostics on Zebra are based on the use of crystals in conjunction with glass capillary converters (GCCs) and multilayer mirrors (MLMs). The GCCs consisting of glass or quartz capillaries collect, guide, focus, filter, and polarize a wide spectrum of x-ray/EUV radiation.¹ The MLMs and crystals are used for dispersing, focusing, and polarizing of a narrow bandwidth of radiation. The NTF x-ray diagnostics (Fig. 1) include six vacuum beamlines with x-ray diagnostic devices. Each vacuum beamline has strong permanent magnets to protect x-ray devices against damage from z-pinch ion beams. X-ray/EUV diagnostics include polarimeter/spectrometers, a survey spectrometer, a multichannel time-gated pinhole camera (MPHC), filtered fast x-ray diodes, a GCC-based two-dimensional (2D) imaging spectrometer, and a six-channel "polychromator." The last two devices are described in detail in the next section. The MPHC (Fig. 1) has been constructed around a six-gold-stripline, 0.1–0.2 ns gated MCP detector from Sandia National Laboratories (SNL). The spatial resolution is 100 μm , the magnification is 0.5, and the distance from the plasma is 70 cm. X-ray polarization-sensitive imaging spectrometers (XPSIS) employ two identical spectrometers² registering spectra in one direction with

different orientation of dispersion planes with respect to the z-pinch discharge axis: one perpendicular and another parallel to the axis. The XPSIS is used in x-ray spectropolarimetry, which is a new powerful method for study of energetic electron distribution functions and magnetic fields.³ Two one-dimensional polarimeter/spectrometers with convex crystals registered polarization-sensitive K- and L-shell spectra produced by Ti x-pinch plasmas at the NTF.^{1–3}

II. NEW NTF X-RAY AND EUV DIAGNOSTICS

A. Novel two-dimensional x-ray imaging capillary spectrometer (2DXIS)

Space and time-resolution for hot z-pinch or laser plasma spectroscopy are essential, as these plasmas contain strong gradients and evolve rapidly. An entire 2D monochromatic plasma image must be captured on each shot. These criteria are not simultaneously satisfied by current spectroscopic methods. A spatial resolution of better than 5–10 μm is achieved now, but for z pinch, the distortion of the image increases up to 50–100 μm for plasma 20–50 mm in length.⁴ However, glass capillaries offer a way to break up and manipulate an x-ray image for spectroscopic analysis.¹ The 2D imaging capillary spectrometer (2DXIS) consists of the entrance pinhole imaging camera for experiments with Sandia National Laboratories Z machine (or imaging x-ray mirror for the NTF scale machines), the 80–100 of individual glass capillary channels, a joint crystal, and a time-gated imaging detector (Fig. 2). The GCC multiplex transforms a 2D image of the plasma into an output array of spatially separated pixels. Cross talk between pixels is prevented by using a separating of pixels with plate sheets (optical insulator). The output x-ray beams array is then spectrally dispersed by a crystal or a MLM, recorded by a MCP imager. The result is

^{a)}Electronic mail: victor@physics.unr.edu

^{b)}On leave from N.I.L.P.R.P., Bucharest, Romania.

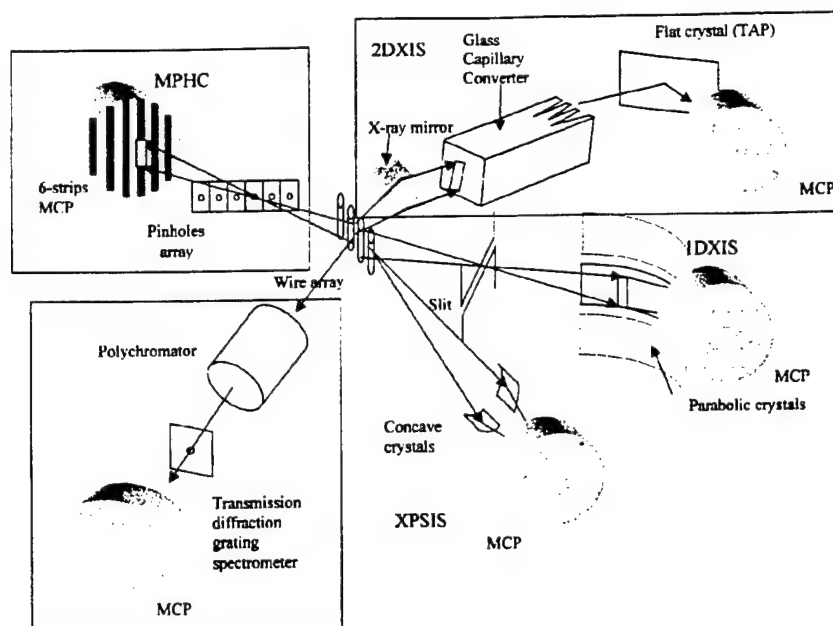


FIG. 1. Scheme of new x-ray and EUV diagnostics at the NTF. 2DXIS: the two-dimensional EUV and x-ray imaging spectrometer with glass capillary optic and a MCP time-gated multistrip imager. This device can be converted to a one-dimensional time-resolved x-ray spectrometer by removing the GCC and installing an imaging slit between a plasma and a crystal (MLM). MPHC, the multichannel x-ray pinhole camera with a MCP time-gated multistrip imager. Polychromator: the five-channel time-resolved crystal (MLM) spectrometer with an additional transmission grating spectrometer channel. XPSIS: the x-ray polarization-sensitive imaging spectrometer. Modification of the device with crossed-placed concave focusing crystals is shown. 1DXIS: the proposed one-dimensional x-ray imaging spectrometer with a set of parabolic crystals for study of z pinches with large dimensions.

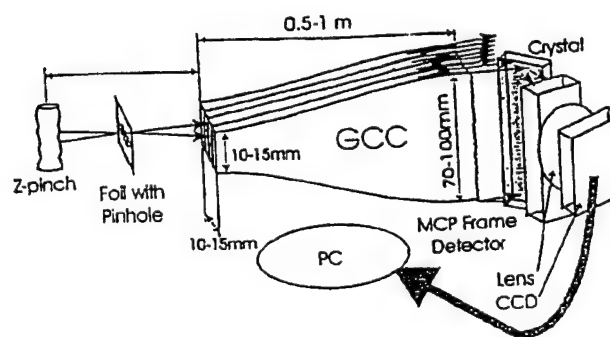
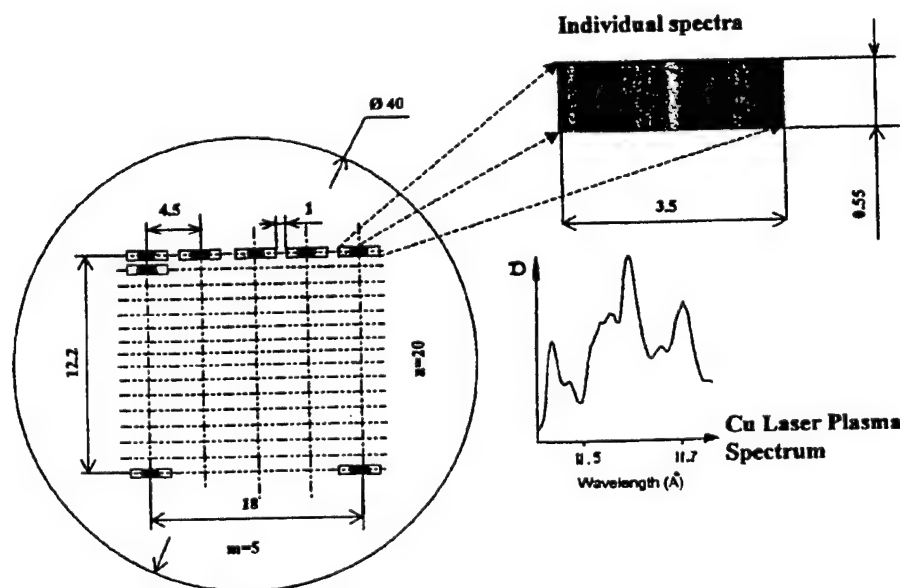


FIG. 2. Two-dimensional EUV/x-ray imaging spectrometer (2DXIS) decomposes an image into pixels, separates, and spectrally disperses these pixels, and records the spectra with a time-gated MCP intensifier.

a time-gated x-ray spectrum for each plasma image point (Fig. 3). The measured spectra, in conjunction with theory and computer modeling, yield two-dimensional maps of important plasma parameters. The distribution of output radiation from an individual capillary with an internal polycapillary structure is much more uniform than that from a simple hollow capillary. The 2DXIS was tested with the NTF laser plasma x-ray calibration facility. A comparison of parameters of a 2DXIS with traditional 2D spectrographs (2DS) with spherically curved crystals^{4,5} for z-pinch study follows. Spectral, spatial, and time resolutions for 2DXIS and 2DS are the same: 800–1000, 100–250 μm , and 1–2 ns, respectively. But, a number of output individual spectra are much bigger for 2DXIS: 80–100 compared with the one



All dimensions are in millimeters.

FIG. 3. Output of the time-gated MCP imager of the 2DXIS. On the right, one of the individual experimental x-ray spectra of Ne-like ions of Cu laser plasma and its densitogram are seen. The laser-plasma x-ray source at the x-ray diagnostics developing laboratory of the NTF was applied to the tests of 2DXIS.

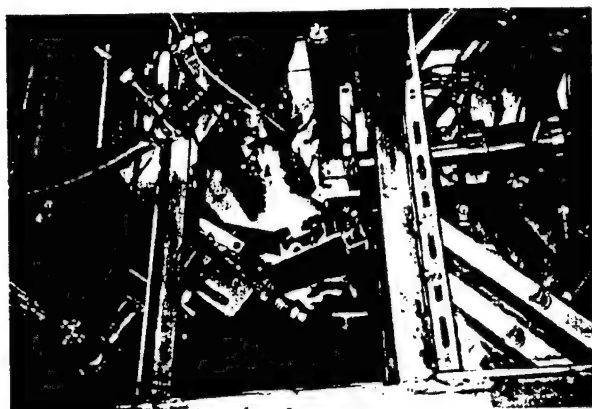


FIG. 4. 2DXIS is prepared for experiments at the NTF (view from the top). At the right, the diagnostics beamlines with bellows and protection magnets are seen. In the center the main vacuum chamber of 2DXIS is shown with a turbopump and an x-ray MCP time-gated multistrip imager. At the left, the screened electronic supply and a part of the MCP vacuum system are seen.

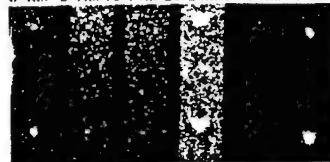
for 2DS. The wavelength observation band $\Delta\lambda$ near the central wavelength λ for a single-shot exposure is better for 2DXIS: $\lambda/10$ – $\lambda/20$ vs $\lambda/25$ – $\lambda/50$ for 2DS. From theoretical estimation of sensitivity of a 2DXIS and experiments with a laser-plasma source (Fig. 3) and the NTF (Fig. 4) it was found, that 2DXIS could be applied to study a z-pinch plasma produced by powerful facilities (SNL-Z scale) during a single shot, even for registering spectroscopic dopant line radiation in plasma with dopant concentration of 10%.

B. Six-channel spectrometer "polychromator"

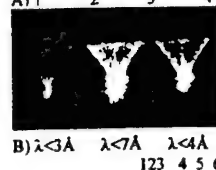
A new six-channel spectrometer (Fig. 1) is designed for registration of x-ray spectral line emission from plasmas with temporal resolution. The device has five channels with fast Si or PCD x-ray detectors and crystals or MLMs. For measurements with spatial and time-gated resolution, a sixth channel with a transmission diffraction grating spectrometer (TGS) and a gated MCP imager are added. Crystal channels record radiation in a wide spectral region from 0.1 to 2.5 nm. EUV radiation has been studied with MLMs. The polychromator characteristics are: spectral regions: 0.1–5.0 nm (three crystal channels and the first MLM channel) and 12.0–24.0 nm (the second MLM channel); spectral resolution: 400–600; time resolution 0.2–0.5 ns. All channels are independent from each other, providing an opportunity to set the particular spectral region for each channel. Adjustment is made by means of a precision linear translation stage for each channel without disturbing the vacuum conditions. The sixth channel (TGS with a gold pinhole transmission diffraction grating) was designed for registration of radiation in a region of 2.0–8.0 nm. Our TGS is designed to work with both an x-ray film and a MCP imager. The TGS spectral resolution is 40–50; the spatial resolution is 150 μm ; the time resolution of the MCP gated imager is 1–2 ns.

Ti x-pinch SHOT#30 (May 18, 2000)

0–4ns 5–9ns 10–14ns 20–24ns 30–34ns 40–44ns (Anode)



Top image $\lambda < 3.5\text{\AA}$
Lower image $\lambda < 5\text{\AA}$



12mm

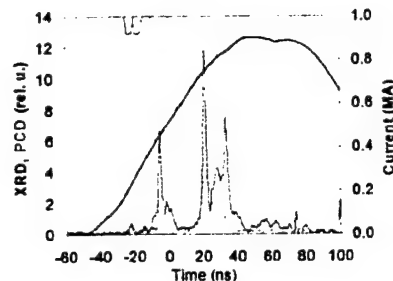


FIG. 5. Ti x-pinch (diameter of wires: 30 μm ; gap, anode–cathode 20 mm) images are at the top; time dependence of an x-pinch current, PCD (8 μm Be filter) and XRD (5 μm Kimfoil filter) diode signals, and time position of frames of a multichannel time-gated x-ray pinhole camera (MPHC) are at the bottom. Time positions of frames are marked 1–6, both on the top images and the bottom of the figure. (a) MPHC time-resolved images, spatial resolution is 100 μm , the anode is on the top of each row of images. (b) Time-integrated multichannel pinhole camera images [the same field of view as on (a)], spatial resolution is 580 μm , the anode is on the top (Kodak DEF-5 x-ray film).

III. EXPERIMENTAL STUDY OF THE HIGH-CURRENT X-PINCH X-RAY SOURCE

Ti and Fe x pinches are being driven on Zebra with high current ($I \geq 900$ kA) and are being investigated with new x-ray diagnostics. The long-term goals of these experiments are: (a) to develop a new (harder) x-ray backlighting source to determine a plasma density profile; (b) to understand the final stage of the z-pinch magnetohydrodynamics (MHD) sausage ($m=0$) instability, when an x pinch turns into a minidiode; (c) to test x-ray spectropolarimetry, a powerful new tool for studying the anisotropy of high-temperature plasmas. Most early experiments were conducted with current smaller than 0.2–0.4 MA and with a wide variety of materials: from Al to Pd.⁶ Only Al x pinch was studied with current near 1 MA.⁷ It was shown that an x pinch could be used as an x-ray source in both the main x-ray optical schemes of backlighting: a monochromatic and direct point-source schemes.⁷ The NTF Ti and Fe x pinches at 0.9 MA yield a bright, nanosecond-duration K-shell x-ray burst from a small bright spot at the intersection of the crossed thin wires. MPHC and XPSIS have been used for the first time for study of x pinches. Time-integrated pinhole cameras also were applied, as well as a survey of convex LiF crystal spectrometer (spectral resolution 700–800), and XPSIS. An array of fast (0.2 ns resolution) filtered diodes were used for mea-

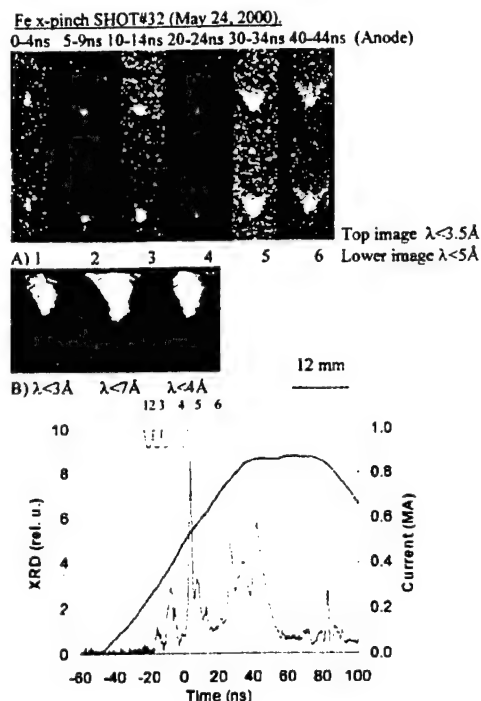


FIG. 6. Fe x-pinch (diameter of wires: $19\text{ }\mu\text{m}$, gap, anode-cathode 20 mm) images are at the top, and time dependence of the x-pinch current, XRD ($5\text{ }\mu\text{m}$ Kimfoil filter) diode signal, and time position of frames of a multichannel time-gated x-ray pinhole camera (MPHC) are at the bottom. Time positions of frames are marked as 1–6, both on the top images and the bottom of the figure. (a) MPHC time-resolved images, spatial resolution is $100\text{ }\mu\text{m}$, the anode is on the top of each row of images. (b) Time-integrated multichannel pinhole camera images [the same field of view as on (A)], spatial resolution is $580\text{ }\mu\text{m}$, the anode is on the top (Kodak DEF-5 x-ray film).

suring of *K*-shell photoconducting diode (PCD) and *L*-shell x-ray radiation diode (XRD) radiation output. The total energy irradiated by plasma in a region from EUV to several keV x rays has been measured with a Ni bolometer from SNL. The main results of the first NTF experiments with Ti and Fe x pinches are as follows.

(1) In Ti spectra, radiation of He-like and H-like ions dominates (for Fe only He-like ions were observed), $T_e \leq 2.4\text{ keV}$, and Ti He-like radiation is polarized.^{1–3} For the Ti x pinch, the *K*-shell radiation output reached $30\text{--}50\text{ J}$ in $2\text{--}4$ x-ray bursts with durations for each of $1.8\text{--}2.5\text{ ns}$, and the *L*-shell consists of $2\text{--}5$ pulses with a total energy of $3\text{--}4.5\text{ kJ}$ (Figs. 5 and 6). The duration of each *L*-shell x-ray burst was $3\text{--}5\text{ ns}$. The total EUV/x-ray energy emitted by a Ti high current x pinch was $7\text{--}9\text{ kJ}$. All these parameters are approximately in $5\text{--}10$ times bigger than a x-ray output of a low current Ti x pinch.⁶ X-ray bursts appear before the current reaches the maximum (Figs. 5 and 6). Most of these pulses form two groups into intervals of $30\text{--}45$ and $60\text{--}80\text{ ns}$ after the current is initiated.

(2) It was found that the structure of x pinches under a high current is more complicated in comparison with a low

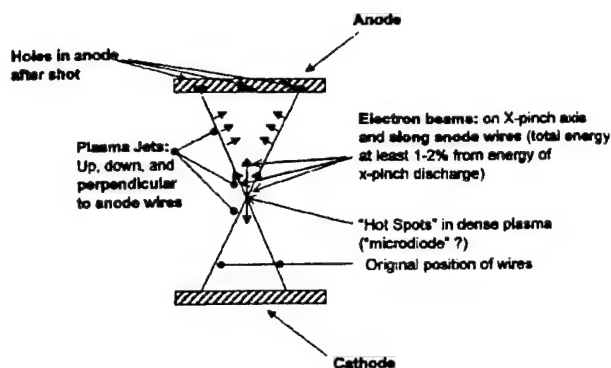


FIG. 7. Ti and Fe x-pinch structure at a high current $I > 900\text{ kA}$.

current x pinch. Particularly, a strong electron beam is directed not only at the center of an anode between the wires, but also in the direction of the anode parts of the wires (Fig. 7). A comparison of time-gated x-ray images with time-integrated images and x-ray diode signals has shown that the x-ray radiating part of the x pinches had a minimum size of $0.6\text{--}0.7\text{ mm}$, and moved during discharge along the discharge axis at the distance of $1.5\text{--}2\text{ mm}$ (Figs. 5 and 6). The formation of the x-pinch structure occurs during the first part of the z-pinch current pulse when most radiation is irradiated by the hot spots of the x pinch. Anode and cathode jets form often near the maximum of the current. Two interesting phenomena were observed. The first is bright jets that are directed to the discharge axis perpendicular to the anode parts of the wires (Figs. 5 and 6). They have a steady-state period of $1.8\text{--}2\text{ mm}$. The second is the appearance of a "V" structure on the x-ray images of the x pinches that were observed not only before the first x-ray pulse, but very often after the first or even the second x-ray pulse (Figs. 5 and 6), which correspond to the first and the second pinching of the plasma.

ACKNOWLEDGMENTS

The authors thank R. Spielman, J. McGurn, D. Jobe, and D. Nielsen from SNL for helpful discussions and help in the x-ray measurements, and W. Cline, G. Newman, and S. Rogowski for their help in the NTF experiments. This work is supported by DOE, DOD, SNL, and UNR.

- ¹ V. Kantsyrev, B. Bauer, A. Shlyaptseva, R. Bruch, and R. Phaneuf, AIP Conf. Proc. **409**, 499 (1997).
- ² A. Shlyaptseva, A. Urnov, and A. Vinogradov, P. N. Phys. Lebedev Inst., USSR, Rep. **12**, 193 (1981).
- ³ A. Shlyaptseva, A. Petrashen, V. Kantsyrev, S. Kazantsev, and U. Safronova, NIFS PROC **44**, 138 (2000).
- ⁴ E. Forster, R. Hutcheon, O. Renner, I. Uschmann, M. Vollbrecht, M. Nantel, A. Klisnick, and P. Jaegle, Appl. Opt. **36**, 831 (1997).
- ⁵ A. Ya. Faenov, S. A. Pikuz, A. I. Erko, B. A. Brunetkin, V. M. Dyakin, G. V. Ivanenkov, T. A. Pikuz, V. M. Romanova, and T. A. Shelkovenko, Phys. Scr. **52**, 333 (1994).
- ⁶ G. Ivanenkov, A. Mingaliev, S. Pikuz, V. Romanova, and T. Shelkovenko, Plasma Phys. Controlled Fusion **22**, 429 (1996).
- ⁷ D. H. Kalantar, D. A. Hammer, K. C. Mittal, N. Qi, F. C. Yong, S. J. Stephanakis, P. G. Burkhalter, G. Mehlman, and D. A. Newman, J. Appl. Phys. **73**, 8134 (1993).

APPENDIX H

X-ray Temporal, Spatial, and Spectral Study of 0.9 MA X-Pinch Ti, Fe, Mo, W, and Pt Radiation Sources. Energetic Electron Beam and Hard X-ray Generation from X-Pinches.

V.L. Kantsyrev, A.S. Shlyaptseva, B.S. Bauer, V.I. Sotnikov, R. Presura,
S. Fuelling, D.A. Fedin, S. Hansen, S. Batie, H. Faretto,
B. Le Galloudec, A. Oxner, N. Ouart, H. LeBeau, S. Keely,
D. Chamberlain, and S. Rogowski

PPPS-2001, Las Vegas, NV, June 17-22, 2001

To be published in PPPS-2001 Proc. Book (June 17-22, 2001, Las Vegas, NV)
**X-RAY TEMPORAL, SPATIAL AND SPECTRAL STUDY OF 0.9 MA
X-PINCH Ti, Fe, Mo, W AND Pt RADIATION SOURCES. ENERGETIC
ELECTRON BEAM AND HARD X-RAY GENERATION.**

**V.L. Kantsyrev, A.S. Shlyaptseva, B.S. Bauer, D.A. Fedin, R. Presura, S. Fuelling,
S. Hansen, S. Batie, A. Oxner, H. Fareto, N. Ouart, S. Keely, H. LeBeau, D. Chamberlain**

The Physics Department, the Nevada Terawatt Facility of the University of Nevada Reno, USA

Abstract

The x-ray emission of Ti, Fe, Mo, W, and Pt x-pinch currently being studied at the Nevada Terawatt Facility (0.9-1.0 MA, 100 ns). New x-ray diagnostics for time-resolved spectroscopy and imaging has been developed and used in x-pinch experiments. Total x-ray/ EUV yield was more than 10 kJ. The minimum x-ray pulse duration was 1.1 ns. For Ti, Mo and W it was observed that x-ray pulses occurred in two or three groups in the narrow time intervals after the start of the current. Most compact emitting region has been observed for a planar-loop Mo x-pinch. Strong jets were observed (Ti, Fe, Mo) directed toward the discharge axis, perpendicular to the wires. A structure of x-pinch includes energetic electron beams directed toward the anode and along wires. A pulse anisotropic hard x-ray radiation was observed moving upwards along the axial axis with an energy of several hundred keV (Mo). The size of the source was smaller than 1 mm.

I. INTRODUCTION

The high current x-pinch [1] is a good candidate for developing a new (harder) x-ray backlighter, for testing x-ray spectropolarimetry [2] (a powerful new tool for studying the anisotropy of high-temperature plasmas), for examining the final stage of the MHD instability, and other applications. The main directions of NTF x-pinch research are: studying of the dynamics of plasma implosion and determinations of plasma conditions in x-pinch that lead to generations of short x-ray pulses; studying of the influence of strong energetic electron beams on the parameters of plasmas; and studying of x-pinch plasma anisotropy.

II. PLASMA DIAGNOSTIC RESEARCH

Plasma diagnostic research at NTF [1,2] includes:

- a) development of x-ray and EUV (extreme ultraviolet) plasma time- and spatial-resolved spectroscopic, imaging, polarimetric, and x-ray backlighter systems, fast x-ray/hard x-ray detectors; b) measurements of

temperature and density of plasma that based on theoretical modeling of K-, L-, and M-shell ions x-ray spectra [3]; c) experimental polarization x-ray measurements and the theoretical polarization study [2, 3] including influence of electron beams in plasma on linear x-ray spectra, measurements of temperature, density and inner magnetic field in z pinch plasma.

The NTF diagnostics includes 12 devices (beginning of development-1997 [4]): side-on one-dimensional time-gated spectrometer (IDXIS [1]); side-on time-resolved "Polychromator" spectrometer with a transmission grating spectrometer (TGS) [5]; side-on one-dimensional x-ray imaging time-integrated crystal spectrometer with a survey pinhole camera [1]; side-on and end-on one-dimensional x-ray imaging time-integrated polarimeter-spectrometers [2]; side-on multichannel time-gated pinhole camera (GXI) [1]; side-on time-integrated high-resolution pinhole camera; end-on time-integrated super-high-resolution pinhole camera; side-on filtered fast PCD and XRD detectors, and a Ni x-ray bolometer [1]; end- and side-on hard x-ray time-integrated imaging detectors with filtered x-ray films; and end-on hard x-ray detector. Side-on two-dimensional glass-capillary imaging spectrometer (2DXIS) [1, 6] decomposes an image into pixels, separates and spectrally disperses these pixels, and records spectra with a time-gate MCP intensifier. The device is under testing at the NTF. Side-on and end-on hard x-ray fast detectors with spatial resolution capability and a side-on EUV imaging diagnostic beamline are under development. The diffraction limitation in spatial resolution for side-on diagnostics due to lack of a minimum distance from plasma to detectors (30-60 cm) was 20-25 μm at $\lambda=10 \text{ \AA}$ and 5-10 μm at $\lambda=1 \text{ \AA}$. All the NTF experiments were proved under vacuum better than 5×10^{-6} torr. Vacuum beamlines have permanent magnets to protect the x-ray devices against the damage from z-pinch ion beams.

III. EXPERIMENTAL RESULTS

X-pinch were made by positioning two thin, straight, crossed wires between the cathode and the anode of the Zebra pulsed-power generator, with wires

contact on the axis of the cathode-anode gap. Two configurations of x-pinch were tested: twisted wires and planar-loop. Other loads for comparison with x-pinch were also studied. Early x-pinch were made from Al to Pd [7] and have been driven by currents of 0.1-0.4 MA. At higher currents, the authors are only aware of three x-pinch publication, on an Al x-pinch driven by 0.8 MA [8], and Ti and Fe driven by 0.9 MA [1, 2]. Here the results on the new study of Ti, Fe, Mo, W and Pt x-pinch driven by 0.85-0.95 MA are reported.

A. Spatial Structure of the High-Current X-Pinch

The high peak current quickly vaporizes and strongly ionizes the wires. Time-integrated and time-gated x-ray pinhole images show the location of the wires, with a bright spot at the cross point (Fig. 1). The structure of x-pinch driven by a high current (0.8-0.9 MA) [1,8] is more complicated than that of low-current x-pinch [7]. First, a strong, energetic electron beam is not only directed to the center of the anode (between the wires), but also toward the anode ends of the wires [1]. Such an energetic electron beam influences the plasma x-ray spectra. For example, polarization of K-shell spectra of Ti x-pinch is observed [2]. In most cases the development of anode-wire directed electron beams occurs when current reached a value of 0.5-1.0 from maximum. Second, strong jets are observed (mostly in softer-than-K-shell Ti and Fe [1], or L-shell Fe and Mo, and x-ray continuum emissions) directed toward the discharge axis (Fig.1 B), perpendicular to the wires [1]. Stagnation of these jets on the axis of discharge forms a strong jet, efficiently radiated in x-ray region, directed to the anode. The same effect was observed for the V-pinch configuration, that can be used to study plasma jet generation. These small jets have a period that varying from 1 to 2 mm for Ti, Fe and Mo. They are presumably spikes of the Rayleigh-Taylor instability of the accelerated wires. The brightness of luminous jets and their wires on the anode side of images was always much stronger, indicating that they are luminous (in the spectral band recorded) because of excitation by fast electrons beams originating from the necked-off contact. Anode and cathode jets appear to be formed during all periods of x-ray generation. In most discharges development of bright spots at the cross point occurs during the first part of the current pulse. High resolution time-gated GXI images, time-integrated pinhole images, TGS spectra, and spatially resolved x-ray spectra [3] show that the line, continuum and harder radiation comes from a region in the same location as the K-, L-or M-shell sources. The size of this region is 2.5-4 mm for Ti K-shell and 2-3 mm for Fe K-shell, Mo L-shell or W, Pt M-shell radiation for planar-loop x-pinch.

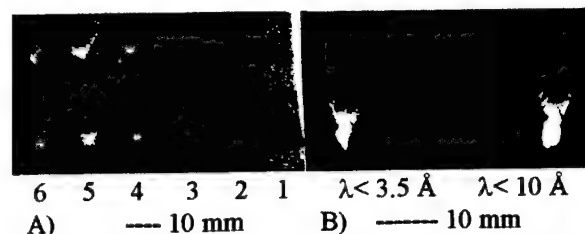


Figure 1. X-ray images from a planar-loop 50 μm Mo wire x-pinch. The anode is above images. A) Gated images. Frame 4 ns, interval between beginning of frames 7 ns. Spatial resolution 230 μm . Top row corresponds to $\lambda < 10 \text{ \AA}$, lower to $\lambda < 3.5 \text{ \AA}$. Frame #1 corresponds to 40 ns after a current start. X-ray bursts (PCD and XRD peaks) were in frames 4-6. B) Time-integrated pinhole camera images. Resolution 60 μm .

The size of L-shell emitting region for Ti is 3-6 mm, for Fe ($\lambda \approx 20-80 \text{ \AA}$) up to 10 mm, and for Mo ($\lambda \approx 20-80 \text{ \AA}$) is 3-4 mm (measured with TGS). All these regions include several small sources of radiation (hot spots) with a minimum size smaller than 30 μm in x-ray (pinhole camera resolution), or 200 μm in soft x-ray (TGS resolution). More compact x-ray source was obtained with planar-loop x-pinch. For example, for wire-twisted Ti x-pinch its size is 4-6 mm. Typically, this region includes from 3-4 to 7-8 hot spots. For the planar-loop x-pinch a number of hot spots is reduced to 1-5. The size of these spots depends on a spectral region of registration. For example, for a Mo x-pinch it has been reduced from several hundred μm to smaller than 30-65 μm (pinhole camera resolution) when a spectral region of observation has been changed from 4-10 \AA (Mo L-shell and continuum) to $\lambda < 1.5-2 \text{ \AA}$ (continuum with planckian spectra) (Fig.2). These short-wavelength hot spots are located in a shape of a chain along a central axis of an x-pinch near the cross point of wires.

A comparison of time-gated images and PCD/XRD signals shows that a x-ray images of the sources moved for a distance of several mm along the discharge axis during the discharge with a maximum speed from $5 \times 10^6 \text{ cm/s}$ (Ti and Fe) to $5 \times 10^7 \text{ cm/s}$ (Mo). The direction of movement can change to opposite during a discharge.

We found that the quality of an x-pinch source (from the point of view of minimization of an effective size of an x-ray source and a number of hot spots) is in strong dependency from original symmetry of an x-pinch and its plainness. An estimated accuracy of an x-pinch must be at least 3-5% from a maximum dimension of a structure.

B. Energetic Electron Beam and Hard X-Ray Generation From High Current X-Pinch

Previous studies of x-pinch plasma sources at lower



Figure 2. X-ray images from a planar-loop 50 μm Mo wire x-pinch. The anode is above images. Time-integrated pinhole camera. Resolution 60 μm . A weak diffuse spot above hot spots images is a result of penetration of hard x-ray through pinhole substrate.

current [7] show that this is a prospective source for x-ray radiography in the 1-10 keV spectral region. Our studies at sufficiently higher currents (~ 900 kA) also confirm a possibility to use an x-pinch as a source for backlighting purposes even with harder x-rays. The presence of a very powerful high energy electron beam in an x-pinch plasma can lead to the generation of hard x-ray radiation in a cross point as a result of interaction of this beam with matter of x-pinch and a local magnetic field. A strong, energetic electron beam is directed not only to the center of the anode (between the wires), but also toward the anode ends of the wires [1, 2]. The experimental estimation of widths of the central jet on x-pinch x-ray images and Fe K_{α} spectral lines (generated on a steel anode) has shown that a diameter of an electron beam in high-current x-pinch may be smaller than 1 mm. The total energy of this electron beam is at least from 2-3 % (Fe) to 16-20 % (Mo and W) of the x-pinch discharge energy $E \approx 100$ -120 kJ (Fig.3). Several tests of the NTF Mo and Fe x-pinch as a possible hard x-ray backlighter source were carried out with a static test object. As test objects, set of Al and Fe parts were used. One of the sets was placed end-on and another side-on. In order to roughly control spectral distribution of hard x-rays, step Al, Fe, Cu and Pb filters with different attenuation were placed in front of the film in both beamlines. The preliminary results of Mo and Fe x-pinch (Fig. 4) show that an x-pinch is an effective source of hard x-ray radiation at high current conditions. Main portion of electrons has the energy smaller 40-50 keV, and some amount of electrons has the energy at least 0.5-1.0 MeV. Note that side-on measured electron temperature is high than end-on measured. It can be explained as a influence of x-pinch local magnetic field on process of interaction of an electron beam with a pinch matter. Time duration of a hard x-ray beam is approximately several tens of ns. Experiments are in progress. A rough estimation of spectral regions available for radiography gives us values of 50-150 keV for Mo x-pinch. Best spatial resolution was approximately 0.2-0.3 mm.

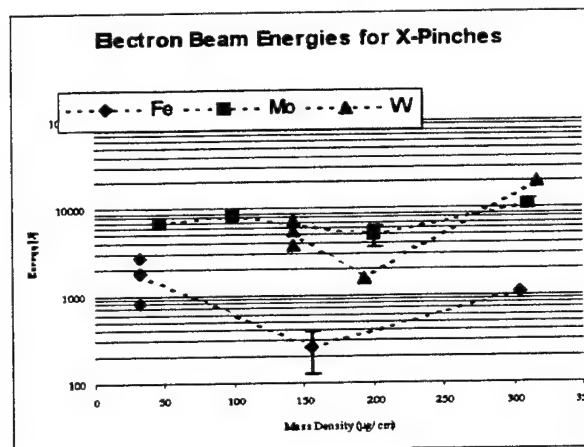


Figure 3. The experimental estimation of the energy needed to generate the observed holes at the points of connection of the wires with the anode of an x-pinch vs mass density of wires.

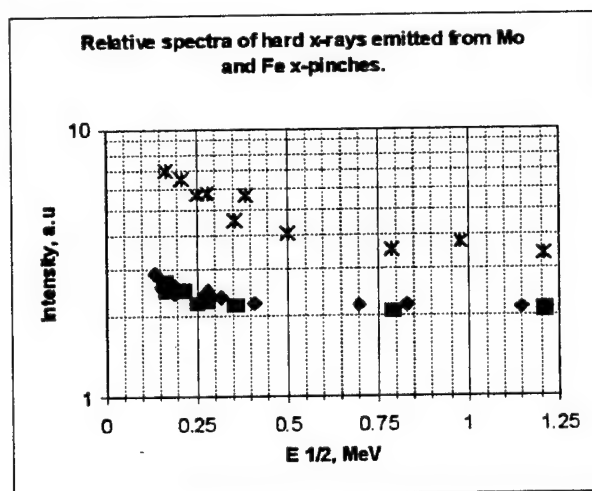


Figure 4. Relative spectra of hard x-ray. * - Mo, 50 μm (end-on); ■ - Mo, 50 μm and ◆ - Fe, 50 μm (side-on).

C. Time, Energy Scaling, and X-ray spectra of High Current X-Pinch X-Ray/EUV Pulses.

The fast filtered PCD and XRD measure x-pinch emission (Table 1,2) and the Ni bolometer (from SNL) measures the total x-ray/EUV energy. X-ray bursts appear before the current reaches maximum. Often x-ray pulses occurred in two or three groups in the narrow time intervals after the start of the current. For example, for a 30 μm Ti x-pinch pulses form two

	PCD (filter)	XRD (filter)
Ti	2.2 \pm 0.4ns (Be 8 μm)	4 \pm 1ns (kimf. 5 μm)
Fe	1.3 \pm 0.7ns (Be 8 μm)	3.7 \pm 0.7ns (kimf. 5 μm)
Mo	1.1 \pm 0.5ns (kapton 25 μm)	1.2 \pm 0.7ns (Be 8 μm)
W	1.1 \pm 0.7ns (kapton 25 μm)	1.1 \pm 0.7ns (Be 8 μm)
Pt	1.2 \pm 0.7ns (kapton 25 μm)	1.1 \pm 0.7ns (Be 8 μm)

Table 2. Probability of generation of one or two x-ray bursts during x-pinch discharge

	One burst	Two bursts
Ti (2x30 μm)	0.35	0.25
Fe (2x50 μm)	0.15	0.15
Mo (2x50 μm)	0.20	0.4-0.5

groups in intervals of 30-45 and 60-80 ns after the current is initiated [1], 20-30 ns and 40-50 ns for a 50 μm Mo x-pinch. Note, that for 50 μm Mo x-pinch first and second x-ray pulses have the same intensity.

The maximum total energy for x-pinch was more than 10-11 kJ for a Mo x-pinch, 7-8 kJ for Fe, Pt and W, and 6 kJ for Ti. For Ti, Fe, and Mo x-pinch maximum x-ray yields were obtained with a wire mass density of 200, 150 and 100-200 $\mu\text{g}/\text{cm}$, respectively. L-shell and 0.7-1keV continuum Mo output was about 250-350 J (XRD), and PCD signals (L-shell and 2 keV continuum) were about 20-30 J. An Fe x-pinch irradiated up to 1 kJ in L-shell and 0.25 keV in continuum (XRD), and 100-150 J in K-shell and several keV in continuum (PCD). The Fe output in a region 0.15-0.6 keV was 1.3 kJ (TGS measurements). Ti results is reported in [1]. The M-shell and 0.7-1 keV continuum (XRD) yield for W varied from 15 to 25 J, and near 15 J for Pt. The L-shell and 2 keV W continuum (PCD) changed from 5 to 20 J.

Currently, the spectra of Ti, Fe Mo, W, and Pt [3] are being processed to measure the main parameters of an x-pinch plasma (electron temperature and density), and to record polarization-dependent spectra. Best K-shell spectra were obtained for Ti and Fe, and L-shell for Mo x-pinch. The measurements of temperature and density of x-pinch plasmas were based on theoretical modeling of K-shell (Ti) and L-shell (Mo) spectra [3]. T_e is 1.5 keV for Ti, 0.8 keV for Mo, N_e is up to $2\text{-}3 \times 10^{22} \text{ cm}^{-3}$ with 1-10 % of hot electrons [3]. The first results of the study of Mo L-shell x-pinch spectra with IDXIS [3] have demonstrated that the shape of spectra changed dramatically during the shot. This instrument can improve results of modeling of plasma parameters. The "Polychromator" [5] spectrometer has been used to study the time evolution of 5 selected x-ray spectral lines from x-pinch. In experiments was observed the difference between time evolutions of selected Mo spectral lines was observed, which can provide us with temporal evolution of N_e and T_e .

IV. CONCLUSIONS

The x-ray emission of Ti, Fe, Mo, W, and Pt x-pinch has been studied at the NTF. Total x-ray/EUV yield and K-, L-, and M-shell radiation were measured. Structure, time and energy scaling of high current x-pinch x-ray/EUV pulses and x-ray spectra

were studied. Strong plasma jets are observed directed toward the discharge axis, perpendicular to the wires. Energetic electron beams and pulse anisotropic hard x-ray radiation were studied and measured moving upwards along the pinch axial axis. The present work is supported by DOE, SNL, and UNR.

V. REFERENCES

- [1]. V. Kantsyrev, B. Bauer, A. Shlyaptseva, D. Fedin, S. Hansen, R. Presura, S. Batie, A. Oxner, B. LeGalloudec, H. Faretto, D. Chamberlain, N. Ouart, A. Jones, H. LeBeau, M. Gharaibeh, "Advanced x-ray and EUV diagnostics and first application to x-pinch plasma experiments at the Nevada Terawatt Facility", *Rev. Sci. Instrum.*, vol.72, 1(II), pp.663-667, 2000.
- [2]. A.S. Shlyaptseva, S. B. Hansen, V.L. Kantsyrev, B.S. Bauer, D.A. Fedin, N. Ouart, S.A. Kazantsev, A.G. Petrashen, U.I. Safronova, "X-ray spectropolarimetry of high-temperature plasmas", submitted to *Rev. Sci. Instrum.*, v.72, 1(II), pp. 1241-1244, 2000.
- [3]. A.S. Shlyaptseva, S. B. Hansen, V.L. Kantsyrev, B.S. Bauer, D.A. Fedin, N. Ouart, S. Keely, H. LeBeau, U.I. Safronova. "X-ray spectropolarimetry and hot electron effects on high-current x-pinch plasma spectra" (at the same conference).
- [4]. V. Kantsyrev, B. Bauer, A. Shlyaptseva, R. Bruch, R. Phaneuf, "New optical instrumentation for hot plasma imaging, polarimetry, and spectroscopy, using glass capillary converters and multilayer mirrors", *Proc. Conf. "Dense Z-pinch"*, AIP Proc., CP409, pp. 499-502, 1997.
- [5]. D. Fedin, V. Kantsyrev, B. Bauer, A. Shlyaptseva, I. Brytov, "Polychromator" five-channel x-ray/EUV spectrometer with imaging transmission grating for plasma diagnostics", *Proc. SPIE*, 3764, pp.80-84, 1999.
- [6]. B. Bauer, V. Kantsyrev, "Capillary spectrometer", The US Patent, #5,991,024, filed May 29, 1998.
- [7]. S.A. Pikuz, T.A. Shelkovenko, V.M. Romanova, G.S. Sarkisov, D.A. Hammer, D.F. Acton, "Studies of X-pinch plasma structure using high resolution x-ray optical and imaging spectroscopy methods", *AIP Proc.* CP 409, pp.429-436, 1997.
- [8]. D. H. Kalantar, D.A. Hammer, K.C. Mittal, N. Qi, F.C. Young, S.J. Stephanakis, P.G. Burkhalter, G. Mehlman, D.A. Newman, "K-shell x-ray yield scaling for aluminum x-pinch plasmas", *J. Appl. Phys.*, vol. 73, pp.8134-8139, 1993.

X-RAY TEMPORAL, SPATIAL and SPECTRAL STUDY of 0.9 MA

X-PINCH Ti, Fe, Mo, W and Pt RADIATION SOURCES.

ENERGETIC ELECTRON BEAM and HARD X-RAY GENERATION

FROM X-PINCHES.

V.L. Kantsyrev, A.S. Shlyaptseva, B. Bauer, V.I. Sotnikov, R. Presura,
S. Fuelling, D. Fedin, S. Hansen, S. Batie, H. Faretto, B. Le Galloudec,
A. Oxner, N. Ouart, H. LeBeau, S. Keely, D. Chamberlain, S. Rogowski

ICOPS, Las Vegas, Nevada, June 17-22, 2001

OUTLINE

- **Plasma Diagnostic Research at the NTF**
- **Physics of High-Current X-Pinch X-ray/EUV Radiation Sources**
- **The NTF X-Pinch Hard X-Ray Experiments**

PLASMA DIAGNOSTIC RESEARCH at the NTF

Plasma diagnostic research at the NTF includes:

- **development of x-ray and EUV plasma time- and spatial-resolved spectroscopic, imaging, polarimetric, and x-ray backlighter systems, fast x-ray and hard x-ray detectors;**
- **measurements of temperature and density of plasma based on theoretical modeling of K-, L-, and M-shell ions x-ray spectra (see A.S. Shlyaptseva et al.);**
- **experimental polarization x-ray measurements and theoretical polarization study (see A.S. Shlyaptseva et al.) of influence of presence of electron beams in plasma on linear x-ray spectra and measurements of temperature, density and inner magnetic field of z-pinch plasma.**

Status of the NTF experimental diagnostics (beginning of the development-1997)**I. X-ray/ EUV spectroscopic and polarimetric systems**

1. Side-on two-dimensional glass-capillary imaging x-ray time-gated spectrometer (2DXIS) :testing in progress

2.Side-on one-dimensional time-gated spectrometer (1DXIS–based on a 2DXIS chamber and a MCP detector): operational.

Spectrometer parameters: λ from 0.5 Å to 30 Å (different flat crystals or multilayer mirrors), observation one shot $\Delta \lambda$ up to 1.5 Å , spectral resolution $\Delta \lambda / \lambda \approx 1000$, temporal resolution $\Delta \tau = 1-9$ ns, number of frames 4, inter-frame time 3-20 ns, spatial resolution 1-5 mm.

3. Side-on 6-channel “Polychromator” time-resolved spectrometer with a transmission grating spectrometer: operational.

4. Side-on one-dimensional x-ray imaging time-integrated crystal spectrometer / time-integrated low-resolution pinhole camera: operational. Spectrometer parameters: λ from 0.5 Å to 20 Å (different convex crystals), spectral resolution $\Delta \lambda / \lambda = 700-800$, spatial resolution 2-7 mm. Camera parameters: spatial resolution 580 μm , $\lambda < 10 \text{ Å}$ (three images behind three different filters).

5. Side-on and end-on one-dimensional x-ray imaging time-integrated polarimeter/spectrometers: side-on is operational, end-on: testing in progress.

6. Extreme ultraviolet (EUV) imaging spectrometer: under development.

II. X-ray imaging systems

- 1. Side-on multichannel time-gated pinhole camera (GXI): operational.**
Camera parameters: 6 frames (1-8 ns), inter-frame time 1-20 ns, spatial resolution 100-250 μm , $\lambda < 10\text{\AA}$ (two rows of images).
- 2. Side-on time-integrated high-resolution pinhole camera: operational.**
Camera parameters: spatial resolution 30-65 μm , $\lambda < 10\text{\AA}$.
- 3. End-on time-integrated high-resolution pinhole camera: operational.**
Camera parameters: spatial resolution 5-10 μm , $\lambda < 4\text{\AA}$.

III. X-ray/EUV fast detectors system

- 1. Side-on filtered fast PCD and XRD detectors (SNL): operational.**
Detectors parameters: $\lambda \approx 500\text{-}0.1\text{ \AA}$, time resolution $\approx 0.2\text{ ns}$.
- 2. Side-on Ni x-ray bolometer (SNL): operational.**

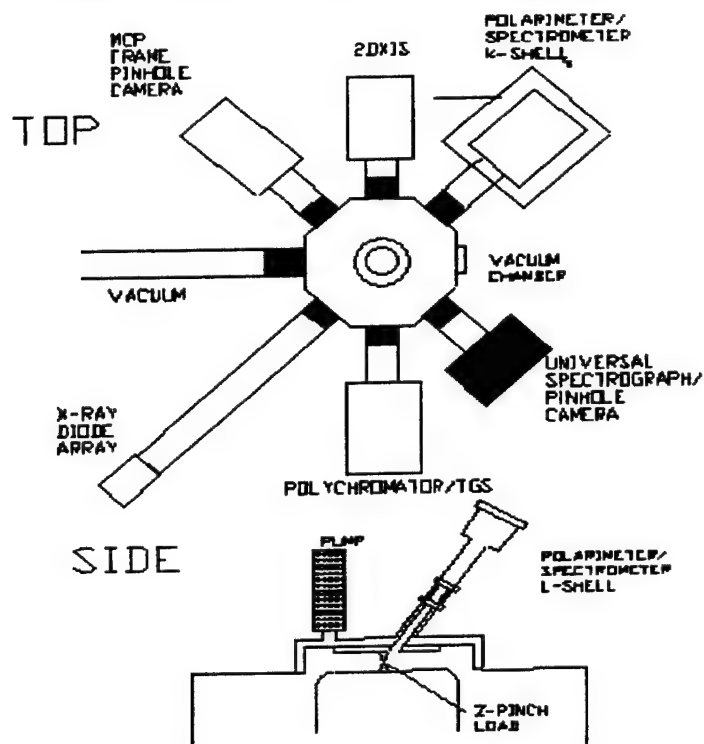
IV. Hard x-ray detectors systems

- 1. End-on hard x-ray time-integrated imaging detector with filtered x-ray films: operational.** Parameters of the detector: energy 25-200 keV.
- 2. Side-on hard x-ray time-integrated imaging detector with filtered x-ray films: operational.** Parameters of the detector: energy 25-200 keV.
- 3. Hard x-ray detector (photomultiplier with scintillator; SNL): operational.** Energy $\approx 1\text{ MeV}$.
- 4. End-on hard x-ray detector with a filtered x-ray diode: operational.**
Detector parameters: energy $\approx 50\text{-}200\text{ keV}$, time resolution $\approx 0.5\text{ ns}$.
- 5. Side-on and end-on hard x-ray fast detectors with spatial resolution capability: under development.** Detector parameters: energy $\approx 1\text{-}200\text{ keV}$, time resolution $\approx 0.2 - 0.5\text{ ns}$, spatial resolution 3-5 mm.

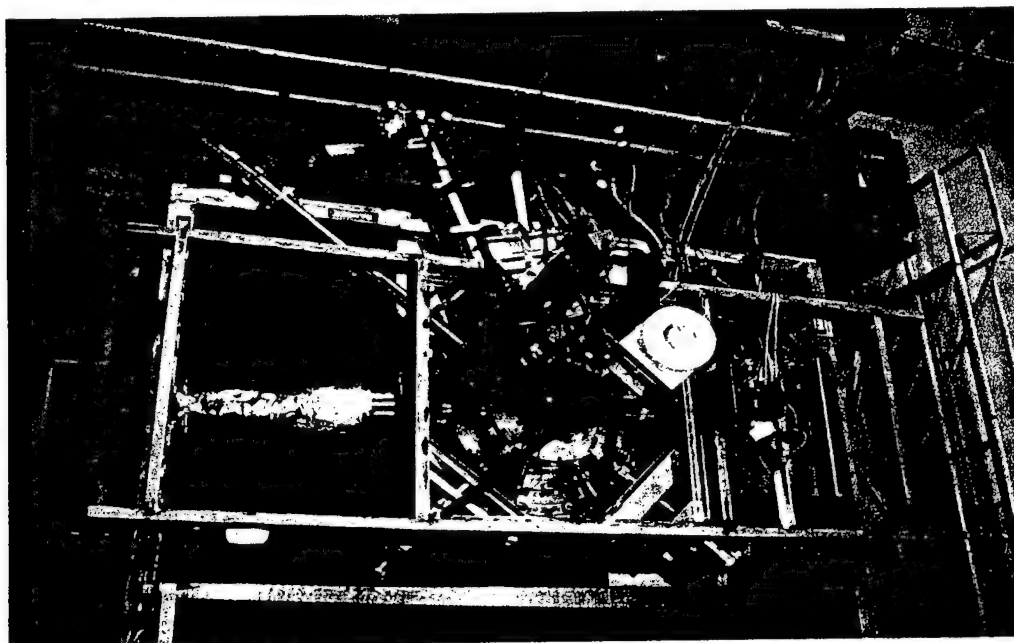
V. X-ray backlighter system

Multi-x-pinch x-ray backlighter: under development.

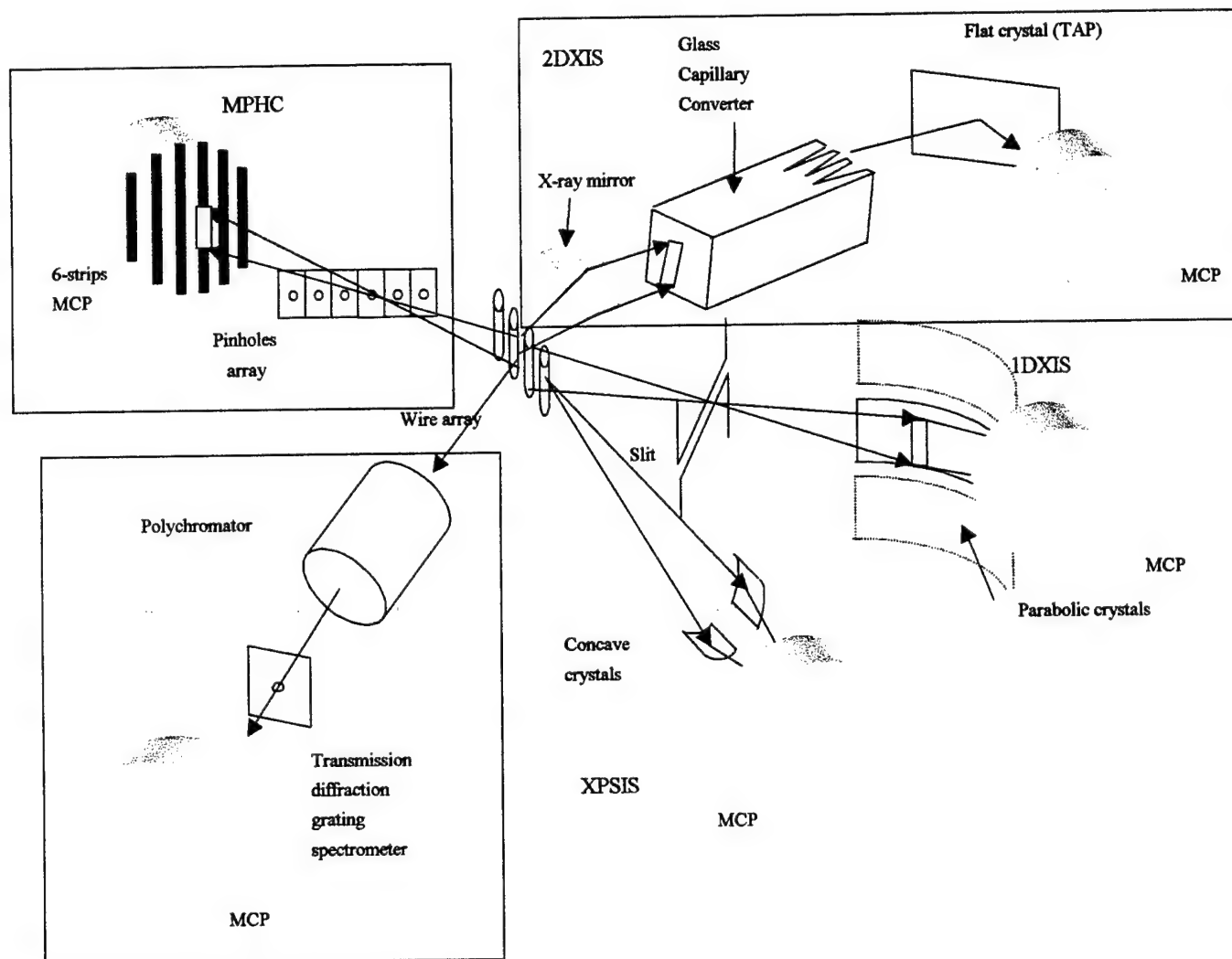
The x-ray diagnostics at the Nevada Terawatt Facility



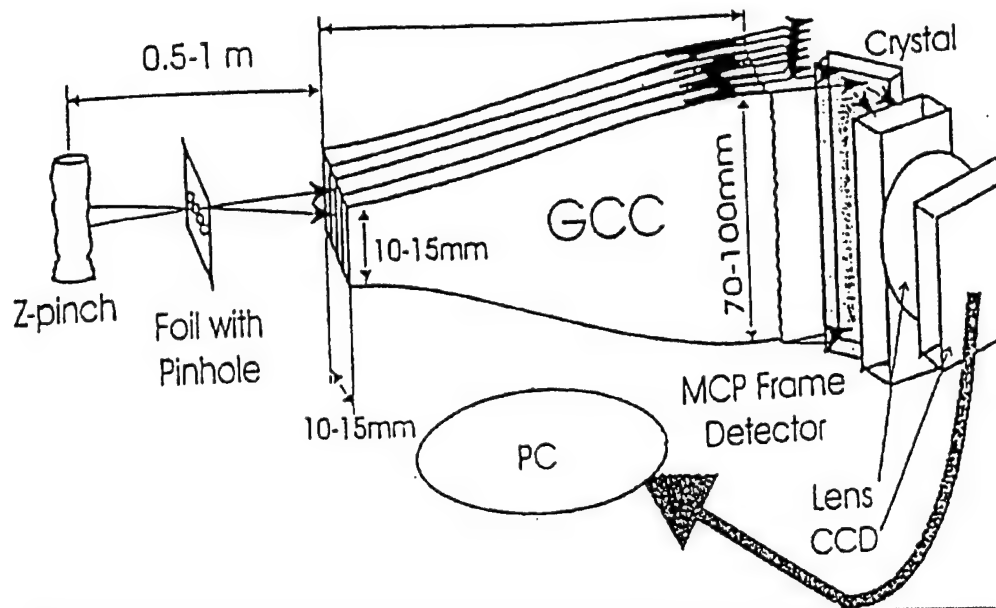
Diffraction limit in spatial resolution due to dimensions of the NTF discharge chamber ($R_{\text{diagn.}} \geq 30\text{-}60\text{ cm}$): $20\text{-}25\text{ }\mu\text{m}$ for $\lambda \approx 10\text{ }\text{\AA}$ and $5\text{-}10\text{ }\mu\text{m}$ for $\lambda \approx 1\text{ }\text{\AA}$



The scheme of new x-ray/EUV diagnostics at the NTF



The two-dimensional EUV/X-ray imaging spectrometer (2DXIS)



The 2DXIS decomposes an image into pixels, separates and spectrally disperses these pixels, and records spectra with a time-gate MCP imager.



The 2DXIS (1DXIS) device at the NTF.

A comparison of parameters of the prototype of the 2DXIS with traditional 2D spectrographs with a spherical curved dispersive elements for Z-pinch studies

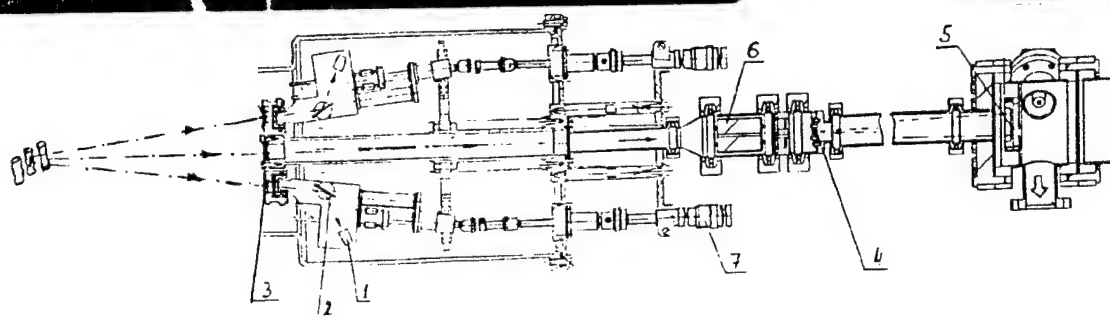
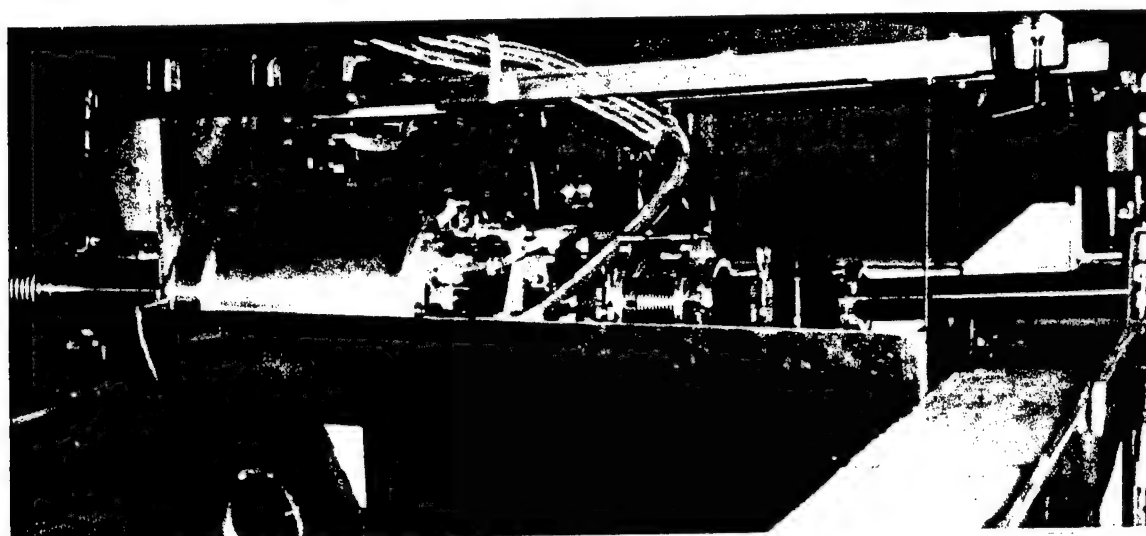
	2DXIS	2D spectrograph
Spectral resolution ($\lambda/\Delta\lambda$):		
crystals	700 - 1000	1000 *
MLMs	50 - 100	50-70**
Spatial resolution (for z-pinch plasma):	100 - 250 μm	100 $\mu\text{m}^{*,**}$
Number of output individual spectra	4- 5 x 20	1 ^{*,**}
Time resolution (gated)	1-2 ns	1-2 ns
Wavelength observation band $\Delta\lambda$:		
single shot exposure	$\lambda / 10 - \lambda / 20$	$\lambda / 25 - \lambda / 50$ ^{*,**}
multi shot exposure	$\lambda / 3$	-----
with rotation of a crystal (MLM)		

* E. Forster, R. Hutcheon, O. Renner, I. Uschmann, M. Vollbrecht, M. Nantel, A. Klisnick, P. Jaegle, "High-resolution x-ray imaging of extended lasing plasmas", *Appl. Opt.*, 36, 4, pp.831-840 (1997);

A.Ya. Faenov, S.A. Pikuz, A.I. Erko, B.A. Brunetkin, V.M. Dyakin, G.V. Ivanenkov, A.R. Mingaliev, T.A. Pikuz, V.M. Romanova, T.A. Shelkovenko, "High-performance x-ray spectroscopic devices for plasma microsources investigations", *Phys. Scripta*, 52, pp. 333-338 (1994).

** V. Kantsyrev, K. Takasugi, K. Tatsumi, T. Miyamoto, A.S. Shlyaptseva, "The structural, spectral and temporal properties of x-ray in regions $\lambda = 3.4 \text{ nm} - 4.6 \text{ nm}$ and $\lambda = 1.0 \text{ nm}$ emitted from the Ar gas-puff z-pinch plasma", *Proc. Intern. Conf. On Plasma Physics (ICPP 96)*, Nagoya, Japan, pp. 1106 - 1109, 1996.

Multichannel Spectrometer "Polychromator"



1. Fast x-ray diodes (5 units) 2. Crystals (5 units) 3. Filters.
 4. Transmission Grating 5. MCP Imager 6. Magnetic Shield
 7. Wavelength controllers 8. 7-inch plasma

5-channel spectrometer

Spectral region: 0.5 - 50 Å
 (3 crystal channels and MLM
 channel)

120 -240 Å (MLM channel)

Spectral resolution: 300-600

Field of view: variable

Spatial resolution: 3-5 mm

Time resolution: 0.2-0.5 ns.

Transmission grating spectrometer (TGS)

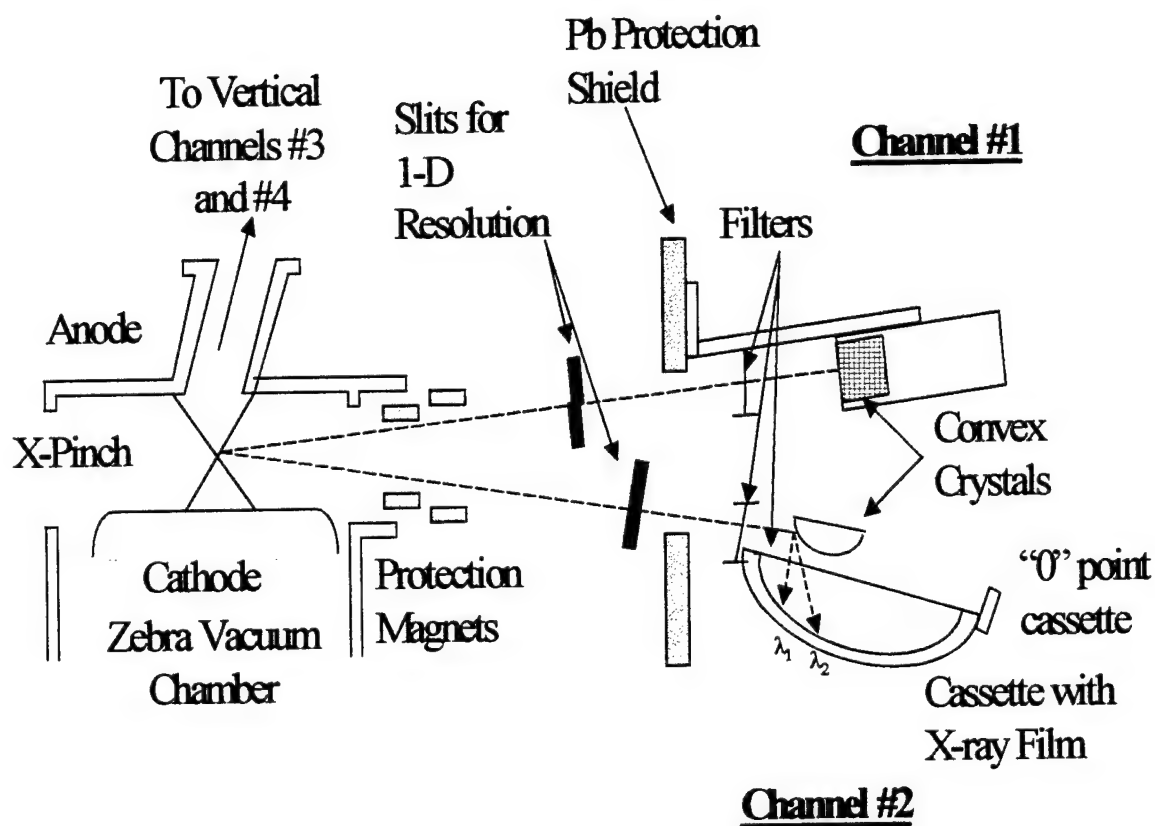
Spectral region: 20-80 Å

Spectral resolution: 20-50

Spatial resolution: 150-200 μm

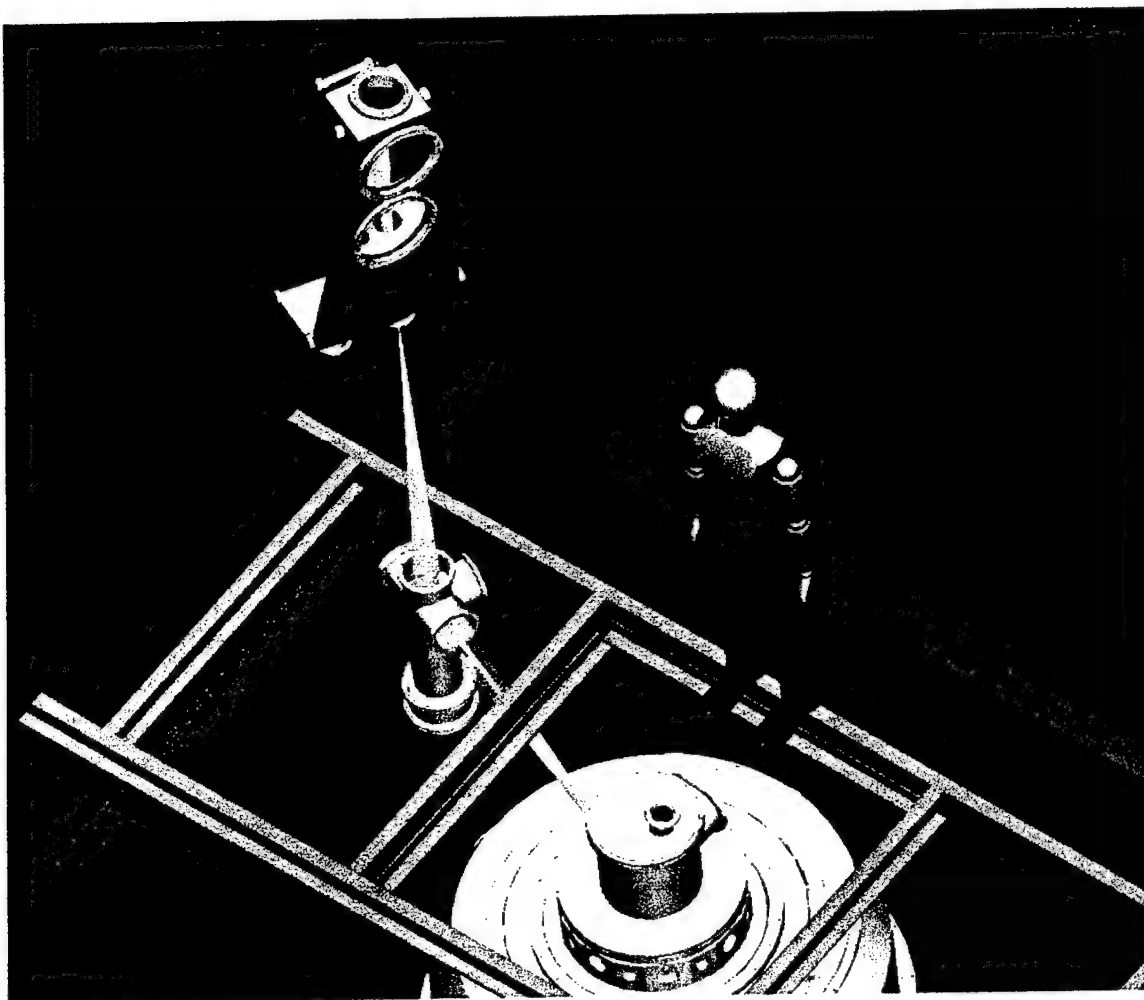
Time resolution (gated): 1-2 ns.

The NTF experimental setup including a one-dimensional x-ray polarimeter/spectrometer for polarization measurements*



* A.S. Shlyaptseva, S.B. Hansen, V. L. Kantsyrev, B.S. Bauer, D.A. Fedin, N. Ouart, "X-ray spectropolarimetry of high-temperature plasmas", *Rev. Sci. Instrum.*, 72, 1(II), 1241-1244 (2001).

Pro/E model of EUV plasma diagnostic beamline

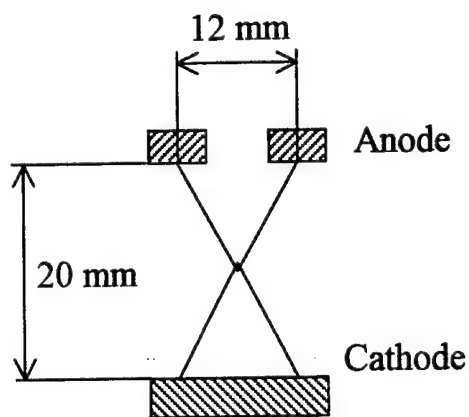


Spectral region $\lambda \approx 700\text{-}1500 \text{ \AA}$
Spatial resolution $\approx 100\text{-}200 \text{ }\mu\text{m}$
Time resolution (gated) \approx several ns

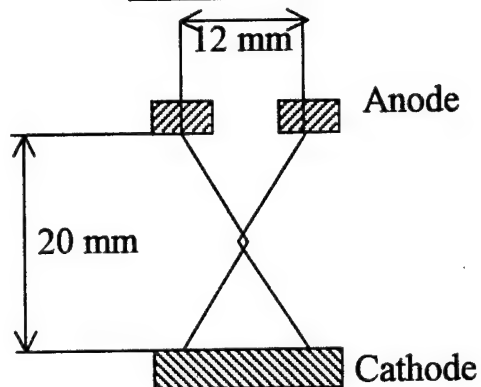
PHYSICS of HIGH-CURRENT (0.9 MA) X-PINCH **X-RAY/EUV RADIATION SOURCES**

Main configurations of loads in the NTF plasma experiments

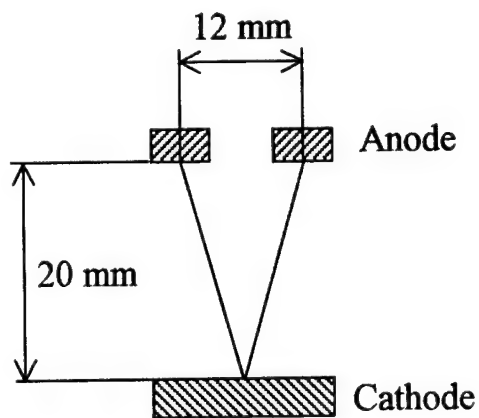
X-pinch
Planar-loop



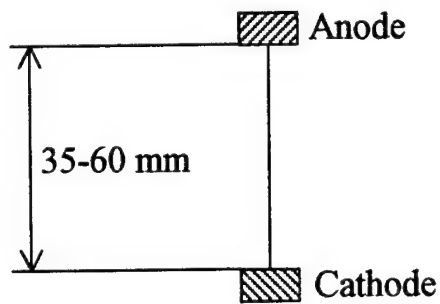
X-pinch
Wire twisted
at $\alpha \approx 25^\circ - 30^\circ$

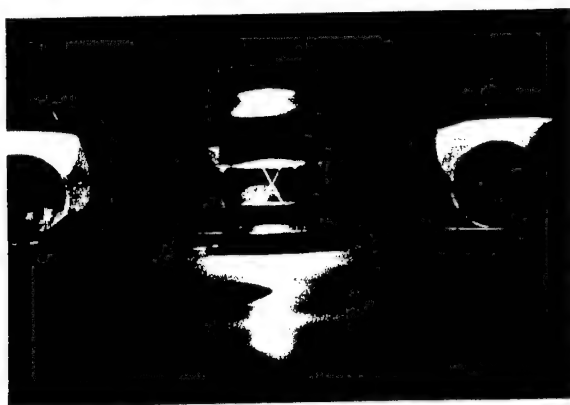


V-pinch

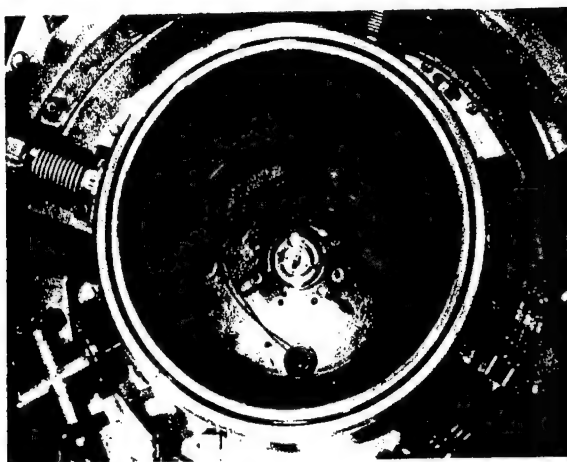


Single
wire





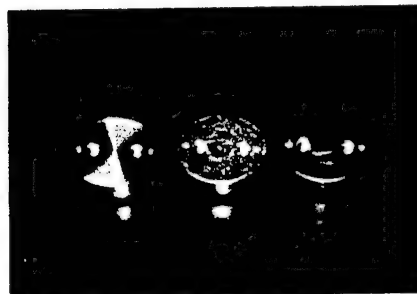
The x-pinch load. Anode is at the top.



View from the top. An x-pinch and wire holders are at the center.



An anode electrode before (left) and after the shot for Fe (center) and Mo x-pinch (right).

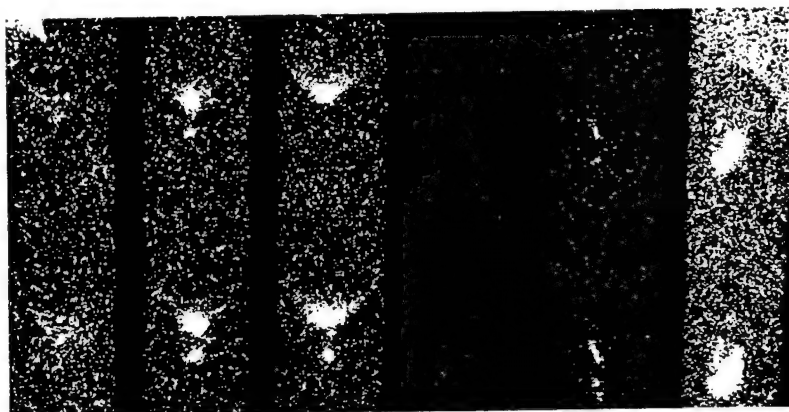


Cathode electrodes before (left) and after the shot (center and right). The central electrode spot corresponds to a symmetrical x-pinch implosion, the right one to asymmetrical with multiple x-ray bursts.

Spatial structure of high-current x-pinch

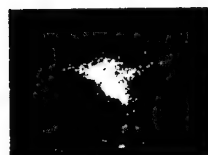
A) Time-gated x-ray images. Anode is just above images.

Top image $\lambda < 3.5 \text{ \AA}$



A) 1 2 3 4 5 6 Lower image $\lambda < 5 \text{ \AA}$

B and C) Time-integrated pinhole camera images; anode is at top of images.



B) $\lambda < 3 \text{ \AA}$

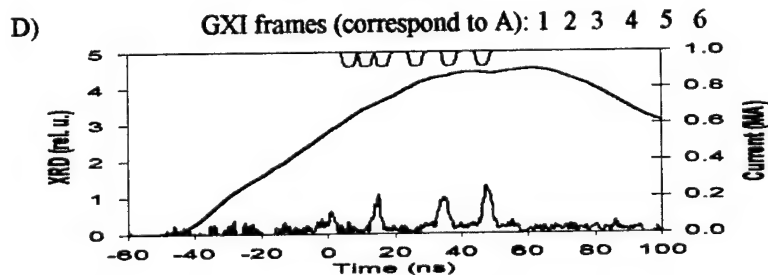
$\lambda < 7 \text{ \AA}$

$\lambda < 4 \text{ \AA}$

C) $\lambda < 4 \text{ \AA}$

12mm

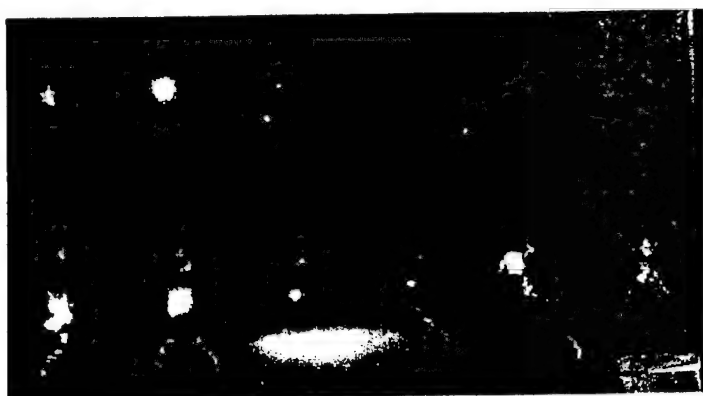
1



Ti wire-twisted x-pinch with 30- μm wire diameter and 20-mm anode-cathode gap (shot #29, May 17, 2000). A) Gated x-ray images. Spatial resolution 100 μm . Top image on each strip filtered for $\lambda < 3.5 \text{ \AA}$, the lower image for $\lambda < 5 \text{ \AA}$. B) Time-integrated pinhole camera images (Kodak DEF-5 x-ray film), with the same view as in A. Spatial resolution 580 μm . C) Time-integrated pinhole camera image as in B), but with a view from the top, at 9 degrees from vertical. Spatial resolution 200 μm . D) X-pinch current (thick smooth line), GXI frames, and XRD (with 5 μm Kimfoil filter; lower thin spiky line) response versus time.

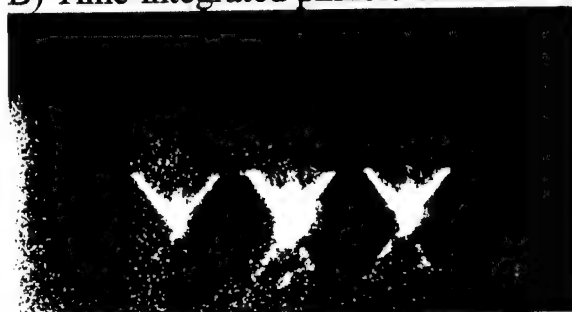
A) Time-gated x-ray images. Anode is just below images.

Top image $\lambda < 3.5 \text{ \AA}$



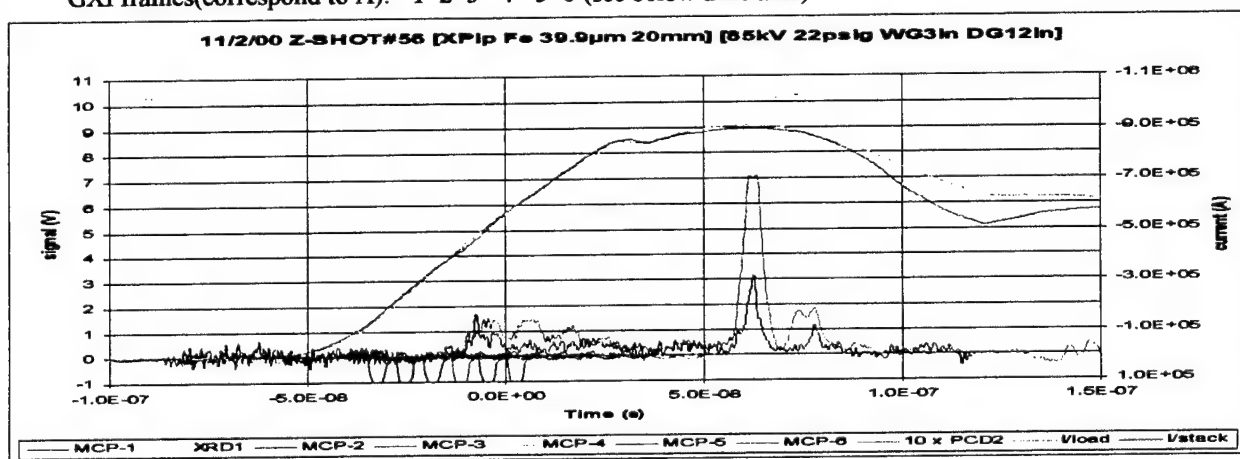
Lower image $\lambda < 10 \text{ \AA}$

B) Time-integrated pinhole camera images; anode is at top of images.



B) $\lambda < 2.6 \text{ \AA}$ $\lambda < 7.9 \text{ \AA}$ $\lambda < 5 \text{ \AA}$

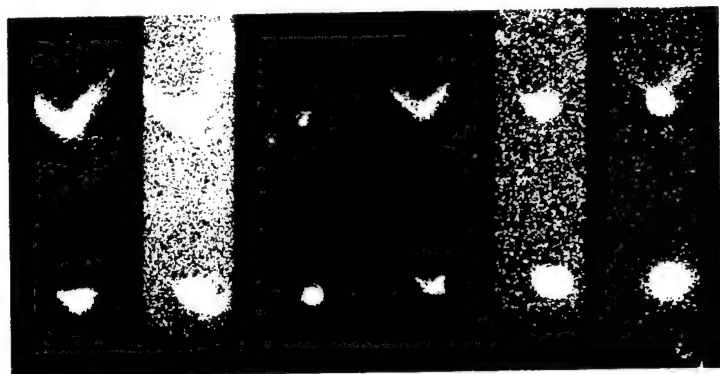
C) GXI frames (correspond to A): 1 2 3 4 5 6 (see below time axis).



X-ray images and signals from a Fe planar-loop x-pinch with a 39.9- μm wire diameter and a 20-mm anode-cathode gap (shot #56, November 02, 2000). A) Gated x-ray images. Frame 4 ns. Spatial resolution 230 μm . Top image on each strip filtered for $\lambda_{1/10} < 10 \text{ \AA}$, the lower image for $\lambda_{1/10} < 3.5 \text{ \AA}$. B) Time-integrated pinhole camera images (Kodak DEF-5 x-ray film), with the same view as in A. Spatial resolution 580 μm . C) X-pinch current (thick smooth line), GXI frames, XRD (with 8 μm Be filter) and PCD (with 25 μm kapton filter) response versus time.

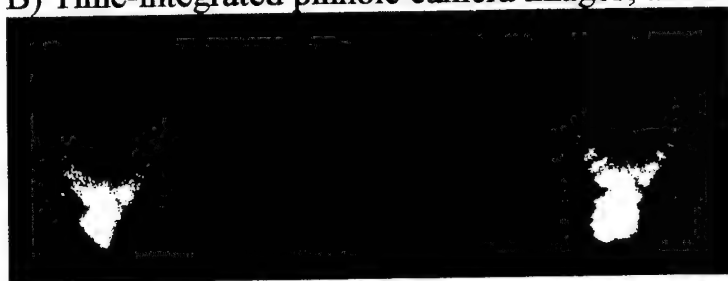
A) Time-gated x-ray images. Anode is just below images.

Top image $\lambda < 10\text{\AA}$



A) 6 5 4 3 2 1 Lower image $\lambda < 3.5\text{\AA}$

B) Time-integrated pinhole camera images; anode is at top of images.

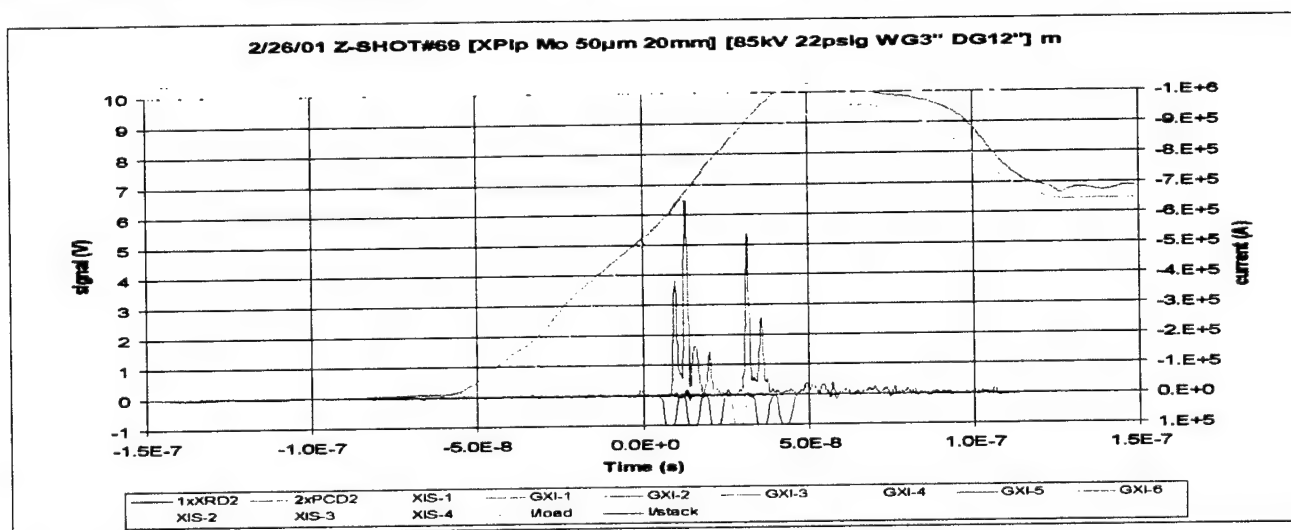


B) $\lambda < 3.5\text{\AA}$

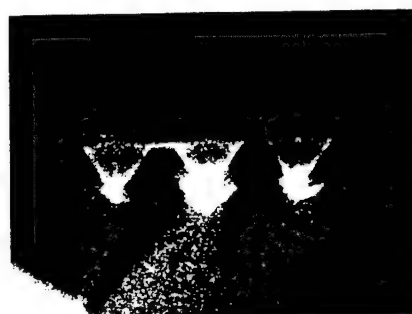
$\lambda < 10\text{\AA}$

— 5mm

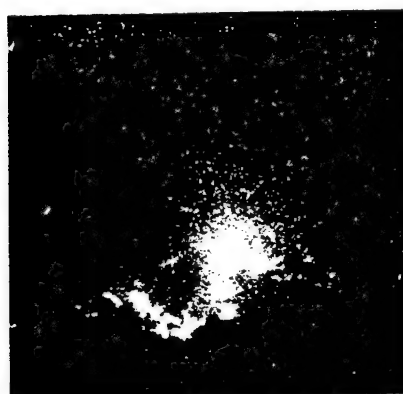
C) GXI frames (correspond to A): 1 2 3 4 5 6 (see below time axis).

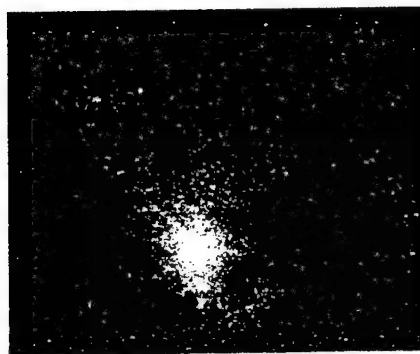


Mo planar-loop x-pinch with a 50- μm wire diameter and a 20-mm anode-cathode gap (shot #69, February 26, 2001). A) Gated x-ray images. Frame 4 ns. Spatial resolution 230 μm . Top image on each strip filtered for $\lambda_{1/10} < 10\text{\AA}$, the lower image for $\lambda_{1/10} < 3.5\text{\AA}$. B) Time-integrated pinhole camera images (Kodak DEF-5 x-ray film), with the same view as in A. Spatial resolution 580 μm . C) X-pinch current (thick smooth line), GXI frames, XRD (with 8 μm Be filter) and PCD (with 25 μm kapton filter) response versus time.


 $\lambda < 5\text{\AA}$ $\lambda < 7.9\text{\AA}$ $\lambda < 2.6\text{\AA}$

---- 10 mm

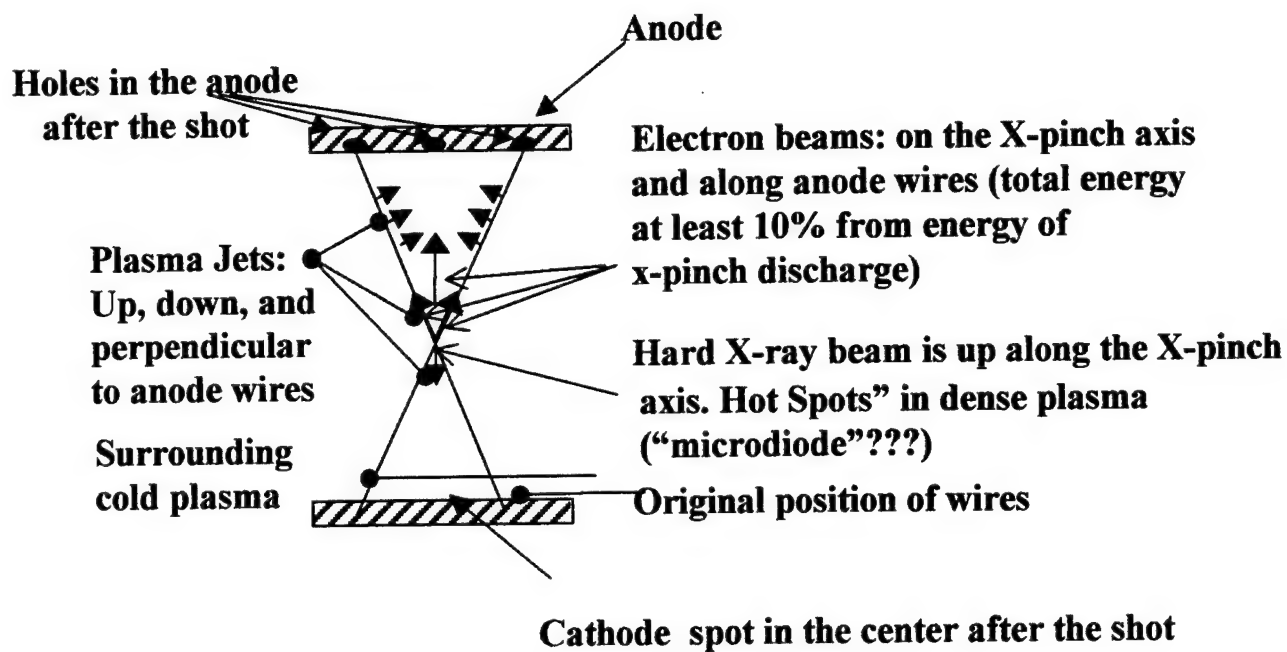

 $\lambda < 7.9\text{\AA}$

 ----- 650 μm

 $\lambda < 2\text{\AA}$

 ----- 650 μm

Mo planar-loop x-pinch with a 50- μm wire diameter and a 20-mm anode-cathode gap (shot #59, November 29, 2000). Anode is at top of images. A) Time-integrated pinhole camera images (Kodak DEF-5 x-ray film). Spatial resolution 580 μm . B) Time-integrated pinhole camera images (Kodak DEF-5 x-ray film). Spatial resolution 60 μm . C) Time-integrated pinhole camera images (Kodak DEF-5 x-ray film). Spatial resolution 60 μm . The spot at the top from hot spots images is a result of penetration of hard x-ray through the Pt/Ir pinhole substrate.

The high-current x-pinch structure

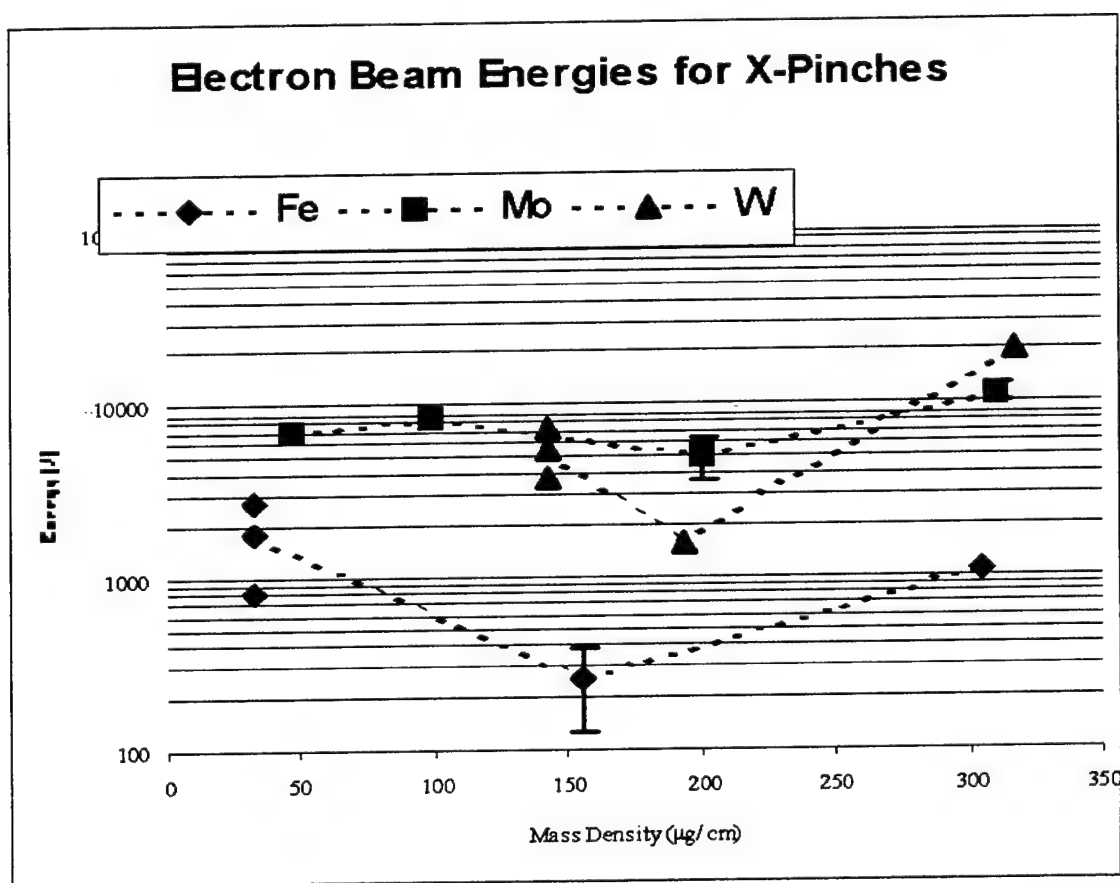


High-energy electron and x-ray beams in high-current x-pinch.

A strong, energetic electron beam is directed not only to the center of the anode (between the wires), but also toward the anode ends of the wires.

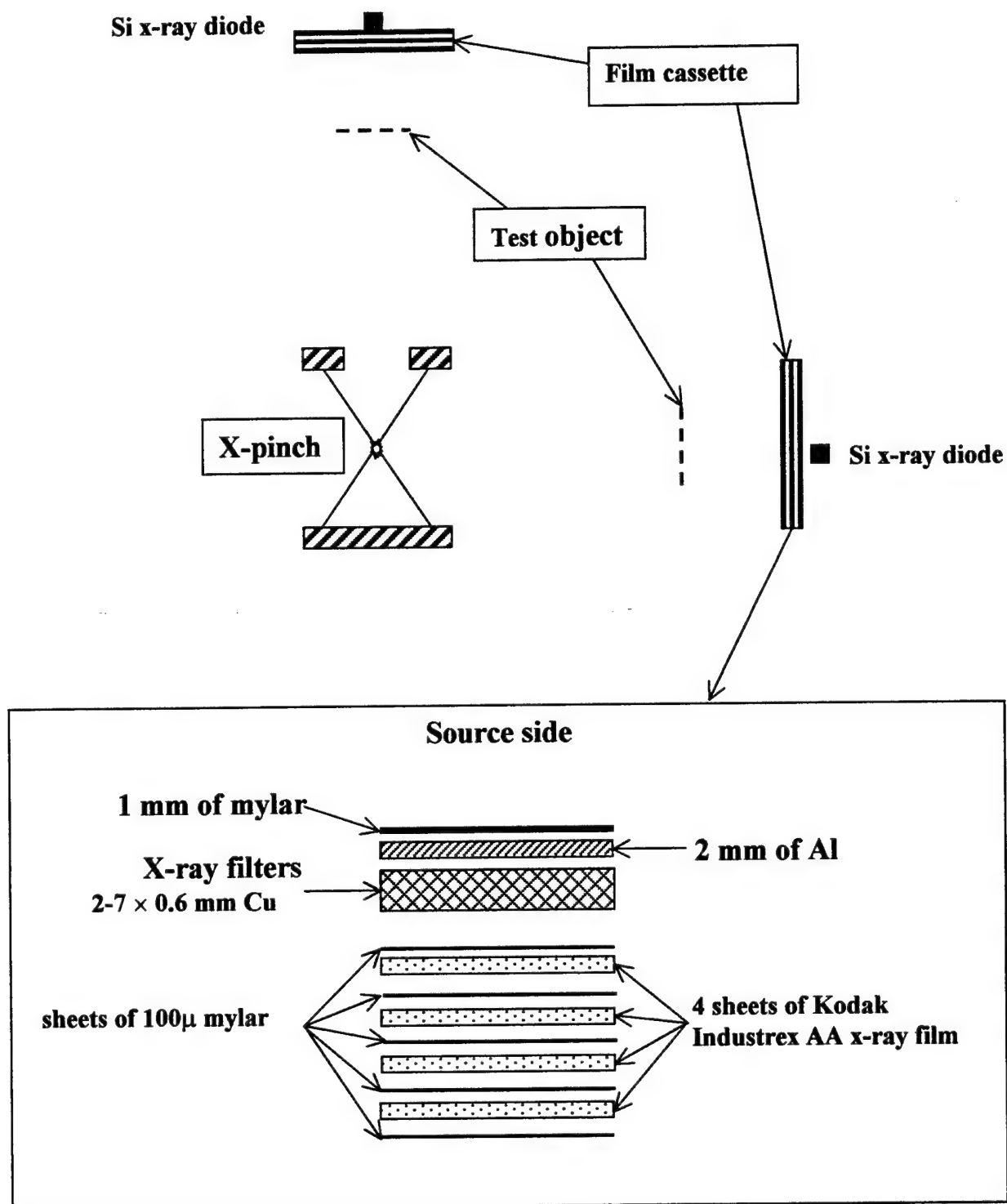
The experimental estimations of the width of the central jet on x-pinch x-ray images and a width of Fe K_{α} spectral lines (generated on a steel anode) in the NTF experiments have shown that a diameter of such electron beam in high-current x-pinchs may be smaller than 1mm.

Presence of a very powerful high energy electron beam in plasma can lead to generation of hard x-ray radiation in a cross point as a result of interaction of this beam with a matter and a local magnetic field.

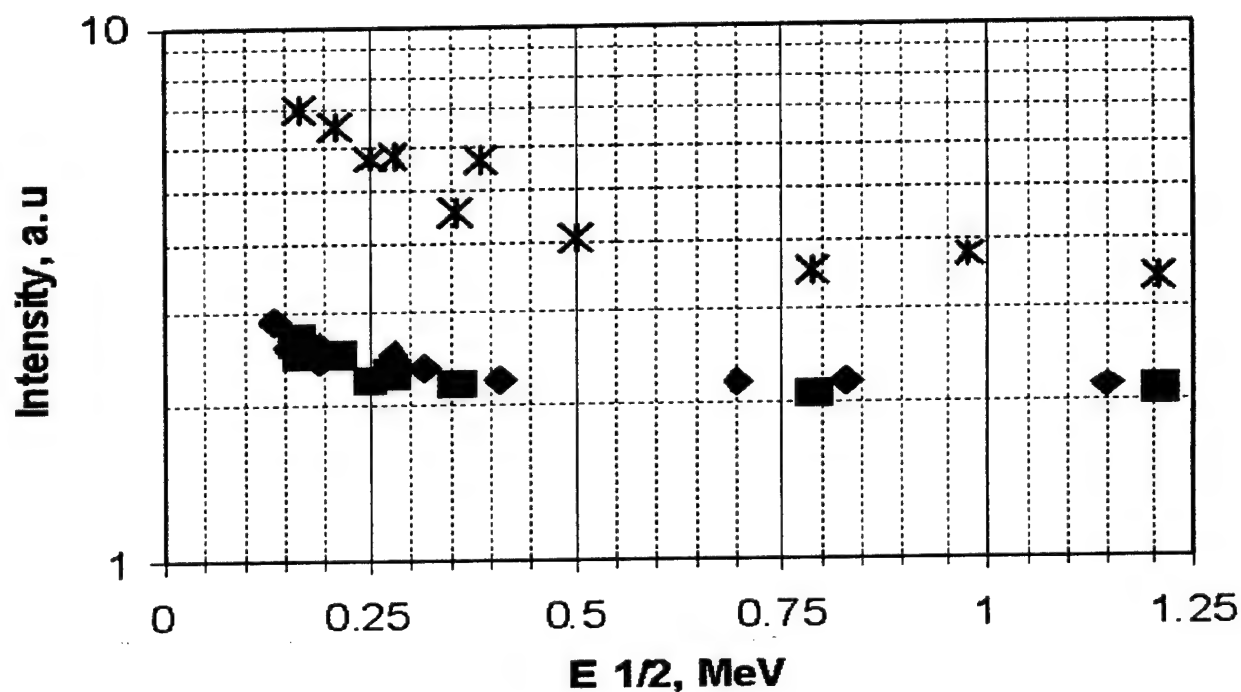


The experimental estimation of the energy needed to generate the observed holes at the points of connection of the wires with the anode of an x-pinch vs mass density of wires.

The NTF hard x-ray experiments



Relative spectra of hard x-rays emitted from Mo and Fe x-pinch.



- × Mo x-pinch 50 μm (end-on detector). Shot # 83
- Mo x-pinch 50 μm (side-on detector). Shot # 83
- ♦ Fe x-pinch 50 μm (end-on detector). Shot # 76

**Main portion of electrons with the energy smaller 40-50 keV,
and some amount of electrons with the energy at least 0.5-1.0 MeV.**

Time-resolved measurements are in progress.

Hard x-ray images of test objects correspond to point source geometry



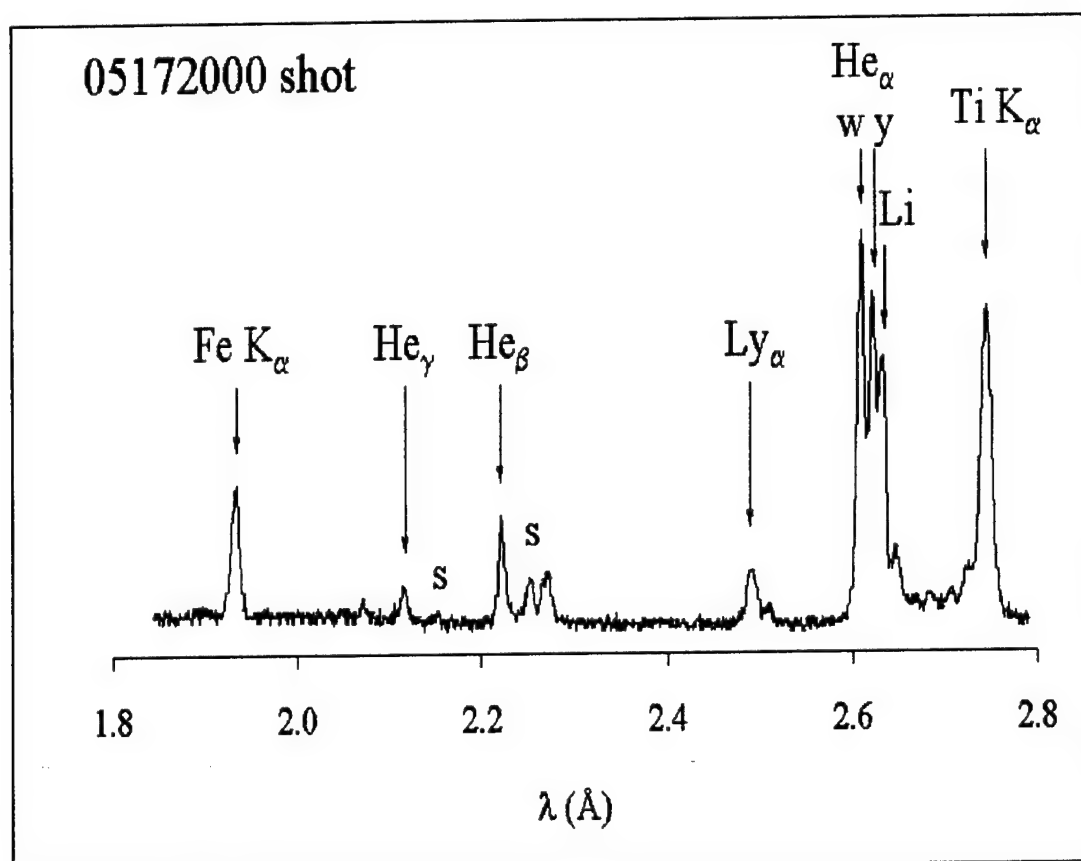
Steel tubes (diameter 15-17mm), and an Al tube (diameter 10-12 mm) connected by a 1 mm thick Cu wire. Shot #71, 50 μ m Mo x-pinch. End-on.
 $E_{\text{cutoff}} \approx 120$ keV for the inner part of steel tubes.



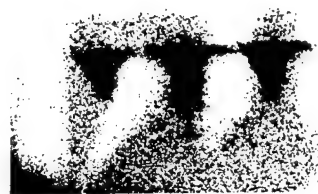
Steel tubes (diameter 15-17mm), and an Al tube (diameter 15-18 mm) connected by a bundle of 0.2 mm thick Cu wires. Shot #71, Mo x-pinch. Side-on.
 $E_{\text{cutoff}} \approx 80$ keV for the inner part of an Al tube.



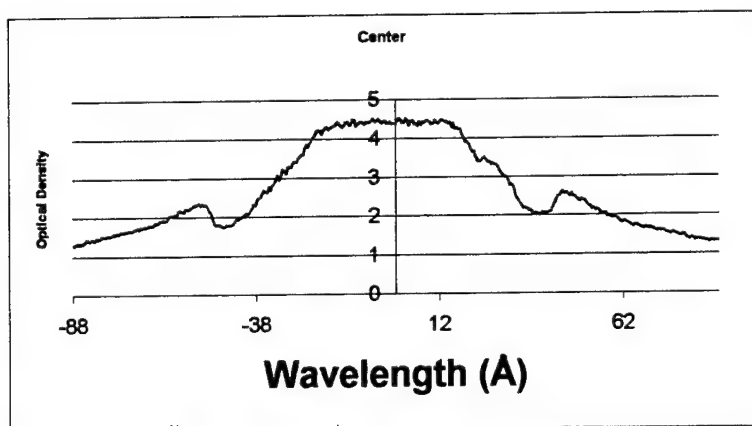
An Al tube with thread (diameter 10-12 mm), and a steel ring (thickness 2.5 mm) connected by a 1 mm thick Cu wire. Shot #69, 50 μ m Mo x-pinch. End-on.
 $E_{\text{cutoff}} \approx 60$ keV for the inner part of an Al tube.

*X-ray spectra of high-current x-pinch sources.*Time-integrated x-pinch spectra ($\lambda < 20 \text{ \AA}$)

Time-integrated TGS x-pinch spectra (20-80 Å)



12mm

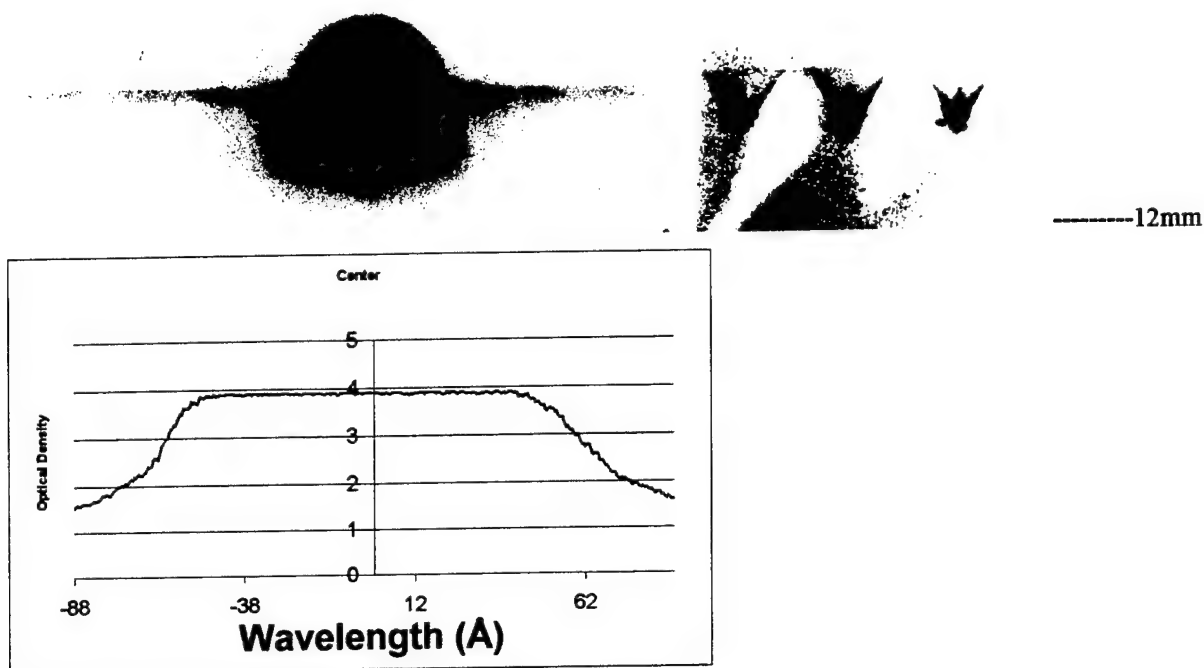


Fe planar-loop x-pinch with a 50 μm wire diameter and a 20-mm anode-cathode gap (shot #50, October 13, 2000). Kodak DEF-5 x-ray film.

Time-integrated x-ray spectrum with 1D resolution (top left). Resolution is 200 μm . The anode is below the image. The profile of Fe L- shell and continuum spectra is just below. The jump in optical density near 44 Å corresponds to a high concentration of a carbon in a x-ray film.

Time-integrated x-ray pinhole (top right, anode is above images).

Resolution is 580 μm . Images are filtered for: right $\lambda < 5$ Å, center $\lambda < 7.9$ Å, left $\lambda < 2.6$ Å.



Mo planar-loop x-pinch with a 62 μm wire diameter and a 20-mm anode-cathode gap (shot #52, October 20, 2000). Kodak DEF-5 x-ray film. Time-integrated x-ray spectrum with 1D resolution (top left). Resolution is 200 μm . The anode is below the image. An overexposed circle is an image of a TGS holder due to a strong hard x-ray radiation from a Mo x-pinch.

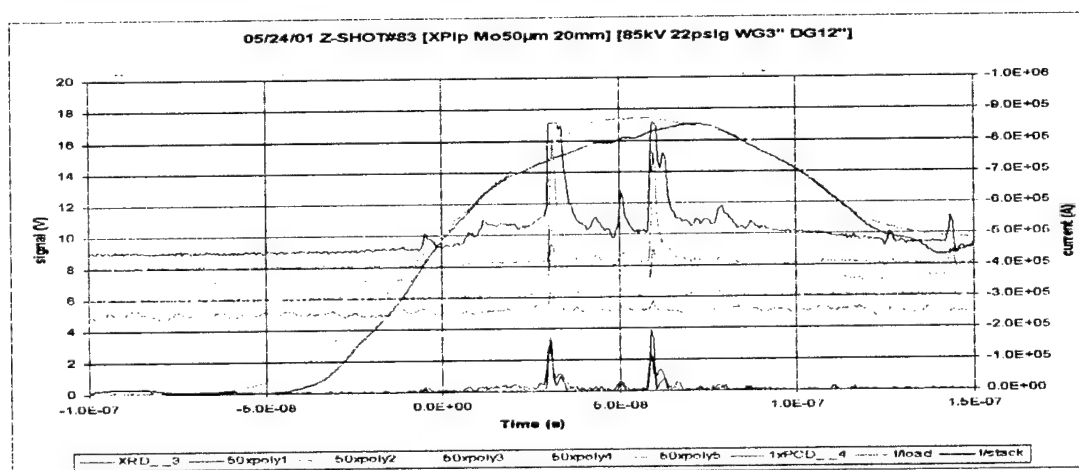
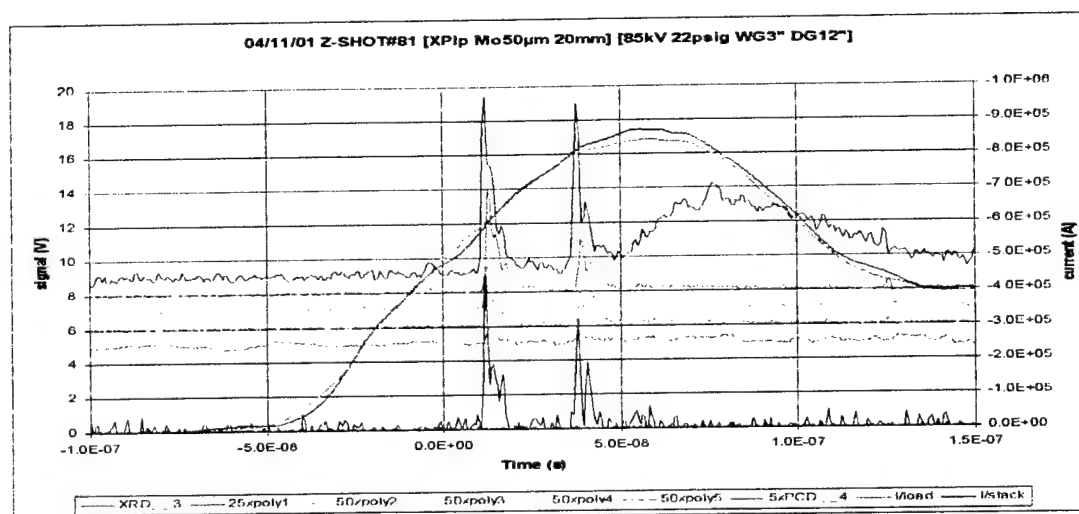
The profile of Mo spectra is just below. The jump in optical density near 44 Å corresponds to a high concentration of a carbon in a x-ray film. Note that size of a Mo longwavelength emitting region is much smaller in comparison with Fe.

Time-integrated x-ray pinhole camera image (top right). The anode is above images. Resolution is 580 μm . Images are filtered for: right $\lambda < 2.6$ Å, center $\lambda < 7.9$ Å, left $\lambda < 5$ Å

Time-resolved x-pinch spectra ($\lambda < 20\text{\AA}$) obtained from "Polychromator" and 1DXIS spectrometers.

X-ray signals from a 50 μm Mo x-pinch (shot # 81, April 11, 2001).

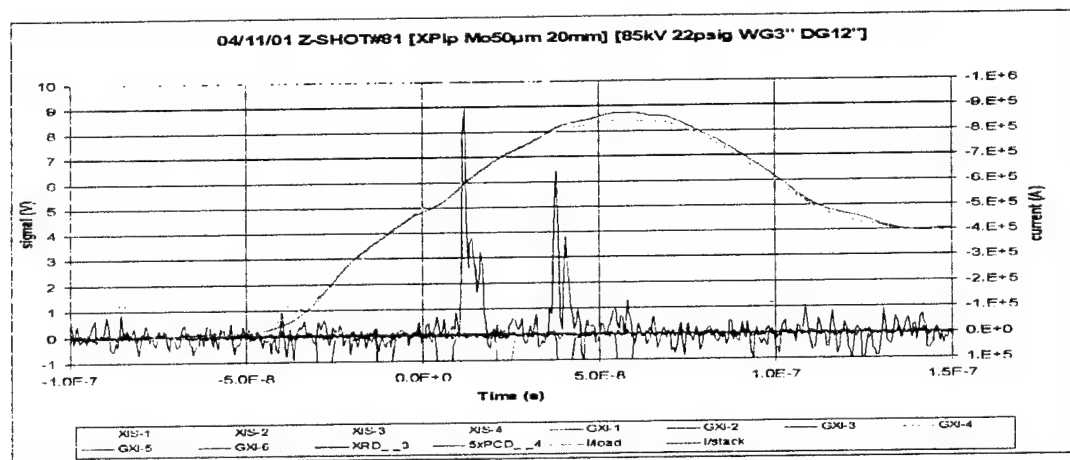
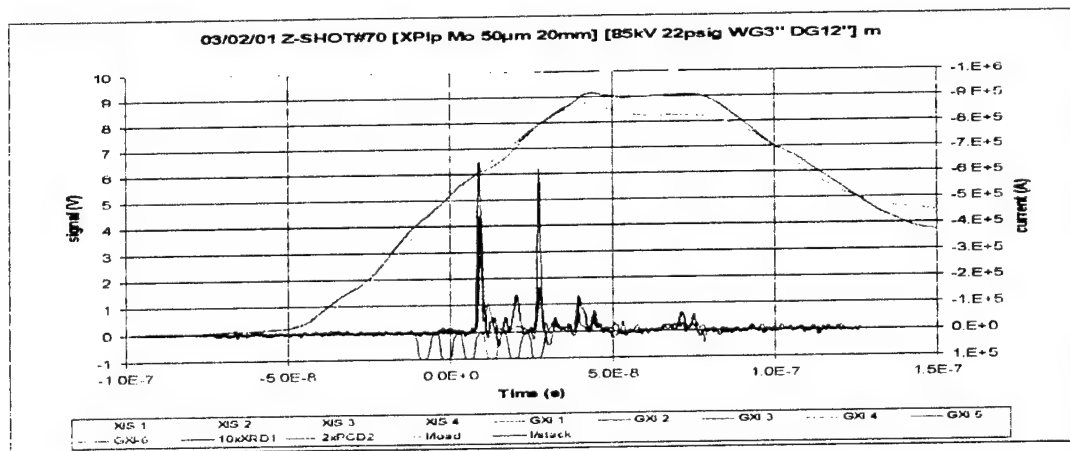
"Polychromator" (chan.1: $\lambda=5.21\text{\AA}$, Ne-like Mo; chan.2: $\lambda=4.80\text{\AA}$, Ne-like Mo; chan.3: $\lambda=1.94\text{\AA}$, "cold" $\text{K}\alpha\text{Fe}$; chan.4: $\lambda=4.41\text{\AA}$, Ne-like Mo; chan.5: $\lambda=5.5\text{\AA}$, continuum, control line). PCD (with 25 μm kapton filter) response versus time.



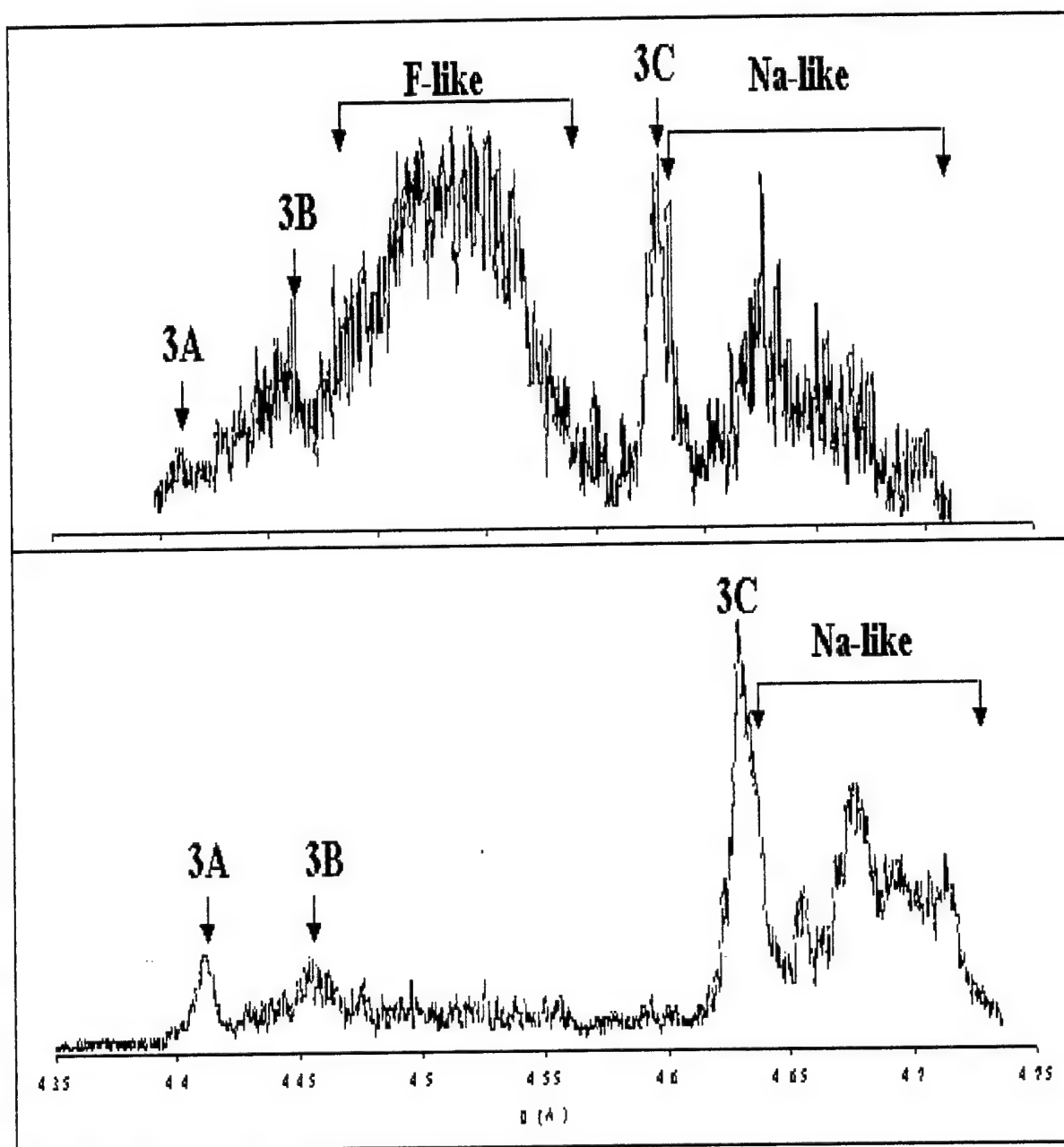
X-ray signals from a 50 μm Mo x-pinch (shot # 83, May 24, 2001).

"Polychromator" (chan.1: $\lambda=5.21\text{\AA}$, Ne-like Mo; chan.2: $\lambda=4.80\text{\AA}$, Ne-like Mo; chan.3: $\lambda=1.94\text{\AA}$, "cold" $\text{K}\alpha\text{Fe}$; chan.4: $\lambda=4.41\text{\AA}$, Ne-like Mo; chan.5: $\lambda=5.5\text{\AA}$, continuum, control line). PCD (with 25 μm kapton filter) and XRD (with 8 μm Be filter) response versus the time.

X-ray signals from a 50 μm Mo x-pinch (shot # 70, March 02, 2001). PCD (with 25 μm kapton filter) and XRD (with 8 μm Be filter) responses versus time. 1DXIS frames just above x-pinch current curves. Frame #3 coincides with the first x-ray burst (current 600 kA).



X-ray signals from a 50 μm Mo x-pinch (shot # 81, April 11, 2001). PCD (with 25 μm kapton filter) response versus time. 1DXIS frames are just above x-pinch current curves. Frame #4 coincides with an x-ray prepulse before the first x-ray burst (current 550 kA).



Time-resolved L-shell Mo x-pinch spectra recorded on 03/02/01 (shot#70, see Fig.18) at the top, and 04/11/01(shot#81, see Fig. 19) at the bottom.

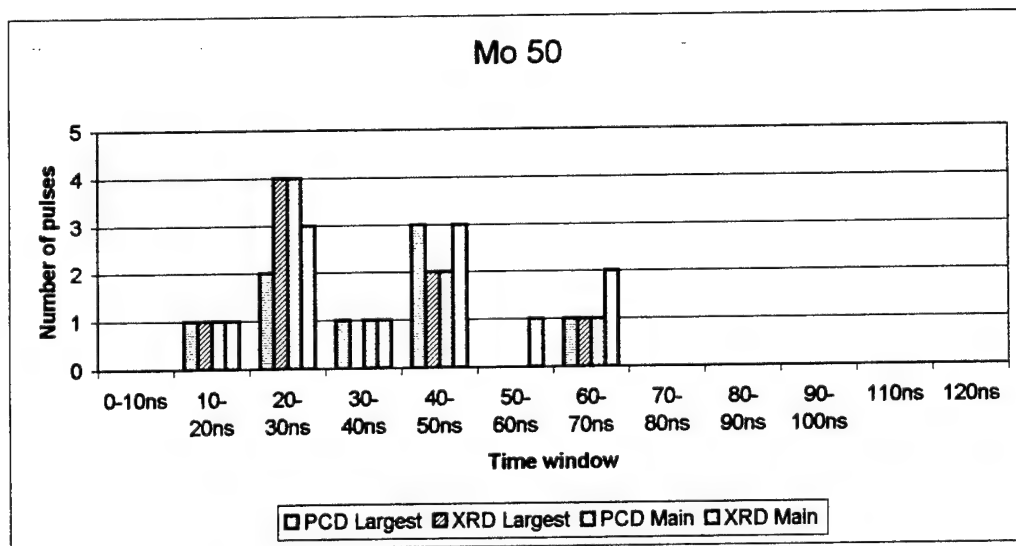
Time scaling of high current x-pinch x-ray/EUV pulses

Minimum pulse duration of a high current x-pinch

	<u>PCD (filter)</u>	<u>XRD (filter)</u>	<u>XRD (filter)</u>
Ti	2.2±0.4 ns (Be8μm)	4±1ns(kimfoil 5μm)	
Fe	1.3±0.7 ns (Be8μm)	3.7±0.7ns(kimfoil 5μm)	
Mo	1.1±0.5 ns (kapton25 μm)	1.2±0.7ns(Be 8μm)	15-20 ns(kimfoil 5μm)
W	1.1±0.7 ns (kapton25 μm)	1.1±0.7 ns(Be 8μm)	15-20 ns(kimfoil 5μm)
Pt	1.2±0.7 ns (kapton25 μm)	1.1±0.7 ns(Be 8μm)	

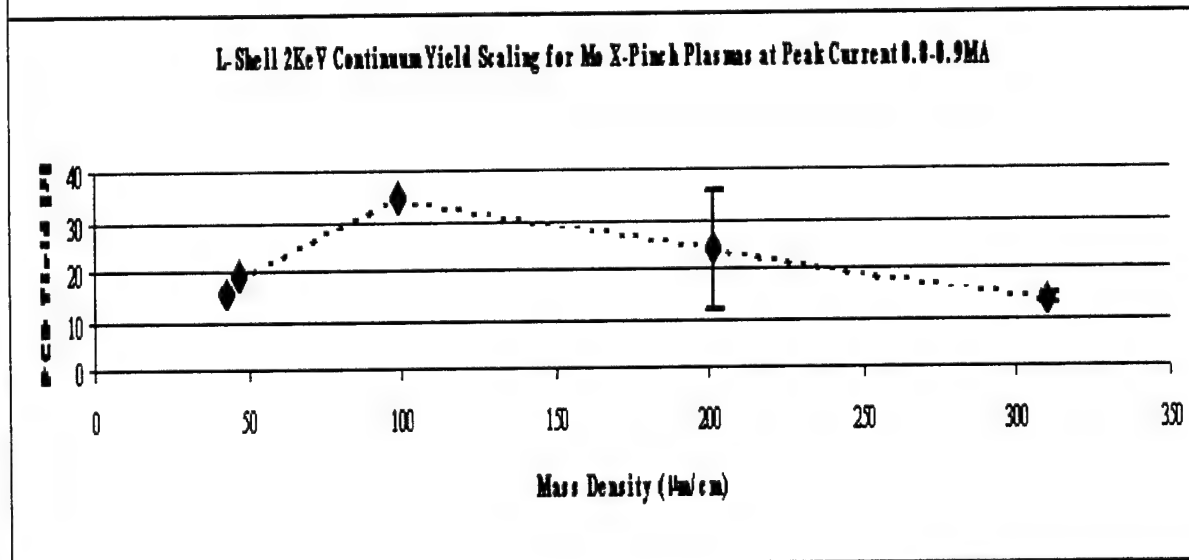
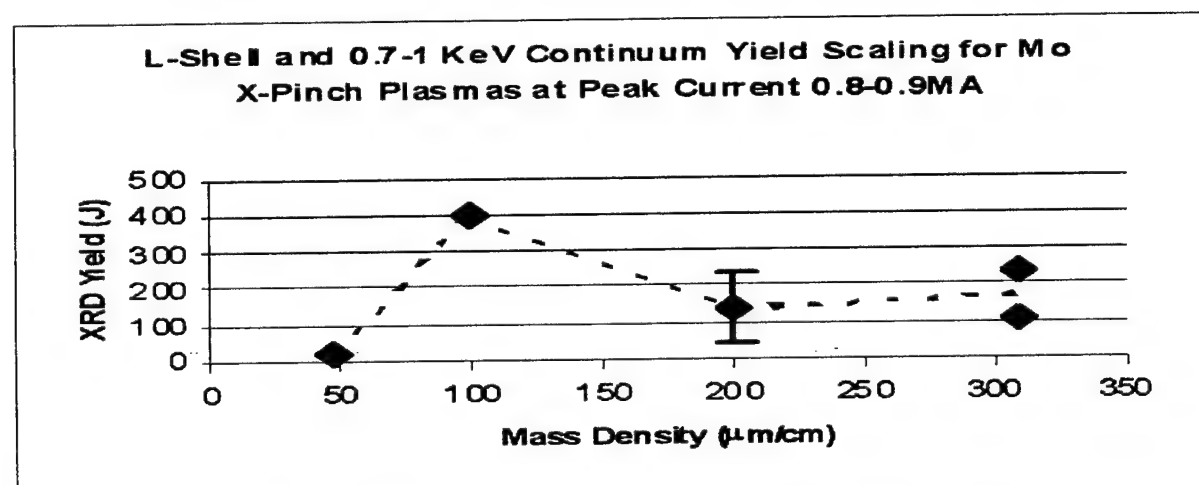
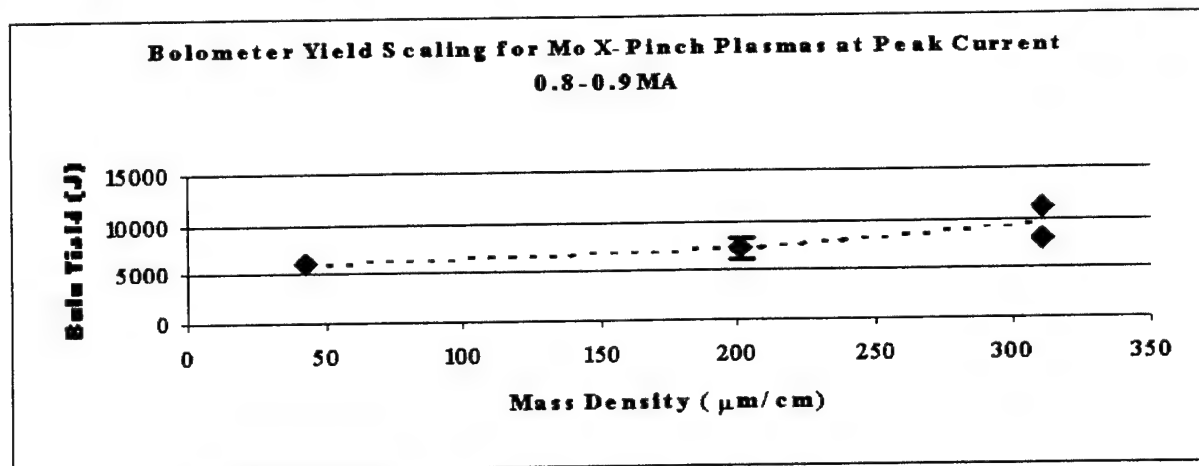
Probability of generation of one or two x-ray bursts during x-pinch discharge

	One burst	Two bursts
Ti (2x30 μm)	0.35	0.25
Fe (2x50 μm)	0.15	0.15
Mo (2x50 μm)	0.20	0.4-0.5



The time distribution of PCD and XRD signals for 50μm Mo x-pinch. Largest: the signals with a maximum amplitude; main: signals with an amplitude from 0.9 to 0.3 of the largest value. The data are based on 8 shots.

The energy scaling of x-ray/EUV pulses from Ti, Fe, Mo x-pinchs, single wires and a V-pinch



The energy scaling of x-ray radiation from Ti, Fe, Mo, W, and Pt 0.9 MA x-pinch

The maximum total energy for x-pinch was measured 10-11 kJ for Mo x-pinch, 7-8 kJ for Fe, W, and Pt, and 6 kJ for Ti.

For a Mo x-pinch optimum yield was obtained with a mass density of 100-200 $\mu\text{g}/\text{cm}$. Mo x-pinch irradiated up to 250-350 J in L-shell and 0.7-1 keV in continuum (XRD signals), and about 20-30 J in L-shell and 2 keV in continuum (PCD signals).

For a Fe x-pinch optimum yields were obtained with a mass density of 150 $\mu\text{g}/\text{cm}$. Fe x-pinch irradiated up to 1 kJ in L-shell and 0.25 keV in continuum (XRD signals), and about 100-150 J in K-shell and several keV in continuum (PCD). Fe x-pinch yield in region 0.5-0.15 keV was about 2 kJ (TGS measurements).

Optimum yields for a Ti x-pinch were obtained with a mass density of 200 $\mu\text{g}/\text{cm}$. The total K-shell radiation was 20-30 J. The total L-shell radiation was 3-4.5 kJ. All these parameters are approximately 3-10 times bigger than those for a lower current (0.2-0.4 MA) Ti x-pinch or for single wire Ti z-pinch at 0.6-0.7 MA.

The M-shell and 0.7-1 keV continuum (XRD) yield for W varied from 25 to 15 J, and L-shell and 2 keV continuum (PCD) changed from 20 to 5-6 J.

The M-shell and 0.7-1 keV continuum (XRD) yield for Pt was around 15 J.

Conclusion

X-pinch at a high current (0.8-0.9 MA) is a bright pulsed source of x-rays in a wide spectral region from 0.1 keV to 100-300 keV. The high current x-pinch is a good candidate to develop a new (harder) x-ray backlighter, to test x-ray spectropolarimetry (a powerful new tool for studying the anisotropy of high-temperature plasmas), to examine the final stage of the MHD instability.

Main directions of the NTF x-pinch studies are:
understanding of dynamics of plasma implosion that lead to generations of very short x-ray pulses;
determinations of plasma conditions in x-pinch hot spots;
understanding of influence of strong energetic electron beams on parameters of plasma and studies of anisotropy of x-pinch plasma.

New x-ray diagnostics have been developed. The new x-ray/EUV instrumentation for time-resolved imaging and spectroscopy has been developed and used in x-pinch experiments.

Polarization measurements of x-ray x-pinch spectra have been started and polarization of Ti K-shell spectra were measured.

Hard x-ray measurements have shown that hard x-ray radiation from a high current x-pinch is anisotropic, and a source of this radiation has a small size.

Theoretical modeling of K-shell (Ti) and L-shell (Mo, Fe) x-ray spectra have been developed and used for measurements of temperature and density of x-pinch plasma in experiments.

Theory of L-shell polarization measurements of magnetic field in dense hot z-pinch plasma was developed.

The preliminary results of high current experiments show that a structure of x-pinch includes strong energetic electron beams, that directed to the anode and along the wires. Strong jets were observed directed toward the discharge axis, perpendicular to the wires.

The emitting region of a x-pinch consists of bright spots formed at the cross point of x-pinch. Minimum size of the emitting region was observed for planar-loop Mo x-pinch with a number of hot spots to 1-5 with minimum size of spots at 1.5-2 Å (continuum with planckian spectra).

The maximum total energy for x-pinch was more than 10-11 kJ for Mo x-pinch, 7-8 kJ for Fe, Pt and W, and 6 kJ for Ti.

Minimum x-ray pulse duration was about 1-1.5 ns. For Mo, Ti, and W we observed that x-ray pulses occurred in two or three groups, in the narrow time intervals after the start of the current.

The quality of an x-pinch structure is in strong dependency from original symmetry of an x-pinch and its plainness.

APPENDIX I

Features of Soft X-Ray and X-Ray Radiation from Point Laser Plasma and Z-Pinch Sources Transported by Glass Capillary Converters (Experiment)

V.L. Kantsyrev, D.A. Fedin, S.V. Kukhlevsky, B.S. Bauer, and N. Quart

Proc. SPIE 4144, 128-136 (2000)

Features of soft x-ray and x-ray radiation from point laser plasma and z-pinch sources transported by glass capillary converters (experiment).

V.L. Kantsyrev*, D.A. Fedin, S.V. Kukhlevsky*, B.S. Bauer, N. Ouart.

Department of Physics / 220, University of Nevada, Reno, Reno, NV 89557, USA.

*Department of Experimental Physics, JPTE University, 7624 Pecs, Hungary.

ABSTRACT

This research is a continuation of our activity on the development and study of glass-capillary optics devices that started in 1974¹. We presented new results of the experimental study of a strongly nonuniform spatial distribution of output keV and sub-keV radiation, that transported by different types of glass mono- and policapillary converters from point x-ray laser plasma and z-pinch plasma sources.

Keywords: glass capillary, x-ray, diagnostics.

1. INTRODUCTION

The application of glass capillaries as a waveguide optical system for transporting, focusing, and analyzing x-ray and extreme ultraviolet (EUV) radiation from plasma sources has more than 25 years history.¹⁻³ X-ray or EUV glass capillary optics operates through multiple reflections of radiation on the inner capillary wall under an angle of incidence smaller than critical. The ability of glass capillaries to capture, to guide, to change cross-section, to modify spectra, and to concentrate into a small size the x-ray or EUV beams from point sources has been employed by various scientific applications⁹⁻¹¹.

The main performances of glass capillaries are as follows: a transmission coefficient, an angle of a divergence of an output radiation beam, size and shape of an output radiation beam. A number of factors affect these characteristics of glass capillary optics. There are:

1) capillary parameters: the chemical composition of the capillary wall (in particular this is ratio of concentration of light and heavy elements), dimensions and the shape of the capillary wall, the waviness and the roughness of the inner reflecting surface of a capillary;

2) x-ray or EUV source parameters: actual dimensions and the divergence of the radiation beam, the distance from the source to the entrance of the capillary, the energy distribution of the source radiation.

The most early and present research of the effects and significance of these parameters on the x-ray properties of capillaries were connected with the study in wavelength region $\lambda \leq 0.3 - 0.4$ nm using synchrotron radiation facilities or x-ray tubes. Our traditional directions of the development and study of glass-capillary optics were concerned of the creation of new types of spectral, imaging and polarimetry diagnostic instrumentation for plasma physics or atomic physics in the spectral region $100 \text{ nm} \geq \lambda \geq 0.2 - 0.3$ nm: soft x-ray and EUV radiation. In this article, we have presented some new results of the experimental investigation of the influence of glass capillary dimensions, shape and structure, distance to the capillary entrance from laser plasma and z-pinch sources of keV and sub-keV radiation on the capillary radiation beam transmission properties. Particularly, new results have been obtained from the experimental study and theoretical modeling of the nonuniform output angular distribution of x-ray radiation transported by different types of glass mono- and policapillary converters (GCCs) from x-ray plasma sources. These GCCs have been used in our new x-ray/EUV diagnostic devices.

*Correspondence: Email: victor@physics.unr.edu; <http://www.physics.unr.edu/faculty/kantsyrev/kantsyrev.html>;
Telephone: (775) 784-6809 or 971-2860; Fax: (775) 784-1398.

like Two-Dimensional X-ray Imaging capillary spectrometer (2DXIS)^{7,8} and glass-capillary polarimeter/spectrometer^{7,12,13}. The new design for GCCs has been developed in collaboration with Collimated Holes, Inc. (Campbell, CA, USA).

2. EXPERIMENT.

The experiments have been conducted at the laser plasma¹⁴ and the pulsed-power Zebra z-pinch sources at the Nevada Terawatt Facility (see report of B.S. Bauer, V.L. Kantsyrev, A.S. Shlyaptseva et al., Session 2 of the Conference 4144). X-ray radiation has been generated by hot, dense plasma with electron temperature 0.1-0.3 keV for laser plasma and 1-2 keV for z-pinch plasma, intense continuum spectra was in the region from 100 nm to 0.1 nm, an x-ray pulse duration was 3 ns for laser plasma and 1-40 ns for z-pinch plasma, the source size was 200-250 μm ¹⁴ for an intense core of a laser plasma flame at the wavelength 11-12 Å (more extended corona has total intensity at least 10 times smaller) and smaller than 100 μm for a z-pinch source (see report of B.S. Bauer, V.L. Kantsyrev, A.S. Shlyaptseva et al., Session 2 of the Conference 4144). Most experiments were conducted with a laser plasma source of x-ray. The structure of this setup is shown on Fig.1. The vacuum in experimental chambers of sources was 10^{-7} torr.

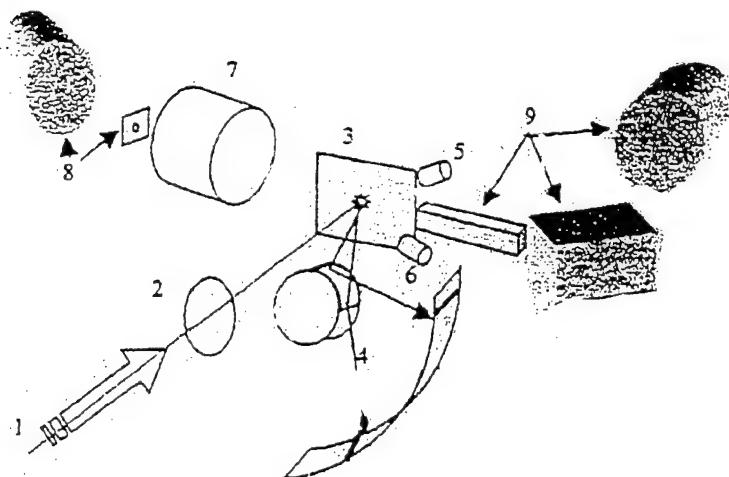


Fig.1. A structure of the laser plasma experimental setup installed during the capillary experiments
1. laser. 2. focusing lens. 3. Flat target. 4. Survey crystal spectrometer. 5. Pinhole camera. 6. Fast x-ray diodes. 7. Multichannel spectrometer. 8. Transmission grating spectrometer. 9. Testing glass-capillary converter with an x-ray film or MCP x-ray/EUV imagers.

Schemes of measurements with different glass capillaries are shown on Fig.2. The distance from x-ray sources to a capillary entrance varied from 0.1 cm to 70 cm. Capillaries used in this experiment were not ideally straight providing no straight rays through capillaries to exit from a device.

The entrance of a GCC was protected by a 25-50 μm Be filter (in experiments at Zebra z-pinch) and 1 μm PET filters (in laser plasma experiments). During all experiments we can monitor main parameters of the x-ray sources: an effective size of the source, x-ray spectra, and a power of the x-ray source. The average wavelength of x-ray that irradiates of capillaries entrance was 11-12 \AA and 2.6 \AA in laser plasma (Cu target) and z-pinch (Ti wire load) experiments respectively.

We tested polycapillaries with an inner diameter of channels 20 μm , 37 μm and 67 μm . These polycapillaries have been made from Corning 7052 glass. From same glass also monocapillaries with an inner diameter 120 μm were made. Another monocapillaries with an inner diameter 390 μm consist from a pure quartz. The length of capillaries varied from 10 cm to 70 cm. The distance from a source to a capillary entrance was from 1 cm to 100 cm to simulate real conditions in plasma experiments.

The observation distance from a capillary exit to a cassette with the UF-ShS x-ray film protected by the aluminized 3 μm PET filter was typically 3-15 cm.

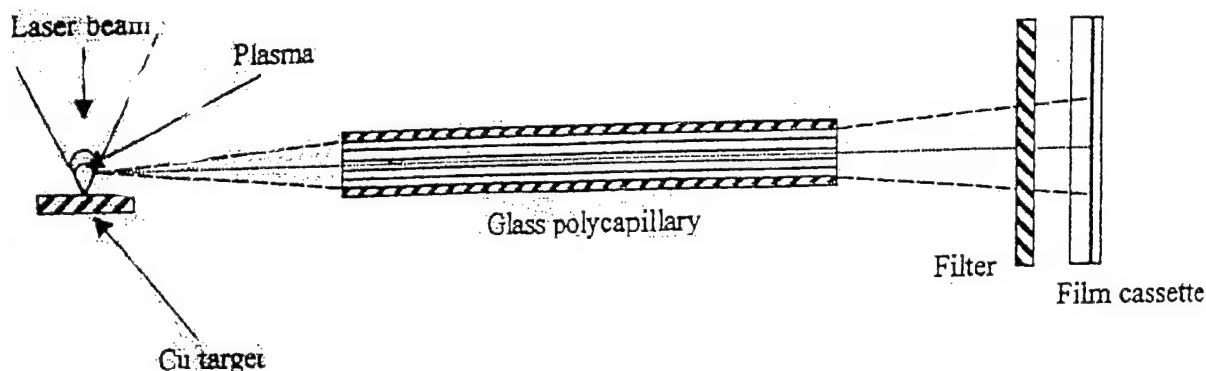


Fig. 2. Scheme of experiments with a straight capillary

Capillaries were aligned to plasma sources by means of a translational/rotational stage having four degrees of freedom (three translations and one rotation). The prealignment was done using a light of a laser spark on the surface of the target without vacuum in the laser plasma source chamber, or He-Ne laser that is placed in the vacuum chamber of a Zebra z-pinch source before shot.

3. RESULTS and DISCUSSION.

In most our experiments capillaries have parallel bore holes. Due to the same entrance and exit dimensions these capillaries serve as x-ray collimators. For an ideal straight capillary the rays which enter the device and reflect from a capillary wall below the critical angle are transmitted through the glass tube retaining the initial angle of incidence during consecutive reflections. Hence, the beam divergence is

The entrance of a GCC was protected by a 25-50 μm Be filter (in experiments at Zebra z-pinch) and 1 μm PET filters (in laser plasma experiments). During all experiments we can monitor main parameters of the x-ray sources: an effective size of the source, x-ray spectra, and a power of the x-ray source. The average wavelength of x-ray that irradiates of capillaries entrance was 11-12 \AA and 2.6 \AA in laser plasma (Cu target) and z-pinch (Ti wire load) experiments respectively.

We tested polycapillaries with an inner diameter of channels 20 μm , 37 μm and 67 μm . These polycapillaries have been made from Corning 7052 glass. From same glass also monicapillaries with an inner diameter 120 μm were made. Another monicapillaries with an inner diameter 390 μm consist from a pure quartz. The length of capillaries varied from 10 cm to 70 cm. The distance from a source to a capillary entrance was from 1 cm to 100 cm to simulate real conditions in plasma experiments.

The observation distance from a capillary exit to a cassette with the UF-ShS x-ray film protected by the aluminized 3 μm PET filter was typically 3-15 cm.

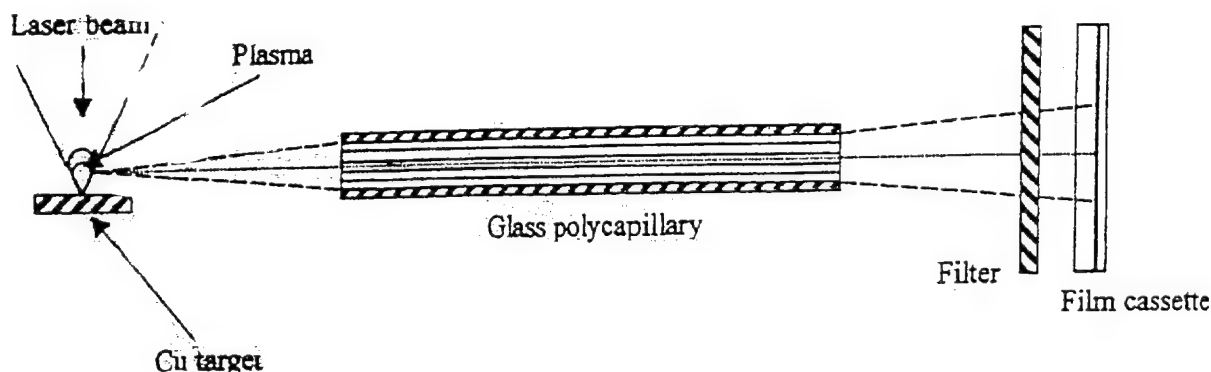


Fig.2. Scheme of experiments with a straight capillary

Capillaries were aligned to plasma sources by means of a translational/rotational stage having four degrees of freedom (three translations and one rotation). The prealignment was done using a light of a laser spark on the surface of the target without vacuum in the laser plasma source chamber, or He-Ne laser that is placed in the vacuum chamber of a Zebra z-pinch source before shot.

3. RESULTS and DISCUSSION.

In most our experiments capillaries have parallel bore holes. Due to the same entrance and exit dimensions these capillaries serve as x-ray collimators. For an ideal straight capillary the rays which enter the device and reflect from a capillary wall below the critical angle are transmitted through the glass tube retaining the initial angle of incidence during consecutive reflections. Hence, the beam divergence is

preserved when such an optical element is used, assuming that it is aligned perfectly with a central ray or an incoming beam. It is the "on axis scheme" when the plasma source is completely fitted with a capture entrance angle (Fig. 3). The situation is different when the optical axis of the capillary is shifted relative to a plasma source ("off axis scheme") (Fig. 3), or a distance from a source to a capillary is large enough that a plasma source could not fill a capture entrance angle of a capillary.

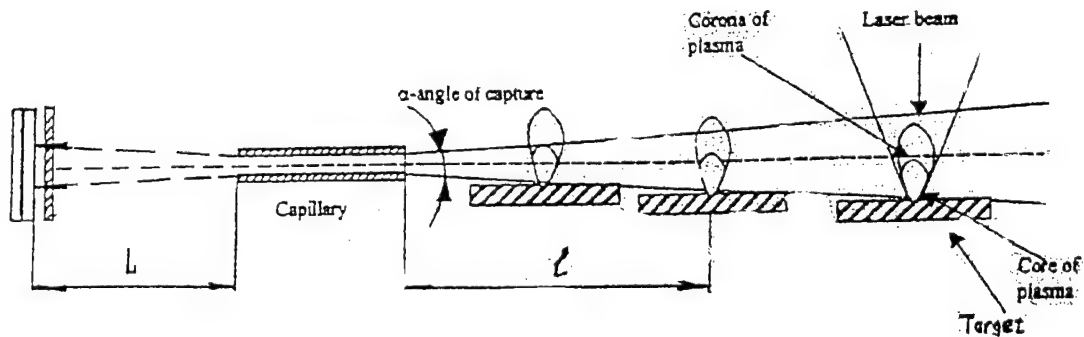


Fig. 3. Scheme of experiments with a straight capillary and different distances from a laser plasma source to a capillary entrance.

Experimental output x-ray images corresponding to various distances from a plasma source to a capillary entrance are shown on Figs. 4. The remarkable difference between images related to short (12-15 mm) and long distances (more than 17-18 mm when the central part of the image is not illuminated) results in the appearance of rings (Figs. 4 a, 4b, 4e) and spiral-like structures (Fig. 4c) instead of continuous spots (Fig. 4d). More interestingly these images also show a clear but irregular ring-like structure (Figs. 4a,b).

The possible reasons for these effects may be a geometrical misalignment of a capillary (Fig. 3) a short range inner surface of a capillary or a long range inner surface of a capillary (waviness)¹⁵. These studies are mainly based on the geometric optics approximation. Recently, the interference of x-rays has been manifested in some experiments on the grazing reflections of x-rays in the capillary.^{14,17}

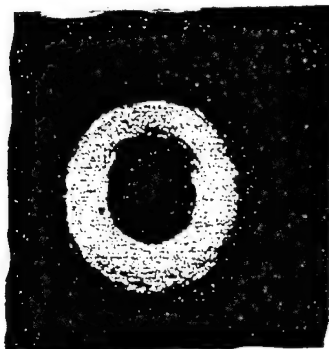
We plan to use a phenomenological explanation for simulation of our experimental results. This model is based on geometric optics and normal waveguides modes have been given for the interference of x-rays in the farfield zone of a capillary output.¹⁸⁻²¹ The results will be published later.

Geometry:
 $l=2.9\text{ mm}$
 $L=150\text{ mm}$

Filter #1: $1\mu\text{m}$ mylar

Filter #2: $6\mu\text{m}$ mylar + $.4\mu\text{m}$ Al

Scale: 1 cm:2 mm



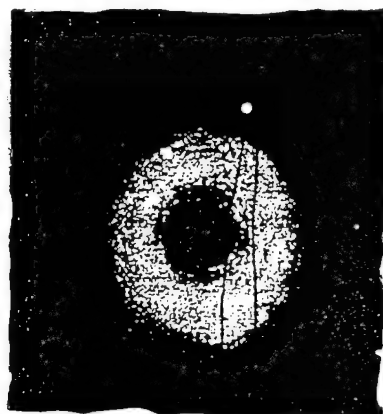
Figs. 4a. Experimental output image corresponding to a monocapillary. Material: quartz;
length of capillary: 290 mm; inner diameter: $390\mu\text{m}$

Geometry:
 $l=40\text{ mm}$
 $L=150\text{ mm}$

Filter #1: $1\mu\text{m}$ mylar

Filter #2: $6\mu\text{m}$ mylar + $.4\mu\text{m}$ Al

Scale: 1 cm:2 mm



Figs. 4b. Experimental output image corresponding to a monocapillary. Material: quartz;
length of capillary: 290 mm; inner diameter: $390\mu\text{m}$.

Geometry:

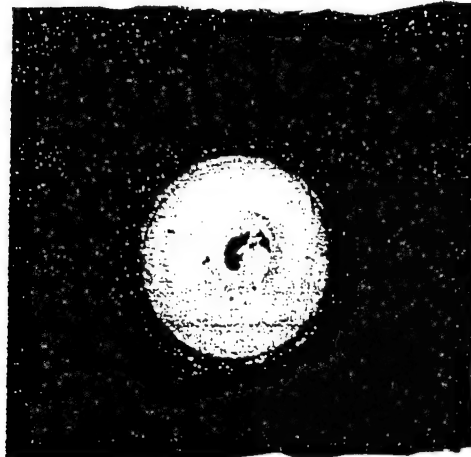
$l=20\text{mm}$

$L=170\text{mm}$

Filter #1: $1\mu\text{m}$ mylar

Filter #2: $6\mu\text{m}$ mylar + $.4\mu\text{m}$ Al

Scale: $1\text{cm}:2\text{mm}$



Figs. 4c. Experimental output image corresponding to a monicapillary. Material: quartz; length of capillary: 290 mm ; inner diameter: $390\text{ }\mu\text{m}$.

Geometry:

$l_1=12\text{ mm}$

$l_2=15\text{ mm}$

$l_3=37\text{ mm}$

$L_1=150\text{ mm}$

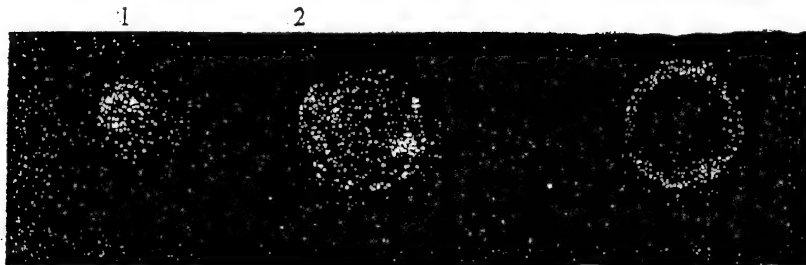
$L_2=150\text{ mm}$

$L_3=150\text{ mm}$

Filter #1: $1\mu\text{m}$ mylar

Filter #2: $6\mu\text{m}$ mylar + $.4\mu\text{m}$ Al

Scale: $1\text{cm}:2\text{mm}$



Figs. 4d. Experimental output image corresponding to various distances from a laser plasma source to a monicapillary entrance. Material: quartz; length of capillary: 290 mm ; inner diameter: $390\text{ }\mu\text{m}$.

Geometry:

$l=28$ mm

$L=150$ mm

Filter #1: $1\mu\text{m}$ mylar

Filter #2: $6\mu\text{m}$ mylar + $.4\mu\text{m}$ Al

Scale: 1cm:2mm

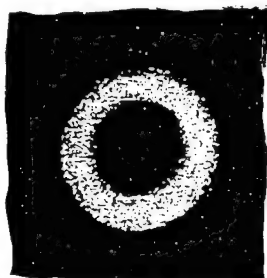


Fig. 4e. Experimental output image corresponding to a monocapillary. Material: Glass K-52 (Corning 7052); length of capillary: 250 mm; inner diameter: $120\mu\text{m}$.

New results have been obtained also from the experimental study of nonuniform output angular distribution of x-ray radiation transported by a glass polycapillary converter from an x-ray plasma source ($\lambda=11-12\text{ \AA}$). The experimental output x-ray image corresponding to the polycapillary is shown on Figs. 5.

Geometry:

$l=22.5$ mm

$L=150$ mm

Filter: $2 \times 3\mu\text{m}$ mylar

Scale: 2 cm : 1 mm

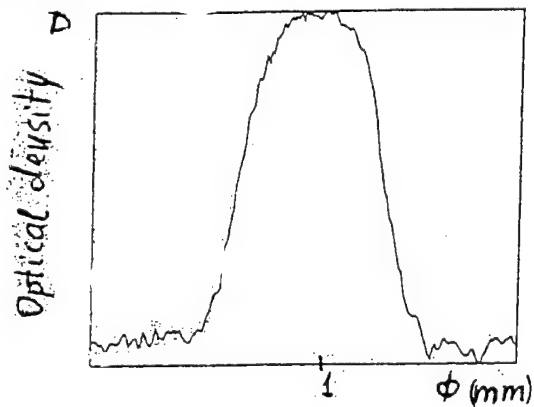


Fig. 5. Experimental output image corresponding to a polycapillary. Material: Glass Corning 7052; length of polycapillary: 250 mm; inner diameter of channels: $20\mu\text{m}$; number of channels: 19; total diameter of polycapillary: $110\mu\text{m}$.

The distribution of the output radiation from a polycapillary is much more uniform than that from monocapillaries (Figs. 4a-4e).

It was experimentally shown (Fig. 6) that the angle of output distribution of x-ray ($\lambda=11-12 \text{ \AA}$) for policapillaries strongly depends from an inner diameter of capillary channels and has been reduced from 1.5° to 0.5° when inner diameter decreases from $67 \text{ }\mu\text{m}$ to $20 \text{ }\mu\text{m}$. The same dependence was found for hard radiation ($\lambda=2.6 \text{ \AA}$).

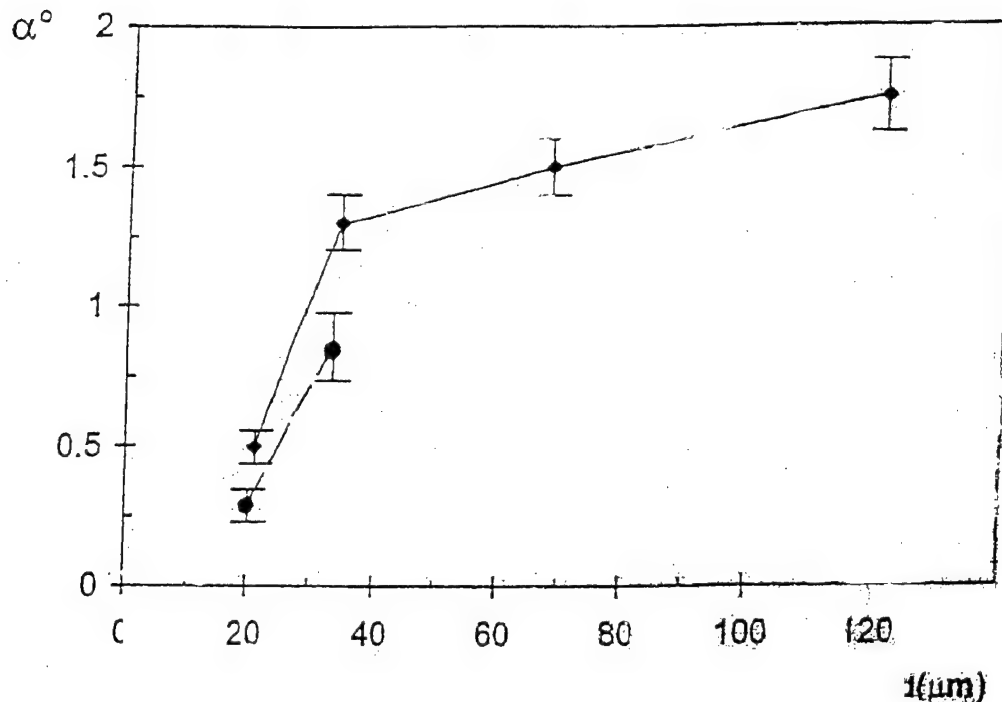


Fig. 6. The experimental dependence of output angle α of distribution of x-ray on the inner diameter d of mono- and policapillary channels: \bullet - $\lambda = 11-12 \text{ \AA}$; \bullet - 2.6 \AA .

These results are very important for application of above-mentioned policapillary structures in new x-ray/EUV diagnostics devices: Two-Dimensional X-ray Imaging capillary Spectrometer (2DXIS)^{7,8} and glass-capillary polarimeter/spectrometer^{7,12,13}.

4. REFERENCES

1. O. Ananyin, Yu. Bykovsky, V. Kantsyrev, Yu. Kozyrev, "Source of x-rays," *Certificate of Authorship* 520863, filed 15 October 1974 (USSR) (*Bull. Izobret. USSR*, N 11, p. 229, 1979).

2. P. Mallozzi, H. Epstein, R. Jung, D. Applebaum, B. Fairand, W. Gallagher, R. Uecker, M. Muckerheide, "Laser plasma as a source of x-rays for medical applications", *J. Appl. Phys.* **45**, pp. 1891-1895, 1974.
3. D. Mosher, S. Stephanakis, "X-ray light - pipe", *Appl. Phys. Lett.* **29**, 2, pp. 105 - 107, 1976.
4. Yu. Bykovsky, V. Kantsyrev, B. Komarov, Yu. Kozyrev, N. Permyakov, P. Pleshanov, "X-ray microscopy with laser plasma source", *Arch. Pathol. (in Russian)*, **12**, 78-82 (1978).
5. V. Kantsyrev, O. Petrukhin, A. Shlyaptseva, N. Mingaliev, S. Pikuz, V. Romanova, T. Shelkovenko, A. Faenov, "Investigating the characteristics of x-ray radiation from hot plasma by means of glass capillary converters", *Quantum Electronics*, **23**, 12, 1026 - 1029, 1993.
6. V. Kantsyrev, R. Bruch, M. Bailey, A. Shlyaptseva, "Enhancement of the flux density of line radiation in the extreme ultraviolet and soft x-ray spectral region for spectroscopic and plasma diagnostic applications using glass capillary converters", *Appl. Phys. Lett.* **66**, pp. 3567-3569 (1995).
7. V. Kantsyrev, B. Bauer, A. Shlyaptseva, R. Bruch, R. Phaneuf, "New optical instrumentation for hot plasma imaging, polarimetry, and spectroscopy, using glass capillary converters and multilayer mirrors", *Proc. Fourth Intern. Conf. "Dense Z-pinches" (1997)*, *ALP Proc.*, **CP409**, pp. 499 - 502, 1997.
8. B. Bauer, V. Kantsyrev, "Capillary spectrometer", The US Patent, # 5,991,024, filed May 29, 1998 (Prov. Appl. Field May, 30, 1997).
9. A. Rindby, "Application of fiber technique in the x-ray region", *Nucl. Instr. and Meth. In Phys. Res. A* **249**, pp. 536-540, 1986.
10. E.A. Stern, Z. Kalman, A. Lewis, K. Liberman, "Simple method for focusing x-rays using tapered capillaries", *Appl. Opt.* **27**, pp. 5135-5139, 1988.
11. V. Arkad'ev, A. Kolomiitsev, M. Kumakhov, I. Ponomarev, I. Knoddeev, Yu. Chertov, I. Shakhparonov, "Wide - band x-ray optics with large angular aperture", *Sov. Phys. Usp.*, **32**, pp. 271 - 279, 1989.
12. V. Kantsyrev, R. Bruch, A. Shlyaptseva, "Spectrometer - polarimeter", The US Patent Applic., 60/014,483, filed April, 01, 1996.
13. V. Kantsyrev, B. Bauer, D. Fedin, A. Shlyaptseva, S. Hansen, I. Paraschiv, "Novel x-ray and EUV two-dimensional glass capillary spectrometer for Z-pinch plasma diagnostics", *Proc. SPIE*, **3766**, pp. 410-417, 1999.
14. V. Kantsyrev, B. Bauer, N. Publicover, D. Fedin, N. Ammons, "Development and application of the x-ray/EUV calibration facility with a laser plasma source for plasma diagnostics and bio-medical x-ray microscopy", *Proc. SPIE*, **3766**, pp. 252-4260, 1999.
15. L. Vincze, K. Janssens, F. Adams, A. Rindby, P. Engstrom, "Interpretation of capillary generated spatial and angular distributions of x rays: Theoretical modeling and experimental verification using the European Synchrotron Radiation Facility Optical beam line", *Rev. Sci. Instrum.*, **69**, 10, pp. 3494-3503 (1998).
16. S.B. Dabagov, M.A. Kumakhov, A.S. Nikitina, "On the interference of x-rays in multiple reflection optics", *Phys. Lett. A* **203**, pp. 279-282, 1995.
17. S. Lagomarcio, A. Cedola, S. Di Fonzo, W. Jark, C. Riwkel, "Hard x-ray waveguides as a new tool in x-ray microscopy", *Notiziario Neutroni E Luce Di Sincrotrone* **3**, pp. 43-54, 1998.
18. S.V. Kukhlevsky, L. Kozma, K. Negrea, "Pulsed-mode analysis of soft x-ray radiation passing through capillary waveguides", *J. Modern Optics*, **43**, pp. 2595-2604 (1996).
19. S.V. Kukhlevsky, L. Kozma, "Guiding of light by short-length multimode waveguides: Part I, II.", *Nuovo Cimento*, **DT 20**, pp. 783-791 (1998).
20. S.V. Kukhlevsky, E. Flora, A. Marinai, L. Palladino, A. Reale, G. Tomassetti, A. Ritucci, G. Nyitray, L. Kozma, "Diffraction of x-rays in capillary optics", *Appl. Opt.*, **39**, pp. 1059-1063 (2000).
21. S.V. Kukhlevsky, E. Flora, A. Marinai, G. Nyitray, A. Ritucci, L. Palladino, A. Reale, G. Tomassetti, "Diffraction of x-rays beams in capillary waveguides", *Nucl. Instrum. Methods, Phys. Res. B* **168**, pp. 276-282 (2000).

APPENDIX J

Fields of Optical Waveguides as Waves in Free Space

S.V. Kukhlevsky and G. Nyitray, University of Pecs, Hungary
V.L. Kantsyrev, UNR

Phys. Rev. E **64** (2001)

herence, and direction of propagation at the guide entrance can be generated in free space by the appropriate equivalent source. The guided waves can be produced in free space provided an appropriate launch pattern containing multiple virtual sources can be constructed. In opposition to the conventional theory of waveguides, the field at the guide entrance can satisfy neither the guide wave equation nor the boundary conditions. That gives possibility to considering not only the mode-matched waves, but also the fields having more complicated spatial and temporal properties at the guide entrance. This approach is illustrated in the following section using several particular fields, such as the diffraction-free, self-imaging, ultrashort, solitonlike, partially coherent waves and laser fractals. The fields are compared, where it is possible (mode-matched fields), to those obtained by solving a boundary condition problem.

III. PARTICULAR FIELDS

Let us consider the optical guiding and the respective free-space propagation of the several particular fields. We first demonstrate that the TEM eigenmodes $\psi_i(x, z, t)$ of the plane-parallel guide ($a = b, \gamma = 0$) having the total-reflection walls can exist and propagate without diffractive broadening not only in the optical guide but also in free space. According to the conventional theory of waveguides, the wave having the mode-matched profile and the plane wave front at the guide entrance propagates down the optical conduit as the waveguide eigenmode. In our consideration, it means that $E_0(x, z=0, t=0) = \psi_i(x)$, $R_m = 1$ and $\Delta\phi_m = \pi m$. For such conditions Eqs. (1)–(5) give

$$E'(x', t) = \frac{1}{\sqrt{i\lambda/2}} \int_{-(2M+1)a}^{(2M+1)a} \frac{\exp[i(kr(x', x) - \omega t)]}{r(x', x)} \psi_i(x) dx. \quad (6)$$

The virtual source producing the waveguide eigenmode in the free space is particularly simple: $E(x, z=0) = \psi_i(x)$ for $x \in [-(2M+1)a, (2M+1)a]$ and $M = d_m/2a - 1$. It should be noted that the beams $E'_m(P', t)$ with $m > M$ do not deliver the energy to the guided field in the region $x' \in [-a, a]$. Therefore, the field $E(x, z=0) = \psi_i(x)$ can be extended to the full region $x \in [-\infty, \infty]$. The interference and diffraction of this field produces the “diffraction-free” beam in the free space. Moreover, it can be easily demonstrated that the superposition of the eigenmodes $\psi_i(x, z, t)$ and $\psi_j(x, z, t)$ is the longitudinally periodic field with the beat length $Z_0 = 2\pi(k_i - k_j)^{-1}$. That means that the respective virtual source produces the self-imaging field in the free space. As an example, Fig. 2 shows the intensity distributions calculated for the eigenmode TE_0 , the “transient modes” $E'_m(x', t)$, and the superposition of the transient modes $E'(P', t) = \sum_{m=-M}^M E'_m(P', t)$. We notice that the distributions of the eigenmode TE_0 and the superposition $E'(P', t)$ are indistinguishable in the “core” region. Figure 3 demonstrates the intensity distributions of the eigenmodes TE_1 and TE_2 and the superposition $TE_1 + TE_2$ calculated using Eqs. (1)–(6) for the different distances z from the virtual source. The respective distributions obtained using the conventional

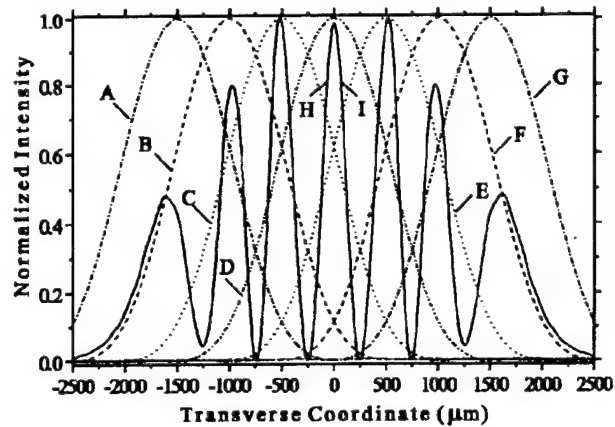


FIG. 2. The normalized intensity distributions of the eigenmode TE_0 , the transient modes $E'_m(x', t)$, and the superposition of the transient modes $E'(P', t) = \sum_{m=-3}^3 E'_m(P', t)$. Curves A, B, C, D, E, F, and G are, respectively, the normalized intensities of the transient modes having $m = -3, -2, -1, 0, 1, 2$, and 3 . Curves H and I are, respectively, the normalized intensities of the TE_0 eigenmode and the superposition $E'(P', t)$ in the core region $x \in [-a, a]$. The intensity distributions of the transient modes and their superposition were calculated for the distance $z = 1$ m from the virtual source using the parameters $\lambda = 500$ nm and $2a = 500$ μm .

theory of waveguides are presented in Fig. 3 for the comparison. One can see that the distributions are indistinguishable. The above presented results demonstrate the unexpected correspondence between the waveguide eigenmodes and the

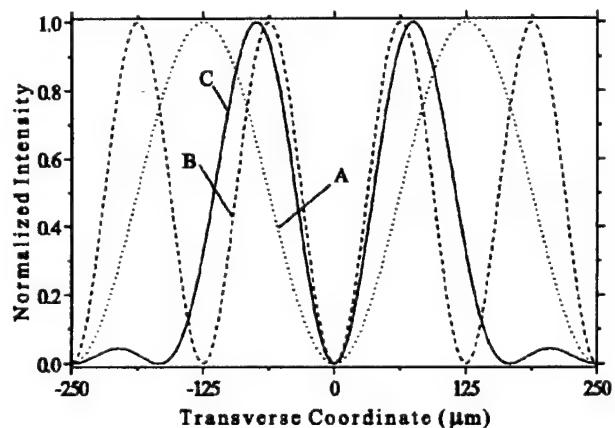


FIG. 3. The normalized intensity distributions of the eigenmodes TE_1 and TE_2 and their superposition $TE_1 + TE_2$ calculated using Eqs. (1)–(6) for the different distances z from the virtual source. The respective distributions obtained using the conventional theory of waveguides are presented for the comparison. Curves A, B, and C show, respectively, the fields TE_1 , TE_3 , and $TE_1 + TE_3$ at the guide entrance. Curves A and B demonstrate, respectively, the fields TE_1 and TE_3 computed for $z = 20, 21, \dots, 600$ cm. Curve C shows the field $TE_1 + TE_3$ calculated for $z = 66.6 \text{ cm} + pZ_0$, where $p = 1, 2, \dots, 10$ and $Z_0 = 33.3$ cm. The distributions were calculated using the parameters $\lambda = 500$ nm and $2a = 500$ μm .

diffraction-free [1–8] and self-imaging [11–14] fields of free space. It is clear now that the diffraction-free Bessel-type beam [1–8] is the free-space equivalent of the eigenmode of the cylindrical waveguide.

Let us now consider the optical guiding and the respective free-space propagation of the field, which at the guide entrance has more complicated temporal properties. We will study an ultrashort light pulse, a wide-frequency-bandwidth field. The input pulse $E_0(x, z=0, t)$ at the guide entrance can be presented in the form of the Fourier integral

$$E_0(P, t) = \int_{-\infty}^{\infty} E_0(P, \omega) \exp(-i\omega t) d\omega. \quad (7)$$

Using Eqs. (1)–(5) for the input harmonic field $E_0(P, \omega) \exp(-i\omega t)$ and substituting the result into Eq. (7), we get the field distribution of the pulse inside the guide. A simple analysis of the equations yields a new prediction, the ultrashort wave propagates through the guide as the superposition of many pulses that diffract in the off-axis direction and interfere with each other. An example of the computer simulation of the evolution of the 10-fs pulse inside the plane-parallel hollow waveguide of the thickness $2a=2b=500 \mu\text{m}$ and the length $z_L=10 \text{ cm}$ is shown in Figs. 4

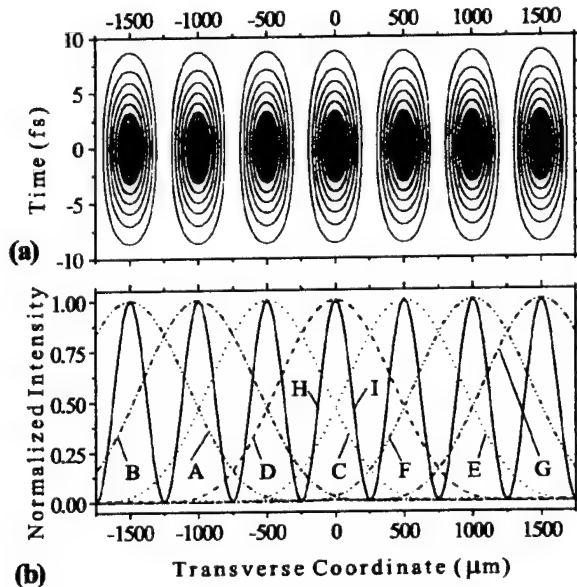


FIG. 4. (a) The normalized intensity distributions calculated for the input pulse, the transient modes $E'_m(x', t)$, and the superposition of the transient modes $E'(P', t) = \sum_{m=-12}^{12} E'_m(P', t)$. The input pulse matches the eigenmode TE_0 . (b) Curves A, B, C, D, E, F, and G are, respectively, the normalized intensities of the transient modes having $m = -3, -2, -1, 0, 1, 2$, and 3. Curves H and I are, respectively, the normalized intensities of the TE_0 eigenmode and the superposition $E'(P', t)$ of the transient modes in the core region $x \in [-a, a]$. The intensity distributions of the transient modes and their superposition were calculated for the distance $z=0.8 \text{ m}$ from the virtual source. Curves A, B, C, D, E, F, G, H, and I show the intensities at the time $t=0 \text{ fs}$.

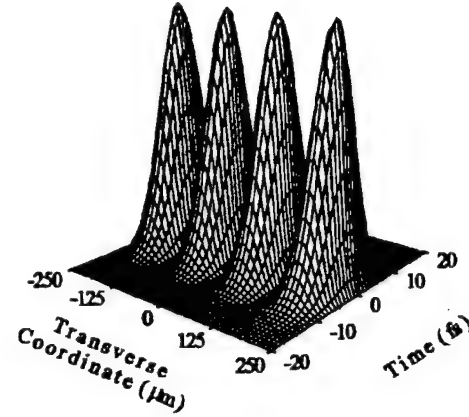


FIG. 5. The normalized intensity distributions of the pulse having $E_0(x) = \text{TE}_3(x)$ calculated using Eqs. (1)–(7) for the different distances $z=0.5, 10 \text{ cm}$ from the virtual source. The respective distributions obtained using the conventional theory of waveguides are shown for comparison.

and 5. At the guide entrance the Gaussian-shaped pulse matches the profile of the TE_0 or TE_3 eigenmodes and has the plane wave front,

$$E_0(x, z=0, t) = E_0(x) \exp[-2 \ln(2)(t/\tau_0)^2] \times \exp\{i[kz - \omega_0 t + \phi_0(x)]\}, \quad (8)$$

where $\tau_0 = 10 \text{ fs}$, $\lambda_0 = 2\pi c/\omega_0 = 500 \text{ nm}$, and $\phi_0(x) = \text{const}$. Figure 4 shows the intensity distributions calculated for the input pulse, the “transient modes” $E'_m(x', t)$ and the superposition of the transient modes $E'(P', t) = \sum_{m=-12}^{12} E'_m(P', t)$. The input pulse matches the eigenmode TE_0 , $E_0(x) = \text{TE}_0(x)$. One can see that the distributions of the input pulse and the superposition $E'(P', t)$ are indistinguishable. Figure 5 shows the intensity distributions of the pulse having $E_0(x) = \text{TE}_3(x)$ calculated using Eqs. (1)–(7) for the different distances from the virtual source. The respective distributions obtained using the conventional theory of waveguides are shown for the comparison. We notice that the distributions are indistinguishable. Thus the usual result of the modal dispersion theory is recovered; the spatial profile of the wave is undistorted along its path of propagation provided the input pulse is mode matched. That means that an ultrashort pulse can exist and propagate without diffractive broadening not only in the optical guide but also in free space. It is interesting to consider also a soliton-like wave, the field that broadens neither transversely nor longitudinally. In order to derive the features of such a field, we recast the previous result for a short wave propagating in the dispersive guide [$n_1 = n_1(\omega)$]. The pulse at the guide entrance is given by $E_0(x, z=0, t) = E_0(x)E_0(t)$. Using Eqs. (1)–(5) for the input field that matches the eigenmode profile $E_0(x) = \psi_i(x)$ and neglecting the unimportant proportionality factor we get the field $E'(P', t')$ at the point $P'(x')$ of the region $x' \in [-a, a]$,

$$E'(P', t') = \psi_i(x') \int_{-\infty}^{\infty} [\omega n_1(\omega)]^{1/2} E_0(\omega) \exp(-i\omega t') d\omega, \quad (9)$$

where $E_0(\omega)$ is the Fourier transform of the field $E_0(t')$. In the case of $\omega n_1(\omega) = \text{const}$ the pulse is a solitonlike field, which broadens neither transversely nor longitudinally. Thus a solitonlike pulse propagating inside the dispersive guide without distortion can be produced by the virtual source in the "free" space.

We now consider the optical guiding and the respective free-space propagation of the partially coherent wave. At the guide entrance, the incoherent or partially coherent wave $E_0(x, z=0, t)$ can be described in terms of the mutual coherence function $\Gamma_{00}(P^i, P^j; \tau)$ (for example, see [17]),

$$\Gamma_{00}(P^i, P^j; \tau) = \langle E_0(P^i, t + \tau) E_0^*(P^j, t) \rangle_t, \quad (10)$$

where the points $P^i, P^j \in [-a, a]$. Using Eqs. (1)–(5) and the mutual intensity function $J_{00}(P^i, P^j) = \Gamma_{00}(P^i, P^j; 0)$, we get the mutual intensity $J(P'^i, P'^j)$ inside the guide

$$J(P'^i, P'^j) = \sum_{m=-M}^M \sum_{n=-M}^M \int_{x_m^{\min}}^{x_m^{\max}} \int_{x_n^{\min}}^{x_n^{\max}} J_{mn}(P_m^i, P_n^j) \times \exp[-n_1 c^{-1} \omega(r_i - r_j)] \times \frac{\chi(\Theta'^i)}{r_i \lambda} \frac{\chi(\Theta'^j)}{r_j \lambda} dx_i dx_j, \quad (11)$$

with

$$J_{mn}(P^i, P^j) = \langle E_0(P_m^i, t) E_0^*(P_n^j, t) \rangle_t, \quad (12)$$

where $\chi(\Theta) = 1 + \cos \Theta$; the points $P_m^i, P_n^j \in [x_m^{\min}, x_m^{\max}]$ can be found using Eqs. (2)–(4). Using the function $J(P'^i, P'^j)$, one can easily find the complex coherence factor $\mu(P'^i, P'^j)$, the mutual coherence function $\Gamma(P'^i, P'^j)$, and the intensity distribution $I(P') = J(P'^i, P'^j; P'^i \rightarrow P'^j)$ of the guided wave [17]. In order to better understand the transformation of the guided waves into the free-space fields, we have numerically examined the guided fields having different degree of the spatial coherence. We considered the intensity distribution of the guided fields that at the guide entrance are incoherent, partially coherent, or coherent. Such fields can be produced by an incoherent, uniform-intensity, quasimonochromatic linear source placed at the different distances from the guide entrance [17]. The input fields can be described by the mutual intensity

$$J_{00}(x_i, x_j) = \int_{-h}^h \int_{-h}^h J(x_i'', x_j'') \exp[-n_0 c^{-1} \omega(r_i'' - r_j'')] \times \frac{\chi(\Theta''^i)}{r_i'' \lambda} \frac{\chi(\Theta''^j)}{r_j'' \lambda} dx_i'' dx_j'', \quad (13)$$

with

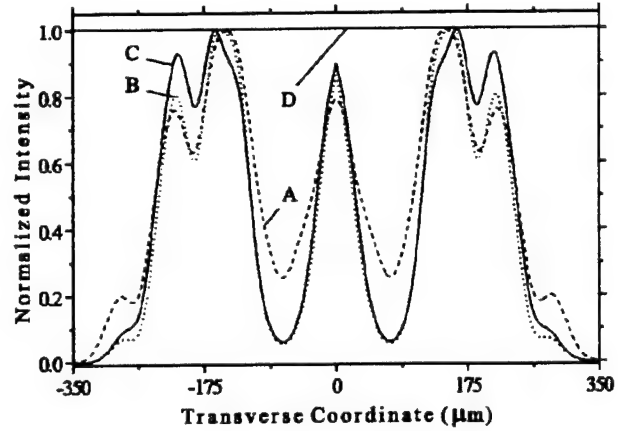


FIG. 6. Normalized intensity distributions of the partially coherent field at the guide exit computed using Eqs. (10)–(14). The parameters of the light at the guide entrance: A, $|\mu|=1$; B, $|\mu|=0.85$; C, $|\mu|=0.75$; and D, $|\mu|=0$.

$$J(x_i'', x_j'') = \sqrt{I(x_i'') I(x_j'')} \left[2 \frac{\sin(2\pi \sqrt{(\Delta x'')^2 / \lambda})}{(2\pi \sqrt{(\Delta x'')^2 / \lambda})} \right]. \quad (14)$$

We computed the intensity distribution at the exit of the straight guide having the thickness $2a = 2b = 700 \mu\text{m}$ and the length $z_L = 10 \text{ cm}$. The input radiation is produced by the linear source having the length $h = 125 \mu\text{m}$ and $\lambda = 500 \text{ nm}$. Figure 6 shows the normalized intensity for the partially coherent fields B and C. The distributions produced by the coherent A and incoherent D input fields are shown for the comparison. At the guide entrance the partially coherent fields, strictly speaking, are not the mode-matched waves. Therefore it is difficult to compare directly the calculations with that of the eigenmode theory. Nevertheless, we notice that the usual result of the theory of partially coherent fields is recovered, the spatial profile of the guided wave broadens with decreasing the coherence degree.

Finally, we consider the relation between the guided waves and the laser fractal fields. Let us consider the formation of light fields in the laser resonator, which consists of a plane-parallel waveguide, two concave mirrors, and an aperture (Fig. 7). The aperture consists of the walls of the guide

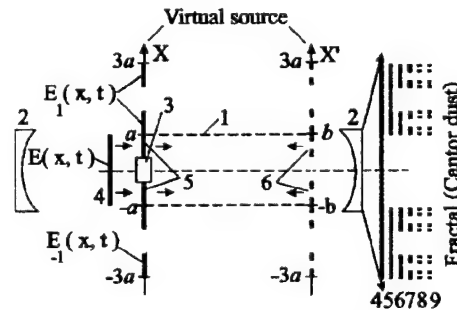


FIG. 7. Formation of the laser fractal (Cantor dust) in the waveguide resonator: 1, guide boundary; 2, mirrors, and 3, obstacle. The triadic Cantor discontinuum (line fractal): 4, C_0 ; 5, C_1 ; 6, C_2 ; 7, C_3 ; 8, C_4 ; and 9, C_5 .

and a light obstacle placed on the laser axis at the guide entrance. The obstacle length is given by $|x| = 2a/q$, where q is a natural number. The transverse dimension of the "step-like" input field E is equal to the guide thickness $2a$. The obstacle cuts the $2a/q$ part of this field creating the field E_0 . Guiding of the field E_0 can be presented as propagation of the fields E'_m generated by the respective fields E_m of the virtual source [Eqs. (1)–(5)]. After reflection from the mirror, the M -times reduced image of the field $E' = \sum_{m=1}^{M-1} E'_m$ arrives to the guide exit. In the limit of small diffraction effect [$E'_m \approx E_m$, see Eq. (1)], the round-trip process can be presented as the mathematical procedure of construction of the line fractals by the tremas [18]. In the case of $2a = 1$, $q = 3$, $m = (-1, 0, 1)$, and $M = 3$, the intersection of the sets C_m is the triadic Cantor dust $C = \cap_m C_m$, the fractal with Hausdorff's dimension $D = \log 2 / \log 3$. Here, $C_0 = E$, $C_1 = E_0$, and C_2 is the reduced image of the field $E' = E'_1 + E'_0 + E'_1$ (see Fig. 5). In order to find the set C_k one should simply repeat the round-trip procedure for the input "field" C_{k-1} . The result means that the laser fractal (triadic Cantor dust) can be generated in the free space by the waveguide resonator. The laser fractals were recently observed in the experiments [9,10]. The studies have shown that a fractal pattern can only appear if the two mirrors form a so-called unstable configuration. In our case such a configuration is formed by the two mirrors and the virtual source of the waveguide.

IV. CONCLUSION

In conclusion, it is shown using the scalar diffraction theory and the method of images that the arbitrary field confined by the optical waveguide can be generated in free space by the appropriate light source. The guided field can be produced in free space provided an appropriate launch pattern containing multiple virtual sources can be constructed. In opposition to the conventional theory of waveguides, the field at the guide entrance can satisfy neither the guide wave equation nor the boundary conditions. That gives possibility to considering not only the mode-matched waves, but also the fields having more complicated spatial and temporal properties at the guide entrance. The correspondence between the guided and free-space waves was illustrated using several particular fields, such as the diffraction-free, self-imaging, ultrashort, solitonlike, partially coherent waves and laser fractals. The fields were compared, where it was possible (mode-matched fields), to those obtained by solving a boundary condition problem. It is expected that our method can be extended to the electron and neutron waves (for the diffraction-free beams the problem was discussed in Ref. [1]).

ACKNOWLEDGMENTS

This work was supported by the Hungarian Scientific Research Foundation (OTKA, Contract No. T 026644) and in part by the U.S. Department of Energy.

-
- [1] J. Durnin, J. J. Miceli, and J. H. Eberly, *Phys. Rev. Lett.* **58**, 1499 (1987).
 - [2] T. Wulle and S. Herminghaus, *Phys. Rev. Lett.* **70**, 1401 (1993).
 - [3] S. Klewitz, P. Leiderer, S. Herminghaus, and S. Sogomonian, *Opt. Lett.* **21**, 248 (1996).
 - [4] Z. Jaroszewicz, A. Kolodziejczyk, A. Kujawski, and C. Gomez-Reino, *Opt. Lett.* **21**, 839 (1996).
 - [5] R. Borghi and M. Santarsiero, *Opt. Lett.* **22**, 262 (1997).
 - [6] V. E. Peet and R. V. Tsubin, *Phys. Rev. A* **56**, 1613 (1997).
 - [7] D. Ding and Z. Lu, *Appl. Phys. Lett.* **71**, 723 (1997).
 - [8] S. Chavez-Cerda, M. A. Meneses-Nava, and J. Miguel Hickmann, *Opt. Lett.* **23**, 1871 (1998).
 - [9] G. P. Karman and J. P. Woerdman, *Opt. Lett.* **23**, 1909 (1998).
 - [10] G. P. Karman, G. S. McDonald, G. H. C. New, and J. P. Woerdman, *Nature (London)* **402**, 138 (1999).
 - [11] W. D. Montgomery, *J. Opt. Soc. Am.* **57**, 772 (1967).
 - [12] R. Sudol and B. J. Thompson, *Opt. Commun.* **31**, 105 (1979).
 - [13] A. W. Lohmann and J. O. Castaneda, *Opt. Acta* **30**, 475 (1983).
 - [14] G. Indebetouw, *J. Mod. Opt.* **35**, 243 (1988).
 - [15] M. Born and E. Wolf, *Principle of Optics* (Pergamon, Oxford, 1980).
 - [16] A. E. Siegman, *Phys. Rev. A* **39**, 1253 (1989).
 - [17] J. W. Goodman, *Statistical Optics* (Wiley-Interscience, New York, 1985).
 - [18] G. A. Edgar, *Measure, Topology, and Fractal Geometry* (Springer-Verlag, New York, 1994).

APPENDIX K

Powerful Microfocus X-Ray and Hard X-Ray 1-MA X-Pinch Plasma Source for Imaging, Spectroscopy, Backlighting, and Polarimetry

V.L. Kantsyrev, B.S. Bauer, A.S. Shlyaptseva, D.A. Fedin, S. Hansen,
R. Presura, S. Fuelling, S. Batie, A. Oxner, H. Faretto, N. Quart,
S. Keely, H. LeBeau, and D. Chamberlain

Proc. SPIE **4502** (2001)

To be published in SPIE Proc. vol. 4502 (July 30-Aug. 3. 2001, San Diego, CA).

Powerful microfocus x-ray and hard x-ray 1 MA x-pinch plasma source for imaging, spectroscopy, backlighting, and polarimetry.

V.L. Kantsyrev, B.S. Bauer, A.S. Shlyaptseva, D.A. Fedin, S. Hansen, R. Presura, S. Fuelling, S. Batie, A. Oxner, H. Faretto, N. Ouart, S. Keely, H. LeBeau, D. Chamberlain

The Physics Department, the Nevada Terawatt Facility of the University of Nevada Reno, MS 220, Reno, NV 89557-0058, USA

ABSTRACT

The x-ray emission of Ti, Fe, Mo, W, and Pt x-pinchs are currently being studied at the Nevada Terawatt Facility z-pinch machine Zebra (0.9-1.0 MA, 100 ns). New x-ray diagnostics for time-resolved spectroscopy and imaging has been developed and used in x-pinch experiments. The total x-ray/ EUV yield was more than 10 kJ. The minimum x-ray pulse duration was 1.1 ns (Mo, W, Pt). For Ti, Mo and W pinchs x-ray pulses occurred in two or three groups in the narrow time intervals after the start of the current. The most compact emitting region has been observed for a planar-loop Mo x-pinch (the number of hot spots ranging from 1-5 with a minimum size smaller than 30 μm at $\lambda < 1.5-2 \text{ \AA}$). Strong jets were observed (Ti, Fe, Mo) directed toward the discharge axis, perpendicular to the wires. A structure of an x-pinch includes energetic electron beams directed toward the anode and along wires. The total beam energy increases from Ti to W. A pulse of anisotropic hard x-ray radiation was observed moving upwards along the axial axis with an energy of several hundred keV (Mo). The size of this source was smaller than 1 mm. The measurements of temperature and density of x-pinch plasmas were based on theoretical modeling of K-shell Ti and L-shell Mo spectra ($T_e = 1.5 \text{ keV}$ for Ti, 0.8 keV for Mo, N_e up to $2-3 \times 10^{22} \text{ cm}^{-3}$ with 1-10 % of hot electrons).

1. INTRODUCTION

The high current x-pinch¹ is a good candidate for developing a new (harder) x-ray backlighter, for testing x-ray spectropolarimetry (a powerful new tool for studying the anisotropy of high-temperature plasmas)², for examining the final stage of the MHD instability, and other applications. The main directions of the Nevada Terawatt Facility (NTF) x-pinchs research are: studying the dynamics of plasma implosion and determinations of plasma conditions in an x-pinchs that lead to generations of short x-ray pulses; studying the influence of strong energetic electron beams on the parameters of plasmas; and studying x-pinch plasma anisotropy. Atomic physics research at the NTF includes line identification of highly ionized ions and the study of isoelectronic sequences with more than one electron above closed shells, up to high-Z elements. X-ray and EUV spectra of a wide variety of chemical elements can be produced on Zebra, and fundamental studies of atomic processes of multiply charged ions in moderate- and high-density z-pinch plasmas have been initiated.

2. PLASMA DIAGNOSTICS

Plasma diagnostic research at NTF [1,2] includes:

a) development of x-ray and EUV time- and spatial-resolved spectroscopic, imaging, polarimetric, x-ray backlighter systems, fast x-ray/hard detectors for plasma monitoring; b) measurements of plasma temperature and density based on theoretical modeling of K-, L-, and M-shell ions x-ray spectra³; c) experimental polarization x-ray measurements and theoretical polarization study^{2,3} of influence of electron beams in plasma on linear x-ray spectra and measurements of temperature, density and inner magnetic field in z-pinch plasmas. The NTF diagnostics include 12 devices (beginning of development-1997⁴): a side-on one-dimensional time-gated spectrometer (1DXIS¹), a side-on 5-channel time-resolved "Polychromator" spectrometer with a transmission grating spectrometer (TGS)⁵, a side-on one-dimensional x-ray imaging time-integrated crystal spectrometer with a low resolution survey pinhole camera¹, a side-on and end-on one-dimensional x-ray imaging time-integrated polarimeter- spectrometers²,

a side-on multichannel time-gated pinhole camera (GXI)¹, a side-on time-integrated high-resolution pinhole camera, an end-on time-integrated super-high-resolution pinhole camera, a side-on filtered fast PCD and XRD detectors, and a Ni x-ray bolometer [1]; an end- and a side-on hard x-ray time-integrated imaging detectors with filtered x-ray films, and an end-on hard x-ray detector. A side-on two-dimensional glass-capillary imaging spectrometer (2DXIS)^{1,6} decomposes an image into pixels, separates and spectrally disperses these pixels, and records spectra with a time-gate MCP intensifier. New results have been obtained from the experimental study and theoretical modeling of the nonuniform output angular distribution of keV and sub-keV radiation transported by different types of capillaries⁷⁻⁹. The device is under testing at the NTF. Side-on and end-on hard x-ray fast detectors with spatial resolution capability and a side-on EUV imaging diagnostic beamline are under development. The diffraction limitation in spatial resolution for side-on diagnostics due to lack of minimum distance from plasma to detectors (30-60 cm) was 20-25 μm at $\lambda=10 \text{ \AA}$ and 5-10 μm at $\lambda=1 \text{ \AA}$. All the NTF experiments were proved under vacuum better than 5×10^{-6} torr. Vacuum beamlines have strong permanent magnets to protect the x-ray devices against the damage from z-pinch ion beams.

3. PHYSICS of HIGH-CURRENT X-PINCH X-RAY/EUV RADIATION SOURCES. EXPERIMENTAL RESULTS.

X-pinchs were made by positioning two thin, straight, crossed wires between the cathode and anode of the Zebra pulsed-power generator, with a wire contact at the axis of the cathode-anode gap. Two typical configurations of x-pinchs were tested: wire twisted (at angle of rotation $\alpha \approx 30^\circ$) and planar-loop. Other loads for comparison with x-pinchs such as single wires and V-pinchs were also tested (see below Fig. 1). Early x-pinchs have been made from Al to Pd¹⁰, and have been driven by currents of 0.1-0.4 MA. At higher currents, the authors are only aware of three x-pinch-related publications, on an Al x-pinch driven by 0.8 MA¹¹, and Ti and Fe driven by 0.9 MA^{1,2}. Here the results on the new study of Ti, Fe, Mo, W and Pt x-pinchs driven by 0.85-0.95 MA are reported.

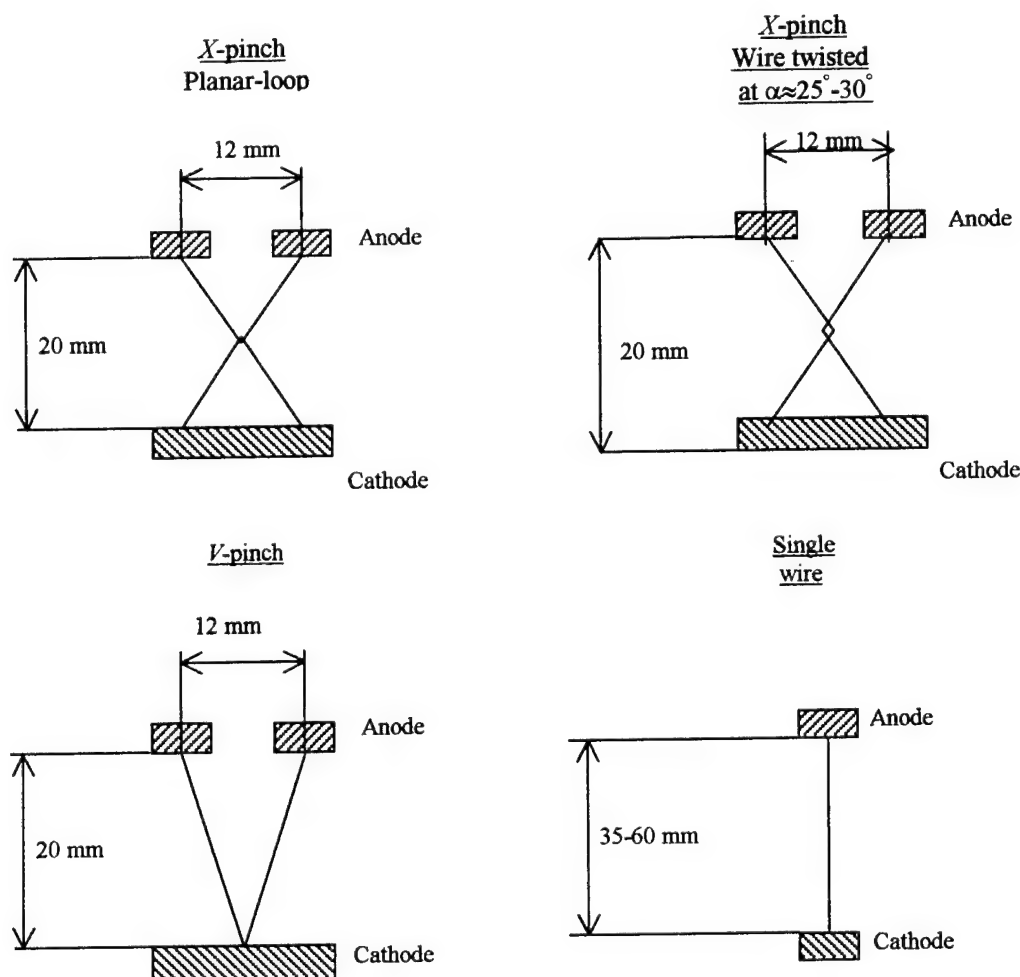


Fig.1. Various x-pinch loads used in NTF experiments.

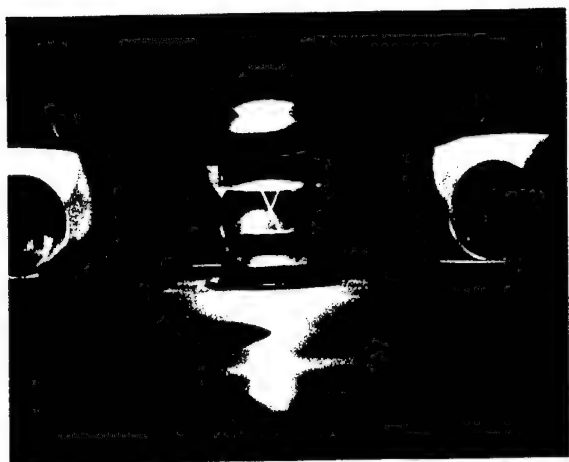


Fig. 2. The x-pinch load in the NTF discharge vacuum chamber. Side view. The anode is at the top.

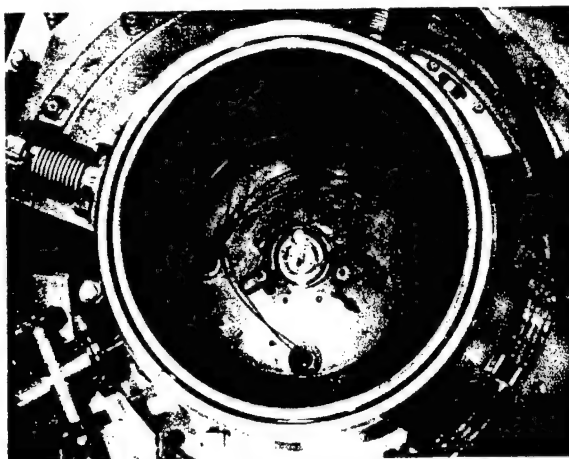


Fig. 3. View from the top of the open discharge chamber. X-pinch and wire holders are at the center.

3.1 Spatial Structure of High-Current X-Pinches

The high peak current quickly vaporizes and strongly ionizes the wires. Time-integrated and time-gated x-ray pinhole images show the location of the wires, with a bright spot at the cross point (Fig. 4).

The structure of x-pinch driven by a high current (0.8-0.9 MA)^{1,11} is more complicated than that of low-current x-pinch¹⁰. First, a strong, energetic electron beam is not only directed to the center of the anode (between the wires), but also toward the anode ends of the wires¹. Such an energetic electron beam influences the x-pinch plasma spectra. For example, polarization of K-shell spectra of Ti x-pinch is observed^{2,3}. In most cases the development of anode-wire directed electron beams occur when the current reaches a value of 0.5-1.0 from maximum. Second, strong jets are observed (mostly in softer-than-K-shell Ti and Fe¹ or L-shell Fe and Mo and x-ray continuum emissions) directed toward the discharge axis (Fig. 4 B), perpendicular to the wires¹. Stagnation of these jets on the discharge axis forms a strong jet, efficiently radiated in a x-ray region, directed to the anode. The same effect was observed for the V-pinch configuration that can be used to study plasma jet generation. These small jets have a period that varying from 1 to 2 mm for Ti, Fe and Mo. They are presumably spikes of the Rayleigh-Taylor instability of the accelerated wires. The luminous jets and their wires are observed on the anode- and cathode-sides of the contact. But brightness of anode side of images were always much stronger, indicating that they are luminous (in the spectral band recorded) because of excitation by fast electrons beams originating from

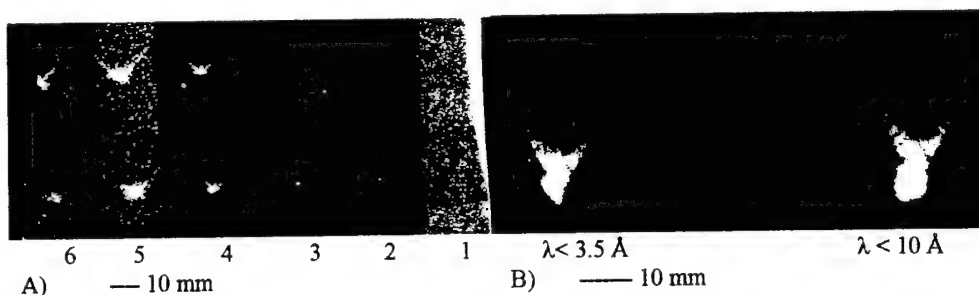
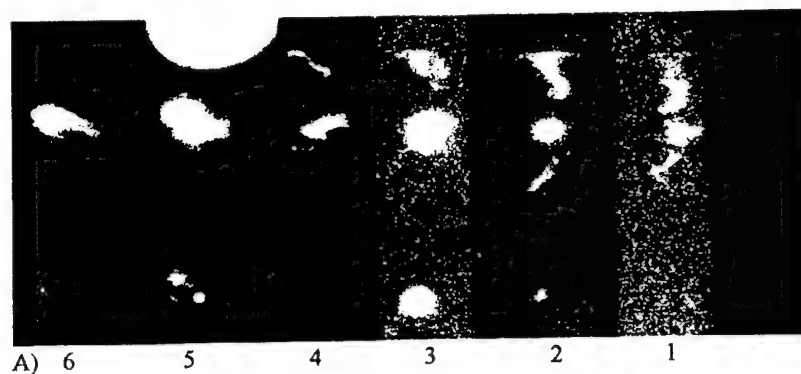


Fig. 4 X-ray images from a planar-loop 50 μm Mo wire x-pinch. The anode is above images. A) Gated images. Frame 4 ns, interval between beginning of frames 7 ns. Spatial resolution 230 μm. The top row corresponds to $\lambda < 10 \text{ Å}$, lower $\lambda < 3.5 \text{ Å}$. Frame #1 corresponds to 40 ns after current start. X-ray bursts (PCD and XRD peaks) were in frames 4, 5 and 6. B) Time-integrated pinhole camera images. Spatial resolution 60 μm.

the necked-off contact. Anode and cathode jets appear to be formed during all periods of x-ray generation. In most discharges development of bright spots at the cross point occur during the first part of the current pulse. High resolution time-gated GXI images, time-integrated pinhole images, TGS spectra (Figs. 5-6), and spatially resolved x-ray spectra [3] show that the line, continuum and harder radiation comes from a region in the same location as the Ti, Fe K-shell, Fe, Mo L-shell or W, Pt M-shell sources. The typical size of this region is 2.5-4 mm for Ti K-shell and 2-3 mm for Fe K-shell, Mo L-shell or W, Pt M-shell radiation (time-integrated image) for planar-loop x-pinch. The

minimum size of L-shell emitting regions for Ti is 3-6 mm, for Fe ($\lambda \approx 20-80$ Å) is up to 10 mm, and for Mo ($\lambda \approx 20-80$ Å) is 3-4 mm (measured with TGS). All these regions include several small sources of radiation (hot spots) with a minimum size smaller than 30 μm in x-ray

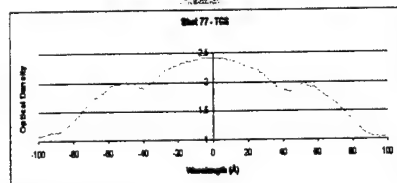
A) Time-gated x-ray images. The anode is just below images.



Top image $\lambda < 10$ Å

Lower image $\lambda < 3.5$ Å — 10 mm

B) Time-integrated pinhole camera images; the anode is at the top of images.



B) $\lambda < 2.6$ Å $\lambda < 7.9$ Å $\lambda < 5$ Å D) Time-integrated TGS images; anode is at top.

C) GXI frames (correspond to A): 1 2 3 4 5 6 (see below time axis). — 10mm

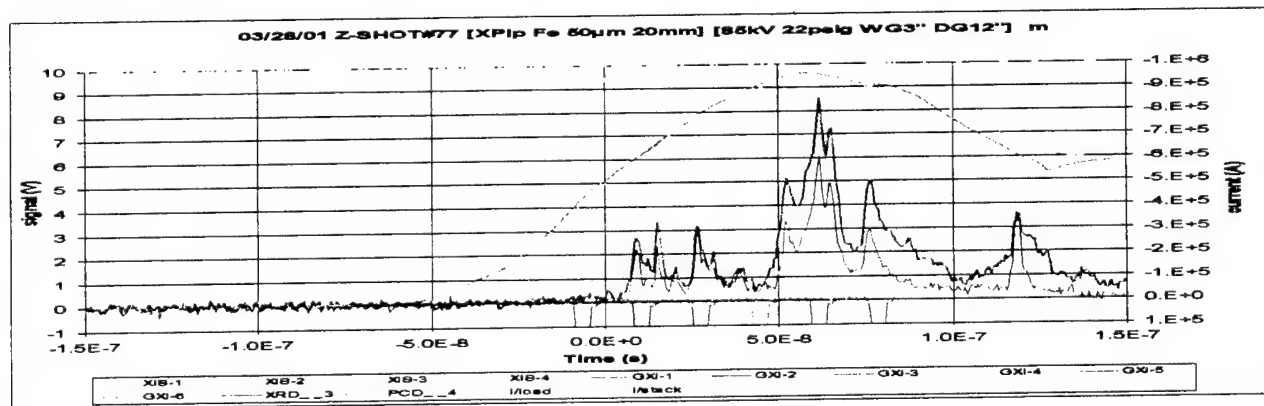
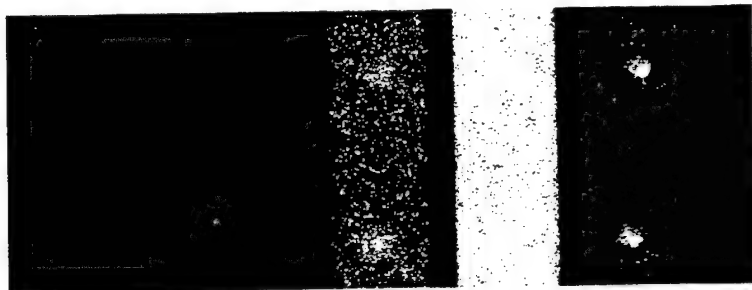


Fig. 5. Fe planar-loop x-pinch with a 50- μm wire diameter and a 20-mm anode-cathode gap (shot #77, March 28, 2001). A) Gated x-ray images. Frame 4 ns. Spatial resolution 230 μm . B) Time-integrated pinhole camera images (Kodak DEF-5 x-ray film), with the same view as in A. Spatial resolution 580 μm . C) X-pinch current (thick smooth line), GXI frames, XRD (5 μm Kimfoil filter) and PCD (8 μm Be filter) response versus time. D) Time-integrated TGS 1D-spectra (20-80 Å). Resolution 200 μm .

(pinhole camera resolution), or 200 μm in soft x-ray (TGS resolution). The most compact x-ray source was obtained with planar-loop x-pinch. For example, for wire-twisted Ti x-pinch its size is 4-6 mm. Typically this region includes from 3-4 to 7-8 hot spots. For the planar-loop x-pinch a number of hot spots is reduced to 1-5. The size of these spots depends on a spectral region of registration. For example, for a Mo x-pinch it has been reduced from several hundred μm to smaller than 30-65 μm (pinhole camera resolution) when a spectral region of observation has

A) Time-gated x-ray images. The anode is just below images.

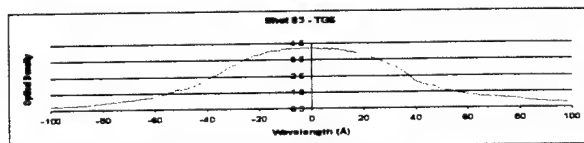
Top image $\lambda < 3.5 \text{ \AA}$



A) 1 2 3 4 5 6
B) Time-integrated pinhole camera images; the anode is at the top of images.



Lower image $\lambda < 10 \text{ \AA}$ — 10 mm



B) $\lambda < 2.6 \text{ \AA}$ $\lambda < 7.9 \text{ \AA}$ $\lambda < 5 \text{ \AA}$ D) Time-integrated TGS images; the anode is at the top.

C) GXI frames (correspond to A): 1 2 3 4 5 6 (see below a time axis).

— 10mm

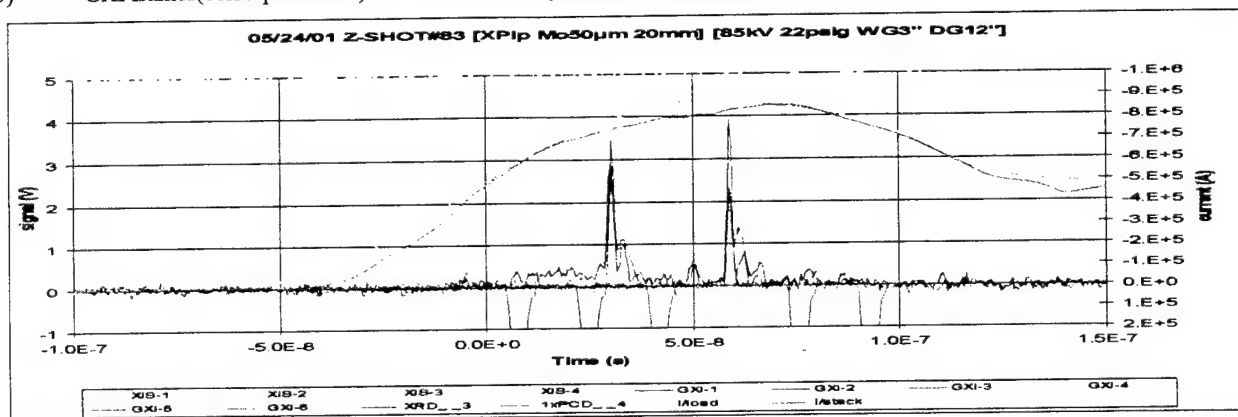


Fig. 6. Mo planar-loop x-pinch with a 50 μm wire diameter and a 20-mm anode-cathode gap (shot #83, May 24, 2001). A) Gated x-ray images. Frame 4 ns. Spatial resolution 230 μm . The top image on the each strip is filtered for $\lambda_{1/10} < 10 \text{ \AA}$, the lower image for $\lambda_{1/10} < 3.5 \text{ \AA}$. B) Time-integrated pinhole camera images (Kodak DEF-5 x-ray film), with the same view as in A. Spatial resolution 580 μm . C) X-pinch current (thick smooth line), GXI frames, XRD (with 8 μm Be filter) and PCD (with 25 μm kapton filter) response versus time. D) Time-integrated TGS 1D-spectra (20-80 \AA). Resolution 200 μm .

been hanged from 4-10 \AA (Mo L-shell and continuum) to $\lambda < 1.5-2 \text{ \AA}$ (continuum with planckian spectra) (Fig.7). These short-wavelength hot spots are located in shape of a chain along a central axis of an x-pinch near the cross point of wires. A comparison of time-gated images and PCD/XRD signals shows that a x-ray image of the source moved for a distance of several mm along the discharge axis during the discharge with a maximum speed from $5 \times 10^6 \text{ cm/s}$ (Ti and Fe) to $5 \times 10^7 \text{ cm/s}$ (Mo). The direction of movement can change to opposite during a discharge. We found that the quality of a x-pinch structure (from the point of view of minimization of an effective size of a x-ray source and a number of hot spots) is in strong dependency from original symmetry of a x-pinch and its plainness. An estimated accuracy of a x-pinch structure must be at least 3-5 % from a maximum dimension of a structure.

3.2 Energetic Electron Beam and Hard X-Ray Generation From High Current X-Pinches.

Previous studies of x-pinch plasma sources at the lower current¹⁰ show that this is a prospective source for x-ray radiography in the 1-10 keV spectral region. Our studies at sufficiently higher currents (<1MA) also confirm a possibility to use a x-pinch as a source for backlighting purposes even with harder x-rays. The presence of a very

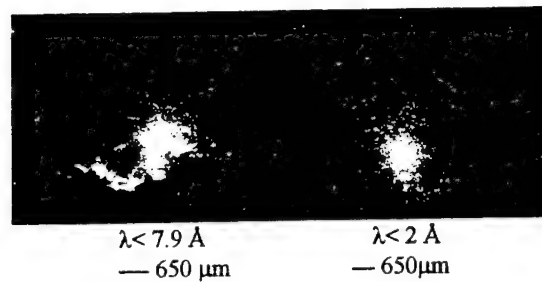


Fig. 7. X-ray images from a planar-loop 50 μm Mo wire x-pinch. The anode is above images. Time-integrated pinhole camera. Spatial resolution 60 μm . A weak diffuse spot above hot spots images is a result of penetration of hard x-ray through a Pt/Ir pinhole substrate.

powerful high energy electron beam in an x-pinch plasma can lead to the generation of hard x-ray radiation in a cross point as a result of interaction of this beam with matter of x-pinch and a local magnetic field. A strong, energetic electron beam is directed not only to the center of the anode (between the wires), but also toward the anode ends of the wires^{1,2}. The experimental estimation of widths of the central jet on x-pinch x-ray images and Fe K_{α} spectral lines (generated on a steel anode) has shown that a diameter of an electron beam in a high-current x-pinch may be smaller than 1mm. The total energy of this electron beam is at least from 2-3 % (Fe) to 15-20 % (Mo and W) of the x-pinch discharge energy $E \approx 100\text{-}120$ kJ (Fig.8). Several tests of the NTF Mo and Fe x-pinch as a possible hard x-ray backlighter source were carried out with a static test object. As test objects, set of Al and Fe parts were used. One of the

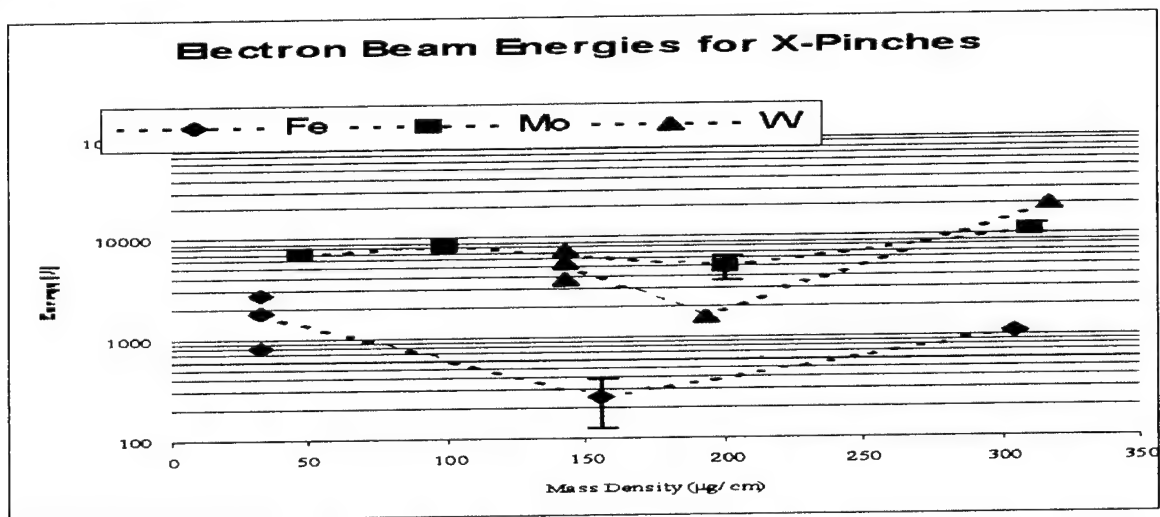


Fig. 8. The experimental estimation of the energy needed to generate the observed holes at the points of connection of the wires with the anode of an x-pinch vs mass density of wires.

sets were placed end-on and another side-on. In order to roughly control spectral distribution of hard x-rays, step Al, Fe, Cu and Pb filters with different attenuations were placed in front of the film in both beamlines (Fig. 9). The preliminary results (Fig. 10) show that a x-pinch is an effective source of hard x-ray radiation at the high current conditions. The main portion of electrons have the energy smaller 40-50 keV, and some amount of electrons has the energy at least 0.5-1.0 MeV. Note that the side-on measured electron temperature is higher than the end-on measured. It can be explained by the influence of a x-pinch local magnetic field on the interaction of an electron beam with a pinch matter. For a hard x-ray backlighter we plan to use only radiation from a cross-wires region in a direction along a x-pinch axis, because preliminary measurements have been shown that time structure of this radiation include several pulses with duration of 10-50 ns. It is shorter than hard x-ray pulses registered from the total gap anode-cathode. Experiments are in progress.

A rough estimation of spectral regions available for radiography gives us values of 50-150 keV for Mo x-pinch (Figs. 11-13, where hard x-ray images of test-objects correspond to a point source geometry). The best spatial resolution in experiments was approximately 0.2-0.3 mm.

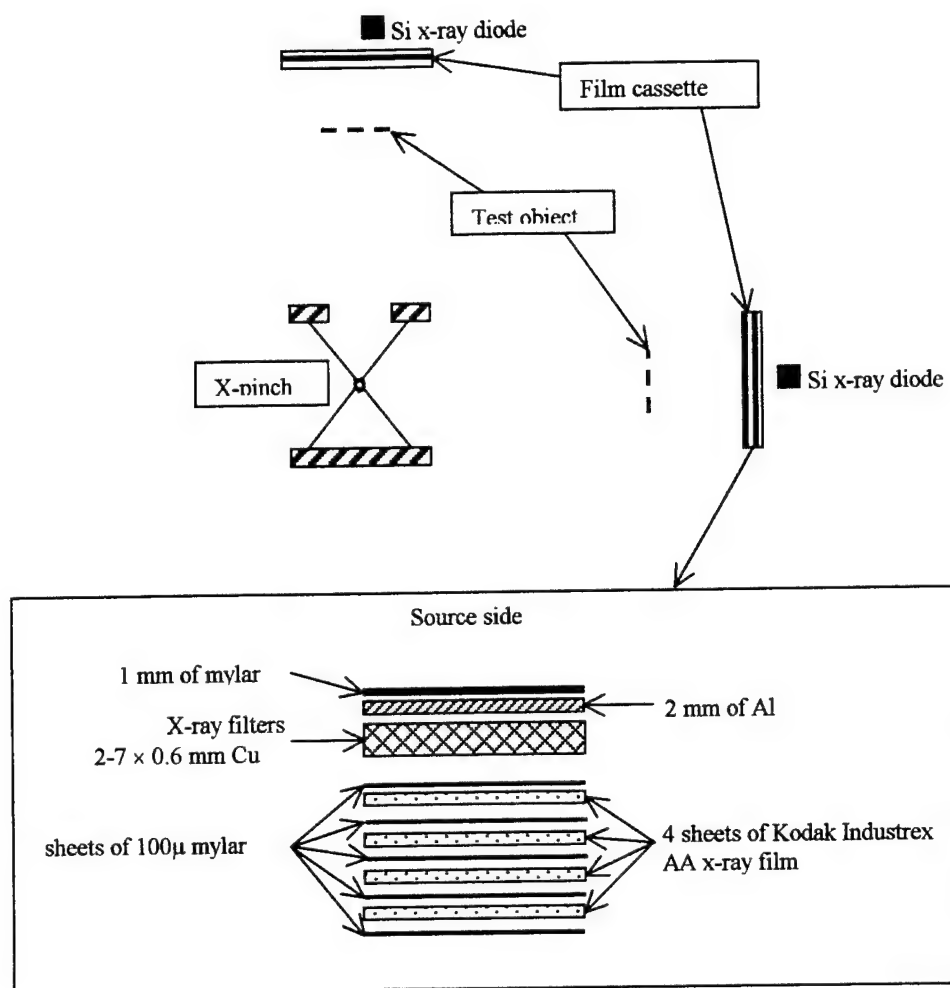


Fig. 9 Scheme of the NTF x-pinch hard x-ray experiments

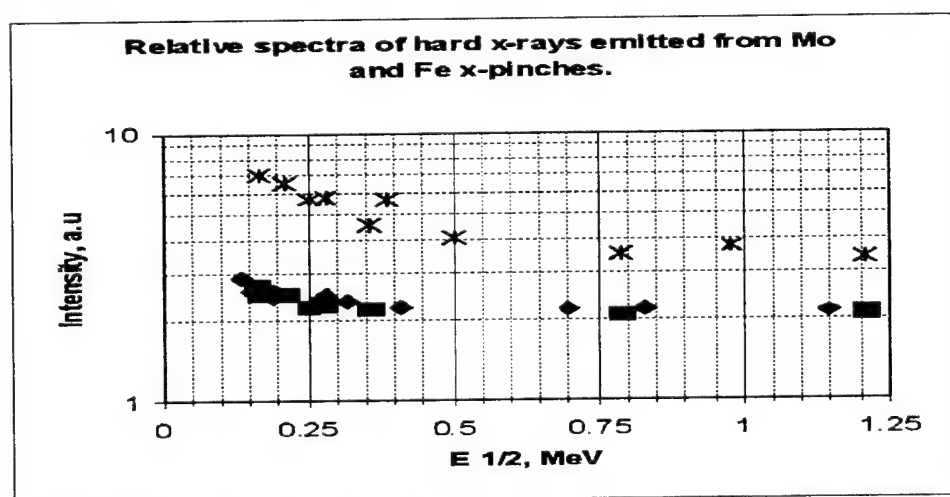


Fig. 10 Relative spectra of hard x-rays. x-Mo, 50 μm (end-on); □-Mo, 50 μm and ♦-Fe, 50 μm (side-on).



Fig. 11. Steel tubes (diameter 15-17mm) at the left and the right, and an Al tube (diameter 10-12 mm) at the center connected by a 1 mm thick Cu wire. Shot #71, 50 μ m Mo x-pinch. End-on. $E_{\text{cutoff}} \approx 120$ keV for the inner part of steel tubes (at the bottom image of a calibrated attenuator).



Fig. 12. Steel tubes (diameter 15-17mm) at the left, and an Al tube (diameter 15-18 mm) at the right connected by a bundle of 0.2 mm thick Cu wires. Shot #71, Mo x-pinch. Side-on. $E_{\text{cutoff}} \approx 80$ keV for the inner part of an Al tube.



Fig. 13. An Al tube with thread (diameter 10-12 mm) at the center, and a steel ring (thickness 2.5 mm) at the center connected by a 1 mm thick Cu wire. Shot #69, 50 μ m Mo x-pinch. End-on. $E_{\text{cutoff}} \approx 60$ keV for the inner part of an Al tube (at the bottom image of a calibrated attenuator).

3.3 Time and Energy Scaling of High Current X-Pinch X-Ray/EUV Pulses.

The fast filtered PCD and XRD measure x-pinch emission (Table 1,2) and the Ni bolometer (from SNL) measures the total x-ray/EUV energy. X-ray bursts appear before the current reaches maximum.

Table 1. Minimum pulse duration of a x-pinch.

	PCD (filter)	XRD (filter)
Ti	2.2 ± 0.4 ns (Be $8\mu\text{m}$)	4 ± 1 ns (kimf. $5\mu\text{m}$)
Fe	1.3 ± 0.7 ns (Be $8\mu\text{m}$)	3.7 ± 0.7 ns (kimf. $5\mu\text{m}$)
Mo	1.1 ± 0.5 ns (kapton $25\mu\text{m}$)	1.2 ± 0.7 ns (Be $8\mu\text{m}$)
W	1.1 ± 0.7 ns (kapton $25\mu\text{m}$)	1.1 ± 0.7 ns (Be $8\mu\text{m}$)
Pt	1.2 ± 0.7 ns (kapton $25\mu\text{m}$)	1.1 ± 0.7 ns (Be $8\mu\text{m}$)

Table 2. Probability of generation of one or two x-ray bursts during the x-pinch discharge.

	1 burst	2 bursts
Ti ($2 \times 30\mu\text{m}$)	0.35	0.25
Fe ($2 \times 50\mu\text{m}$)	0.15	0.15
Mo ($2 \times 50\mu\text{m}$)	0.20	0.4-0.5

Often x-ray pulses occurred in two or three groups, in the narrow time intervals after the start of the current. For example, for a $30\mu\text{m}$ Ti x-pinch pulses form two groups into intervals 30-45 and 60-80 ns after the current is initiated¹, 20-30 ns and 40-50 ns for a $50\mu\text{m}$ Mo x-pinch. Note, that for Mo first and second x-ray pulses have the same intensity.

The maximum total energy for x-pinch was more than 10-11 kJ for a Mo x-pinch, 7-8 kJ for Fe, Pt and W, and 6 kJ for Ti. For Ti, Fe, and Mo x-pinch optimum x-ray yields were obtained with a wire mass density of 200, 150 and 100-200 $\mu\text{g}/\text{cm}$ respectively. L-shell and 0.7-1keV continuum Mo output was about 250-350 J (XRD), and PCD signal (L-shell and 2 keV continuum) was about 20-30 J. An Fe x-pinch irradiated up to 1 kJ in L-shell and 0.25 keV in continuum (XRD), and 100-150 J in K-shell and several keV in continuum (PCD). The Fe output in region

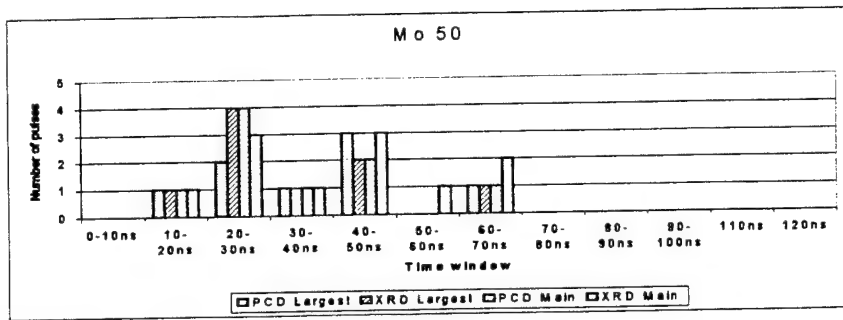


Fig. 15. The time distribution of PCD and XRD signals for a 50μm Mo x-pinch. Largest: the signals with a maximum amplitude; main: signals with an amplitude from 0.9 to 0.3 of the largest value. The data are based on 8 shots.

0.15-0.6 keV was 1.3 kJ (TGS measurements). Ti results were reported in [1]. The M-shell and 0.7-1 keV continuum (XRD) yield for W varied from 15 to 25 J, and near 15 J for Pt. The L-shell and 2 keV W continuum (PCD) changed from 5 to 20 J. Power of 1 MA x-pinch x-ray source pulses can reach $(1-5) \times 10^{11}$ W.

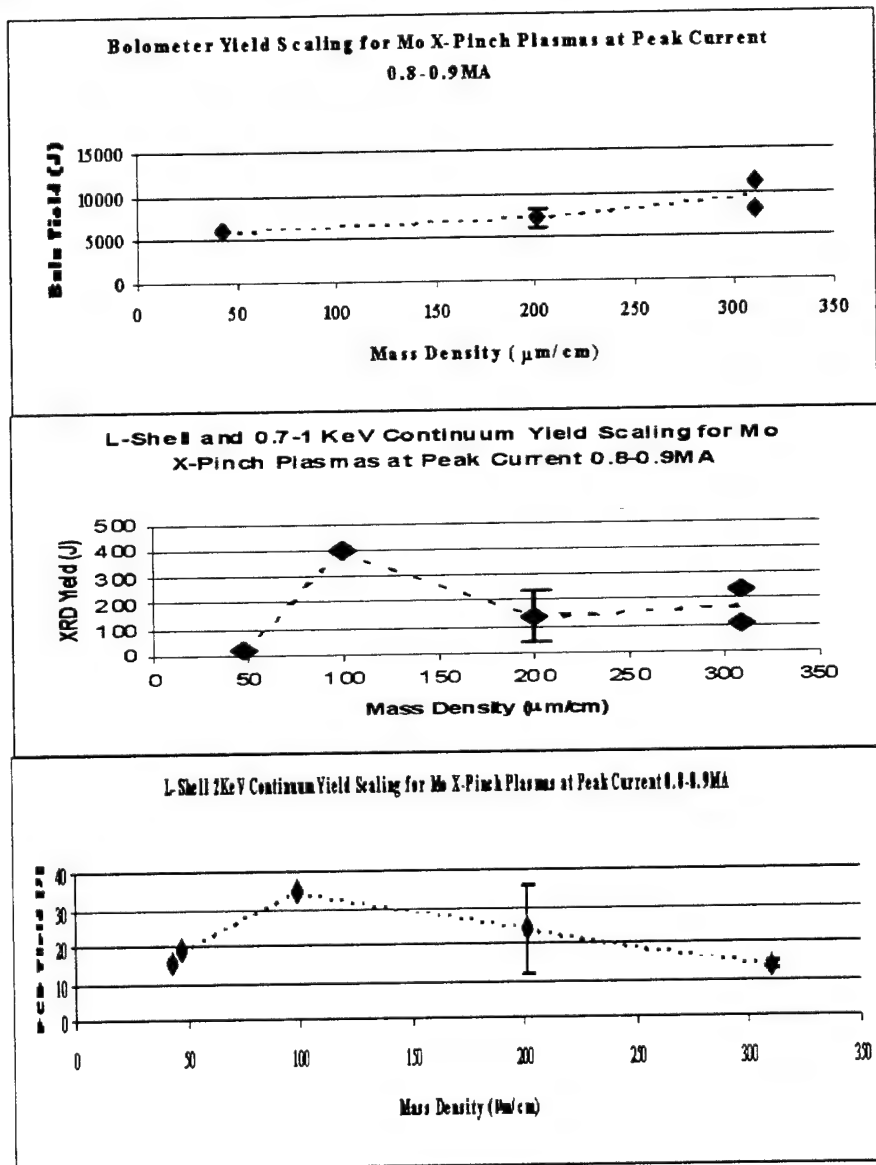


Fig. 16. The results of the study of variation of an x-ray yield with a linear mass-density of the x-pinch Mo wires.

3.4 X-ray spectra of high-current x-pinch sources.

Currently, the X-ray spectra of Ti, Fe Mo, W, and Pt³ are being processed to measure the main parameters of an x-pinch plasma (electron temperature, density and anisotropy). Best K-shell spectra were obtained for Ti and Fe, and L-shell for Mo x-pinch. The measurements of temperature and density of x-pinch plasmas were based on theoretical modeling of K-shell Ti and L-shell Mo spectra³. T_e is 1.5 keV for Ti, 0.8 keV for Mo, N_e is up to $2-3 \times 10^{22} \text{ cm}^{-3}$ for Mo x-pinch with 1-10% of hot electrons. The first results of the study of Mo L-shell x-pinch spectra with 1DXIS³ have demonstrated that the shape of spectra changed dramatically during the shot. This instrument can improve results of modeling of plasma parameters. The multichannel "Polychromator"⁵ spectrometer has been used to study the time evolution of up to 5 selected x-ray spectral lines from x-pinch. In experiments the difference between time evolutions of different Ne- and F-like Mo spectral lines has detected, which can provide us with temporal evolution of electron density and temperature.

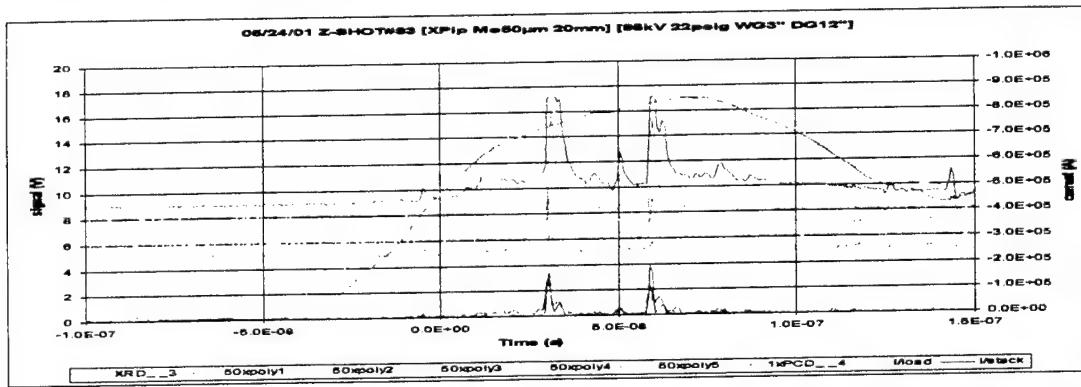


Fig. 17. X-ray signals from a 50 μm Mo x-pinch (shot # 83, May 24, 2001). "Polychromator" from the top: chan.1: $\lambda=5.21 \text{ \AA}$, Ne-like Mo; chan.2: $\lambda=4.80 \text{ \AA}$, Ne-like Mo; chan.3: $\lambda=1.94 \text{ \AA}$, "cold" $K_{\alpha}\text{Fe}$; chan.4: $\lambda=4.41 \text{ \AA}$, Ne-like Mo; chan.5: $\lambda=5.5 \text{ \AA}$, continuum, control line; PCD (with 25 μm kapton filter) and XRD (with 8 μm Be filter) response versus the time.

Fig. 18. X-ray signals from a 50 μm Mo x-pinch (shot # 70, March 02, 2001). PCD (with 25 μm kapton filter) and XRD (with 8 μm Be filter) responses versus time. 1DXIS frames just above x-pinch current curves. Frame #3 coincides with the first x-ray burst (current 600 kA).

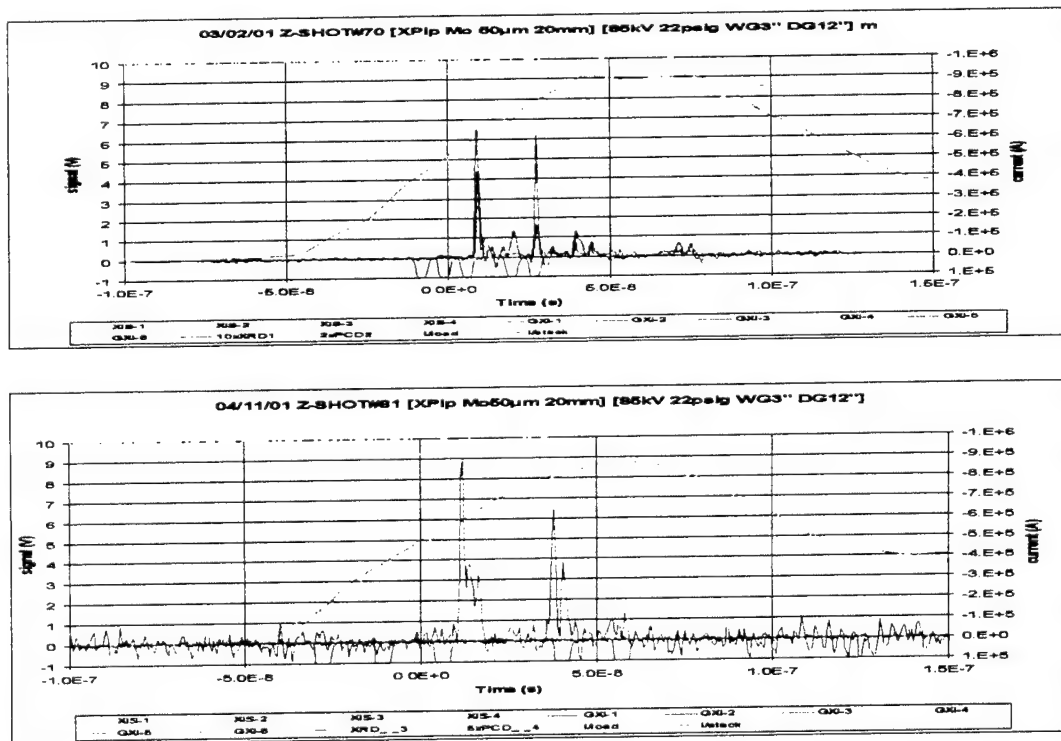


Fig. 19. X-ray signals from a 50 μm Mo x-pinch (shot # 81, April 11, 2001). PCD (with 25 μm kapton filter) response versus time. 1DXIS frames are just above x-pinch current curves. Frame #4 coincides with an x-ray prepulse before the first x-ray burst.

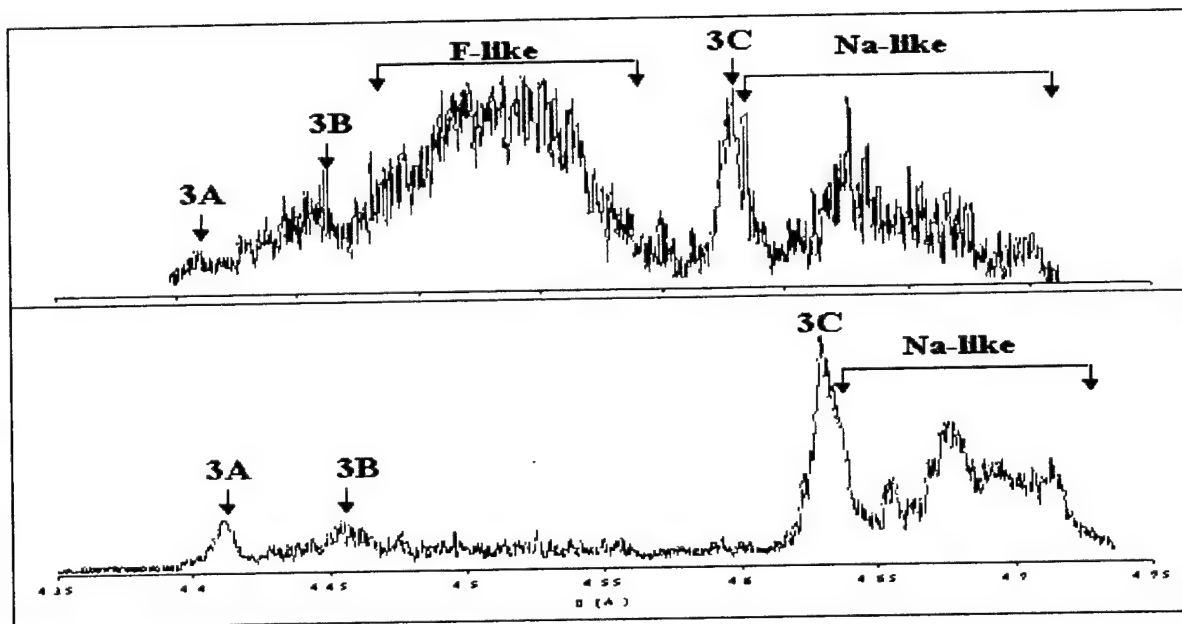


Fig. 20. Time-resolved L-shell Mo x-pinch spectra recorded on 03/02/01 (shot#70, see Fig.18) at the top, and 04/11/01(shot#81, see Fig. 19) at the bottom.

In Ti x-pinch spectra, x-ray radiation of He-like ions was polarized^{2,3}. From calculations and modeling^{2,3} we concluded that K-shell lines, in particular a He-like resonance line and satellite lines, can be successfully used for the diagnostics of energetic electron beams in z-pinch plasmas.

4. FUTURE APPLICATIONS of HIGH-CURRENT X-PINCH SOURCE

In the future, Zebra will be used for the study of surface physics and for x-ray microscopy.

In surface physics a powerful microfocus x-ray and hard x-ray 1 MA x-pinch plasma source can be used together with glass-capillary converters (GCC). Results of estimations that are based on our measurements (see above), experiments with GCC and a small vacuum spark source¹² have shown, that the 1 MA x-pinch source coupled with GCC^{13,14} for collecting and focusing x-ray on a flat surface in a 1-2 mm spot, can reach an energy density from 50-100 mJ/cm² (8-10 keV region) to 1-2 J/cm² (1-1.5 keV region), and flux density from 5×10^6 - 10^7 W/cm² (8-10 keV region) to $(1-5) \times 10^8$ W/cm² (1-1.5 keV region). Such facility can be used for research in fields of surface modification, annealing, and implantation for microelectronic technology.

For biomedical x-ray microscopy applications, two key properties of x-pinch sources were exploited: (i) spatial resolution which exceeds that possible with UV and visible light microscopy –much better than 0.2 - $0.5 \mu\text{m}$ ¹⁵, and (ii) distinct absorbcency properties at different wavelengths by different chemical elements present in intracellular and extracellular environments –the x-ray chemical contrast microscopy (XCCM). Using a such powerful x-ray source in combination with crystal x-ray monochromators (for example, compact devices with cylindrical crystals¹⁶) it is possible to study the spatial distribution of a wide variety of chemical elements in biological tissues with nanosecond temporal resolution.

5. ACKNOWLEDGEMENTS

The authors acknowledge the many collaborators whose work and help are excerpted in this paper, particularly R. Spielman, K. Struve, J. McGurn, D. Jobe from Sandia National Laboratories, W. Cline, B. Le Galloudec, G. Newman, A. Astanovitskiy, S. Rogowski from UNR. This study has been supported by DOE, DOD, SNL, and UNR.

6. REFERENCES

- 1.V. Kantsyrev, B. Bauer, A. Shlyaptseva, D. Fedin, S. Hansen, R. Presura, S. Batie, A. Oxner, B. LeGalloudec, H. Faretto, D. Chamberlain, N. Ouart, A. Jones, H. LeBeau, M. Gharaibeh, "Advanced x-ray and EUV diagnostics and

first application to x-pinch plasma experiments at the Nevada Terawatt Facility", *Rev. Sci. Instrum.*, v.72, 1(II), pp.663-667(2000).

2.A.S. Shlyaptseva, S. B. Hansen, V.L. Kantsyrev, B.S. Bauer, D.A. Fedin, N. Ouart, S.A. Kazantsev, A.G. Petrashen, U.I. Safronova, "X-ray spectropolarimetry of high-temperature plasmas", *Rev. Sci. Instrum.*, 72, 1(II), pp. 1241-1244, 2000.

3. A.S. Shlyaptseva, S. B. Hansen, V.L. Kantsyrev, B.S. Bauer, D.A. Fedin, N. Ouart, S. Keely, H. LeBeau, U.I. Safronova. "X-ray spectropolarimetry and hot electron effects on high-current x-pinch plasma spectra", *Abstr. IEEE International Conference on Pulsed Power Plasma Science PPPS 2001*, p.190, 2001.

4. V. Kantsyrev, B. Bauer, A. Shlyaptseva, R. Bruch, R. Phaneuf, "New optical instrumentation for hot plasma imaging, polarimetry, and spectroscopy, using glass capillary converters and multilayer mirrors", *Proc. Conf. "Dense Z-pinch" (1997)*, *AIP Proc.*, CP409, pp. 499 - 502, 1997.

5. D. Fedin, V. Kantsyrev, B. Bauer, A. Shlyaptseva, I. Brytov, "Polychromator" five-channel x-ray/EUV spectrometer with imaging transmission grating for plasma diagnostics", *Proc. SPIE*, 3764, pp.80-84, 1999.

6. B. Bauer, V. Kantsyrev, "Capillary spectrometer", *The US Patent*, #5,991,024, filed May 29, 1998.

7. V. Kantsyrev, D. Fedin, S. V. Kukhlevsky, B. Bauer, N. Ouart, "Features of soft x-ray and x-ray radiation from point laser plasma and z-pinch sources transported by glass capillary converters (experiment)", *SPIE Proc.* 4144, pp. 128-136, 2000.

8. S. V. Kukhlevsky, F. Flora, A. Marinai, L. Palladino, A. Reale, G. Tomassetti, A. Ritucci, G. Nyitray, L. Kozma, "Diffraction of x-rays in capillary optics", *Appl. Opt.*, 39, pp. 1059-1063, 2000.

9. S. V. Kukhlevsky, F. Flora, A. Marinai, G. Nyitray, A. Ritucci, L. Palladino, A. Reale, G. Tomassetti, "Diffraction of x-rays beams in capillary waveguides", *Nucl. Instrum. Methods, Res.*, B 168, pp. 276-282, 2000.

10. S.A. Pikuz, T.A. Shelkovenko, V.M. Romanova, G.S. Sarkisov, D.A. Hammer, D.F. Acton, "Studies of x-pinch plasma structure using high resolution x-ray optical and imaging spectroscopy methods", *AIP Proc.* CP 409, pp.429-436, 1997.

11. D. H. Kalantar, D.A. Hammer, K.C. Mittal, N. Qi, F.C. Young, S.J. Stephanakis, P.G. Burkhalter, G. Mehlman, D.A. Newman, "K-shell x-ray yield scaling for aluminum x-pinch plasmas", *J. Appl. Phys.*, 73, pp.8134-8139, 1993.

12. O.B. Ananyin, Yu.A. Bykovsky, V.L. Kantsyrev, A.A. Kologrivov, K.I. Kopytok, A.S. Shlyaptseva, M.Ya. Yakovlev, "Small plasma source with a capillary concentrator of soft x-rays", *Sov. Tech. Phys. Lett.*, 18, 5, pp. 331-332, 1992.

13. V. Kantsyrev, O. Petrukhin, A. Shlyaptseva, N. Mingaliev, S. Pikuz, V. Romanova, T. Shelkovenko, A. Faenov, "Investigation the characteristics of x-ray radiation from hot plasma by means of glass capillary converters", *Quantum Electronics*, 23, 12, 1026-1029, 1993.

14. Lei Wang, B.K. Rath, W.M. Gibson, J.C. Kimball, C.A. MacDonald, "Performance study of polycapillary optics performance for hard x-rays", *J. Appl. Phys.*, 80, 7, pp. 3628-3638, 1996.

15. P.C. Cheng, H.B. Peng, K.H. Tan, J. Wm. McGowan, R. Feder, D.M. Shinozaki, "Contact x-ray microscopy and micro-chemical analysis of biological objects", in "X-ray Microscopy", Edit. G. Schmahl, D. Rudolph, Springer-Verlag, Berlin, pp. 383-395, 1984.

16. V. Kantsyrev, R. Bruch, P. Phaneuf, N. Publicover, "New concepts for x-ray, soft x-ray, and EUV optical instrumentation including applications in spectroscopy, plasma diagnostics, and biomedical microscopy: A status report", *J. X-ray Sci. Technol.*, 7, pp. 139-158, 1997.

APPENDIX L

Application of New Five-Channel X-Ray/EUV Spectrometer with an Imaging Transmission Diffraction Grating for Study of Z-Pinch Plasma Sources

D.A. Fedin, V.L. Kantsyrev, B.S. Bauer, S. Fuelling, H. LeBeau,
and W. Cline, UNR
G. Newman, Nevada Technical Design

Proc. SPIE **4506** (2001)

To be published in SPIE Proc. Vol.4506 (July30-Aug.3. 2001, San Diego, CA).
**Application of new five-channel x-ray/EUV spectrometer with an
imaging transmission diffraction grating for study of z-pinch plasma
sources.**

Dmitry Fedin^{a*}, Victor Kantsyrev^a, Bruno Bauer^a, Stephan Fuelling^a, Sean Keely^a, Hank LeBeau^a, Gene Newman^b, Wade Cline^a.

^a Nevada Terawatt Facility, Department of Physics, University of Nevada Reno, Reno, NV, 89557

^b Nevada Technical Design, Reno, NV, 89506

ABSTRACT

A new five- channel spectrometer is designed for registration of x-ray spectral line emissions from plasmas with temporal resolution. All channels are independent from each other and include wide variety of dispersing elements (crystals and/or multiplayer mirrors) and detectors (*Si*-diodes or PCD). Sixth channel is used for device alignments with minimum adjustments can be used as channel for transmission diffraction grating spectrometer or channel for another time resolved detector. The device was used in experiments with different plasma sources in different configurations and showed its reliability and flexibility.

Keywords: X-ray diagnostics, spectrometer, crystal, multiplayer mirror, transmission grating.

1.INTRODUCTION

The monitoring of time evolution of x-ray emission from hot dense plasma is very important for estimation of electron density and temperature behavior¹. A device described has 5 high spectral and temporal resolution channels based on fast *Si* or PCD x-ray detectors. Different types of crystals and multiplayer mirrors are used as dispersing elements. This allows us to observe different spectral groups of spectral lines in wide wavelength range. An additional channel at an axis of the device is used as transmission diffraction grating spectrometer (TGS) and for alignments.

2. FIVE- CHANNEL SPECTROMETER "POLYCHROMATOR"

Five- channel spectrometer "Polychromator" (Fig.1) is designed for registration of x-ray emission from hot dense plasmas with spectral and spatial resolution^{2, 3}. Observing spectral region is defined by set of dispersing elements used in each channel. For studying *K*- and *L*- shell radiation we use four different types of crystals: KAP ($2d=26.63$ Å), PET 002 ($2d=8.742$ Å), *LiF* 200 ($2d=4.027$ Å) and α -quartz ($2d=$ Å) This set of crystals allows us to study properties of plasma radiation in wide spectral region (from 1 to 25 Å). 25 μ Be filters are used in each channel for protection from visible light and debris. In order to select other spectral range filters can be easily replaced by another material.

A registration system is based on application of fast *Si* diodes^{4, 5}. Additional protection from visible light made from 1 μ mylar coated on both sides by 0.1 μ Al. Flexible design of registration system allows us to substitute currently used detectors to practically any type of time resolving detector, which fits standard SMA connector.

First tests of the device were performed³ with laser plasma source⁶. After minor adjustments "Polychromator" was installed in one of beamlines at z-pinch pulsed power machine at Nevada Terawatt Facility (NTF)⁵ for studying properties of plasma emission from different types of loads such as single wire, x-pinch, conical and cylindrical arrays and materials ranging from Al to W with wire diameters from 10 to 200 μ .

* Correspondence: e-mail: fedin@physics.unr.edu ; phone (775) 971-2862; fax: (775) 972-2690; Nevada Terawatt Facility 5625 Fox Ave., Reno, NV, 89506.

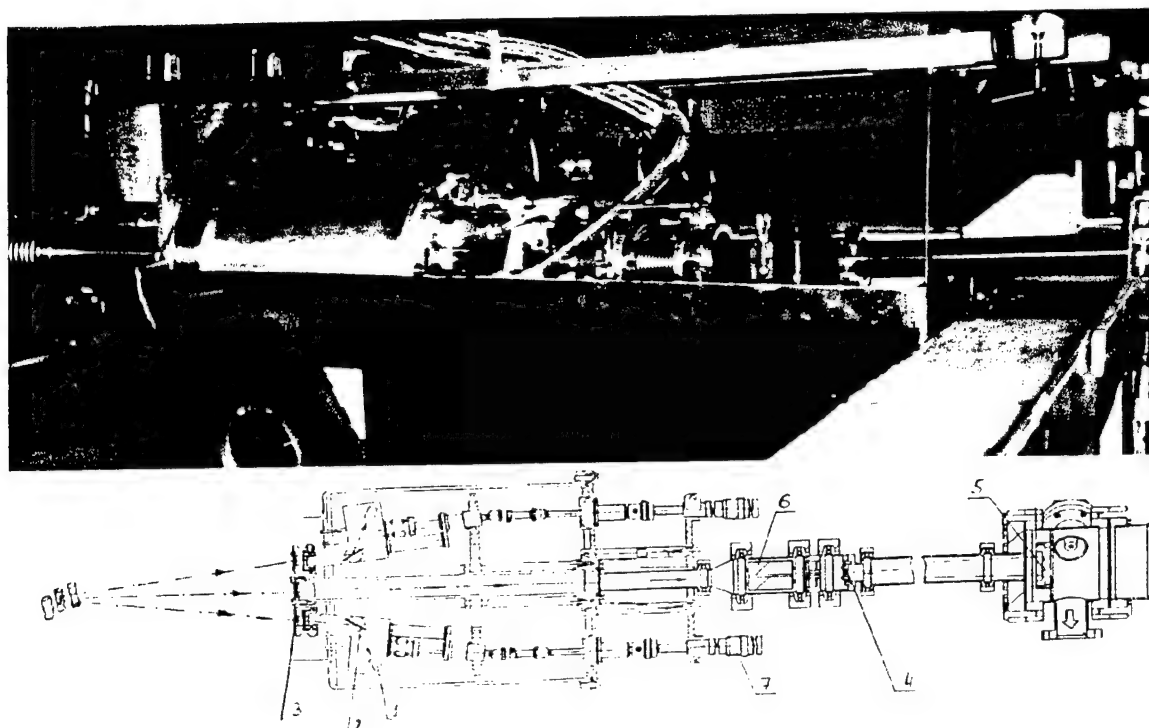


Fig. 1. Polychromator at the NTF (top) and its detailed drawing (bottom).

1. Fast x-ray diodes (5 units) 2. Crystals (5 units) 3. Filters (5 units) 4. Transmission Grating 5. MCP Imager 6. Magnetic Shield
7. Wavelength controllers (5 units) 8. Z-pinch plasma

Table 1. 6-channel "Polychromator" X-ray Spectrometer Characteristics.

5-channel spectrometer	Transmission grating spectrometer (TGS)
Spectral region: 0.5 - 50 Å	Spectral region: 20 - 80 Å
(3 crystal channels and MLM channel)	
120 - 240 Å (MLM channel)	
Spectral resolution: 400-600	Spectral resolution: 20-50
Field of view: variable with	Spatial resolution: 150-200 μm
Spatial resolution: 3 - 5 mm	
Time resolution: 0.2 - 0.5 ns.	Possible time resolution (gated): 1 - 2 ns.

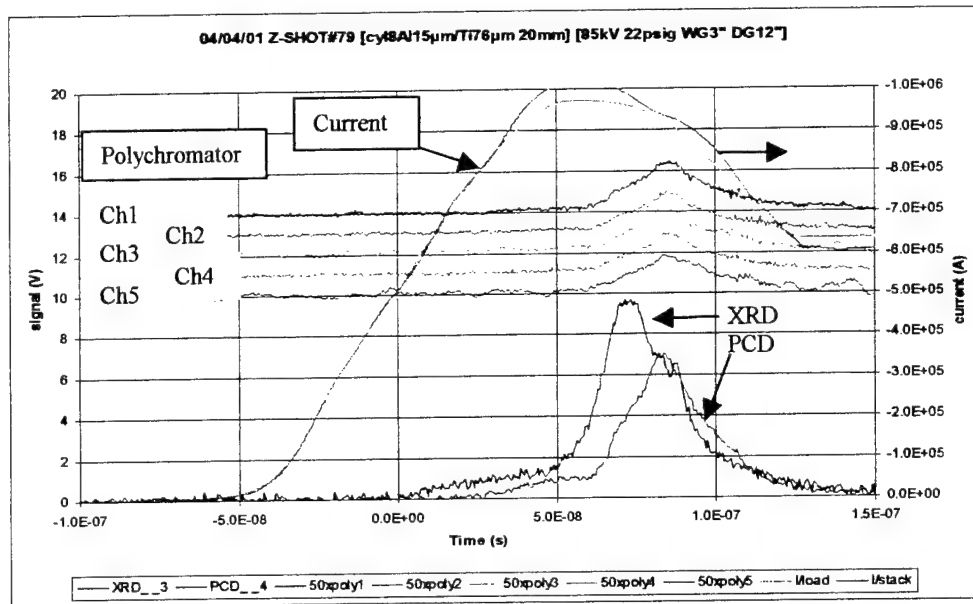


Figure 2: X-ray signals from an Al /Ti cylindrical wire array (Al 15 μm x8, 76 μm Ti central wire) (shot # 79, April 04, 2001). "Polychromator" ($\lambda=2.74$ \AA , "cold" $K_{\alpha}\text{Ti}$) PCD (with 8 μm Be filter) and XRD (with 5 μm kimfoil filter) response versus the time. Note, that maximum of "Polychromator" signals correlated in time with PCD signal (Ti K-shell radiation).

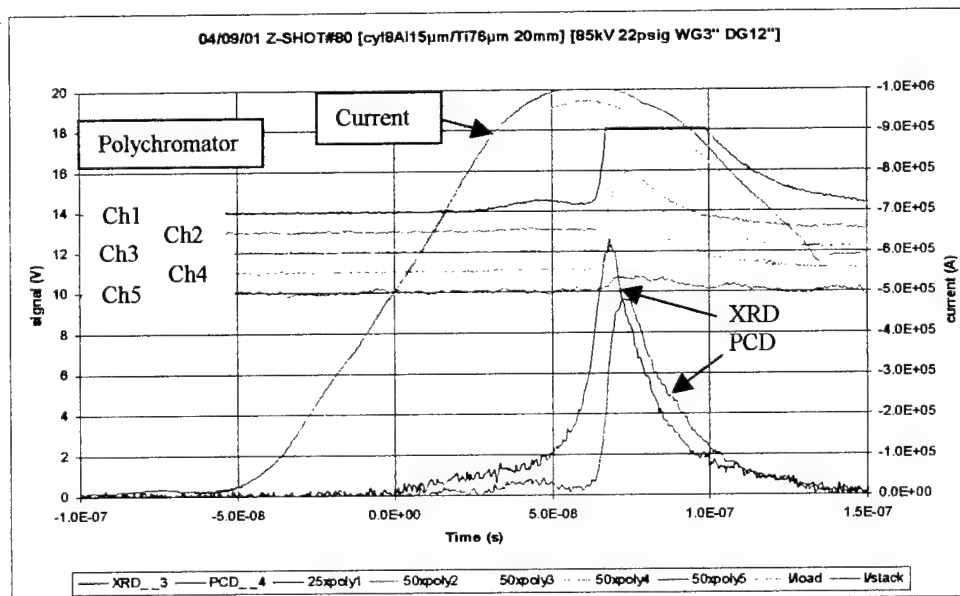


Figure 3: X-ray signals from an Al /Ti cylindrical wire array (Al 15 μm x8, 76 μm Ti central wire) (shot # 80, April 09, 2001). "Polychromator" (chan.1: $\lambda=7.765$ \AA , He-like Al; chan.2,3,4: $\lambda=2.74$ \AA , "cold" $K_{\alpha}\text{Ti}$; chan.5: $\lambda=7.174$ \AA , H-like Al) PCD (with 8 μm Be

filter) and XRD (with 5 μm kimfoil filter) response versus the time. Note, that maximum of "Polychromator" Ti signals correlated in time with PCD signal (Ti K-shell radiation).

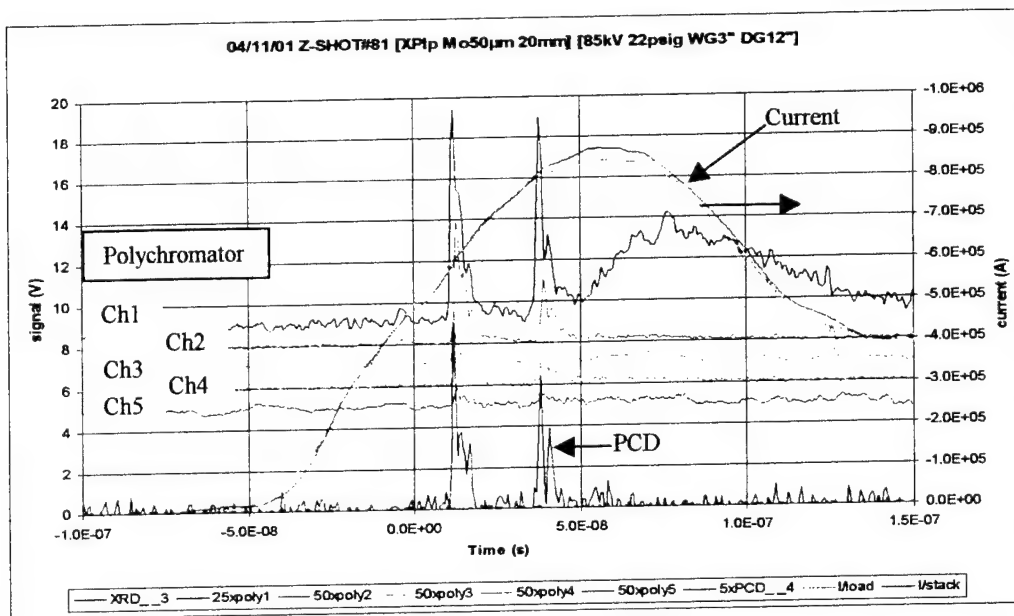


Fig. 4. X-ray signals from an 50 μm Mo x-pinch (shot # 81, April 11, 2001). "Polychromator" (chan.1: $\lambda=5.21$ Å, Ne-like Mo; chan.2: $\lambda=4.80$ Å, Na-like Mo; chan.3: $\lambda=1.94$ Å, "cold" $K_{\alpha}\text{Fe}$; chan.4: $\lambda=4.41$ Å, Ne-like Mo; chan.5: $\lambda=5.5$ Å, continuum, control line). PCD (with 25 μm kapton filter) response versus the time. Note, that maximum of "Polychromator" signals correlated in time with PCD signal (Mo L-shell radiation).

Due to strong kinetic shock during the shot of the machine periodic check of device alignment is necessary. Positioning system of crystal and detector are checking by standard procedure and, if necessary correcting. During first shot after alignment we install a set of five identical crystals (α -quartz) and adjust all channels to the same spectral line. Difference in waveforms was within the limits of crystals reflection and detectors sensitivity variations, which gave us a proof of alignment (Fig. 2).

For next shots two of α -quartz crystals were substituted to KAP crystals to observe temporal behavior of softer lines. In the shot with Al-Ti wire array (Fig. 3) one of channels was adjusted to He-like Al (7.765 Å) and another to H-like Al (7.174 Å). Those channels had KAP crystal as a dispersing element. Waveform from the first (He-like Al) channel was completely out of scale, at the same time signal from H-like Al channel was barely visible, which is an evidence of predominance of He-like line of Al in plasma emission. Analysis of signals from three other channels with α -quartz crystals (adjusted to Ti lines) shows no significant difference in temporal evolution and these lines were more intensive than H-like Al and much less intensive than He-like. The waveforms of the signal are very close to signal from PCD and approximately 5 ns later than signal from XRD, which was filtered for softer radiation.

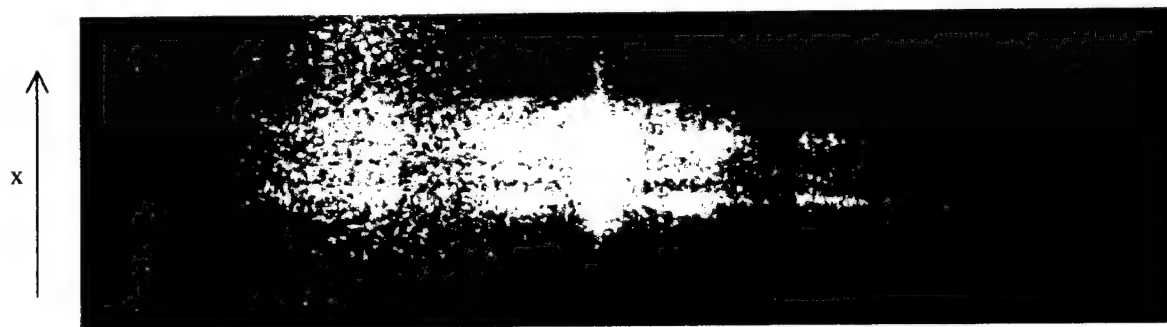
For the analysis of experiments (Fig. 4) with 50 μm Mo x-pinch "Polychromator" channels with KAP crystal were adjusted to Ne-like lines at 5.21 Å, two channels with α -quartz crystals were adjusted to another Mo L-shell lines (4.80 Å and 4.41 Å) and the last channel with α -quartz was adjusted to Fe K_{α} line (1.94 Å). With such alignments signals from channel 1 and 5 (KAP) had to be nearly the same. Such dramatic difference can be explained by fact that the crystals were at the limit of "Polychromator" angle change range and very high sensitivity of this device to alignment inaccuracies at limiting points. Nevertheless one can see the difference between time evolutions of different Mo spectral lines and Fe K_{α} line. To avoid such situation in later experiments KAP crystals were replaced by PET 002 and LiF 200 crystals when PET crystal was looking at Ne-like lines of Mo at 5.21 Å and LiF crystal at Fe K_{α} line.

3. TRANSMISSION DIFFRACTION GRATING SPECTROMETER.

Sixth (axial) channel of the device was equipped with TGS to make spectroscopic measurements with spatial and spectral resolution in wavelength range from 20 to 80 Å. TGS is very well described and reliable diagnostics for studying soft x-ray radiation from different plasma sources^{7,8,9}. Spectrometers with transmission gratings used as dispersing element has number of advantages in comparison with spectrometers based on crystals or reflecting gratings. These advantages are: TGS is easy to align, it usually has higher aperture, covers wide spectral diapason and relatively non expensive. With known absolute response of detector used⁸ absolutely calibrated spectrometer is an excellent device to use it with other soft x-ray radiation detectors to prove and calibrate data. With diffraction grating (period 1 μ , gap to period ratio $\frac{1}{2}$, substrate thickness 0.5 μ) and detector (Kodak DEF-5 film⁸) used in our experiment the spectral range was limited by wavelengths from 20 Å to 80 Å. Lower limit of registration is provided by decreasing of efficiency of grating and higher limit by strong second diffraction order of grating. In experiments with heavy elements such as *Mo*, *W* and *Pt* our spectral range limited by 50-80 Å because of hard x-ray radiation penetrating trough 5 μ Au substrate of grating. The grating is placed in 50 μ in diameter pinhole, which provides spatial resolution. Geometrical spatial resolution of the device is 150-200 μ and spectral resolution $\lambda/\Delta\lambda = 40-50$. For protection from charged particles system with strong bending magnets is used.

Spatially resolved spectra can provide more information about source structure and characteristics. Absolute calibration of the device allows evaluating of total energy radiated from the source as well as particular hot spot. Also in higher diffraction orders (4th in our case) it is possible to resolve certain lines or groups of lines. Because of lower diffraction efficiency at 4th diffraction order only strongest lines (groups) could be resolved. Addition of time-resolving gated MCP imager gives an opportunity to obtain time evolution of plasma radiation. Together with waveforms obtained from other five channels one can collect practically complete set of information necessary to calculate very important plasma parameters such as electron temperature and density. Comparison of calculated spectral shapes with Plank radiation spectrum allows evaluating of black body temperature of plasma. Integrated spectral distribution gives a yield of x-ray emission in wavelength range specified. The value obtained and signals from absolutely calibrated XRD and bolometer (also employed in these experiments) are in good agreement, which confirms, that methods of data processing are correct.

Typical spatially resolved spectra for different materials and load configurations are shown on fig. 5,6,7.



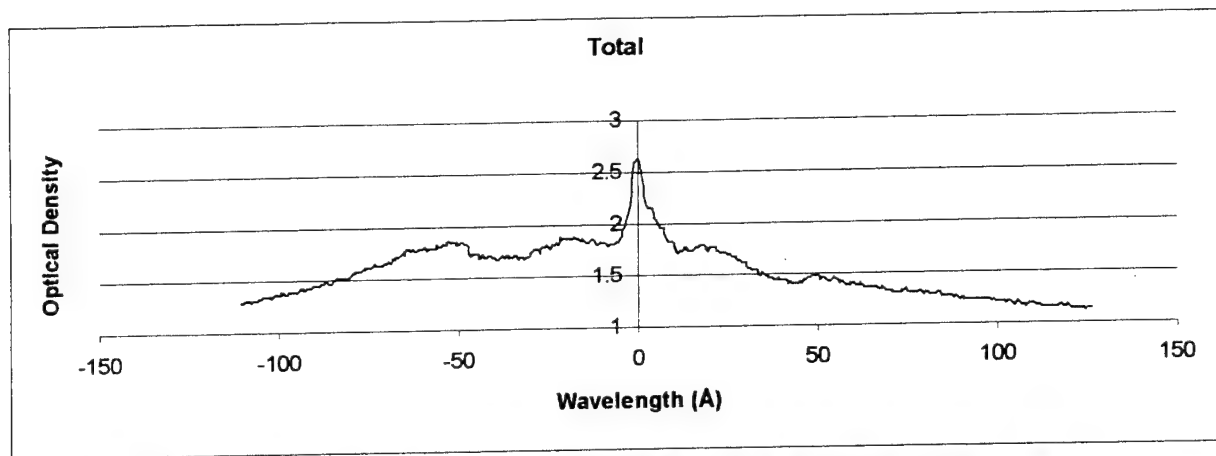


Figure 5. Typical spatially resolved spectrum and its densitometric trace for *Ti* single wire plasma source.

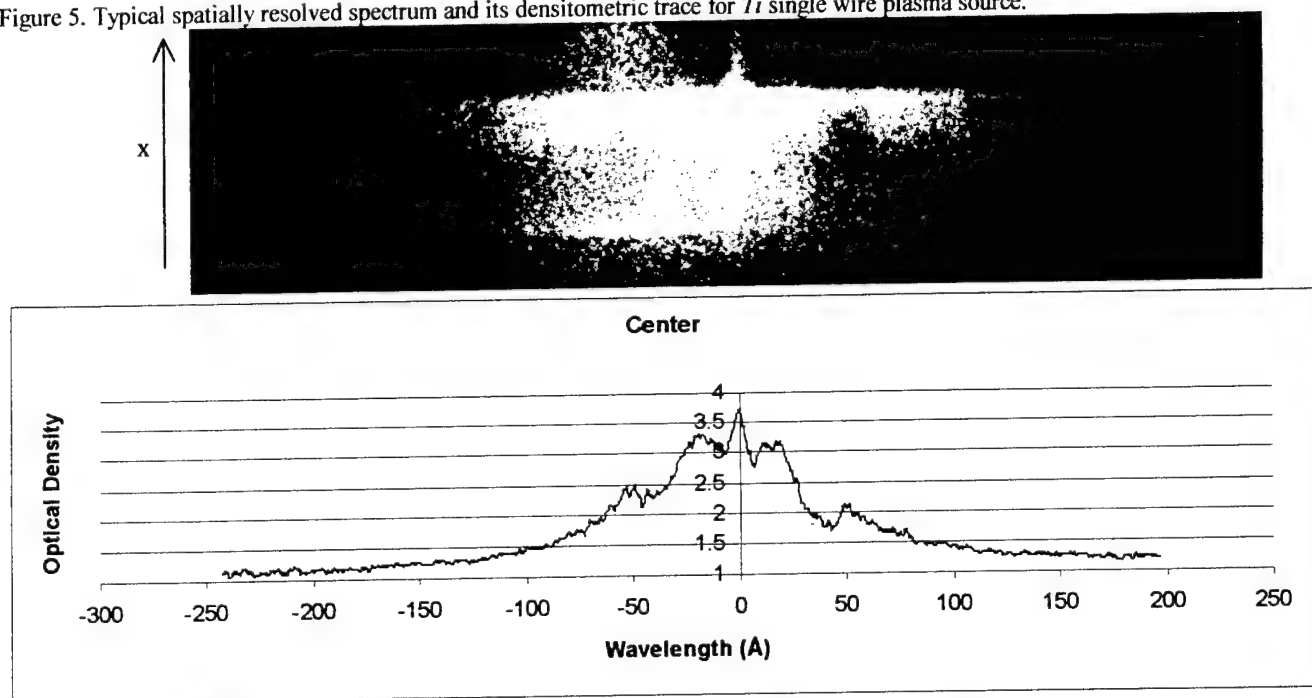


Figure 6. Typical spatially resolved spectrum and its densitometric trace for central part for *Ti* x-pinch.



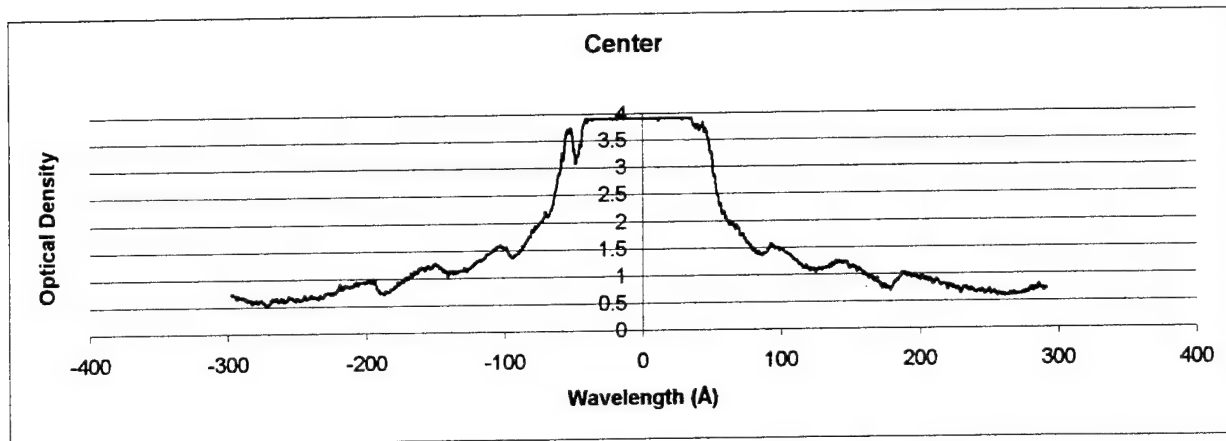


Figure 7. Typical spatially resolved spectrum and its densitometric trace for central part for Mo x-pinch.

4. CONCLUSION

A multichannel crystal spectrometer/transmission diffraction grating spectrometer "Polychromator" was designed to study a time history of an x-ray/EUV spectral line radiation from powerful plasma sources such as z-pinch. Flexible design of device allows us to use it also with other x-ray sources. High time and spectral resolution of the device described gives us an opportunity to study an evolution of very important plasma parameters such as electron density and temperature. Five time resolving channels are also used as relative time markers for time resolving gated pinhole camera and spectrometer. An additional time integrated channel with TGS collects data about a source under study in wide wavelength region with reasonable spectral and spatial resolution. TGS can be easily converted in time resolving device by substituting x-ray film by gated MCP detector. Tests performed with different plasma sources showed that "Polychromator" is a reliable powerful tool for investigation of different plasma sources.

5. ACKNOWLEDGEMENTS

The authors acknowledge many collaborators whose work and help is excerpted in this paper, in particular, S.Batie, A.Oxner, R.Pesura, H.Faretto, B.LeGalloudec and S.Rogowski. This study was supported by DOE, DOD, SNL and UNR.

6. REFERENCES

1. K.L.Wong, P.T.Springer, C.A.Iglesias, A.L.Ostenfeld, M.E.Foord, H.C.Bruns, J.A.Eming, "One and two dimensional density and temperature measurements of an argon-neon z-pinch plasma at stagnation", *AIP Proc.CP* **392** pp.1211-1214, 1996.
2. Technical press-release of "Bourestnic" Inc., 1993.
3. D.Fedin, V.Kantsyrev, B.Bauer, A.Shlyaptseva, I.Brytov, "Polychromator" five channel x-ray/EUV spectrometer with imaging transmission grating for plasma diagnostics", *SPIE 3764 Ultraviolet and X-Ray Detection, Spectroscopy and Polarimetry III* pp.80-84, 1999.
4. R.Korde, J.C.Cable, L.R.Canfield, "One Giga-rad passivating nitrided oxides for 100% internal quantum efficiency silicon photodiodes", *IEEE Transactions on Nuclear Science*, **40**, 6, pp.1655-59, 1993.
5. L.R.Canfield, R.West, T.N.Woods, R.Korde, "Silicon photodiodes with integrated thin film filters for selective bandpasses in extreme ultraviolet", *SPIE 2282 Ultraviolet Technology V*, pp. 31-38, 1994.
6. V.Kantsyrev, B.Bauer, N.Publicover, D.Fedin, N.Ammons, "Development and application of x-ray/EUV calibration facility with laser plasma source for plasma diagnostics and bio-medical x-ray microscopy", *SPIE 3766 Ultraviolet and X-Ray Detection, Spectroscopy and Polarimetry III* pp.252-260, 1999.

7. Yu.M.Alexandrov, M.O.Koshevoi, V.A.Murasheva, T.F.Nikitina, A.A.Rupasov, G.V.Sklizkov, A.S.Shikanov, M.N.Yakimenko, Yu.A.Zakharenkov, K.Eidmann, R.Siegel, G.D.Tsakiris, "X-ray spectrometer using a free-standing transmission grating and microchannel plate as a detector for plasma studies", *Laser and Particle Beams*, **6**, (3), pp.561-567, 1988.
8. Yu.M.Alexandrov, K.Eidmann, D.A.Fedin, R.V.Fedorchuk, M.O.Koshevoi, V.A.Murasheva, A.A.Rupasov, A.S.Shikanov, M.R.Shpol'sky, M.N.Yakimenko, "Investigation of sensitometric characteristics of x-ray photoemulsions in the spectral range 15-80 Å", *Nucl. Instrum. and Methods in Phys. Research*, **A308**, pp.343-346, 1991.
9. R.B.Baksht, V.I.Oreshkin, A.V.Fediunin, M.O.Koshevoi, A.A.Rupasov, D.A.Fedin, A.S.Shikanov, "Definition of Kr-liner plasma b radiation characteristics" *Soviet Journal Fizika Plazmy (Plasma Physics)*, **20**, 11, pp.962-967, 1994.

APPENDIX M

Multi-Channel Fast Hard X-Ray Spectrometer with Spatial Resolution Capability for Extended Z-Pinch Plasma Sources

H. LeBeau, D.A. Fedin, V.L. Kantsyrev, B.S. Bauer, S. Keely,
A. Kessler, and W. Cline, UNR
G. Newman, Nevada Technical Design

Proc. SPIE **4506** (2001)

Multi-channel fast hard x-ray spectrometer with spatial resolution capability for extended z-pinch plasma sources

H. LeBeau*, D.A. Fedin, V.L. Kantsyrev, B.S. Bauer, S. Keely, A. Kessler,
W. Cline, G. Newman

Dept. of Physics/220, University of Nevada, Reno, NV 89557, USA

ABSTRACT

A multi-channel, fast, hard x-ray diode spectrometer is being developed at the Nevada Terawatt facility. This spectrometer helps facilitate the study of the time evolution of hard x-ray emissions from hot, dense plasma. Each channel in the array can be adjusted individually with shielded view areas, allowing small areas of an x-ray source to be isolated and studied by region. This spatial resolution capability will permit a better understanding of the mechanisms present in hot, dense plasma. Results will be presented of experimental tests, and their interpretation, pertaining to the hard x-ray emissions generated from an x-pinch source in a pulse-power type device.

Keywords: Hard x-ray, multi-channel, spectrometer, z-pinch.

1. INTRODUCTION

A hot, dense extended z-pinch, plasma source will often contain regions with extremely different characteristics that change rapidly and drastically. Recent experimental observations, such as the generation of strong, energetic electron beams, highlight the ambiguity surrounding the cause of such phenomena.^{1,2} For instance, experiments show that for an x-pinch, a strong electron beam is directed not only axially toward the anode, but also along the ends of the wires toward the anode.² The energy contained in this e-beam is estimated to be 10-20 % of the total discharge energy.³ High current (1 MA) x-pinch plasma emits unexpectedly strong high-energy x-rays, whose energy far exceeds the values expected from the applied anode-cathode voltage. Some acceleration mechanism causes electrons to gain the high kinetic energy necessary for producing such hard x-ray radiation. Although many theories abound, the exact mechanism of this physical process has not been well established, and has lead to the need for a deeper understanding of the properties of hot, dense plasma.^{4,5,6,7} In response the Nevada Terawatt Facility (NTF), a laboratory run by the University of Nevada at Reno, is developing a variety of new x-ray and extreme ultra-violet diagnostic devices.¹ One of the devices being developed is a multi-channel hard x-ray spectrometer. The facility where this research is being conducted is built around Zebra, a 2 terawatt, pulse-power machine with a maximum current of 1.2 MA, a maximum voltage of 2 MV, and a rise-time of 100 ns (fig.1).⁸ Zebra can deliver a maximum energy of 100-120 kJ down a 1.9 Ohm high voltage transmission line to the target load.

2. HARD X-RAY SPECTROMETER

This new spectrometer has spatial resolution capability with a fast response time of 0.7 nanoseconds. The spectrometer has four channels that can be targeted individually, with movement in two dimensions across a source. Each channel is attached to a 154 mm tungsten-carbide collimating tube. Each tube has an inner diameter of 1.5 mm and an outer diameter of 3 mm. These high-Z tubes shield the detector diode from scattering radiation and limit the view area to a 5 mm diameter (at 500 mm from the source), allowing the time evolution of specific areas to be isolated and studied. Through a swivel mechanism, the collimating tubes themselves can be articulated up to 5 mm, which leads to a proportionally larger view change at the source (~20 mm at 500 mm from the source). The collimating tubes can be checked for precision and correct view area through the use of soft x-ray equipment.

*correspondence: Email: lebeaux@excite.com ; phone: 775.971.2859; fax: 775.784.1398

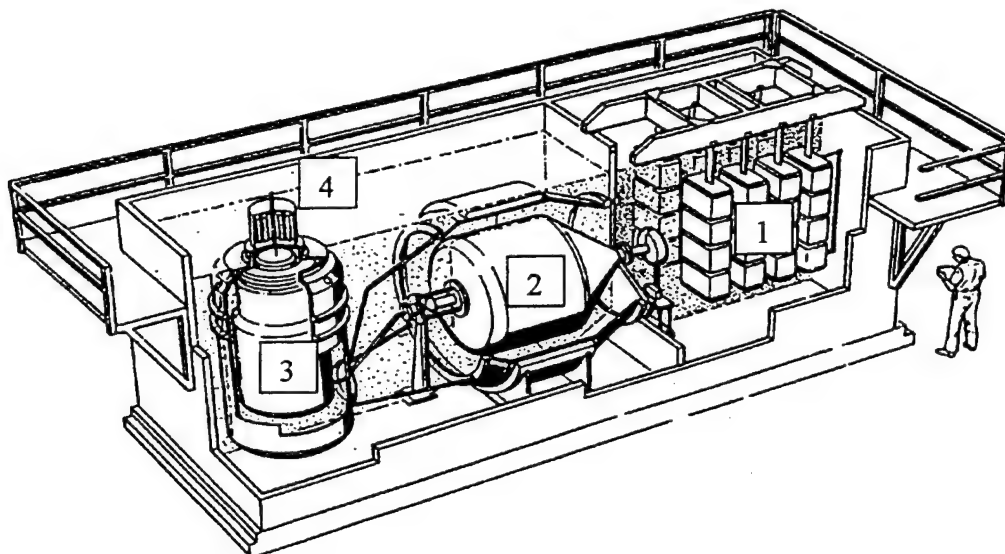


Fig. 1: The Nevada Terawatt Facility pulsed power generator-Zebra.

- | | |
|---|--|
| 1. Marx high-voltage generator (in a oil tank). | 2. Intermediate store |
| 3. Vertical pulse forming line (in a water tank). | 4. Vacuum chamber with z-pinch load and diagnostics. |

The diode array itself, and its associated articulated collimating tubes, are housed inside a vacuum tight metal case that is attached to the Zebra load chamber. A bellows is mounted between the spectrometer and the load chamber to minimize the kinetic shock associated with discharging a 2-terawatt pulse-power device. The main cover of the spectrometer is designed for easy removal and access to the diode array assembly. This facilitates convenient manipulation and alignment of the collimating tubes, and allows filters to be changed with little effort. The individual collimating tubes can be targeted with precision at widely separated areas of the plasma source. This articulation is accomplished by a collection of easily operated, micrometer-head controls located near the rear of the diode array assembly. A specially designed eyepiece attachment can be rapidly affixed to each individual channel that will allow quick and accurate optical alignment of each diode. To improve the signal to noise ratio, the spectrometer can be connected via a signal amplifier to an oscilloscope. The amplifier can be contained in a small Faraday cage near the spectrometer for protection and signal preservation.

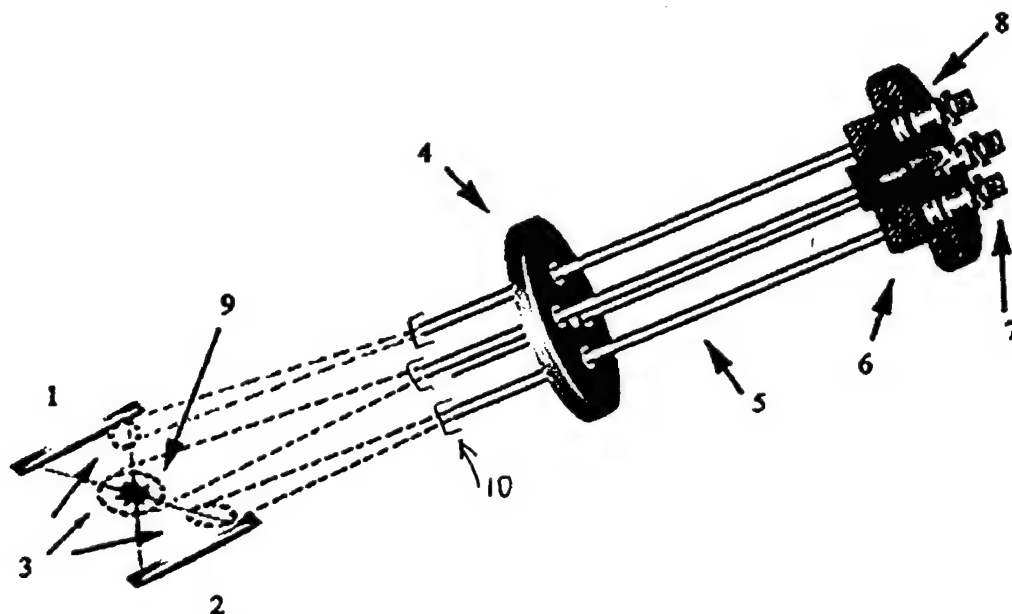


Figure 2: Multi-channel Hard X-ray Spectrometer.

- | | | |
|-----------------------|---------------------|-----------------------------------|
| 1. Cathode | 2. Anode | 3. Diode view areas |
| 4. Front tube support | 5. Collimating tube | 6. Tube adjuster and Pb shielding |
| 7. Diodes | 8. Filter holder | 9. Plasma |
| | | 10. Mylar/Al filters. |

The diodes employed in this spectrometer are doped silicon p-i-n diodes of the type AXUV-HS5, which are produced by International Radiation Detectors (IRD). The detector diodes are internal photoelectric devices and therefore are less sensitive to vacuum system contaminants than conventional detectors based on the external photoelectric effect.⁹ These photodiodes can maintain stable, high quantum efficiencies and have confirmed response capacity beyond 200 keV.¹⁰ In addition, as indicated by IRD literature, AXUV-HS5 diodes are radiation hardened to a level much greater than that of commonly available p-i-n silicon photodiodes, which allows for prolonged survivability when used in conjunction with a high-energy pulse-power device. The detectors are also reverse biased to increase resolution and sensitivity, and also to avoid saturation. The diodes are covered in lead protective sheaths and attached to the collimating tubes through a filter holder.

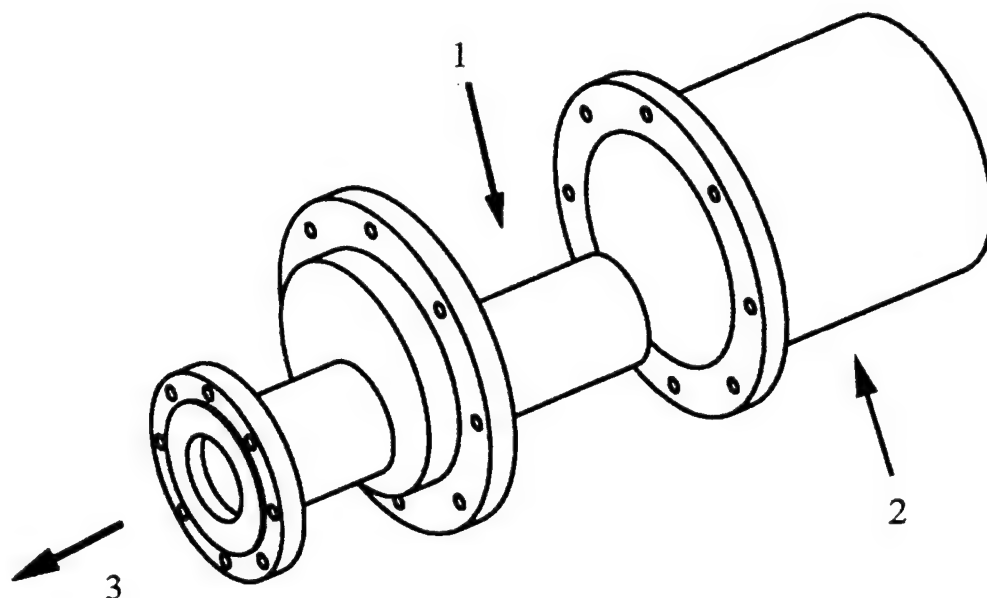


Figure 3: Spectrometer Assembly

1. Spectrometer 2. Vacuum cover 3. To plasma

3. EXPERIMENTAL PROCEDURE

The x-ray source configurations used during our experiments were x-pinch wire loads. The x-pinch configuration consists of two wires, typically 2 cm in length, which cross over each other in the middle like an x. This allows for the consistent appearance of a single bright emission source at the cross-over point.⁸ X-pinch wire materials and diameters were varied shot to shot but largely consisted of W, Mo, and Ti loads, all of which, when employed, result in the emission of intense bursts of x-rays at the cross-over point. To limit the radiation wavelengths seen by the silicon diodes from these bursts, filters are necessary. In order to isolate spectral regions of interest, Be-kapton filters for the 1-10 keV range and Cu-Al filters for the 50-150 keV range are employed.

Below the alignment process is briefly described. A scale size, simulation x-pinch load is inserted into the load chamber, with a visible-light point source attached to the exact position that is intended for viewing by a given diode. Usually these points of viewing interest will be at the center of the x-pinch, and along the wire near the anode or cathode. The main cover of the spectrometer is removed exposing the diode array assembly. The diode and filter holder are then removed. The diode itself is housed in an SMA connector and can easily be unscrewed, while the filter holder is contained in an SMA sized nut attached to the front of the diode, which is also readily removed. A specially designed eyepiece is then attached to allow for the accurate and prompt alignment of each individual diode channel in turn. The alignment mechanism is actuated through a collection of precision micrometer-heads. Once aligned each channel is secured against accidental movement. Filters and diodes are then re-attached, and the vacuum cover is re-fitted.

Testing has commenced on this spectrometer and data is being acquired. The collimating tubes themselves are checked, using an x-ray tube, for precision and accuracy of view area. The diodes have been tested in a horizontal position, and in a vertical position (9 degrees off axis above the load chamber). The diodes are shielded with lead tubing and filtered with Cu. During testing the diodes received signals whose time evolution correlated correctly with other calibrated diagnostics (see fig. 4). The acquired signals show a difference in amplitude that is caused by the relative collimation of emissions from the plasma source. The source when viewed from top, has been found to be partially collimated and narrow (10mm), and when viewed side-on has no collimation. In further tests the spectrometer will make use of its independently targeted channels to isolate distinct regions of the source plasma. This will allow the study and comparison of the anode surface, where Bremsstrahlung radiation is thought to be predominately generated, and the pinch area. This may provide insight into the different mechanisms that exist in hot, dense plasma by effectively separating the emissions from these different regions.

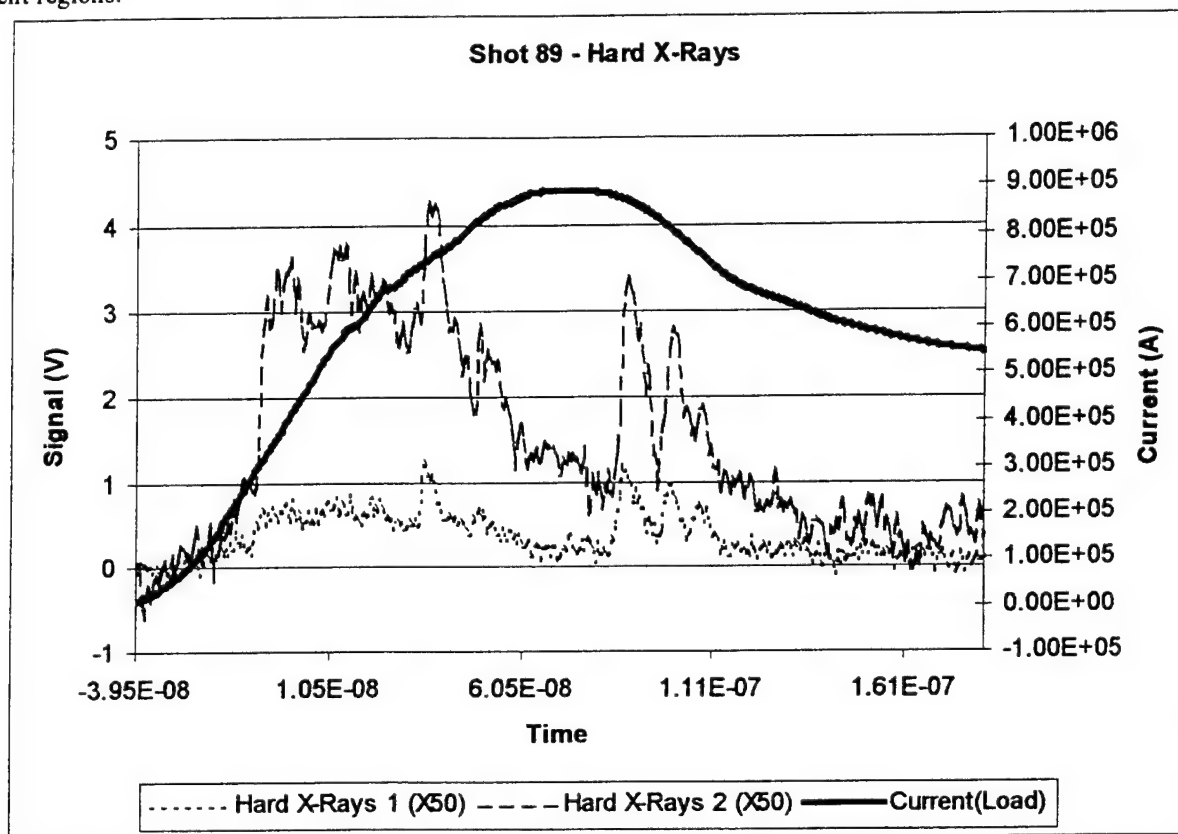


Fig. 4: Time dependence of an x-pinch current with hard x-ray diode signals. Hard x-ray 1 is positioned vertically above the load with a 4.8 mm Cu filter. Hard x-ray 2 is positioned side-on to the load with a 4.2 mm Cu filter.

4. CONCLUSION

The multi-channel fast hard x-ray spectrometer was specifically designed to study the time evolution of hard radiation emissions in a wide spectral region from 10 keV to 200 keV. Quantitative information concerning diverse regions of a plasma source can be obtained from the use of this spectrometer's individually targeted channels and their spatial resolution capabilities. A special design allows for ease of use and rapid preparation during experiments. The multi-channel, fast hard x-ray spectrometer is a useful new tool for understanding of the time evolution of hard x-ray emissions. This work is supported by DOE, SNL, and UNR.

5. ACKNOWLEDGEMENTS

The assistance and advice received from the following people is appreciated: Stephan Fuelling, Andrew Oxner, Harold Faretto, and Steve Batie.

6. REFERENCES

1. V. Kantsyrev, B. Bauer, A. Shlyapseva, D. Fedin, S. Hansen, R. Presura, S. Batie, W. Brinsmead, H. Faretto, B. Le Galloudec, A. Oxner, D. Chamberlain, N. Ouart, A. Jones, H. LeBeau, "Advanced X-ray/EUV diagnostics for spectroscopy, imaging and polarimetry at the Nevada Terawatt Facility z-pinch plasma source", *Rev. Sci. Instrum.*, **72**, 1 (II), 2001.
2. A.S. Shlyapseva, S.B. Hansen, V.L. Kantsyrev, B.S. Bauer, D.A. Fedin, and N. Ouart, "X-ray spectropolarimetry of high-temperature plasmas", *Rev. Sci. Instrum.*, **72**, 1 (II), 2001.
3. V.L. Kantsyrev, A.S. Shlyapseva, B.S. Bauer, R. Pressura, S. Fuelling, D.A. Fedin, S. Hansen, S. Batie, H. Faretto, B. LeGalloudec, A. Oxner, N. Ouart, H. LeBeau, S. Keely, D. Chamberlain, S. Rogowski, "X-Ray Temporal, Spatial and Spectral Study of .9 MA X-Pinch Ti, Fe, Mo, W, and Pt Radiation Sources", *ICOPS 2001 Proceedings*, Las Vegas, 2001, in press.
4. A. Robledo, I.H. Mitchell, R. Aliaga-Rossel, J.P. Chittenden, A.E. Dangor, M.G. Haines, "Time-resolved energy measurements of electron beams in fiber Z-pinch discharges", *Physics of Plasmas*, **4**, 1997.
5. J. Fukai, E.J. Clothiaux, "Mechanism for the Hard X-ray Emission in Vacuum Spark Discharges", *Physical Review Letters*, **34**, 14, 1975.
6. M.G. Haines, "Ion Beam Formation in an $m=0$ Unstable Z-Pinch", *Nuclear Instruments and Methods*, **207**, pp. 179-185, 1983.
7. Hans Uhm, Tong Nyong Lee, "High-energy x-ray emission in vacuum spark discharge", *Phys. Rev. A*, **40**, 7, 1989.
8. V.L. Kantsyrev, B. Bauer, A.S. Shlyapseva, D.A. Fedin, S. Hansen, R. Pressura, S. Batie, W. Cline, H. Faretto, B. LeGalloudec, A. Oxner, D. McCrory, N. Ouart, H. LeBeau, "The X-Pinch Driven by 0.9 MA: a powerful pulsed soft x-ray point source", *Proceedings of SPIE: advances in Laboratory-based x-ray sources and optics*, **4144**, San Diego, 2000.
9. H.O. Funsten, D.M. Suszcynsky, S.M. Ritzau, and R. Korde, "Response of 100% Internal Quantum Efficiency Silicon Photodiodes to 200 eV to 40 keV Electrons", *IEEE Transactions on Nuclear Science*, **44**, 6, pp. 2561-2565, 1997.
10. B. Planskoy, "X-Ray Response Vs. Energy", *Phys Med. Biol.*, **25**, 3, pp. 519-532, 1980.

APPENDIX N

X-Ray Spectropolarimetry of High-Temperature Plasmas

A.S. Shlyaptseva, S.B. Hansen, V.L. Kantsyrev,

B.S. Bauer, D.A. Fedin, and N. Ouart, UNR

S.A. Kazantsev, Observatoire de Paris

A.G. Petrashen, State Institute of Fine Mechanics and Optics

U.I. Safronova, University of Notre Dame

Rev. Sci. Instrum. **72**, 1241-1244 (2001)

X-ray spectropolarimetry of high-temperature plasmas

A. S. Shlyaptseva,^{a)} S. B. Hansen, V. L. Kantsyrev, B. S. Bauer, D. A. Fedin, and N. Quart
Department of Physics, University of Nevada, Reno, Nevada 89557-0058

S. A. Kazantsev

DASOP-L.P.S.H. Section Meudon, Observatoire de Paris, 92195 Meudon Cedex, France

A. G. Petrashen

State Institute of Fine Mechanics and Optics, St. Petersburg, 199101 Russia

U. I. Safronova

Department of Physics, University of Notre Dame, Indiana 46556

(Presented on 22 June 2000)

X-ray spectropolarimetry is a powerful new tool for investigating the anisotropy of high-temperature plasmas. It is sensitive to the energetic electron distribution function and magnetic field, which, in general, have not been measured adequately. This diagnostic is based on the theoretical modeling of x-ray line polarization-dependent spectra measured simultaneously by spectrometers with different sensitivities to polarization. The increasing sophistication of spectroscopic monitoring of high-temperature plasmas has led to the necessity to account for both non-Maxwellian electron distribution functions and polarization properties of lines. This diagnostic can be applied to a broad range of plasmas, from low-density astrophysical plasmas to dense z-pinch plasmas. This work shows how x-ray spectropolarimetry complements the usual spectroscopic monitoring of hot plasmas and demonstrates the importance of accounting for x-ray line polarization in plasma diagnostics. © 2001 American Institute of Physics. [DOI: 10.1063/1.1324752]

I. INTRODUCTION

Polarization plasma spectroscopy provides information about the anisotropy of processes occurring in plasmas. In particular, x-ray line polarization plasma spectroscopy is a powerful new tool for the investigation of plasma anisotropy. It can be used for diagnostics of plasmas with very different densities, from low-density astrophysical to dense z-pinch plasmas. This is a multi-step problem which requires creation of a new type of atomic database and appropriate theoretical modeling and experimental monitoring of polarization-dependent spectra. X-ray line polarization is sensitive to the electron distribution function and magnetic field, important plasma characteristics, that, in general, have not been measured adequately. The difference in line intensities between two polarization states will yield information on these plasma characteristics. In particular, it was justified in Refs. 1–3 that K-shell polarization-dependent spectra of dielectronic satellites can be used to diagnose the energy, density, and directionality of electron beams. In this article, results of the first experimental polarization-sensitive measurements of K-shell emission generated by high-density z-pinch plasmas are presented and diagnostics of the magnetic field based on polarization-sensitive L-shell spectra are discussed.

II. K-SHELL SPECTROPOLARIMETRY OF X-PINCH PLASMAS

To diagnose electron beams of high-energy electrons, we propose to use K-shell spectra of Ti or Fe ions in z-pinch

plasma. The first polarization-sensitive experiments at the Nevada Terawatt Facility (NTF) proved that the best object for the study of these effects is an x-pinch plasma, because of the presence of a strong electron beam along the discharge axis. The core of the NTF is the Zebra z-pinch, which has a maximum voltage of 2 MV, a current of 1.2 MA, a rise time of 100 ns, and a maximum energy in the Marx generator of 200 kJ (formerly the HDZP-II z-pinch facility at LANL). The diagnostic method first suggested in Ref. 4 employs an x-ray polarimeter/spectrometer that includes two identical LiF ($2d=0.4027$ nm) convex crystal spectrometers with additional slits (Fig. 1, channels 1 and 2) used with one-dimensional (1D) spatial resolution for the study of Ti K-shell radiation. At the first phase of our research these spectra are recorded with time and spatial integration. Experimental polarization-sensitive spectra produced by Ti x-pinch plasma are presented in Fig. 2. In each experimental data set, two spectra were collected simultaneously using two identical spectrometer setups. The “horizontal” spectrometer (Fig. 1, channel 1) has a dispersion plane perpendicular to the discharge axis, and the “vertical” spectrometer (Fig. 1, channel 2) has a dispersion plane parallel to the discharge axis. The LiF crystal has a spacing corresponding to the nominal Bragg angle of 40° at the wavelength of 2.6 \AA ; the Ti lines most likely to be polarized with λ close to 2.6 \AA are He-like lines [a resonance line w ($\text{He}\alpha$) and intercombination line y] and Li-like line q (here Gabriel’s line notations are employed from Ref. 5). The difference in K-shell polarization-dependent spectra related to polarization states parallel and perpendicular to the electron beam (horizontal

^{a)}Electronic mail: alla@physics.unr.edu

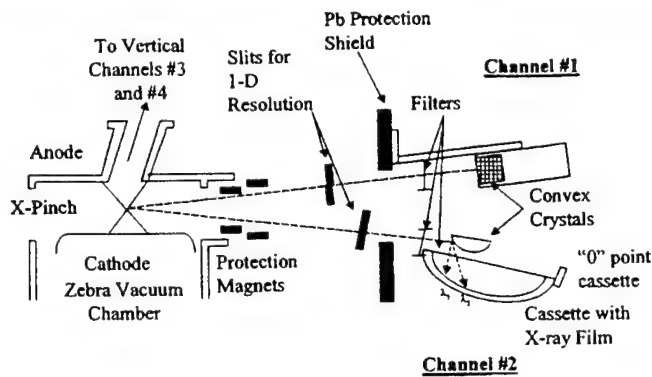


FIG. 1. Experimental setup including a one-dimensional x-ray polarimeter/spectrometer for polarization measurements.

and vertical traces in the figures) can be used to diagnose the energy, density, and directionality of electron beams in laboratory plasmas.

Eight sets of x-ray spectra of $K\alpha$ line radiation produced by Ti x-pinch in May 2000 indicate that line radiation from helium-like Ti dominates. The lines $He\alpha$, β , and γ and their satellite lines are seen on all spectra. Also, line radiation of H-like and Li-to F-like Ti ions is observed. The cold $K\alpha$ line of Ti is present on all spectra, but the $K\alpha$ line of Fe is observed only on the "vertical" spectrometer spectra because the "horizontal" spectrometer was not seeing an anode. Preliminary estimates based on spectral line intensity ratios indicate an electron temperature in the range 1.8–2.4 keV. The polarization-dependent x-ray spectra indicate that

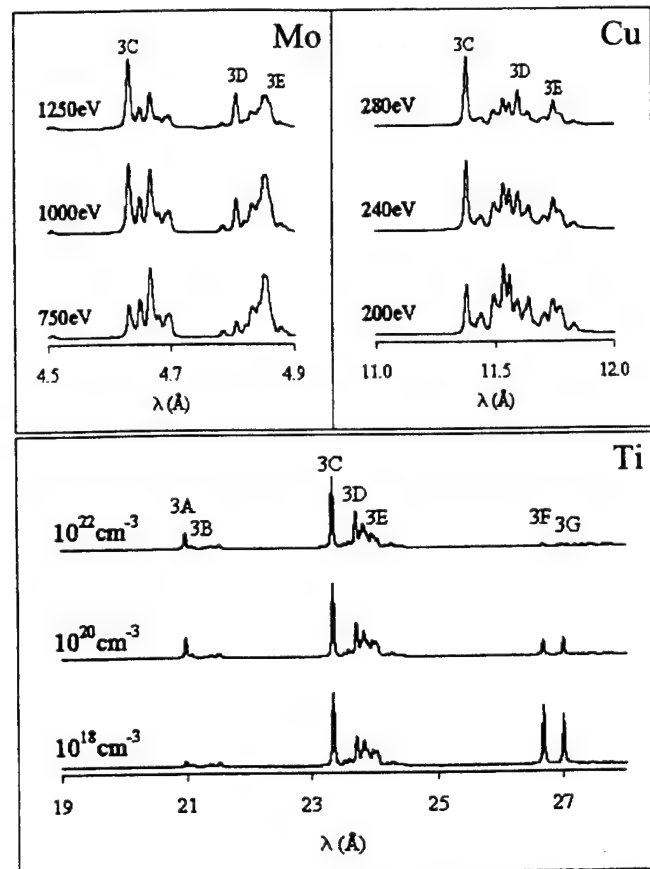


FIG. 3. (top) Synthetic L-shell spectra of Cu and Mo ions calculated at $Ne=10^{20} \text{ cm}^{-3}$ and various Te (bottom). Synthetic L-shell spectra of Ti ions calculated at $Te=90 \text{ eV}$ and various Ne.

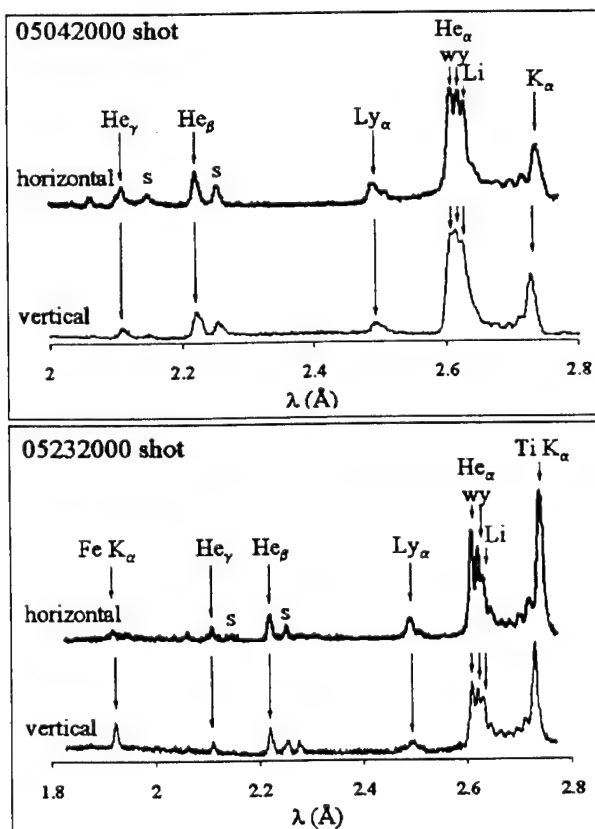


FIG. 2. Experimental polarization-sensitive x-ray spectra produced by Ti x-pinch plasma on 4 May 2000 (top) and on 23 May 2000 (bottom).

x-ray spectral lines of Ti ions in the spectral region above 2.6 Å are polarized. The distribution of relative intensities within w, y, and q lines is different in the horizontal and vertical spectra; this indicates polarization of these lines and the existence of a strong electron beam with an energy above 5 keV. Calculations are in progress to estimate the energy and density of the electron beam. The x-ray spectral lines of Be-, B-, C-, N-, and O-like Ti ions in the spectral region above 2.6 Å are probably also polarized; relative intensities of the lines are different in the horizontal and vertical spectra. The relative intensities of short-wavelength lines below 2.6 Å ($He\beta$ and $He\gamma$ of Ti ions) are almost the same in the horizontal and vertical spectra; this indicates that these lines are not polarized. Polarization in the x-ray lines of Fe ions is not observed with these LiF crystals; the distribution of relative intensities within w, y, and q lines is almost identical in the horizontal and vertical spectra (the corresponding Bragg angle is 27°).

III. L-SHELL SPECTROPOLARIMETRY OF HIGH-TEMPERATURE PLASMAS

The increasing sophistication of time-dependent L-shell spectroscopic monitoring of high-temperature plasmas has led to the necessity to account for both non-Maxwellian electron distribution functions and polarization properties of L-shell lines. Moreover, the influence of the magnetic field on polarization of x-ray L-shell fine radiation is large enough

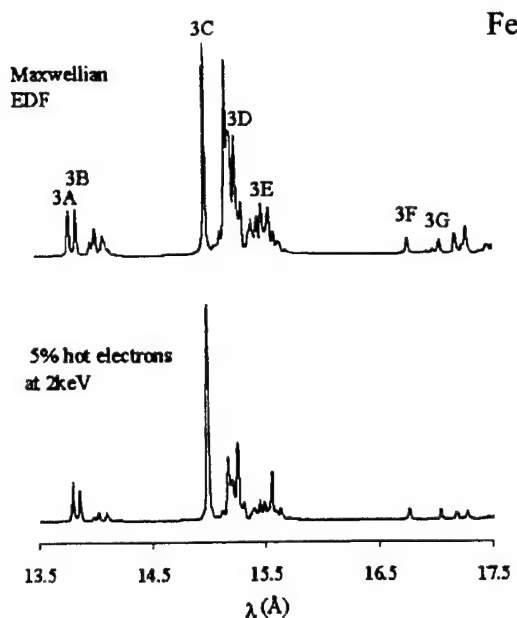


FIG. 4. Synthetic L-shell spectra of Fe calculated at $T_e=175$ eV and $N_e=10^{20}$ cm $^{-3}$ illustrating the effect of a non-Maxwellian EDF.

to be measured. In the present article, the time-dependent model for L-shell spectra modeling will be briefly overviewed and then diagnostics involving polarization properties of L-shell lines will be discussed.

A. L-shell spectroscopic monitoring of high-temperature plasmas

A time-dependent collisional-radiative atomic kinetic model of the neon- and sodium-like states for ions with a nuclear charge ranging from 18 to 42 has been developed. The model includes all of the important resonance and mixing CR processes among the 36 $n=3$ excited states of the neon-like ion and the neon-like ground state. More than 200 autoionizing sodium-like $3l3l'$ states are included, populated by inner-shell excitation from five non-autoionizing sodium-like states and dielectronic recombination from the neon-like ground state. Both the electron temperature and electron density of laser-produced plasmas have been successfully diagnosed with 10% precision by comparison of their spectra with synthetic L-shell spectra produced by our kinetic model. Electron temperature is diagnosed by the relative intensities of the neon-like $2p-3d^1P_1$ (3C) resonance line to the dielectronic satellite line structure, in an analysis similar to that of Ref. 5. Electron density is diagnosed by the total relative intensities of $2p-3s$ (3F and 3G) and $2s-3p$ (3A and 3B) neon-like lines, following the work in Ref. 6. The spectra in Fig. 3 illustrate the Te and Ne dependence of L-shell spectral line intensities. Evidence of a strong electron beam in x-pinch plasmas produced by Zebra has prompted the use of rates calculated with non-Maxwellian electron distribution functions in the model. Only a few percent nonthermal electrons are sufficient to make significant contributions to the synthetic spectra (see Fig. 4).

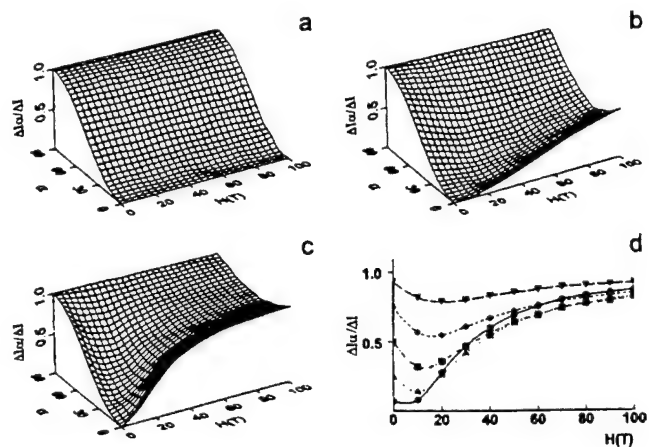


FIG. 5. The 3D plot of the dependence of the ratio of the intensities $\Delta I_\alpha/\Delta I$ on the value of magnetic field H (in T) and the angle of observation to the symmetry axis α calculated for the following transitions in Ti ions: (a) the K-shell resonance transition $1s^2-1s2p^1P_1$, (b) the L-shell transition $2p-3d^1P_1(3C)$, (c) the L-shell transition $2s-3p^1P_1(3A)$; and (d) 2D plot of the dependence displayed in (c) calculated for the following values of the angle α : 15° (circle), 30° (triangle up), 45° (square), 60° (rhombus), and 75° (triangle down).

B. The influence of the magnetic field on the polarized line radiation of multiply-charged ions

A model incorporating anisotropy of electron impact excitation and the internal magnetic field is analyzed by means of a solution of the equation for the density matrix. The particular case of multiply-charged Ti ions is considered when alignment of the excited states is created in the axially symmetric plasma source. The diagnostic possibilities of x-ray line polarization spectroscopy for estimation of the magnetic field are numerically studied. The following Liouville equation describes the evolution density operator $\hat{\rho}$ and accounts for radiation damping, magnetic field effect, and an excitation process determined by the operator \hat{N} :⁷

$$\frac{\partial}{\partial t} \hat{\rho} = -\frac{\hat{\rho}}{\tau_0} - \frac{i}{\hbar} [\hat{\rho}, \hat{V}] + \hat{N}, \quad (1)$$

where τ_0 is the lifetime of the excited state, and \hat{V} is the operator of the interaction of electron shells of the atomic system with a magnetic field. In our case when Zeeman splitting is much smaller than the fine structure splitting, a weak-field approximation can be employed. The following Cartesian reference system XYZ is used: the X axis is in the direction of observation, the Y axis is in the direction of the magnetic field, and the Z axis is in the direction of the electron beam. In such a system Eq. (1) takes the form

$$\begin{aligned} \frac{\partial}{\partial t} \rho_q^k = & -\rho_q^k + \frac{\omega_L}{2} [\sqrt{(k-q)(k+q+1)} \rho_{q+1}^k \\ & - \sqrt{(k+q)(k-q+1)} \rho_{q-1}^k] + N_q^k, \end{aligned} \quad (2)$$

where ρ_q^k is a polarization moment, $\omega_L = \mu_0 \tau_0 H / \hbar$ is the dimensionless Larmor frequency, $N_q^k = N_e v \tau_0 \sigma_q^k$ is the efficiency of the induction of the ordering of angular moments in the ensemble of ions, σ_q^k is the cross section of the collisional process, and N_e and v are the electron density and velocity, respectively. In a stationary regime, taking into ac-

count the axial symmetry of an excitation process $N_q^2 \sim \delta_{q,0}$, the solution of this equation has the simple form

$$\begin{aligned}\rho_2^2 &= N_0^2 \sqrt{\frac{3}{2}} \frac{\omega_L^2}{(1+4\omega_L^2)}; \\ \rho_1^2 &= -N_0^2 \sqrt{\frac{3}{2}} \frac{\omega_L}{(1+4\omega_L^2)}; \quad \rho_0^2 = N_0^2 \frac{1+\omega_L^2}{(1+4\omega_L^2)}.\end{aligned}\quad (3)$$

These expressions can be used to evaluate the difference of intensities $\Delta I = I_z - I_y$:

$$\Delta I = I_0 N_0^2 K_2 \sqrt{\frac{3}{2}} \frac{1+2\omega_L^2}{1+4\omega_L^2}, \quad (4)$$

where I_0 includes the fundamental constants and other factors independent from the angular momenta, and K_2 is a 6j symbol.

The same difference of intensities but measured at the angle α with the Z axis (the Y axis is in the same direction) may be written in the form

$$\Delta I_\alpha = I_0 K_2 N_0^2 \sqrt{\frac{3}{2}} \frac{1+2\omega_L^2 - \cos^2 \alpha - \omega_L \sin 2\alpha}{1+4\omega_L^2}. \quad (5)$$

The ratio of the polarized intensities is equal to

$$\frac{\Delta I_\alpha}{\Delta I} = \frac{1+2\omega_L^2 - \cos^2 \alpha - \omega_L \sin 2\alpha}{1+2\omega_L^2}. \quad (6)$$

It is very important to emphasize that this ratio does not depend on the process of excitation and is a function only of the value of the Larmor frequency and the angle α .

For diagnostics purposes, K- and L-shell transitions in Ti ions are considered. For example, for the He α transition, the lifetime is $\tau_0 = 4.5 \times 10^{-15}$ s, and for Ne-like transitions $2l-3l'$, the lifetimes are 1.0×10^{-13} and 3.4×10^{-13} s [for the transitions $2p-3d^1P_1(3C)$ and $2s-3p^1P_1(3A)$, respectively]. For a value of the magnetic field of about ~ 10 T, the corresponding values of dimensionless Larmor frequencies vary from 0.003 to 0.3. In Figs. 5(a)–5(d), the theoretical values of the ratio $\Delta I_\alpha/\Delta I$ are presented in the form of 3D plots calculated for the specified K- and L-shell transitions. Because of the particularly small value of the ratio $\mu_0 \tau_0 H/\hbar$ for the states of K-shell in the range of the value of a magnetic field between 10 and 100 T, the polarization characteristics of this type of transition do not depend on the value of the magnetic field [see Fig. 5(a)]. On the contrary, for L-shell transitions (3A and 3C lines) in Ti ions, the ratio $\Delta I_\alpha/\Delta I$ depends significantly on the value of the magnetic field for small angles $\alpha \leq 45^\circ$ [see Figs. 5(b) and 5(c)]. Figure 5(d) illustrates the sensitivity of the ratio $\Delta I_\alpha/\Delta I$ for the

3A line to the value of the magnetic field calculated for different values of the observation angle. Other L-shell lines (see Fig. 3) have longer lifetimes of the upper levels and are not useful for this diagnostic. It is important to emphasize that lines appropriate to this diagnostic method should have not only moderate values of lifetimes but should be polarized by electron beam excitation. Polarization of these L-shell lines has been discussed in Ref. 8. To perform polarization-sensitive experiments aimed to the measurement of the magnetic field, crystals will be chosen with an appropriate integrated reflectivity for x rays polarized parallel and perpendicular to the electron beam axis. The set of two identical lead stearate (for Ti) or KAP (for Fe) convex crystal spectrometers with additional slits (Fig. 1, channels 3 and 4) should be used as the second polarimeter/spectrometer with 1D spatial resolution for this diagnostic. The polarimeter/spectrometer observes photons emitted at angles less than 10° to the electron beam axis (the z-pinch discharge axis) through the hole in the anode.

In conclusion, from our preliminary calculations and modeling we learned that K-shell Ti and Fe lines, in particular a He-like resonance line and satellite lines, can be successfully used for the diagnostics of electron beams. They will have no influence from the magnetic field on their polarization. On the other hand, L-shell Ti or Fe lines are very good candidates for the diagnostics of magnetic fields through line polarization. In particular, some of the Ne-like lines are very sensitive to the effect of the magnetic field, and few of them are nonsensitive.

ACKNOWLEDGMENTS

The authors thank R. Presura, S. Batie, H. Faretto, B. LeGalloudec, G. Newman, A. Oxner, H. LeBeau, and A. Jones for their help in NTF experiments. This work was supported by DOE, SNL, UNR, and NSF.

¹A. S. Shlyaptseva, R. C. Mancini, P. Neill, and P. Beiersdorfer, *Rev. Sci. Instrum.* **68**, 1095 (1997).

²A. S. Shlyaptseva, R. C. Mancini, P. Neill, P. Beiersdorfer, J. Crespo López-Urrutia, and K. Widmann, *Phys. Rev. A* **57**, 888 (1998).

³A. Shlyaptseva, A. Petrashen, V. Kantsyrev, S. Kazantsev, and U. Safronova, in *Proceedings of the International Seminar on Atomic Processes in Plasmas* 29–30 July 1999, Toki, Japan (2000), NIFS-PROC-44, p. 138.

⁴A. S. Shlyaptseva, A. M. Urnov, and A. V. Vinogradov, P. N. Physical Lebedev Institute, Moscow, Russia, Report Vol. **193** (1981).

⁵A. H. Gabriel, *Mon. Not. R. Astron. Soc.* **160**, 99 (1972).

⁶J. Bailey *et al.*, *J. Phys. B* **19**, 2639 (1986).

⁷S. A. Kazantsev and J.-C. Henoux, *Polarization Spectroscopy of Ionized Gases* (Kluwer Academic, Dordrecht, 1995).

⁸S. B. Utter, G. V. Brown, P. Beiersdorfer, E. J. Clothiaux, and N. K. Podder, *Rev. Sci. Instrum.* **70**, 284 (1999).

APPENDIX O

X-Ray Spectropolarimetry and the Effect of Hot Electrons on Modeling of High-Current X-Pinch Plasma Spectra

A.S. Shlyaptseva, S.B. Hansen, V.L. Kantsyrev,
B.S. Bauer, D.A. Fedin, N. Quart, and H. LeBeau, UNR

U.I. Safronova, University of Notre Dame

PPPS-2001, Las Vegas, NV, June 17-22, 2001

To be published in PPPS-2001 Proc. Book (June 17-22, 2001, Las Vegas, NV)
**X-RAY SPECTROPOLARIMETRY AND HOT ELECTRON EFFECTS ON
HIGH-CURRENT X-PINCH PLASMA SPECTRA**

**A.S. Shlyaptseva, S.B. Hansen, V.L. Kantsyrev, B.S. Bauer, D.A. Fedin, N. Ouart,
S. Keely, H. LeBeau**

Physics Department/220, University of Nevada, Reno, NV 89557

U.I. Safronova

Department of Physics, University of Notre Dame, Notre Dame, IN 46556

Abstract

Accurate K-and L-shell spectroscopic modeling of high-temperature and high-density x-pinch plasmas requires the consideration of anisotropic plasma characteristics: non-maxwellian electron distribution functions and the polarization properties of x-ray lines. Experimental evidence for the existence of strong electron beams in x-pinch plasmas has motivated the development of a new tool, x-ray spectropolarimetry, for investigating the anisotropy of such plasmas. This diagnostic includes both space- and time-resolved x-ray spectroscopy and polarimetry and is based on theoretical modeling of x-ray line polarization-dependent spectra measured simultaneously by spectrometers with different sensitivities to polarization. Specifically, K-shell Ti and L-shell Mo x-ray spectra have been thoroughly modeled. Experimental spectra have been generated by Ti and Mo x-pinch plasmas produced at the Nevada Terawatt Facility. The detailed spectroscopic analysis of more than 20 shots with these x-pinch plasmas shows how x-ray spectropolarimetry complements the usual spectroscopic monitoring of z-pinch plasmas and demonstrates the importance of accounting for hot, non-maxwellian electrons in plasma diagnostics.

I. INTRODUCTION

X-pinch plasmas produce a bright, small x-ray source with a well-defined location. They can yield x-ray spectra of numerous ions with very high resolution. A distinct feature of x-pinch plasmas is the existence of strong electron beams, which makes them attractive objects for spectropolarimetry. X-ray spectropolarimetry is a new diagnostic that can provide detailed information about the electron distribution function and the magnetic field in x-pinch plasmas. Recent results on x-pinch plasmas and x-ray spectropolarimetry at the NTF were published in [1,2]. It has been shown that the polarization properties of Ti K-shell radiation can be successfully used for diagnostics of electron beams, whereas L-shell lines are

good candidates for the diagnostics of magnetic fields. From studying L-shell radiation of Ti, Fe, and Mo x-pinch plasmas, it was decided that Mo x-pinch plasmas are the best for magnetic field spectropolarimetry. In this paper, new polarization-sensitive diagnostics of Ti x-pinch plasmas are discussed briefly. The main topic of the paper is x-ray L-shell diagnostics of Mo x-pinch plasmas.

**II. X-RAY LINE POLARIZATION
SPECTROSCOPY OF TI X-PINCH
PLASMAS**

Ti plasmas have been produced at the NTF from a wide variety of pinches including single wires, x-pinch plasmas, and conical and cylindrical arrays with Al wires. The pinhole images of Ti x-pinch plasmas indicate that they are fairly inhomogeneous much more so than pinch plasmas of heavier elements. These images and damage to the anodes after shots also evidence the presence of beams of hot electrons. Thus, accurate K-shell spectropolarimetry of Ti x-pinch plasmas requires detailed plasma modeling that can account for the effects of hot electrons.

New polarization-sensitive experiments of Ti x-pinch plasmas were performed at the NTF in May-August 2000. The polarization-dependent spectra of K-shell line radiation produced by Ti x-pinch plasmas were recorded simultaneously by horizontal (with a slit for spatial resolution) and vertical (w/o a slit) spectrometers. The horizontal spectrometer has a dispersion plane perpendicular to the discharge axis and records mostly the parallel polarization state. The vertical spectrometer has a dispersion plane parallel to the discharge axis and records mostly the perpendicular polarization state. Both convex crystal spectrometers have identical LiF ($2d=4.027 \text{ \AA}$) crystals with spacing corresponding to the nominal Bragg angle of 40° at the wavelength of 2.6 \AA . For the polarization analysis, only shots with x-ray images representing one bright hot spot are chosen. Two typical polarization-sensitive spectra simultaneously recorded by horizontal and vertical spectrometers are presented in Fig. 1.

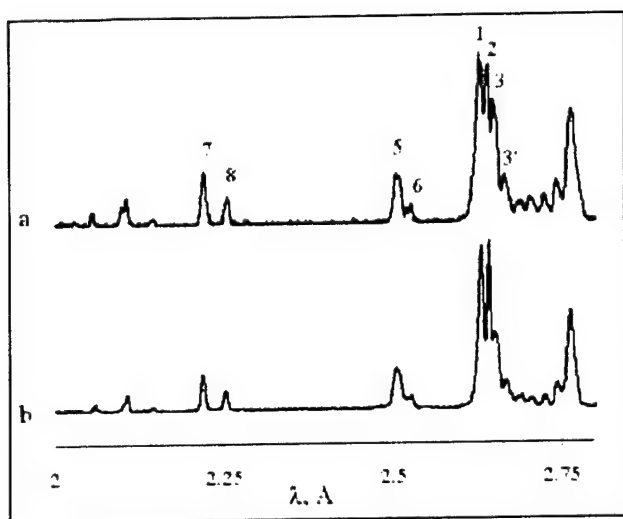


Figure 1. Typical Ti x-pinch spectra from horizontal (a) and vertical (b) spectrometers. Lines 1, 2, 5, and 7 are respectively $\text{He}\alpha$ (w), $\text{He}\alpha$ (y), $\text{Ly}\alpha$, and $\text{He}\beta$. Lines 3', 3, 6, and 8 are respectively Be-, Li-, He-, and Li-like satellite structures.

The most intense spectral feature belongs to He-like ions. The intensities associated with different polarization states I_{\parallel}/I_{\perp} for each of the spectral lines (1, 2, 3, 3', 5, 6, 7, and 8) and the line ratios of the satellite lines to their resonance lines (3/1, 3'/1, 6/5, and 8/7) from horizontal and vertical spectra have been analyzed. The ratio I_{\parallel}/I_{\perp} greater (less) than unity indicates the positive (negative) polarization of the line. The polarization of dielectronic satellite peaks and the positive polarization of resonance lines indicate that the electron beam has a low energy (3–5 keV). A negative polarization of resonance lines would indicate an electron beam with a much higher energy (>30 keV). The polarization of x-ray lines has been observed for most of the Ti x-pinch shots. The detailed modeling of the polarization-dependent features of Ti is the subject of another publication.

III. L-SHELL DIAGNOSTICS OF MO X-PINCH PLASMAS

The NTF has produced a number of Mo x-pinch plasmas from which L-shell spectra have been collected. A typical Mo x-pinch spectrum is shown in Fig. 2. The brightest lines, labeled with letters 3A–3G, belong to Ne-like Mo. The group of lines between 3B and 3C is generated mostly by F-like Mo and the groups between 3C and 3F are mostly Na-like and Mg-like satellite lines. The relative intensities of these features vary from shot to shot and indicate variations of plasma conditions.

A detailed atomic kinetic model has been developed to diagnose the electron density, temperature, and electron beam fractions (T_e , N_e , and f) of these plasmas.

It should be emphasized that while hot electron effects have been studied for Al and Ar ions [3,4], this is the first study of their effects on high-Z (Mo) ions.

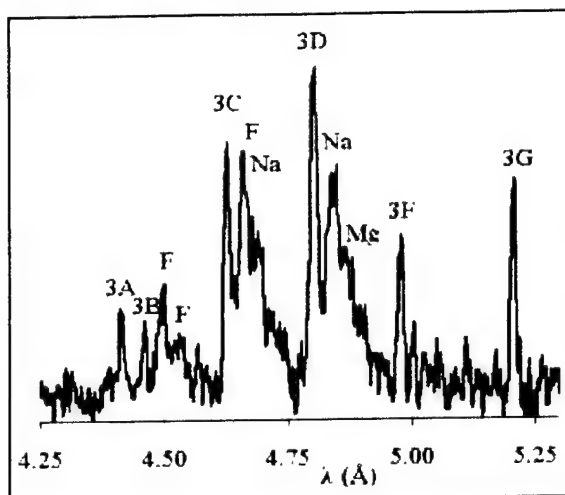


Figure 2. Identification of spectral lines and structures of a typical experimental Mo x-pinch spectrum.

The collisional-radiative (CR) atomic kinetic model developed for these diagnostics includes the ground states of every ionization stage of Mo from the bare ion with to neutral Mo. Detailed atomic structure is included for the O-, F-, Ne-, Na-, and Mg-like ionization stages. Each fine structure state is linked to other states within its ionization stage via collisional excitation, collisional de-excitation, and radiative decay. Ground states and low-lying non-autoionizing excited states of ions are linked via collisional ionization, three-body recombination, and radiative recombination. Autoionizing states of ions with charge z are linked to the ground state of the ion with charge $z+1$ via Auger decay and dielectronic recombination. The atomic structure and rate data were calculated with the MZ [5] and Cowan codes or taken from published tables [6–9]. The effects of hot electrons are incorporated into the model by integrating collision cross sections over a non-maxwellian EDF.

The electron density diagnostic used here is straightforward. Calculations performed at 900 eV with densities from 10^{21} to 10^{23} cm^{-3} indicate a consistent decrease in the intensity of the Ne-like 3F and 3G lines with increasing density. These two lines are relatively isolated from the lines of other ions, which makes their intensities independent of the ionization balance. Their intensities are also almost independent of T_e (see Fig. 3) and only slightly dependent on the presence and characteristics of hot electrons (see Fig. 4). Also, the intensities of other spectral features are only slightly sensitive to the electron density.

The temperature dependence of synthetic spectra is illustrated in Fig. 3. The Ne-like lines and three features

from other ionization stages are indicated on the figure. As T_e increases, the intensity of the Na- and Mg-like features decrease and the intensity of the F-like feature increases. However, since the F-like feature includes some contributions from Na- and Mg-like ions, its increase is less marked than the decrease of Na- and Mg-like features. The experimental spectra have significant amounts of both Mg- and F-like features and cannot be described by a single temperature.

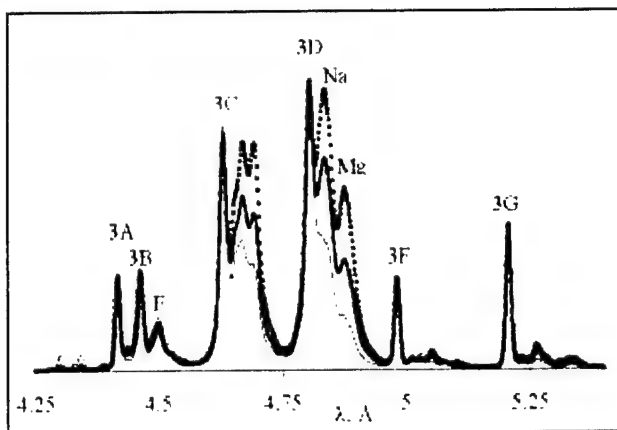


Figure 3. Theoretical Mo spectra with no hot electrons at 10^{22}cm^{-3} and 800 eV (dotted line), 900 eV (thick solid line), and 1.1 keV (thin solid line).

Adding hot electrons to the EDF has the effect of increasing the ionization balance and the overall intensity of the lines. Fig. 4 shows the effects of various percentages of hot electrons.

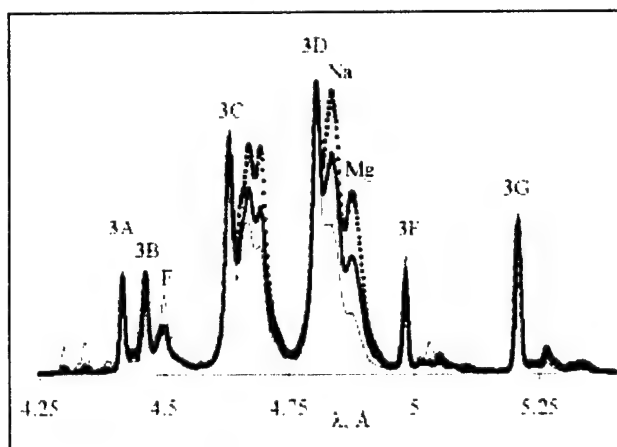


Figure 4. Theoretical Mo spectra at 10^{22}cm^{-3} and 800 eV with 0% (dotted line), 3% (thick solid line), and 10% (thin solid line) hot electrons at 10 keV.

These effects are different than those due to changing T_e , since changing the fraction of hot electrons tends to leave more population behind in lower ionization stages as the overall ionization balances shifts higher. This means that significant fractions of Mg-like ions can co-

exist with significant fractions of F-like ions, which is exactly what is needed to fit the experimental spectra. It was shown that the temperature of the hot electrons is relatively unimportant.

In order to fit the experimental spectra, many synthetic spectra were constructed over a range of T_e , N_e , and f . The density of the experimental spectra was estimated and then matched to that synthetic spectrum which had a minimum deviation from the experimental F-, Na-, and Mg- like spectral feature intensities. Comparisons of the best-fitting synthetic spectra with two different experimental spectra are shown in Figs. 5 and 6. Overall, the fits are good and indicate n_e between 10^{22} and $3 \times 10^{22}\text{cm}^{-3}$, T_e between 700 and 800 eV, and hot electron fractions between 5 and 10%. In general, thinner wires had higher T_e and greater f .

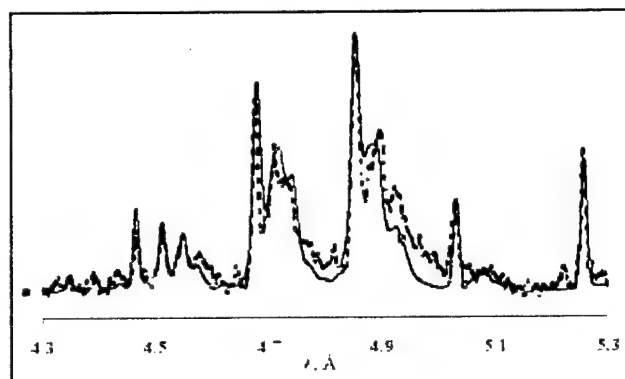


Figure 5. Comparison of the experimental 62 μm Mo wire x-pinch spectrum produced on October 10, 2000 (dotted line) and theoretical spectrum (solid line) at 700 eV and 10^{22}cm^{-3} with 10% hot electrons at 10 keV.

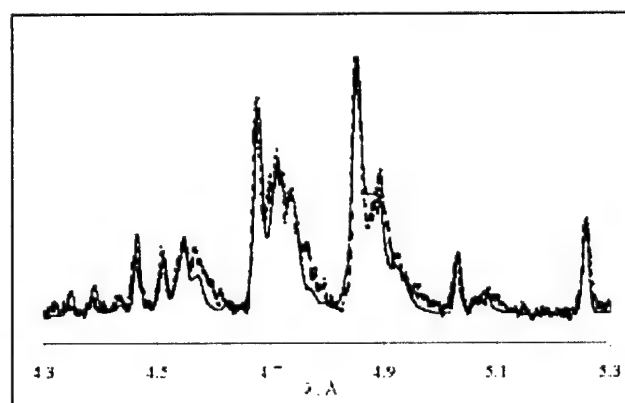


Figure 6. Comparison of experimental 24 μm Mo wire x-pinch spectrum produced on December 7, 2000 (dotted line) and theoretical spectrum (solid line) at 800 eV and $3 \times 10^{22}\text{cm}^{-3}$ with 10% hot electrons at 10 keV.

Recently, the first NTF time-resolved Mo spectra have been produced (see Fig. 7). The details of experiments are described in [10]. These spectra were recorded by a time-resolved spectrometer with frame intervals of 10ns and frame duration of 9 ns. There are four time frames that begin approximately 40ns after the rising of the current and end approximately 20ns before the maximum of the current. During the first frame no x-ray burst and no time-resolved spectrum were recorded. The spectrum (b) recorded during the second time frame coincided exactly with the first non-intense x-ray burst. The spectrum (c) recorded during the third time frame coincided with the second and the third intense x-ray bursts. The spectrum (d) recorded during the fourth time frame coincided with the fourth, most intense x-ray burst.

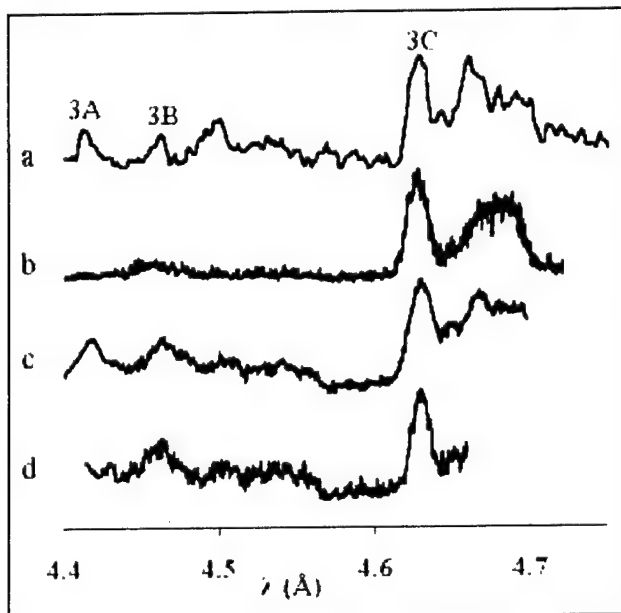


Figure 7. Time-integrated (a) and time-resolved (b-d) x-ray spectra of Mo x-pinch produced on May 25, 2001.

All time-integrated spectra have intense lines from F-like ions, which require higher temperatures or higher hot electron fractions than lines from Ne-like ions. The time resolved spectra show an increase of the ratio of F- to Ne-like emission over time, indicating an increase of either T_e or f . Detailed diagnostics of time-resolved spectra will be done in the nearest future.

IV. CONCLUSIONS

Effects of electron density, temperature, and electron beam fractions on synthetic spectra have been isolated. Good diagnostic techniques for each of those plasma parameters have been developed and used to determine the properties of a number of Ti and Mo x-pinch

plasmas. X-ray spectropolarimetry can be a valuable diagnostic tool, complementing kinetic modeling which includes hot electron effects. In the near future, polarization-sensitive Mo x-pinch experiments will be performed.

The present work is supported by DOE, SNL, and UNR.

V. REFERENCES

- [1] A. S. Shlyaptseva, S. B. Hansen, V. L. Kantsyrev et al, "X-ray spectropolarimetry of high-temperature plasmas," *Rev. Sci. Instr.*, vol. 72, pp. 1241-1244, 2001.
- [2] V. L. Kantsyrev, B. S. Bauer, A. S. Shlyaptseva et al, "Advanced x-ray and extreme ultraviolet diagnostics and first applications to x-pinch plasma experiments at the Nevada Terawatt Facility," *Rev. Sci. Instr.*, vol. 72, pp. 663-667, 2001.
- [3] J. Abdallah et al, "Electron beam effects on the spectroscopy of satellite lines in Aluminum x-pinch plasmas," *Physica Scripta*, vol. 53, pp. 705-711, 1996.
- [4] J. Abdallah et al, "Electron beam effects on the spectroscopy of multiply charged ions in plasma focus experiments," *JQSRT*, vol. 62, pp. 85-96, 1999.
- [5] L. A. Vainshtein and U. I. Safronova, *Atomic Data and Nuclear Data Tables*, vol. 21, p. 49, 1979.
- [6] J. Nilsen, "Dielectronic satellite spectra for neon-like ions," *Atomic Data and Nuclear Data Tables*, vol. 41, pp. 131-177, 1989.
- [7] D. H. Sampson et al, "Relativistic distorted-wave collision strengths and oscillator strengths for F-like ions with $22 \leq Z \leq 92$," *Atomic Data and Nuclear Data Tables*, vol. 48, pp. 25-90, 1991.
- [8] H. Zhang et al, "Collision strengths and oscillator strengths for excitation to the $n = 3$ and 4 levels of neon-like ions," *Atomic Data and Nuclear Data Tables*, vol. 37, pp. 17-51, 1987.
- [9] H. Zhang et al, "Collision strengths and oscillator strengths for inner-shell excitation of Na-like ions," *Atomic Data and Nuclear Data Tables*, vol. 4, pp 1-58, 1989.
- [10] V. L. Kantsyrev, A. S. Shlyaptseva, B. S. Bauer et al, "X-ray temporal, spatial and spectral study of 0.9 MA x-pinch Ti, Fe, Mo, W and Pt radiation sources. Energetic electron beam and hard x-ray generation" (at the same conference).

**X-RAY SPECTROPOLARIMETRY
AND THE EFFECT OF HOT ELECTRONS
ON MODELING
OF HIGH-CURRENT X-PINCH PLASMA
SPECTRA**

Lake Tahoe

ICOPS, Las Vegas, Nevada, June 17-22, 2001

X-ray spectropolarimetry...

N_7
 Z_F

A.S. Shlyaptseva, S.B. Hansen V.L. Kantsyrev, B.S. Bauer,

D.A. Fedin, N. Ouart, S. Keely, H. LeBeau

Physics Department, University of Nevada, Reno, USA

U.I. Safronova

Department of Physics, University of Notre Dame, USA

Lake Tahoe

ICOPS, Las Vegas, Nevada, June 17-22, 2001

ABSTRACT

N7
T
Z-F

The development of time-dependent K- and L-shell spectroscopic monitoring of high-temperature and high-density z-pinch plasmas necessitates accounting for non-maxwellian electron distribution functions and polarization properties of x-ray lines. The existence of strong electron beams in x-pinch plasmas motivated the development of a new tool, x-ray spectropolarimetry, for investigating the anisotropy of such plasmas. This diagnostic includes both space- and time-resolved x-ray spectroscopy and polarimetry and is based on the theoretical modeling of x-ray line polarization-dependent spectra measured simultaneously by spectrometers with different sensitivities to polarization. Specifically, K-shell Ti and L-shell Mo x-ray spectra have been thoroughly modeled. Experimental spectra have been generated by Ti and Mo x-pinch plasmas produced at the Nevada Terawatt Facility. The detailed spectroscopic analysis of more than 20 shots with these x-pinch plasmas shows how x-ray spectropolarimetry complements the usual spectroscopic monitoring of z-pinch plasmas and demonstrates the importance of accounting for hot, non-maxwellian electrons in plasma diagnostics. The present work is supported by DOE, SNL, and UNR.

Lake Tahoe

ICOPS, Las Vegas, Nevada, June 17-22, 2001

OUTLINE

**NZ
ZF**

§ 1. Introduction

**§ 2. X-ray spectropolarimetry of Ti x-pinch
plasmas**

§ 3. L-shell diagnostics of Mo x-pinch plasmas

§ 4. Conclusions

§1. Introduction

N7
ZF

X-pinchs produce a bright, small x-ray source with a well-defined location. They can yield x-ray spectra of numerous ions with very high resolution. A distinct feature of x-pinchs is the existence of strong electron beams, which makes them attractive objects for spectropolarimetry. X-ray spectropolarimetry is a new diagnostic that can provide detailed information about the electron distribution function and the magnetic field in x-pinch plasmas. Recent results on x-pinchs and x-ray spectropolarimetry at the NTF were published in [1,2]. It has been shown that the polarization properties of Ti K-shell radiation can be successfully used for diagnostics of electron beams, whereas L-shell lines are good candidates for the diagnostics of magnetic fields. From studying L-shell radiation from Ti, Fe, and Mo x-pinchs, it was decided that Mo x-pinchs are the best for magnetic field spectropolarimetry. In this presentation, new polarization-sensitive diagnostics of Ti x-pinch experiments are briefly discussed. The main topic is x-ray L-shell diagnostics of Mo x-pinchs.

[1] A. S. Shlyaptseva, S. B. Hansen, V. L. Kantsyrev et al, "X-ray spectropolarimetry of high-temperature plasmas," Rev. Sci. Instr., vol. 72, pp. 1241-1244, 2001.

[2] V. L. Kantsyrev, B. S. Bauer, A. S. Shlyaptseva et al, "Advanced x-ray and extreme ultraviolet diagnostics and first applications to x-pinch plasma experiments at the Nevada Terawatt Facility," Rev. Sci. Instr., vol. 72, pp. 663-667, 2001.

§ 2. X-ray spectropolarimetry of Ti x-pinch plasmas

N_Z
 Z_F

Ti plasmas have been produced at the NTF from a wide variety of pinches including single wires, x-pinches, and conical and cylindrical arrays with Al wires. The pinhole images of Ti x-pinch plasmas indicate that they are fairly inhomogeneous -- much more so than pinch plasmas of heavier elements. These images and damage to the anodes after shots also evidence the presence of beams of hot electrons. Thus, accurate K-shell spectropolarimetry of Ti x-pinch plasmas requires detailed plasma modeling that can account for the effects of hot electrons.

First polarization-sensitive experiments at the Nevada Terawatt Facility

**N7
ZF**

● An x-pinch produces a bright, small-sized x-ray source, with a well-defined location. It can yield x-ray spectra of numerous ions with very high resolution. A new diagnostic, x-ray spectropolarimetry, applied to x-pinch plasmas, can provide detailed information about the electron distribution function and the magnetic field;

● Polarization-sensitive experiments of x-pinch plasmas were performed at the NTF on May 04, 16, 17, 18, 23, 24, and 25; July 12, 13, 18, 19, 21 and 26, and August 16 and 17.

New polarization-sensitive experiments of Ti x-pinch plasmas

N7
ZF

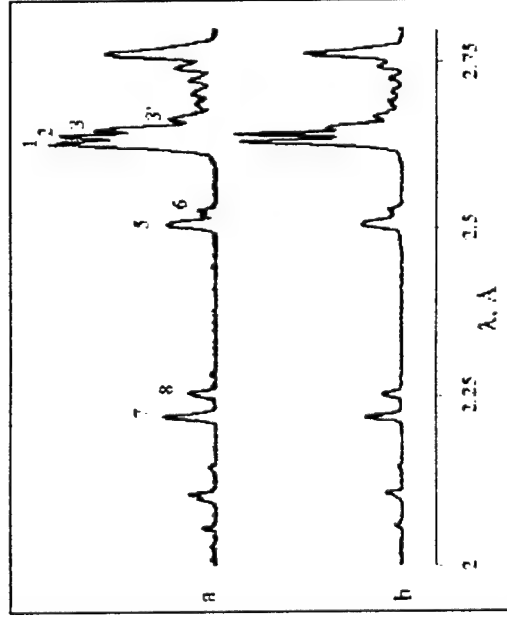


Figure 1. Typical Ti x-pinch spectra from horizontal (a) and vertical (b) spectrometers. Lines 1, 2, 5, and 7 are respectively Hea (w), Hea (y), Lya, and Heb. Lines 3', 3, 6, and 8 are respectively Be-, Li-, He-, and Li-like satellite structures.

New polarization-sensitive experiments of Ti x-pinch plasmas were performed at the NTF in May-August 2000. The polarization-dependent spectra of K-shell line radiation produced by Ti x-pinch were recorded simultaneously by horizontal (with a slit for spatial resolution) and vertical (w/o a slit) spectrometers. The horizontal spectrometer has a dispersion plane perpendicular to the discharge axis and records mostly the parallel polarization state. The vertical spectrometer has a dispersion plane parallel to the discharge axis and records mostly the perpendicular polarization state. Both convex crystal spectrometers have identical LiF ($2d=4.027\text{\AA}$) crystals with spacing corresponding to the nominal Bragg angle of 40° at the wavelength of 2.6 \AA . For the polarization analysis, only shots with x-ray images representing one bright hot spot are chosen. Two typical polarization-sensitive spectra simultaneously recorded by horizontal and vertical spectrometers are presented in Fig. 1.

Lake Tahoe

ICOPS, Las Vegas, Nevada, June 17-22, 2001

New polarization-sensitive experiments... (continued)

$N \neq Z$
 Z_F

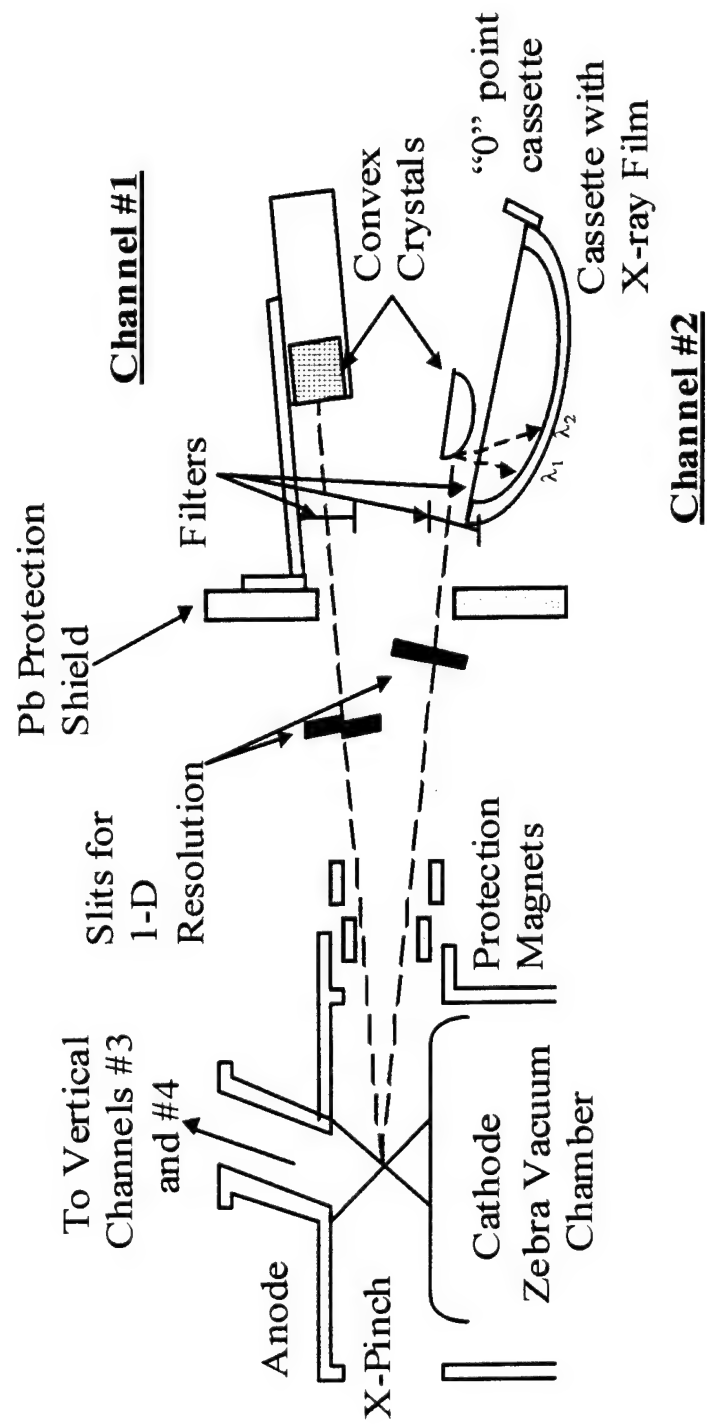
- The most intense spectral feature belongs to He-like ions.
- The intensities associated with different polarization states I_{\parallel}/I_{\perp} for each of the spectral lines (1, 2, 3, 3', 5, 6, 7, and 8) and the line ratios of the satellite lines to their resonance lines (3/1, 3'/1, 6/5, and 8/7) from horizontal and vertical spectra have been analyzed. The ratio I_{\parallel}/I_{\perp} greater (less) than unity indicates the positive (negative) polarization of the line.
- The polarization of dielectronic satellite peaks and the positive polarization of resonance lines indicate that the electron beam has a low energy (3-5keV).
- A negative polarization of resonance lines would indicate an electron beam with a much higher energy (>30keV).
- The polarization of x-ray lines has been observed for most of the Ti x-pinch shots. The detailed modeling of the polarization-dependent features of Ti is the subject of another publication.

Lake Tahoe

ICOPS, Las Vegas, Nevada, June 17-22, 2001

Experimental setup includes a one-dimensional x-ray polarimeter/spectrometer for polarization measurements

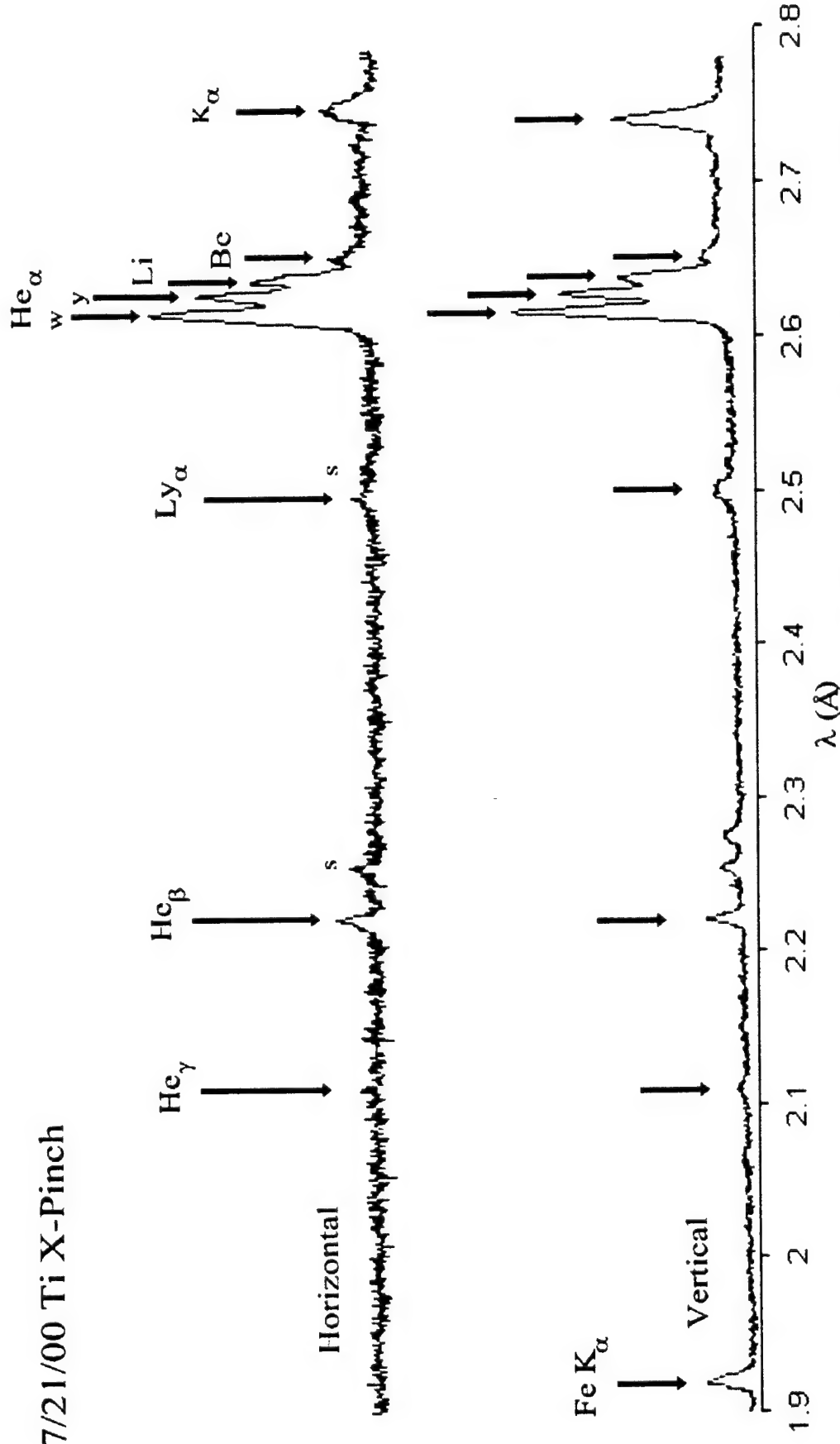
N7
I
F



Polarization-sensitive Ti spectra

NZ
TF

7/21/00 Ti X-Pinch

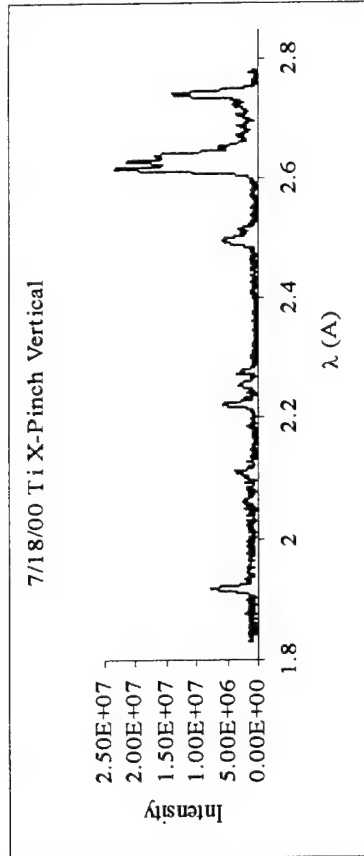
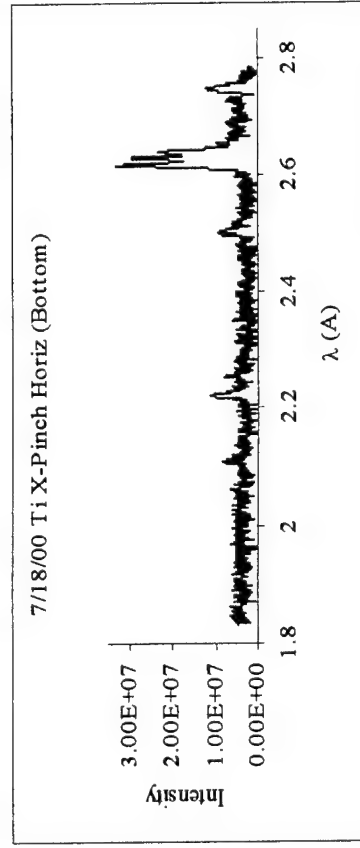
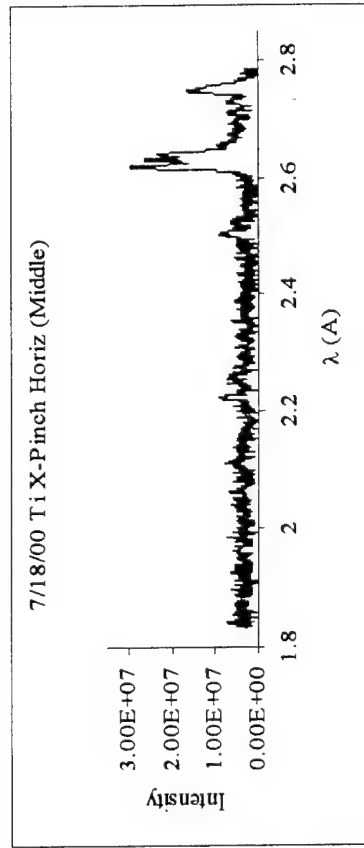
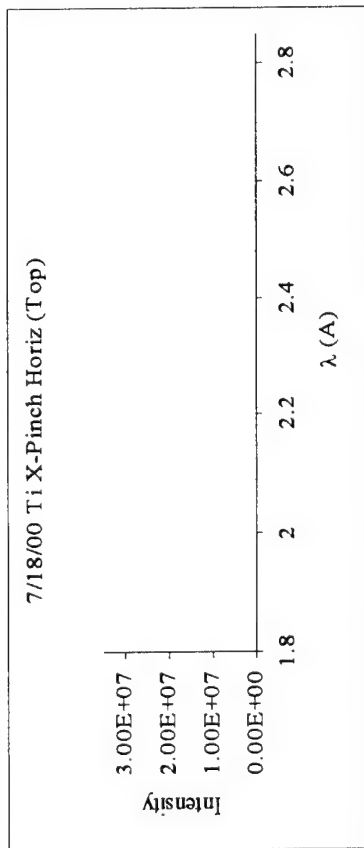


Lake Tahoe

ICOPS, Las Vegas, Nevada, June 17-22, 2001

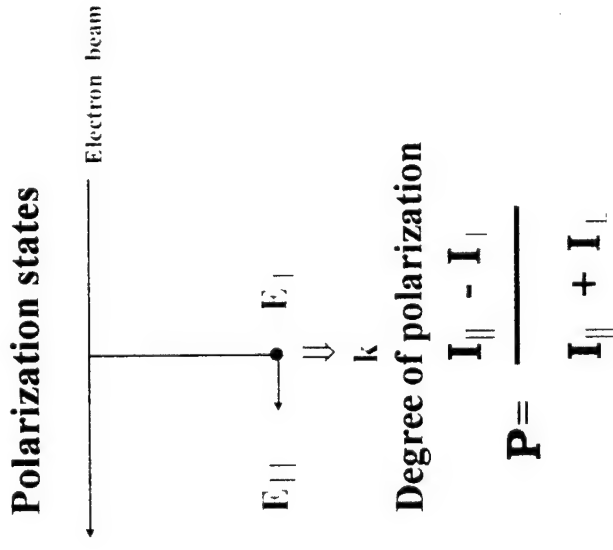
Ti X-Pinch ($\phi=30\text{ }\mu$) Spectrum produced on July 18, 2000 (shot 38)

NZ
ZF



The ratio of intensities of different polarization states ($I_{||}/I_{\perp}$)

N
T
F



Ratio of polarized intensities

$$I_{||} / I_{\perp} = (1+P)/(1-P)$$

The intensity of observed radiation

$$I_{obs} = R_{||} I_{||} + R_{\perp} I_{\perp}$$

Horizontal spectrometer: $I_{||}$
(Channel 1)

Vertical spectrometer: I_{\perp}
(Channel 2)

$I_{||} / I_{\perp} > 1$ when **P(line) > 0**

$I_{||} / I_{\perp} < 1$ when **P(line) < 0**

$P(He_{\alpha})$: decreases from 60% (at the threshold) to 0 (near 7 thresholds) and then <0;

$P(y)$: increases from -33% (at the threshold) to 0 and then tends to $P(He_{\alpha})$;

$P(Li)$: decreases from 34% (at the threshold) to 0 and then <0.

ICOPS, Las Vegas, Nevada, June 17-22, 2001

Lake Tahoe

Illustration of polarization of Ti K-shell lines through the measured ratio of line intensities

N7
I
F

Table. Illustration of polarization of Ti K-shell lines through the measured ratio of relative intensities of the lines recorded by a horizontal (H) and vertical (V) spectrometers.

Line ratio	7/12/00		7/18/00			7/19/00			7/21/00			
	H	V	H/V	H	V	H/V	H	V	H/V	H	V	H/V
2/1	0.90	0.83	1.09	0.88	0.91	0.96	0.88	0.88	1.0	0.82	0.86	0.95
3/1	0.77	0.68	1.13	0.80	0.73	1.1	0.79	0.60	1.32	0.62	0.64	0.98
3'/1	0.30	0.27	1.08	0.33	0.28	1.2	0.33	0.2	1.65	0.35	0.33	1.04
6/5	0.56	0.35	1.61	0.68	0.53	1.27	0.66	0.46	1.42	0.80	0.71	1.13
8/7	0.70	0.50	1.41	0.79	0.58	1.37	0.77	0.57	1.35	0.80	0.75	1.06

Illustration of polarization of Ti K-shell lines through the measured ratio of intensities ($I_{||}/I_{\perp}$)

N_Z
 Z_F

Line	Ion	λ (Å)	7/12/00	7/18/00	7/19/00	7/21/00
1 He α	He	2.618	0.93	1.02	0.65	1.09
2 γ	He	2.631	1.01	0.98	0.66	1.04
3 q	Li	2.640	1.05	1.12	0.86	1.06
3' sat	Be	2.655	1.0	1.22	1.07	1.13
5 Ly α	H	2.500	0.97	1.25	1.06	1.02
6 sat	H	2.515	1.29	1.58	1.52	1.14
7 He β	He	2.221	0.91	1.29	0.69	1.12
8 sat	He	2.253	1.28	1.75	0.94	1.19

Lake Tahoe

ICOPS, Las Vegas, Nevada, June 17-22, 2001

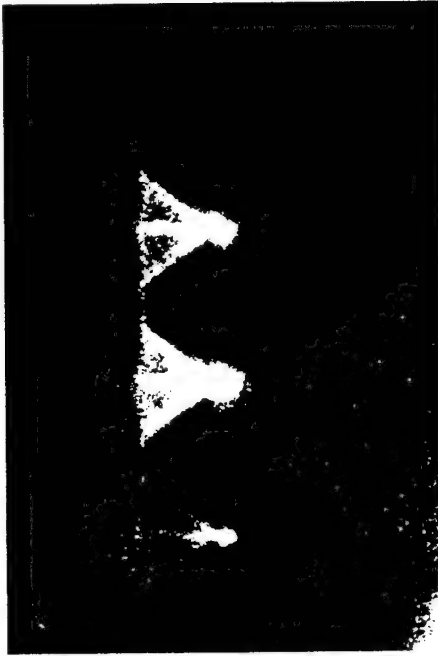
Electron beam energies for Ti x-pinch

N7
ZF

Shot #	Material	Date	Anode Holes (mm)		Depth(mm)	Mass Lost (g)		Electron Beam Energy (J)		
			$\phi 1$	$\phi 2$		$\phi 1$	$\phi 2$	$\phi 1$	$\phi 2$	Total
36	Ti	7/12/00	1.5	1	1.4	9.41E-02	2.55E-02	1.43E+03	3.88E+02	1.82E+03
38	Ti	7/18/00	1	0.9	1.5	2.73E-02	1.82E-02	4.16E+02	2.77E+02	6.93E+02
39	Ti	7/19/00	0.8	1	1.4	1.02E-02	2.55E-02	1.55E+02	3.88E+02	5.43E+02
40	Ti	7/21/00	1.2	0.3	1.3	4.43E-02	1.98E-03	6.76E+02	3.03E+01	7.06E+02
47	Ti	8/16/00	0.5	0.4	1.3	2.32E-03	3.91E-04	3.53E+01	5.96E+00	4.13E+01

NTF time-integrated x-ray pinhole camera images of Ti x-pinch (shots 36-39)

N
T
F



Shot 36 (07/12/00)



Shot 37 (07/13/00)



Shot 38 (07/18/00)



Shot 39 (07/19/00)

Lake Tahoe

ICOPS, Las Vegas, Nevada, June 17-22, 2001

**NTF time-integrated x-ray pinhole camera images
of Ti x-pinch (shots 41,42,47, and 48)**

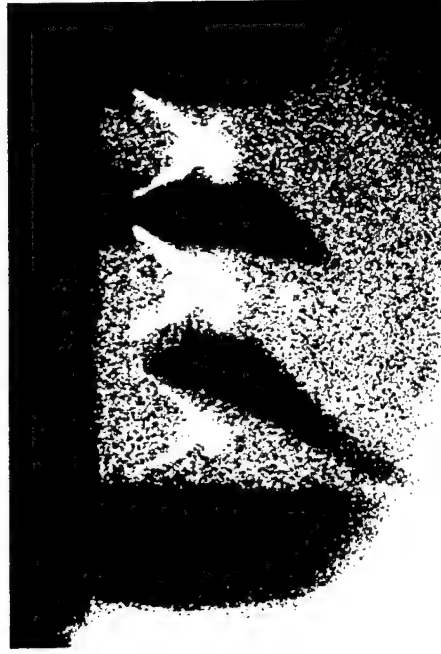
**N7
TF**



Shot 40 (07/21/00)



Shot 41 (07/26/00)



Shot 47 (08/16/00)



Shot 48 (08/17/00)

Lake Tahoe

ICOPS, Las Vegas, Nevada, June 17-22, 2001

§ 3. L-shell diagnostics of Mo x-pinch plasma

NZ
TF

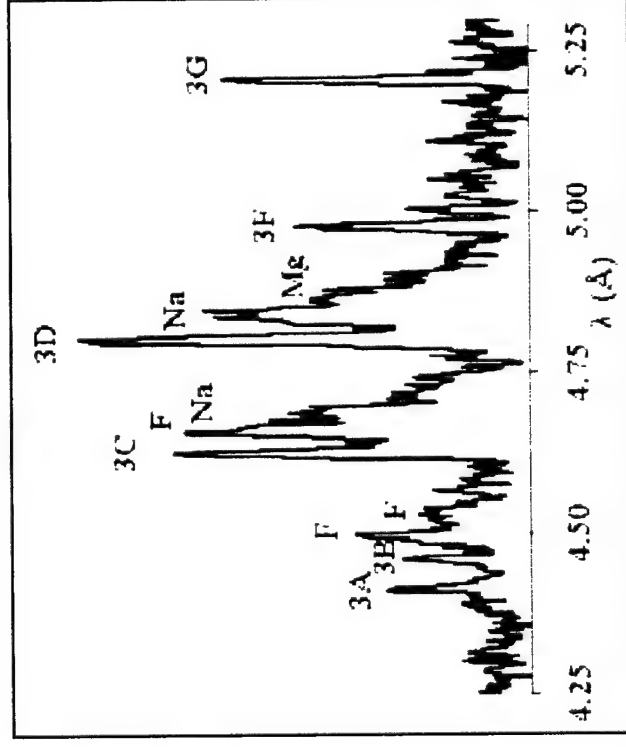
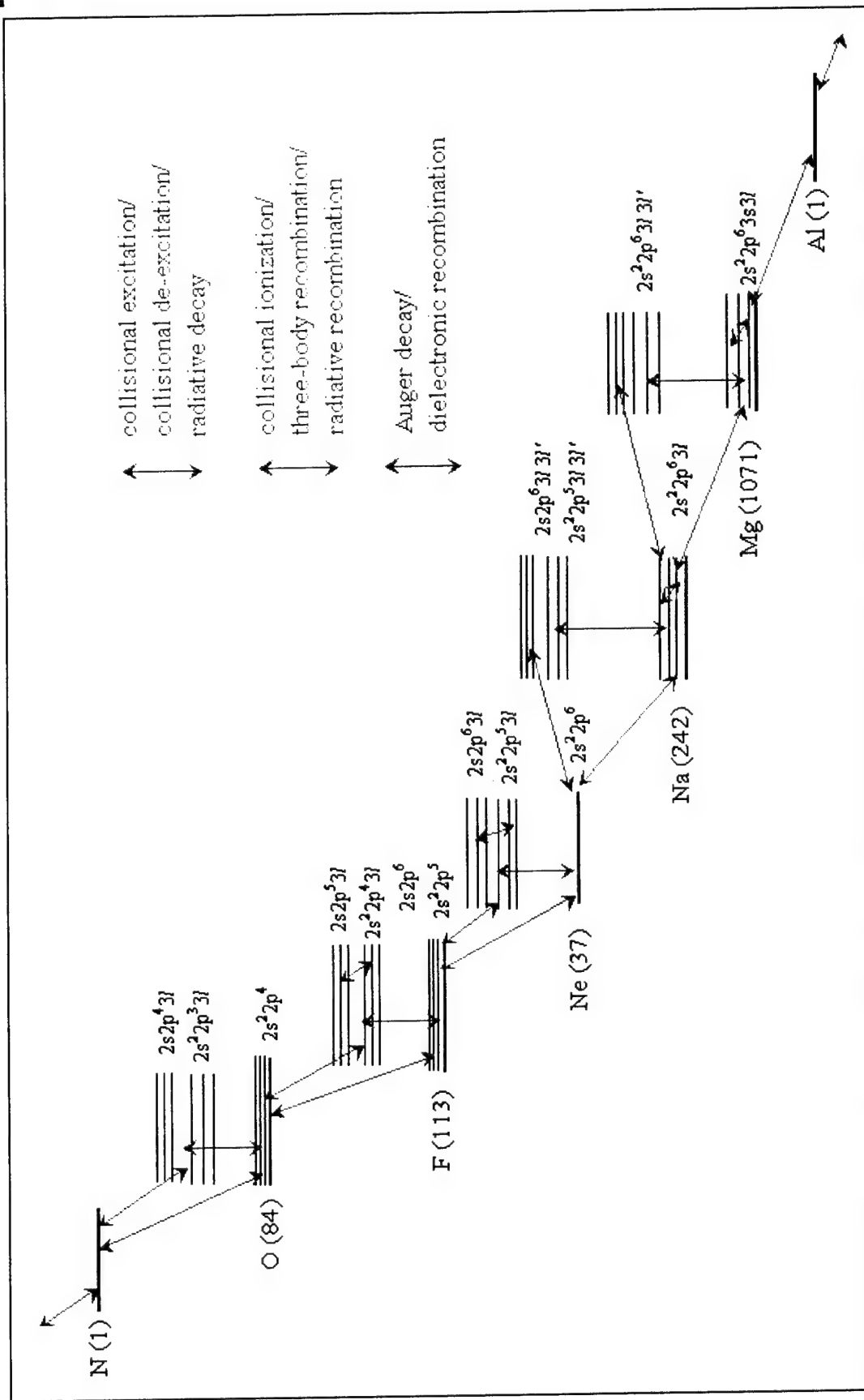


Figure 2. Identification of spectral lines and structures of a typical experimental Mo x-pinch spectrum.

The NTF has produced a number of Mo x-pinch plasmas from which L-shell spectra have been collected. A typical Mo x-pinch spectrum is shown in Fig. 2. The brightest lines, labeled with letters 3A-3G, belong to Ne-like Mo. The group of lines between 3B and 3C is generated mostly by F-like Mo and the groups between 3C and 3F are mostly Na-like and Mg-like satellite lines. The relative intensities of these features vary from shot to shot and indicate variations of plasma conditions.

L-shell atomic kinetic model

N
T
F

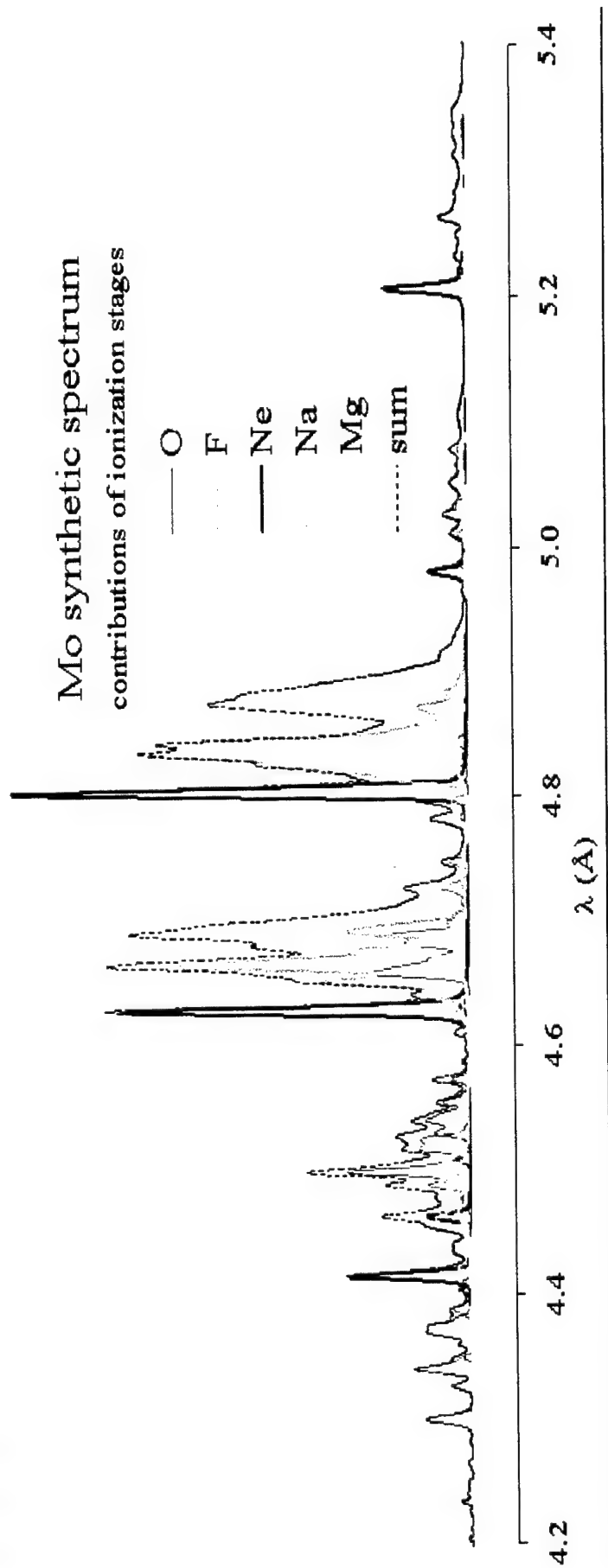


Lake Tahoe

ICOPS, Las Vegas, Nevada, June 17-22, 200

Contribution of different Mo ions

N₂
T
F



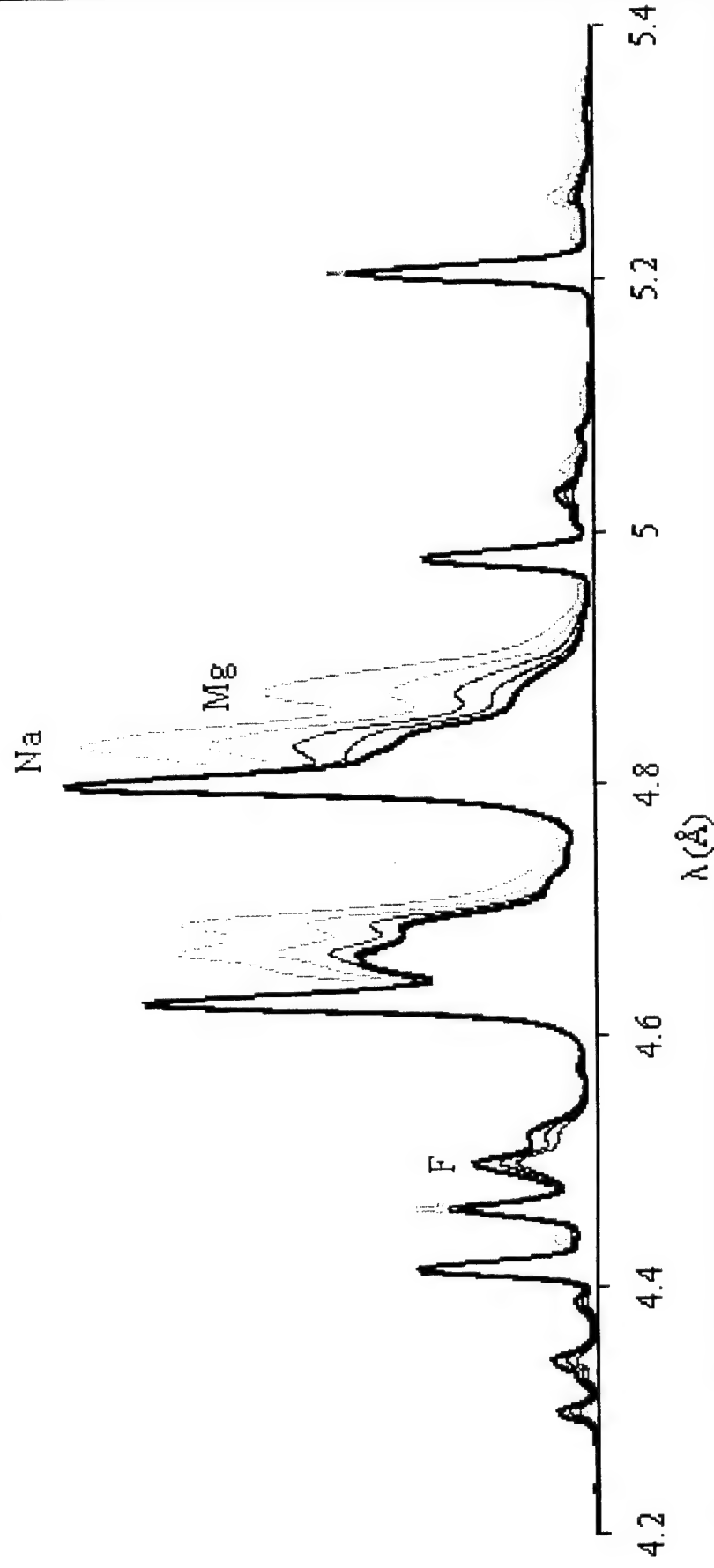
ICOPS, Las Vegas, Nevada, June 17-22, 2001

Lake Tahoe

T_e dependence of L-shell Mo spectra

N7
T_F

Mo synthetic spectra: $n_e = 10^{22} \text{ cm}^{-3}$; $T_e = 1000, 1100, 1200 \text{ eV}$; no hot electrons



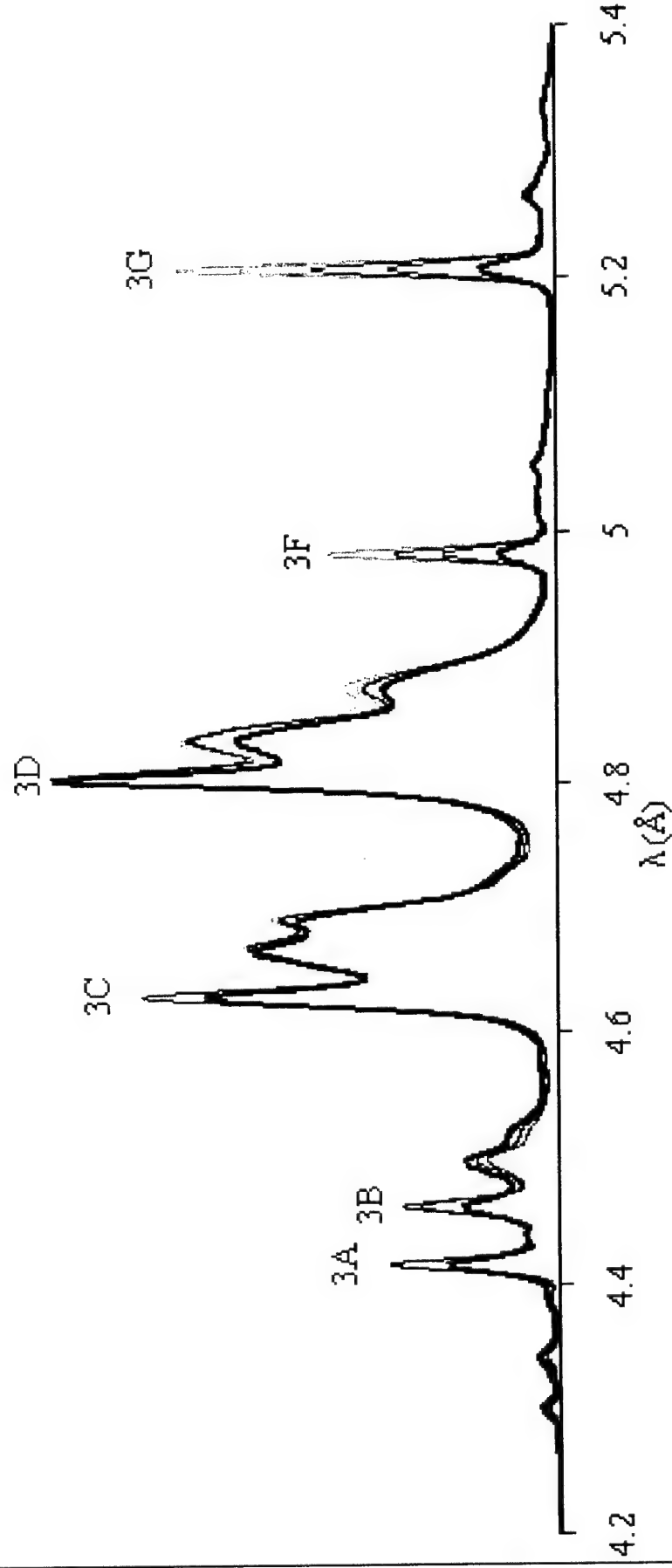
Lake Tahoe

ICOPS, Las Vegas, Nevada, June 17-22, 2001

N_e dependence of L-shell Mo spectra

N_Z
 Z_F

Mo synthetic spectra: $T_e = 900\text{eV}$; $n_e = 10^{21}, 3 \times 10^{21}, 10^{22}, 3 \times 10^{22}, 10^{23}\text{cm}^{-3}$; no hot electrons



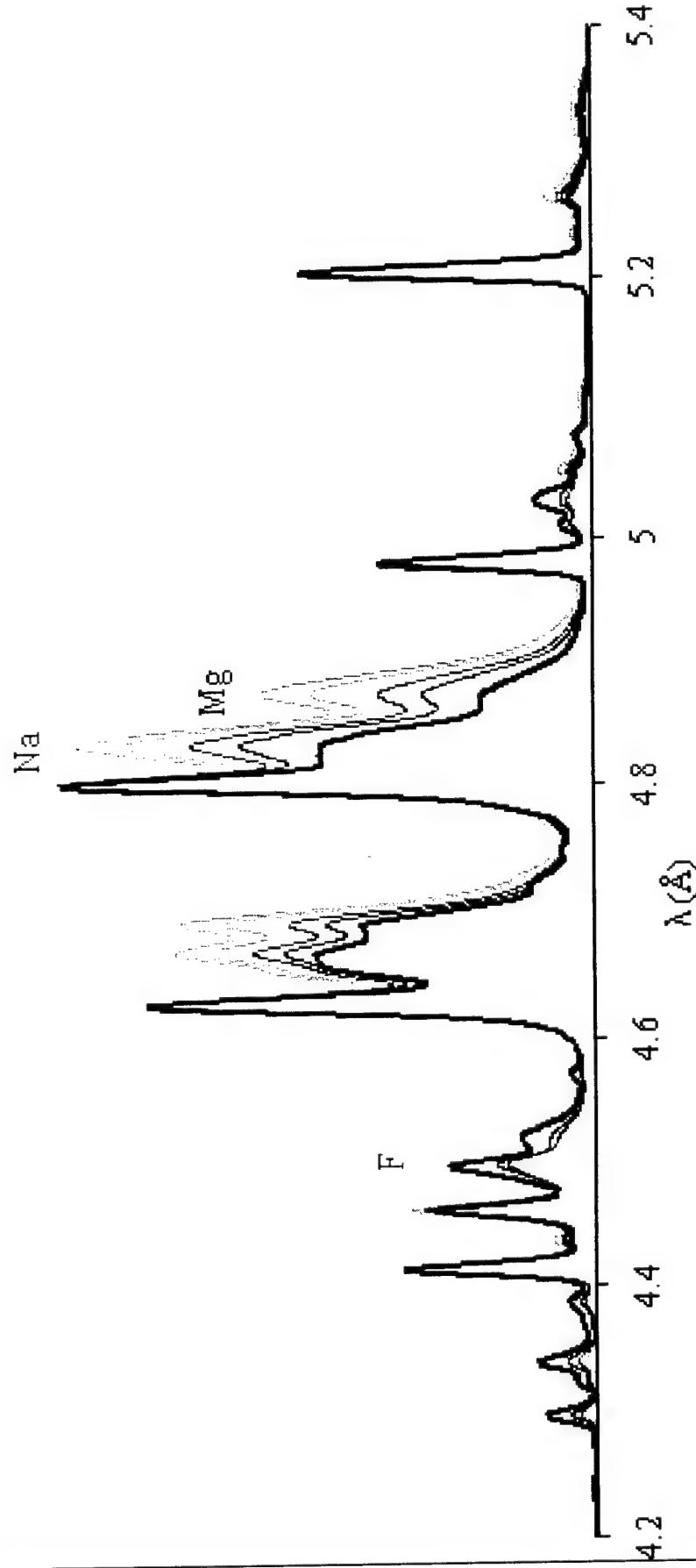
ICOPS, Las Vegas, Nevada, June 17-22, 2001

Lake Tahoe

The effect of hot electrons on L-shell Mo spectra

N_F
 T_F

Mo synthetic spectra: $n_e = 10^{22} \text{ cm}^{-3}$, $T_e = 800 \text{ eV}$, 10%, 3%, 5%, & 10% hot electrons @ 10keV



ICOPS, Las Vegas, Nevada, June 17-22, 2001

Lake Tahoe

Comparison of experimental and theoretical spectra of Mo x-pinch plasmas produced on 10/20/2000 (shot 52)

$\frac{N}{Z}$
 $\frac{T}{F}$

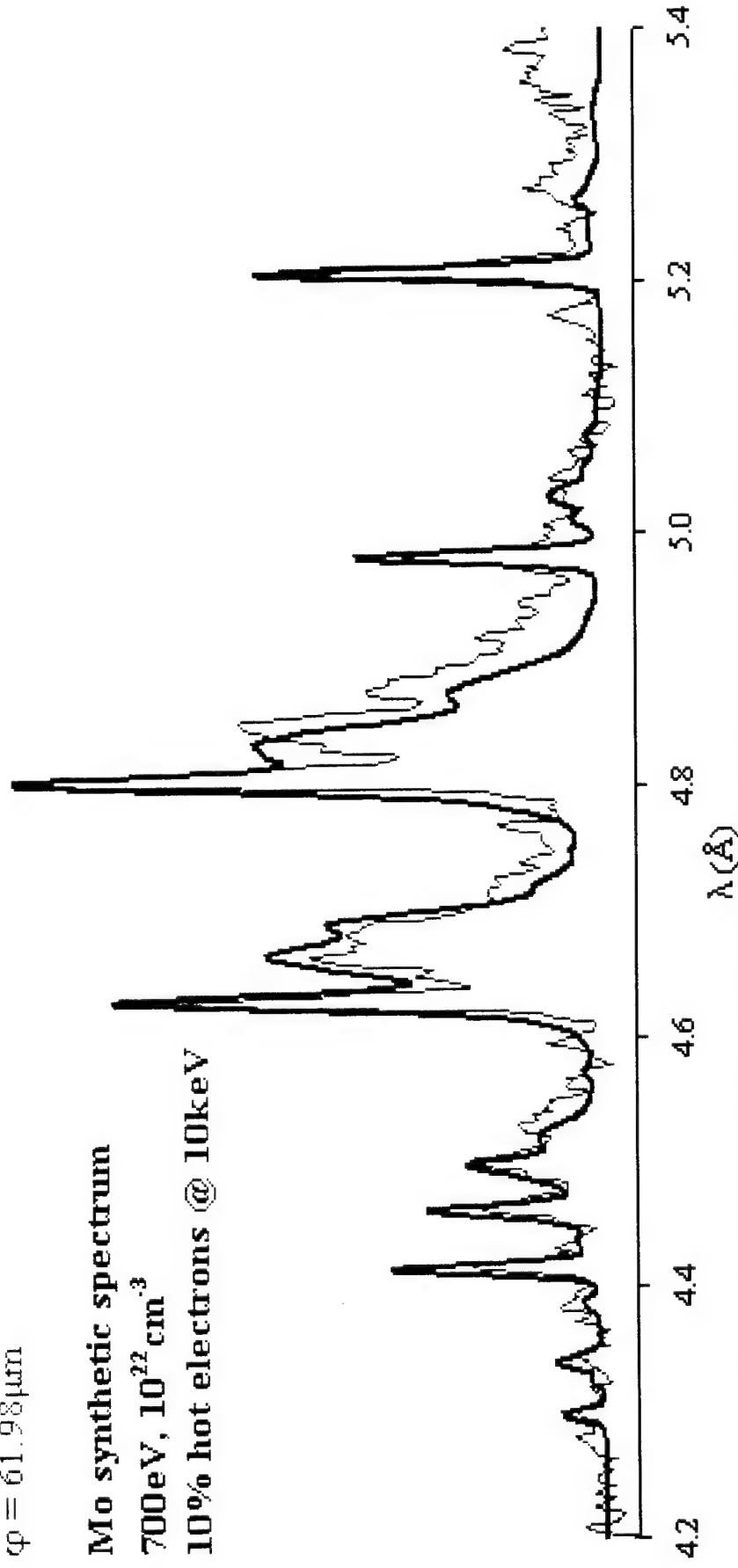
Shot 52: Mo x-pinch 10/20/00, 1st order

$\varphi = 61.98 \mu\text{m}$

Mo synthetic spectrum

700eV, 10^{22}cm^{-3}

10% hot electrons @ 10keV



ICOPS, Las Vegas, Nevada, June 17-22, 2001

Lake Tahoe

Comparison of experimental and theoretical spectra of Mo x-pinch plasmas produced on 12/07/2000 (shot 62)

N7
ZF

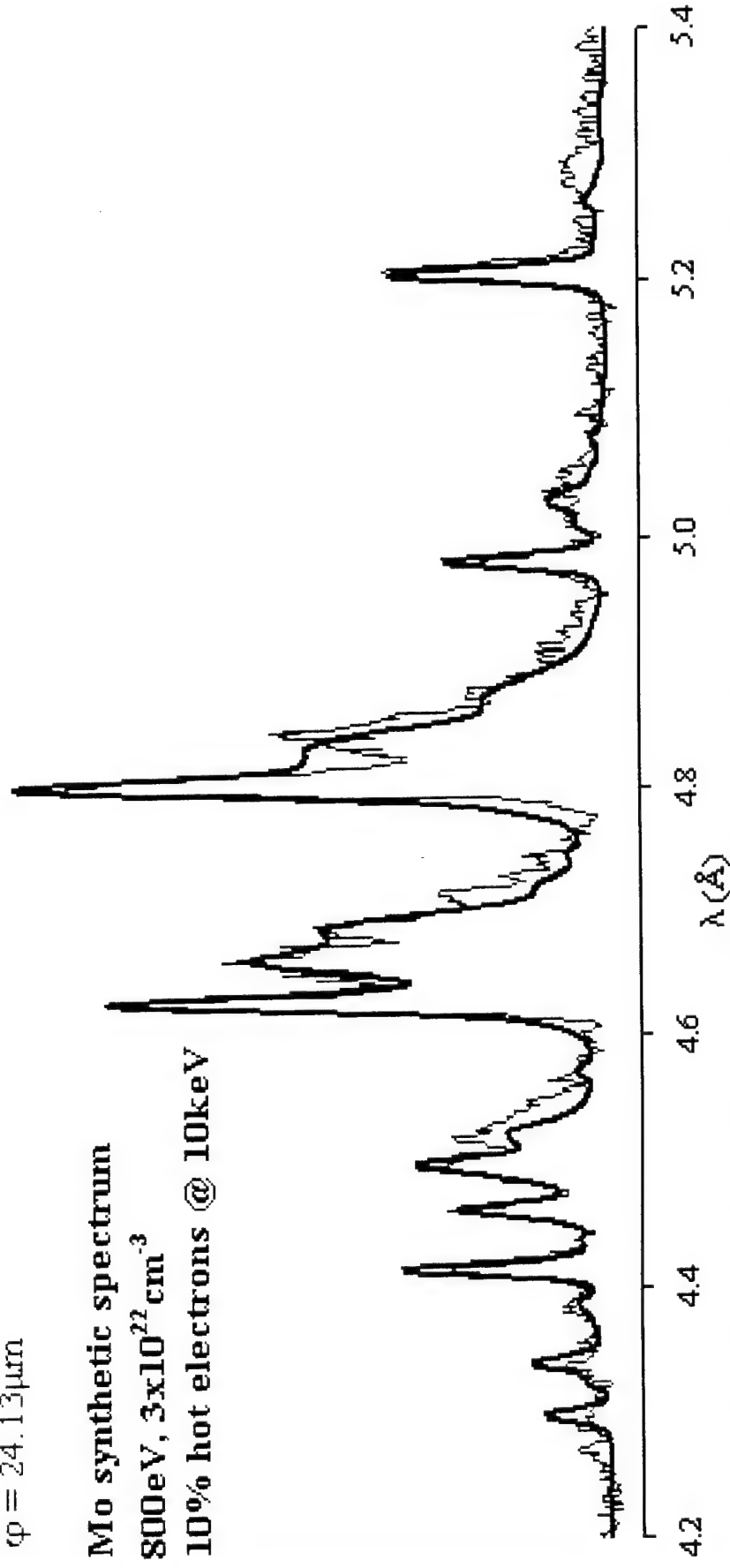
Shot 62: Mo x-pinch 12/7/00, 1st order

$\varphi = 24.13\mu\text{m}$

Mo synthetic spectrum

800eV, $3 \times 10^{22} \text{ cm}^{-3}$

10% hot electrons @ 10keV



Lake Tahoe

ICOPS, Las Vegas, Nevada, June 17-22, 2001

Electron beam energies for Mo x-pinch

N7
ZF

Shot #	Material	Date	Anode Holes (mm)		Depth(mm)	Mass Lost (g)		Electron Beam Energy (J)		
			φ1	φ2		φ1	φ2	φ1	φ2	Total
33	Mo	5/25/2000	0.2	0.3	1.4	1.47E-03	7.89E-05	2.24E+01	1.20E+00	2.36E+01
52	Mo	10/20/2000	2.3	2	1.6	3.84E-01	2.76E-01	5.85E+03	4.20E+03	1.00E+04
54	Mo	10/26/2000	0.5	2.5	1.5	2.67E-03	4.36E-01	4.07E+01	6.65E+03	6.69E+03
57	Mo	11/9/2000	2.3	2.4	1.5	3.60E-01	3.97E-01	5.48E+03	6.05E+03	1.15E+04
59	Mo	11/29/2000	1.7	1.4	1.6	1.85E-01	1.13E-01	2.83E+03	1.72E+03	4.55E+03
60	Mo	12/1/2000	2	2.2	1.4	2.41E-01	3.02E-01	3.68E+03	4.61E+03	8.29E+03
62	Mo	12/7/2000	1.9	1.8	1.6	2.44E-01	2.14E-01	3.71E+03	3.26E+03	6.97E+03
65	Mo	1/11/2001	2.6	2.1	1.6	5.09E-01	3.10E-01	7.76E+03	4.72E+03	1.25E+04
67	Mo	2/15/2001	1.7	1.6	1.6	1.85E-01	1.59E-01	2.83E+03	2.43E+03	5.26E+03
70	Mo	3/2/2001	2.1	1.9	1.4	2.71E-01	2.13E-01	4.13E+03	3.25E+03	7.38E+03
71	Mo	3/5/2001	1.9	1.5	1.3	1.98E-01	1.10E-01	3.02E+03	1.68E+03	4.69E+03
81	Mo	4/11/2001	2.56	2.62	1.6	4.91E-01	5.18E-01	7.49E+03	7.90E+03	1.54E+04
83	Mo	5/24/2001	1.6	1.63	1.5	1.49E-01	1.57E-01	2.28E+03	2.39E+03	4.66E+03
84	Mo	5/25/2001	2.17	2.84	1.4	2.93E-01	5.45E-01	4.46E+03	8.31E+03	1.28E+04
86	Mo	6/4/2001	0.96	1.1	1.3	3.19E-02	4.76E-02	4.86E+02	7.26E+02	1.21E+03
69	Mo	2/26/2001	1.3	1.4	1.6	9.30E-02	1.13E-01	1.42E+03	1.72E+03	3.14E+03

Lake Tahoe

ICOPS, Las Vegas, Nevada, June 17-22, 2001

L-shell Mo Time-resolved Spectra

N7
ZF

Recently, the first NTF time-resolved Mo spectra have been produced. The details of experiments are described in [3]. These spectra were recorded by a time-resolved spectrometer with frame intervals of 10ns and frame duration of 9 ns. There are four time frames that begin approximately 40ns after the rising of the current and end approximately 20ns before the maximum of the current. During the first frame no x-ray burst and no time-resolved spectrum were recorded. The spectrum (b) recorded during the second time frame coincided exactly with the first non-intense x-ray burst. The spectrum (c) recorded during the third time frame coincided with the second and the third intense x-ray bursts. The spectrum (d) recorded during the fourth time frame coincided with the fourth, most intense x-ray burst.

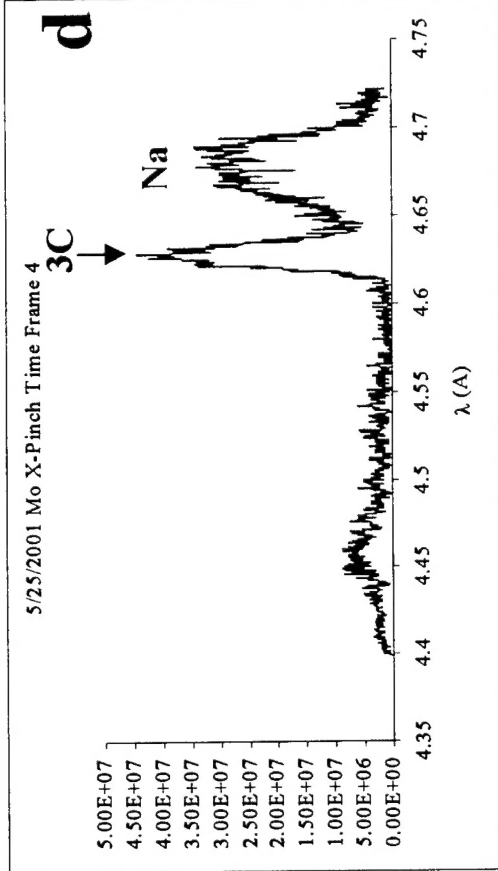
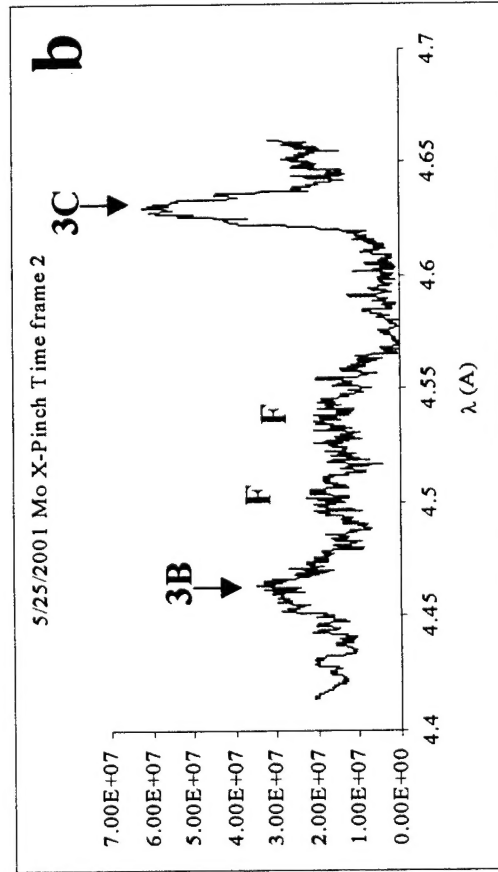
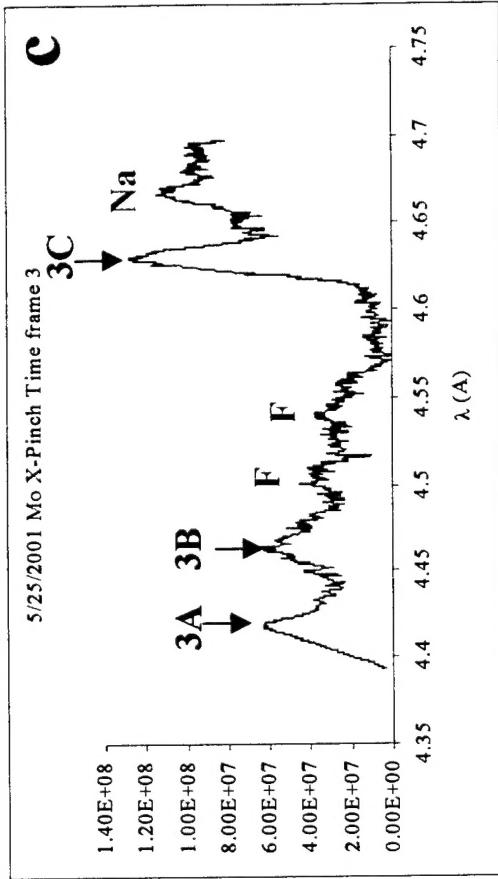
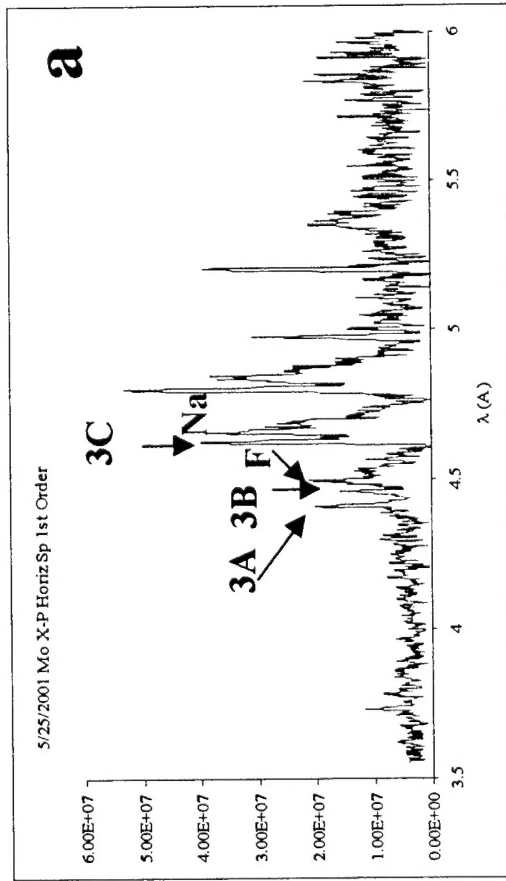
[3] V. L. Kantsyrev, A. S. Shlyaptseva, B. S. Bauer et al, "X-ray temporal, spatial and spectral study of 0.9 MA x-pinch Ti, Fe, Mo, W and Pt radiation sources. Energetic electron beam and hard x-ray generation" (at the same conference)

Lake Tahoe

ICOPS, Las Vegas, Nevada, June 17-22, 200

L-shell Mo X-Pinch Time-integrated and Time-resolved X-ray Spectra (shot 84)

N_Z
I_F



ICOPS, Las Vegas, Nevada, June 17-22, 2001

§ 4. Conclusions

N_Z
Z_F

Effects of electron density, temperature, and electron beam fractions on synthetic spectra have been isolated. Good diagnostic techniques for each of those plasma parameters have been developed and used to determine the properties of a number of Ti and Mo x-pinch plasmas. X-ray spectropolarimetry can be a valuable diagnostic tool, complementing kinetic modeling which includes hot electron effects. In the near future, polarization-sensitive Mo x-pinch experiments will be performed

REPORT DOCUMENTATION PAGE

Form Approved
OMB No. 0704-0188

Public reporting burden for this collection of information is estimated to average 1 hour per response, including the time for reviewing instructions, searching data sources, gathering and maintaining the data needed, and completing and reviewing the collection of information. Send comments regarding this burden estimate or any other aspect of this collection of information, including suggestions for reducing this burden to Washington Headquarters Service, Directorate for Information Operations and Reports, 1215 Jefferson Davis Highway, Suite 1204, Arlington, VA 22202-4302, and to the Office of Management and Budget, Paperwork Reduction Project (0704-0188) Washington, DC 20503.

PLEASE DO NOT RETURN YOUR FORM TO THE ABOVE ADDRESS.

1. REPORT DATE (DD-MM-YYYY) 14/02/2002			2. REPORT TYPE FINAL		3. DATES COVERED (From - To) 1 Sept 1998-31 Dec 2002	
4. TITLE AND SUBTITLE Stabilization and Confinement of Hot, Dense, High-Beta Plasma				5a. CONTRACT NUMBER		
				5b. GRANT NUMBER N00014-98-1-0857		
				5c. PROGRAM ELEMENT NUMBER 98PR07448-00		
				5d. PROJECT NUMBER		
6. AUTHOR(S) Bauer, Bruno S. Shlyaptseva, Alla S. Kantsyrev, Victor L. Sotnikov, Vladimir I. Le Galloudec, Nathalie Makhin, Volodymyr Mancini, Roberto C. Sarkisov, Gennady S.				5e. TASK NUMBER		
				5f. WORK UNIT NUMBER		
7. PERFORMING ORGANIZATION NAME(S) AND ADDRESS(ES) University of Nevada, Reno Reno, NV 89557				8. PERFORMING ORGANIZATION REPORT NUMBER		
9. SPONSORING/MONITORING AGENCY NAME(S) AND ADDRESS(ES) Charles W. Roberson - Program Officer ONR 331, Office of Naval Research Ballston Centre Tower One - 800 North Quincy Street Arlington, VA 22217-5660				10. SPONSOR/MONITOR'S ACRONYM(S)		
				11. SPONSORING/MONITORING AGENCY REPORT NUMBER		
12. DISTRIBUTION AVAILABILITY STATEMENT APPROVED FOR PUBLIC RELEASE						
13. SUPPLEMENTARY NOTES						
14. ABSTRACT A calibrated, high-repetition rate 2-terawatt z-pinch (Zebra) was developed, and new z-pinch physics was investigated. Investigation of axial-shear-flow z-pinch stabilization was initiated, with experiments, computer modeling, and theory. An experiment on single wires driven by current prepulses similar to, and faster than, those at Z (SNL) found that faster rising pulses are much more effective at exploding single tungsten wires than Z-like pulses. Experiments on x-pinch driven at 900 kA characterized x-pinch in an almost unexplored regime.						
15. SUBJECT TERMS Plasma physics, z-pinch, instability, experiment, computer simulation, linear theory, diagnostics.						
16. SECURITY CLASSIFICATION OF:			17. LIMITATION OF ABSTRACT	18. NUMBER OF PAGES	19a. NAME OF RESPONSIBLE PERSON	
a. REPORT	b. ABSTRACT	c. THIS PAGE			Bruno Bauer	
UU	UU	UU	UU	432	19b. TELEPHONE NUMBER (Include area code) 775-784-1363	

INSTRUCTIONS FOR COMPLETING SF 298

1. REPORT DATE. Full publication date, including day, month, if available. Must cite at least the year and be Year 2000 compliant, e.g., 30-06-1998; xx-08-1998; xx-xx-1998.

2. REPORT TYPE. State the type of report, such as final, technical, interim, memorandum, master's thesis, progress, quarterly, research, special, group study, etc.

3. DATES COVERED. Indicate the time during which the work was performed and the report was written, e.g., Jun 1997 - Jun 1998; 1-10 Jun 1996; May - Nov 1998; Nov 1998.

4. TITLE. Enter title and subtitle with volume number and part number, if applicable. On classified documents, enter the title classification in parentheses.

5a. CONTRACT NUMBER. Enter all contract numbers as they appear in the report, e.g. F33615-86-C-5169.

5b. GRANT NUMBER. Enter all grant numbers as they appear in the report, e.g. 1F665702D1257.

5c. PROGRAM ELEMENT NUMBER. Enter all program element numbers as they appear in the report, e.g. AFOSR-82-1234.

5d. PROJECT NUMBER. Enter all project numbers as they appear in the report, e.g. 1F665702D1257; ILIR.

5e. TASK NUMBER. Enter all task numbers as they appear in the report, e.g. 05; RF0330201; T4112.

5f. WORK UNIT NUMBER. Enter all work unit numbers as they appear in the report, e.g. 001; AFAPL30480105.

6. AUTHOR(S). Enter name(s) of person(s) responsible for writing the report, performing the research, or credited with the content of the report. The form of entry is the last name, first name, middle initial, and additional qualifiers separated by commas, e.g. Smith, Richard, Jr.

7. PERFORMING ORGANIZATION NAME(S) AND ADDRESS(ES). Self-explanatory.

8. PERFORMING ORGANIZATION REPORT NUMBER. Enter all unique alphanumeric report numbers assigned by the performing organization, e.g. BRL-1234; AFWL-TR-85-4017-Vol-21-PT-2.

9. SPONSORING/MONITORS AGENCY NAME(S) AND ADDRESS(ES). Enter the name and address of the organization(s) financially responsible for and monitoring the work.

10. SPONSOR/MONITOR'S ACRONYM(S). Enter, if available, e.g. BRL, ARDEC, NADC.

11. SPONSOR/MONITOR'S REPORT NUMBER(S). Enter report number as assigned by the sponsoring/monitoring agency, if available, e.g. BRL-TR-829; -215.

12. DISTRIBUTION/AVAILABILITY STATEMENT. Use agency-mandated availability statements to indicate the public availability or distribution limitations of the report. If additional limitations/restrictions or special markings are indicated, follow agency authorization procedures, e.g. RD/FRD, PROPIN, ITAR, etc. Include copyright information.

13. SUPPLEMENTARY NOTES. Enter information not included elsewhere such as: prepared in cooperation with; translation of; report supersedes; old edition number, etc.

14. ABSTRACT. A brief (approximately 200 words) factual summary of the most significant information.

15. SUBJECT TERMS. Key words or phrases identifying major concepts in the report.

16. SECURITY CLASSIFICATION. Enter security classification in accordance with security classification regulations, e.g. U, C, S, etc. If this form contains classified information, stamp classification level on the top and bottom of this page.

17. LIMITATION OF ABSTRACT. This block must be completed to assign a distribution limitation to the abstract. Enter UU (Unclassified Unlimited) or SAR (Same as Report). An entry in this block is necessary if the abstract is to be limited.